

Identification of apoptosis-inducing natural products and derivatives for the elimination of tumor cells

Inaugural-Dissertation

zur Erlangung des Doktorgrades
der Mathematisch-Naturwissenschaftlichen Fakultät
der Heinrich-Heine-Universität Düsseldorf

vorgelegt von

Fabian Stuhldreier

aus Dortmund

Düsseldorf, Juni 2021

aus dem Institut für Molekulare Medizin I
der Heinrich-Heine-Universität Düsseldorf

Gedruckt mit der Genehmigung der
Mathematisch-Naturwissenschaftlichen Fakultät der
Heinrich-Heine-Universität Düsseldorf

Berichterstatter:

1. Prof. Dr. Sebastian Wesselborg
2. Prof. Dr. Peter Proksch

Tag der mündlichen Prüfung: 01.09.2021

Acknowledgement

Auch wenn das Titelblatt lediglich meinen Namen trägt, waren doch eine Vielzahl an Personen an der Entstehung dieser Dissertation beteiligt, denen ich an dieser Stelle danken möchte. Mein besonderer Dank gilt meinem Doktorvater Prof. Dr. Sebastian Wesselborg für seine vertrauensvolle Betreuung, sein stets offenes Ohr und seine umfassende Unterstützung meiner fachlichen Weiterbildung.

Gleichermaßen möchte ich Prof. Dr. Peter Proksch für seine Betreuung dieser Arbeit als Zweitgutachter danken und für seine ansteckende Begeisterungsfähigkeit für die Naturstoffforschung.

Auch bei Prof. Dr. Björn Stork möchte ich mich für die herzliche Aufnahme in seine Arbeitsgruppe und seine vielfältige Unterstützung bedanken.

Bei Paul Jäger, Stefanie Geyh und Thomas Lenz bedanke ich mich für ihre Hilfsbereitschaft, mit der sie mir ihre wissenschaftliche Methodik zeigten und für ihre Beiträge zu gemeinsamen Experimenten und Projekten.

Mein Dank gilt auch der Düsseldorf School of Oncology sowie dem Graduiertenkolleg GRK2158 für ihre finanzielle Unterstützung, die Ausrichtung von vielen bereichernden Veranstaltungen und die Bereitschaft meine fachliche Weiterbildung zu fördern. Bedanken möchte ich mich insbesondere bei den Koordinatorinnen Cornelia Höner und Martina Holz.

Besonderer Dank gilt auch allen Mitgliedern des Instituts für Molekulare Medizin I und des Instituts für Molekulare Radioonkologie für ihren Beitrag zu der warmherzigen Arbeitsatmosphäre, die einen auch nach misslungenen Experimenten nie die Freude an der Forschung verlieren ließ und wesentlich zum Gelingen dieser Arbeit beitrug. Ich werde auch in Zukunft oft an die gemeinsame Zeit zurückdenken und bin sehr froh über die persönlichen Freundschaften, die sich entwickeln konnten.

Sonja Miletzki danke ich für das kritische Korrekturlesen der Dissertation und ihren konstruktiven Anregungen.

Bei meiner Familie, insbesondere meinen Eltern, die mir stets ein Rückhalt waren, möchte ich mich besonders herzlich bedanken für ihre uneingeschränkte und vielseitige Unterstützung sowie ihre Geduld. Auch Martin, auf den ich mich immer verlassen kann, gilt mein Dank.

Zu guter Letzt möchte ich Steffi danken für ihr geduldiges Zuhören, ihre Rücksichtnahme und ihre Aufmunterungen gerade in stressigen Arbeitsphasen.

Abbreviations

2-ME	2-methoxyoestradiol	HDAC	histone deacetylase
ACINUS	apoptotic chromatin condensation inducer in the nucleus	HSPC	hematopoietic stem and progenitor cell
ADP	adenosine diphosphate	IAP	inhibitor of apoptosis
AIF	apoptosis-inducing factor	ICAM1	intercellular adhesion molecule 1
ANT	adenine nucleotide translocator	IL	interleukin
APAF1	apoptotic protease-activating factor 1	IMM	inner mitochondrial membrane
ARF	ADP ribosylation factor	INDF	internucleosomal DNA fragmentation
ASC	apoptosis-associated speck-like protein containing a CARD	IRF3	interferon regulatory factor 3
ATG	autophagy-related	JAK	Janus kinase
ATP	adenosine triphosphate	JNK	Jun N-terminal kinase
AVD	apoptotic volume decrease	logP	octanol-water partition coefficient
BAD	BCL2-associated agonist of cell death	MFN	mitofusin
BAK	BCL2 antagonist/killer	miR-21	microRNA 21
BAX	BCL2-associated X protein	MLC	myosin light chain
BCL2	B-cell lymphoma 2	MLKL	mixed lineage kinase domain-like protein
BCL-xL	B-cell lymphoma-extra large	MOMP	mitochondrial outer membrane permeabilization
BH	BCL2 homology	mTOR	mammalian target of rapamycin
BID	BH3-interacting domain death agonist	mPTP	mitochondrial permeability transition pore
BIM	BCL2-interacting mediator of cell death	NF- κ B	Nuclear factor NF-kappa-B p105 subunit
BIR	baculovirus IAP repeat	OMM	outer mitochondrial membrane
BIRC	BIR-containing protein	OPA1	optic atrophy protein 1 / dynamin-like 120 kDa protein, mitochondrial
BMF	Bcl-2-modifying factor	MAPK	mitogen-activated protein kinase
CAD	caspase-activated DNase	PARP1	Poly [ADP-ribose] polymerase 1
cAMP	cyclic adenosine monophosphate	PBMC	peripheral blood mononuclear cell
CARD	caspase activation and recruitment domain	PEITC	phenethyl isothiocyanate
CASP	caspase	PIDD	p53-induced death domain-containing protein
CD	cluster of differentiation	PS	phosphatidylserine
ced-3	cell death protein 3	PUMA	p53 upregulated modulator of apoptosis
CFLAR	CASP8 and FADD-like apoptosis regulator	PXA	phomoxanthone A
CHOP	C/EBP-homologous protein	RB1	retinoblastoma-associated protein
CML	chronic myelogenous leukemia	(rh)TRAIL	(recombinant human) TNF-related apoptosis-inducing ligand
CRADD	caspase and RIP adapter with death domain	RING	really interesting new protein
CUL9	cullin-9	RIPK1	receptor-interacting serine/threonine-protein kinase 1
CYCS	cytochrome c	ROCK1	Rho-associated protein kinase 1
DD	death domain	ROS	reactive oxygen species
DDX3	DEAD box protein 3, X-chromosomal	S1P	sphingosine 1-phosphate
DED	death effector domain	SMAC	second mitochondria-derived activator of caspase
DFF	DNA fragmentation factor	STAT	signal transducer and activator of transcription
DISC	death-inducing signaling complex	TBDP	4,5,6-tribromo-2-(2',4'-dibromophenoxy)phenol
DNA-PK	DNA-dependent protein kinase	TNFR1	tumor necrosis factor receptor 1
DR	death receptor	TRA	TRAIL receptor agonist
DRP1	dynamin-1-like protein	TRADD	tumor necrosis factor receptor type 1-associated DEATH domain protein
ER	endoplasmic reticulum	UPR	unfolded protein response
ETC	electron transport chain	VDAC	voltage-dependent anion channel
FADD	FAS-associated death domain protein	VDT	viriditoxin
FASL	FAS ligand	XIAP	X-linked inhibitor of apoptosis protein
GRASP65	golgi reassembly-stacking protein of 65 kDa	$\Delta\Psi_m$	mitochondrial inner membrane potential
GSH	glutathione		

Summary

Tight regulation of the total cell count is essential for the viability of multicellular organisms. The instrument through which this control is exerted is a form of programmed cell death termed apoptosis, which allows the organism to selectively eliminate cells that are damaged, degenerated or no longer needed. Deregulation of apoptosis is usually associated with serious disorders such as autoimmune diseases or cancer. Malignant cells undergo evolutionary processes in which they frequently acquire a severely reduced sensitivity to proapoptotic signals, which favors their unhindered proliferation and thereby provides them with a survival advantage.

Despite therapeutic advancements over the last decades, malignant tumors still represent the second leading cause of mortality worldwide. In fact, a major drawback of conventional and novel targeted therapies is the development of treatment resistance. Accordingly, it is urgently required to establish strategies to effectively induce apoptosis in cancer cells, including those carrying mutations in canonical apoptosis signaling pathways. The focus thereby must be on identifying cellular structures or molecules that are of central importance for cancer cells, whose addressing by suitable bioactive substances can therefore force them to undergo apoptosis without being accompanied by undesired toxicity to healthy neighboring cells.

By testing more than 150 natural compounds, most of them derived from the natural product library of Prof. Proksch (Institute for Pharmaceutical Biology and Biotechnology, HHU Düsseldorf) for proapoptotic efficacy in a multi-step procedure, we were able to identify and characterize several potent inducers of apoptotic cell death: We demonstrated that the mycotoxin phomoxanthone A depolarizes mitochondria, reduces the activity of the electron transport chain, inhibits cellular respiration and can cause fragmentation of the inner mitochondrial membrane within seconds, resulting in the release of proapoptotic factors. Likewise, we characterized viriditoxin as a potent mitochondrial toxin that depolarizes mitochondria and inhibits oxidative phosphorylation, presumably by inhibiting complex I of the respiratory chain. In addition, we were able to show that viriditoxin and 4,5,6-tribromo-2-(2',4'-dibromophenoxy)phenol, which is also presumed to inhibit the electron transport chain, have a selective effect on cancer cells with significantly reduced toxicity in healthy cells. Furthermore, we demonstrated that arzanol can sensitize cancer cells to cisplatin, which can at least partly be attributed to mitochondrial effects such as the inhibition of complex I and II of the respiratory chain.

Following a review of the publications resulting from the research projects of this thesis, the activities of the tested substances are discussed comparatively, mitochondria are evaluated as a possible target of antineoplastic effects and prospects for a possible future therapeutic use of these findings in cancer therapy are given.

Zusammenfassung

Für die Lebensfähigkeit multizellulärer Organismen ist die strikte Kontrolle der Gesamtzahl ihrer Zellen von essenzieller Bedeutung. Das Werkzeug, mit dem diese Kontrolle ausgeübt wird, ist eine Form des programmierten Zelltods, die man Apoptose nennt und mithilfe derer der Organismus sich geschädigter, entarteter oder nicht länger benötigter Zellen entledigt. Eine Deregulation dieses Prozesses ist in der Regel mit schwerwiegenden Krankheiten wie Autoimmunerkrankungen oder Krebs assoziiert. Trotz der therapeutischen Fortschritte der letzten Jahrzehnte stellen maligne Tumore weiterhin weltweit die zweithäufigste Todesursache dar, was primär in der Entstehung von Therapieresistenz begründet liegt. Entsprechend ist es dringend geboten, Wege zu finden, auch in Krebszellen effektiv Apoptose herbeizuführen, selbst wenn diese Mutationen in kanonischen Apoptosesignalwegen tragen. Der Fokus muss dabei darauf liegen, zelluläre Strukturen oder Moleküle mit gesteigerter Bedeutung für Krebszellen zu identifizieren, deren Adressierung durch geeignete bioaktive Substanzen daher gezielt in diesen Zellen Apoptose induzieren kann, ohne dabei von unerwünschter Toxizität auf gesunde Nachbarzellen begleitet zu sein.

Indem wir über 150 Naturstoffe, von denen die meisten aus der Naturstoffbibliothek von Prof. Proksch (Institut für Pharmazeutische Biologie und Biotechnologie, HHU Düsseldorf) stammten, in einem mehrstufigen Vorgehen auf proapoptotische Wirksamkeit untersuchten, konnten wir mehrere potente Auslöser von apoptotischem Zelltod identifizieren und charakterisieren: Wir zeigten, dass das Mykotoxin Phomoxanthon A Mitochondrien depolarisiert, die Aktivität der Elektronentransportkette herabsetzt sowie die zelluläre Atmung inhibiert und innerhalb von Sekunden eine Fragmentierung der inneren Mitochondrienmembran bewirken kann, wodurch es zur Freisetzung von proapoptotischen Faktoren kommt. Auch Viriditoxin charakterisierten wir als potentes Mitochondriengift, das Mitochondrien depolarisiert und die oxidative Phosphorylierung hemmt, mutmaßlich durch Inhibierung von Komplex I der Atmungskette. Darüber hinaus konnten wir für Viriditoxin und 4,5,6-tribromo-2-(2',4'-dibromophenoxy)phenol, für das ebenfalls eine Inhibierung der Elektronentransportkette vermutet wird, eine selektive Wirkung auf Krebszellen mit vergleichsweise deutlich herabgesetzter Toxizität in gesunden Zellen nachweisen. Ergänzend konnten wir demonstrieren, dass Arzanol Krebszellen gegenüber Cisplatin sensitivieren kann, was unter anderem auf mitochondriale Effekte wie die Inhibierung von Komplex I und II der Atmungskette zurückzuführen ist.

Im Anschluss an die Betrachtung der aus den Forschungsprojekten dieser Arbeit hervorgegangenen Publikationen werden die Aktivitäten der untersuchten Substanzen vergleichend diskutiert, Mitochondrien als mögliches Ziel antineoplastischer Effekte betrachtet und Ausblicke auf eine mögliche zukünftige therapeutische Nutzung dieser Erkenntnisse im Rahmen der Krebstherapie gegeben.

Acknowledgement	I
Abbreviations	II
Summary	III
Zusammenfassung	IV
1 Introduction	1
1.1 A brief overview of apoptosis and the history of its exploration	1
1.2 Morphological and biochemical hallmarks of apoptotic cells	3
1.2.1 Cytoplasmic shrinkage and plasma membrane blebbing.....	3
1.2.2 Chromatin condensation	3
1.2.3 DNA fragmentation	4
1.2.4 Organelle fragmentation.....	4
1.2.5 Release of find-me and eat-me signals.....	5
1.2.6 Distinction from necrotic cell death	6
1.3 The caspase protein family as the “swiss army knife” of apoptosis	8
1.4 Extrinsic apoptosis pathway	10
1.5 Intrinsic apoptosis pathway	11
1.5.1 Induction of intrinsic apoptosis.....	11
1.5.2 Regulation of intrinsic apoptosis by BCL2 family members and IAPs.....	13
1.5.3 Stress stimuli initiating intrinsic apoptosis	14
1.5.4 The role of mitochondria in intrinsic apoptosis	17
1.6 Apoptosis, cancer and therapeutic implications	18
1.7 Natural products in drug discovery	21
1.8 Natural products as inducers of apoptosis	22
1.8.1 Inducers of extrinsic apoptosis	22
1.8.2 Inducers of intrinsic apoptosis.....	23
1.9 Aims	25
2 Manuscripts	26
2.1 Publications within the scope of this dissertation	26
2.1.1 Pleiotropic effects of spongean alkaloids on mechanisms of cell death, cell cycle progression and DNA damage response (DDR) of acute myeloid leukemia (AML) cells	26
2.1.2 Cyclic Cystine-Bridged Peptides from the Marine Sponge <i>Clathria basilana</i> Induce Apoptosis in Tumor Cells and Depolarize the Bacterial Cytoplasmic Membrane.....	26
2.1.3 Daldinone derivatives from the mangrove-derived endophytic fungus <i>Annulohyphoxylon</i> sp.	26

Table of contents

2.1.4	The mycotoxin phomoxanthone A disturbs the form and function of the inner mitochondrial membrane	27
2.1.5	Dithiodiketopiperazine derivatives from endophytic fungi <i>Trichoderma harzianum</i> and <i>Epicoecum nigrum</i>	27
2.1.6	First Results from a Screening of 300 Naturally Occurring Compounds: 4,6-dibromo-2-(2',4'-dibromophenoxy)phenol, 4,5,6-tribromo-2-(2',4'-dibromophenoxy)phenol, and 5-epi-nakijinone Q as Substances with the Potential for Anticancer Therapy	27
2.1.7	Novel meriolin derivatives as rapid apoptosis inducers	27
2.1.8	Azaphilone pigments and macrodiolides from the coprophilous fungus <i>Coniella fragariae</i>	28
2.1.9	Sesterterpenes and macrolide derivatives from the endophytic fungus <i>Aplosporella javeedii</i>	28
2.1.10	Didymellanosine, a new decahydrofluorene analogue, and ascolactone C from <i>Didymella</i> sp. IEA-3B.1, an endophyte of <i>Terminalia catappa</i>	28
2.1.11	Induction of New Lactam Derivatives From the Endophytic Fungus <i>Aplosporella javeedii</i> Through an OSMAC Approach	28
2.1.12	High-throughput screening for natural compound-based autophagy modulators reveals novel chemotherapeutic mode of action for arzanol	28
2.1.13	Cancer-specific pro-apoptotic effects of the mycotoxin viriditoxin	29
2.2	Publications beyond the scope of this dissertation	29
2.2.1	Deubiquitinase inhibition by WP1130 leads to ULK1 aggregation and blockade of autophagy.....	29
2.2.2	Expression of a ULK1/2 binding-deficient ATG13 variant can partially restore autophagic activity in ATG13-deficient cells	29
2.2.3	Systematic analysis of ATG13 domain requirements for autophagy induction.....	30
2.2.4	Targeting urothelial carcinoma cells by combining cisplatin with a specific inhibitor of the autophagy-inducing class III PtdIns3K complex	30
2.2.5	Multiple DNA damage-dependent and DNA damage-independent stress responses define the outcome of ATR/Chk1 targeting in medulloblastoma cells....	30
2.2.6	The Autophagy-Initiating Kinase ULK1 Controls RIPK1-Mediated Cell Death	30
2.2.7	Natural Products Impacting DNA Methyltransferases and Histone Deacetylases	30
2.2.8	TNF-induced necroptosis initiates early autophagy events via RIPK3-dependent AMPK activation, but inhibits late autophagy	31
2.2.9	FIP200 controls TBK1 activation threshold at SQSTM1/p62-positive condensates.....	31
3	Discussion.....	32
4	References.....	38
5	Licensing & Copyright.....	65

1 Introduction

1.1 A brief overview of apoptosis and the history of its exploration

The biology of multicellular organisms knows many states of equilibrium, which are maintained by continuous fine corrections and whose imbalance almost always leads to pathological conditions. Some obvious examples for such states of equilibrium are transcriptional regulation, proteostasis or arterial blood pressure and body temperature of mammals. The total number of cells in an organism is also subject to homeostatic processes. Since the body of an adult human being is supplied with billions of new cells every day through the process of mitosis, it is obvious that there has to be an opposing process in order to keep the total cell number constant.¹ This process of programmed cell death is known as apoptosis. Apoptotic processes ensure the degradation and disposal of cells no longer useful for the organism and potentially harmful cells such as damaged or transformed cells or cells infected by pathogens. Consequently, in addition to controlling cellular turnover, apoptosis is of central importance for a number of further biological processes, such as embryonic development or immune defense.² In order to prevent the release of inflammatory factors, the apoptotically dying cell maintains the integrity of its plasma membrane throughout the entire time lapse of apoptosis. The process of apoptosis ends with the dying cell collapsing into individual membrane-enveloped vesicles, termed apoptotic bodies, which are finally engulfed by neighboring cells or specialized phagocytes.² Since even small alterations in the equilibrium between mitosis and apoptosis are associated with severe consequences such as the occurrence of autoimmune disorders or neoplasia, the initiation and execution of apoptosis is, like mitosis, subject to a complex control machinery.³ The center of this control apparatus comprises the caspase protease family, whose activity orchestrates most cellular subprocesses of apoptotic cell death.⁴ Before the regulation of apoptosis is illuminated in detail in the following chapters, it is worth taking a look at the history of the discovery of what we now refer to as apoptosis.

The Greek term “apoptosis” originally denotes the programmed shedding of leaves in autumn. Hippocrates of Cos already used the term in ancient times in medical context when he described gangrenes.⁵ Interestingly, the term was thus assigned to a cell death process long before any understanding of the cellular order of life existed. The cell theory of life was postulated by Schleiden and Schwann in 1839 and, remarkably, only three years later Carl Vogt extended it by the concept of natural cell death after studies on toads, making the idea of physiologically occurring cell death to one of the oldest in cell biology.^{6,7} By the end of the 19th century at the latest, when the processes of cell division became the subject of extensive investigations and Walter Flemming had established the term mitosis in 1882, it became evident that there must be a physiological counterpart.⁸ Flemming also described in 1885 for the first time important morphological hallmarks of apoptosis, including nuclear

fragmentation, cell shrinkage and the formation of apoptotic bodies.⁷ Surprisingly, his observations did not receive much attention at first, nor did those of Glucksman, who more than 60 years later described a form of cell death characterized by chromatin condensation and whose corresponding publication has only been highly cited in recent years.⁹

In the end, the ultimate starting point of intensive apoptosis research is closely tied to the name Kerr. In 1965, Kerr recorded in a short section of his publication on ischemic injury in rat liver the secondary observation that in ischemically damaged liver tissue cells died whose morphology differed significantly from that of necrotic areas, showing characteristics like chromatin condensation and cell shrinkage.¹⁰ He thereby independently repeated the observations of Flemming and Glucksman and named this specific type of cell death “shrinkage necrosis”. When Kerr came across Glucksman's paper, he recognized the omnipresent nature of apoptosis. Together with his colleagues Wyllie and Currie, Kerr thereafter laid the foundations for the understanding of apoptosis in the following years. After Lockshin proposed the term “programmed cell death” in 1965, Kerr introduced the term “apoptosis” into the scientific literature in 1972.^{11,12} Two landmark publications from 1980 then fueled the emergence of broad academic research on apoptosis. Wyllie described in a Nature publication that DNA fragmentation as a hallmark of apoptotic cells can be visualized by means of gel electrophoretic separation of genomic DNA and subsequent staining, resulting in a characteristic DNA ladder pattern.¹³ This provided for the first time a simple biochemical detection method of apoptotic processes. In a second publication Wyllie highlighted together with Kerr and Currie the biological importance of apoptosis in a review that gained a large amount of attention.¹⁴

Whereas apoptosis had previously been described mainly based on morphological observations, the next 20 years up to the year 2000 saw the discovery and description of central proteins of apoptosis signaling. In 1988 *B-cell lymphoma 2* (BCL2) was discovered as the first member of the BCL2 protein family, in 1995 *cluster of differentiation 95* (CD95) was cloned and sequenced, in 1993 *BCL2-associated X protein* (BAX) was identified, in 1995 *BCL2 antagonist/killer* (BAK) and in 2000 *second mitochondria-derived activator of caspase* (SMAC/DIABLO).¹⁵⁻²¹ The numerous discoveries in the field of apoptosis signaling finally culminated in the Nobel Prize for Howard Robert Horvitz in 2002. He had previously used the nematode *c. elegans* as a model organism to show central aspects of apoptosis and discovered the first cell death gene (*ced-3*, human orthologue is CASP9).^{5,22} Based on the observation that during the development of the nematode always the same number of cells die in a controlled manner, he was able to prove that apoptosis is a programmed process.²

1.2 Morphological and biochemical hallmarks of apoptotic cells

1.2.1 Cytoplasmic shrinkage and plasma membrane blebbing

Apoptotic cells are characterized by a multitude of morphological alterations that can help to distinguish them from other forms of cell death, like necrosis as an accidental and proinflammatory type of cell death resulting from acute cell damage. The most obvious changes of apoptotic cells are cell shrinkage and membrane blebbing, which affect the external appearance of the cell itself and have therefore already been described as hallmarks in Kerr's first definition of apoptosis.¹² Cellular shrinkage is also referred to in the literature as cellular condensation or apoptotic volume decrease (AVD) in order to distinguish it from physiological cellular volume loss, for example in response to increased osmotic pressure.²³ The mechanisms that control AVD have not been fully understood in detail so far, but a central role of ion efflux through K⁺ and Cl⁻ channels is suspected.²⁴ Severe cellular volume loss in the absence of other apoptotic stimuli is by itself sufficient to induce apoptotic cell death.²³ Furthermore, activation of cysteine proteases of the caspase-family may depend on prior apoptotic volume decrease, although there are contradictory reports on this issue.²³⁻²⁵

The appearance of balloon-like protuberances of the plasma membrane, termed blebs, is one of the first apoptotic events, whose exact temporal onset depends on the cell type and sometimes even occurs before caspase activation.²⁶⁻³⁰ It is driven by the contractile cortex, a submembranous cytoskeleton with a high actomyosin content, whose structure and motility is regulated by Rho GTPases.^{26,31} The central effector for apoptosis-related membrane blebbing is the kinase *Rho-associated protein kinase 1* (ROCK1), which undergoes activating cleavage by caspases during apoptosis and consequently phosphorylates *myosin light chain* (MLC) filaments of the cortex. This results in an actomyosin-dependent increase in cell contractility, leading to a delamination of the plasma membrane from the contractile cortex.³² Without the shape-retaining role of the cytoskeleton, membrane blebbing occurs due to the increased hydrostatic pressure caused by cellular condensation in apoptotic cells.³³ Membrane blebbing is a reversible event and can also occur in non-apoptotic cells, for example in the context of cell migration.³⁴ Thus, like cellular shrinkage, it is in itself not a sufficient criterion for identifying apoptotic cells.

1.2.2 Chromatin condensation

Another well-known characteristic of apoptotic cells is a distinct condensation of nuclear DNA.² Even though chromatin condensation also occurs during mitosis, DNA only reaches its maximum condensation status during apoptosis. The process of condensation can be divided into three phases. In the first phase, a homogeneous ring of condensed chromatin forms at the interior surface of the nuclear envelope. In the second phase, the ring loses its homogeneous shape and takes on a form that Toné *et al.* compare to a necklace. At the same time the whole nucleus begins to shrink. The third phase is

characterized by progressive chromatin condensation and nucleus shrinkage, finally causing the nucleus to break up into individual fragments.³⁵ The control of these processes is not yet fully understood, although several factors involved have been identified. Two of these effectors, *apoptosis inducing factor* (AIF) and *caspase-activated DNase* (CAD) are released by the mitochondria during apoptosis and then translocate into the nucleus where they cause chromatin condensation and DNA fragmentation.^{2,36-38} An involvement of the caspase substrate *apoptotic chromatin condensation inducer in the nucleus* (ACINUS) in this process is also discussed.³⁹ Since separate inhibition of AIF, CAD or ACINUS cannot prevent chromatin condensation, it is apparently a result of the combined action of these proteins.⁴⁰⁻⁴²

1.2.3 DNA fragmentation

While non-apoptotic cells may also show signs such as cell shrinkage, plasma membrane blebbing and chromatin condensation, internucleosomal DNA fragmentation (INDF) is a distinctive indicator of apoptotic cell death.⁴³ Although its effectors are partly the same as those involved in chromatin condensation, INDF occurs much later in the course of apoptosis than the hallmarks mentioned above.⁴⁴ INDF refers to the cleavage of genomic DNA at internucleosomal linker regions, resulting in DNA fragments with a length of around 180 base pairs or multiples thereof. The first broadly applied apoptosis assay is based on the detection of these characteristic fragments, giving a typical ladder pattern after gel electrophoretic separation.¹³ INDF is mainly caused by *DNA fragmentation factor* (DFF), a heterodimeric protein build up of two subunits DFFA and DFFB, also known as *caspase-activated DNase* (CAD) and *inhibitor of caspase-activated DNase* (ICAD), respectively. CAD carries the catalytic DNase activity, that takes effect as soon as ICAD is cleaved by activated caspases.^{45,46} In the last years, a large number of further endonucleases have been described that are associated with fragmentation of DNA in apoptotic cells, some but not all of which are caspase-dependent.^{43,47-49}

1.2.4 Organelle fragmentation

Apoptotic cell death is accompanied by a restructuring of the entire vacuolar system, including endoplasmic reticulum, Golgi apparatus, lysosomes and mitochondria. The endoplasmic reticulum (ER) is an interconnected system of membrane-enclosed cavities which represents the primary site of chaperone-mediated protein folding.⁵⁰ Although the ER possesses important functions in apoptotic signaling and can even serve as an apoptotic source in case of malfunction due to pathological accumulation of unfolded proteins, the morphological changes it experiences during apoptosis are not fully understood.^{50,51} However, it has been described that the ER of apoptotic cells undergoes severe swelling, loses its homogeneous distribution in the cytoplasm and finally ruptures.^{52,53} Subsequently, it is transported into membrane blebs in an active process that depends on both actin cytoskeleton and microtubules and is regulated via caspase-6 (CASP6).⁵⁴ The Golgi apparatus is a system of disc-shaped,

membrane-enclosed cisterns arranged in stacks, whose primary functions are the uptake and redistribution of cargo as well as synthesis of membranes and processing of proteins.⁵⁵ In apoptotic cells the Golgi apparatus swells, aggregates, loses its typical stacking form and finally fragments.⁵⁶⁻⁵⁸ This drastic change in shape is attributed to a caspase-dependent cleavage of a number of proteins, which are thought to play an important role in maintaining the structure of the Golgi apparatus, namely *golgin subfamily A member 3* (GOLGA3 / Golgin-160), *golgi reassembly-stacking protein of 65 kDa* (GRASP65) and *general vesicular transport factor p115* (USO1).⁵⁸⁻⁶⁰

The lysosomes, membrane-enclosed vesicles that serve the hydrolytic digestion of biomolecules, are also the target of apoptotic effects. However, these effects do not appear to be fundamental components of the apoptotic program, but only appear in certain pathological contexts, such as neurodegenerative processes or ischemia.⁶¹ Described are mainly destabilization of the lysosomes by increased cytosolic Ca²⁺ levels as well as lysosomal permeabilization by insertion of BAX, a proapoptotic protein of the BCL2 family, into the lysosomal membrane.⁶²⁻⁶⁴ Loss of lysosomal membrane integrity results in the release of cathepsins, a group of endoproteases. Although cathepsins cannot directly activate caspases, they are able to cleave other apoptotic effectors such as *BH3-interacting domain death agonist* (BID) and thus contribute to the apoptotic cascade.⁶⁵ The structure of the mitochondrion as the central organelle of apoptotic signal transmission is subject to drastic changes during apoptosis. Since mitochondrial dynamics are of particular importance for the control and execution of apoptosis, the processes involved are discussed in detail in chapter 1.5.4.

1.2.5 Release of find-me and eat-me signals

Apoptotic cells need to be rapidly cleared, as otherwise they enter a state known as secondary necrosis, which is associated with inflammatory reactions due to the uncontrolled release of intracellular components. For this purpose, apoptotic cells secrete soluble find-me signals that attract phagocytes and eat-me signals to be selectively recognizable to them. Find-me signals are a heterogeneous group of different molecules including lysophosphatidylcholine, fractalkine, ATP and sphingosine 1-phosphate (S1P), which are secreted in an active and caspase-dependent manner. The radius of action of the individual find-me signals is limited and it is assumed that the combination of the different signals orchestrates phagocyte attraction.⁶⁶⁻⁶⁸ To ensure that the process of clearance remains immunologically silent, additional anti-inflammatory signals are secreted to prevent recruitment of neutrophils.⁶⁹ In order to be recognized as a target for phagocytic cells, apoptotic cells start to present eat-me signals on their surface as early as 1-2 hours after the onset of the apoptotic cascade. Eat-me signals include the externalization of phosphatidylserine (PS) and calreticulin as well as alteration in glycosylation patterns or *intercellular adhesion molecule 1* (ICAM1) epitopes on the cell surface, of which PS has the most universal function. The significance of PS is also reflected by the presence of a multitude of different

receptors in phagocytes enabling binding to PS, whose concentration on the surface of the plasma membrane increases more than 200-fold during apoptosis.^{66,70} This enrichment is due to the apoptotic control of flippases and scramblases. Flippases translocate PS from the inner to the outer leaflet of the cell membrane, while scramblases can move PS bidirectionally between both sides. In the course of apoptosis, caspases inactivate flippases and activate scramblases.⁷¹ This leads to the described PS accumulation on the outside of the cells, which then serves as a recognition signal for phagocytic cells (macrophages, immature dendritic cells).⁶⁶ Furthermore, apoptotic clearance can also be carried out by neighboring cells (e.g. fibroblasts).⁷²

1.2.6 Distinction from necrotic cell death

Apoptotic cells can be distinguished from necrotic cells based on their biochemical and morphological characteristics. Necrotic cells experience swelling of the cytoplasm, rupture of the plasma membrane and induce local inflammation, whereas apoptotic cells are characterized by shrinkage of the cytoplasm, maintenance of plasma membrane integrity and absence of inflammatory processes. However, apoptotic cells that are not rapidly cleared by phagocytes enter a state of secondary necrosis, which sometimes renders distinction difficult.⁷³ In addition, necrosis can also show features that typically characterize apoptotic cells, such as the externalization of PS as well as plasma membrane alterations.^{74,75} According to Rello *et al.* necrotic cells lose the control over water influx through the plasma membrane, leading to the formation of small membrane bubbles, which ultimately culminate in a single macrobubble, the rupture of which eventually results in loss of membrane integrity.⁷⁵ However, even in the absence of caspase activity, phenotypic signs of intrinsic apoptosis can occur.⁷⁶ Therefore, for the distinction between apoptotic and necrotic cell death, ideally several different endpoints should be examined.

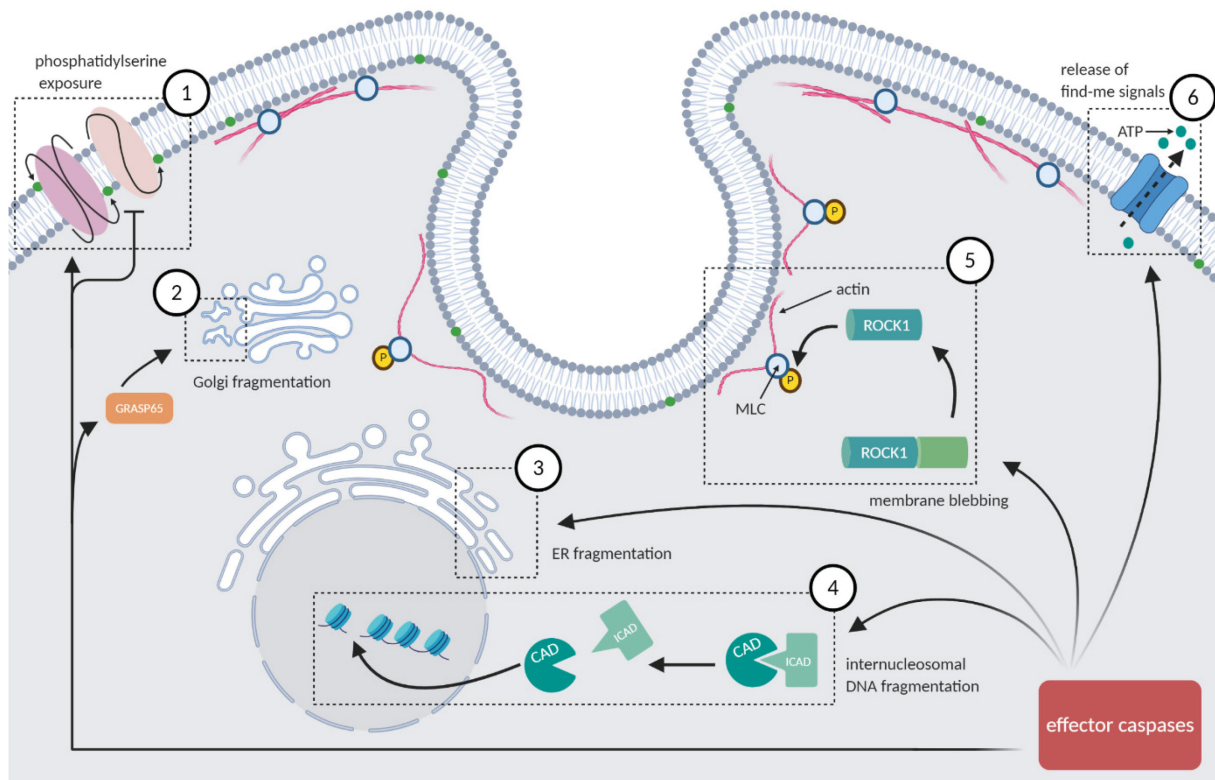


Figure 1: Hallmarks of apoptosis. Apoptotic cells undergo a multitude of functional as well as morphological changes, the majority of which are orchestrated by activated effector caspases. While **fragmentation of the ER (3)** during apoptosis is not yet well understood, **fragmentation of the Golgi apparatus (2)** can be attributed to caspase-dependent cleavage of proteins preserving its structure, such as **GRASP65**. Another hallmark of apoptotic cell death is **internucleosomal DNA fragmentation (4)**, which arises as soon as effector caspases cleave **ICAD**, thereby abrogating its inhibitory effect on the DNase **CAD**. The most prominent alteration of apoptotic cells is the deformation of the plasma membrane and the subsequent formation of **apoptotic blebs (5)**, which can be attributed to an activating cleavage of **ROCK1** by effector caspases. After cleavage, ROCK1 is constitutively activated and causes phosphorylation of **MLC**, which in turn gives rise to an actomyosin-dependent increase in cell contractility and delamination of the plasma membrane from the contractile cortex. Subsequently, the high hydrostatic pressure of the condensed apoptotic cell results in the formation of the characteristic blebs. In order to ensure rapid clearance, apoptotic cells secrete **find-me signals (6)** such as ATP, which attract phagocytes. **Eat-me signals** secreted in parallel (1) allow phagocytes recognition of the apoptotic cells. The most important eat-me signal is **phosphatidylserine (PS)**, whose localization in the plasma membrane is controlled by flippases and scramblases. While flippases translocate PS from the outer to the inner leaflet of the cell membrane, scramblases can move PS bidirectionally between both sides. Effector caspases activate scramblases while inactivating flippases, resulting in a net externalization of PS.

1.3 The caspase protein family as the “swiss army knife” of apoptosis

Caspases are a family of endoproteases that play a central role in the control and regulation of apoptosis. Their name is an acronym of **cysteine-aspartic protease** and derives from the fact that they cleave their substrates only after an aspartic acid residue by hydrolyzing the peptide bond and always carry a cysteine residue in their active center.⁴ Dysregulation of caspase activity can trigger severe diseases such as cancer or inflammatory disorders, therefore the activation of caspases is subject to tight control mechanisms. Caspases are produced as inactive zymogens, also called procaspases, and obtain their catalytic activity after dimerization or cleavage by activated caspases.⁷⁷ Currently, 18 different caspases are known in mammals, whose degree of expression can vary significantly between species.⁷⁸ Some caspases, such as caspase-3 (CASP3), have hundreds of different substrates, which indicates a wide range of functions.⁷⁹ In general, besides their role in the regulation of cell death, caspases are involved in inflammation, proliferation and differentiation.^{77,78}

Out of the 18 known caspases, CASP1, CASP4, CASP5 and CASP12 are associated with inflammatory reactions within the innate immune response in humans.⁷⁷ The activation of CASP1, the central pro-inflammatory caspase, depends on the assembly of multiprotein complexes referred to as *inflammasomes*. Depending on their composition, different inflammasomes can be distinguished, which, however, all share the same tripartite structure. In addition to CASP1, inflammasomes contain a sensor complex and the adapter protein *apoptosis-associated speck-like protein containing a CARD* (ASC), both of which possess a *caspase recruitment domain* (CARD). Bacterial proteins are typical stimuli that are recognized by the sensor complex, resulting in recruitment of CASP1 by ASC and assembly of the inflammasome. In the assembled inflammasome, multiple CASP1 molecules are brought into close proximity, whereupon they are activated by autocatalytic cleavage and subsequently cause the secretion of *interleukin-1 β* (IL1B) and *interleukin-18* (IL18).⁸⁰ CASP12 attenuates inflammatory responses as an inhibitory counterpart of CASP1.⁷⁷ Inhibition of CASP1 can also be caused by CASP8 independently of apoptotic signaling by constitutive activation of *interferon regulatory factor 3* (IRF3).⁸¹

Caspases are also contributing to the regulation of cell fate decisions outside of apoptosis, namely those of autophagy and non-apoptotic cell death forms such as pyroptosis, necroptosis and mitotic catastrophe.⁷⁷ Autophagy is an intracellular degradation system for misfolded or aggregated proteins and damaged organelles and therefore serves as a pro-survival pathway.⁸² Consequently, autophagic processes are inhibited by caspases via cleavage of central proteins of autophagy signaling. It has been described that *Beclin-1* (BECN1) can be cleaved by CASP3 and CASP8, *ubiquitin-binding protein p62* (p62) by CASP6 and CASP8 and *autophagy related 3* (ATG3) by CASP6.⁸³⁻⁸⁶

Pyroptosis is a pro-inflammatory, programmed form of cell death triggered by sustained CASP1 activity in response to infection with cellular pathogens.⁸⁷ In this setting, CASP1 causes pore formation in the plasma membrane, resulting in water influx and subsequent osmotic lysis of the cell.⁸⁸ Necroptosis is the programmed form of cell death that occurs upon inhibition of caspase activity, for example by viral caspase inhibitors. CASP8 acts as a central inhibitor of necroptosis. Without CASP8 activity, *receptor-interacting serine/threonine-protein kinase 1* (RIPK1) and RIPK3 form an activation complex called *necrosome* and thus activate the effector of necroptosis, the pore forming pseudokinase *mixed lineage kinase domain-like protein* (MLKL) via phosphorylation.⁸⁹ Finally, caspases also contribute to the mitotic catastrophe, a mechanism of cell death intended to shut down cells with defective mitosis apparatus, since the main executor here is CASP2.⁹⁰

Basically, apoptotic caspases are divided into two distinct groups, the initiator caspases (CASP2, CASP8, CASP9, CASP10,) and the effector caspases (CASP3, CASP6, CASP7), according to their hierarchical position in the caspase cascade and the resulting function.⁷⁸

The primary purpose of initiator caspases is the activation of effector caspases while effector caspases are responsible for loss-of-function or gain-of-function cleavage of apoptotic substrates, which ultimately leads to apoptotic cell death. Since the activation of the two most prominent initiator caspases CASP8 and CASP9 will be discussed in detail in the following two subchapters and the main substrates of the effector caspases have already been presented in chapter 1.2, a brief view at the remaining apoptotic caspases follows at this point. In contrast to effector caspases, (apoptotic as well as inflammatory) initiator caspases feature specific protein interaction domains (CARD or *death effector domains* [DED]) at their N-terminus. These are necessary for the dimerization of the inactive monomeric procaspases or for recruitment into multi-protein complexes serving for activation (*apoptosome* for CASP9, *inflammasomes* for CASP1).⁷⁸ CASP10 is dispensable for initiating apoptosis and can even inhibit CASP8.^{91,92} CASP2, however, can be activated after a variety of stress signals such as DNA damage, heat shock or accumulation of β -amyloids. Canonically, activation of CASP2 is based on the aggregation of a multiprotein complex called *PIDDosome*, which is composed of several *p53-induced death domain-containing protein 1* (PIDD1) fragments and *caspase and RIP adapter with death domain* (CRADD) molecules. CRADD serves as an adapter molecule that binds with a conserved cytosolic motif termed *death domain* (DD) to the DD of PIDD1 and concurrently recruits the still inactive procaspase-2 with its N-terminal CARD. Two procaspase-2 molecules are brought into close proximity, resulting in dimerization and activation by autocatalytic cleavage.⁹³ The effector caspases, on the contrary, are not activated by dimerization but by activated initiator caspases that cleave them between the small and the large subunit, resulting in a conformational change so that the two active sites experience spatial proximity

and can thereby form an active effector caspase. Likewise, activated effector caspases can in turn activate other effector caspases, thus creating a potent amplification loop.⁷⁷

During the execution phase of apoptosis, caspases cleave a variety of substrates, preferably C-terminal of aspartate and less frequently C-terminal of glutamate or phosphoserine residues. The most prevalent recognition sequence of effector caspases is aspartic acid-glutamic acid-valine-aspartic acid (translated into the single letter amino acid code as DEVD), which is also found in *poly [ADP-ribose] polymerase 1* (PARP1).⁷⁹ To date, more than 1500 caspase substrates have been identified, most of which can be attributed to CASP3.^{4,79} However, the substrate specificities of caspases partly overlap, especially those of CASP3 and CASP7.⁴

The substrates cleaved by effector caspases can be loosely divided into two subgroups. The first group includes proteins that are involved in processes that are either unnecessary or even counterproductive for apoptotic cells, such as pro-survival signaling like autophagy, or in processes with a high ATP demand like DNA damage response. An example of the latter is PARP1, which is a high abundance protein with about 1-2 million copies per cell.⁹⁴ PARP1 is involved in DNA repair and requires large amounts of energy for its ATP-dependent function, therefore hyperactivation of PARP1 leads to an energy crisis and subsequent necrosis.⁹⁵ Under apoptotic DNA degradation due to CAD activation, functional PARP1 would deplete the cellular ATP pool and thus prevent the completion of apoptosis, which is why it is inactivated by caspases. PARP1 is cleaved into an 89 kDa and a 24 kDa fragment, the larger fragment carrying the catalytic activity and the smaller one carrying the DNA binding domain. The separated 24 kDa fragment can additionally inhibit active PARP1, making the inactivation process highly effective.⁹⁶ Similarly, other proteins of the DNA damage response are inactivated, such as *DNA-dependent protein kinase* (DNA-PK), or proteins like *retinoblastoma-associated protein* (RB1), which are involved in proliferation.⁹⁷⁻⁹⁹ The second group of substrates comprises proteins whose cleavage by caspases directly serves the progress of the apoptosis program. Examples include ROCK1 (membrane blebbing), CAD (DNA fragmentation), Golgin-160 (fragmentation of Golgi apparatus), the caspase-dependent secretion of find-me signals, and the caspase-dependent remodeling of the plasma membrane leading to PS externalization.^{32,45,59,66,71}

1.4 Extrinsic apoptosis pathway

The signaling leading to the activation of effector caspases can be divided into two fundamental pathways, the extrinsic or death receptor pathway and the intrinsic or mitochondrial pathway, depending on the origin of the apoptotic triggers. The extrinsic pathway is characterized by transmission of extracellular stress signals into the cytoplasm via transmembrane receptors, resulting in the activation of CASP8 and consequently in the activation of effector caspases.⁷⁶ Extrinsic apoptosis

is triggered by the binding of a proapoptotic ligand termed death ligand, usually secreted by immunocompetent cells such as T cells, macrophages or dendritic cells, to its corresponding receptor of the family of tumor necrosis factor receptors, termed death receptor.^{100,101} Known pairs of death receptors and their death ligands include *Fas ligand* (FASL, CD95L, APO1L), binding to *cluster of differentiation 95* (CD95, also known as FAS or APO1), *tumor necrosis factor* (TNF, formerly called TNF- α) binding to *tumor necrosis factor receptor 1* (TNFR1) and *TNF-related apoptosis-inducing ligand* (TRAIL) binding to death receptor 4 (DR4) or death receptor 5 (DR5).²

The mechanism of death receptor dependent activation of CASP8 is best understood for the Fas pathway. Binding of the Fas ligand causes stabilization of spontaneously forming receptor trimers, leading to a conformational change which exposes their DDs. These DDs now acts as a binding site for the DDs of adapter proteins, whose N-terminal death-effector domain (DED) serves as a platform for the recruitment of procaspase-8, which in turn binds with its DED.⁷⁶ While *FAS-associated death domain protein* (FADD) is the only adapter protein required for the recruitment of procaspase-8 to the Fas receptor, *Tumor necrosis factor receptor type 1-associated DEATH domain protein* (TRADD) is additionally involved in its recruitment to the TNFR1 receptor.² According to the commonly accepted *induced proximity model*, the local enrichment of procaspase-8 in the multiprotein complex formed by death receptor, adapter protein and procaspase-8, which is termed *death-inducing signaling complex* (DISC), leads to autoproteolytic caspase activation.¹⁰⁰ Since inhibitory proteins such as *CASP8 and FADD-like apoptosis regulator* (CFLAR, also known as c-FLIP) and *Baculoviral IAP repeat-containing protein 2* (BIRC2, also known as CIAP1) can also be recruited to the DISC, the DISC acts as an integrative platform that controls the activation of CASP8.⁷⁶ While BIRC2 causes a higher expression of CFLAR, the latter in turn directly inhibits the processing of procaspase-8 at the DISC.^{102,103} As soon as CASP8 is activated, it cleaves the downstream effector caspases, which ultimately leads to apoptotic cell death.¹⁰³ An additional CASP8-substrate is *BH3-interacting domain death agonist* (BID). BID cleaved by CASP8 (truncated BID, t-BID) translocates to the mitochondria, where it causes the release of proapoptotic factors and the cytochrome c (CYCS) dependent activation of procaspase-9 and thus leads to an amplification of the apoptotic signal.^{104,105} However, the extent to which this lateral axis of apoptosis signaling is only supportive or even indispensable for the execution of apoptosis after death ligand binding depends on the cell type.⁷⁶

1.5 Intrinsic apoptosis pathway

1.5.1 Induction of intrinsic apoptosis

In contrast to extrinsic apoptosis, which is triggered by external signals reaching the cell membrane, intrinsic apoptosis is initiated by intracellular stress signals, reaching the outer mitochondrial

membrane (OMM).² Since the release of cytochrome c from the mitochondrial intermembrane space is a crucial step in the initiation of intrinsic apoptosis and furthermore central control circuits of this cell death pathway are located in the mitochondria, intrinsic apoptosis is also referred to as mitochondrial apoptosis. The outer mitochondrial membrane is the site where antiapoptotic and proapoptotic signals get integrated, determining the cell's fate. If proapoptotic signals predominate, mitochondrial outer membrane permeabilization (MOMP) occurs, resulting in release of cytochrome c into the cytosol.

Two different models are discussed as drivers of MOMP. The first model attributes permeabilization to the pore-forming proteins of the BCL2 family (BAK and BAX).⁷⁶ While it is known that BAX is recruited in apoptotic cells from cytosol to mitochondria, where it oligomerizes with BAK and forms pores together with lipids of the OMM, the exact mechanism of this pore formation is still unknown.¹⁰⁶ However, MOMP in BAK/BAX double knockout cells proves the existence of at least one alternative mechanism.¹⁰⁷ Accordingly, the second model indirectly attributes the permeabilization of OMM to the opening of a supramolecular pore called *mitochondrial permeability transition pore* (mPTP) at the contact site of inner mitochondrial membrane (IMM) and OMM. The opening of the mPTP causes depolarization of the mitochondria, matrix swelling and thus rupture of the OMM. Presumed components of the pore are *voltage-dependent anion channel* (VDAC), *adenine nucleotide translocator* (ANT), *cyclophilin D* (PPIF) and *hexokinases*.^{108,109} Apparently, it depends on the cell type and the apoptosis stimulus which mechanism is prevailing. In some studies it is also assumed that BAX and mPTP together cause MOMP.¹¹⁰

Irreversible induction of MOMP causes a breakdown of the mitochondrial inner membrane potential ($\Delta\Psi_m$) and thus the inhibition of the $\Delta\Psi_m$ -driven ATP production and protein transport processes, the release of proapoptotic factors into the cytosol, an inhibition of cellular respiration due to the release of cytochrome c as a fundamental component of complex III of the respiratory chain and finally an increase in mitochondrial reactive oxygen species (ROS) levels.⁷⁶ Overall, a mitotoxic, proapoptotic amplification loop is formed, with the release of proapoptotic factors from the intermembrane space as the most relevant component: AIF and *endonuclease G* (ENDOG) translocate into the nucleus after their release to cause caspase-independent DNA fragmentation (see also chapter 1.2.3).^{111,112} SMAC enhances the apoptotic signal by inhibiting the antiapoptotic proteins of the *inhibitor of apoptosis* (IAP) family.¹¹³ And finally, cytochrome c itself aggregates with *apoptotic protease-activating factor 1* (APAF1) and dATP to form the multi-protein complex called apoptosome.⁷⁶ More precisely, the binding of cytochrome c to the C-terminus of inactive, dADP-bound APAF1 causes the transition to the active, dATP-bound form.^{114,115} In the absence of dATP, however, only dysfunctional protein complexes are formed.¹¹⁶ The binding of cytochrome c leads to the uncovering of the N-terminal CARD of APAF1, which can then serve as a binding site for procaspase-9.^{108,115} Seven cytochrome c/APAF1/dADP heteromers finally assemble into

a functional apoptosome in a wheel-shaped structure allowing procaspase-9 to be recruited and activated.¹⁰⁸

1.5.2 Regulation of intrinsic apoptosis by BCL2 family members and IAPs

The regulation of the two crucial switches for the activation of intrinsic apoptosis, firstly the release of cytochrome c into the cytosol and secondly the downstream activation of caspases, are each particularly associated with one distinct protein family. While the release of cytochrome c is mainly controlled by proteins of the BCL2 family, the activation of caspases is mainly regulated by proteins of the IAP family as well as their antagonists.^{117,118}

Proteins of the BCL2 family are basically divided into three subgroups according to the number of their *Bcl-2 homology* (BH) regions.¹¹⁹ The first group contains the classical inhibitory BCL2 family members with four BH regions (BH1234), the second group is the BH123 subgroup and the third group comprises the proapoptotic BH3-only proteins.¹¹⁴ The BH123 subgroup includes the two pore-forming proteins that directly affect cytochrome c release, namely BAK and BAX. While the proteins of the BH1234 subfamily including BCL2, *B-cell lymphoma-extra large* (BCL-xL) and *induced myeloid leukemia cell differentiation protein Mcl-1* (MCL1) inhibit the activity of BAK/BAX, proteins of the BH3-only subfamily including *BCL2-associated agonist of cell death* (BAD), BID, *BCL2-interacting mediator of cell death* (BIM), *Bcl-2-modifying factor* (BMF), *p53 upregulated modulator of apoptosis* (PUMA) and NOXA (PMAIP1) increase the activity of BAK/BAX.^{108,120} Under physiological conditions BCL2 and BCL-xL form heterodimers with BAK and BAX, which inhibits the activity of these and thus maintains the integrity of the OMM. Stress signals lead to increased expression of BH3-only proteins, which in turn can bind to BH1234 proteins and neutralize their antiapoptotic effect, allowing BAK and BAX to eventually oligomerize, form pores and release cytochrome c.¹¹⁴ The central importance of BAK and BAX is underlined by the fact that in their absence neither activation of BH3-only proteins nor inactivation of BH1234 proteins are sufficient stimuli for the release of cytochrome c.¹²¹

Proteins of the IAP family possess antiapoptotic activity and are characterized by one to three baculoviral IAP repeats (BIR domains).¹¹⁴ So far, eight different IAP proteins are known, namely BIRC1 (NAIP), BIRC2 (CIAP1), BIRC3 (CIAP2), BIRC4 (XIAP), BIRC5 (survivin), BIRC6 (BRUCE), BIRC7 (ML-IAP/Livin) and BIRC8 (Ts-IAP). In addition to their BIR domains, CIAP1 and CIAP2 feature a CARD that allows them to bind to the DISC.¹²² In general, IAPs can bind to and inhibit CASP3, CASP7 and CASP9.¹¹⁴ Initiator caspases as well as effector caspases can thus become targets of the antiapoptotic activity of IAP proteins. Moreover, most IAPs carry RING finger domains that allow them to ubiquitinate active caspases and other proapoptotic factors, thereby inducing their proteasomal degradation.^{122,123}

The two most prominent antagonists of IAP proteins, SMAC and OMI, are released from the mitochondria into the cytosol in the course of MOMP and bind to IAPs via their N-terminal IAP-binding motif (AVPS), thus preventing their binding to caspases.^{124,125} In contrast to SMAC, the inhibitory effect of OMI is irreversible, as it can additionally degrade *X-linked inhibitor of apoptosis protein* (XIAP), CIAP1 and CIAP2 by means of its serine protease activity.^{114,126} SMAC on the other hand is capable of additionally enhancing the proteasomal degradation of CIAP1 and CIAP2.¹¹³

1.5.3 Stress stimuli initiating intrinsic apoptosis

A wide variety of different intracellular stress signals can trigger MOMP and thus initiate intrinsic apoptosis. A particularly well described cause is the emergence of DNA damage. DNA damage leads to activation of the tumor suppressor and transcription factor *cellular tumor antigen p53* (TP53), which can induce either cell cycle arrest or cellular senescence via *cyclin-dependent kinase inhibitor 1* (CDKN1A, also known as p21) or apoptosis via activation of BAX, depending on the severity of the damage.¹¹⁹ This switch between pro-survival signaling or proapoptotic action apparently depends on the phosphorylation state of TP53.¹²⁷ The proapoptotic effect of TP53 is mechanistically attributable to an increase in the expression of proapoptotic BCL2 proteins, in particular PUMA, NOXA, BIM, ASC (which promotes BAX activation) and PIDD1 (see chapter 1.3), while the expression of antiapoptotic BCL2 proteins is inhibited.^{119,128} Moreover, TP53 can directly activate BAK and can cause nuclear release of the histone H1.2, which also promotes MOMP.¹²⁹

Another possible trigger for the induction of MOMP is endoplasmic reticulum stress. The ER is the central intracellular storage for Ca²⁺. Stress factors such as impaired regulation of the Ca²⁺ gradient reduce the protein folding capacity of the ER, causing misfolded proteins to aggregate and unfolded protein response (UPR) to be induced as a rescue mechanism from this toxic aggregation.^{130,131} If the stress persists, MOMP can be promoted by various signaling pathways, including activation of the transcription factor *C/EBP-homologous protein* (CHOP), which upregulates the expression of BIM and PUMA.^{132,133} Sustained release of Ca²⁺ from the ER followed by uptake into the mitochondria can also serve as a stimulus for MOMP.¹³⁴

The stress kinases *c-Jun N-terminal kinase 1* (JNK1), JNK2, JNK3 and *p38 mitogen-activated protein kinases* (p38-MAPK) as proapoptotic members of the MAP kinase family play an important role in the promotion of MOMP. When activated by stress such as DNA damage, heat shock or oxidative stress, they activate transcription factors including TP53 and thus stimulate the expression of proapoptotic proteins like BAX. Moreover, they support the translocation of BAX to the mitochondria.^{135,136}

Oxidative stress causes DNA damage and thus an activation of TP53 as well as an activation of the above-mentioned stress kinases. In addition, ROS can oxidize mPTP proteins and thereby induce their

opening. Finally, ROS can weaken the binding of cytochrome c to the outer leaflet of the IMM by oxidizing cardiolipin as an anchor of cytochrome c and consequently promote the release of cytochrome c.¹³³

Lysosomes are also possible starting points for the induction of MOMP. Rupture of the lysosomal membrane, e.g. as a result of oxidative stress, causes release of cathepsins into the cytosol. These can then activate BID and thus induce apoptosis.^{119,137}

Another way to induce MOMP is to inhibit histone deacetylases (HDACs), a class of enzymes that modulate chromatin structure and transcription by deacetylation of histones. Since cancer cells frequently exhibit highly upregulated expression levels of HDACs and thus experience oncogenic addiction, inhibition of HDACs is a potent way to force cancer cells into apoptotic cell death.^{138,139} Apoptosis of cancer cells following HDAC inhibition is usually characterized by increased activity of BCL-2 family members (BCL-2, BCL-XL, MCL1, BCL-6, and BCL-11) and BIM.^{140,141}

Finally, microtubules, which are often targeted by anticancer drugs, represent a possible starting point for the induction of MOMP.¹¹⁹ Under physiological conditions, microtubules sequester BH3-only proteins, but severe damage by microtubule poisons like taxanes results in the release and activation of these proapoptotic proteins.¹⁴² In particular, activation of BIM is found after treatment with taxanes.¹⁴³

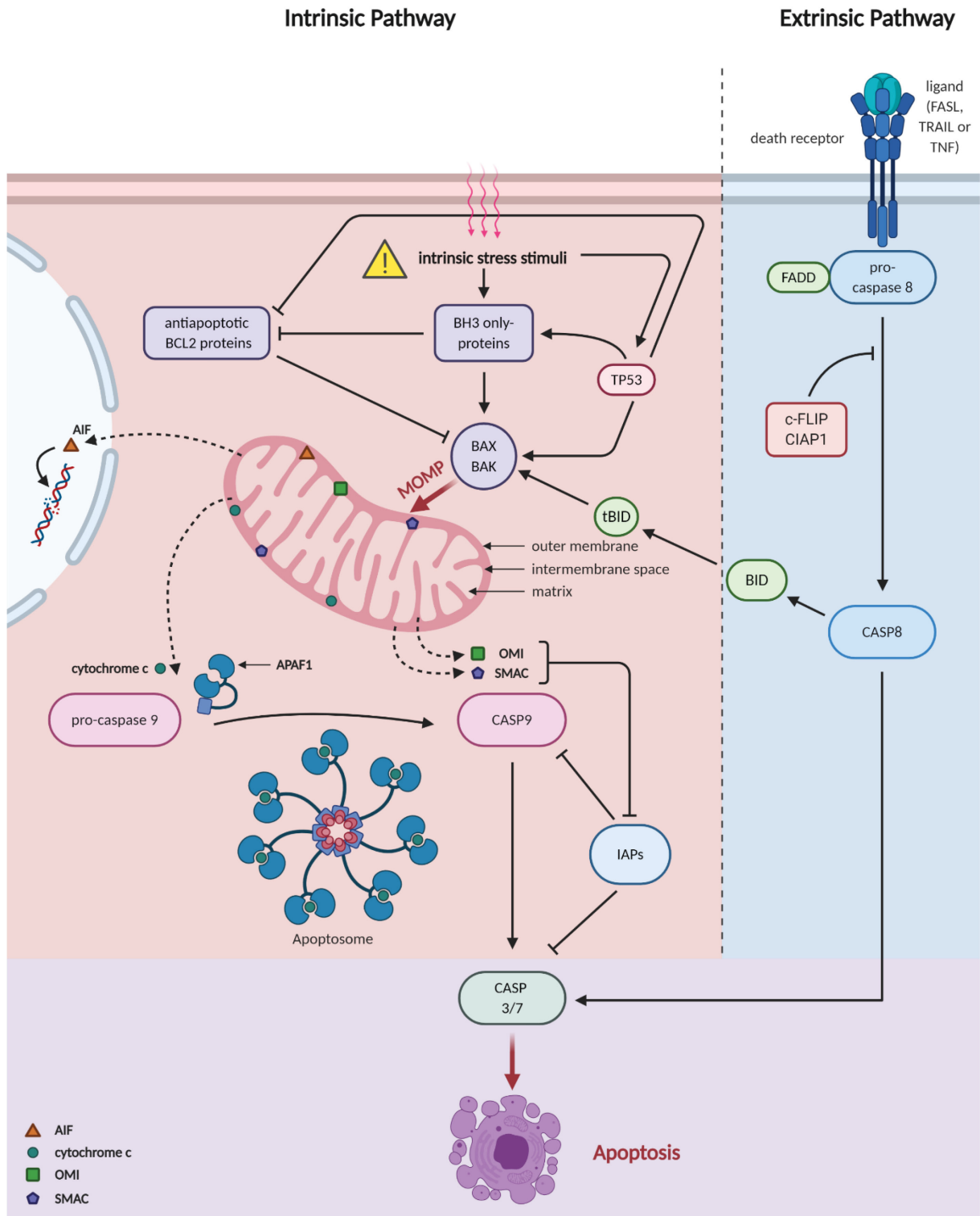


Figure 2: Signaling of extrinsic and intrinsic apoptosis. The two most central signaling pathways of apoptosis are the intrinsic and the extrinsic pathway, which differ in the proteins involved but also in the events that trigger them. The extrinsic pathway is triggered by the binding of a ligand to its corresponding death receptor, such as the binding of FASL to Fas (CD95). This results in a trimerization of the transmembrane receptor, which allows the adaptor protein FADD to bind, forming a platform for the recruitment of **procaspase-8**. The resulting local enrichment of procaspase-8 leads to its autoproteolytic activation unless this process is inhibited by **CIAP1** or **c-FLIP**. In contrast, the intrinsic pathway, also called the mitochondrial pathway, is triggered by **intrinsic stress stimuli** such as DNA

damage, ER stress, or growth factor withdrawal. Intrinsic stress signals may cause mitochondrial outer membrane permeabilization (**MOMP**) via a regulatory network of pro- and antiapoptotic BCL2 proteins. In this process, stress signals lead to the activation of **BH3-only proteins**, which in turn activate **BAK** and **BAX**, leading them to oligomerize into pore complexes in the outer mitochondrial membrane, thereby inducing MOMP. **Antiapoptotic BCL2 proteins**, which are inhibited by BH3-only proteins, can inhibit the activation of BAK and BAX and thus the initiation of MOMP. In the presence of DNA damage, **TP53** gets activated, which can then promote MOMP by activating BH3-only proteins as well as BAK and BAX and additionally by inhibiting antiapoptotic BCL2 proteins. MOMP is accompanied by release of proapoptotic factors such as **AIF**, **cytochrome c**, **OMI** or **SMAC** from the mitochondrial intermembrane space. After release into the cytosol, cytochrome c assembles together with **APAF1** and dATP into a multi-protein complex called **apoptosome** that catalyzes the activation of **procaspase-9**. AIF translocates to the nucleus where it leads to DNA degradation. OMI and SMAC abolish the inhibitory effect of **IAPs** on **CASP3**, **CASP7** and **CASP9**, thus acting proapoptotically. The activated initiator caspases of the extrinsic and intrinsic pathways (CASP8 and CASP9, respectively) finally activate the effector caspases (CASP3 and CASP7), which ultimately cause the apoptotic death of the cell. CASP8 also cleaves **BID** to **tBID**, whereupon the latter can activate BAK and BAX, thus providing a cross-link to intrinsic apoptosis, allowing the additional activation of CASP9 to cause amplification of the proapoptotic signal.

1.5.4 The role of mitochondria in intrinsic apoptosis

Since the release of cytochrome c is an essential switch in the direction of intrinsic apoptotic cell death, it is subject to complex regulatory mechanisms. The majority of mitochondrial cytochrome c is localized in compartments termed cristae, which are formed by folds of the inner mitochondrial membrane and which experience a spatial separation and diffusion barrier from the intermembrane space through narrow cristae junctions. Control mechanisms that regulate mitochondrial morphology, especially cristae structure and size of cristae junctions, can therefore affect the release of cytochrome c and thus the initiation of apoptosis.¹¹⁹

This is also reflected by the observations that mitochondrial fragmentation is one of the first apoptotic events and occurs even prior to membrane blebbing and activation of caspases, and that intensive mitochondrial fragmentation promotes the initiation of apoptosis.¹⁴⁴ Mitochondria form a highly dynamic network and their membranes are subject to continuous fusion and fission processes, termed mitochondrial dynamics.¹⁴⁵ Fusion and fission serve as quality control mechanisms since they allow the separation of dysfunctional mitochondria and their disposal via mitophagy.^{146,147} The mechanisms underlying mitochondrial dynamics and their involved proteins can be subdivided into three processes.

The first process is the fusion of the outer mitochondrial membrane by *mitofusin-1* (MFN1) and *mitofusin-2* (MFN2). The second process is the fusion of the inner mitochondrial membrane by *optic atrophy protein 1* (OPA1) and the third the mitochondrial fission mediated by *dynamamin-1-like protein* (DRP1).¹⁴⁷ The proteins involved in the fusion of the inner and outer mitochondrial membrane (MFN1, MFN2, OPA1)

exert antiapoptotic effects whereas DRP1 as a mediator of mitochondrial fission exerts proapoptotic effects.¹⁴⁸⁻¹⁵²

Mitofusins are capable of binding to BAX in the cytosol and thereby inhibiting its activation. Moreover, they are able to prevent opening of the mPTP.¹⁴⁸ Accordingly, MFN1 is inhibited early in apoptotic cells.¹⁴⁹ In contrast, OPA1 shows antiapoptotic potency by preserving cristae structure and preventing cristae tubules from dilating, thus delaying and reducing the release of cytochrome c.¹⁵⁰ In fact, loss of OPA1 alone is sufficient to induce apoptosis.¹⁵¹ Proapoptotic members of the BCL2 family can inhibit OPA1 and thus induce cristae fusion and cristae junction opening, which facilitates the release of cytochrome c.^{150,153,154} Activity of OPA1 is regulated by cleavage at two proteolytic cleavage sites S1 and S2 by the two proteases *metalloendopeptidase OMA1, mitochondrial* (OMA1) and *ATP-dependent zinc metalloprotease YME1L1* (YMEL1), respectively. Physiologically, both proteases exhibit moderate activity, resulting in a balanced ratio of short (S-OPA) and long (L-OPA) isoforms, favoring mitochondrial fusion. Stress conditions result in OMA1-dependent total cleavage in S-OPA, which lacks the transmembrane domain. Loss of L-OPA leads to disorganization of the cristae, while accumulation of S-OPA favors mitochondrial fission, which in sum leads to an increased sensitivity to apoptotic stimuli.¹⁴⁷

The proapoptotic effect of DRP1, by contrast, is less well understood and still subject to ongoing debate. The consensus is that DRP1 activity promotes the release of cytochrome c.¹⁵⁵ However, while there are reports attributing this to the finding that DRP1 may promote BAK activation downstream of OPA1-dependent cristae modelling, there are contrary reports attributing the effect of DRP1 on cytochrome c release to proapoptotic cristae modelling without interaction with BAK or BAX.^{152,156}

1.6 Apoptosis, cancer and therapeutic implications

In order to ensure their survival, cancer cells have to develop strategies to escape apoptotic cell death. Dysregulation of apoptosis signaling, resulting in an acquired resistance to apoptosis induction, is therefore an important hallmark for tumorigenesis and cancer progression.¹⁵⁷ Even more often than the extrinsic pathway, the mitochondrial pathway in cancer cells is affected by severe dysregulation.¹⁵⁸ Due to the short generation times, high selection pressure and genetic instability, tumors can rapidly accumulate a multitude of mutations that provide them with a certain degree of apoptosis resistance and thus a survival advantage. However, since tumor cells exhibit a high inherent stress level due to stressors such as hypoxia, nutrient deficiency or oncogenic stress, they are usually still susceptible to therapies that aim to shift the fragile balance between cell death and survival signaling by acting on apoptosis signaling.¹⁵⁸ Thus, already in 1970, Kerr described the connection between apoptosis and the elimination of malignant cells and nowadays the induction of apoptosis is one of the main mechanisms

of anticancer drugs.^{158,159} In the following, therefore, the various adaptations, that cancer cells use to evade apoptosis, and possible pharmacological countermeasures are discussed. Basically, the mechanisms of apoptosis evasion can be divided into five groups, the elimination of TP53 as the “guardian of the genome”, dysregulated death receptor signaling, disrupted triggering of MOMP, impaired caspase activity and effects on IAPs and their antagonists.^{114,159} In many cancer cells, TP53 is inactivated by missense mutations, which drastically reduce the apoptosis rate of affected cells.¹¹⁴ To counteract this, small compounds have been developed that stabilize the conformation of TP53 against inhibitory unfolding, neutralize upstream inhibitors of TP53 such as Mdm2, or induce proteasomal degradation of mutated TP53.¹⁶⁰ The death receptors DR4 and DR5 as binding sites for their ligand TRAIL are commonly upregulated in cancer cells, which is why they have been intensively evaluated as therapeutic targets.^{161,162} The use of recombinant human trail (rhTRAIL) or other synthetic TRAIL receptor agonists (TRAs) offers the advantage that ligation with DR4 and DR5 can trigger apoptosis independently of the cancer’s TP53-status. However, clinical studies have shown that monotherapy with these ligands is usually not efficient and that a combination therapy is necessary for therapeutic success.¹⁶³

Cancer cells can escape MOMP either by acting on mPTP or by shifting the balance of proapoptotic and antiapoptotic BCL2 proteins.¹⁵⁸ The expression levels of mPTP proteins such as ANT and VDAC are upregulated in many cancer cells, resulting in a deregulation of their interactions.¹¹⁹ One example is the increased binding of VDAC to hexokinases, which in turn causes a reduced recruitment of BAX to the mitochondria and thus inhibition of MOMP and consequently of apoptosis. Therefore, various substances that can suppress this binding are being investigated in clinical trials.¹⁶⁴ However, in other cancer cells MOMP is inhibited by a strong upregulation of antiapoptotic BCL2 proteins.¹¹⁴ An increased expression of antiapoptotic BCL2 proteins directly correlates with accelerated tumorigenesis upon activation of oncogenes.¹⁶⁵ The mechanisms underlying the increase in expression range from copy number amplification, transcriptional upregulation to downregulation of microRNAs that inhibit BCL2 expression. In addition, cancer cells can also experience transcriptional silencing of proapoptotic BH3-only proteins by promoter methylation or deletion.¹⁵⁸ BH3 mimetics can induce BAK/BAX activation even in case of a dysregulated BCL2 balance by neutralizing the antiapoptotic BCL2 family members. This direct form of BAK/BAX activation appears to be attractive for application in cancer therapy because it does not rely on upstream signals and thus bypasses signaling pathways and frequently mutated mediators such as TP53.¹²⁸ But although the BCL2 protein family has been known for over 30 years, BH3 mimetics have so far shown little benefit in therapy due to their complex chemical requirements for the necessary affinity to the hydrophobic grooves of the target proteins.¹⁶⁶ Since the antiapoptotic BCL2 proteins also fulfill physiological functions independent of apoptosis, e.g.

in the regulation of glucose metabolism or macroautophagy, the use of BH3 mimetics moreover is often associated with severe side effects.¹⁶⁷ For example, BH3 mimetics targeting BCL-xL may induce thrombocytopenia, as platelets depend on BCL-xL for survival.¹⁶⁸

Further potential drivers of apoptosis evasion are alterations in the expression and activation of caspases. Cancer cells frequently exhibit reduced caspase-levels. Colon cancer for example is usually characterized by low CASP9 levels and choriocarcinoma by low CASP8 levels.^{169,170} Downregulated CASP3 levels are also found in many cancer cells.¹¹⁴ Apart from regulation at the transcriptional level, reduced caspase function may also result from inhibition of caspase activation in cancer cells. Epigenetic silencing of APAF1 is one well-known mechanism of cancer cells to inhibit caspase activation.¹⁵⁸ The discovery that staurosporine, an ATP-competitive multikinase inhibitor, can induce intrinsic apoptosis even in APAF1 deficient cells, i.e. without assembly of the apoptosome, nourishes the hope that induction of apoptosis in cancer cells with mutated classical apoptosis pathways can be used therapeutically by targeting non-canonical apoptosis pathways.¹⁷¹ Given the central function of cytochrome c in the activation of CASP9, it is not surprising that this segment of intrinsic signaling also becomes the target of mutations in cancer cells. In neuroblastoma and glioblastoma cells, for example, proteasomal degradation of cytochrome c released into the cytosol can occur, which is dependent on the E3 ligase cullin-9 (CUL9) and leads to increased resistance to intrinsic apoptosis.¹⁷²

Finally, the last remaining target of tumorigenic apoptosis evasion is the expression of IAPs. Overexpression of IAPs, present in many cancer cells, is associated with a poor prognosis.^{114,173} A suitable example for IAPs overexpression is survivin, which is silenced in most differentiated tissues, but is highly expressed in tumor tissue.¹⁷⁴ A pharmacological approach to IAP inhibition is the use of antisense oligonucleotides, which can bind to the mRNA of IAPs and thus prevent their expression. In preclinical studies, the administration of antisense oligonucleotides significantly increased the sensitivity of cancer cells to the initiation of apoptosis and showed synergistic effects in combination with chemotherapeutic agents.^{175,176} However, in clinical trials neither single-agent treatment nor co-treatment with chemotherapeutic agents lead to improved remission rates, which was attributed to limited knockdown efficacy.¹⁷⁷ Improved study results were obtained with SMAC mimetics, small molecules that bind to the BIR2 domain of cIAPs and the BIR3 domain of XIAP, thereby inducing proteasomal degradation and thus antagonization of cIAPs and XIAP.¹⁷⁸ Degradation of XIAP leads to the direct activation of caspases, while degradation of cIAPs causes NF- κ B-dependent transcriptional activation of TNF- α and subsequently triggers extrinsic apoptosis via the TNFR1 receptor.¹⁷⁹

1.7 Natural products in drug discovery

Natural products are bioactive compounds derived from natural sources such as plants, fungi, bacteria or animals.¹⁸⁰ Starting with biosynthetic intermediates from the metabolic pathways of primary biochemical processes such as photosynthesis or glycolysis, a multitude of modifying chemical reactions leads to the overwhelming structural diversity of natural products.¹⁸¹ From an evolutionary point of view, the energy-intensive synthesis of high-molecular structures only makes sense if they can convey a distinct survival advantage for the host organism. For natural products, this survival advantage is primarily based on protection against predators.¹⁸² To fulfill this function, natural compounds have been evolutionary tailored to target biological receptors and to provide ideal interactions with biological macromolecules over millions of years. Their usually high number of chiral centers enables them to occupy even complex binding sites.¹⁸² It is now assumed that all natural compounds bind to at least one receptor.¹⁸³ Summing up, due to their long evolution in biological systems, natural compounds have developed a high target affinity and specificity and are similar in many respects to the demands made on drugs.¹⁸² It is therefore not surprising that already ancient civilizations such as those of the Mesopotamians or Egyptians used hundreds of different natural compounds for medical purposes.¹⁸³

A major challenge in the transition of natural products into medical use is the need for efficient methods for isolation and structure elucidation as well as the often limited availability of source materials.¹⁸² Modern synthetic chemistry is a valuable tool to circumvent potential supply problems with source materials. Friedrich Wöhler can be regarded as a pioneer in the synthesis of natural products and in organic chemistry, having first succeeded in synthesizing urea in 1828.¹⁸⁴ While the synthesis of highly complex scaffolds remained too challenging for decades, advances in this discipline have made it possible to synthesize many natural products and derivatives originated from natural products. One example is the 62-step synthesis of eribulin, a cytostatic drug whose structure is basically derived from the natural substance halichondrin B, but which has been simplified in order to enable total synthesis.¹⁸⁵ Meanwhile, the sophisticated total synthesis of halichondrines on a 10 g scale is also feasible, underlining the potency of modern synthesis chemistry.¹⁸⁶ Advances in synthetic chemistry also allow for semi-synthesis from more readily available starting substances as well as enhancement of potency of natural products by means of derivatization.^{182,187}

The pharmacological applicability of natural products becomes evident when looking at the statistics. In the period from 1981 - 2010 40% of the new chemical entities were natural products or derived from natural products. They accounted for 64% of the cancer drugs and even 75% of the antibiotics that were developed during this period.¹⁸⁴ The range of applications addressed by natural product-derived drugs is diverse and includes analgesics (e.g. ziconotide¹⁸⁸), anticancer drugs (e.g. trabectedin¹⁸⁹), antibiotics

(e.g. penicillin¹⁹⁰), antifungals (e.g. caspofungin¹⁹¹), anti-malaria drugs (e.g. artemether¹⁹²), diabetes drugs (e.g. exenatide¹⁹³), anti-HIV drugs (e.g. bevirimat¹⁹⁴) or Alzheimer's drugs (e.g. galantamine¹⁹⁵). In addition to their use in drug development, natural products have often demonstrated in the past to be useful for a better understanding of cellular processes. Some examples are the relevance of brefeldin A (for the understanding of protein transport), of forskolin (cAMP signaling), of cyclosporine A (lymphocyte signaling), of rapamycin (mTOR signaling) and of trapoxin B (epigenetics).¹⁸⁴ As a look into the future, it should be noted that due to the fact that only 6% of higher plants have been systematically investigated and only a negligible percentage of all microorganisms have ever been cultivated, the absolute majority of all natural compounds are still waiting to be discovered.¹⁸³ If host organisms are to be harvested, top priority must be given to safeguarding the rights of the host country and protecting nature by complying with the *Convention on Biological Diversity* (CBD).¹⁸²

1.8 Natural products as inducers of apoptosis

Their large structural diversity allows natural products to theoretically target all biological macromolecules, so it is not surprising that for virtually all apoptosis-involved signaling pathways and proteins described in the previous chapters, natural products interacting with them are described. On the one hand, many of these pathways are evolutionarily highly conserved and thus useful targets for defense purposes. On the other hand, due to the vast mass of different natural compounds, these interactions are certainly to some extent also of a random nature. In the following, the different targets for proapoptotic natural products are classified and corresponding exemplary compounds are named and discussed.

1.8.1 Inducers of extrinsic apoptosis

Although the majority of natural product-induced apoptosis is related to the mitochondrial pathway, there are examples of natural products that target the extrinsic apoptosis pathway. Thymoquinone causes relocation of cytoplasmic CD95 to the cell membrane and thus increases sensitivity to extrinsic apoptosis.¹⁹⁶ The traditional Chinese medicine cantharidine leads to an increase in the expression of CD95, which combined with other effects of the substance triggers apoptosis.¹⁹⁷ And honokiol, an active component purified from magnolia is a weak apoptosis inducer, when used alone. However, since the substance ubiquitinates the antiapoptotic c-FLIP, it potently sensitizes to death-receptor-mediated apoptosis and is therefore highly effective in combination with TRAIL.¹⁹⁸

1.8.2 Inducers of intrinsic apoptosis

Natural compounds that induce intrinsic apoptosis can be divided into three subgroups, compounds that increase the cellular stress level and thus induce downstream apoptosis and compounds that act directly on apoptosis signaling, either by affecting MOMP or by interacting with IAPs.

Increasing the stress level

Induction of DNA damage has been described for a large number of natural compounds, such as leinamycin, maximiscin, eusynstyelamide B, β -thujaplicin or berberine. Mechanistically, this can be attributed to the induction of ROS, the inhibition of repair mechanisms or the inhibition of *topoisomerase II* (TOP2), for example.¹⁹⁹⁻²⁰³ Natural compounds are also known to trigger ER stress, e.g. by disrupting the ER-Golgi vesicular transport via inhibition of *ADP ribosylation factor* (ARF) as it has been shown for brefeldin A.²⁰⁴ As another example, polyphyllin D induces ER stress, presumably by disruption of Ca^{2+} homeostasis.²⁰⁵ The increase of cellular ROS levels is a frequently observed effect of natural products and is caused by chaetocin, levistolide A, neoantimycin F or ramentaceone for example.²⁰⁶⁻²⁰⁹ In some cases, the effect on ROS levels can also be mechanistically pinpointed. For 2-methoxyestradiol (2-ME), inhibition of *superoxide dismutase* (SOD) is described, β -phenylethyl isothiocyanate (PEITC) is known to cause *glutathione* (GSH) depletion and avenanthramide targets the oncogenic RNA helicase *DEAD box protein 3, X-chromosomal* (DDX3) and thus affects mitoribosomal translation and therefore the translation of components of the electron transport chain (ETC).²¹⁰⁻²¹² Since the disruption of microtubule dynamics leads to cellular stress by inhibition of mitosis and induction of cell cycle arrest, microtubule poisons are particularly effective in rapidly proliferating cells such as cancer cells and are therefore frequently used in cancer therapy.²¹³ Many potent microtubule poisons are of natural origin, for example paclitaxel, colchicine, epothilone A or discodermolide.²¹⁴⁻²¹⁷ As cancer cells depend on the expression of oncogenes, the inhibition of their expression by HDAC inhibitors can also elevate cellular stress levels and trigger apoptosis.²¹⁸ Known natural compounds that inhibit HDACs include curcumin, resveratrol, genistein and (-)-epigallocatechin-3-gallate.²¹⁹⁻²²² As described in chapter 1.2.4, the release of cathepsins from lysosomes may result in apoptosis.¹³⁷ A relevant example is IMB-6G, a derivative of sophoridin that induces apoptosis by permeabilizing the lysosomal membrane.²²³ Oxidative phosphorylation is a highly conserved process of central relevance for energy homeostasis, which makes its disruption toxic to most predators and explains why so many natural products target the respiratory complexes. For example rotenone, nafuredin and eliamid are known inhibitors of complex I, α -tocopheryl succinate, gracillin, caulerpin and harzianopyridone inhibitors of complex II, antimycin A, stigmatellin and cyrmenin A inhibitors of complex III, psychosine and metarhizin A inhibitors of complex IV and oligomycin, apoptolidin and resveratrol inhibitors of complex V (ATP synthase).²²⁴⁻²³⁸

Affecting MOMP

Natural compounds that induce apoptosis by promoting the process of MOMP either facilitate opening of mPTP or shift the balance between pro- and antiapoptotic BCL2 family members, both resulting in MOMP. Betulinic acid has been shown to be capable of opening mPTP directly in isolated mitochondria in a caspase-independent manner.²³⁹ 6[3-adamantyl-4-hydroxyphenyl]-2-naphthalene carboxylic acid (CD437) and all-trans-retinoic acid appear to act as ligands of ANT and thus promote the opening of mPTP.^{240,241} Finally, methyl jasmonate detaches hexokinase from VDAC.²⁴² Since binding of hexokinase stabilizes the closed configuration of the pore, methyl jasmonate thereby causes opening of the mPTP.²⁴³ A large variety of natural compounds are known to affect either expression or activity of proteins of the BCL2 family. Direct inhibition of antiapoptotic BCL2 proteins has been described for antimycin A3, gossypol and tetrocarcin A, among others.²⁴⁴⁻²⁴⁶ Berberine reduces the expression of BCL2 by inhibiting its regulator *miR-21*.²⁴⁷ Genipin, resveratrol and the active ginseng saponin metabolite compound K decrease the expression of BCL2 and BCL-xL by suppressing the JAK1/STAT3 pathway as their upstream regulator.²⁴⁸⁻²⁵⁰ Finally, oridonin reduces the expression of BCL-xL and MCL1 and thereby triggers apoptosis in leukemia cells while the survival of healthy lymphoid cells is not affected.²⁵¹

Inhibitors of IAPs

Targeting of IAPs by natural products can either induce extrinsic or intrinsic apoptosis. The drimane sesquiterpene lactone SF002-96-1 reduces the expression of survivin by inhibiting the survivin promoter activity.²⁵² Embelin, an active compound isolated from the Japanese *ardisia* herb, binds to the BIR3 domain of XIAP and thereby inhibits its activity.²⁵³ Finally, resveratrol causes a JAK1/STAT3-dependent down-regulation of CIAP2, XIAP and survivin.²⁴⁹ Resveratrol with its broad range of proapoptotic effects (e.g. inhibition of HDACs, BCL2 proteins, *topoisomerase II*, *ATP synthase* and IAPs) is a prototypical example of how natural compounds usually address several targets simultaneously, which together determine the apoptotic phenotype of the compound.^{221,238,249,254}

1.9 Aims

The primary aim of the present work as a subproject of the Düsseldorf School of Oncology (DSO) and the Research Training Group 2158 (GRK2158) was the identification and characterization of natural products as inducers of apoptosis in cancer cells on the background of a potential therapeutic use. For this purpose, substances derived from organisms from highly competitive habitats as catalysts for the generation of potent bioactive natural products were tested for their suitability in a multi-stage test procedure. The absolute majority of the over 150 substances tested originated from Prof. Proksch's extensive library of natural products or were isolated and made available by his team (Institute for Pharmaceutical Biology and Biotechnology, HHU Düsseldorf) in the course of the project.

After an initial screening for cytotoxicity in leukemia and lymphoma cells, toxic natural compounds were examined for their potential to induce apoptotic cell death. Potent apoptosis inducers with rapid onset of action were then investigated for possible selectivity by comparative testing in healthy hematopoietic stem and progenitor cells. Natural compounds that displayed particularly beneficial properties were finally evaluated for the underlying mode of action.

Likewise, the mode of action of the mycotoxin phomoxanthone A, which has already been identified in preliminary work as a strong apoptosis inducer, should be characterized and described. In addition, cooperation partners should be supported in the testing of synthesized substances, whose structure was inspired by scaffolds from natural products, with respect to existing bioactivity and in the derivation of particularly potent apoptosis inducers. The addressing of these aims culminated in the publication of a number of manuscripts, selected ones of which are discussed in the following. The corresponding manuscripts are provided in the appendix to this dissertation.

2 Manuscripts

2.1 Publications within the scope of this dissertation

The full texts of these manuscripts are attached in the appendix to this dissertation.

2.1.1 Pleiotropic effects of spongean alkaloids on mechanisms of cell death, cell cycle progression and DNA damage response (DDR) of acute myeloid leukemia (AML) cells

Stuhldreier F, Kassel S, Schumacher L, Wesselborg S, Proksch P, Fritz G. (2015) Cancer Letters 361:39–48. doi: 10.1016/j.canlet.2015.02.030

Author contribution:

This publication is primarily based on the data collected by the author of this dissertation during the work on his master thesis. During an extensive revision process in the framework of his PhD thesis, the author performed the experiments on apoptosis induction (caspase-3 activity measurements and immunoblot analyses), which then supplemented the revised version of the manuscript as Figures 3c, 3d and 5b. Relative contribution (within context of his PhD): about 5%

2.1.2 Cyclic Cystine-Bridged Peptides from the Marine Sponge *Clathria basilana* Induce Apoptosis in Tumor Cells and Depolarize the Bacterial Cytoplasmic Membrane

Mokhlesi A, Stuhldreier F, Wex KW, Berscheid A, Hartmann R, Rehberg N, Sureechatchaiyan P, Chaidir C, Kassack MU, Kalscheuer R, Brötz-Oesterhelt H, Wesselborg S, Stork B, Daletos G, Proksch P. (2017) Journal of Natural Products 80:2941–2952. doi: 10.1021/acs.jnatprod.7b00477

Author contribution:

The author of this dissertation independently planned, designed and carried out the experiments on apoptosis, autophagy and cytotoxicity in leukemia and lymphoma cells and wrote parts of the manuscript. Relative contribution: about 15%

2.1.3 Daldinone derivatives from the mangrove-derived endophytic fungus *Annulohyphylon* sp.

Liu Y, Stuhldreier F, Kurtán T, Mándi A, Arumugam S, Lin W, Stork B, Wesselborg S, Weber H, Henrich B, Daletos G, Proksch P. (2017) RSC Advances 7:5381–5393. doi: 10.1039/C6RA27306H

Author contribution:

The author of this dissertation independently planned, designed and carried out the experiments on apoptosis, autophagy and cytotoxicity in leukemia and lymphoma cells and wrote parts of the manuscript. Relative contribution: about 15%

2.1.4 The mycotoxin phomoxanthone A disturbs the form and function of the inner mitochondrial membrane

Böhler P*, Stuhldreier F*, Anand R, Kondadi AK, Schlütermann D, Berleth N, Deitersen J, Wallot-Hieke N, Wu W, Frank M, Niemann H, Wesbuer E, Barbian A, Luyten T, Parys JB, Weidtkamp-Peters S, Borchardt A, Reichert AS, Peña-Blanco A, García-Sáez AJ, Itskanov S, van der Blik AM, Proksch P, Wesselborg S*, Stork B*. (2018) Cell Death & Disease 9:286. doi: 10.1038/s41419-018-0312-8

* authors contributed equally to the manuscript

Author contribution:

The author of this dissertation carried out part of the experiments (preliminary tests, caspase-3 activity measurements, parts of the immunoblot analyses), participated in the development of the project, contributed ideas, discussed the results and commented on the manuscript. Relative contribution: about 20%

2.1.5 Dithiodiketopiperazine derivatives from endophytic fungi *Trichoderma harzianum* and *Epicoccum nigrum*

Harwoko H, Daletos G, Stuhldreier E, Lee J, Wesselborg S, Feldbrügge M, Müller WEG, Kalscheuer R, Ancheeva E, Proksch P. (2019) Natural Product Research. doi: 10.1080/14786419.2019.1627348

Author contribution:

The author of this dissertation designed and performed the experiments on cytotoxicity and apoptosis in leukemia and lymphoma cells. Relative contribution: about 10%

2.1.6 First Results from a Screening of 300 Naturally Occurring Compounds: 4,6-dibromo-2-(2',4'-dibromophenoxy)phenol, 4,5,6-tribromo-2-(2',4'-dibromophenoxy)phenol, and 5-epi-nakijinone Q as Substances with the Potential for Anticancer Therapy

Mayer S, Prechtel M, Liebfried P, Cadeddu RP, Stuhldreier E, Kohl M, Wenzel F, Stork B, Wesselborg S, Proksch P, Germing U, Haas R, Jäger P. (2019) Marine Drugs 17:521. doi: 10.3390/md17090521

Author contribution:

The author of this dissertation contributed several ideas, developed parts of the experimental designs, provided technical assistance and helped to evaluate the data. Relative contribution: about 5%

2.1.7 Novel meriolin derivatives as rapid apoptosis inducers

Drießen D, Stuhldreier E, Frank A, Stark H, Wesselborg S, Stork B, Müller TJJ. (2019) Bioorganic & Medicinal Chemistry 27:3463–3468. doi: 10.1016/j.bmc.2019.06.029

Author contribution:

The author of this dissertation designed and conducted the experiments on cytotoxicity and apoptosis and wrote parts of the manuscript. Relative contribution: about 20%

2.1.8 Azaphilone pigments and macrodialides from the coprophilous fungus *Coniella fragariae*

Yu H, Sperlich J, Höfert SP, Janiak C, Teusch N, Stuhldreier F, Wesselborg S, Wang C, Kassack MU, Dai H, Liu Z, Proksch P. (2019) *Fitoterapia* 137:104249. doi: 10.1016/j.fitote.2019.104249

Author contribution:

The author of this dissertation designed and performed the experiments on cytotoxicity in leukemia and lymphoma cell lines. Relative contribution: about 5%

2.1.9 Sesterterpenes and macrolide derivatives from the endophytic fungus *Aplosporella javeedii*

Gao Y, Stuhldreier F, Schmitt L, Wesselborg S, Wang L, Müller WEG, Kalscheuer R, Guo Z, Zou K, Liu Z, Proksch P. (2020) *Fitoterapia* 146:104652. doi: 10.1016/j.fitote.2020.104652

Author contribution:

The author of this dissertation designed and performed the experiments on cytotoxicity and apoptosis in leukemia and lymphoma cell lines together with L. Schmitt. Relative contribution: about 5%

2.1.10 Didymellanosine, a new decahydrofluorene analogue, and ascolactone C from *Didymella* sp. IEA-3B.1, an endophyte of *Terminalia catappa*

Ariantari NP, Ancheeva E, Frank M, Stuhldreier F, Meier D, Gröner Y, Reimche I, Teusch N, Wesselborg S, Müller WEG, Kalscheuer R, Liu Z, Proksch P (2020) *RSC Advances* 10:7232–7240. doi: 10.1039/c9ra10685e

Author contribution:

The author of this dissertation designed and performed the experiments on cytotoxicity in leukemia and lymphoma cell lines. Relative contribution: about 5%

2.1.11 Induction of New Lactam Derivatives From the Endophytic Fungus *Aplosporella javeedii* Through an OSMAC Approach

Gao Y, Stuhldreier F, Schmitt L, Wesselborg S, Guo Z, Zou K, Mándi A, Kurtán T, Liu Z, Proksch P (2020) *Frontiers in Microbiology* 11:600983. doi: 10.3389/fmicb.2020.600983

Author contribution:

The author of this dissertation designed and performed the experiments on cytotoxicity and apoptosis in leukemia and lymphoma cell lines together with L. Schmitt. Relative contribution: about 5%

2.1.12 High-throughput screening for natural compound-based autophagy modulators reveals novel chemotherapeutic mode of action for arzanol

Deitersen J, Stuhldreier F, Ceccacci S, Schlütermann D, Berning L, Wu W, Sun Y, Berleth N, Mendiburo MJ, Seggewiß S, Monti MC, Proksch P, Stork B *Manuscript in preparation*

Author contribution:

The author of this dissertation performed the activity measurements of the respiratory chain complexes, helped in isolating the mitochondria and commented on the manuscript. Relative contribution: about 5%

2.1.13 Cancer-specific pro-apoptotic effects of the mycotoxin viriditoxin

Stuhldreier F, Lenz T, Jäger P, Schmitt L, Liu Y, Geyh S, Berleth N, Berning L, Deitersen J, Hinxlage I, Schlütermann D, Sun Y, Wu W, Haas R, Stühler K, Proksch P, Stork B, Wesselborg S

Manuscript in preparation

Author contribution:

The author of this dissertation developed and managed the project, independently planned, designed and carried out the majority of the experiments and wrote the manuscript. Relative contribution: about 80%

2.2 Publications beyond the scope of this dissertation

During his doctorate, the author of this work made contributions to several other publications. However, since these publications go beyond the thematic scope of this dissertation, it was waived to include them to the appendix.

2.2.1 Deubiquitinase inhibition by WP1130 leads to ULK1 aggregation and blockade of autophagy

Drießen S, Berleth N, Friesen O, Löffler AS, Böhler P, Hieke N, Stuhldreier F, Peter C, Schink KO, Schultz SW, Stenmark H, Holland P, Simonsen A, Wesselborg S, Stork B. (2015) *Autophagy* 11: 1458–1470. doi: 10.1080/15548627.2015.1067359

Author contribution:

The author of this dissertation gave technical support, discussed the results and commented on the manuscript. Relative contribution: about 2%

2.2.2 Expression of a ULK1/2 binding-deficient ATG13 variant can partially restore autophagic activity in ATG13-deficient cells

Hieke N, Löffler AS, Kaizuka T, Berleth N, Böhler P, Drießen S, Stuhldreier F, Friesen O, Assani K, Schmitz K, Peter C, Diedrich B, Dengjel J, Holland P, Simonsen A, Wesselborg S, Mizushima N, Stork B. (2015) *Autophagy* 11:1471-1483. doi: 10.1080/15548627.2015.1068488

Author contribution:

The author of this dissertation gave technical support, discussed the results and commented on the manuscript. Relative contribution: about 2%

2.2.3 Systematic analysis of ATG13 domain requirements for autophagy induction

Wallot-Hieke N, Verma N, Schlütermann D, Berleth N, Deitersen J, Böhler P, Stuhldreier E, Wu W, Seggewiß S, Peter C, Gohlke H, Mizushima N, Stork B. (2018) *Autophagy* 14:743-763. doi: 10.1080/15548627.2017.1387342

Author contribution:

The author of this dissertation gave technical support, discussed the results and commented on the manuscript. Relative contribution: about 2%

2.2.4 Targeting urothelial carcinoma cells by combining cisplatin with a specific inhibitor of the autophagy-inducing class III PtdIns3K complex

Schlütermann D, Skowron MA, Berleth N, Böhler P, Deitersen J, Stuhldreier E, Wallot-Hieke N, Wu W, Peter C, Hoffmann MJ, Niegisch G, Stork B. (2018) *Urologic Oncology* 36:160.e1-160.e13. doi: 10.1016/j.urolonc.2017.11.021

Author contribution:

The author of this dissertation gave technical support, discussed the results and commented on the manuscript. Relative contribution: about 2%

2.2.5 Multiple DNA damage-dependent and DNA damage-independent stress responses define the outcome of ATR/Chk1 targeting in medulloblastoma cells

Krüger K, Geist K, Stuhldreier E, Schumacher L, Blümel L, Remke M, Wesselborg S, Stork B, Klöcker N, Bormann S, Roos WP, Honnen S, Fritz G. (2018) *Cancer Letters* 430:34-46. doi: 10.1016/j.canlet.2018.05.011

Author contribution:

The author of this dissertation performed part of the experiments (Fig. 2a, Fig. 2c, Fig. 4c, Fig. 4e) and commented on the manuscript. Relative contribution: about 5%

2.2.6 The Autophagy-Initiating Kinase ULK1 Controls RIPK1-Mediated Cell Death

Wu W, Wang X, Berleth N, Deitersen J, Wallot-Hieke N, Böhler P, Schlütermann D, Stuhldreier E, Cox J, Schmitz K, Seggewiß S, Peter C, Kasof G, Stefanski A, Stühler K, Tschapek A, Gödecke A, Stork B. (2020) *Cell Reports* 31:107547. doi: 10.1016/j.celrep.2020.107547

Author contribution:

The author of this dissertation gave technical support, discussed the results and commented on the manuscript. Relative contribution: about 2%

2.2.7 Natural Products Impacting DNA Methyltransferases and Histone Deacetylases

Akone SH, Ntie-Kang F, Stuhldreier E, Ewonkem MB, Noah AM, Mouelle SEM, Müller R. (2020) *Frontiers in Pharmacology* 11:992. doi: 10.3389/fphar.2020.00992

Author contribution:

The author of this dissertation wrote parts of the manuscript and made several suggestions for its refinement. Relative contribution: about 20%

2.2.8 TNF-induced necroptosis initiates early autophagy events via RIPK3-dependent AMPK activation, but inhibits late autophagy

Wu W, Wang X, Sun Y, Berleth N, Deitersen J, Schlütermann D, Stuhldreier F, Wallot-Hieke N, José Mendiburo M, Cox J, Peter C, Bergmann AK, Stork B. (2021) *Autophagy* 28:1-18.

doi: 10.1080/15548627.2021.1899667

Author contribution:

The author of this dissertation gave technical support, discussed the results and commented on the manuscript. Relative contribution: about 2%

2.2.9 FIP200 controls TBK1 activation threshold at SQSTM1/p62-positive condensates

Schlütermann D, Berleth N, Deitersen J, Wallot-Hieke N, Friesen O, Wu W, Stuhldreier F, Sun Y, Berning L, Friedrich A, Mendiburo MJ, Peter C, Wiek C, Hanenberg H, Stefanski A, Stühler K, Stork B.

Manuscript submitted to Scientific Reports

Author contribution:

The author of this dissertation gave technical support, discussed the results and commented on the manuscript. Relative contribution: about 2%

3 Discussion

Despite major advances in recent decades in fields such as prevention, early detection, surgical techniques and chemotherapy, cancer remains one of the leading causes of death worldwide, as demonstrated by the fact that one in six deaths is still caused by cancer.²⁵⁵ Therapeutic failure after treatment with chemotherapeutics is frequently caused by premature termination of therapy due to excessive side effects. However, the main cause of therapy failure is either the initial presence of resistance-mediating somatic mutations in the signaling pathways targeted by anticancer drugs, or the development of such mutations under the evolutionary pressure exerted by both the toxic treatment conditions and the hostile microenvironment cancer cells are embedded in.²⁵⁶ The tyrosine kinase inhibitor imatinib is a shining example of the potency of targeted therapy approaches. By inhibiting a constitutively active tyrosine kinase encoded by the oncogenic fusion gene BCR-ABL, it can act as a “magic bullet” to inhibit leukemogenesis of chronic myelogenous leukemia (CML), resulting in complete and sustained hematological remission in most patients.²⁵⁷ The development and progression of very few cancers, however, can be traced back to a single mutation. And even if such a mutation can be identified, this does not necessarily mean that it can be pharmacologically addressed or that its inhibition stops further mutagenesis. Negative examples include inactivation of the tumor suppressor protein *retinoblastoma-associated protein* (RB1) as the driver of retinoblastoma development and the frequency of resistance emergence during treatment with the BRAF antagonist vemurafenib.^{258,259} The overwhelming majority of tumors are characterized by a pronounced genetic heterogeneity in which a large number of different mutations determine the phenotype, making targeted therapy difficult or even impossible.²⁶⁰ Casás-Selves *et al.* have provided a vividly illustration of the mutagenic potency of cancer by pointing out that a similar number of generations can occur in the development of an adult tumor as in the complete evolutionary development of *Homo sapiens*.²⁶¹ Due to this incontrovertible reality, it is still necessary to fight cancer conventionally through the induction of cell death. Ideally, this is done by induction of apoptosis rather than necrosis to prevent uncontrollable inflammatory events, rapidly to avoid therapy-induced potential resistance-mediating mutations, as well as via non-canonical signaling pathways to maintain efficacy even in already resistant tumors.

In the search for new potent apoptosis inducers, the importance of nature as an almost infinite source of bioactive substances should not be underestimated. Paclitaxel as a representative of plant-derived drugs, mitomycin C as a representative of drugs derived from microorganisms or cytarabine as a representative of marine substances are just a few examples of the many important anticancer drugs directly isolated or adapted from natural sources.^{215,262,263}

In order to identify new potent apoptosis inducers with promising properties for future therapeutic use from natural sources, we have applied a tiered strategy. As a first pre-selection, we specifically used host organisms for the isolation of natural products whose habitat exhibits high biodiversity. The inherent competition in these habitats leads to an intensified evolutionary pressure and promotes the biogenesis of bioactive compounds for defense purposes, which increases the probability to discover valuable compounds there. In the first experimental stage, we pre-sorted natural products for the presence of bioactivity by measuring cytotoxicity in Ramos cells (human Burkitt's lymphoma B lymphocytes) and Jurkat cells (human acute T-cell leukemia T lymphocytes). Substances that proved to be particularly cytotoxic in the used cancer cell lines were subsequently characterized in a second step with respect to their potency to induce apoptosis. Necrosis-inducing substances were sorted out due to their unsuitability for therapeutic use and were not further investigated. In a third step, we tested the natural products for specificity against cancer cells by investigating possible toxic effects on hematopoietic stem and progenitor cells (HSPC) as well as peripheral blood mononuclear cells (PBMCs) from healthy donors using cytotoxicity tests and colony forming assays. Finally, we further characterized the molecular mechanisms of viriditoxin (VDT), the compound that offered the most convincing overall profile of strong and rapid apoptosis induction on the one hand and lower off-target toxicity on the other. The functionality of our approach was demonstrated by the identification of several natural products and natural product-derived compounds as apoptosis inducers, which culminated in a double-digit number of publications.²⁶⁴⁻²⁷⁴ For these substances a variety of different proapoptotic mechanisms such as oxidative stress, mediation of autophagy, inhibition of the electron transport chain, multifaceted disturbance of mitochondrial homeostasis and pan-kinase inhibition could be shown and moreover for two substances, VDT and 4,5,6-tribromo-2-(2',4'-dibromophenoxy)phenol (TBDP) distinct specificity to cancer could be demonstrated.

Already in 2013, Rönnsberg *et al.* identified the tetrahydroxanthone dimer phomoxanthone A (PXA) as a potent apoptosis stimulus in Jurkat cells. The compound was extracted from the endophytic fungus *Phomopsis longicolla*, which was isolated and cultivated from leaves of the plant *Sonneratia caseolaris*. In this study, PXA was attributed two features that particularly qualified the substance for further investigation of the underlying mechanism of apoptosis induction. First, healthy PBMCs were found to be approximately 100 times less sensitive to PXA-mediated cytotoxicity, indicating specificity of PXA to cancer and second, PXA was shown to be capable of inducing apoptosis in DG-75 cells, suggesting efficacy against cancer with deregulated pathways of intrinsic apoptosis.²⁷⁵ DG-75 cells are exceptionally resistant to BAK/BAX-dependent apoptosis since their BAK/BAX genes are expressed but not translated into functional proteins, probably due to post-translational gene silencing.^{276,277} In our follow-up study, we could demonstrate that PXA acts directly on the mitochondria and triggers a variety of effects such

as the release of mitochondrial Ca^{2+} , depolarization of the mitochondria, inhibition of ETC and cellular respiration as well as fragmentation of the inner but not the outer mitochondrial membrane, resulting in release of cytochrome c and SMAC and execution of intrinsic apoptosis.²⁶⁶ The selectivity of PXA towards cancer cells reported by Rönnsberg *et al.* could not be reproduced in our later experiments. When the study of Rönnsberg *et al.* was published, the low stability of PXA in organic solvents was not yet known, therefore it cannot be excluded that in the experiments performed with PBMCs already isomerized and therefore inactive PXA was used. Even if the substance thus appears unsuitable for therapeutic use, its unique mechanism of fragmentation of the inner mitochondrial membrane renders it relevant for the study of mitochondrial dynamics. In fact, we could show that PXA is capable of inducing exclusive fragmentation of the inner mitochondrial membrane within seconds without affecting the outer mitochondrial membrane, independent of the known canonical effectors of mitochondrial fission, OPA1 and DRP1. This unexpected result raises questions regarding the comprehensiveness of our current understanding of the mitochondrial fission machinery. A profound understanding of these processes and possible alterations in cancer cells is of great importance for the applicability in cancer therapy. Based on the cumulative evidence that the mitochondrial fusion and fission machinery can represent a vulnerability of cancer cells, there are ongoing attempts to pharmacologically exploit it by means of suitable inhibitors or activators. Several inhibitors have already been specifically developed for DRP1, which is upregulated in many types of cancer and whose function is required for the rapid proliferation of cancer cells, for example due to its importance for the mitochondrial division during mitosis.²⁷⁸⁻²⁸¹ Increased DRP1 activity also enhances apoptosis, consequently it has been shown that activation of DRP1 by natural products in cancer cells can cause them to die.^{156,282} Furthermore, the gene expression levels of OMA1 and OPA1 are known to be a strong predictive marker for the overall survival of cancer patients with certain cancers. Inhibition of OMA1 has therefore been suggested as a potential target for cancer therapy, but so far, no specific OMA1 inhibitor has been identified.²⁸³ For OPA1, which mediates its antiapoptotic effect by preserving mitochondrial cristae structure, a small-molecule inhibitor has recently been presented and its efficacy in cancer cells was demonstrated.^{150,151,284}

Our characterization of PXA as a potent mitochondrial toxin brought the mitochondria into our focus as a potential target of natural products and consequently led to the discovery of further mitochondrial toxins. One of these substances is arzanol, a phloroglucinol α -pyrone isolated from *Helichrysum italicum*.²⁸⁵ Originally brought into our focus when screening for autophagy inhibitors, we subsequently showed that it causes OPA1 cleavage and fragmentation of both the inner and outer mitochondrial membrane and inhibits the complexes of ETC, in particular complex II and complex III. In addition, we demonstrated that co-treatment with arzanol sensitizes bladder cancer to cisplatin, further confirming

that mitochondria are an excellent target for cancer elimination (publication in preparation, see chapter 2.1.12). Strong inhibition of autophagy in combination with induction of apoptosis and high efficacy in cancer cells we could also observe for the natural compound daldinone I, isolated from the endophytic fungus *Annulohypoxyton sp.*, which was obtained from the mangrove plant *Rhizophora racemosa*.²⁶⁷

When screening natural products previously characterized by us as apoptosis inducers for selectivity towards cancer cells, the first substance that appeared less toxic in PBMCs than in the tested leukemia or lymphoma cell lines was the polybrominated diphenyl ether derivative 4,5,6-tribromo-2-(2',4'-dibromophenoxy)phenol (TBDP) derived from the marine sponge *Dysidea sp.* The selectivity of the substance is shown by reduced cytotoxicity and less potent induction of apoptosis in PBMCs, and the fact that it hardly affects the colony-forming capacity of healthy HSPC, even at concentrations above the IC₅₀ values determined for the cancer cell lines. Interestingly, Arai *et al.* reported that the highly structurally related 3,4,5-tribromo-2-(2',4'-dibromophenoxy)-phenol acts by inhibiting complex I, suggesting a similar mechanism of action for TBDP and further emphasizing the electron transport chain as a valuable target for cancer elimination.²⁸⁶ However, TBDP does not fully meet the requirements of an ideal drug candidate, as it exhibits only moderate potency, a comparatively long onset of its effects and a mild specificity, which suggests a narrow therapeutic range.²⁷¹

As a substance which, like PXA, acts directly on the mitochondria but shows a higher stability in solvents and, like TBDP, displays selectivity towards cancer cells, we were able to identify the mycotoxin viriditoxin (VDT). In comparison to TBDP, VDT acts faster and more potent and offers a higher specificity. In addition, like PXA, it can induce apoptosis in BAK/BAX double-deficient DG-75 cells (unpublished data). The VDT we used for our experiments was isolated from *Cladosporium cladosporioides*, but in principle the substance is formed by various fungi, including *Aspergillus fumigatus*, *Aspergillus viridinutans*, *Aspergillus brevipipes* and *Paecilomyces variotii* (formerly named as *Spicaria divaricata*) which were found in habitats as diverse as herbivore dung, sediments of a hypersaline lake or inside the jellyfish *Nemopilema nomurai*.²⁸⁷⁻²⁹¹ The ubiquitous production of VDT by different organisms indicates its high bioactivity, which provides survival advantages for the host organisms. These will primarily be attributable to the strong antibiotic activity of VDT.²⁸⁸ Given the assumed bacterial origin of mitochondria, it is not surprising that many antibiotics can exert toxic effects on mammalian mitochondria.²⁹²⁻²⁹⁵ The antibiotic activity of VDT is mediated by inhibition of the bacterial cell division protein FtsZ.²⁸⁸ Consequently, Kundu *et al.* suggested that the mild apoptosis induction by VDT they observed in prostate cancer cells can be attributed to the inhibition of tubulin, which is a close structural homologue of bacterial FtsZ.²⁸⁹

Nevertheless, we were able to show that the potent and rapid apoptosis initiation in our cell system is not due to an effect of VDT on tubulin polymerization, but rather to direct damage to the mitochondria.

This is reflected by cleavage of OPA1 within minutes, depolarization and fragmentation of the mitochondria, induction of ROS and inhibition of ETC, especially complex I (publication in preparation, see chapter 2.1.13). In comparison with PXA, whose mode of action is in many respects similar to that of VDT, the differences in the induction of mitochondrial fragmentation and the associated processing of OPA1 are particularly noticeable. VDT causes a loss of L-OPA1 within 15 - 30 min, which is of a reversible nature since the stress-induced activation of OMA1 as an OPA1-processing protease is generally accompanied by an autocatalytic inactivation of the protease. In contrast, PXA causes irreversible OPA1 cleavage in less than 5 minutes, suggesting a deviating mechanism of OPA1 cleavage. Moreover, the mitochondrial fragmentation also occurs significantly faster upon treatment with PXA (within seconds) and is not dependent on the canonical fission mediator DRP1. The rapidity of the effect suggests an immediate, unregulated effect on the mitochondrial membrane, which similarly occurs in the mitochondria of untransformed cells and could thus explain the lack of selectivity of PXA compared to VDT. Since we could observe cleavage of OPA1 for several natural compounds (VDT, PXA, arzanol), we examined if OPA1 cleavage is not just a ubiquitous event in the course of intrinsic apoptosis. This is not the case, as we could determine by testing a panel of intrinsic apoptosis inducers including paclitaxel, staurosporine and vinblastine regarding OPA1 cleavage (unpublished data).

First attempts to elucidate the molecular target of VDT using thermal proteome profiling indicate an involvement of the mitochondrial ribosomes. Furthermore, we could show for the first time that lymphoma cells are more than 20 times more sensitive to VDT-mediated effects than healthy HSPC. In summary, the strong potency, rapid mechanism, high selectivity and stability in solution encourage further investigation of VDT as a lead compound for anticancer drug development. The rise of combinatorial chemistry in the last decades led to the demand of predicting the druglikeness of a substance and to the formulation of Lipinski's Rule of 5, which states that an orally bioavailable substance should have a logP less than 5, a molecular mass less than 500 g/mol, a number of hydrogen bond acceptors less than 10, and a number of hydrogen bond donors less than 5.²⁹⁶ VDT fulfills only three of these rules (miLogP of 4.08 predicted by *Molinspiration property engine* v2018.10)²⁹⁷ since its molecular mass is above 600 g/mol and the sum of its hydrogen bond acceptors is 14. However, oral bioavailability is of little relevance for anticancer drugs that are usually administered intravenously. Moreover, we could not detect any problems with VDT's permeability into lipophilic environments such as the cell membrane, given that intracellular effects occurred within minutes. Future lead optimization processes benefit from the fact that several synthesis routes of VDT have been published and that its biosynthesis is comparably well understood.^{287,298} Open questions, which should be addressed before conducting future in vivo tests, are to which extent mitochondrial ribosomes are involved in the observed processes and whether co-treatment with apoptosis modulators could further

enhance the potency of the VDT. Due to the induction of the intrinsic apoptosis route and the limited BAK/BAX dependence, the combination of VDT with IAP inhibitors seems particularly promising. IAPs are pathologically up-regulated in many cancers and the efficacy of their inhibition to enhance the effect of intrinsic apoptosis inducers has been shown repeatedly.²⁹⁹⁻³⁰³

In extension to our approach to screen isolated natural compounds for bioactivity, we tested a number of meriolin derivatives structurally similar to natural products, that have been synthesized in the laboratory of Prof. Thomas J. J. Müller (Institute for Organic Chemistry and Macromolecular Chemistry, HHU Düsseldorf) for their ability to induce apoptosis. Meriolins carry structural motifs of the meridianins originating from *Ascidia Aplidium meridianum* as well as of the variolins isolated from the sponge *Kirkpatrickia variolosa*.³⁰⁴ We could characterize the synthesized derivatives as kinase inhibitors and potent apoptosis inducers.²⁶⁸ Similarities in target profile and kinetics to the well-known pan-kinase inhibitor staurosporine (STS) suggest a similar mechanism. Since STS is able to induce intrinsic apoptosis independent of apoptosome formation and is therefore prototypical for targeting cancer cells with a mutated intrinsic pathway, future studies will have to show whether meriolins are able to do so.¹⁷¹

In summary, we have identified on the one hand several natural products that selectively induce apoptosis in cancer cells and are therefore promising candidates as lead compounds for drug development in cancer therapy. On the other hand, we were able to characterize PXA as a substance which, due to its unique mechanism of fragmentation of the inner mitochondrial membrane, may in the future be a valuable tool for a deeper understanding of the dynamic processes to which the mitochondrial membranes are subject. Furthermore, the characterization of meriolin derivatives as potent apoptosis inducers has underlined that nature is not only of tremendous value as a direct source of bioactive compounds, but that the structural diversity of natural compounds can be effectively used as templates for the synthesis of new proapoptotic substance classes.

4 References

- 1 Renehan AG, Booth C, Potten CS. (2001) What is apoptosis, and why is it important ? *BMJ* **322**:1536–1538. doi:10.1136/bmj.322.7301.1536.
- 2 Elmore S. (2007) Apoptosis: a review of programmed cell death. *Toxicol Pathol* **35**:495–516. doi:10.1080/01926230701320337.
- 3 Favaloro B, Allocati N, Graziano V, De Ilio C, De Laurenzi V. (2012) Role of apoptosis in disease. *Aging (Albany NY)* **4**:330–349. doi:10.18632/aging.100459.
- 4 Cohen GM. (1997) Caspases: the executioners of apoptosis. *Biochem J* **326**:1–16. doi:10.1042/bj3260001.
- 5 Diamantis A, Magiorkinis E, Sakorafas GH, Androutsos G. (2008) A brief history of apoptosis: From ancient to modern times. *Onkologie* **31**:702–706. doi:10.1159/000165071.
- 6 Müller-Wille S. (2010) Cell theory, specificity, and reproduction, 1837 – 1870. *Stud Hist Philos Biol Biomed Sci* **41**:225–231. doi:10.1016/j.shpsc.2010.07.008.Cell.
- 7 Cotter TG. (2009) Apoptosis and cancer: The genesis of a research field. *Nat Rev Cancer* **9**:501–507. doi:10.1038/nrc2663.
- 8 Paweletz N. (2001) Walther Flemming: pioneer of mitosis research. *Nat Rev Mol Cell Biol* **2**:72–75. doi:10.1038/35048077.
- 9 Glücksmann A. (1951) Cell deaths in normal vertebrate ontogeny. *Biol Rev Camb Philos Soc* **26**:59–86. doi:10.1111/j.1469-185x.1951.tb00774.x.
- 10 Kerr JFR. (1965) A histochemical study of hypertrophy and ischaemic injury of rat liver with special reference to changes in lysosomes. *J Pathol Bacteriol* **90**:419–435. doi:10.1002/path.1700900210.
- 11 Lockshin RA, Williams CM. (1965) Programmed cell death - I. Cytology of degeneration in the intersegmental muscles of the Pernyi silkmoth. *J Insect Physiol* **11**:123–133. doi:10.1016/0022-1910(65)90099-5.
- 12 Kerr JFR, Wyllie AH, Currie AR. (1972) Apoptosis: A basic biological phenomenon with wide-ranging implications in tissue kinetics. *Br J Cancer* **26**:239–257. doi:10.1038/bjc.1972.33.
- 13 Wyllie AH. (1980) Glucocorticoid-induced thymocyte apoptosis is associated with endogenous endonuclease activation. *Nature* **284**:555–556. doi:10.1038/284555a0.

- 14 Wyllie AH, Kerr JFR, Currie AR. (1980) Cell death : The significance of apoptosis. *Int Rev Cytol* **68**:251–306. doi:10.1016/s0074-7696(08)62312-8.
- 15 Chittenden T, Harrington EA, Connor RO, Flemington C, ... Guild BC. (1995) Induction of apoptosis by the Bcl-2 homologue Bak. *Nature* **374**:733–736. doi:10.1038/374733a0.
- 16 Trauth BC, Kias C, Peters AMJ, Matzku S, ... Krammer PH. (1989) Monoclonal antibody-mediated tumor regression by induction of apoptosis. *Science* **245**:301–305. doi:10.1126/science.2787530.
- 17 Yonehara S, Ishii A, Yonehara M. (1989) A cell-killing monoclonal antibody (anti-Fas) to a cell surface antigen co-downregulated with the receptor of tumor necrosis factor. *J Exp Med* **169**:1747–1756. doi:10.1084/jem.169.5.1747.
- 18 Itoh N, Yonehara S, Ishii A, Yonehara M, ... Nagata S. (1991) The polypeptide encoded by the cDNA for human cell surface antigen Fas can mediate apoptosis. *Cell* **66**:233–243. doi:10.1016/0092-8674(91)90614-5.
- 19 Vaux DL, Cory S, Adams JM. (1988) Bcl-2 gene promotes haemopoietic cell survival and cooperates with c-myc to immortalize pre-B cells. *Nature* **335**:440–442. doi:10.1038/335440a0.
- 20 Du C, Fang M, Li Y, Li L, Wang X. (2000) Smac, a mitochondrial Protein that promotes cytochrome c – dependent caspase activation by eliminating IAP inhibition. *Cell* **102**:33–42. doi:10.1016/S0092-8674(00)00008-8.
- 21 Oltvai ZN, Milkman CL, Korsmeyer SJ. (1993) Bcl-2 heterodimerizes in vivo with a conserved homolog, Bax, that accelerates programmed cell death. *Cell* **74**:609–619. doi:10.1016/0092-8674(93)90509-o.
- 22 Ellis HM, Horvitz HR. (1986) Genetic control of programmed cell death in the nematode *C. elegans*. *Cell* **44**:817–829. doi:10.1016/0092-8674(86)90004-8.
- 23 Ernest NJ, Habela CW, Sontheimer H. (2008) Cytoplasmic condensation is both necessary and sufficient to induce apoptotic cell death. *J Cell Sci* **121**:290–297. doi:10.1242/jcs.017343.
- 24 Wei L, Ai YX, Jin C, Yang A, ... Shan PY. (2004) Effects of chloride and potassium channel blockers on apoptotic cell shrinkage and apoptosis in cortical neurons. *Pflugers Arch Eur J Physiol* **448**:325–334. doi:10.1007/s00424-004-1277-2.
- 25 Nietsch HH, Roe MW, Fiekers JF, Moore AL, Lidofsky SD. (2000) Activation of potassium and chloride channels by tumor necrosis Factor α . *J Biol Chem* **275**:20556–20561. doi:10.1074/jbc.M002535200.

- 26 Wickman G, Julian L, Olson MF. (2012) How apoptotic cells aid in the removal of their own cold dead bodies. *Cell Death Differ* **19**:735–742. doi:10.1038/cdd.2012.25.
- 27 Mills JC, Stone NL, Erhardt J, Pittman RN. (1998) Apoptotic membrane blebbing is regulated by myosin light chain phosphorylation. *J Cell Biol* **140**:627–636. doi:10.1083/jcb.140.3.627.
- 28 McCarthy NJ, Whyte MKB, Gilbert CS, Evan GI. (1997) Inhibition of Ced-3/ICE-related proteases does not prevent cell death induced by oncogenes, DNA damage, or the Bcl-2 homologue Bak. *J Cell Biol* **136**:215–227. doi:10.1083/jcb.136.1.215.
- 29 Zheng TS, Schlosser SF, Dao T, Hingorani R, ... Flavell RA. (1998) Caspase-3 controls both cytoplasmic and nuclear events associated with Fas-mediated apoptosis in vivo. *Proc Natl Acad Sci U S A* **95**:13618–13623. doi:10.1073/pnas.95.23.13618.
- 30 Jänicke RU, Ng P, Sprengart ML, Porter AG. (1998) Caspase-3 is required for α -fodrin cleavage but dispensable for cleavage of other death substrates in apoptosis. *J Biol Chem* **273**:15540–15545. doi:10.1074/jbc.273.25.15540.
- 31 Charras GT, Hu C-K, Coughlin M, Mitchison TJ. (2006) Reassembly of contractile actin cortex in cell blebs. *J Cell Biol* **175**:477–490. doi:10.1083/jcb.200602085.
- 32 Coleman ML, Sahai EA, Yeo M, Bosch M, ... Olson MF. (2001) Membrane blebbing during apoptosis results from caspase-mediated activation of ROCK I. *Nat Cell Biol* **3**:339–346. doi:10.1038/35070009.
- 33 Zhang Y, Chen X, Gueydan C, Han J. (2018) Plasma membrane changes during programmed cell deaths. *Cell Res* **28**:9–21. doi:10.1038/cr.2017.133.
- 34 Fackler OT, Grosse R. (2008) Cell motility through plasma membrane blebbing. *J Cell Biol* **181**:879–884. doi:10.1083/jcb.200802081.
- 35 Toné S, Sugimoto K, Tanda K, Suda T, ... Earnshaw WC. (2007) Three distinct stages of apoptotic nuclear condensation revealed by time-lapse imaging, biochemical and electron microscopy analysis of cell-free apoptosis. *Exp Cell Res* **313**:3635–3644. doi:10.1016/j.yexcr.2007.06.018.
- 36 Susin SA, Lorenzo HK, Zamzami N, Marzo I, ... Kroemer G. (1999) Molecular characterization of mitochondrial apoptosis-inducing factor. *Nature* **39**:441–446. doi:10.1038/17135.
- 37 Enari M, Sakahiri H, Yokoyama H, Okawa K, ... Nagata S. (1998) Acaspase-activated DNase that degrades DNA during apoptosis, and its inhibitor ICAD. *Nature* **391**:43–50. doi:10.1038/34112.

- 38 Sakahira H, Enari M, Ohsawa Y, Uchiyama Y, Nagata S. (1999) Apoptotic nuclear morphological change without DNA fragmentation. *Curr Biol* **9**:543–546. doi:10.1016/s0960-9822(99)80240-1.
- 39 Setsuko S, Aoto M, Eguchi Y, Imamto N, ... Tsujimoto Y. (1999) Acinus is a caspase-3-activated protein required for apoptotic chromatin condensation. *Nature* **401**:168–173. doi:10.1038/43678.
- 40 Yuste VJ, Sanchez-Lopez I, Sole C, Moubarak RS, ... Comella JX. (2005) The Contribution of apoptosis-inducing factor, caspase-activated DNase, and inhibitor of caspase-activated DNase to the nuclear phenotype and DNA degradation during apoptosis. *J Biol Chem* **280**:35670–35683. doi:10.1074/jbc.M504015200.
- 41 Samejima K, Tone S, Earnshaw WC. (2001) CAD/DFF40 nuclease is dispensable for high molecular weight DNA cleavage and stage I chromatin condensation in apoptosis. *J Biol Chem* **276**:45427–45432. doi:10.1074/jbc.M108844200.
- 42 Joselin AP, Schulze-Osthoff K, Schwerk C. (2006) Loss of acinus inhibits oligonucleosomal DNA fragmentation but not chromatin condensation during apoptosis. *J Biol Chem* **281**:12475–12484. doi:10.1074/jbc.M509859200.
- 43 Errami Y, Naura AS, Kim H, Ju J, ... Boulares AH. (2013) Apoptotic DNA fragmentation may be a cooperative activity between caspase-activated deoxyribonuclease and the poly(ADP-ribose) polymerase-regulated DNAS1L3, an endoplasmic reticulum-localized endonuclease that translocates to the nucleus during apoptosis. *J Biol Chem* **288**:3460–3468. doi:10.1074/jbc.M112.423061.
- 44 Collins JA, Schandl CA, Young KK, Vesely J, Willingham MC. (1997) Major DNA fragmentation is a late event in apoptosis. *J Histochem Cytochem* **45**:923–934. doi:10.1177/002215549704500702.
- 45 Liu X, Li P, Widlak P, Zou H, ... Wang X. (1998) The 40-kDa subunit of DNA fragmentation factor induces DNA fragmentation and chromatin condensation during apoptosis. *Proc Natl Acad Sci U S A* **95**:8461–8466. doi:10.1073/pnas.95.15.8461.
- 46 Liu X, Zou H, Slaughter C, Wang X. (1997) DFF, a heterodimeric protein that functions downstream of caspase-3 to trigger DNA fragmentation during apoptosis. *Cell* **89**:175–184. doi:10.1016/S0092-8674(00)80197-X.
- 47 Urbano A, McCaffrey R, Foss F. (1998) Isolation and characterization of NUC70, a cytoplasmic hematopoietic apoptotic endonuclease. *J Biol Chem* **273**:34820–34827.

- doi:10.1074/jbc.273.52.34820.
- 48 Los M, Neubüser D, Coy JF, Mozoluk M, ... Schulze-Osthoff K. (2000) Functional characterization of DNase X, a novel endonuclease expressed in muscle cells. *Biochemistry* **39**:7365–7373. doi:10.1021/bi000158w.
- 49 Oberhammer F, Wilson JW, Dive C, Morris ID, ... Sikorska M. (1993) Apoptotic death in epithelial cells: Cleavage of DNA to 300 and/or 50 kb fragments prior to or in the absence of internucleosomal fragmentation. *EMBO J* **12**:3679–3684. doi:10.1002/j.1460-2075.1993.tb06042.x.
- 50 Szegezdi E, Logue SE, Gorman AM, Samali A. (2006) Mediators of endoplasmic reticulum stress-induced apoptosis. *EMBO Rep* **7**:880–885. doi:10.1038/sj.embor.7400779.
- 51 Breckenridge DG, Germain M, Mathai JP, Nguyen M, Shore GC. (2003) Regulation of apoptosis by endoplasmic reticulum pathways. *Oncogene* **22**:8608–8618. doi:10.1038/sj.onc.1207108.
- 52 Soldani C, Croce AC, Bottone MG, Frascini A, ... Pellicciari C. (2007) Apoptosis in tumour cells photosensitized with rose bengal acetate is induced by multiple organelle photodamage. *Histochem Cell Biol* **128**:485–495. doi:10.1007/s00418-007-0333-3.
- 53 Bottone MG, Santin G, Aredia F, Bernocchi G, ... Scovassi AI. (2013) Morphological features of organelles during spoptosis: an overview. *Cells* **2**:294–305. doi:10.3390/cells2020294.
- 54 Lane JD, Allan VJ, Woodman PG. (2005) Active relocation of chromatin and endoplasmic reticulum into blebs in late apoptotic cells. *J Cell Sci* **118**:4059–4071. doi:10.1242/jcs.02529.
- 55 Day KJ, Staehelin LA, Glick BS. (2013) A three-stage model of golgi structure and function. *Histochem Cell Biol* **140**:239–249. doi:10.1007/s00418-013-1128-3.
- 56 Jiang Z, Hu Z, Zeng L, Lu W, ... Xiao H. (2011) The role of the Golgi apparatus in oxidative stress: Is this organelle less significant than mitochondria? *Free Radic Biol Med* **50**:907–917. doi:10.1016/j.freeradbiomed.2011.01.011.
- 57 Machamer CE. (2003) Golgi disassembly in apoptosis: Cause or effect? *Trends Cell Biol* **13**:279–281. doi:10.1016/S0962-8924(03)00101-6.
- 58 Lane JD, Lucocq J, Pryde J, Barr FA, ... Lowe M. (2002) Caspase-mediated cleavage of the stacking protein GRASP65 is required for Golgi fragmentation during apoptosis. *J Cell Biol* **156**:495–509. doi:10.1083/jcb.200110007.
- 59 Mancini M, Machamer CE, Roy S, Nicholson DW, ... Rosen A. (2000) Caspase-2 is localized at the golgi complex and cleaves Golgin-160 during apoptosis. *J Cell Biol* **149**:603–612.

- doi:10.1083/jcb.149.3.603.
- 60 Chiu R, Novikov L, Mukherjee S, Shields D. (2002) A caspase cleavage fragment of p115 induces fragmentation of the Golgi apparatus and apoptosis. *J Cell Biol* **159**:637–648. doi:10.1083/jcb.200208013.
- 61 Guicciardi ME, Leist M, Gores GJ. (2004) Lysosomes in cell death. *Oncogene* **23**:2881–2890. doi:10.1038/sj.onc.1207512.
- 62 Stoka V, Turk V, Turk B. (2007) Lysosomal cysteine cathepsins: Signaling pathways in apoptosis. *Biol Chem* **388**:555–560. doi:10.1515/BC.2007.064.
- 63 Yap YW, Whiteman M, Bay BH, Li Y, ... Cheung NS. (2006) Hypochlorous acid induces apoptosis of cultured cortical neurons through activation of calpains and rupture of lysosomes. *J Neurochem* **98**:1597–1609. doi:10.1111/j.1471-4159.2006.03996.x.
- 64 Kågedal K, Johansson AC, Johansson U, Heimlich G, ... Öllinger K. (2005) Lysosomal membrane permeabilization during apoptosis - Involvement of Bax? *Int J Exp Pathol* **86**:309–321. doi:10.1111/j.0959-9673.2005.00442.x.
- 65 Stoka V, Turk B, Schendel SL, Kim TH, ... Salvesen GS. (2001) Lysosomal protease pathways to apoptosis: Cleavage of Bid, not pro-caspases, is the most likely route. *J Biol Chem* **276**:3149–3157. doi:10.1074/jbc.M008944200.
- 66 Ravichandran KS. (2010) Find-me and eat-me signals in apoptotic cell clearance: progress and conundrums. *J Exp Med* **207**:1807–1817. doi:10.1084/jem.20101157.
- 67 Peter C, Wesselborg S, Herrmann M, Lauber K. (2010) Dangerous attraction: phagocyte recruitment and danger signals of apoptotic and necrotic cells. *Apoptosis* **15**:1007–1028. doi:10.1007/s10495-010-0472-1.
- 68 Ravichandran KS. (2011) Beginnings of a good apoptotic meal: the find-me and eat-me signaling pathways. *Immunity* **35**:445–455. doi:10.1016/j.immuni.2011.09.004.
- 69 Bournazou I, Pound JD, Duffin R, Bournazos S, ... Gregory CD. (2009) Apoptotic human cells inhibit migration of granulocytes via release of lactoferrin. *J Clin Invest* **119**:20–32. doi:10.1172/JCI36226.20.
- 70 Borisenko GG, Matsura T, Liu S-X, Tyurin VA, ... Kagan VE. (2003) Macrophage recognition of externalized phosphatidylserine and phagocytosis of apoptotic Jurkat cells — existence of a threshold. *Arch Biochem Biophys* **413**:41–52. doi:10.1016/S0003-9861(03)00083-3.

- 71 Segawa K, Nagata S. (2015) An apoptotic 'eat me' signal: phosphatidylserine exposure. *Trends Cell Biol* **25**:639–650. doi:10.1016/j.tcb.2015.08.003.
- 72 Monks J, Smith-Steinhart C, Kruk ER, Fadok VA, Henson PM. (2008) Epithelial cells remove apoptotic epithelial cells during post-lactation involution of the mouse mammary gland. *Biol Reprod* **78**:586–594. doi:10.1095/biolreprod.107.065045.
- 73 Vanden Berghe T, Grootjans S, Goossens V, Dondelinger Y, ... Vandenabeele P. (2013) Determination of apoptotic and necrotic cell death in vitro and in vivo. *Methods* **61**:117–129. doi:10.1016/j.ymeth.2013.02.011.
- 74 Lecoeur H, Prévost M-C, Gougeon M-L. (2001) Oncosis is associated with exposure of phosphatidylserine residues on the outside layer of the plasma membrane: A reconsideration of the specificity of the annexin V/propidium iodide assay. *Cytometry* **44**:65–72. doi:10.1002/1097-0320(20010501)44:1<65::AID-CYTO1083>3.0.CO;2-Q.
- 75 Rello S, Stockert JC, Moreno V, Pacheco M, ... Villanueva A. (2005) Morphological criteria to distinguish cell death induced by apoptotic and necrotic treatments. *Apoptosis* **10**:201–208. doi:10.1007/s10495-005-6075-6.
- 76 Galluzzi L, Vitale I, Abrams JM, Alnemri ES, ... Kroemer G. (2012) Molecular definitions of cell death subroutines: Recommendations of the Nomenclature Committee on Cell Death 2012. *Cell Death Differ* **19**:107–120. doi:10.1038/cdd.2011.96.
- 77 McIlwain DR, Berger T, Mak TW. (2013) Caspase functions in cell death and disease. *Cold Spring Harb Perspect Biol* **5**:a008656. doi:10.1101/cshperspect.a008656.
- 78 Shalini S, Dorstyn L, Dawar S, Kumar S. (2015) Old, new and emerging functions of caspases. *Cell Death Differ* **22**:526–539. doi:10.1038/cdd.2014.216.
- 79 Julien O, Wells JA. (2017) Caspases and their substrates. *Cell Death Differ* **24**:1380–1389. doi:10.1038/cdd.2017.44.
- 80 Latz E, Xiao TS, Stutz A. (2013) Activation and regulation of the inflammasomes. *Nat Rev Immunol* **13**:397–411. doi:10.1038/nri3452.
- 81 Kovalenko A, Kim J, Kang T, Rajput A, ... Wallach D. (2009) Caspase-8 deficiency in epidermal keratinocytes triggers an inflammatory skin disease. *J Exp Med* **206**:2161–2177. doi:10.1084/jem.20090616.
- 82 Mizushima N, Levine B, Cuervo AM, Klionsky DJ. (2008) Autophagy fights disease through cellular self-digestion. *Nature* **451**:1069–1075. doi:10.1038/nature06639.

- 83 Zhu Y, Zhao L, Liu L, Gao P, ... Chen Q. (2010) Beclin 1 cleavage by caspase-3 inactivates autophagy and promotes apoptosis. *Protein Cell* **1**:468–477. doi:10.1007/s13238-010-0048-4.
- 84 Norman JM, Cohen GM, Bampton ETW. (2010) The in vitro cleavage of the hAtg proteins by cell death proteases. *Autophagy* **6**:1042–1056. doi:10.4161/auto.6.8.13337.
- 85 You M, Savaraj N, Kuo MT, Wangpaichitr M, ... Feun L. (2013) TRAIL induces autophagic protein cleavage through caspase activation in melanoma cell lines under arginine deprivation. *Mol Cell Biochem* **374**:181–190. doi:10.1007/s11010-012-1518-1.
- 86 Matsuzawa Y, Oshima S, Nibe Y, Kobayashi M, ... Watanabe M. (2015) RIPK3 regulates p62 – LC3 complex formation via the caspase-8-dependent cleavage of p62. *Biochem Biophys Res Commun* **456**:298–304. doi:10.1016/j.bbrc.2014.11.075.
- 87 Bergsbaken T, Fink SL, Cookson BT. (2009) Pyroptosis: host cell death and inflammation. *Nat Rev Microbiol* **7**:99–109. doi:10.1038/nrmicro2070.
- 88 Fink SL, Cookson BT. (2006) Caspase-1-dependent pore formation during pyroptosis leads to osmotic lysis of infected host macrophages. *Cell Microbiol* **8**:1812–1825. doi:10.1111/j.1462-5822.2006.00751.x.
- 89 Yuan J, Najafov A, Py B. (2016) Roles of caspases in necrotic cell death. *Cell* **167**:1693–1704. doi:10.1016/j.cell.2016.11.047.
- 90 Vitale I, Manic G, Castedo M, Kroemer G. (2017) Caspase 2 in mitotic catastrophe: The terminator of aneuploid and tetraploid cells. *Mol Cell Oncol* **4**:e1299274. doi:10.1080/23723556.2017.1299274.
- 91 Sprick MR, Rieser E, Stahl H, Grosse-Wilde A, ... Walczak H. (2002) Caspase-10 is recruited to and activated at the native TRAIL and CD95 death-inducing signalling complexes in a FADD-dependent manner but can not functionally substitute caspase-8. *EMBO J* **21**:4520–4530. doi:10.1093/emboj/cdf441.
- 92 Horn S, Hughes MA, Schilling R, Sticht C, ... Leverkus M. (2017) Caspase-10 negatively regulates caspase-8-mediated cell death, switching the response to CD95L in favor of NF-κB activation and Cell survival. *Cell Rep* **19**:785–797. doi:10.1016/j.celrep.2017.04.010.
- 93 Sladky VC, Villunger A. (2020) Uncovering the PIDDosome and caspase-2 as regulators of organogenesis and cellular differentiation. *Cell Death Differ* **27**:2037–2047. doi:10.1038/s41418-020-0556-6.
- 94 Yamanaka H, Penning CA, Willis EH, Wasson DB, Carson DA. (1989) Characterization of

- poly(ADP-ribose) polymerase with human autoantibodies. *Adv Exp Med Biol* **253B**:259–265. doi:10.1007/978-1-4684-5676-9_38.
- 95 Formentini L, Macchiarulo A, Cipriani G, Camaioni E, ... Chiarugi A. (2009) Poly(ADP-ribose) catabolism triggers AMP-dependent mitochondrial energy failure. *J Biol Chem* **284**:17668–17676. doi:10.1074/jbc.M109.002931.
- 96 Chaitanya GV, Alexander JS, Babu PP. (2010) PARP-1 cleavage fragments: Signatures of cell-death proteases in neurodegeneration. *Cell Commun Signal* **8**:31. doi:10.1186/1478-811X-8-31.
- 97 Mukherjee B, Kessinger C, Kobayashi J, Chen BPC, ... Burma S. (2006) DNA-PK phosphorylates histone H2AX during apoptotic DNA fragmentation in mammalian cells. *DNA Repair (Amst)* **5**:575–590. doi:10.1016/j.dnarep.2006.01.011.
- 98 Fattman CL, Delach SM, Dou QP, Johnson DE. (2001) Sequential two-step cleavage of the retinoblastoma protein by caspase-3/-7 during etoposide-induced apoptosis. *Oncogene* **20**:2918–2926. doi:10.1038/sj.onc.1204414.
- 99 Boutillier A-L, Trinh E, Loeffler J-P. (2000) Caspase-dependent cleavage of the retinoblastoma protein is an early step in neuronal apoptosis. *Oncogene* **19**:2171–2178. doi:10.1038/sj.onc.1203532.
- 100 Lavrik I, Golks A, Krammer PH. (2005) Death receptor signaling. *J Cell Sci* **118**:265–267. doi:10.1242/jcs.01610.
- 101 Sayers TJ. (2011) Targeting the extrinsic apoptosis signaling pathway for cancer therapy. *Cancer Immunol Immunother* **60**:1173–1180. doi:10.1007/s00262-011-1008-4.
- 102 Safa AR. (2013) Roles of c-FLIP in apoptosis, necroptosis, and autophagy. *J Carcinog Mutagen Suppl* **6**:003. doi:10.1038/jid.2014.371.
- 103 Tummers B, Green DR. (2017) Caspase-8; regulating life and death. *Immunol Rev* **277**:76–89. doi:10.1111/imr.12541.
- 104 Wei MC, Lindsten T, Mootha VK, Weiler S, ... Korsmeyer SJ. (2000) tBID, a membrane-targeted death ligand, oligomerizes BAK to release cytochrome c. *Genes Dev* **14**:2060–2071. doi:10.1101/gad.14.16.2060.
- 105 Li H, Zhu H, Xu C-J, Yuan J. (1998) Cleavage of BID by caspase 8 mediates the mitochondrial damage in the Fas pathway of apoptosis. *Cell* **94**:491–501. doi:10.1016/S0092-8674(00)81590-1.
- 106 Cosentino K, García-Sáez AJ. (2017) Bax and Bak pores: Are we closing the circle? Bax and Bak

- are key players in mitochondrial apoptosis. *Trends Cell Biol* **27**:266–275.
doi:10.1016/j.tcb.2016.11.004.
- 107 De Marchi U, Campello S, Tombola F, Martinou J-C, Zoratti M. (2004) Bax does not directly participate in the Ca²⁺-induced permeability transition of isolated mitochondria. *J Biol Chem* **279**:37415–37422. doi:10.1074/jbc.M314093200.
- 108 Wang C, Youle RJ. (2009) The role of mitochondria in apoptosis. *Annu Rev Genet* **43**:95–118. doi:10.1146/annurev-genet-102108-134850.
- 109 Bernardi P, Di Lisa F. (2015) The mitochondrial permeability transition pore: Molecular nature and role as a target in cardioprotection. *J Mol Cell Cardiol* **78**:100–106. doi:10.1016/j.yjmcc.2014.09.023.
- 110 Pastorino JG, Tafani M, Rothman RJ, Marcineviciute A, ... Farber JL. (1999) Functional consequences of the sustained or transient activation by Bax of the mitochondrial permeability transition pore. *J Biol Chem* **274**:31734–31739. doi:10.1074/jbc.274.44.31734.
- 111 Lorenzo HK, Susin SA, Penninger J, Kroemer G. (1999) Apoptosis inducing factor (AIF): a phylogenetically old, caspase-independent effector of cell death. *Cell Death Differ* **6**:516–524. doi:10.1038/sj.cdd.4400527.
- 112 Li LY, Luo X, Wang X. (2001) Endonuclease G is an apoptotic DNase when released from mitochondria. *Nature* **412**:95–99. doi:10.1038/35083620.
- 113 Yang Q-H, Du C. (2004) Smac/DIABLO selectively reduces the levels of c-IAP1 and c-IAP2 but not that of XIAP and Livin in HeLa cells. *J Biol Chem* **279**:16963–16970. doi:10.1074/jbc.M401253200.
- 114 Xiong S, Mu T, Wang G, Jiang X. (2014) Mitochondria-mediated apoptosis in mammals. *Protein Cell* **5**:737–749. doi:10.1007/s13238-014-0089-1.
- 115 Acehan D, Jiang X, Morgan DG, Heuser JE, ... Akey CW. (2002) Three-dimensional structure of the apoptosome: Implications for assembly, procaspase-9 binding, and activation. *Mol Cell* **9**:423–432. doi:10.1016/S1097-2765(02)00442-2.
- 116 Kim H-E, Du F, Fang M, Wang X. (2005) Formation of apoptosome is initiated by cytochrome c-induced dATP hydrolysis and subsequent nucleotide exchange on Apaf-1. *Proc Natl Acad Sci U S A* **102**:17545–17550. doi:10.1073/pnas.0507900102.
- 117 Kale J, Osterlund EJ, Andrews DW. (2018) BCL-2 family proteins: changing partners in the dance towards death. *Cell Death Differ* **25**:65–80. doi:10.1038/cdd.2017.186.

- 118 Silke J, Meier P. (2013) Inhibitor of apoptosis (IAP) proteins – modulators of cell death and inflammation. *Cold Spring Harb Perspect Biol* **5**:a008730.
- 119 Kroemer G, Galluzzi L, Brenner C. (2007) Mitochondrial membrane permeabilization in cell death. *Physiol Rev* **87**:99–163. doi:10.1152/physrev.00013.2006.
- 120 Shamas-Din A, Brahmabhatt H, Leber B, Andrews DW. (2011) BH3-only proteins: Orchestrators of apoptosis. *Biochim Biophys Acta* **1813**:508–520. doi:10.1016/j.bbamcr.2010.11.024.
- 121 Zong W, Lindsten T, Ross AJ, Macgregor GR, Thompson CB. (2001) BH3-only proteins that bind pro-survival Bcl-2 family members fail to induce apoptosis in the absence of Bax and Bak. *Genes Dev* **15**:1481–1486. doi:10.1101/gad.897601.
- 122 Oberoi-Khanuja TK, Murali A, Rajalingam K. (2013) IAPs on the move: role of inhibitors of apoptosis proteins in cell migration. *Cell Death Dis* **4**:e784. doi:10.1038/cddis.2013.311.
- 123 MacFarlane M, Merrison W, Bratton SB, Cohen GM. (2002) Proteasome-mediated degradation of Smac during apoptosis : XIAP promotes Smac ubiquitination in vitro. *J Biol Chem* **277**:36611–36616. doi:10.1074/jbc.M200317200.
- 124 Hegde R, Srinivasula SM, Zhang Z, Wassell R, ... Alnemri ES. (2002) Identification of Omi/HtrA2 as a mitochondrial apoptotic serine protease that disrupts inhibitor of apoptosis protein-caspase interaction. *J Biol Chem* **277**:432–438. doi:10.1074/jbc.M109721200.
- 125 Liu Z, Sun C, Olejniczak ET, Meadows RP, ... Fesik SW. (2000) Structural basis for binding of Smac/DIABLO to the XIAP BIR3 domain. *Nature* **408**:1004–1008. doi:10.1038/35050006.
- 126 Yang Q-H, Church-Hajduk R, Ren J, Newton ML, Du C. (2003) Omi/HtrA2 catalytic cleavage of inhibitor of apoptosis (IAP) irreversibly inactivates IAPs and facilitates caspase activity in apoptosis. *Genes Dev* **17**:1487–1496. doi:10.1101/gad.1097903.
- 127 Vousden KH, Lu X. (2002) Live or let die: The cell's response to p53. *Nat Rev Cancer* **2**:594–604. doi:10.1038/nrc864.
- 128 Delbridge ARD, Strasser A. (2015) The BCL-2 protein family, BH3-mimetics and cancer therapy. *Cell Death Differ* **22**:1071–1080. doi:10.1038/cdd.2015.50.
- 129 Chipuk JE, Kuwana T, Bouchier-Hayes L, Droin NM, ... Green DR. (2004) Direct activation of Bax by p53 mediates mitochondrial membrane permeabilization and apoptosis. *Science* **303**:1010–1015. doi:10.1126/science.1092734.
- 130 Hajnoczky G, Davies E, Madesh M. (2003) Calcium signaling and apoptosis. *Biochem Biophys*

- Res Commun* **304**:445–454. doi:10.1016/S0006-291X(03)00616-8.
- 131 Bahar E, Kim H, Yoon H. (2016) ER stress-mediated signaling: action potential and Ca²⁺ as key players. *Int J Mol Sci* **17**:1558. doi:10.3390/ijms17091558.
- 132 Hu H, Tian M, Ding C, Yu S. (2019) The C/EBP homologous protein (CHOP) transcription factor functions in endoplasmic reticulum stress-induced apoptosis and microbial infection. *Front Immunol* **9**:3083. doi:10.3389/fimmu.2018.03083.
- 133 Redza-Dutordoir M, Averill-Bates DA. (2016) Activation of apoptosis signalling pathways by reactive oxygen species. *Biochim Biophys Acta* **1863**:2977–2992. doi:10.1016/j.bbamcr.2016.09.012.
- 134 Deniaud A, Sharaf el dein O, Maillier E, Poncet D, ... Brenner C. (2008) Endoplasmic reticulum stress induces calcium-dependent permeability transition, mitochondrial outer membrane permeabilization and apoptosis. *Oncogene* **27**:285–299. doi:10.1038/sj.onc.1210638.
- 135 Wada T, Penninger JM. (2004) Mitogen-activated protein kinases in apoptosis regulation. *Oncogene* **23**:2838–2849. doi:10.1038/sj.onc.1207556.
- 136 Dhanasekaran DN, Reddy EP. (2017) JNK-signaling: A multiplexing hub in programmed cell death. *Genes and Cancer* **8**:682–694. doi:10.18632/genesandcancer.155.
- 137 Mrschtik M, Ryan KM. (2015) Lysosomal proteins in cell death and autophagy. *FEBS J* **282**:1858–1870. doi:10.1111/febs.13253.
- 138 Seto E, Yoshida M. (2014) Erasers of histone acetylation: The histone deacetylase enzymes. *Cold Spring Harb Perspect Biol* **6**:a018713. doi:10.1101/cshperspect.a018713.
- 139 Akone SH, Ntie-Kang F, Stuhldreier F, Ewonkem MB, ... Müller R. (2020) Natural products impacting DNA methyltransferases and histone deacetylases. *Front Pharmacol* **11**:992. doi:10.3389/fphar.2020.00992.
- 140 Zhang Y, Adachi M, Kawamura R, Imai K. (2006) Bmf is a possible mediator in histone deacetylase inhibitors FK228 and CBHA-induced apoptosis. *Cell Death Differ* **13**:129–140. doi:10.1038/sj.cdd.4401686.
- 141 Lindemann RK, Newbold A, Whitecross KF, Cluse LA, ... Johnstone RW. (2007) Analysis of the apoptotic and therapeutic activities of histone deacetylase inhibitors by using a mouse model of B cell lymphoma. *Proc Natl Acad Sci U S A* **104**:8071–8076. doi:10.1073/pnas.0702294104.
- 142 Mollinedo F, Gajate C. (2003) Microtubules, microtubule-interfering agents and apoptosis. *Apoptosis* **8**:413–450. doi:10.1023/a:1025513106330.

- 143 Sunters A, Fernández De Mattos S, Stahl M, Brosens JJ, ... Lam EWF. (2003) FoxO3a transcriptional regulation of Bim controls apoptosis in paclitaxel-treated breast cancer cell lines. *J Biol Chem* **278**:49795–49805. doi:10.1074/jbc.M309523200.
- 144 Suen D-F, Norris KL, Youle RJ. (2008) Mitochondrial dynamics and apoptosis. *Genes Dev* **22**:1577–1590. doi:10.1101/gad.1658508.
- 145 van der Blik AM, Shen Q, Kawajiri S. (2013) Mechanisms of mitochondrial fission and fusion. *Cold Spring Harb Perspect Biol* **5**:a011072. doi:10.1101/cshperspect.a011072.
- 146 Kubli DA, Gustafsson AB. (2012) Mitochondria and mitophagy: The Yin and Yang of cell death control. *Circ Res* **111**:1208–1221. doi:10.1161/CIRCRESAHA.112.265819.
- 147 Anand R, Wai T, Baker MJ, Kladt N, ... Langer T. (2014) The i-AAA protease YME1L and OMA1 cleave OPA1 to balance mitochondrial fusion and fission. *J Cell Biol* **204**:919–929. doi:10.1083/jcb.201308006.
- 148 Neuspiel M, Zunino R, Gangaraju S, Rippstein P, McBride H. (2005) Activated Mitofusin 2 signals mitochondrial fusion, interferes with Bax activation, and reduces susceptibility to radical induced depolarization. *J Biol Chem* **280**:25060–25070. doi:10.1074/jbc.M501599200.
- 149 Karbowski M, Arnoult D, Chen H, Chan DC, ... Youle RJ. (2004) Quantitation of mitochondrial dynamics by photolabeling of individual organelles shows that mitochondrial fusion is blocked during the Bax activation phase of apoptosis. *J Cell Biol* **164**:493–499. doi:10.1083/jcb.200309082.
- 150 Frezza C, Cipolat S, Martins de Brito O, Micaroni M, ... Scorrano L. (2006) OPA1 controls apoptotic cristae remodeling independently from mitochondrial fusion. *Cell* **126**:177–189. doi:10.1016/j.cell.2006.06.025.
- 151 Olichon A, Baricault L, Gas N, Guillou E, ... Lenaers G. (2002) Loss of OPA1 perturbs the mitochondrial inner membrane structure and integrity, leading to cytochrome c release and apoptosis. *J Biol Chem* **278**:7743–7747. doi:10.1074/jbc.C200677200.
- 152 Oettinghaus B, D'Alonzo D, Barbieri E, Restelli LM, ... Scorrano L. (2016) DRP1-dependent apoptotic mitochondrial fission occurs independently of BAX, BAK and APAF1 to amplify cell death by BID and oxidative stress. *Biochim Biophys Acta* **1857**:1267–1276. doi:10.1016/j.bbabi.2016.03.016.
- 153 Yamaguchi R, Lartigue L, Perkins G, Scott RT, ... Newmeyer DD. (2008) Opa1-mediated cristae opening is Bax/Bak- and BH3-dependent, required for apoptosis, and independent of Bak oligomerization. *Mol Cell* **31**:557–569. doi:10.1016/j.molcel.2008.07.010.

- 154 Scorrano L, Ashiya M, Buttle K, Weiler S, ... Korsmeyer SJ. (2002) A distinct pathway remodels mitochondrial cristae and mobilizes cytochrome c during apoptosis. *Dev Cell* **2**:55–67. doi:10.1016/s1534-5807(01)00116-2.
- 155 Trotta AP, Chipuk JE. (2017) Mitochondrial dynamics as regulators of cancer biology. *Cell Mol Life Sci* **74**:1999–2017. doi:10.1007/s00018-016-2451-3.
- 156 Milani M, Beckett AJ, Al-Zabeeby A, Luo X, ... Varadarajan S. (2019) DRP-1 functions independently of mitochondrial structural perturbations to facilitate BH3 mimetic-mediated apoptosis. *Cell Death Discov* **5**:117. doi:10.1038/s41420-019-0199-x.
- 157 Hanahan D, Weinberg RA. (2011) Hallmarks of cancer : The next generation. *Cell* **144**:646–674. doi:10.1016/j.cell.2011.02.013.
- 158 Lopez J, Tait SWG. (2015) Mitochondrial apoptosis: killing cancer using the enemy within. *Br J Cancer* **112**:957–962. doi:10.1038/bjc.2015.85.
- 159 Wong RSY. (2011) Apoptosis in cancer: From pathogenesis to treatment. *J Exp Clin Cancer Res* **30**:87. doi:10.1186/1756-9966-30-87.
- 160 Zawacka-Pankau J, Selivanova G. (2015) Pharmacological reactivation of p53 as a strategy to treat cancer. *J Intern Med* **277**:248–259. doi:10.1111/joim.12336.
- 161 De Miguel D, Lemke J, Anel A, Walczak H, Martinez-Lostao L. (2016) Onto better TRAILs for cancer treatment. *Cell Death Differ* **23**:733–747. doi:10.1038/cdd.2015.174.
- 162 Walczak H, Miller RE, Ariail K, Gliniak B, ... Lynch DH. (1999) Tumoricidal activity of tumor necrosis factor-related apoptosis-inducing ligand in vivo. *Nat Med* **5**:157–163. doi:10.1038/5517.
- 163 Mahmood Z, Shukla Y. (2010) Death receptors: Targets for cancer therapy. *Exp Cell Res* **316**:887–899. doi:10.1016/j.yexcr.2009.12.011.
- 164 Magrì A, Reina S, De Pinto V. (2018) VDAC1 as pharmacological target in cancer and neurodegeneration: Focus on its role in apoptosis. *Front Chem* **6**:108. doi:10.3389/fchem.2018.00108.
- 165 Strasser A, Harris AW, Bath ML, Cory S. (1990) Novel primitive lymphoid tumours induced in transgenic mice by cooperation between myc and bcl-2. *Nature* **348**:331–333. doi:10.1038/348331a0.
- 166 Merino D, Kelly GL, Lessene G, Wei AH, ... Strasser A. (2018) BH3-mimetic drugs: Blazing the trail for new cancer medicines. *Cancer Cell* **34**:879–891. doi:10.1016/j.ccell.2018.11.004.

- 167 Gross A, Katz SG. (2017) Non-apoptotic functions of BCL-2 family proteins. *Cell Death Differ* **24**:1348–1358. doi:10.1038/cdd.2017.22.
- 168 Zhang H, Nimmer PM, Tahir SK, Chen J, ... Tse C. (2007) Bcl-2 family proteins are essential for platelet survival. *Cell Death Differ* **14**:943–951. doi:10.1038/sj.cdd.4402081.
- 169 Shen XG, Wang C, Li Y, Wang L, ... Sun XF. (2010) Downregulation of caspase-9 is a frequent event in patients with stage II colorectal cancer and correlates with poor clinical outcome. *Color Dis* **12**:1213–1218. doi:10.1111/j.1463-1318.2009.02009.x.
- 170 Fong PY, Xue WC, Ngan HYS, Chiu PM, ... Cheung ANY. (2006) Caspase activity is downregulated in choriocarcinoma: A cDNA array differential expression study. *J Clin Pathol* **59**:179–183. doi:10.1136/jcp.2005.028027.
- 171 Manns J, Daubrawa M, Driessen S, Paasch F, ... Wesselborg S. (2011) Triggering of a novel intrinsic apoptosis pathway by the kinase inhibitor staurosporine: activation of caspase-9 in the absence of Apaf-1. *FASEB J* **25**:3250–3261. doi:10.1096/fj.10-177527.
- 172 Gama V, Swahari V, Schafer J, Kole AJ, ... Desmukh M. (2015) PARC/CUL9 mediates the degradation of mitochondrial-released cytochrome c and promotes survival in neurons and cancer cells. *Sci Signal* **7**:ra67. doi:10.1126/scisignal.2005309.
- 173 LaCasse EC, Mahoney DJ, Cheung HH, Plenchette S, ... Korneluk RG. (2008) IAP-targeted therapies for cancer. *Oncogene* **27**:6252–6275. doi:10.1038/onc.2008.302.
- 174 Ambrosini G, Adida C, Altieri DC. (1997) A novel anti-apoptosis gene, survivin, expressed in cancer and lymphoma. *Nat Med* **3**:917–921. doi:10.1038/nm0897-917.
- 175 Olie RA, Simões-Wüst AP, Baumann B, Leech SH, ... Zangemeister-Wittke U. (2000) A novel antisense oligonucleotide targeting survivin expression induces apoptosis and sensitizes lung cancer cells to chemotherapy. *Cancer Res* **60**:2805–2809.
- 176 Amantana A, London CA, Iversen PL, Devi GR. (2004) X-linked inhibitor of apoptosis protein inhibition induces apoptosis and enhances chemotherapy sensitivity in human prostate cancer cells. *Mol Cancer Ther* **3**:699–707.
- 177 Schimmer AD, Herr W, Hänel M, Borthakur G, ... Koschmieder S. (2011) Addition of AEG35156 XIAP antisense oligonucleotide in reinduction chemotherapy does not improve remission rates in patients with primary refractory acute myeloid leukemia in a randomized phase II study. *Clin Lymphoma, Myeloma Leuk* **11**:433–438. doi:10.1016/j.clml.2011.03.033.
- 178 Boddu P, Carter BZ, Verstovsek S, Pemmaraju N. (2019) SMAC mimetics as potential cancer

- therapeutics in myeloid malignancies. *Br J Haematol* **185**:219–231. doi:10.1111/bjh.15829.
- 179 Fulda S. (2017) Smac mimetics to therapeutically target IAP proteins in cancer. *Int Rev Cell Mol Biol* **330**:157–169. doi:10.1016/bs.ircmb.2016.09.004.
- 180 Baker DD, Chu M, Oza U, Rajgarhia V. (2007) The value of natural products to future pharmaceutical discovery. *Nat Prod Rep* **24**:1225–1244. doi:10.1039/b602241n.
- 181 Bernardini S, Tiezzi A, Laghezza Masci V, Ovidi E. (2018) Natural products for human health: an historical overview of the drug discovery approaches. *Nat Prod Res* **32**:1926–1950. doi:10.1080/14786419.2017.1356838.
- 182 Kingston DGI, Kingston DGI. (2008) A natural love of natural products. *J Org Chem* **73**:3975–3984. doi:10.1021/jo800239a.
- 183 Cragg GM, Newman DJ. (2013) Natural products: A continuing source of novel drug leads. *Biochim Biophys Acta* **1830**:3670–3695. doi:10.1016/j.bbagen.2013.02.008.
- 184 Hong J. (2014) Natural product synthesis at the interface of chemistry and biology. *Chemistry (Easton)* **20**:10204–10212. doi:10.1002/chem.201402804.
- 185 Zheng W, Seletsky BM, Palme MH, Lydon PJ, ... Yu MJ. (2004) Macrocyclic ketone analogues of halichondrin B. *Bioorg Med Chem Lett* **14**:5551–5554. doi:10.1016/j.bmcl.2004.08.069.
- 186 Kawano S, Ito K, Yahata K, Kira K, ... Kishi Y. (2019) A landmark in drug discovery based on complex natural product synthesis. *Sci Rep* **9**:8656. doi:10.1038/s41598-019-45001-9.
- 187 Cuevas C, Perez M, Martin MJ, Chicharro JL, ... Manzanares I. (2000) Synthesis of Ecteinascidin ET-743 and Phthalascidin Pt-650 from Cyanosafracin B. *Org Lett* **2**:2545–2548. doi:10.1021/ol0062502.
- 188 Schmidtko A, Lötsch J, Freynhagen R, Geisslinger G. (2010) Ziconotide for treatment of severe chronic pain. *Lancet* **375**:1569–1577. doi:10.1016/S0140-6736(10)60354-6.
- 189 Cuevas C, Francesch A. (2009) Development of Yondelis (trabectedin, ET-743). A semisynthetic process solves the supply problem. *Nat Prod Rep* **26**:322–337. doi:10.1039/b808331m.
- 190 Lobanovska M, Pilla G. (2017) Penicillin's discovery and antibiotic resistance: Lessons for the future? *Yale J Biol Med* **90**:135–145.
- 191 Stone EA, Fung HB, Kirschenbaum HL. (2002) Caspofungin: An echinocandin antifungal agent. *Clin Ther* **24**:351–377. doi:10.1016/s0149-2918(02)85039-1.

- 192 Efferth T. (2017) From ancient herb to modern drug: Artemisia annua and artemisinin for cancer therapy. *Semin Cancer Biol* **46**:65–83. doi:10.1016/j.semcancer.2017.02.009.
- 193 Bond A. (2006) Exenatide (Byetta) as a novel treatment option for type 2 diabetes mellitus. *Proc (Bayl Univ Med Cent)* **19**:281–284. doi:10.1080/08998280.2006.11928181.
- 194 Keller PW, Adamson CS, Heymann JB, Freed EO, Steven AC. (2011) HIV-1 maturation inhibitor bevirimat stabilizes the immature gag lattice. *J Virol* **85**:1420–1428. doi:10.1128/JVI.01926-10.
- 195 Loy C, Schneider L. (2006) Galantamine for Alzheimer's disease and mild cognitive impairment. *Cochrane Database Syst Rev* **1**:CD001747. doi:10.1002/14651858.cd001747.pub3.
- 196 Badr G, Lefevre EA, Mohany M. (2011) Thymoquinone inhibits the CXCL12-induced chemotaxis of multiple myeloma cells and increases their susceptibility to Fas-mediated apoptosis. *PLoS One* **6**:e23741. doi:10.1371/journal.pone.0023741.
- 197 Sagawa M, Nakazato T, Uchida H, Ikeda Y, Kizaki M. (2008) Cantharidin induces apoptosis of human multiple myeloma cells via inhibition of the JAK/STAT pathway. *Cancer Sci* **99**:1820–1826. doi:10.1111/j.1349-7006.2008.00872.x.
- 198 Raja SM, Chen S, Yue P, Acker TM, ... Sun S-Y. (2008) The natural product honokiol preferentially inhibits c-FLIP and augments death receptor-induced apoptosis. *Mol Cancer Ther* **7**:2212–2223. doi:10.1158/1535-7163.MCT-07-2409.
- 199 Viswesh V, Gates K, Sun D. (2011) Characterization of DNA damage induced by a natural product antitumor antibiotic leinamycin in human cancer cells. *Chem Res Toxicol* **23**:99–107. doi:10.1021/tx900301r.
- 200 Robles AJ, Du L, Cichewicz RH, Mooberry SL. (2016) Maximiscin induces DNA damage, activates DNA damage response pathways, and has selective cytotoxic activity against a subtype of triple-negative breast cancer. *J Nat Prod* **79**:1822–1827. doi:10.1021/acs.jnatprod.6b00290.
- 201 Liberio MS, Sadowski MC, Davis RA, Rockstroh A, ... Nelson CC. (2015) The ascidian natural product eusynstyelamide B is a novel topoisomerase II poison that induces DNA damage and growth arrest in prostate and breast cancer cells. *Oncotarget* **6**:43944–43963. doi:10.18632/oncotarget.6267.
- 202 Zhang L, Peng Y, Uray IP, Shen J, ... Peng G. (2017) Natural product β -thujaplicin inhibits homologous recombination repair and sensitizes cancer cells to radiation therapy. *DNA Repair*

- (*Amst*) **60**:89–101. doi:10.1016/j.dnarep.2017.10.009.
- 203 Zhu Y, Ma N, Li H-X, Tian L, ... Hao B. (2014) Berberine induces apoptosis and DNA damage in MG-63 human osteosarcoma cells. *Mol Med Rep* **10**:1734–1738. doi:10.3892/mmr.2014.2405.
- 204 Moon JL, Kim SY, Shin SW, Park J-W. (2012) Regulation of brefeldin A-induced ER stress and apoptosis by mitochondrial NADP⁺-dependent isocitrate dehydrogenase. *Biochem Biophys Res Commun* **417**:760–764. doi:10.1016/j.bbrc.2011.12.030.
- 205 Siu F-M, Cheung Y-W, Lok C-N, Yan K, ... Che C-M. (2008) Proteomic and transcriptomic study on the action of a cytotoxic saponin (Polyphyllin D): Induction of endoplasmic reticulum stress and mitochondria-mediated apoptotic pathways. *Proteomics* **8**:3105–3117. doi:10.1002/pmic.200700829.
- 206 Li Z, Huang L, Wei L, Hou Z, ... Huang S. (2019) Chaetocin induces caspase-dependent apoptosis in ovarian cancer cells via the generation of reactive oxygen species. *Oncol Lett* **18**:1915–1921. doi:10.3892/ol.2019.10507.
- 207 Yang Y, Zhang Y, Wang L, Lee S. (2017) Levistolide A induces apoptosis via ROS-mediated ER stress pathway in colon cancer cells. *Cell Physiol Biochem* **42**:929–938. doi:10.1159/000478647.
- 208 Liu L, Zhu H, Wu W, Shen Y, ... Lin H-W. (2019) Neoantimycin F, a streptomyces-derived natural product induces mitochondria-related apoptotic death in human non-small cell lung cancer cells. *Front Pharmacol* **10**:1042. doi:10.3389/fphar.2019.01042.
- 209 Kawiak A, Zawacka-Pankau J, Wasilewska A, Stasiłojc G, ... Lojkowska E. (2012) Induction of apoptosis in HL-60 cells through the ROS-mediated mitochondrial pathway by ramentaceone from *drosera aliciae*. *J Nat Prod* **75**:9–14. doi:10.1021/np200247g.
- 210 Huang P, Feng L, Oldham EA, Keating MJ, Plunkett W. (2000) Superoxide dismutase as a target for the selective killing of cancer cells. *Nature* **407**:390–395. doi:10.1038/35030140.
- 211 Trachootham D, Zhou Y, Zhang H, Demizu Y, ... Huang P. (2006) Selective killing of oncogenically transformed cells through a ROS-mediated mechanism by β -phenylethyl isothiocyanate. *Cancer Cell* **10**:241–252. doi:10.1016/j.ccr.2006.08.009.
- 212 Fu R, Yang P, Li Z, Liu W, ... Li Z. (2019) Avenanthramide A triggers potent ROS-mediated anti-tumor effects in colorectal cancer by directly targeting DDX3. *Cell Death Dis* **10**:593. doi:10.1038/s41419-019-1825-5.
- 213 Mukhtar E, Adhami VM, Mukhtar H. (2014) Targeting microtubules by natural agents for cancer therapy. *Mol Cancer Ther* **13**:275–284. doi:10.1158/1535-7163.MCT-13-0791.

- 214 Leung YY, Yao Hui LL, Kraus VB. (2015) Colchicine-Update on mechanisms of action and therapeutic uses. *Semin Arthritis Rheum* **45**:341–350. doi:10.1016/j.semarthrit.2015.06.013.
- 215 Weaver BA. (2014) How Taxol/paclitaxel kills cancer cells. *Mol Biol Cell* **25**:2677–2681. doi:10.1091/mbc.E14-04-0916.
- 216 Bollag DM, McQueney PA, Zhu J, Hensens O, ... Woods CM. (1995) Epothilones, a new class of microtubule-stabilizing agents with a taxol-like mechanism of action. *Cancer Res* **55**:2325–2333.
- 217 De Souza MVN. (2004) (+)-Discodermolide: a marine natural product against cancer. *Sci World J* **4**:415–436. doi:10.1100/tsw.2004.96.
- 218 Dawson MA, Kouzarides T. (2012) Cancer epigenetics: From mechanism to therapy. *Cell* **150**:12–27. doi:10.1016/j.cell.2012.06.013.
- 219 Liu H-L, Chen Y, Cui G-H, Zhou J-F. (2005) Curcumin, a potent anti-tumor reagent, is a novel histone deacetylase inhibitor regulating B-NHL cell line Raji proliferation. *Acta Pharmacol Sin* **26**:603–609. doi:10.1111/j.1745-7254.2005.00081.x.
- 220 Khan MA, Hussain A, Sundaram MK, Alalami U, ... Quraishi U. (2015) (-)-Epigallocatechin-3-gallate reverses the expression of various tumor-suppressor genes by inhibiting DNA methyltransferases and histone deacetylases in human cervical cancer cells. *Oncol Rep* **33**:1976–1984. doi:10.3892/or.2015.3802.
- 221 Venturelli S, Berger A, Böcker A, Busch C, ... Bitzer M. (2013) Resveratrol as a pan-HDAC inhibitor alters the acetylation status of histone proteins in human-derived hepatoblastoma cells. *PLoS One* **8**:e73097. doi:10.1371/journal.pone.0073097.
- 222 Groh IAM, Chen C, Lüske C, Cartus AT, Esselen M. (2013) Plant polyphenols and oxidative metabolites of the herbal alkenylbenzene methyleugenol suppress histone deacetylase activity in human colon carcinoma cells. *J Nutr Metab* **2013**:821082. doi:10.1155/2013/821082.
- 223 Liu L, Zhang N, Dou Y, Mao G, ... Deng H. (2017) Lysosomal dysfunction and autophagy blockade contribute to IMB-6G-induced apoptosis in pancreatic cancer cells. *Sci Rep* **7**:41862. doi:10.1038/srep41862.
- 224 Li N, Ragheb K, Lawler G, Sturgis J, ... Robinson JP. (2003) Mitochondrial complex I inhibitor rotenone induces apoptosis through enhancing mitochondrial reactive oxygen species production. *J Biol Chem* **278**:8516–8525. doi:10.1074/jbc.M210432200.
- 225 Omura S, Miyadera H, Ui H, Shiomi K, ... Kita K. (2001) An anthelmintic compound, nafuredin, shows selective inhibition of complex I in helminth mitochondria. *Proc Natl Acad Sci*

- U S A* **98**:60–62. doi:10.1073/pnas.98.1.60.
- 226 Höfle G, Gerth K, Reichenbach H, Kunze B, ... Prusov E V. (2012) Isolation, biological activity evaluation, structure elucidation, and total synthesis of eliamid: A novel complex i inhibitor. *Chem Eur J* **18**:11362–11370. doi:10.1002/chem.201201879.
- 227 Dong LF, Low P, Dyason JC, Wang XF, ... Neuzil J. (2008) α -Tocopheryl succinate induces apoptosis by targeting ubiquinone-binding sites in mitochondrial respiratory complex II. *Oncogene* **27**:4324–4335. doi:10.1038/onc.2008.69.
- 228 Min H-Y, Jang H-J, Park KH, Hyun SY, ... Lee H-Y. (2019) The natural compound gracillin exerts potent antitumor activity by targeting mitochondrial complex II. *Cell Death Dis* **10**:810. doi:10.1038/s41419-019-2041-z.
- 229 Miyadera H, Shiomi K, Ui H, Yamaguchi Y, ... Omura S. (2003) Atpenins, potent and specific inhibitors of mitochondrial complex II (succinate-ubiquinone oxidoreductase). *Proc Natl Acad Sci U S A* **100**:473–477. doi:10.1073/pnas.0237315100.
- 230 Ferramosca A, Conte A, Guerra F, Felling S, ... Terlizzi A. (2016) Metabolites from invasive pests inhibit mitochondrial complex II: A potential strategy for the treatment of human ovarian carcinoma? *Biochem Biophys Res Commun* **473**:1133–1138. doi:10.1016/j.bbrc.2016.04.028.
- 231 Han YH, Kim SH, Kim ZS, Park WH. (2008) Antimycin A as a mitochondrial electron transport inhibitor prevents the growth of human lung cancer A549 cells. *Oncol Rep* **20**:689–693. doi:10.3892/or_00000061.
- 232 Gurung B, Yu L, Yu C-A. (2008) Stigmatellin induces reduction of iron-sulfur protein in the oxidized cytochrome bc1 complex. *J Biol Chem* **283**:28087–28094. doi:10.1074/jbc.M804229200.
- 233 Sasse F, Leibold T, Kunze B, Höfle G, Reichenbach H. (2003) Cyrmenins, new β -methoxyacrylate inhibitors of the electron transport. Production, isolation, physico-chemical and biological properties. *J Antibiot (Tokyo)* **56**:827–831. doi:10.7164/antibiotics.56.827.
- 234 Igisu H, Nakamura M. (1986) Inhibition of cytochrome c oxidase by psychosine (galactosylsphingosine). *Biochem Biophys Res Commun* **137**:323–327. doi:10.1016/0006-291X(86)91213-1.
- 235 Katou Y, Endo N, Suzuki T, Yu J, ... Homma Y. (2014) Metarhizin A suppresses cell proliferation by inhibiting cytochrome c oxidase activity. *Life Sci* **103**:1–7. doi:10.1016/j.lfs.2014.03.023.
- 236 Symersky J, Osowski D, Walters DE, Mueller DM. (2012) Oligomycin frames a common drug-

- binding site in the ATP synthase. *Proc Natl Acad Sci U S A* **109**:13961–13965.
doi:10.1073/pnas.1207912109.
- 237 Daniel PT, Koert U, Schuppan J. (2006) Apoptolidin: Induction of apoptosis by a natural product. *Angew Chemie - Int Ed* **45**:872–893. doi:10.1002/anie.200502698.
- 238 Gledhill JR, Montgomery MG, Leslie AGW, Walker JE. (2007) Mechanism of inhibition of bovine F1-ATPase by resveratrol and related polyphenols. *Proc Natl Acad Sci U S A* **104**:13632–13637. doi:10.1073/pnas.0706290104.
- 239 Fulda S, Scaffidi G, Susin SA, Krammer PH, ... Debatin KM. (1998) Activation of mitochondria and release of mitochondrial apoptogenic factors by betulinic acid. *J Biol Chem* **273**:33942–33948. doi:10.1074/jbc.273.51.33942.
- 240 Belzacq AS, El Hamel C, Vieira HLA, Cohen I, ... Kroemer G. (2001) Adenine nucleotide translocator mediates the mitochondrial membrane permeabilization induced by lonidamine, arsenite and CD437. *Oncogene* **20**:7579–7587. doi:10.1038/sj.onc.1204953.
- 241 Notario B, Zamora M, Viñas O, Mampel T. (2003) All-trans-retinoic acid binds to and inhibits adenine nucleotide translocase and induces mitochondrial permeability transition. *Mol Pharmacol* **63**:224–231. doi:10.1124/mol.63.1.224.
- 242 Goldin N, Arzoine L, Heyfets A, Israelson A, ... Flescher E. (2008) Methyl jasmonate binds to and detaches mitochondria-bound hexokinase. *Oncogene* **27**:4636–4643.
doi:10.1038/onc.2008.108.
- 243 Abu-Hamad S, Zaid H, Israelson A, Nahon E, Shoshan-Barmatz V. (2008) Hexokinase-I protection against apoptotic cell death is mediated via interaction with the voltage-dependent anion channel-1: Mapping the site of binding. *J Biol Chem* **283**:13482–13490.
doi:10.1074/jbc.M708216200.
- 244 Tzung S, Kim KM, Basañez G, Giedt CD, ... Hockenbery DM. (2001) Antimycin A mimics cell death inducing Bcl2 homology. *Nat Cell Biol* **3**:183–191. doi:10.1038/35055095.
- 245 Meng Y, Tang W, Dai Y, Wu X, ... Xu L. (2008) Natural BH3 mimetic (-)-gossypol chemosensitizes human prostate cancer via Bcl-xL inhibition accompanied by increase of Puma and Noxa. *Mol Cancer Ther* **7**:2192–2202. doi:10.1158/1535-7163.MCT-08-0333.
- 246 Nakashima T, Miura M, Hara M. (2000) Tetrocarcin A inhibits mitochondrial functions of Bcl-2 and suppresses its anti-apoptotic activity. *Cancer Res* **60**:1229–1235.
- 247 Hu H-Y, Li K-P, Wang X-J, Liu Y, ... Zhang M-X. (2013) Set9, NF- κ B, and microRNA-21

- mediate berberine-induced apoptosis of human multiple myeloma cells. *Acta Pharmacol Sin* **34**:157–166. doi:10.1038/aps.2012.161.
- 248 Kim SH, Lee JC, Ahn KS, Jeong SJ, ... Chen CY. (2011) Signal transducer and activator of transcription 3 pathway mediates genipin-induced apoptosis in U266 multiple myeloma cells. *J Cell Biochem* **112**:1552–1562. doi:10.1002/jcb.23077.
- 249 Bhardwaj A, Sethi G, Vadhan-Raj S, Bueso-Ramos C, ... Aggarwal BB. (2007) Resveratrol inhibits proliferation, induces apoptosis, and overcomes chemoresistance through down-regulation of STAT3 and nuclear factor- κ B-regulated antiapoptotic and cell survival gene products in human multiple myeloma cells. *Blood* **109**:2293–2302. doi:10.1182/blood-2006-02-003988.
- 250 Park S, Lee H-J, Jeong S-J, Song HS, ... Kim S-H. (2011) Inhibition of JAK1/STAT3 signaling mediates compound K-induced apoptosis in human multiple myeloma U266 cells. *Food Chem Toxicol* **49**:1367–1372. doi:10.1016/j.fct.2011.03.021.
- 251 Ikezoe T, Yang Y, Bandobashi K, Saito T, ... Taguchi H. (2005) Oridonin, a diterpenoid purified from *Rabdosia rubescens*, inhibits the proliferation of cells from lymphoid malignancies in association with blockade of the NF- κ B signal pathways. *Mol Cancer Ther* **4**:578–586. doi:10.1158/1535-7163.MCT-04-0277.
- 252 Felix S, Sandjo LP, Opatz T, Erkel G. (2013) SF002-96-1, a new drimane sesquiterpene lactone from an *Aspergillus* species, inhibits survivin expression. *Beilstein J Org Chem* **9**:2866–2876. doi:10.3762/bjoc.9.323.
- 253 Nikolovska-Coleska Z, Xu L, Hu Z, Tomita Y, ... Wang S. (2004) Discovery of embelin as a cell-permeable, small-molecular weight inhibitor of XIAP through structure-based computational screening of a traditional herbal medicine three-dimensional structure database. *J Med Chem* **47**:2430–2440. doi:10.1021/jm030420+.
- 254 Lee JH, Wendorff TJ, Berger JM. (2017) Resveratrol: A novel type of topoisomerase II inhibitor. *J Biol Chem* **292**:21011–21022. doi:10.1074/jbc.M117.810580.
- 255 Ferlay J, Colombet M, Soerjomataram I, Mathers C, ... Bray F. (2019) Estimating the global cancer incidence and mortality in 2018: GLOBOCAN sources and methods. *Int J Cancer* **144**:1941–1953. doi:10.1002/ijc.31937.
- 256 Gatenby RA, Smallbone K, Maini PK, Rose F, ... Gillies RJ. (2007) Cellular adaptations to hypoxia and acidosis during somatic evolution of breast cancer. *Br J Cancer* **97**:646–653.

- doi:10.1038/sj.bjc.6603922.
- 257 Iqbal N, Iqbal N. (2014) Imatinib: A Breakthrough of targeted therapy in cancer. *Chemother Res Pract* **2014**:357027. doi:10.1155/2014/357027.
- 258 Dimaras H, Corson TW, Cobrinik D, White A, ... Gallie BL. (2015) Retinoblastoma. *Nat Rev Dis Prim* **1**:15021. doi:10.1038/nrdp.2015.21.
- 259 Wagenaar TR, Ma L, Roscoe B, Park SM, ... Green MR. (2014) Resistance to vemurafenib resulting from a novel mutation in the BRAFV600E kinase domain. *Pigment Cell Melanoma Res* **27**:124–133. doi:10.1111/pcmr.12171.
- 260 Yates LR, Campbell PJ. (2012) Evolution of the cancer genome. *Nat Rev Genet* **13**:795–806. doi:10.1038/nrg3317.
- 261 Casás-Selves M, DeGregori J. (2011) How cancer shapes evolution and how evolution shapes cancer. *Evolution (N Y)* **4**:624–634. doi:10.1007/s12052-011-0373-y.
- 262 Crooke ST, Bradner WT. (1976) Mitomycin C: a review. *Cancer Treat Rev* **3**:121–139. doi:10.1016/S0305-7372(76)80019-9.
- 263 Murphy T, Yee KWL. (2017) Cytarabine and daunorubicin for the treatment of acute myeloid leukemia. *Expert Opin Pharmacother* **18**:1765–1780. doi:10.1080/14656566.2017.1391216.
- 264 Stuhldreier F, Kassel S, Schumacher L, Wesselborg S, ... Fritz G. (2015) Pleiotropic effects of spongean alkaloids on mechanisms of cell death, cell cycle progression and DNA damage response (DDR) of acute myeloid leukemia (AML) cells. *Cancer Lett* **361**:39–48. doi:10.1016/j.canlet.2015.02.030.
- 265 Mokhlesi A, Stuhldreier F, Wex KW, Berscheid A, ... Proksch P. (2017) Cyclic cystine-bridged peptides from the marine sponge *Clathria basilana* induce apoptosis in tumor cells and depolarize the bacterial cytoplasmic membrane. *J Nat Prod* **80**:2941–2952. doi:10.1021/acs.jnatprod.7b00477.
- 266 Böhler P, Stuhldreier F, Anand R, Kondadi AK, ... Wesselborg S, Stork B. (2018) The mycotoxin phomoxanthone A disturbs the form and function of the inner mitochondrial membrane. *Cell Death Dis* **9**:286. doi:10.1038/s41419-018-0312-8.
- 267 Liu Y, Stuhldreier F, Kurtán T, Mándi A, ... Proksch P. (2017) Daldinone derivatives from the mangrove-derived endophytic fungus *Annulohyphoxylon* sp. *RSC Adv* **7**:5381–5393. doi:10.1039/C6RA27306H.

- 268 Drießen D, Stuhldreier F, Frank A, Stark H, ... Müller TJJ. (2019) Novel meriolin derivatives as rapid apoptosis inducers. *Bioorganic Med Chem* **27**:3463–3468. doi:10.1016/j.bmc.2019.06.029.
- 269 Yu H, Sperlich J, Höfert S-P, Janiak C, ... Proksch P. (2019) Azaphilone pigments and macrodiolides from the coprophilous fungus *Coniella fragariae*. *Fitoterapia* **137**:104249. doi:10.1016/j.fitote.2019.104249.
- 270 Harwoko H, Daletos G, Stuhldreier F, Lee J, ... Proksch P. (2019) Dithiodiketopiperazine derivatives from endophytic fungi *Trichoderma harzianum* and *Epicoccum nigrum*. *Nat Prod Res* 1–9. doi:10.1080/14786419.2019.1627348.
- 271 Mayer S, Prechtel M, Liebfried P, Cadeddu RP, ... Jäger P. (2019) First results from a screening of 300 naturally occurring compounds: 4,6-dibromo-2-(2',4'-dibromophenoxy)phenol, 4,5,6-tribromo-2-(2',4'-dibromophenoxy)phenol, and 5-epi-nakijinone Q as substances with the potential for anticancer therapy. *Mar Drugs* **17**:521. doi:10.3390/md17090521.
- 272 Ariantari NP, Ancheeva E, Frank M, Stuhldreier F, ... Proksch P. (2020) Didymellanosine, a new decahydrofluorene analogue, and ascolactone C from *Didymella* sp. IEA-3B.1, an endophyte of *Terminalia catappa*. *RSC Adv* **10**:7232–7240. doi:10.1039/c9ra10685e.
- 273 Gao Y, Stuhldreier F, Schmitt L, Wesselborg S, ... Proksch P. (2020) Sesterterpenes and macrolide derivatives from the endophytic fungus *Aplosporella javeedii*. *Fitoterapia* **146**:104652. doi:10.1016/j.fitote.2020.104652.
- 274 Gao Y, Stuhldreier F, Schmitt L, Wesselborg S, ... Proksch P. (2020) Induction of New Lactam Derivatives From the Endophytic Fungus *Aplosporella javeedii* Through an OSMAC Approach. *Front Microbiol* **11**:600983. doi:10.3389/fmicb.2020.600983.
- 275 Rösberg D, Debbab A, Mándi A, Vasylyeva V, ..., Wesselborg S, ..., Proksch P. (2013) Pro-apoptotic and immunostimulatory tetrahydroxanthone dimers from the endophytic fungus *Phomopsis longicolla*. *J Org Chem* **78**:12409–12425. doi:10.1021/jo402066b.
- 276 Ierano C, Chakraborty AR, Nicolae A, Bahr JC, ... Robey RW. (2013) Loss of the proteins Bak and Bax prevents apoptosis mediated by histone deacetylase inhibitors. *Cell Cycle* **12**:2829–2838. doi:10.4161/cc.25914.
- 277 Müller A, Gillissen B, Richter A, Richter A, ... Scholz CW. (2018) Pan-class I PI3-kinase inhibitor BKM120 induces MEK1/2-dependent mitotic catastrophe in non-Hodgkin lymphoma leading to apoptosis or polyploidy determined by Bax/Bak and p53. *Cell Death Dis* **9**:384. doi:10.1038/s41419-018-0413-4.

- 278 Liang J, Yang Y, Bai L, Li F, Li E. (2020) DRP1 upregulation promotes pancreatic cancer growth and metastasis through increased aerobic glycolysis. *J Gastroenterol Hepatol* **35**:885–895. doi:10.1111/jgh.14912.
- 279 Yu L, Xiao Z, Tu H, Tong B, Chen S. (2019) The expression and prognostic significance of Drp1 in lung cancer. *Medicine (Baltimore)* **98**:e18228. doi:10.1097/md.00000000000018228.
- 280 Rehman J, Zhang HJ, Toth PT, Zhang Y, ... Archer SL. (2012) Inhibition of mitochondrial fission prevents cell cycle progression in lung cancer. *FASEB J* **26**:2175–2186. doi:10.1096/fj.11-196543.
- 281 Wu D, Dasgupta A, Chen KH, Neuber-Hess M, ... Archer SL. (2020) Identification of novel dynamin-related protein 1 (Drp1) GTPase inhibitors: Therapeutic potential of Drpitor1 and Drpitor1a in cancer and cardiac ischemia-reperfusion injury. *FASEB J* **34**:1447–1464. doi:10.1096/fj.201901467R.
- 282 You Y, He Q, Lu H, Zhou X, ... Zhao X. (2020) Silibinin Induces G2/M cell cycle arrest by activating Drp1-dependent mitochondrial fission in cervical cancer. *Front Pharmacol* **11**:271. doi:10.3389/fphar.2020.00271.
- 283 Alavi M V. (2019) Targeted OMA1 therapies for cancer. *Int J Cancer* **145**:2330–2341. doi:10.1002/ijc.32177.
- 284 Herkenne S, Ek O, Zamberlan M, Pellattiero A, ... Scorrano L. (2020) Developmental and tumor angiogenesis requires the mitochondria-shaping protein Opa1. *Cell Metab* **31**:886–887. doi:10.1016/j.cmet.2020.04.007.
- 285 Werner J, Ebrahim W, Özkaya FC, Mándi A, ... Proksch P. (2019) Pyrone derivatives from *Helichrysum italicum*. *Fitoterapia* **133**:80–84. doi:10.1016/j.fitote.2018.12.018.
- 286 Arai M, Shin D, Kamiya K, Ishida R. (2017) Marine spongean polybrominated diphenyl ethers, selective growth inhibitors against the cancer cells adapted to glucose starvation, inhibits mitochondrial complex II. *J Nat Med* **71**:44–49. doi:10.1007/s11418-016-1025-x.
- 287 Park YS, Grove CI, González-López M, Uргаonkar S, ... Shaw JT. (2011) Synthesis of (-)-viriditoxin: A 6,6'-binaphthopyran-2-one that targets the bacterial cell division protein FtsZ. *Angew Chemie - Int Ed* **50**:3730–3733. doi:10.1002/anie.201007298.
- 288 Wang J, Galgoci A, Kodali S, Herath KB, ... Singh S. (2003) Discovery of a small molecule that inhibits cell division by blocking FtsZ, a novel therapeutic target of antibiotics. *J Biol Chem* **278**:44424–44428. doi:10.1074/jbc.M307625200.

- 289 Kundu S, Kim TH, Yoon JH, Shin H-S, ... Kim HS. (2014) Viriditoxin regulates apoptosis and autophagy via mitotic catastrophe and microtubule formation in human prostate cancer cells. *Int J Oncol* **45**:2331–2340. doi:10.3892/ijo.2014.2659.
- 290 Suzuki K, Nozawa K, Nakajima S, Kawai K. (1990) Structure revision of mycotoxin, viriditoxin, and its derivatives. *Chem Pharm Bull* **38**:3180–3181. doi:10.1248/cpb.38.3180.
- 291 Jiu J, Mizuba S. (1974) Metabolic products from *Spicaria divaricata* NRRL 5771. *J Antibiot (Tokyo)* **27**:760–765. doi:10.7164/antibiotics.27.760.
- 292 Kalghatgi S, Spina CS, Costello JC, Liesa M, ... Collins JJ. (2013) Bactericidal antibiotics induce mitochondrial dysfunction and oxidative damage in mammalian cells. *Sci Transl Med* **5**:192ra85. doi:10.1126/scitranslmed.3006055.
- 293 Stefano GB, Samuel J, Kream RM. (2017) Antibiotics may trigger mitochondrial dysfunction inducing psychiatric disorders. *Med Sci Monit* **23**:101–106. doi:10.12659/MSM.899478.
- 294 Jones CN, Miller C, Tenenbaum A, Spremulli LL, Saada A. (2009) Antibiotic effects on mitochondrial translation and in patients with mitochondrial translational defects. *Mitochondrion* **9**:429–437. doi:10.1016/j.mito.2009.08.001.
- 295 Chatzisprou IA, Held NM, Mouchiroud L, Auwerx J, Houtkooper RH. (2015) Tetracycline antibiotics impair mitochondrial function. *Cancer Res* **75**:4446–4449. doi:10.1158/0008-5472.CAN-15-1626.
- 296 Pollastri MP. (2010) Overview on the rule of five. *Curr Protoc Pharmacol* chapter 9: unit 9.12. doi:10.1002/0471141755.ph0912s49.
- 297 Molinspiration Cheminformatics. <https://www.molinspiration.com/cgi-bin/properties> (accessed 28 Sep 2020).
- 298 Grove CI, Shaw JT. (2012) Second-generation synthesis of (–)-viriditoxin. *Synthesis (Stuttg)* **2012**:362–371. doi:10.1055/s-0031-1289651.
- 299 Lopes RB, Gangeswaran R, McNeish IA, Wang Y, Lemoine NR. (2007) Expression of the IAP protein family is dysregulated in pancreatic cancer cells and is important for resistance to chemotherapy. *Int J Cancer* **120**:2344–2352. doi:10.1002/ijc.22554.
- 300 Gerges S, Rohde K, Fulda S. (2016) Cotreatment with Smac mimetics and demethylating agents induces both apoptotic and necroptotic cell death pathways in acute lymphoblastic leukemia cells. *Cancer Lett* **375**:127–132. doi:10.1016/j.canlet.2016.02.040.

References

- 301 Perimenis P, Galaris A, Voulgari A, Prassa M, Pintzas A. (2016) IAP antagonists Birinapant and AT-406 efficiently synergise with either TRAIL, BRAF, or BCL-2 inhibitors to sensitise BRAFV600E colorectal tumour cells to apoptosis. *BMC Cancer* **16**:624. doi:10.1186/s12885-016-2606-5.
- 302 Hu J, Li H, Chooi Y-H. (2019) Fungal dirigent protein controls the stereoselectivity of multicopper oxidase-catalyzed phenol coupling in viriditoxin biosynthesis. *J Am Chem Soc* **141**:8068–8072. doi:10.1021/jacs.9b03354.
- 303 Urquhart AS, Hu J, Chooi YH, Idnurm A. (2019) The fungal gene cluster for biosynthesis of the antibacterial agent viriditoxin. *Fungal Biol Biotechnol* **6**:9. doi:10.1186/s40694-019-0072-y.
- 304 Jarry M, Lecointre C, Malleval C, Desrues L, ... Castel H. (2014) Impact of meriolins, a new class of cyclin-dependent kinase inhibitors, on malignant glioma proliferation and neo-angiogenesis. *Neuro Oncol* **16**:1484–1498. doi:10.1093/neuonc/nou102.

The figures depicted on page 7 and page 16 were created using <http://www.biorender.com>.

5 Licensing & Copyright

I the author hereby grant anyone the right to reuse any part of this dissertation that is not subject to explicit copyright, provided that credit is given (license CC BY 4.0). Please cite as follows:

Stuhldreier, Fabian (2021) *Identification of apoptosis-inducing natural products and derivatives for the elimination of tumor cells*. Heinrich Heine University, Düsseldorf.

All non-copyrighted parts of this work are licensed under the Creative Commons Attribution 4.0 International License.

To view a copy of this license, visit <http://creativecommons.org/licenses/by/4.0/legalcode> or send a letter to Creative Commons, PO Box 1866, Mountain View, CA 94042, USA.

The following parts of this dissertation are subject to copyright and have been reproduced without changes:

- 1) **Manuscript “Pleiotropic effects of spongean alkaloids on mechanisms of cell death, cell cycle progression and DNA damage response (DDR) of acute myeloid leukemia (AML) cells”**: Reproduced with permission from Stuhldreier F et al. (2015) *Cancer Letters* 361:39–48. doi: 10.1016/j.canlet.2015.02.030. Copyright 2015 Elsevier.
- 2) **Manuscript “Cyclic Cystine-Bridged Peptides from the Marine Sponge *Clathria basilana* Induce Apoptosis in Tumor Cells and Depolarize the Bacterial Cytoplasmic Membrane”**: Reproduced with permission from Mokhlesi A et al. (2017) *Journal of Natural Products* 80:2941–2952. doi:10.1021/acs.jnatprod.7b00477N. Copyright 2017 American Chemical Society.
- 3) **Manuscript “Daldinone derivatives from the mangrove-derived endophytic fungus *Annulohyphoxylon* sp.”**: Reproduced from Liu Y et al. (2017) *RSC Advances* 7:5381–5393. doi: 10.1039/C6RA27306H with permission from the Royal Society of Chemistry. This article is licensed under the Creative Commons Attribution-NonCommercial 3.0 Unported Licence (<https://creativecommons.org/licenses/by-nc/3.0/legalcode>).
- 4) **Manuscript “The mycotoxin phomoxanthone A disturbs the form and function of the inner mitochondrial membrane”**: Reproduced from Böhler et al. (2018) *Cell Death & Disease* 9:286. doi: 10.1038/s41419-018-0312-8 under the Creative Commons CC BY-NC-ND 4.0 license (as indicated by Nature).
- 5) **Manuscript “Dithiodiketopiperazine derivatives from endophytic fungi *Trichoderma harzianum* and *Epicoccum nigrum*”**: Reproduced from Harwoko H et al. (2019) *Natural Product Research*. doi: 10.1080/14786419.2019.1627348 with permission of the publisher (Taylor & Francis Ltd, <http://www.tandfonline.com>).

- 6) **Manuscript “First Results from a Screening of 300 Naturally Occurring Compounds: 4,6-dibromo-2-(2',4'-dibromophenoxy)phenol,4,5,6-tribromo-2-(2',4'-dibromophenoxy)phenol, and 5-epi-nakijinone Q as Substances with the Potential for Anticancer Therapy”**: Reproduced from Mayer S et al. (2019) *Marine Drugs* 17:521. doi: 10.3390/md17090521 under the Creative Commons CC BY 4.0 license (as indicated by MDPI).
- 7) **Manuscript “Novel meriolin derivatives as rapid apoptosis inducers”**: Reproduced with permission from Drießen D et al. (2019) *Bioorganic & Medicinal Chemistry* 27:3463–3468. doi: 10.1016/j.bmc.2019.06.029. Copyright 2019 Elsevier.
- 8) **Manuscript “Azaphilone pigments and macrodiolides from the coprophilous fungus *Coniella fragariae*”**: Reproduced with permission from Hu H et al. (2019) *Fitoterapia* 137:104249. doi: 10.1016/j.fitote.2019.104249. Copyright 2019 Elsevier.
- 9) **Manuscript “Sesterterpenes and macrolide derivatives from the endophytic fungus *Aplosporella javeedii*”**: Reproduced with permission from Gao Y et al. (2020) *Fitoterapia* 146:104652. doi: 10.1016/j.fitote.2020.104652. Copyright 2020 Elsevier.
- 10) **Manuscript “Didymellanosine, a new decahydrofluorene analogue, and ascolactone C from *Didymella* sp. IEA-3B.1, an endophyte of *Terminalia catappa*”**: Reproduced from Ariantari NP et al. (2020) *RSC Advances* 10:7232–7240. doi: 10.1039/c9ra10685e with permission from the Royal Society of Chemistry. This article is licensed under the Creative Commons Attribution-NonCommercial 3.0 Unported Licence (<https://creativecommons.org/licenses/by-nc/3.0/legalcode>).
- 11) **Manuscript “Induction of New Lactam Derivatives From the Endophytic Fungus *Aplosporella javeedii* Through an OSMAC Approach”**: Reproduced from Gao Y et al. (2020) *Frontiers in Microbiology* 11:600983. doi: 10.3389/fmicb.2020.600983 under the Creative Commons CC BY 4.0 license (as indicated by Frontiers Media).
- 12) **Manuscript “High-throughput screening for natural compound-based autophagy modulators reveals novel chemotherapeutic mode of action for arzanol”**: Reproduced with the copyright as author, and protected by the German copyright laws (including § 16, § 17, § 18, § 19a UrhG). Any reproduction of any parts of this manuscript in any form is not permitted without the explicit consent of these authors.
- 13) **Manuscript “Cancer-specific pro-apoptotic effects of the mycotoxin viriditoxin”**: Reproduced with the copyright as author, and protected by the German copyright laws (including § 16, § 17, § 18, § 19a UrhG). Any reproduction of any parts of this manuscript in any form is not permitted without the explicit consent of these authors.

Appendix

Publication 1

Manuscript “Pleiotropic effects of spongean alkaloids on mechanisms of cell death, cell cycle progression and DNA damage response (DDR) of acute myeloid leukemia (AML) cells”:

Stuhldreier E, Kassel S, Schumacher L, Wesselborg S, Proksch P, Fritz G.

Cancer Letters 361:39–48 (2015). doi: 10.1016/j.canlet.2015.02.030



Original Articles

Pleiotropic effects of spongean alkaloids on mechanisms of cell death, cell cycle progression and DNA damage response (DDR) of acute myeloid leukemia (AML) cells



Fabian Stuhldreier ^{a,b}, Stefanie Kassel ^{a,c}, Lena Schumacher ^a, Sebastian Wesselborg ^b, Peter Proksch ^c, Gerhard Fritz ^{a,*}

^a Institute of Toxicology, Heinrich Heine University Düsseldorf, Moorenstrasse 5, Düsseldorf 40225, Germany

^b Institute of Molecular Medicine I, Heinrich Heine University Düsseldorf, Moorenstrasse 5, Düsseldorf 40225, Germany

^c Institute of Pharmaceutical Biology and Biotechnology, Heinrich Heine University Düsseldorf Universitätsstrasse 1, Düsseldorf 40225, Germany

ARTICLE INFO

Article history:

Received 10 December 2014

Received in revised form 10 February 2015

Accepted 12 February 2015

Keywords:

DNA damage response

Cell death

Acute myeloid leukemia

Natural compounds

Spongean alkaloids

Anthracyclines

ABSTRACT

We investigated cytotoxic mechanisms evoked by the spongean alkaloids aaptamine (Aa) and aeropylsinin-1 (Ap), applied alone and in combination with daunorubicin, employing acute myeloid leukemia (AML) cells. Aa and Ap reduced the viability of AML cells in a dose dependent manner with IC₅₀ of 10–20 μM. Ap triggered apoptotic cell death more efficiently than Aa. Both alkaloids increased the protein level of S139-phosphorylated H2AX (γH2AX), which however was independent of the induction of DNA damage. Expression of the senescence markers p21 and p16 was increased, while the phosphorylation level of p-Chk-2 was reduced following Aa treatment. As a function of dose, Aa and Ap protected or sensitized AML cells against daunorubicin. Protection by Aa was paralleled by reduced formation of ROS and lower level of DNA damage. Both Aa and Ap attenuated daunorubicin-stimulated activation of the DNA damage response (DDR) as reflected on the levels of γH2AX, p-Kap-1 and p-Chk-1. Specifically Ap restored the decrease in S10 phosphorylation of histone H3 resulting from daunorubicin treatment. The cytoprotective effects of Aa and Ap were independent of daunorubicin import/export. Both Aa and Ap abrogated daunorubicin-induced accumulation of cells in S-phase. Inhibition of DNA synthesis was specific for Ap. The data show that Aa and Ap have both congruent and agent-specific pleiotropic effects that are preferential for anticancer drugs. Since Ap showed a broader spectrum of anticancer activities, this compound is suggested as novel lead compound for forthcoming in vivo studies elucidating the usefulness of spongean alkaloids in AML therapy.

© 2015 Elsevier Ireland Ltd. All rights reserved.

Introduction

Natural compounds (NC) are a promising source for the identification of novel lead compounds with anticancer activity. Apart from exhibiting anticancer potency on their own, NC might also be useful to increase the efficacy of approved anticancer therapeutics if used in combinatorial treatments [1,2]. Multiple mechanisms contribute to the anticancer effects of NC, including ROS formation [3], inhibition of microtubular function [4] or inhibition of topoisomerases [5]. Marine sponges are considered as an encouraging source for novel anticancer agents. For instance, the spongean alkaloids aeropylsinin-1 and aaptamine are reported to have

multiple activities useful for cancer treatment. Aeropylsinin-1 (Ap) is known to inhibit EGF receptor signaling [6], is anti-proliferative [7], causes growth arrest and apoptosis in Ehrlich ascites and HeLa tumor cells [8] and, moreover, has anti-angiogenic potency by inducing apoptosis in endothelial cells [9]. Aaptamine (Aa) causes a p53-independent induction of p21 in chronic myeloid leukemia (CML) cells [10]. Whether this holds true also for other types of leukemic cells, such as acute myeloid leukemia cells, is unknown. p53-independent activation of the p21 promotor by Aa was also reported in osteosarcoma cells and is accompanied by G2/M arrest [11]. Notably, the biological effect of Aa depends on the concentration: at lower concentrations it causes G2/M arrest, as shown in human embryonal carcinoma NT2 cells, whereas higher concentrations resulted in apoptosis [12]. Proteome-based pathway analyses showed a cross-talk of Aa with c-myc and p53 network [13]. The cytotoxic and anti-viral activity of Aa might be related to its ability to intercalate into the DNA [14]. Recently, Aa was described to protect normal rat kidney tubular cells from the cytotoxic effects of the anticancer drug cisplatin [15].

Abbreviations: Aa, aaptamine; AML, acute myeloid leukemia; Ap, aeropylsinin-1; dauno, daunorubicin; DDR, DNA damage response; H2AX, histone H2AX; γH2AX, S139-phosphorylated H2AX; ROS, reactive oxygen species.

* Corresponding author. Tel.: +49 211 8113022; fax: +49 211 8113013.

E-mail address: fritz@uni-duesseldorf.de (G. Fritz).

<http://dx.doi.org/10.1016/j.canlet.2015.02.030>

0304-3835/© 2015 Elsevier Ireland Ltd. All rights reserved.

Acute myeloid leukemia (AML) is the most frequent type of leukemia in adults and can occur as a late adverse effect of anticancer therapeutics, in particular topoisomerase type II poisons (= therapy-related AML; t-AML) [16]. AML and t-AML are characterized by different types of chromosomal rearrangements, most notably translocations involving the mixed lineage leukemia (MLL) gene [17]. It is assumed that the resulting oncogenes, for instance MLL-AF9, control myeloproliferation [18], likely by stimulating the association of transcriptional regulators with genes that produce critical factors for leukemia development [19,20]. Recently, it was demonstrated that MLL interferes with the regulation of Ataxia telangiectasia and Rad3-related kinase (ATR) [21], which is a key regulator of the DNA damage response (DDR) because it is crucial for a proper control of intra-S-phase checkpoints [22–24]. This finding indicates that ATR-regulated checkpoint mechanisms might be disturbed in AML cells expressing MLL fusion proteins. Nowadays, anti-metabolites such as cytarabine and anthracycline derivatives such as daunorubicin are frequently used in AML therapy [25,26]. A drawback of these agents is their limited anticancer efficacy and induction of normal tissue damage. Therefore, alternative therapeutic options are preferential. Here, we addressed the question whether the spongean alkaloids Aa and Ap might be useful in the therapy of AML, either alone or in combination with daunorubicin. To this end, cell viability, apoptosis and cell cycle progression were analyzed. Moreover, we aimed to elucidate the stress responses of AML cells that are evoked by Aa and Ap on the molecular level by focusing on mechanisms of the DNA damage response (DDR).

Materials and methods

Materials

The anthracycline derivative daunorubicin was obtained from the central pharmaceutical department of the University Hospital Düsseldorf and originates from Cell Pharm GmbH (Bad Vilbel, Germany). Acute monocytic leukemia (THP-1) and acute myeloid leukemia (NOMO-1) cells originate from the German collection of microorganisms (DSMZ, Braunschweig, Germany). The antibody detecting Ser139 phosphorylated histone H2AX (γ H2AX) was obtained from Millipore (Billerica, MA, USA), ERK2, p21, PARP and β -actin specific antibodies are from Santa Cruz Biotechnology (Santa Cruz, CA, USA), p-JNK (Thr183/Tyr18), p-p38 (Thr180/Tyr182), p-Chk1 (S345), p-Chk2 (Thr68) and p-p53 (S15) antibodies originate from New England Biolabs (Frankfurt am Main, Germany). Antibody specifically detecting the cleaved (i.e. activated) form of pro-caspase 3 was obtained from Cell Signaling Technology (Frankfurt am Main, Germany) (#9664) and antibody detecting non-cleaved pro-caspase 3 protein was purchased from R&D Systems (Wiesbaden, Germany) (AF-605-NA). Aaptamine and aeropylsin-1 were provided by the Institute of Pharmaceutical Biology and Biotechnology of the Heinrich Heine University (Düsseldorf, Germany). Isolation of the marine sponge alkaloids aaptamine and aeropylsin-1 has been described earlier [27–29]. Chemical structures and HPLC chromatograms showing the purity of the isolated spongean alkaloids are shown in [Supplementary Fig. S1](#). Substances were dissolved in DMSO. When treating cells, stock solutions were diluted thus far that the final DMSO concentration was $\leq 0.1\%$, (w/v), which is non toxic.

Cell culture and drug treatments

Acute monocytic leukemia cells (THP-1) and acute myeloid leukemia cells (NOMO-1), both harboring the t(11q23;MLL-AF9) translocation, originate from the German collection of microorganisms (DSMZ, Braunschweig, Germany). AML cells were routinely cultured in RPMI medium containing 10% fetal bovine serum at 37 °C in humidified atmosphere containing 5% (v/v) CO₂. If not stated otherwise, treatment of the proliferating cells started 24–36h after seeding ($2-5 \times 10^5$ cells/ml). Treatment with different concentrations of the spongean alkaloids was performed for 24 hours and daunorubicin was added at the indicated concentrations as described in the legends.

Analysis of DNA damage

In order to analyze DNA damage, the level of Ser139-phosphorylated H2AX (γ H2AX), which is a surrogate marker of DNA damage [30], was monitored by western blot analysis or by immunohistochemistry-based analysis of the number of γ H2AX foci/cell. For immunohistochemical analysis, cells were centrifuged onto glass slides (cytospin method). After treatment, cells were fixed with 4% paraformaldehyde (v/v) (15 min, RT) and ice-cold methanol (-20 °C, 1 h). After treatment with blocking solution (PBS containing 0.3% Triton X-100/5% BSA (w/v), 1 h, RT), the antibody specifically detecting phosphorylated (Ser139) histone H2AX (γ H2AX) (1:500) was added.

After overnight incubation at 4 °C and washing, secondary fluorescent labeled antibody (Alexa Fluor 488; Invitrogen) was added for 2 h (RT in the dark). Afterwards, cells were mounted in Vectashield containing the DNA staining dye DAPI. Relative level of γ H2AX as detected in untreated control cells by western blot analysis was set to 1.0. Analysis of DNA strand breaks was monitored using the alkaline Comet assay according to the protocol of Olive and Banath [31]. Briefly, cells were embedded in 0.5% low melting point-agarose and transferred onto agarose-precoated slides and allowed to gel. Subsequently, the slides were incubated in lysis buffer containing 2.5 M NaCl, 100 mM EDTA, 1% sodium lauryl sarcosinate, 10 mM Tris (pH 10) for 1 h followed by an unwinding step in electrophoresis buffer comprising 300 mM NaOH and 1 mM EDTA (pH 13) for 25 min at 4 °C. Electrophoresis was carried out for 15 min at 25 V and 300 mA, respectively, and samples were neutralized three times with 0.4 M Tris (pH 7.5). Finally, samples were fixed in 100% ethanol, air-dried and then stained with 50 μ g/ml propidium iodide. Comets were analyzed by microscopy (Olympus BX43). Quantification of migrated DNA was performed with TriTek Comet Score™ software Version 1.5 evaluating ≥ 50 cells per condition. Results showing the olive tail moment (OTM) are displayed as mean \pm SD of $n = 3$ independent experiments.

Determination of cell viability

$2-3 \times 10^4$ cells/well (96 well plate; 100 μ l culture medium per well) were seeded for cell viability analyses. In general, viability was analyzed 72 h after treatment using the water-soluble tetrazolium salt (WST) assay according to the manufacturers protocol (Boehringer Mannheim, Germany). Briefly, the WST reagent was added to each well (1:10), followed by an incubation period of 30–60 min. During this time, WST is metabolized to a formazan dye by mitochondrial dehydrogenase, which is active in living cells only. Absorption was measured at 440 nm. Relative viability in corresponding untreated (i.e. non anticancer drug treated) controls was set to 100%. If not stated otherwise, data shown are the mean \pm SD from 3 independent experiments each performed in triplicate.

FACS-based analysis of cell cycle distribution and cell death

Cell cycle distribution was analyzed by flow cytometry (FACS). To this end, cells were washed twice with PBS, resuspended in 100 μ l PBS and fixed with 2 ml of ice-cold ethanol (-20 °C, ≥ 20 min). After centrifugation (1000 \times g, 5 min, 4 °C) the supernatant was discarded. The cells were resuspended in PBS containing RNase (1 μ g/ μ l) and incubated for 1 h at room temperature. After adding propidium iodide (50 μ g/ml) the cells were subjected to FACS analysis for quantification of the percentage of cells present in SubG1, G1-, S- and G2-phase of the cell cycle. The subG1-fraction is considered as a measure of dead (apoptotic) cells. Caspase 3 activity was analyzed by measuring the cleavage of the fluorescent caspase 3 substrate Ac-DEVD-AMC (Biomol#ABD-13042) (Ex 360 nm, Em 450 nm) as described [32]. Measurements were performed in triplicate and relative caspase 3 activity in the untreated control cells was set to 100%. Moreover, cleavage of PARP protein and pro-caspase 3 were determined by Western blot analysis.

Determination of daunorubicin transport

Due to its inherent fluorescence, transport (i.e. import and export) of the anthracycline derivative daunorubicin can be analyzed by FACS-based method. To detect drug import, pulse treatment with daunorubicin (1 μ M) was performed for 2 h. To analyze daunorubicin export, the daunorubicin-labeled cells were post-incubated for another 6 h in the absence of the drug. The decrease in intracellular fluorescence is taken as measure of daunorubicin export. For FACS analysis, the cells were washed three times with PBS and resuspended in PBS.

Analysis of S-phase activity by measuring EdU incorporation

Incorporation of EdU was determined using the EdU Click-iT assay according to the manufacturers protocol (Life Technologies GmbH, Darmstadt, Germany). Cells were pulse-labeled with 5-ethynyl-2'-deoxyuridin (EdU) for 2 hours. After addition of Alexa Fluor 488-conjugated dye, the incorporation of the nucleoside into the DNA was determined by flow cytometry.

Determination of ROS formation

Reactive oxygen species (ROS) were measured using the DCF-assay according to the manufacturer's protocol (Life Technologies GmbH, Darmstadt, Germany). Briefly, in the presence of ROS, the substrate 2,7-dichlorodihydrofluorescein (H₂DCF) is cleaved into the fluorescent dye DCF, which is detected by flow cytometry.

Western blot analysis

After drug treatment, total cell extracts were prepared by lysing of $5 \times 10^5-10^6$ cells in 100–200 μ l of Roti-Load buffer (Carl Roth GmbH, Karlsruhe, Germany). After heating to 95 °C for 5 min, 20–30 μ l of the protein extract (containing $\sim 20-30$ μ g protein) was separated by SDS-PAGE (8–15% gel (v/v)) using the Mini-Protean system from Biorad (Munich, Germany). After electrophoresis (30 mA per gel), proteins were

transferred onto a nitrocellulose membrane by wet blotting using the aforementioned system from Biorad (transfer buffer: 25 mM Tris, 192 mM Glycin, 20% (v/v) MeOH). After blocking in 5% non-fat milk in TBS (w/v)/0.1% Tween (v/v) for 1 h at RT, incubation with the primary antibodies (1:200 – 1:1000) was performed overnight at 4 °C. After washing with TBS/0.1% Tween (v/v) (3 × 5 min, RT), incubation with peroxidase conjugated secondary antibody (1:2000) was performed for 2 h at RT. After washing, the bound antibodies were visualized using the Fusion FX7 imaging system (PepLab, Erlangen, Germany).

Statistical analysis

The Student's t-test was used for statistical analysis. $p \leq 0.05$ was considered as a statistically significant difference.

Results and discussion

Aaptamine and aeroplysinin-1 influence cell viability of AML cells and induce p21 expression

Aaptamine (Aa) and aeroplysinin-1 (Ap) reduced the viability of THP-1 and NOMO-1 cells in a dose dependent manner (Fig. 1A and C). The IC_{50} of Aa was $\sim 8 \mu\text{M}$ for both NOMO-1 and THP-1 cells, the IC_{50} of Ap was ~ 17 and $\sim 10 \mu\text{M}$ for NOMO-1 and THP-1 cells, respectively (Fig. 1A and C). Regarding HL-60 cells, IC_{50} of about $10 \mu\text{M}$ and $5 \mu\text{M}$ were observed for Aa and Ap, respectively (data not shown). These data do not support the hypothesis of a major selectivity of the spongean alkaloids toward specific subtypes of AML cells. Because Aa is known to cause a p53 independent induction of p21 in chronic myeloid leukemia (CML) cells [10], we examined whether the alkaloids stimulate p21 induction also in AML cells. Both alkaloids caused a substantial increase in p21 protein levels in THP-1 and NOMO-1 cells if used at a concentration of $5 \mu\text{M}$ (Fig. 1B and

D). Aa and Ap did not activate checkpoint kinase-1 (p-Chk-1), checkpoint kinase-2 (p-Chk-2) or p53 (p-p53) by their own (Fig. 1B). Ionizing radiation (IR), which was included as positive control, evoked these responses (Fig. 1B and D). Taken together, loss of cell viability following treatment of AML cells with the spongean alkaloids Aa and Ap was accompanied by increased protein expression of the cyclin-dependent kinase inhibitor p21. Already $5 \mu\text{M}$ of Aa and Ap were sufficient to increase p21 levels, whereas viability was only moderately affected at this concentration (Fig. 1).

Aaptamine and aeroplysinin-1 stimulate S139 phosphorylation of histone H2AX independent of the formation of DNA damage

Because part of the cytotoxic activity of Aa was discussed as a result from DNA intercalation [14], we next addressed the question whether Aa and Ap cause formation of DNA damage in AML cells. To this end, S139 phosphorylation of histone H2AX (γH2AX), which is a frequently used surrogate marker of the DNA damage response [30], was analyzed by Western blot. Both spongean alkaloids stimulated a substantial increase in γH2AX protein level if used at a concentration of $5 \mu\text{M}$ (Fig. 2A). At first sight, this finding indicates that Aa and Ap induce DNA damage. Immunocytochemical analysis, however, showed that Aa and Ap did not increase the number of nuclear γH2AX foci (Fig. 2B), which are indicative of DNA double-strand breaks [30,33], whereas ionizing radiation (IR) did so (Fig. 2B). Moreover, measuring DNA damage by employing the alkaline comet assay, which detects DNA single- and double-strand breaks [31], we also failed to detect DNA damage following treatment with Aa and Ap (Fig. 2C). Taken together, the data

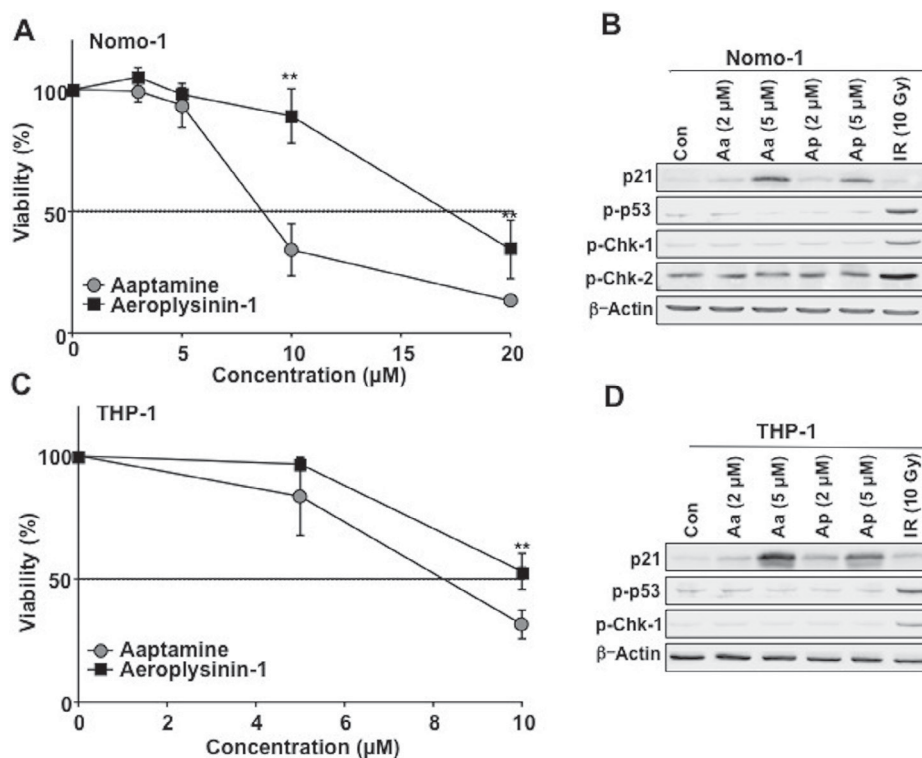


Fig. 1. Spongean alkaloids reduce viability and stimulate p21 expression in AML cells. (A, C) Logarithmically growing human acute myeloid leukemia cells (NOMO-1) (A) and acute monocytic leukemia cells (THP-1) (C) were treated with increasing concentrations of the spongean alkaloids aaptamine (Aa) or aeroplysinin-1 (Ap). After incubation period of 72 h, cell viability was monitored using the WST assay as described in methods. Relative viability in untreated control cells was set to 100%. Shown are the mean \pm SEM from at least 3 independent experiments each performed in triplicate. $**p \leq 0.01$. (B, D) NOMO-1 (B) and THP-1 (D) cells were treated with the indicated concentrations of aaptamine (Aa) or aeroplysinin-1 (Ap). Twenty-four hours later cells were harvested and the expression of a selected subset of cell cycle regulatory factors (p21, p-p53, p-Chk-1, p-Chk-2) was analyzed by Western blot analysis. For control, cells were exposed to ionizing radiation (IR, 10 Gy) and protein extracts were isolated 0.5 h later. The expression of β -actin was determined as protein loading control. Shown are representative blots from ≥ 3 independent experiments.

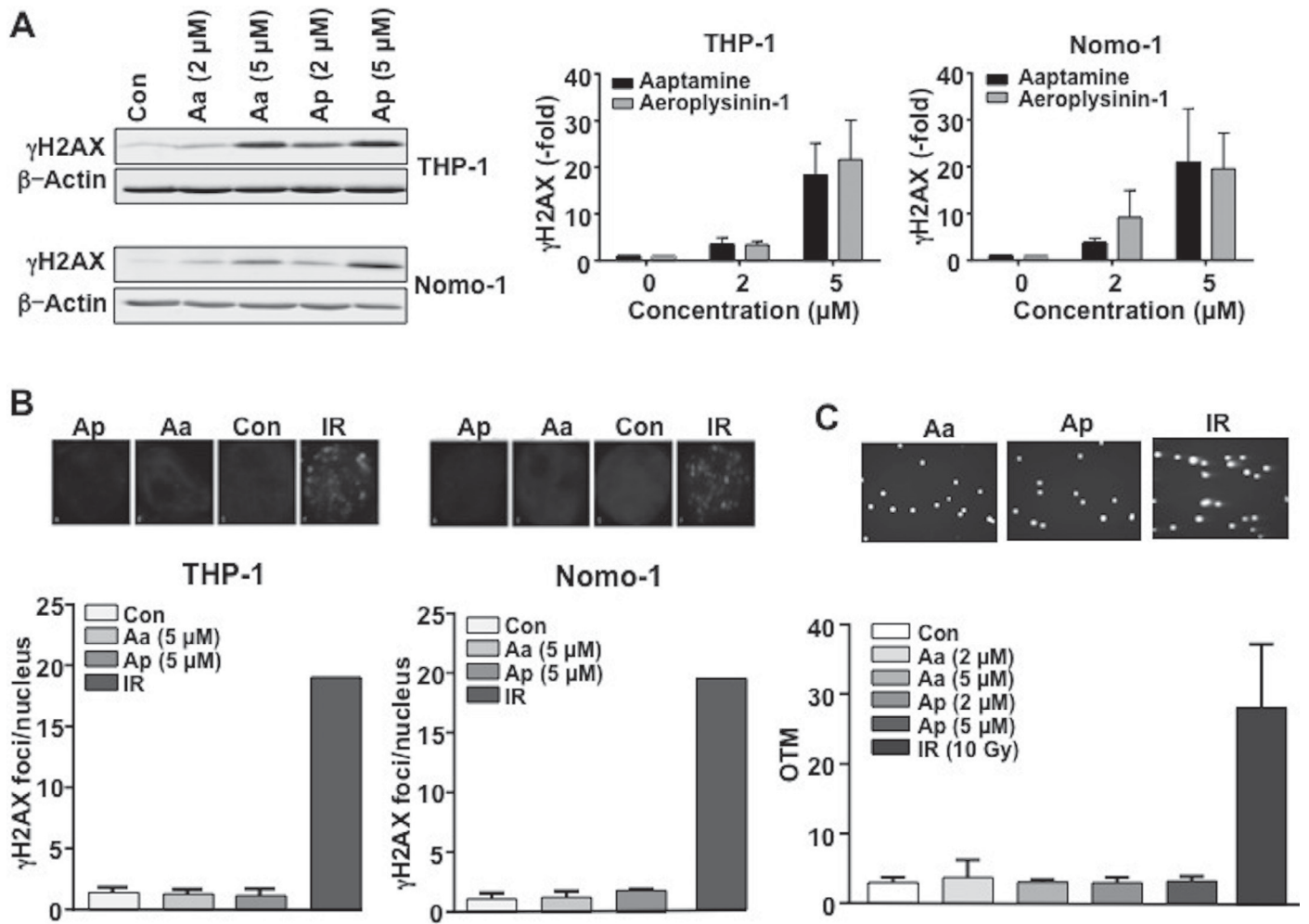


Fig. 2. Aaptamine and aeroplysinin-1 stimulate S139 phosphorylation of histone H2AX, which is independent of DNA damage induction. (A) Logarithmically growing NOMO-1 and THP-1 cells were treated with the indicated concentrations of aaptamine (Aa) or aeroplysinin-1 (Ap). After incubation period of 24 h, S139 phosphorylation of H2AX (γ H2AX) was determined by Western blot analysis. Shown is the result of a representative blot. On the right panel quantitative data (mean \pm SEM) obtained from densitometrical analysis of ≥ 3 independent experiments are shown. (B) 24 h after treatment of AML cells to 5 μ M of aaptamine (Aa) or aeroplysinin-1 (Ap), formation of nuclear γ H2AX foci, which are indicative of DNA double-strand breaks, was analyzed by immunohistochemistry as described in “Materials and methods” section. For control, cells were irradiated (IR, 2 Gy) and analysis was performed 0.5 h later. Shown are representative microscopic pictures. Data shown in the histograms were obtained from at least 2 independent experiments with each ≥ 50 nuclei being analyzed. (C) AML cells were treated as described under (B). For control, cells were irradiated with 10 Gy (IR) and analysis was performed 0.5 h later. The formation of strand breaks was analyzed using the alkaline Comet assay as described in “Materials and methods” section. Data shown are the mean \pm SD from 3 independent experiments with each ≥ 50 cells being analyzed.

indicate that the Aa- and Ap-stimulated increase in γ H2AX protein level does not result from the induction of DNA damage. It rather appears feasible that the alkaloids influence the chromatin structure, which eventually favors phosphorylation of H2AX. This hypothesis is mainly based on a report showing that alterations in chromatin structure, as induced by hypotonic conditions, also results in increased γ H2AX levels [34]. In this context, it should be noted that apart from the key regulatory kinases of the DDR (i.e. ATM/ATR/DNA-PKcs [23]), which use the amino acid motif S/TQ as consensus sequence for phosphorylation, other stress responsive kinases such as stress-activated protein kinases/c-Jun-N-terminal kinases (SAPK/JNK [35,36] (typical consensus sequence PXS/TP) and ribosomal S6 kinase (RSK [37] (typical consensus sequence RXXS) can also phosphorylate H2AX at position S139. Noteworthy was that UVA-induced S139 phosphorylation of H2AX by SAPK/JNK, does not result in the formation of distinct nuclear γ H2AX foci but rather causes a pan-staining of the nucleus [38]. It has been suggested that S139 of H2AX acts as a site of signal integration between the SAPK/JNK pathway and DDR mechanisms regulated by the PIKK group of kinases, including ATM, ATR and DNA-PKcs [37]. Bearing this in mind,

we speculate that the observed increase in γ H2AX protein levels following Aa and Ap treatment of AML cells is related to alterations in the chromatin structure and is catalyzed by kinases others than ATM/ATR/DNA-PKcs.

Influence of aaptamine and aeroplysinin-1 on the expression of factors involved in the regulation of cell cycle progression, DDR and apoptosis

Next, we aimed to figure out whether Aa and Ap affect the expression of cell cycle regulatory factors others than p21 (see Fig. 1). To this end, NOMO-1 cells were treated with different concentrations of Aa and Ap and the expression of CDK inhibitory proteins p16 and p21 was analyzed. As shown in Fig. 3A, Aa and Ap concomitantly caused an increase in the expression of p21 and p16, which both are involved in the regulation of the G1/S checkpoint and are frequently used as markers of senescence [39,40]. Notably yet, the dose response of p21 expression following Aa and Ap treatment was not linear but showed an inverse U-shaped form (Fig. 3A). A maximum p21 expression was observed at a dose of 5 μ M and

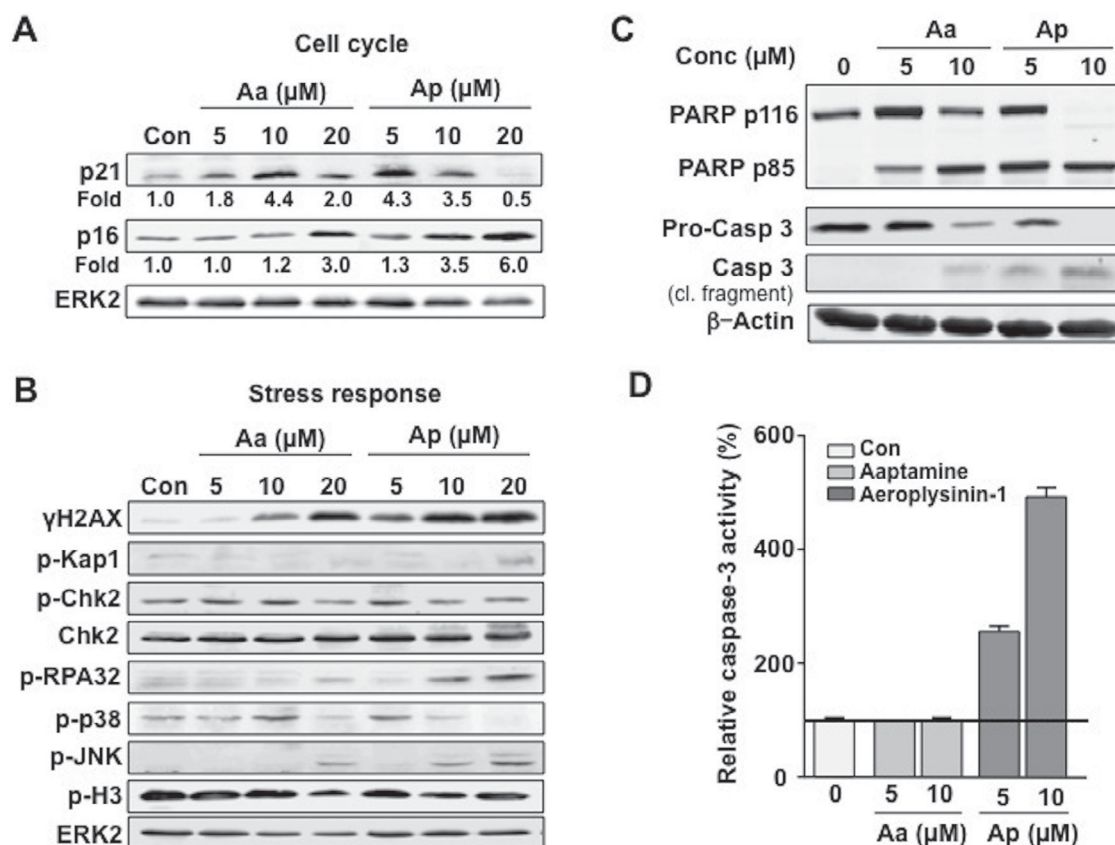


Fig. 3. Dose dependent effects of Aa and Ap on mechanisms of cell cycle, DNA damage response and cell death of AML cells. (A) NOMO-1 cells were treated with increasing concentrations of aaptamine (Aa) or aerplysinin-1 (Ap). After incubation period of 24 h, cells were harvested and the expression level of the cell cycle regulatory factors p21 and p16 was analyzed by Western blot analysis. Expression of ERK2 was determined as protein loading control. After densitometrical analysis of the blots, relative protein expression of p21 (or p16) in untreated controls was set to 1.0. (B) NOMO-1 cells were treated with increasing concentrations of aaptamine (Aa) or aerplysinin-1 (Ap). After incubation period of 24 h, cells were harvested and the expression level of phosphorylated factors that are indicative of stress responses was analyzed by Western blot analysis. Expression of ERK2 was determined as protein loading control. (C, D) Following treatment of NOMO-1 cells for 24 h with the indicated concentrations of Aa or Ap, activation of apoptotic mechanisms was investigated by monitoring the cleavage of PARP, the level of cleaved (i.e. activated) pro-caspase 3 (Casp 3) and the amount of non-cleaved pro-caspase 3 (Pro-Casp 3) (C) or measuring caspase 3 activity as described in “Materials and methods” section (D). Quantitative data shown in (D) are the mean \pm SD from a representative experiment performed in triplicate. Relative caspase 3 activity in untreated control cells was set to 100%.

10 μM for Ap and Aa, respectively. Stimulation of p16 expression was most efficient by Ap (Fig. 3A). These data indicate that the spongean alkaloids can trigger mechanisms of senescence in AML cells which are independent of DNA damage.

In further analyses we examined the impact of Aa and Ap on signal mechanisms that are related to the DDR. While Aa and Ap caused a substantial increase in γH2AX level, the phosphorylation of the heterochromatin regulatory factor Kap-1 [41] was only slightly increased by a high dose of Ap (Fig. 3B). If used at high concentration, Ap also stimulated the phosphorylation of replication protein RPA32 (Fig. 3B). Since RPA32 is substrate of ATR kinase, which is a key player in the regulation of replicative stress responses [42], this finding indicates that Ap triggers ATR-regulated S-phase specific stress responses. Moreover, phosphorylation of histone H3, which naturally occurs during mitosis [43], was mitigated by high concentrations of Aa and, to a weaker extent, also by Ap. Stress kinases belonging to the MAPK family (p38 kinase and SAPK/JNK) were also weakly activated by Aa and Ap (Fig. 3B).

Regarding mechanisms associated with apoptosis we found that Ap is particular efficient in stimulating apoptotic pathways. For instance, 5 μM of Ap stimulated the cleavage of the caspase substrate PARP and proteolytic activation of pro-caspase 3 more efficient than 5 μM Aa (Fig. 3C). In line with this, a substantial stimulation of caspase 3 activity was observed only after Ap treatment (Fig. 3D). Taken together, these data indicate that the spongean alkaloids differ

from each other regarding their efficacy to stimulate mechanisms of cell death. Ap showed a higher potency than Aa. Hence, the loss of cell viability occurring in response to Aa and Ap treatment (see Fig. 1) seems to involve different mechanisms, with the induction of apoptosis being more relevant for Ap. However, application of a pan-caspase inhibitor only moderately rescued cells from Ap-induced loss of viability (Supplementary Fig. S2). Similar effects were observed for Aa (Supplementary Fig. S2). This indicates that Aa and Ap-stimulated cell death is either largely independent of caspase activation or that other types death mechanisms become compensatorily activated if caspases are inhibited.

Influence of Aa and Ap on daunorubicin-induced cytotoxicity

Since daunorubicin is a major part of the current therapeutic regimen of AML therapy [26], we wondered whether Aa and Ap can potentiate the cytotoxicity of this anthracycline derivative. As shown in Fig. 4A, daunorubicin decreases viability in Nomo-1 cells in a dose dependent manner with an IC_{50} of ~ 0.12 μM in both NOMO-1 and THP-1 cells. To figure out whether the spongean alkaloids modulate daunorubicin-induced cytotoxicity, NOMO-1 cells were co-treated for 72 h with different concentrations of the corresponding alkaloid and the IC_{50} dose of daunorubicin (i.e. 0.12 μM). The data show that Aa and Ap significantly increased the viability of NOMO-1 cells toward daunorubicin if used in low, subtoxic concentrations

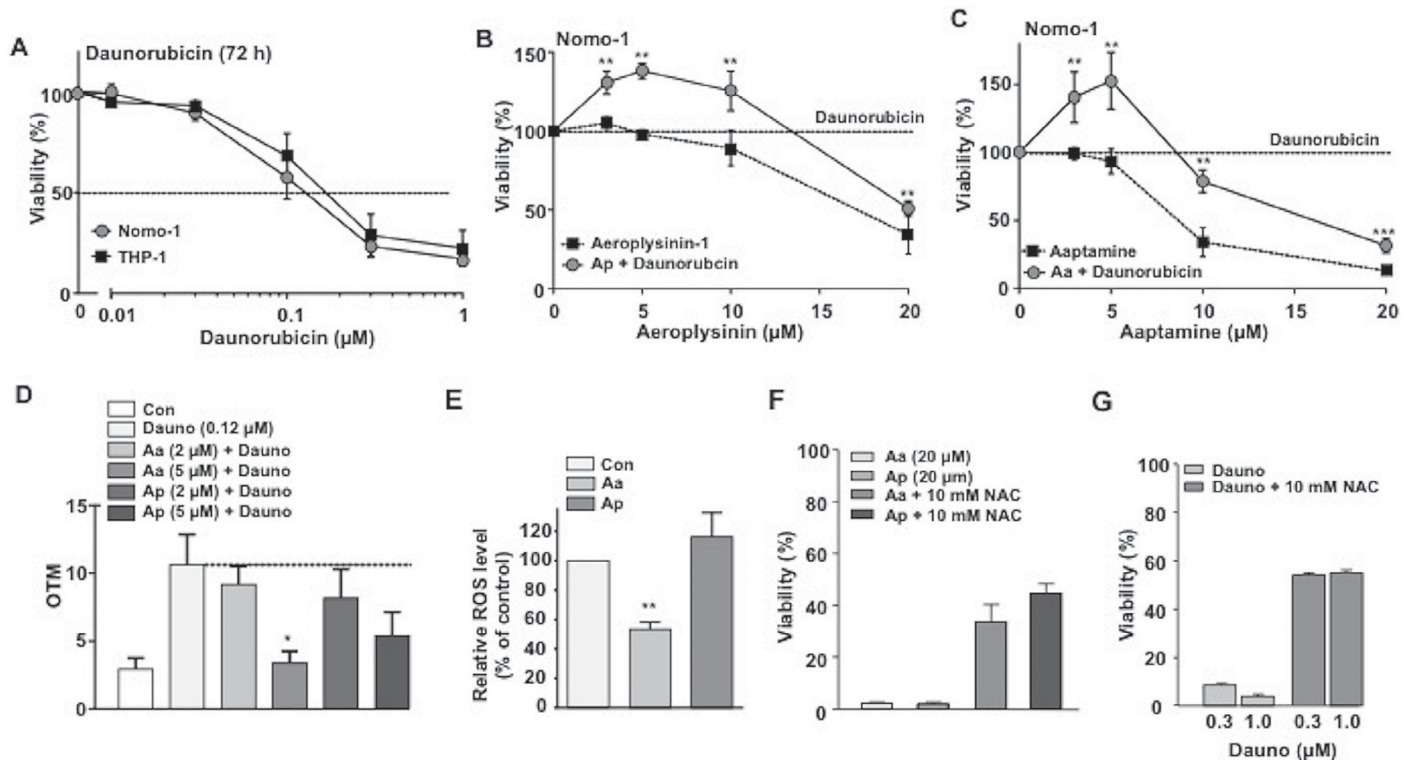


Fig. 4. As a function of dose, the spongean alkaloids Aa and Ap can either reduce or increase the cytotoxicity of the anthracycline derivative daunorubicin. (A) Cell viability was determined 72 h after treatment of NOMO-1 or THP-1 cells with increasing doses of daunorubicin. Data shown are the mean \pm SD from ≥ 3 independent experiments each performed in triplicate. The dashed line illustrates the IC_{50} , which is $\sim 0.12 \mu\text{M}$ for both cell lines. (B, C) NOMO-1 cells were co-treated with the IC_{50} concentration of daunorubicin (0.12 μM), which was set to 100% (dashed line) and increasing concentrations of aeropylsinin-1 (B) or aptamine (C). After incubation period of 72 h, cell viability was determined as described in “Materials and methods” section. Data shown are the mean \pm SEM from 3 independent experiments each performed in triplicate. $**p \leq 0.01$. (D) Cells were treated with the indicated concentrations of daunorubicin, aptamine and aeropylsinin-1. After incubation period of 24 h, cells were harvested and the level of DNA damage (i.e. DNA strand breaks) was measured using the alkaline comet assay as described in “Materials and methods” section. The olive tail moment (OTM) is indicative of DNA strand breaks. Data shown are the mean \pm SD from two independent experiments with ≥ 50 nuclei being analyzed per sample. $*p \leq 0.05$. (E) After incubation period of 24 h with 5 μM of aptamine (Aa) or aeropylsinin-1 (Ap), the level of ROS was determined by fluorescence-based method as described in “Materials and methods” section. Data shown are the mean \pm SD from 2 independent experiments. $**p \leq 0.01$. (F) Cells were treated with 20 μM of Aa or Ap in the presence or absence of N-acetyl-cysteine (NAC) (10 mM). After incubation period of 24 h, cell viability was monitored as described in “Materials and methods” section. Data shown are the mean \pm SD from a representative experiment performed in quadruplicate. (G) Cells were treated with 0.3 or 1.0 μM of daunorubicin (Dauno) and co-treated or not with N-acetyl-cysteine (NAC) (10 mM). After incubation period of 24 h, cell viability was monitored as described in methods. Data shown are the mean \pm SD from a representative experiment performed in quadruplicate.

of $\leq 5 \mu\text{M}$ (Fig. 4B). While protecting from daunorubicin-induced cytotoxicity at low doses, higher doses of the alkaloids (i.e. $> 10 \mu\text{M}$) promoted the toxic effects of the anthracycline (Fig. 4B and C). Protection from daunorubicin-induced cytotoxicity by Aa was paralleled by a reduced formation of DNA strand breaks (Fig. 4D) and antioxidative capacity (Fig. 4E). Taken together, the data show that the spongean alkaloids Aa and Ap influence the cytotoxicity of daunorubicin in a dual manner: depending on the dose they can act either in a protective or sensitizing manner. While protection mediated by Aa is related to its antioxidative capacity and reduced DNA damage formation, mechanisms underlying the cytoprotective effect of Ap are likely independent of ROS and DNA damage induction. In this context we would like to note that the cytotoxicity of Aa and Ap (Fig. 4F) as well as of daunorubicin (Fig. 4G) can be prevented by co-incubation with the antioxidant N-acetyl-cysteine (NAC), indicating that oxidative stress contributes to the cytotoxicity evoked by Aa, Ap and daunorubicin in AML cells.

Influence of Aa and Ap on daunorubicin-induced stress responses and cell cycle progression

In a next step, we investigated the influence of Aa and Ap on stress responses evoked by daunorubicin treatment. Both Aa and Ap inhibited the increase in γH2AX , p-KAP1 and p-Chk-1 levels

following treatment with 0.12 μM of daunorubicin (Fig. 5A). Such inhibitory effects were not observed if higher concentrations of daunorubicin were used (Fig. 5A). Notably, the attenuation of daunorubicin-induced DDR by spongean alkaloids is independent of transport mechanisms. Neither Aa nor Ap affected the uptake of daunorubicin into the cells (Fig. 5C). Moreover, export of daunorubicin was also not influenced (Fig. 5C). Monitoring S10 phosphorylation of histone H3 (p-H3), which is a marker of mitosis, daunorubicin caused a strong decrease in the protein level of pH3, which was specifically prevented by Ap but not by Aa (Fig. 5A). Regarding the activation of apoptotic pathways, neither Ap nor Aa showed substantial effects on the cleavage of the caspase substrate PARP following daunorubicin treatment (Fig. 5B). Similar results were obtained if the level of cleaved (i.e. activated) pro-caspase 3 was measured (Fig. 5B).

Furthermore, both alkaloids modulated daunorubicin-induced alterations in cell cycle progression as analyzed 24 h after treatment by flow cytometry. The increase in the S-phase population as caused by daunorubicin treatment was significantly prevented by co-treatment with Aa and Ap (Fig. 6A). Identical effects were observed when THP-1 cells were used (Supplementary Fig. S3). Measuring cell cycle distribution by flow cytometry 72 h after drug addition, no major interference of Aa and Ap with daunorubicin-stimulated effects were detectable. Noteworthy, while Ap caused a

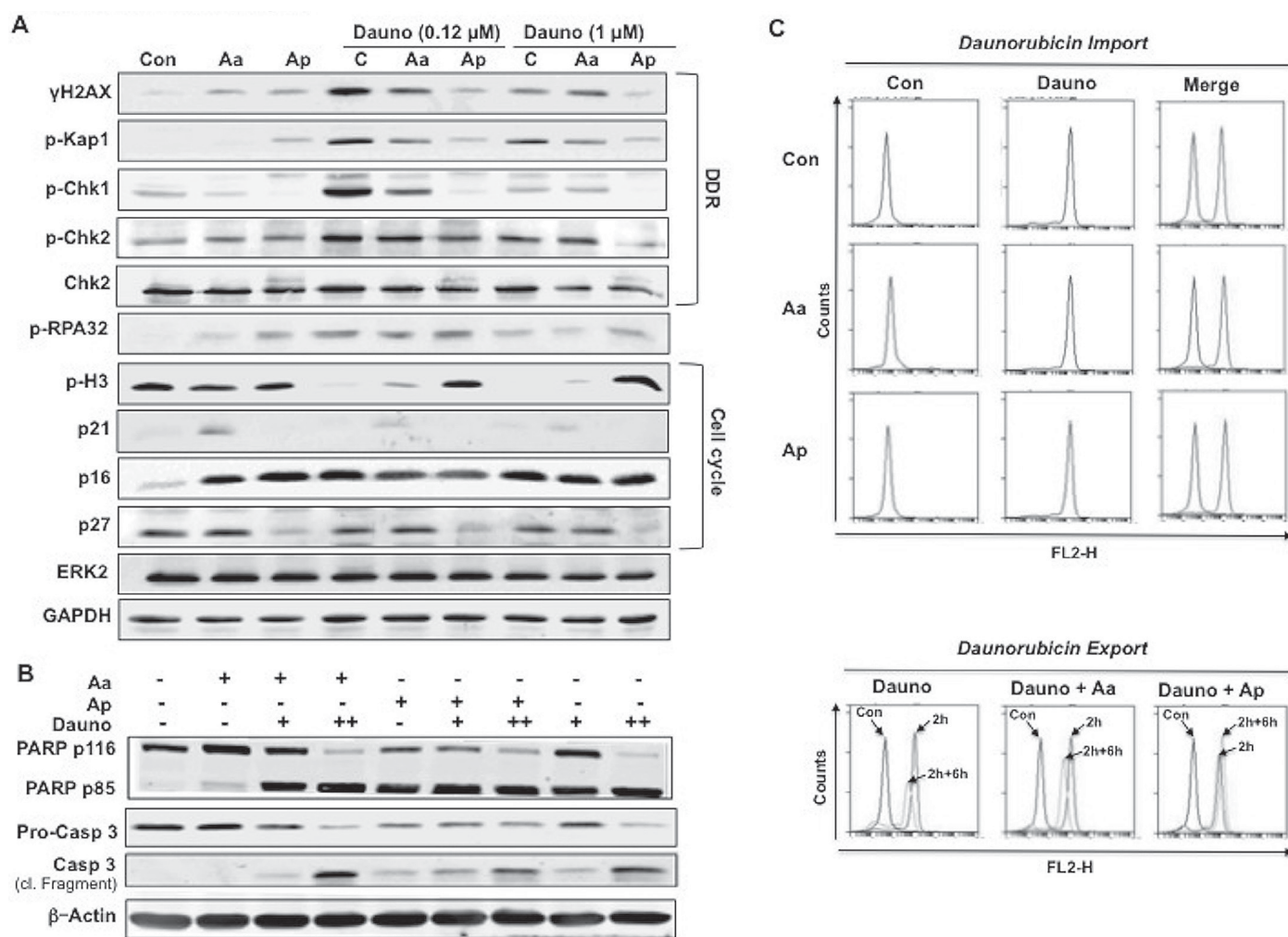


Fig. 5. Modulation of daunorubicin-induced DNA damage response (DDR) and apoptotic mechanisms by Aa and Ap. (A) NOMO-1 cells were treated with aaptamine (Aa) (10 μM), aeropylsinin-1 (Ap) (10 μM) and/or daunorubicin (dauno) (0.12 or 1 μM). After incubation period of 24 h, cells were harvested and the phosphorylation level of DDR factors and expression level of cell cycle regulatory factors were analyzed by Western blot analysis. Expression of ERK2 and GAPDH were determined as protein loading control. (B) Cells were treated with aaptamine (Aa) (5 μM), aeropylsinin-1 (Ap) (5 μM) and/or daunorubicin (dauno) (0.12 or 1 μM). Twenty-four hours after addition of daunorubicin, activation of apoptotic mechanisms was determined by measuring cleavage of PARP as well as the levels of cleaved (i.e. activated) pro-caspase 3 (Casp 3) and the non-cleaved pro-caspase 3 (Pro-Casp 3) by Western blot. Expression of β-actin was determined as protein loading control. Aa (+), 5 μM; Ap (+), 5 μM; Dauno (+, ++), 0.12 μM (+) or 1.0 μM (++) (C) Analysis of daunorubicin import and export. Cells were treated with 1 μM of daunorubicin in the presence or absence of 5 μM of Aa or Ap. After incubation period of 2 h, intracellular daunorubicin concentration was determined by FACS analysis as described in "Materials and methods" section. Moreover, residual intracellular level of daunorubicin was analyzed after a post-incubation period of 6 h in the absence of daunorubicin. Shown are representative data from two independent experiments.

substantial increase in SubG1 cells, which is indicative of apoptotic cells, Aa did not provoke this response (Fig. 6B). These data are in line with data shown in Fig. 3C and D, again pointing to a preferential induction of proapoptotic mechanisms by Ap but not by Aa. The increase in SubG1 fraction observed after daunorubicin treatment was not further enhanced by Ap co-treatment, indicating a saturation effect (Fig. 6B).

Specific inhibition of DNA synthesis by Ap

To analyze the influence of spongean alkaloids on DNA synthesis, cells were pulse-labeled with the fluorescent nucleotide EdU after single or combined treatments for 24 h. The incorporation of EdU was monitored by flow cytometry. As shown in Fig. 6C, untreated and Aa only treated cells revealed a clear DNA synthesis as reflected by an increase in the number of cells present in the FL1-A channel. By contrast, Ap treated cells completely lack EdU incorporation, suggesting a massive block of DNA synthesis (Fig. 6C). Similar to Ap, daunorubicin treatment also caused a large

decrease in DNA synthesis (Fig. 6C). Next, EdU labeling was performed first and EdU positive cells were monitored 24 h after treatment with the spongean alkaloids and daunorubicin. Whereas non-treated control cells revealed EdU positive cells in both G1- and G2-phase, all drug treatments prevented the progression of EdU-labeled S-phase cells into the next G1 phase (Fig. 6D). Hence, we conclude that Aa and Ap as well as daunorubicin disturb normal cell cycle progression through S- and G2/M-phase. It is feasible that part of the cell cycle-related effects of the spongean alkaloids are related to a stimulation of differentiation processes, as described for instance for retinoic acid derivatives in the context of APL therapy [44]. Yet, to our knowledge, effects of Aa or Ap on the differentiation status of AML cells have not been reported so far.

Taken together, the spongean alkaloids Aa and Ap have pleiotropic effects on AML cells (Fig. 7). They decrease cell viability of AML cells by their own, with Ap being a more potent inducer of apoptosis than Aa. It should be noted that stimulation of apoptotic mechanisms by Ap was not restricted to AML cells but was also observed in endothelial cells (Supplementary Fig. S4). Both Aa and Ap

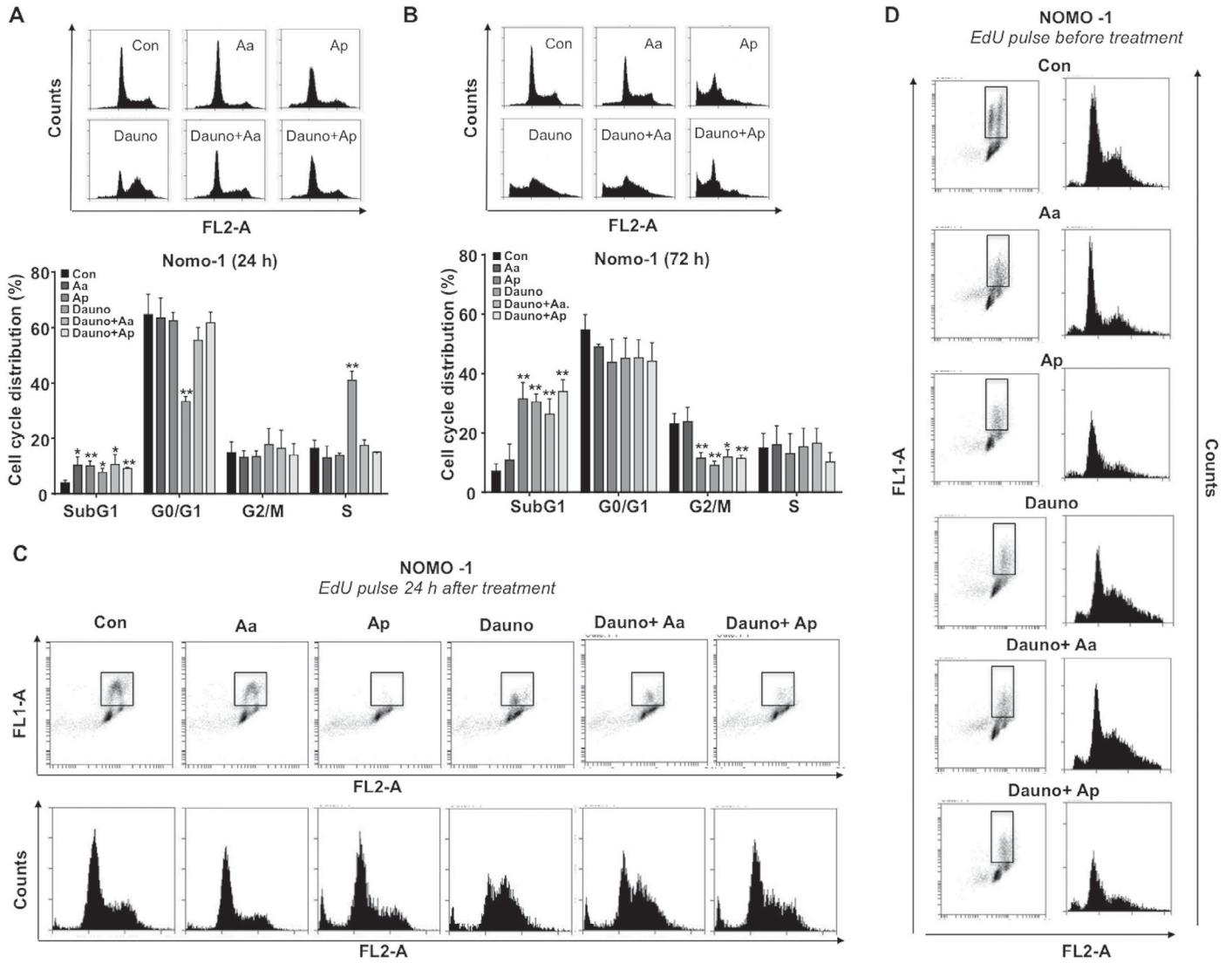


Fig. 6. Aa and Ap influence cell cycle progression of AML cells following daunorubicin treatment. (A, B) Logarithmically growing NOMO-1 cells were treated or not with aaptamine (Aa) (5 μM), aerplysinin-1 (Ap) (10 μM) and/or daunorubicin (Dauno) (0.12 μM). After incubation periods of 24 h (A) or 72 h (B) cells were fixed and cell cycle distribution was determined by flow cytometry as described in methods. Data shown are the mean ± SD from ≥3 independent analyses. *p ≤ 0.05; **p ≤ 0.01. (C) NOMO-1 cells were treated with 10 μM of aaptamine (Aa), aerplysinin-1 (Ap) and/or daunorubicin (Dauno) (0.12 μM). After incubation period of 24 h cells were pulse-labeled with EdU as described in “Materials and methods” section. Incorporation of EdU into the DNA was determined by flow cytometry as described in “Materials and methods” section. Shown are representative data from 2 independent experiments each performed in duplicate. (D) Cells were pulse-labeled with EdU as described in “Materials and methods” section. Afterwards, aaptamine (Aa) (10 μM), aerplysinin-1 (Ap) (10 μM) and daunorubicin (dauno) (0.12 μM) were added. After incubation period of 24 h, cells were subjected to flow cytometry analysis. Shown are representative data from 2 independent experiments.

modulate daunorubicin-stimulated cytotoxicity in a complex (non linear) manner; at low doses they have protective effects whereas at higher doses they promote the cytotoxicity of the anthracycline derivate. The cytoprotective effects of Aa likely involves antioxidative and genoprotective mechanisms. On the molecular level, Aa and Ap show qualitatively congruent responses such as an increase in the level of S139 phosphorylated H2AX protein (γH2AX). Although γH2AX is a widely used marker of DNA damage, Aa and Ap-stimulated H2AX phosphorylation is independent of DNA damage formation as shown by the comet assay and by measuring nuclear γH2AX foci. We hypothesize that mechanism underlying H2AX phosphorylation by Aa and Ap resemble the mechanisms described for osmotic stress [34] and involve kinases others than ATM/ATR. Moreover, both Aa and Ap are able to stimulate senescence-related mechanisms as indicated by an enhanced protein expression of p21 and p16 [39]. Notably, daunorubicin-stimulated DDR, as reflected

on the levels of γH2AX, p-Kap1 and p-Chk1 are blocked by Aa and, even more efficiently, by Ap. Remarkably, Ap fully reversed the inhibitory effects of daunorubicin on S10 phosphorylation of histone H3, while Aa did not. On the other hand, both spongean alkaloids prevent the accumulation of cells in S-phase following daunorubicin treatment. Apparently, apart from common effects on daunorubicin-induced stress responses, Aa and Ap accomplish specific effects as well. Importantly, the aforementioned impact of the spongean alkaloids on daunorubicin-induced stress responses is independent of the transport of the anthracycline. Another intriguing finding was that DNA synthesis gets specifically blocked by Ap (and daunorubicin) but not by Aa. This indicates that specifically Ap interferes with mechanisms of DNA synthesis and S-phase progression. Summarizing, Aa and Ap have various, both unique and common, biological activities on AML cells that occur in a narrow dose window. Because Ap comprises a broader spectrum of activities useful for anticancer

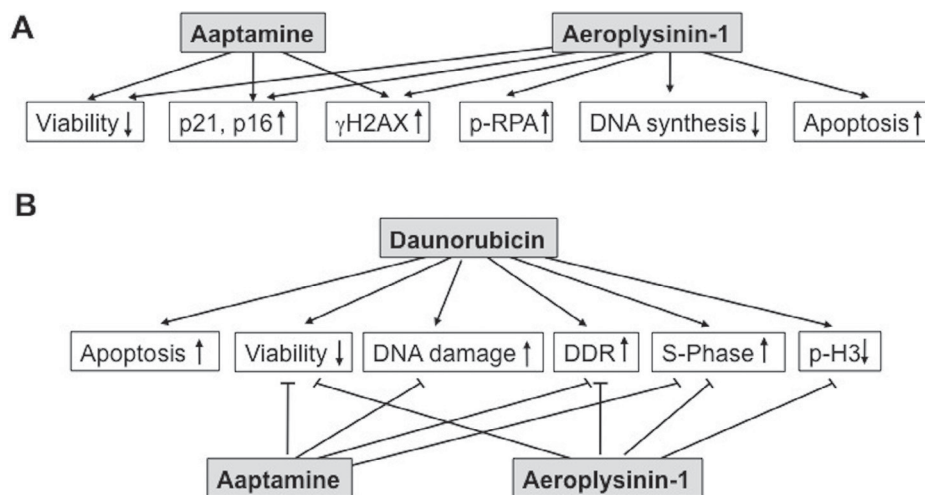


Fig. 7. Summary of Aa and Ap-mediated effects on AML cells (A) and daunorubicin-stimulated stress responses (B).

therapy (Fig. 7), this spongan alkaloid appears to be particular appropriate for further analyses. The in vitro data presented here encourage forthcoming in vivo studies to elucidate their usefulness in AML therapy, either as monotherapeutics or in combination with established AML therapeutics, including anthracyclines and antimetabolites.

Funding

This work was supported by the Düsseldorf „School of Oncology“ and the Medical Faculty of the Heinrich Heine University Düsseldorf.

Conflict of interest

There is no conflict of interest to be disclosed.

Appendix: Supplementary material

Supplementary data to this article can be found online at doi:10.1016/j.canlet.2015.02.030.

References

- [1] A. Mohan, S. Narayanan, S. Sethuraman, U.M. Krishnan, Combinations of plant polyphenols and anti-cancer molecules: a novel treatment strategy for cancer chemotherapy, *Anticancer Agents Med. Chem.* 13 (2013) 281–295.
- [2] C. Spatafora, C. Tringali, Natural-derived polyphenols as potential anticancer agents, *Anticancer Agents Med. Chem.* 12 (2012) 902–918.
- [3] S.M. Hadi, S.H. Bhat, A.S. Azmi, S. Hanif, U. Shamim, M.F. Ullah, Oxidative breakage of cellular DNA by plant polyphenols: a putative mechanism for anticancer properties, *Semin. Cancer Biol.* 17 (2007) 370–376.
- [4] K. Ferrante, B. Winograd, R. Canetta, Promising new developments in cancer chemotherapy, *Cancer Chemother. Pharmacol.* 43 (Suppl.) (1999) S61–S68.
- [5] G. Shao Rong, X. Cao Chun, H. Zhang, W. Kohn Kurt, S. Wold Marc, Y. Pommier, Replication-mediated DNA damage by camptothecin induces phosphorylation of RPA by DNA-dependent protein kinase and dissociates RPA:DNA-PK complexes, *EMBO J.* 18 (1999) 1397–1406.
- [6] M.H. Kreuter, R.E. Leake, F. Rinaldi, W. Muller-Klieser, A. Maidhof, W.E. Muller, et al., Inhibition of intrinsic protein tyrosine kinase activity of EGF-receptor kinase complex from human breast cancer cells by the marine sponge metabolite (+)-aeropylsinin-1, *Comp. Biochem. Physiol. B.* 97 (1990) 151–158.
- [7] B. Martinez-Poveda, J.A. Garcia-Vilas, C. Cardenas, E. Melgarejo, A.R. Quesada, M.A. Medina, The brominated compound aeropylsinin-1 inhibits proliferation and the expression of key pro-inflammatory molecules in human endothelial and monocyte cells, *PLoS ONE* 8 (2013) e55203.
- [8] A. Koulman, P. Proksch, R. Ebel, A.C. Beekman, W. van Uden, A.W. Konings, et al., Cytotoxicity and mode of action of aeropylsinin-1 and a related dione from the sponge *Aplysina aerophoba*, *J. Nat. Prod.* 59 (1996) 591–594.
- [9] B. Martinez-Poveda, S. Rodriguez-Nieto, M. Garcia-Caballero, M.A. Medina, A.R. Quesada, The antiangiogenic compound aeropylsinin-1 induces apoptosis in endothelial cells by activating the mitochondrial pathway, *Mar. Drugs* 10 (2012) 2033–2046.
- [10] M. Jin, W. Zhao, Y. Zhang, M. Kobayashi, H. Duan, D. Kong, Antiproliferative effect of aaptamine on human chronic myeloid leukemia k562 cells, *Int. J. Mol. Sci.* 12 (2011) 7352–7359.
- [11] S. Aoki, D. Kong, H. Suna, Y. Sowa, T. Sakai, A. Setiawan, et al., Aaptamine, a spongan alkaloid, activates p21 promoter in a p53-independent manner, *Biochem. Biophys. Res. Commun.* 342 (2006) 101–106.
- [12] S.A. Dyshlovoy, I. Naeth, S. Venz, M. Preukschas, H. Sievert, C. Jacobsen, et al., Proteomic profiling of germ cell cancer cells treated with aaptamine, a marine alkaloid with antiproliferative activity, *J. Proteome Res.* 11 (2012) 2316–2330.
- [13] S.A. Dyshlovoy, S. Venz, L.K. Shubina, S.N. Fedorov, R. Walthers, C. Jacobsen, et al., Activity of aaptamine and two derivatives, demethoxyaaptamine and iso-aaptamine, in cisplatin-resistant germ cell cancer, *J. Proteomics* 96 (2014) 223–239.
- [14] J.J. Bowling, H.K. Pennaka, K. Ivey, S. Wahyuono, M. Kelly, R.F. Schinazi, et al., Antiviral and anticancer optimization studies of the DNA-binding marine natural product aaptamine, *Chem. Biol. Drug Des.* 71 (2008) 205–215.
- [15] F. Funk, K. Kruger, C. Henninger, W. Watjen, P. Proksch, J. Thomale, et al., Spongan alkaloids protect rat kidney cells against cisplatin-induced cytotoxicity, *Anticancer Drugs* 25 (2014) 917–929.
- [16] H.J. Super, N.R. McCabe, M.J. Thirman, R.A. Larson, M.M. Le Beau, J. Pedersen-Bjergaard, et al., Rearrangements of the MLL gene in therapy-related acute myeloid leukemia in patients previously treated with agents targeting DNA-topoisomerase II, *Blood* 82 (1993) 3705–3711.
- [17] C. Schoch, S. Schnittger, M. Klaus, W. Kern, W. Hiddemann, T. Haferlach, AML with 11q23/MLL abnormalities as defined by the WHO classification: incidence, partner chromosomes, FAB subtype, age distribution, and prognostic impact in an unselected series of 1897 cytogenetically analyzed AML cases, *Blood* 102 (2003) 2395–2402.
- [18] C.L. Dobson, A.J. Warren, R. Pannell, A. Forster, I. Lavenir, J. Corral, et al., The mll-AF9 gene fusion in mice controls myeloproliferation and specifies acute myeloid leukaemogenesis, *EMBO J.* 18 (1999) 3564–3574.
- [19] S.C. Monroe, S.Y. Jo, D.S. Sanders, V. Basrur, K.S. Elenitoba-Johnson, R.K. Slany, et al., MLL-AF9 and MLL-ENL alter the dynamic association of transcriptional regulators with genes critical for leukemia, *Exp. Hematol.* 39 (2011) 77–86, e71–75.
- [20] A.G. Muntean, J. Tan, K. Sitwala, Y. Huang, J. Bronstein, J.A. Connelly, et al., The PAF complex synergizes with MLL fusion proteins at HOX loci to promote leukemogenesis, *Cancer Cell* 17 (2010) 609–621.
- [21] H. Liu, S. Takeda, R. Kumar, T.D. Westergaard, E.J. Brown, T.K. Pandita, et al., Phosphorylation of MLL by ATR is required for execution of mammalian S-phase checkpoint, *Nature* 467 (2010) 343–346.
- [22] D. Cortez, S. Guntuku, J. Qin, S.J. Elledge, ATR and ATRIP: partners in checkpoint signaling, *Science* 294 (2001) 1713–1716.
- [23] J.W. Harper, S.J. Elledge, The DNA damage response: ten years after, *Mol. Cell* 28 (2007) 739–745.
- [24] R.D. Paulsen, K.A. Cimprich, The ATR pathway: fine-tuning the fork, *DNA Repair (Amst)* 6 (2007) 953–966.
- [25] A. Burnett, M. Wetzler, B. Lowenberg, Therapeutic advances in acute myeloid leukemia, *J. Clin. Oncol.* 29 (2011) 487–494.
- [26] G.J. Roboz, Current treatment of acute myeloid leukemia, *Curr. Opin. Oncol.* 24 (2012) 711–719.
- [27] R. Ebel, M. Brenzinger, A. Kunze, H.J. Gross, P. Proksch, Wound activation of protoxins in the marine sponge *Aplysina aerophoba*, *J. Chem. Ecol.* 23 (1997) 1451–1462.

- [28] T. Hertiani, R. Edrada-Ebel, S. Ortlepp, R.W. van Soest, N.J. de Voogd, V. Wray, et al., From anti-fouling to biofilm inhibition: new cytotoxic secondary metabolites from two Indonesian *Agelas* sponges, *Bioorg. Med. Chem.* 18 (2010) 1297–1311.
- [29] C.D. Pham, R. Hartmann, W.E. Muller, N. de Voogd, D. Lai, P. Proksch, Aaptamine derivatives from the Indonesian sponge *Aaptos suberitoides*, *J. Nat. Prod.* 76 (2013) 103–106.
- [30] P.L. Olive, Detection of DNA damage in individual cells by analysis of histone H2AX phosphorylation, *Methods Cell Biol.* 75 (2004) 355–373.
- [31] P.L. Olive, J.P. Banath, The comet assay: a method to measure DNA damage in individual cells, *Nat. Protoc.* 1 (2006) 23–29.
- [32] J. Manns, M. Daubrawa, S. Driessen, F. Paasch, N. Hoffmann, A. Loffler, et al., Triggering of a novel intrinsic apoptosis pathway by the kinase inhibitor staurosporine: activation of caspase-9 in the absence of Apaf-1, *FASEB J.* 25 (2011) 3250–3261.
- [33] E.P. Rogakou, D.R. Pilch, A.H. Orr, V.S. Ivanova, W.M. Bonner, DNA double-stranded breaks induce histone H2AX phosphorylation on serine 139, *J. Biol. Chem.* 273 (1998) 5858–5868.
- [34] J. Baure, A. Izadi, V. Suarez, E. Giedzinski, J.E. Cleaver, J.R. Fike, et al., Histone H2AX phosphorylation in response to changes in chromatin structure induced by altered osmolarity, *Mutagenesis* 24 (2009) 161–167.
- [35] M.A. Bogoyevitch, B. Kobe, Uses for JNK: the many and varied substrates of the c-Jun N-terminal kinases, *Microbiol. Mol. Biol. Rev.* 70 (2006) 1061–1095.
- [36] C. Lu, F. Zhu, Y.Y. Cho, F. Tang, T. Zykova, W.Y. Ma, et al., Cell apoptosis: requirement of H2AX in DNA ladder formation, but not for the activation of caspase-3, *Mol. Cell* 23 (2006) 121–132.
- [37] F. Zhu, T.A. Zykova, C. Peng, J. Zhang, Y.Y. Cho, D. Zheng, et al., Phosphorylation of H2AX at Ser139 and a new phosphorylation site Ser16 by RSK2 decreases H2AX ubiquitination and inhibits cell transformation, *Cancer Res.* 71 (2011) 393–403.
- [38] T.M. Marti, E. Hefner, L. Feeny, V. Natale, J.E. Cleaver, H2AX phosphorylation within the G1 phase after UV irradiation depends on nucleotide excision repair and not DNA double-strand breaks, *Proc. Natl. Acad. Sci. U.S.A.* 103 (2006) 9891–9896.
- [39] C. Lopez-Otin, M.A. Blasco, L. Partridge, M. Serrano, G. Kroemer, The hallmarks of aging, *Cell* 153 (2013) 1194–1217.
- [40] J. Robles Steven, R. Adami Guy, Agents that cause DNA double strand breaks lead to p16^{INK4a} enrichment and the premature senescence of normal fibroblasts, *Oncogene* 16 (1998) 1113–1123.
- [41] D. White, I.U. Rafalska-Metcalf, A.V. Ivanov, A. Corsinotti, H. Peng, S.C. Lee, et al., The ATM substrate KAP1 controls DNA repair in heterochromatin: regulation by HP1 proteins and serine 473/824 phosphorylation, *Mol. Cancer Res.* 10 (2012) 401–414.
- [42] Y. Shiloh, ATM and ATR: networking cellular responses to DNA damage, *Curr. Opin. Genet. Dev.* 11 (2001) 71–77.
- [43] F. Hans, S. Dimitrov, Histone H3 phosphorylation and cell division, *Oncogene* 20 (2001) 3021–3027.
- [44] P. Johnson, H. McKenzie, How I treat advanced classical Hodgkin lymphoma, *Blood* (2015).

Publication 2

Manuscript “Cyclic Cystine-Bridged Peptides from the Marine Sponge *Clathria basilana* Induce Apoptosis in Tumor Cells and Depolarize the Bacterial Cytoplasmic Membrane”:

Mokhlesi A, Stuhldreier E, Wex KW, Berscheid A, Hartmann R, Rehberg N, Sureechatchaiyan P, Chaidir C, Kassack MU, Kalscheuer R, Brötz-Oesterhelt H, Wesselborg S, Stork B, Daletos G, Proksch P.

Journal of Natural Products 80:2941–2952 (2017). doi: 10.1021/acs.jnatprod.7b00477

Cyclic Cystine-Bridged Peptides from the Marine Sponge *Clathria basilana* Induce Apoptosis in Tumor Cells and Depolarize the Bacterial Cytoplasmic Membrane

Amin Mokhlesi,^{†,‡} Fabian Stuhldreier,[§] Katharina W. Wex,[⊥] Anne Berscheid,[⊥] Rudolf Hartmann,^{||} Nidja Rehberg,[†] Parichat Sureechatchaiyan,[▽] Chaidir Chaidir,[○] Matthias U. Kassack,[▽] Rainer Kalscheuer,[†] Heike Brötz-Oesterhelt,[⊥] Sebastian Wesselborg,[§] Björn Stork,[§] Georgios Daletos,^{*,†} and Peter Proksch^{*,†}

[†]Institute of Pharmaceutical Biology and Biotechnology, Heinrich Heine University, Universitätsstraße 1, D-40225 Düsseldorf, Germany

[‡]Department of Marine Biology, Faculty of Marine Sciences, Tarbiat Modares University, Noor, Iran

[§]Institute of Molecular Medicine I, Medical Faculty, Heinrich Heine University, Universitätsstraße 1, D-40225 Düsseldorf, Germany

[⊥]Department of Microbial Bioactive Compounds, Interfaculty Institute of Microbiology and Infection Medicine, University of Tübingen, Auf der Morgenstelle 28/E8, 72076 Tübingen, Germany

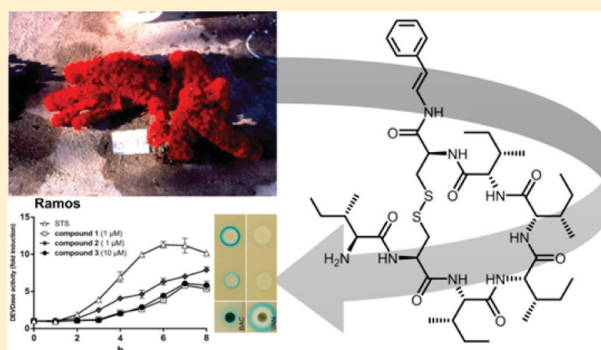
^{||}Institute of Complex Systems: Strukturbiochemie, Forschungszentrum Jülich, Wilhelm-Johnenstrasse, 52428 Jülich, Germany

[▽]Institute of Pharmaceutical and Medicinal Chemistry, Heinrich Heine University, Universitätsstraße 1, D-40225 Düsseldorf, Germany

[○]Center for Pharmaceutical and Medical Technology, Agency for the Assessment and Application Technology, 10340 Jakarta, Indonesia

Supporting Information

ABSTRACT: Investigation of the sponge *Clathria basilana* collected in Indonesia afforded five new peptides, including microcionamides C (1) and D (2), gombamides B (4), C (5), and D (6), and an unusual amide, (*E*)-2-amino-3-methyl-*N*-styrylbutanamide (7), along with 11 known compounds, among them microcionamide A (3). The structures of the new compounds were elucidated by one- and two-dimensional NMR spectroscopy as well as by high-resolution mass spectrometry. The absolute configurations of the constituent amino acid residues in 1–7 were determined by Marfey's analysis. Microcionamides A, C, and D (1–3) showed *in vitro* cytotoxicity against lymphoma (Ramos) and leukemia cell lines (HL-60, Nomo-1, Jurkat J16), as well as against a human ovarian carcinoma cell line (A2780) with IC₅₀ values ranging from 0.45 to 28 μM. Mechanistic studies showed that compounds 1–3 rapidly induce apoptotic cell death in Jurkat J16 and Ramos cells and that 1 and 2 potently block autophagy upon starvation conditions, thereby impairing pro-survival signaling of cancer cells. In addition, microcionamides C and A (1 and 3) inhibited bacterial growth of *Staphylococcus aureus* and *Enterococcus faecium* with minimal inhibitory concentrations between 6.2 and 12 μM. Mechanistic studies indicate dissipation of the bacterial membrane potential.



Marine sponges represent a prolific source of structurally unique peptides possessing diverse bioactivities, primarily as antibiotic, anticancer, and neuroprotective agents, thus suggesting their potential value for the development of leads in drug discovery.¹ Prominent examples of bioactive sponge-derived peptides include koshikamide A₁ and calyxamide A reported from *Theonella* sp. and *Discodermia calyx*, respectively, both showing strong cytotoxicity toward P388 murine leukemia cells,^{2,3} as well as the diaminoacrylic acid-containing cyclic peptides callyaerins A and B possessing inhibitory activity against *Mycobacterium tuberculosis*.⁴

The genus *Clathria* (order Poecilosclerida, family Microcionidae)⁵ includes more than 800 species that are widely distributed in the shallow waters of tropical and temperate regions. Chemical investigation of sponges belonging to this genus has provided a diverse array of secondary metabolites, such as alkaloids,^{6,7} carotenoids,⁸ steroids,^{9,10} and peptides.^{11,12} The latter class of compounds includes microcionamides A and B as well as gombamide A from *Clathria abietina* and *Clathria*

Received: June 4, 2017

Published: November 2, 2017

Table 1. ¹H (600 MHz), ¹³C (150 MHz), HMBC, and ROESY NMR Data (DMSO-*d*₆, δ in ppm) of Microcionamide C (1)

Unit	position	δ _C ^a type	δ _H (J in Hz)	HMBC	ROESY ^b	
E-PEA	NH		10.02, d (10.0)		Cys ₁ -α, E-PEA-β	
	α	122.8, CH	7.35, dd (10.0, 14.8)	Cys ₁ -CO, E-PEA-β, E-PEA-1		
	β	112.5, CH	6.26, d (14.8)	E-PEA-α, E-PEA-1, E-PEA-2/6	Ile ₂ -γ'	
	aromatic	1:136.0, C				
		2:124.9, CH	7.32, br dd (7.4, 1.4)	E-PEA-β, E-PEA-1, E-PEA-6, E-PEA-4		
		3:128.5, CH	7.28, br dd (7.4, 7.1)	E-PEA-1, E-PEA-5, E-PEA-4		
		4:126.1, CH	7.16, tt (7.1, 1.4)	E-PEA-2/6, E-PEA-3/5		
		5:128.5, CH	7.28, br dd (7.4, 7.1)	E-PEA-1, E-PEA-3, E-PEA-4		
6:124.9, CH	7.32, br dd (7.4, 1.4)	E-PEA-β, E-PEA-1, E-PEA-2, E-PEA-4				
Cys ₁	NH		8.15, d (7.8)	Ile ₂ -CO	Ile ₂ -α	
	CO	167.2, C				
	α	52.6, CH	4.34 ^c	Cys ₁ -CO, Cys ₁ -β, Ile ₂ -CO	E-PEA-α, E-PEA-NH	
Ile ₂	β	40.7, CH ₂	3.19, br t (13.2); 3.30, dd (13.2, 4.7)	Cys ₁ -CO, Cys ₁ -α		
	NH		7.99, br s			
	CO	170.4, C				
	α	57.7, CH	3.96, t (7.6)	Ile ₂ -CO, Ile ₃ -CO, Ile ₂ -β, Ile ₂ -γ, Ile ₂ -γ'	Cys ₁ -NH	
	β	34.6, CH	1.88, m	Ile ₂ -α		
	γ	24.5, CH ₂	1.51, m; 1.06, m	Ile ₂ -α	Ile ₃ -α	
	γ'	15.4, CH ₃	0.86, d (6.9)	Ile ₂ -α		
	δ	11.0, CH ₃	0.81 ^c			
Ile ₃	NH		7.75, br s			
	CO	171.2, C				
	α	57.6, CH	4.04, br s	Ile ₃ -γ, Ile ₃ -γ'	Ile ₂ -γ	
	β	36.2, CH	1.82, m	Ile ₃ -γ, Ile ₃ -γ', Ile ₃ -δ, Ile ₃ -CO		
	γ	24.5, CH ₂	1.20, m; 1.54, m	Ile ₃ -α		
	γ'	15.1, CH ₃	0.93, d (6.8)	Ile ₃ -α		
	δ	11.2, CH ₃	0.87 ^c			
			7.34 ^c			
Ile ₄	NH					
	CO	n.d. ^d				
	α	56.7, CH	4.33 ^c	Ile ₄ -γ, Ile ₄ -γ'	Ile ₅ -β	
	β	35.9, CH	2.00, br s			
	γ	23.5, CH ₂	1.16, m; 1.35, m	Ile ₄ -α, Ile ₄ -γ', Ile ₄ -δ		
	γ'	15.6, CH ₃	0.89 ^c	Ile ₄ -α, Ile ₄ -γ		
	δ	11.1, CH ₃	0.82 ^c	Ile ₄ -β		
			8.53, d (9.8)	Cys ₆ -CO	Cys ₆ -α	
Ile ₅	NH					
	CO	170.4, C				
	α	57.8, CH	4.19, dd (9.8, 6.9)	Ile ₅ -CO, Cys ₆ -CO, Ile ₅ -β, Ile ₅ -γ, Ile ₅ -γ'		
	β	36.2, CH	1.84, m	Ile ₅ -α, Ile ₅ -γ'	Ile ₄ -α	
	γ	23.9, CH ₂	1.40, m; 1.10, m	Ile ₅ -α		
	γ'	15.2, CH ₃	0.84 ^c	Ile ₅ -α, Ile ₅ -β		
	δ	10.7, CH ₃	0.80 ^c			
			8.83, d (8.1)	Cys ₆ -β	Ile ₇ -α, Ile ₇ -β, Ile ₇ -γ	
Cys ₆	NH					
	CO	168.9, C				
	α	52.3, CH	4.62, br ddd (10.3, 8.1, 4.6)	Cys ₆ -CO, Ile ₇ -CO, Cys ₆ -β	Ile ₅ -NH	
	β	40.1, CH ₂	3.11, br dd (12.8, 10.3); 3.39, dd (12.8, 4.6)	Cys ₆ -CO, Cys ₆ -α		
Ile ₇	NH ₂		8.10, br d (5.4)	Ile ₇ -CO, Ile ₇ -α, Ile ₇ -β	Ile ₇ -α, Ile ₇ -β, Ile ₇ -γ'	
	CO	167.8, C				
	α	56.0, CH	3.66, br t (5.4)	Ile ₇ -CO, Ile ₇ -γ, Ile ₇ -γ'	Cys ₆ -NH	
	β	36.2, CH	1.79, m	Ile ₇ -CO, Ile ₇ -δ	Cys ₆ -NH	
	γ	23.4, CH ₂	1.10, m; 1.47, m	Ile ₇ -α	Cys ₆ -NH	
	γ'	14.1, CH ₃	0.89 ^c	Ile ₇ -α		
	δ	10.8, CH ₃	0.83 ^c			

^aData extracted from HSQC and HMBC spectra. ^bSequential NOEs. ^cSignal overlap prevents determination of couplings. ^dn.d.: not detected.

gombawuiensis, respectively, all featuring a disulfide linkage that is rarely found in sponge-derived metabolites.^{11,12}

During our ongoing research for bioactive metabolites from marine sponges, we investigated a specimen of the marine sponge *Clathria basilana*, which was collected at Ambon Island, Indonesia. Notably, the MeOH extract completely inhibited the

growth of the murine lymphoma L5178Y cell line at a concentration of 10 μg/mL. Bioactivity-guided isolation afforded five new peptides (1, 2, 4–6) and one new amide derivative (7), in addition to one known peptide (3) and 10 known, structurally unrelated aromatic compounds. In this study, the structure elucidation of the new compounds as well as results of cytotoxicity

and antibacterial assays, followed by mechanistic studies, are reported.

RESULTS AND DISCUSSION

The MeOH extract of *C. basilana* was subjected to liquid–liquid fractionation to yield *n*-hexane, EtOAc, and *n*-BuOH fractions. Subsequent column chromatography of the EtOAc or *n*-BuOH fraction followed by semipreparative reversed-phase HPLC afforded five new peptides (**1**, **2**, **4**–**6**) and a new amide derivative (**7**).

Compound **1** was obtained as a white, amorphous solid. Its molecular formula was determined to be $C_{44}H_{72}N_8O_7S_2$ on the basis of the prominent ion peak at m/z 889.5033 $[M + H]^+$ in the HRESIMS spectrum, accounting for 13 degrees of unsaturation. In the 1H NMR spectrum, measured in DMSO- d_6 , the peptidic nature of **1** was evident from the presence of NH signals in the amide region (δ_H 7.34–10.02) and characteristic signals of α -amino protons (δ_H 3.66–4.62), as well as from a cluster of primary and secondary methyl groups in the aliphatic region (δ_H 0.81–2.00). Detailed analysis of the 2D NMR (HSQC, TOCSY, ROESY, and HMBC) spectra of **1** allowed the assignment of seven spin systems, including those of five isoleucine (Ile) and two cysteine (Cys) residues (Table 1). The remaining signals included those of a monosubstituted phenyl ring [δ_H 7.32 (2H, dd, $J = 7.4, 1.4$ Hz), 7.28 (2H, dd, $J = 7.4, 7.1$ Hz), and 7.16 (1H, tt, $J = 7.1, 1.4$ Hz)] and two olefinic protons at δ_H 6.26 (PEA-H β) and 7.35 (PEA-H α), suggesting the presence of a 2-phenylethen-1-amine (PEA) unit, as supported by the HMBC correlations from PEA-H α to PEA-C1 (δ_C 136.0) and from PEA-H β to PEA-C2/6 (δ_C 124.9), as well as by the TOCSY correlations of both PEA-H α and PEA-H β with PEA-NH. The configuration of the double bond of PEA was deduced as *E* on the basis of the large coupling constant ($^3J = 14.8$ Hz) measured for the respective protons.

The connectivity of the amino acid residues and of *E*-PEA was established by key HMBC and ROESY correlations (Figure 1).

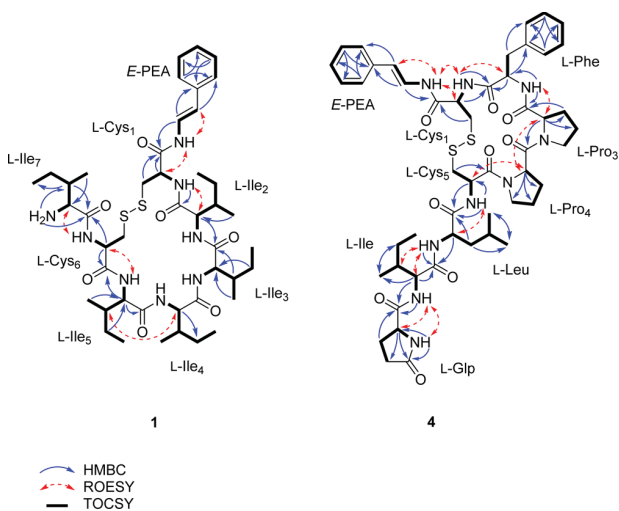
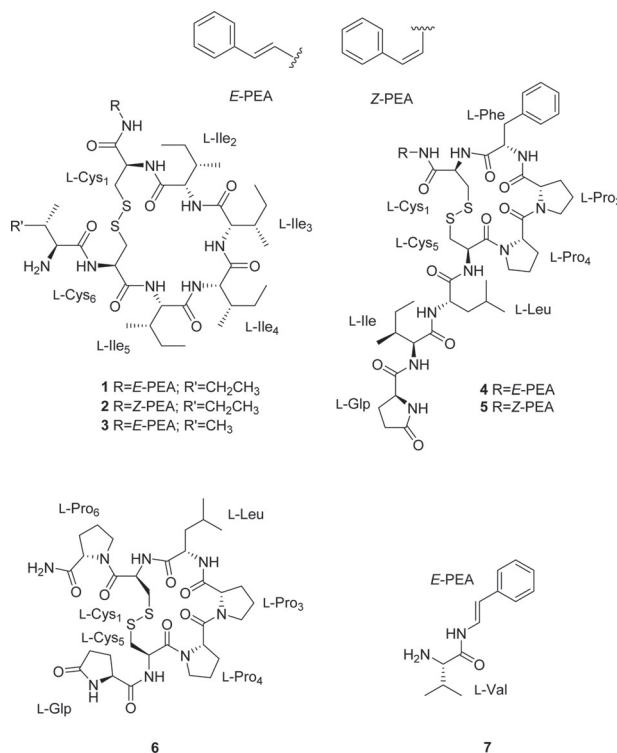


Figure 1. Key HMBC, ROESY, and TOCSY correlations of **1** and **4**.

Accordingly, the HMBC correlations from *E*-PEA-H α to Cys $_1$ -CO (δ_C 167.2), from Cys $_1$ -NH to Ile $_2$ -CO (δ_C 170.4), and from Ile $_2$ -H α to Ile $_3$ -CO (δ_C 171.2), along with the ROESY correlations between Cys $_1$ -H α and *E*-PEA-NH and between Ile $_2$ -H α and Cys $_1$ -NH, suggested the peptide substructure *E*-PEA-Cys $_1$ -Ile $_2$ -Ile $_3$. Moreover, the sequence Ile $_4$ -Ile $_5$ -Cys $_6$ was

supported by the HMBC correlations from Ile $_5$ -NH and Ile $_5$ -H α to Cys $_6$ -CO, as well as by the ROESY correlations between Ile $_4$ -H α and Ile $_5$ -H β and between Ile $_5$ -NH and Cys $_6$ -H α (Figure 1). The latter cysteine moiety (Cys $_6$) was linked to Ile $_7$ based on the HMBC cross-peak from Cys $_6$ -H α to Ile $_7$ -CO (δ_C 167.8) and the ROESY correlation between Cys $_6$ -NH and Ile $_7$ -H α , thus leading to the overall peptide structure *E*-PEA-Cys $_1$ -Ile $_2$ -Ile $_3$ -Ile $_4$ -Ile $_5$ -Cys $_6$ -Ile $_7$. Additionally, the cyclic nature of **1** was evident from the disulfide linkage of the two cysteine residues that formed a cystine moiety, thus accounting for the last degree of unsaturation based on the molecular formula ($C_{44}H_{72}N_8O_7S_2$). The assignment was further supported by HRESIMS/MS, which showed the fragmentation ions at m/z 770.4297 for $[M - E\text{-PEA}]^+$ and at m/z 657.3454 for $[M - (E\text{-PEA} + \text{Ile}_7)]^+$, originating from subsequent cleavage of the *E*-PEA and Ile $_7$ units, both located at the linear parts of the peptide (Figure S1-7). Hence, compound **1** was identified as a new natural product, and the name microcionamide C was proposed given the structural relationship between this compound and the known compounds microcionamides A (**3**) and B.¹¹



Compound **2** was isolated as a white, amorphous solid. The molecular formula of **2** was established as $C_{44}H_{72}N_8O_7S_2$ by HRESIMS, identical to that found for **1**. Moreover, the 1H NMR data of **2** were almost superimposable to those of **1**, the only notable difference being the resonances and coupling constants of the olefinic protons at δ_H 5.74 (1H, d, $J = 10.0$ Hz) and 6.72 (1H, t, $J = 10.0$ Hz), suggesting a (*Z*)-2-phenylethen-1-amine (*Z*-PEA) unit in **2** instead of a *E*-PEA unit, as in the case of **1** (Table S2-1). Likewise, HRESIMS/MS of **2** showed fragmentation ions originating from cleavage of the *Z*-PEA and Ile $_7$ units (Figure S2-9). Hence, the structure of **2** was assigned as the *Z* isomer of **1** and was named microcionamide D.

Compound **4** was obtained as a white, amorphous solid. The molecular formula of **4** was deduced to be $C_{50}H_{67}N_9O_9S_2$ based on the prominent ion peak at m/z 1002.4572 $[M + H]^+$ in

Table 2. ¹H (600 MHz), ¹³C (150 MHz), HMBC, and ROESY NMR Data (DMSO-*d*₆, δ in ppm) of Gombamide B (4)

unit	position	δ _C , type	δ _H (J in Hz)	HMBC	ROESY ^a	
E-PEA	NH		10.32, d (10.0)		Cys ₁ -NH, Cys ₁ -α	
	α	123.0, CH	7.36, dd (14.7, 10.0)	Cys ₁ -CO, E-PEA-1		
	β	113.2, CH	6.33, d (14.7)	E-PEA-NH, E-PEA-α, E-PEA-2/6, E-PEA-1	E-PEA-NH	
	aromatic	1:	136.2, C			
		2:	125.3, CH	7.37, br d (7.7)	E-PEA-β, E-PEA-1, E-PEA-6, E-PEA-4	
		3:	128.6, CH	7.30, br t (7.7)	E-PEA-1, E-PEA-5	
4:		126.4, CH	7.17, br t (7.7)	E-PEA-2/6		
Cys ₁	5:	128.6, CH	7.30, br t (7.7)	E-PEA-1, E-PEA-3		
	6:	125.3, CH	7.37, br d (7.7)	E-PEA-β, E-PEA-1, E-PEA-2		
	NH		7.72, d (8.6)	Phe-CO, Cys ₁ -α, Cys ₁ -β	E-PEA-NH, Phe-α	
	CO	167.8, C				
	α	51.6, CH	4.64, ddd (12.0, 8.6, 3.5)	Cys ₁ -CO, Cys ₁ -β, Phe-CO	E-PEA-NH	
	β	42.1, CH ₂	2.93, dd (14.4, 12.0); 3.15, dd (14.4, 3.5)	Cys ₁ -CO, Cys ₁ -α		
Phe	NH		8.97, d (8.8)	Phe-α, Phe-β, Pro ₃ -CO	Pro ₃ -α	
	CO	170.8, C				
	α	53.5, CH	4.81, m	Phe-CO, Phe-β, Phe-1, Pro ₃ -CO	Cys ₁ -NH	
	β	34.0, CH ₂	2.99, m; 3.02, m	Phe-CO, Phe-α, Phe-1, Phe-2/6		
	aromatic	1:	138.3, C			
		2:	129.3, CH	7.43, br d (7.5)	Phe-β, Phe-6, Phe-4	
3:		128.1, CH	7.29, br t (7.5)	Phe-1, Phe-5		
4:		126.2, CH	7.20, br t (7.5)	Phe-2/6		
5:		128.1, CH	7.29, br t (7.5)	Phe-1, Phe-3		
6:		129.3, CH	7.43, br d (7.5)	Phe-β, Phe-2, Phe-4		
Pro ₃	CO	171.4, C				
	α	60.3, CH	4.36, d (7.8)	Pro ₃ -CO, Pro ₄ -CO, Pro ₃ -β, Pro ₃ -γ, Pro ₃ -δ	Pro ₄ -α, Pro ₄ -β, Phe-NH	
	β	31.2, CH ₂	1.73, m; 1.88, m	Pro ₃ -CO, Pro ₃ -α, Pro ₃ -γ		
	γ	20.1, CH ₂	1.42, m; 0.55, m	Pro ₃ -α		
	δ	45.9, CH ₂	3.29, m; 3.26, m	Pro ₃ -α, Pro ₃ -β		
Pro ₄	CO	169.3, C				
	α	59.2, CH	4.84, dd (9.5, 2.0)	Pro ₄ -β, Pro ₄ -γ, Pro ₄ -δ	Pro ₃ -α, Cys ₅ -α	
	β	30.2, CH ₂	1.87, m; 2.22, m	Pro ₄ -CO, Pro ₄ -α, Pro ₄ -δ	Pro ₃ -α	
	γ	21.9, CH ₂	1.76, m	Pro ₄ -α		
	δ	46.3, CH ₂	3.34, m; 3.48, m	Pro ₄ -β, Pro ₄ -γ		
Cys ₅	NH		8.01, d (10.0)	Leu-CO, Cys ₅ -α, Cys ₅ -β	Leu-α	
	CO	167.9, C				
	α	48.4, CH	4.56, td (10.0, 5.2)	Leu-CO, Cys ₅ -CO, Cys ₅ -β	Pro ₄ -α	
Leu	β	38.0, CH ₂	2.61, br dd (12.0, 10.0); 3.22, br dd (12.0, 5.2)	Cys ₅ -α, Cys ₅ -CO		
	NH		8.05, d (9.2)	Leu-α, Leu-β, Ile-CO	Ile-α, Ile-β	
Leu	CO	170.5, C				
	α	50.5, CH	4.49, ddd (9.2, 8.0, 7.7)	Leu-CO, Leu-β, Leu-γ, Ile-CO	Cys ₅ -NH	
	β	41.2, CH ₂	1.58, m	Leu-CO, Leu-α, Leu-γ, Leu-δ, Leu-δ'		
	γ	24.0, CH	1.63, m	Leu-δ, Leu-δ'		
	δ	21.3, CH ₃	0.86, d (6.3)	Leu-β, Leu-γ, Leu-δ'		
	δ'	23.3, CH ₃	0.89, d (6.4)	Leu-β, Leu-γ, Leu-δ		
	NH		8.07, d (8.8)	Glp-CO, Ile-α, Ile-β	Glp-α, Glp-NH	
	CO	170.7, C				
Ile	α	57.0, CH	4.16, t (8.8)	Ile-CO, Ile-β, Ile-γ, Ile-γ', Glp-CO	Leu-NH	
	β	35.5, CH	1.73, m	Ile-CO, Ile-α, Ile-γ		
	γ	24.2, CH ₂	1.02, m; 1.42, m	Ile-α, Ile-β, Ile-δ, Ile-γ'		
	γ'	15.4, CH ₃	0.75, d (6.7)	Ile-α, Ile-β, Ile-γ		
	δ	10.4, CH ₃	0.72, t (7.4)	Ile-β, Ile-γ		
	NH		7.80, s	Glp-CO', Glp-α, Glp-β, Glp-γ	Ile-NH	
	CO	172.4, C				
	CO'	177.4, C				
Glp	α	55.1, CH	4.10, dd (8.7, 4.0)	Glp-CO, Glp-CO', Glp-β, Glp-γ	Ile-NH	
	β	25.3, CH ₂	1.78, m; 2.21, m	Glp-CO, Glp-CO'		
	γ	29.0, CH ₂	2.09, m; 2.07, m	Glp-CO', Glp-α, Glp-β		

^aSequential NOEs.

the HRESIMS spectrum, accounting for 22 degrees of unsaturation. The planar peptidic structure of **4** was distinguished by the abundance of the amide (NH) (δ_{H} 7.72–10.32) and α -amino (δ_{H} 4.10–4.84) protons, as well as by the cluster of primary and secondary methyl groups in the aliphatic region of the ^1H NMR spectrum (Table 2). Analysis of the COSY and TOCSY NMR spectra revealed the spin systems of seven amino acid residues, including Pro (2 equiv), Cys (2 equiv), Phe, Leu, and Ile, together with the *E*-PEA unit and the unusual amino acid residue pyroglutamic acid (Glp). The presence of the latter was confirmed by key HMBC correlations from Glp-H α to Glp-CO' (δ_{C} 177.4) and Glp-C γ (δ_{C} 29.0), from Glp-NH to Glp-CO' and Glp-C α (δ_{C} 55.1), and from Glp-H β to Glp-CO (δ_{C} 172.4). In analogy to **1** and **2**, the linkages and assignments of the amino acid residues in **4** were established by HMBC and ROESY NMR data (Table 2). Accordingly, the connection between *E*-PEA and Cys₁ was deduced by the HMBC correlation from *E*-PEA-H α to Cys₁-CO (δ_{C} 167.8) as well as the ROESY cross-peak between *E*-PEA-NH and Cys₁-H α . Moreover, the HMBC correlations from Cys₁-H α and Cys₁-NH to Phe-CO (δ_{C} 170.8), from Phe-H α and Phe-NH to Pro₃-CO (δ_{C} 171.4), and from Pro₃-H α to Pro₄-CO (δ_{C} 169.3) disclosed the peptide fragment *E*-PEA-Cys₁-Phe-Pro₃-Pro₄ (Figure 1). This was further corroborated by the ROESY cross-peaks between Cys₁-NH/Phe-H α , Phe-NH/Pro₃-H α , and Pro₃-H α /Pro₄-H α . Likewise, the HMBC correlations from Cys₅-H α to Leu-CO (δ_{C} 170.5), from Leu-H α to Ile-CO (δ_{C} 170.7), as well as from Ile-H α to Glp-CO (δ_{C} 172.4), in addition to the ROESY correlations between Pro₄-H α /Cys₅-H α , Cys₅-NH/Leu-H α , Leu-NH/Ile-H α , and Ile-NH/Glp-H α extended this fragment, leading to the overall peptide sequence *E*-PEA-Cys₁-Phe-Pro₃-Pro₄-Cys₅-Leu-Ile-Glp. Finally, a disulfide bond between the two Cys residues was evident, consistent with the 22 elements of unsaturation required by the molecular formula. The structure of **4** was further corroborated by the fragment ions at m/z 665.2566 [$\text{M} - \text{Leu-Ile-Glp}$]⁺ and 883.3826 [$\text{M} - \text{E-PEA}$]⁺ in the HRESIMS/MS spectrum, originating from cleavage of the linear peptide sequence Leu-Ile-Glp and the PEA unit, respectively (Figure S4-9). Hence, compound **4** was identified as a new natural product and was named gombamide B, based on the structural relationship with the known compound gombamide A.¹²

Compound **5** was isolated as a white, amorphous solid. The molecular formula of **5** was deduced to be C₅₀H₆₇N₉O₉S₂ by HRESIMS analysis, as in the case of **4**. In analogy to **1** and **2**, the ^1H NMR spectrum of **5** was similar to that of **4**, the only difference being the *Z*-configuration of the ethylene protons in the PEA moiety instead of the *E*-configuration, as deduced by their vicinal coupling constant ($^3J_{\text{H}\alpha,\text{H}\beta} = 9.7$ Hz; Table S5-1). In a similar manner to **4**, HRESIMS/MS of **5** showed MS fragment ions of [$\text{M} - \text{Z-PEA}$]⁺ and [$\text{M} - \text{Leu-Ile-Glp}$]⁺ (Figure S5-7). Thus, compound **5** was characterized as a new natural product and was named gombamide C.

Compound **6** was isolated as a white, amorphous solid. The molecular formula of **6** was determined as C₃₂H₄₈N₈O₈S₂ by HRESIMS, consistent with 13 degrees of unsaturation. Detailed interpretation of the COSY and HMBC NMR spectra of **6** established the presence of six amino acid residues, including Pro (3 equiv), Cys (2 equiv), and Leu, along with a Glp unit. As described for peptides **1**, **2**, **4**, and **5**, key HMBC correlations from Pro₆-H α to Cys₁-CO (δ_{C} 168.1), from Cys₁-NH to Leu-CO (δ_{C} 170.9), from Leu-NH to Pro₃-CO (δ_{C} 171.0), from Pro₃-H α to Pro₄-CO (δ_{C} 169.6), and from Cys₅-NH to Glp-CO (δ_{C} 171.5) established the overall amino acid sequence of **6** as

Pro₆-Cys₁-Leu-Pro₃-Pro₄-Cys₅-Glp. This assignment was also evident by the ROESY cross-peaks between Cys₁-NH/Leu-NH, Leu-NH/Pro₃-H α , and Cys₅-NH/Glp-H α . The remaining two NH protons at δ_{H} 6.90 (1H, s) and 7.27 (1H, s) were attributed to a terminal carboxamide group, as supported by their HMBC correlations to Pro₆-CO and Pro₆-C α (Figure 2, Table 3). Finally,

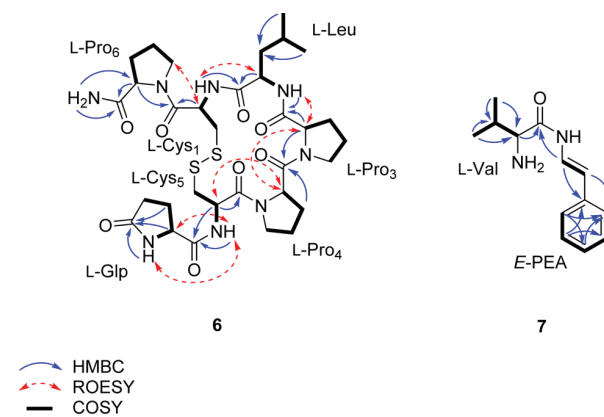


Figure 2. Key HMBC, ROESY, and COSY correlations of **6** and **7**.

cyclization via a disulfide bond between the two Cys residues was suggested to satisfy the remaining element of unsaturation in the structure of **6**. This assignment was further corroborated by the fragment ions at m/z 623.2317 [$\text{M} - \text{Pro}_6\text{-NH}_2$]⁺ and 595.2367 [$\text{M} - (\text{Pro}_6\text{-NH}_2 + \text{CO})$]⁺, which were observed in the HRESIMS/MS spectrum of **6** (Figure S6-8). Accordingly, compound **6** was identified as a new natural product and was given the name gombamide D.

Compound **7** was isolated as a white, amorphous solid. The molecular formula of **7** was determined as C₁₃H₁₈N₂O based on HRESIMS analysis, consistent with six degrees of unsaturation. Detailed analysis of the 2D NMR (COSY and HMBC) spectra of **7** allowed the assignment of an unusual amide consisting of Val and *E*-PEA residues, connected through an amide linkage, as supported by the HMBC correlation from *E*-PEA-H α to Val-CO (δ_{C} 167.2) (Figure 2, Table 4). Thus, compound **7** was assigned as (*E*)-2-amino-3-methyl-*N*-styrylbutanamide, which is a new natural product.

The remaining compounds were identified on the basis of NMR, HRESIMS, and specific rotation data analysis, as well as by comparison with published data as microcinamide A (**3**),¹¹ six indole derivatives, namely, 1*H*-indole-3-carbaldehyde, 1*H*-indole-3-carboxylic acid, 6-bromo-1*H*-indole-3-carbaldehyde, 6-bromo-1*H*-indole-3-carboxylic acid, methyl 6-bromo-1*H*-indole-3-carboxylate, and ethyl 6-bromo-1*H*-indole-3-carboxylate,^{13,14} along with 7-bromo-4(1*H*)-quinolinone,¹⁵ the δ -lactam derivative (3-(2-(4-hydroxyphenyl)-2-oxoethyl)-5,6-dihydropyridin-2(1*H*)-one),¹⁶ 2-deoxythymidine,¹⁷ and 4-hydroxybenzoic acid (Figure S9-1).

The absolute configuration of each amino acid residue was determined by Marfey's method following acid hydrolysis (6 N HCl) of the isolated peptides **1**–**7** (0.5 mg each).¹⁸ Comparison of the resulting derivatives with those of standard amino acids by HPLC led to the assignment of the *L*-configuration for all amino acid residues (Table S8-1). Moreover, in an attempt to improve the HPLC resolution between *L*/*D*-Ile and *L*/*D*-*allo*-Ile residues, a C₄ HPLC RP-column was successfully employed, instead of the commonly used C₁₈ column, in analogy to the C₃ Marfey's method,¹⁹ revealing the presence of only *L*-Ile residues

Table 3. ¹H (600 MHz), ¹³C (150 MHz), HMBC, and ROESY NMR Data (DMSO-*d*₆, δ in ppm) of Gombamide D (6)

unit	position	δ _C , type	δ _H (J in Hz)	HMBC	ROESY ^a
Pro ₆	CONH ₂		6.90, s; 7.27, s	Pro ₆ -CO, Pro ₆ -α	Pro ₆ -α, Cys ₁ -β
	CO	173.4, C			
	α	59.9, CH	4.16, dd (8.8, 3.5)	Pro ₆ -CO, Cys ₁ -CO, Pro ₆ -β, Pro ₆ -γ, Pro ₆ -δ	
	β	29.3, CH ₂	1.80, m; 2.02, m	Pro ₆ -CO, Pro ₆ -α, Pro ₆ -γ, Pro ₆ -δ	
	γ	24.3, CH ₂	1.87, m	Pro ₆ -α, Pro ₆ -β, Pro ₆ -δ	
Cys ₁	δ	46.6, CH ₂	3.52 ^b ; 3.63, ddd (9.7, 7.4, 4.5)	Pro ₆ -α, Pro ₆ -β	Cys ₁ -α
	NH		7.87, d (8.3)	Leu-CO, Cys ₁ -β, Cys ₁ -α	Leu-α, Leu-NH
	CO	168.1, C			
	α	49.2, CH	4.75, ddd (11.6, 8.3, 3.2)	Cys ₁ -CO, Cys ₁ -β	Pro ₆ -δ
	β	41.3, CH ₂	2.78, dd (14.6, 11.6); 3.12, dd (14.6, 3.2)	Cys ₁ -CO, Cys ₁ -α	
Leu	NH		9.17, d (9.0)	Leu-α, Pro ₃ -CO	Cys ₁ -NH, Pro ₃ -α, Pro ₃ -δ
	CO	170.9, C			
	α	50.1, CH	4.53 ^b	Leu-CO, Leu-β, Leu-γ	Cys ₁ -NH
	β	37.7, CH ₂	1.37, m; 1.71, m	Leu-CO, Leu-α, Leu-γ, Leu-δ, Leu-δ'	
	γ	24.2, CH	1.42, m	Leu-α, Leu-δ, Leu-δ'	
	δ	21.4, CH ₃	0.79, d (6.4)	Leu-β, Leu-γ, Leu-δ'	
	δ'	23.1, CH ₃	0.88, d (6.4)	Leu-β, Leu-γ, Leu-δ	
Pro ₃	CO	171.0, C			
	α	60.6, CH	4.52 ^b	Pro ₃ -CO, Pro ₄ -CO, Pro ₃ -β, Pro ₃ -γ, Pro ₃ -δ	Leu-NH, Pro ₄ -α
	β	31.2, CH ₂	2.08, m; 2.21, m	Pro ₃ -CO, Pro ₃ -α, Pro ₃ -γ, Pro ₃ -δ	
	γ	21.2, CH ₂	1.56, m; 1.91, m	Pro ₃ -α	
	δ	45.9, CH ₂	3.27, br t (10.4); 3.43 ^b	Pro ₃ -β, Pro ₃ -γ	Leu-NH
Pro ₄	CO	169.6, C			
	α	59.4, CH	4.91, dd (8.7, 2.5)	Pro ₄ -β, Pro ₄ -γ, Pro ₄ -δ	Pro ₃ -α, Cys ₅ -α
	β	30.4, CH ₂	2.30, m; 1.94, m	Pro ₄ -CO, Pro ₄ -α, Pro ₄ -δ	
	γ	21.8, CH ₂	1.73, m; 1.79, m		
	δ	46.5, CH ₂	3.50 ^b ; 3.35, dt (11.7, 7.7)	Pro ₄ -β	
Cys ₅	NH		8.54, d (9.7)	Glp-CO, Cys ₅ -α	Glp-α, Glp-NH
	CO	168.2, C			
	α	48.4, CH	4.58, ddd (11.1, 9.7, 5.2)	Cys ₅ -CO, Glp-CO, Cys ₅ -β	Pro ₄ -α
Glp	β	37.5, CH ₂	2.62, dd (12.4, 11.1); 3.23, dd (12.4, 5.2)	Cys ₅ -α, Cys ₅ -CO	
	NH		7.67, s	Glp-CO', Glp-α, Glp-β, Glp-γ	Cys ₅ -NH
	CO	171.5, C			
	CO'	177.6, C			
	α	54.9, CH	4.02, br dd (9.0, 2.6)	Glp-CO', Glp-β	Cys ₅ -NH
	β	25.1, CH ₂	2.07, m; 2.15, td (9.2, 3.4)	Glp-CO, Glp-CO', Glp-γ	
	γ	28.9, CH ₂	2.00, m; 2.24, m	Glp-CO', Glp-α	

^aSequential NOEs. ^bSignal overlap prevents determination of couplings.

as constituents of the respective peptides (1–5) (Table S8-2). Moreover, the ROESY correlations between Pro₃-Ha/Pro₄-Ha and Pro₄-Ha/Cys₅-Ha (Figure 1) in 4 and 5 suggested a *cis* configuration for the amide peptide bonds, which was further corroborated by the large Pro-Cβ and Pro-Cγ shift difference values ($\Delta\delta_{C\beta-C\gamma} \approx 8-11$ ppm). Similarly, in the case of 6 a *cis* peptide bond was deduced between Pro₃-Pro₄ and Pro₄-Cys₅, whereas the ROESY correlation between Cys₁-Ha and Pro₆-Hδ in addition to the carbon resonances of Cβ and Cγ in Pro₆ (29.3 and 24.3 ppm, respectively) suggested a *trans* peptide bond between Pro₆-Cys₁.^{4,20}

Microcionamides C (1) and D (2) are stereoisomers differing in the *E/Z* double-bond configuration of the PEA moiety, as previously observed for the known analogues microcionamides A (3) and B.¹¹ The only difference between the structures of 1 and 2 compared to 3 and microcionamide B is the replacement of the terminal Val residue in the latter compounds by Ile. In analogy to 1 and 2, compounds 4 and 5 were found to be *E/Z* stereoisomers. It should be noted, however, that the *Z*-PEA derivatives 2 and 5 were detected as the minor components in the crude extract, and thus these compounds may be artifacts arising from the

respective *E*-PEA analogues 1 and 4 during extraction and/or isolation (e.g., upon exposure to natural light), as previously suggested for 3 and microcionamide B.¹¹ Compounds 4 and 5 are structurally related to the known peptide gombamide A from the sponge *Clathria gombawuiensis*, the latter compound bearing pyroglutamic acid (Glp) and *para*-hydroxystyrylamide units instead of the linear peptide chain Leu-Ile-Glp and PEA, respectively.¹² Interestingly, Glp is rarely reported from marine invertebrates. In addition to the aforementioned gombamide A, other examples of peptides bearing this unit include didemnins from the tunicate *Trididemnum solidum*,²¹ as well as asteropsin A and two pyroglutamyl dipeptides from *Asteropus* sp. sponges.^{22,23} The intramolecular cyclization of N-terminal glutamine residues into Glp is of special interest, as it protects peptides from degradation by the action of exopeptidase enzymes or even enables them to adopt the right conformation for binding to their receptors.²⁴ Gombamide D (6) possesses a similar cyclic part to 4 and 5, the only difference being that the Phe residue is substituted by Leu, as in the case of the cyclic thiopeptides eudistomides A and B, reported from a Fijian ascidian of the genus *Eudistoma*.²⁵ The promiscuous occurrence of these

Table 4. ^1H (600 MHz), ^{13}C (150 MHz), and HMBC NMR Data (MeOH- d_4 , δ in ppm) of (*E*)-2-Amino-3-methyl-N-styrylbutanamide (7)

unit	position	δ_c , type	δ_H (J in Hz)	HMBC	
E-PEA	α	122.8, CH	7.46, d (14.7)	Val-CO, E-PEA-1	
	β	116.4, CH	6.32, d (14.7)	E-PEA-2/6	
	aromatic	1: 137.2, C			
		2: 126.6, CH	7.35, dt (8.3, 1.5)	E-PEA- β , E-PEA-6, E-PEA-4	
		3: 129.8, CH	7.29, br dd (8.3, 7.3)	E-PEA-1, E-PEA-5	
		4: 128.1, CH	7.19, tt (7.3, 1.5)	E-PEA-2/6	
5: 129.8, CH	7.29, br dd (8.3, 7.3)	E-PEA-1, E-PEA-3			
6: 126.6, CH	7.35, dt (8.3, 1.5)	E-PEA- β , E-PEA-2, E-PEA-4			
Val	CO	167.2, C			
	α	59.9, CH	3.69, d (5.8)	Val-CO, Val- γ , Val- γ'	
	β	31.6, CH	2.24, m	Val- γ , Val- γ'	
	γ	17.8, CH ₃	1.07, d (6.9)	Val- β , Val- α	
	γ'	18.9, CH ₃	1.10, d (6.9)	Val- β , Val- α	

peptide analogues in different phyla of marine invertebrates argues for symbiont microorganisms as true producers.

Cytotoxicity of the isolated metabolites (1–7 and known compounds) was investigated using different tumor cell lines. Microcionamides A, C, and D (1–3) showed *in vitro* cytotoxicity against lymphoma (Ramos) and leukemia cell lines (HL-60, Nomo-1, Jurkat J16), as well as against a human ovarian carcinoma cell line (A2780) with IC₅₀ values ranging from 0.45 to 28 μM (Figures S10-1 and 3, Table 5). The remaining

Table 5. Cytotoxicity of Compounds 1–3 after Incubation for 24 h Reported as IC₅₀ (μM)

compd	A 2780	Ramos	Jurkat J16	Nomo-1	HL-60
1	0.45	1.4	0.81	1.4	1.9
2	0.53	1.9	1.3	2.4	2.5
3	2.6	5.9	4.6	10	28

isolated compounds proved to be inactive in concentrations up to 10 μM .

Due to their strong cytotoxic activity, we next addressed the question of whether 1–3 cause apoptotic cell death. Activation of caspase-3 was measured employing two different methods: first by immunoblotting for the cleavage of the caspase-3 substrate poly(ADP-ribose) polymerase-1 (PARP-1) and second by measuring the fluorescence of the profluorescent caspase-3 substrate Ac-DEVD-AMC. Activated caspase-3 cleaves the latter substrate between aspartate (D) and 7-amino-4-methylcoumarin (AMC), hence releasing the fluorogenic AMC, which can be subsequently detected with a spectrofluorometer. Because cysteine-dependent aspartate-directed proteases (caspases) in general and caspase-3 as an effector caspase in particular are central players of apoptotic processes, activation of caspase-3 indicates induction of apoptosis. As shown in Figure 3A, compounds 1–3 induced the activation of caspases in Jurkat and Ramos cells with rapid kinetics within 4 h and reached a maximum after 6 to 7 h, indicating a fast induction of apoptotic processes. However, compound 3 induced caspase activation only at 10 μM , whereas in contrast to 1 and 2 it displayed no effect at 1 μM (data not shown), which is in accordance with the higher IC₅₀. To confirm activation of caspase-3 via a further end point, we detected cleavage of the

caspase-3 substrate PARP after treatment with 1, 2, and 3 (same concentrations as in Figure 3A). In line with the results of the caspase-3 activity assay, all compounds induced cleavage of PARP within 4 to 8 h, indicating again activation of caspase-3 and thus execution of apoptosis. To prove caspase dependency of the observed PARP cleavage, we additionally performed co-incubation with the pan-caspase inhibitor QVD (Figure 3B). QVD completely blocked cleavage of PARP after treatment with 1, 2, and 3, demonstrating a causative role of caspases and thereby occurrence of apoptosis.

Autophagy is a major intracellular degradation route responsible for the lysosome-mediated breakdown of soluble cytosolic components and therefore plays a crucial role in maintaining cellular homeostasis.²⁶ Cancer cells in particular suffer from metabolic stress and nutrient deprivation due to fast proliferation. Thus, autophagy can support cancer cells to overcome microenvironmental stress by allowing them to recycle dysfunctional or unessential components. Autophagy thereby acts as a mechanism of cell survival. Accordingly, inhibition of autophagy is a promising therapeutic target for anticancer chemotherapy.^{27,28} In order to investigate potential inhibitory or stimulating effects of 1–3 with regard to autophagy, we used murine embryonic fibroblast (MEF) cells stably expressing mCitrine-hLC3B and measured lysosomal degradation of mCitrine-hLC3B under starvation conditions and after treatment with compounds 1–3 or alternatively with the known autophagy inhibitor bafilomycin A1 via flow cytometry.²⁹ LC3 is an essential component of autophagosomes (double-membraned key structures of autophagy), which deliver engulfed cytoplasmic components to lysosomes and get degraded by the lysosomal system during autophagy. Thus, breakdown of LC3 is a suitable indicator of autophagic processes. Incubation with 10 μM compound 1 or 2 distinctly blocked starvation-induced degradation of LC3, indicating inhibition of autophagy by these compounds (Figure 4). Compound 3 on the other hand was inactive in this experiment, indicating the relevance of the terminal Ile for the autophagy-inhibitory effect. In order to determine whether the observed inhibition of autophagy by compounds 1 and 2 is caspase-dependent, we additionally performed experiments with cotreatment of QVD. Because QVD counteracted compound 1-related inhibition of autophagy, this inhibitory effect was at least partially due to apoptotic processes. In contrast, the inhibitory effect mediated by compound 2 was completely unaffected by cotreatment with QVD, indicating independence of apoptosis.

Finding new antibacterial agents unaffected by available resistance determinants is of paramount importance in light of increasing bacterial resistance development. Thus, we were also interested in the antibacterial potential of the compounds (Table S10-2). Compounds 1 and 3 showed antibacterial activity against the Gram-positive bacterial species *Enterococcus faecium* and *Staphylococcus aureus* in the low μM range. For both compounds, the minimal inhibitory concentrations (defined as the lowest concentrations completely preventing visible bacterial growth) were 6.2 μM for *S. aureus* and 12 μM for *E. faecium*, respectively (Table S10-2). *Mycobacterium tuberculosis* as well as the Gram-negative species *Klebsiella pneumoniae*, *Enterobacter aerogenes*, *Escherichia coli*, *Pseudomonas aeruginosa*, and *Acinetobacter baumannii* were not inhibited up to 100 μM . Compounds 2 and 5 were not investigated due to compound limitation. The remaining compounds showed no antibacterial activity.

In order to investigate the mechanism of bacterial growth inhibition, we employed as a first step a panel of bacterial reporter strains that we constructed in the background of the Gram-positive

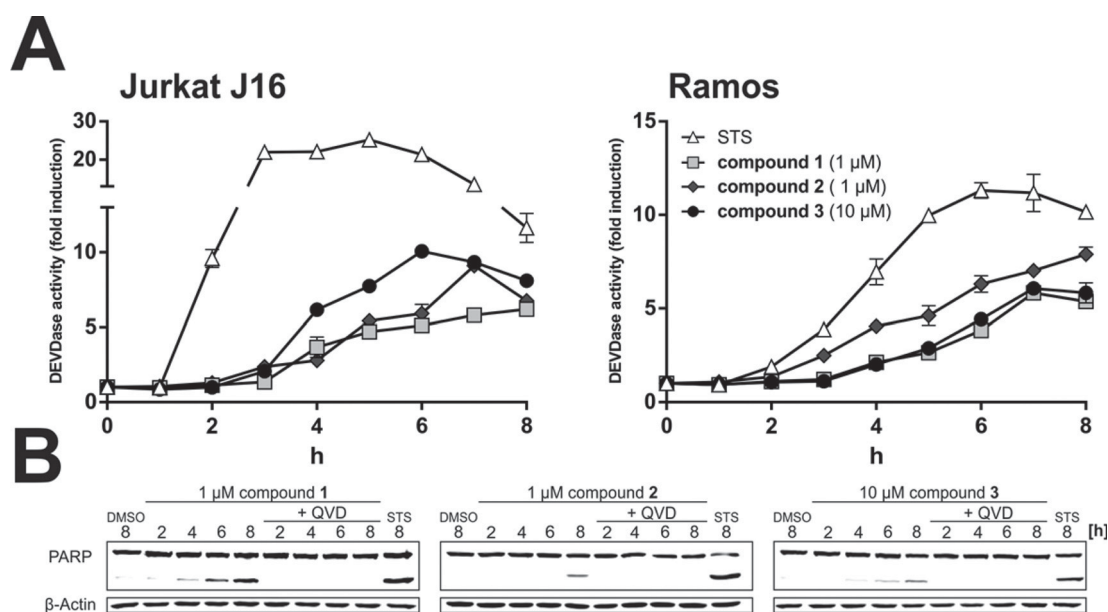


Figure 3. Compounds 1–3 rapidly induce apoptosis in human lymphoma and leukemia cell lines. (A) The kinetics of caspase-3 activation in Jurkat J16 (acute T cell leukemia; left panel) and Ramos (Burkitt's lymphoma; right panel) cells after treatment with indicated concentrations of compounds 1–3 were compared to those of staurosporine (STS, 2.5 μM), a well-established inducer of apoptosis. Caspase-3 activity was measured by the rate of cleavage of the profluorescent caspase-3 substrate Ac-DEVD-AMC. Relative caspase-3 activity in DMSO (0.1% v/v)-treated control cells was set to 1. Data shown are the mean ± SD from a representative experiment performed in triplicate. (B) Ramos cells were treated with compounds 1 (1 μM), 2 (1 μM), or 3 (10 μM) in the absence or presence of the caspase inhibitor Q-VD-OPh (QVD, 10 μM) for the indicated duration between 2 and 8 h. After the incubation period cleavage of PARP was determined by Western blot analysis. The expression of β-actin was determined as a protein loading control. Shown is the result of a representative blot. STS (2.5 μM) served as the positive control for caspase-dependent cleavage of PARP.

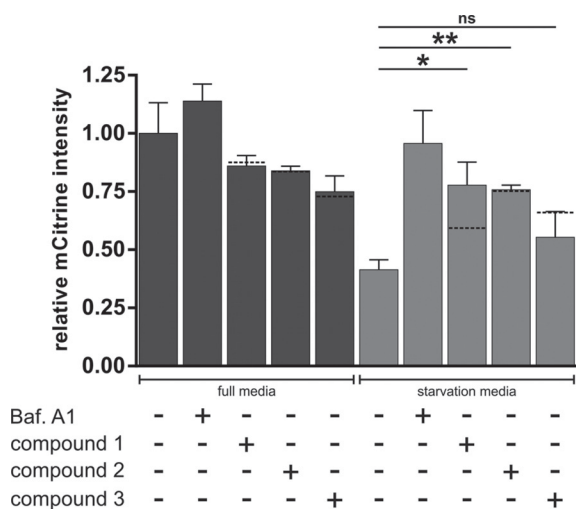


Figure 4. Compounds 1 and 2 impair amino acid starvation-induced autophagy. MEFs stably expressing mCitrine-hLC3B were cultivated in full medium or starvation medium (EBSS) with 10 μM compounds 1, 2, or 3 for 4 h. Ten nM bafilomycin A₁ (Baf. A1) served as the positive control for inhibition of autophagy. Total cellular mCitrine-hLC3B signals were analyzed by flow cytometry. The median of fluorescence intensity was plotted in a bar diagram. Values are normalized to DMSO (0.1% v/v)-treated cells cultivated in full medium (1.0) and represent mean ± SD of 3 independent analyses. * = $p \leq 0.05$, ** = $p \leq 0.01$ (Student's *t* test, two-sample assuming unequal variances). Dashed lines represent median mCitrine fluorescence intensity of cells cotreated with caspase inhibitor Q-VD-OPh (10 μM) performed in triplicate.

model organism *Bacillus subtilis*. These strains express the reporter gene β-galactosidase from five selected promoters that were

previously found and validated to react specifically to disturbances of certain metabolic pathways or cell structures.³⁰ Previous whole genome mRNA profiling of *B. subtilis* after treatment with a broad range of antibiotic classes had identified these promoters as particularly responsive to DNA, RNA, protein, or cell envelope damage. Compounds 1 and 3 showed a specific induction of the cell envelope stress sensing promoters *liaI* and *ypuA* (Figure 5). While *ypuA* is known to respond broadly to disturbances at the bacterial cell envelope, *liaI* showed in previous studies a particularly strong reaction to compounds that interfere with cycling of undecaprenyl precursors in cell wall synthesis.³¹

With the aim to further explore the effects of the microciconamides on the bacterial cell envelope, we determined effects of compounds 1 and 3 on the membrane potential of *S. aureus*. The membrane potential is an electrical gradient across the bacterial cytoplasmic membrane, with a surplus of positive charge outside, that bacteria establish in the course of respiration. The membrane potential is essential for ATP generation by the F₀F₁-ATPase and for active transport processes across the cytoplasmic membrane. For measurement of the membrane potential the fluorescent dye DiOC₂(3) was used, which enters bacterial cells to some extent and emits green fluorescence. The higher the membrane potential, the more dye molecules accumulate in the cells and aggregation triggers a red-shift of fluorescence emission. Addition of compounds 1 and 3 efficiently dissipated the membrane potential of *S. aureus*, as indicated by the strong loss of red fluorescence (Figure 6). The effect occurred already at sub-micromolar concentrations of 1 and 3, the latter compound being slightly more potent. Consequently, microciconamides A (3) and C (1) seem to kill bacteria by energy depletion.

Notably, while some energy depleting agents induce the *liaI* promoter, e.g. the lantibiotic nisin, which uses the undecaprenyl

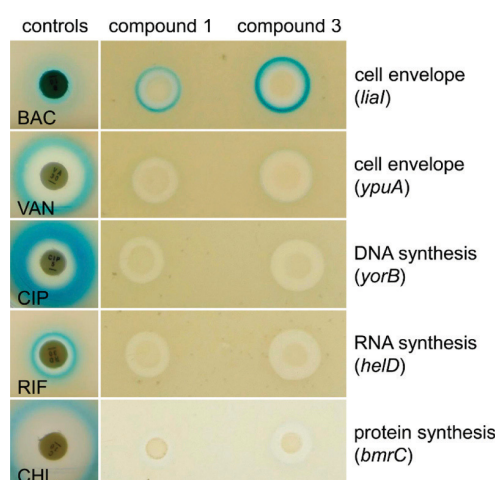


Figure 5. Reporter gene assay with compounds **1** and **3** for orienting mode of action studies. Compounds **1** and **3** strongly induced the *liaI* promoter, and a weak induction was detected for the *yjuA* promoter, indicating that these compounds cause cell envelope stress. The other three promoters indicating DNA damage (*yorB*), RNA damage (*helD*), or translation arrest (*bmrC*) were not induced. The five different promoters showed a strong induction when treated with the respective positive controls: bacitracin (BAC), vancomycin (VAN), ciprofloxacin (CIP), rifampicin (RIF), and chloramphenicol (CHL).

precursor lipid II as a docking molecule to form pores within the bacterial cytoplasmic membrane,³² many energy-depleting agents, such as ionophores, do not effectively induce *liaI*. Whether or not the strong *liaI* signal triggered by the microcionamides indicates that bacterial cells sense an interference with their undecaprenyl precursor cycle will require further studies.

In summary, microcionamides A, B, and C (**1–3**) exhibited cytotoxicity on different human cancer cell lines via both induction of apoptosis and inhibition of starvation-induced autophagy. Furthermore, microcionamides A (**3**) and C (**1**) showed a significant inhibitory effect on Gram-positive bacteria, which is probably correlated with their abilities to depolarize bacterial cytoplasmic membranes. It is noteworthy that microcionamide C (**1**) showed increased cytotoxic activity over microcionamide A (**3**) by a factor of 5 or more on different eukaryotic cell lines, while **3** was more potent against Gram-positive bacteria compared to **1**. Even though the difference in the MIC between **1** and **3** against *S. aureus* was smaller than a whole titration step in the MIC assay, a larger zone of inhibition of **3** was detected on agar (Figure 5), and lower concentrations of **3** were able to cause a disruption of the membrane potential in comparison to **1** (Figure 6). Conversely, gombamides B (**4**) and D (**6**) proved to be inactive against both human and bacterial cells.

EXPERIMENTAL SECTION

General Experimental Procedures. Optical rotations were measured with a JASCO P-2000 polarimeter. UV data were recorded on a PerkinElmer Lambda 2S UV/vis spectrometer. ¹H, ¹³C, and 2D NMR spectra (HH-ROESY, HH-TOCSY, HC-HSQC, and HC-HMBC) were recorded with standard pulse sequences on a Bruker AVIII HD 600 spectrometer equipped with a QXI/QCI cryoprobe. The sweep width for the homonuclear experiments (HH-ROESY, HH-TOCSY) was 7000 Hz in F2 and F1. Two thousand data points were collected in F2, and 512 data points in F1 with quadrature detection in both dimensions. The mixing time for the HH-ROESY experiment was 450 ms with a spin lock field of 5000 Hz and 80ms for the HH-TOCSY with a spin lock field of 9500 Hz. The HC-HSQC

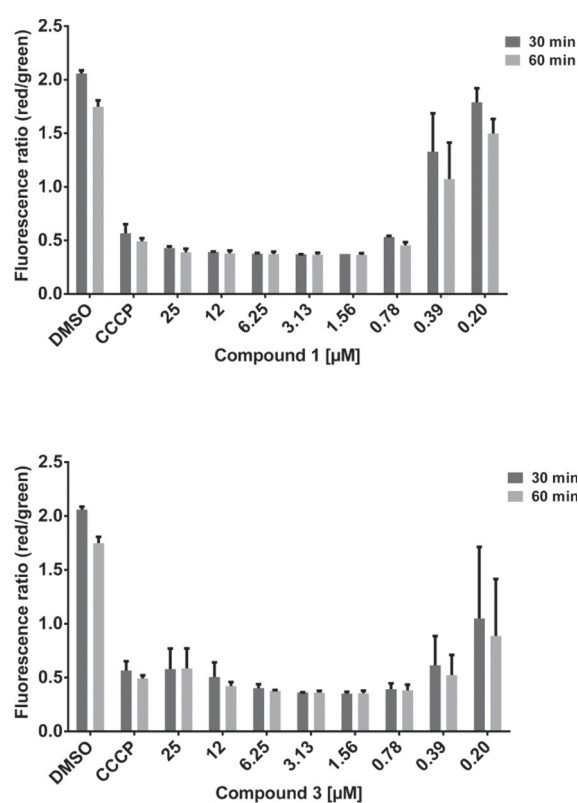


Figure 6. Effect of microcionamides A (**3**) and C (**1**) on the membrane potential of *Staphylococcus aureus* NCTC 8325. A prominent loss of red fluorescence indicative of strong membrane potential dissipation occurs already at 0.8 μM of **1** or 0.2 μM of **3**. The protonophore carbonyl cyanide *m*-chlorophenyl hydrazone (CCCP) at 5 μM served as a positive control, and DMSO was the negative control. Samples were analyzed after 30 and 60 min of exposure to compounds. The experiment was performed two times on two different days with independent bacterial cultures. Results for both biological replicates are shown in the graphs. Error bars indicate the standard error of the mean.

experiment was measured with a sweep width of 7000 Hz in F2 and 26400 Hz in F1. Two thousand data points were collected in F2, and 512 data points in F1 with quadrature detection in both dimensions. The sweep width for the HC-HMBC experiments was set to 7000 Hz in F2 and 27900 Hz in F1. Two thousand data points in F2 and 512 data points in F1 were collected with quadrature detection in F2. The chemical shifts were referenced to the residual solvent peaks at δ_{H} 3.31 (MeOH-*d*₄) and 2.50 (DMSO-*d*₆) for ¹H and at δ_{C} 49.0 (MeOH-*d*₄) and 39.5 (DMSO-*d*₆) for ¹³C NMR. Low-resolution ESI mass spectra were recorded on a Thermoquest Finnigan LCQ Deca connected to an Agilent 1100 series LC. High-resolution mass measurements were obtained on an LTQ Orbitrap Velos Pro (Thermo Scientific). Solvents were distilled prior to use, and spectral grade solvents were used for spectroscopic measurements. HPLC analysis was performed using a Dionex UltiMate3400 SD coupled to a photodiode array detector (DAD3000RS) with detection wavelengths at 235, 254, 280, and 340 nm. The separation column (125 \times 4 mm, L \times i.d) was prefiltered with Eurospher 100-10, C18 (Knauer, Germany). HPLC analysis of L/D-Ile and L/D-*allo*-Ile following Marfey's derivatization was carried out on the EC 250/4.6 Nucleosil 120-5, C₄ (Macherey-Nagel) separation column. Column chromatography was performed using Sephadex LH-20 or reversed-phase silica (RP C₁₈) as stationary phase. Semipreparative purification was accomplished on a Merck Hitachi system (pump L7100 and UV detector L7400; Eurospher 100 C₁₈, 300 \times 8 mm, L \times i.d; Knauer) with a flow rate of 5.0 mL/min. Thin-layer chromatography (TLC) was performed using

precoated silica gel 60 F₂₅₄ plates (Merck) followed by detection under UV at 254 nm or after spraying the plates with anisaldehyde reagent.

Sponge Material. The sponge was collected by scuba at Ambon, Indonesia. The sponge was identified as *Clathria basilana* by Dr. Nicole de Voogd (Naturalis Biodiversity Center, Leiden, The Netherlands), and a voucher specimen was deposited at the Naturalis Biodiversity Center, Leiden, The Netherlands (reference number RMNH POR 8636). The sponge was preserved in a mixture of EtOH and H₂O (70:30) and stored in a -20 °C freezer prior to extraction.

Extraction and Isolation. The thawed sponge material (820 g wet) was cut into small pieces and exhaustively extracted with MeOH (3 × 2L) at room temperature (rt). The extracts were combined and concentrated under vacuum to yield 6.5 g of crude extract. Subsequent liquid-liquid partitioning afforded *n*-hexane, EtOAc, *n*-BuOH, and aqueous fractions at amounts of 420 mg, 700 mg, 540 mg, and 4.9 g, respectively. The EtOAc fraction was further purified by column chromatography on Sephadex LH-20 (MeOH as mobile phase), followed by reversed-phase vacuum liquid chromatography (RP-VLC) and semipreparative HPLC in a gradient system of H₂O/MeOH, respectively, to yield **1** (7.7 mg), **2** (2 mg), **3** (1 mg), **4** (4.5 mg), **5** (1 mg), **7** (0.8 mg), 1*H*-indole-3-carbaldehyde (0.6 mg), 1*H*-indole-3-carboxylic acid (0.5 mg), 6-bromo-1*H*-indole-3-carbaldehyde (1.2 mg), 6-bromo-1*H*-indole-3-carboxylic acid (1 mg), methyl 6-bromo-1*H*-indole-3-carboxylate (1 mg), ethyl 6-bromo-1*H*-indole-3-carboxylate (1.7 mg), 7-bromo-4(1*H*)-quinolinone (1 mg), (3-(2-(4-hydroxyphenyl)-2-oxoethyl)-5,6-dihydropyridin-2(1*H*)-one) (2.2 mg), 2-deoxythymidine (2.5 mg), and 4-hydroxybenzoic acid (4 mg). The *n*-BuOH fraction was subjected to column chromatography on Sephadex LH-20 (MeOH as mobile phase), followed by RP-VLC and semipreparative HPLC to yield **6** (5.6 mg).

Microconamide C (1): white, amorphous solid; $[\alpha]_D^{20}$ -56 (*c* 0.1, MeOH); UV (λ_{max} MeOH) (log ϵ) 201 (3.72), 287 (3.09); ¹H (600 MHz) and ¹³C (150 MHz) NMR data (DMSO-*d*₆), Table 1; HRESIMS *m/z* 889.5033 [M + H]⁺ (calcd for C₄₄H₇₃N₈O₇S₂, 889.5038); HRESIMS/MS *m/z* 770.4297 [M - E-PEA]⁺ (calcd for C₃₆H₆₄N₇O₇S₂, 770.4303); 657.3454 [M - (E-PEA + Ile₇)⁺ (calcd for C₃₀H₅₂N₆O₆S₂, 657.3463).

Microconamide D (2): white, amorphous solid; $[\alpha]_D^{20}$ -40 (*c* 0.1, MeOH); UV (λ_{max} MeOH) (log ϵ) 210 (3.8), 271 (4.01); ¹H (600 MHz) and ¹³C (150 MHz) NMR data (DMSO-*d*₆), Table S2-1; HRESIMS *m/z* 889.5034 [M + H]⁺ (calcd for C₄₄H₇₃N₈O₇S₂, 889.5038); HRESIMS/MS *m/z* 770.4294 [M - Z-PEA]⁺ (calcd for C₃₆H₆₄N₇O₇S₂, 770.4294); 657.3451 [M - (Z-PEA + Ile₇)⁺ (calcd for C₃₀H₅₂N₆O₆S₂, 657.3451); 776.4184 [M - Ile₇]⁺ (calcd for C₃₈H₆₀N₇O₆S₂, 776.4184).

Gombamide B (4): white, amorphous solid; $[\alpha]_D^{20}$ +28 (*c* 0.1, MeOH); UV (λ_{max} MeOH) (log ϵ) 212 (4.1), 290 (4.56); ¹H (600 MHz) and ¹³C (150 MHz) NMR data (DMSO-*d*₆), Table 2; HRESIMS *m/z* 1002.4572 [M + H]⁺ (calcd for C₅₀H₆₈N₉O₉S₂, 1002.4576); HRESIMS/MS *m/z* 883.3826 [M - E-PEA]⁺ (calcd for C₄₂H₅₉N₈O₉S₂, 883.3826); 665.2566 [M - Leu-Ile-Glp]⁺ (calcd for C₃₃H₄₁N₆O₅S₂, 665.2566); 546.1833 [M - (E-PEA + Leu-Ile-Glp)]⁺ (calcd for C₂₅H₃₂N₅O₅S₂, 546.1833).

Gombamide C (5): white, amorphous solid; $[\alpha]_D^{20}$ +16 (*c* 0.1, MeOH); UV (λ_{max} MeOH) (log ϵ) 214 (4.01), 288 (4.4); ¹H (600 MHz) and ¹³C (150 MHz) NMR data (DMSO-*d*₆), Table S5-1; HRESIMS *m/z* 1002.4576 [M + H]⁺ (calcd for C₅₀H₆₈N₉O₉S₂, 1002.4576); HRESIMS/MS *m/z* 883.3826 [M - Z-PEA]⁺ (calcd for C₄₂H₅₉N₈O₉S₂, 883.3841); 665.2566 [M - Leu-Ile-Glp]⁺ (calcd for C₃₃H₄₁N₆O₅S₂, 665.2566); 546.1833 [M - (Z-PEA + Leu-Ile-Glp)]⁺ (calcd for C₂₅H₃₂N₅O₅S₂, 546.1839).

Gombamide D (6): white, amorphous solid; $[\alpha]_D^{20}$ -6 (*c* 0.1, MeOH); UV (λ_{max} MeOH) (log ϵ) 210 (3.8), 271 (4.01); ¹H (600 MHz) and ¹³C (150 MHz) NMR data (DMSO-*d*₆), Table 3; HRESIMS *m/z* 737.3107 [M + H]⁺ (calcd for C₃₃H₄₉N₈O₈S₂, 737.3109); HRESIMS/MS *m/z* 623.2317 [M - Pro₆-NH₂]⁺ (calcd for C₂₇H₃₉N₆O₇S₂, 623.2317); 595.2367 [M - (Pro₆-NH₂ + CO)]⁺ (calcd for C₂₆H₃₉N₆O₆S₂, 595.2367).

(E)-2-Amino-3-methyl-N-styrylbutanamide (7): white, amorphous solid; $[\alpha]_D^{20}$ -38 (*c* 0.1, MeOH); UV (λ_{max} MeOH) (log ϵ) 220 (3.07),

285 (3.22); ¹H (600 MHz) and ¹³C (150 MHz) NMR data (MeOH-*d*₄), Table 4; HRESIMS *m/z* 219.1490 [M + H]⁺ (calcd for C₁₃H₁₉N₂O, 219.1492).

Marfey's Analysis. For acid hydrolysis of the isolated peptides (**1**–**7**), 0.5 mg of each was treated separately with 2 mL of 6 N HCl and heated at 110 °C for 24 h. The resulting solutions were concentrated, with consecutive addition of H₂O (5 mL each) to ensure complete elimination of HCl. Accordingly, the mixture of 50 μL of each acid hydrolysate, 100 μL of FDNPL (1% *N*-(5-fluoro-2,4-dinitrophenyl)-L-leucinamide in acetone), and 20 μL of 1 M NaHCO₃ was heated at 40 °C for 1 h with frequent mixing. After cooling, 10 μL of 2 N HCl was added into the reaction solution. Subsequently, the derivatized product was concentrated to dryness and prepared for HPLC analysis by dissolving in 1000 μL of MeOH. The same procedure was followed for L- and D-amino acid standards. HPLC (C₁₈) analysis of the derivatized amino acids was performed by comparing their retention times with those of standards [gradient (MeOH, 0.1% HCOOH in H₂O): 0 min (10% MeOH); 5 min (10% MeOH); 35 min (100% MeOH); 45 min (100% MeOH); 25 °C, 1 mL/min] (Table S8-1). For improved resolution, HPLC analysis of the derivatized L/D-Ile and L/D-*allo*-Ile residues was performed on a C₄ analytical column [gradient (MeOH, 0.1% HCOOH in H₂O): 0% to 60% (MeOH) for 160 min; 25 °C, 1 mL/min] (Table S8-2).^{18,33}

Eukaryotic Cell Lines and Reagents. Acute T cell leukemia cells (Jurkat J16, no. ACC-282), Burkitt's lymphoma B lymphocytes (Ramos, no. ACC-603), acute promyelocytic leukemia cells (HL-60, no. ACC-3), and acute myeloid leukemia cells (Nomo-1, no. ACC-542) were obtained from the German Collection of Microorganisms and Cell Cultures (DSMZ). Wild-type murine embryonic fibroblasts (kindly provided by Xiaodong Wang)³⁴ expressing mCitrine-hLc3B were generated by retroviral gene transfer using pMSCVpuro/mCitrine-hLc3B. To generate pMSCVpuro/mCitrine-hLc3B, full-length human MAP1LC3B cDNA was cloned into pMSCVpuro/mCitrine vector (kindly provided by Michael Engelke, University of Göttingen). All cell lines were grown at 37 °C under humidified air supplemented with 5% CO₂ in RPMI 1640 (HL-60, Jurkat J16, Nomo-1, Ramos) or DMEM (mCitrine-hLc3B-MEF) containing 10% fetal calf serum, 1% HEPES, 120 IU/mL penicillin, and 120 μg/mL streptomycin. The broad-range caspase inhibitor *N*-(2-quinolyl)-L-valyl-L-aspartyl-(2,6-difluorophenoxy) methyl ketone [(QVD) #SML0063], the autophagy inhibitor bafilomycin A1 [(Baf. A1) #B1793], and the kinase inhibitor staurosporine [(STS) #SS921], used as positive control for induction of apoptosis, were obtained from Sigma-Aldrich. The profluorescent caspase-3 substrate Ac-DEVD-AMC was purchased from Biomol (#ABD-13402). Human ovarian carcinoma (A2780) cells were obtained from ECACC (Salisbury, Wiltshire, UK) and cultivated in RPMI-1640 medium supplemented with 10% fetal bovine serum, 120 μg/mL streptomycin, and 120 U/mL penicillin. Cells were grown at 37 °C in a humidified atmosphere containing 5% CO₂.

Determination of Eukaryotic Cell Viability. HL-60, Jurkat J16, Nomo-1, and Ramos cells were seeded at a density of 5 × 10⁵ cells/mL and incubated with different concentrations of compounds **1**, **2**, and **3** for 24 h. Cells treated with DMSO (0.1% v/v) for 24 h were used as the negative control. After the incubation period MTT (3-(4,5-dimethyl-2-thiazolyl)-2,5-diphenyl-2*H*-tetrazolium bromide; Calbiochem #475989) was added to the cells to a final concentration of 1 mg/mL, and the cells were incubated further for 60 min and then centrifuged at 600 rcf for 5 min. The medium was aspirated, and 100 μL of DMSO was added to each well to extract the formazan product from the cells. After 25 min of incubation on a shaker at rt, the absorbances at 650 nm (reference wavelength) and 570 nm (test wavelength) were measured using a multiplate reader (Synergy Mx, BioTek). Viability and IC₅₀ values (IC₅₀ = half-maximal inhibitory concentration) were calculated using Prism 6 (GraphPad Software). Relative viability in DMSO (0.1% v/v)-treated control cells was set to 100%. A2780 cells were plated into 96-well microtiter plates (approximately 9000 cells/well) (Sarstedt) and preincubated with growth medium overnight. Then, cells were incubated with increasing concentrations of test compounds for 72 h. After 72 h, 25 μL of a solution of MTT was added to each well. After approximately 10 min, formazan crystals were formed, and

medium was removed. Formazan crystals were then dissolved in 75 μL of DMSO. Absorptions were measured at 544 nm (test wavelength) and 690 nm (reference wavelength) using the BMG FLUOstar (BMG Labtechnologies, Offenburg, Germany). Absorption of the reference wavelength was subtracted from the absorption of the test wavelength.

Determination of Antibacterial Activity. MIC values for bacterial strains were determined in cation-adjusted Mueller-Hinton broth by the broth microdilution method according to the recommendations of the Clinical and Laboratory Standards Institute (CLSI).³⁵ For preparation of the inoculum the direct colony suspension method was used. Briefly, serial 2-fold dilutions of test compounds were prepared in microtiter plates and seeded with a final bacterial inoculum of 5×10^5 colony forming units per mL (CFU/mL). After 16 to 20 h at 37 °C and ambient air, the minimal inhibitory concentration was read as the lowest compound concentration preventing visible bacterial growth. The strain panel included antibiotic-susceptible CLSI quality control strains obtained from the American Type Culture Collection as indicated by the ATCC strain label. *E. faecium* BM 4147-1 is a clinical isolate cured of its vancomycin resistance plasmid,³⁶ and *A. baumannii* 09987 is a clinical isolate from the University of Bonn, Germany.

Cells of *M. tuberculosis* H37Rv were grown aerobically in Middlebrook 7H9 medium supplemented with 10% (v/v) ADS enrichment (5%, w/v, bovine serum albumin fraction V; 2%, w/v, glucose; 0.85%, w/v, sodium chloride), 0.5% (v/v) glycerol, and 0.05% (v/v) tyloxapol at 37 °C. For the determination of MIC against *M. tuberculosis*, bacteria were precultured until log-phase ($\text{OD}_{600\text{nm}} = 0.5-1$) and then seeded at 1×10^5 cells per well in a total volume of 100 μL in 96-well round-bottom microtiter plates containing 2-fold serially diluted compounds at a concentration range of 100–0.78 μM . Microplates were incubated at 37 °C for 5 days. Afterward, 10 μL /well of a 100 $\mu\text{g}/\text{mL}$ resazurin solution was added and incubated at ambient temperature for a further 16 h. Then cells were fixed for 30 min after formalin addition (5%, v/v, final concentration). For viability determination, fluorescence was quantified using a microplate reader (excitation 540 nm, emission 590 nm). Percentage of growth was calculated relative to rifampicin-treated (0% growth) and DMSO-treated (100% growth) controls.

Western Blot Analysis. Ramos cells were treated for the indicated durations with 1 μM of **1**, 1 μM of **2**, or 10 μM of **3**, respectively. Co-incubation with the caspase inhibitor QVD at a concentration of 10 μM was used as proof of caspase dependency of the observed effects. Subsequently, cells were pelleted at 600 rcf at 4 °C for 5 min, washed with phosphate-buffered saline (PBS), and frozen in liquid nitrogen. The cells were lysed in ice-cold lysis buffer [20 mM Tris-HCl, pH 7.5, 150 mM NaCl, 0.5 mM EDTA, 1% Triton X-100, 10 mM NaF, 2.5 mM $\text{Na}_4\text{P}_2\text{O}_7$, 10 μM Na_2MoO_4 , 1 mM Na_3VO_4 , protease inhibitor cocktail (Sigma #P2714)]. The lysates were cleared from cell debris by centrifugation at 11 000 rcf at 4 °C for 15 min, and the total protein concentration was measured by Bradford assay and adjusted to equal concentrations. After loading with Laemmli buffer and heating to 95 °C for 5 min, 25 μg of the protein extract was separated by SDS-PAGE [10% tris-glycine polyacrylamide gel (v/v)] and transferred to a PVDF membrane by Western blotting according to the standard protocol. Analysis of proteins of interest was performed using primary mouse antibodies to poly(ADP-ribose) polymerase-1 (Enzo Life Sciences #BML-SA250) or β -actin (Sigma-Aldrich #A5316) and IRDye800-conjugated secondary antibodies (LI-COR Biosciences #926-32210/11). Signals were detected with an infrared imaging system.

Caspase-3 Activity Assay. Caspase activity was analyzed as previously described.³⁷ Briefly, Jurkat J16 cells and Ramos cells were seeded at a density of 1×10^6 cells/mL in 96-well microtiter plates and incubated with different concentrations of **1**, **2**, and **3** for the indicated times. Cells treated with DMSO (0.1% v/v) were used as negative control. After the incubation period, cells were harvested by centrifugation at 600 rcf at 4 °C and lysed by incubation with ice-cold lysis buffer (20 mM HEPES, 84 mM KCl, 10 mM MgCl_2 , 200 μM EDTA, 200 μM EGTA, 0.5% NP-40, 1 $\mu\text{g}/\text{mL}$ leupeptin, 1 $\mu\text{g}/\text{mL}$ pepstatin, 5 $\mu\text{g}/\text{mL}$ aprotinin) for 10 min. After addition of 150 μL of reaction buffer (50 mM HEPES, 100 mM NaCl, 10% sucrose, 0.1% CHAPS, 2 mM CaCl_2 , 13.35 mM DTT, 70 μM DEVD-AMC) per well, fluorescence (Ex 360 nm, Em 450 nm) was measured at 37 °C over a time course of

150 min using a multiplate reader (Synergy Mx, BioTek). Caspase activity was determined as the slope of the resulting linear regressions. Data points shown are the mean of triplicates; error bars = SD. Values are normalized to DMSO (0.1% v/v)-treated cells (fold change = 1.00).

FACS-Based Analysis of Autophagy. The FACS-based analysis of autophagy was adapted from a protocol previously described by Shvets et al.³⁸ MEF cells stably expressing mCitrine-hLC3B were cultured in the indicated medium for 4 h with bafilomycin A1 (10 nM) and compound **1**, **2**, or **3** (10 μM), harvested with 0.05% trypsin-EDTA, and washed once with PBS. Subsequently, the intensity of mCitrine fluorescence was analyzed by flow cytometry using FACSDiva software. Reduction of mCitrine-hLC3B compared to medium control indicates autophagy induction. Baf. A1 served as positive control for inhibition of autophagy. Co-treatment with QVD was performed to exclude caspase-dependent processes.

Bacterial Reporter Gene Assay. For mode of action studies, five bacterial reporter strains were constructed in the genetic background of *B. subtilis* 1S34, each carrying one of the following promoters fused to the β -galactosidase reporter gene and inserted into the chromosomal *amyE* locus. Induction of the *yorB* promoter indicates DNA damage, the *hcdD* promoter (synonym *yvgS*) senses RNA damage, and the *bmrC* promoter senses translation arrest. Induction of the *ypuA* or *lial* (synonym *yvqI*) promoters indicates cell envelope stress. Promoter regions were chosen according to a previous publication by Urban et al.³⁰ For the agar-based reporter gene assay 20 mL of lysogeny broth (LB) containing spectinomycin (50 $\mu\text{g}/\text{mL}$) were inoculated with 500 μL of an overnight culture of *B. subtilis* 1S34 and grown to the stationary phase. Cells were adjusted to a total cell number of 3×10^7 CFU/mL in 50 mL of LB soft agar (0.7% agar) containing 150 $\mu\text{g}/\text{mL}$ of 5-bromo-4-chloro-3-indolyl- β -D-galactopyranoside (X-Gal) and poured into a square Petri dish. After solidification, test compounds (20 nmol) were spotted onto the agar plates. Paper discs (Oxoid) containing the following reference antibiotics were used as positive controls: bacitracin (10 μg), chloramphenicol (10 μg), ciprofloxacin (5 μg), rifampicin (30 μg), and vancomycin (30 μg). Plates were analyzed for promoter induction after incubation at 30 °C for 14 to 18 h. In the case of the *bmrC* promoter, soft agar was prepared from Belitzky minimal medium, and the plates were incubated at 37 °C.³⁹

Measurement of Bacterial Membrane Potential. Determination of membrane potential changes upon antibiotic treatment was performed using the membrane potential-sensitive fluorescent dye 3,3'-diethyloxycarbocyanine iodide ($\text{DiOC}_2(3)$, Molecular Probes). *S. aureus* NCTC 8325 was grown to the exponential phase in LB medium, harvested, and resuspended to an optical density at 600 nm (OD_{600}) of 0.5 in PBS. Cells were incubated with 30 μM $\text{DiOC}_2(3)$ for 15 min and subsequently treated with compounds **1** and **3** at different concentrations for 30 min. The protonophore carbonyl cyanide *m*-chlorophenyl hydrazone (Sigma-Aldrich) at a concentration of 5 μM was used as a positive control and DMSO as a negative control. Fluorescence was measured 30 and 60 min after addition of the respective compound at an excitation wavelength of 485 nm and two emission wavelengths, 530 nm (green) as well as 630 nm (red), using a microplate reader (TECAN Infinite M200). Increased membrane potential promotes intracellular dye accumulation, self-association of which causes a red-shift of the fluorescence emission signal.

■ ASSOCIATED CONTENT

📄 Supporting Information

The Supporting Information is available free of charge on the ACS Publications website at DOI: 10.1021/acs.jnatprod.7b00477.

¹H NMR spectra of **1–7**; ¹³C NMR spectra of **4**, **6**, and **7**; 2D NMR and HRESIMS spectra of the new compounds **1**, **2**, and **4–7**; HRESIMS/MS spectra of **1**, **2**, and **4–6**; tables of ¹H, ¹³C, and 2D NMR data for **2** and **5**; HPLC analysis of the acid hydrolysates of **1–7** using Marfey's method; structures of known compounds; cytotoxicity effects of **1–3** on human lymphoma and leukemia cell lines, measured by MTT assay; table of antibacterial

activity of 1–7 and known compounds reported as MIC (PDF)

AUTHOR INFORMATION

Corresponding Authors

*Tel: ++492118114163. E-mail: georgios.daletos@uni-duesseldorf.de.

*E-mail: proksch@uni-duesseldorf.de.

ORCID

Georgios Daletos: 0000-0002-1636-6424

Notes

The authors declare no competing financial interest.

ACKNOWLEDGMENTS

Support of this project to P.P., H.B.-O., M.U.K., R.K., and A.B. by the BMBF (project BALIPEND) and to K.W.W. by the German Center for Infection Research is gratefully acknowledged. We thank Dr. N. de Voogd (Leiden, Naturalis Biodiversity Center, Leiden, The Netherlands) for identification of the sponge. We appreciate the help of Prof. W. E. G. Müller (Johannes Gutenberg University, Mainz, Germany) for cytotoxicity assays with the L5178Y mouse lymphoma cell line. A.M. gratefully acknowledges the Ministry of Science, Research and Technology (MSRT) of Iran for awarding him a scholarship. The authors acknowledge access to the Jülich-Düsseldorf Biomolecular NMR Center. We furthermore wish to acknowledge Ms. Okoniewski and Mr. Straetener for expert technical assistance. The authors wish to thank Dr. E. Ferdinandus (University Pattimura, Ambon, Indonesia) and Prof. Dr. S. Wiryowidagdo (University Hassanudin, Makassar, Indonesia) for their support and help during sponge collection.

REFERENCES

- Toshiyuki, W.; Karen, C. T.; Hiroki, T.; Ikuro, A. Cytotoxic Cyclic Peptides from the Marine Sponges. In *Handbook of Anticancer Drugs from Marine Origin*; Springer International Publishing: Switzerland, 2015; pp 113–144.
- Fusetani, N.; Warabi, K.; Nogata, Y.; Nakao, Y.; Matsunaga, S.; Van Soest, R. R. M. *Tetrahedron Lett.* **1999**, *40*, 4687–4690.
- Kimura, M.; Wakimoto, T.; Egami, Y.; Tan, K. C.; Ise, Y.; Abe, I. *J. Nat. Prod.* **2012**, *75*, 290–294.
- Daletos, G.; Kalscheuer, R.; Koliwer, B. H.; Hartmann, R.; de Voogd, N. J.; Wray, V.; Lin, W.; Proksch, P. *J. Nat. Prod.* **2015**, *78*, 1910–1925.
- Van Soest, R. W. M.; Boury-Esnault, N.; Hooper, J. N. A.; Rützler, K.; de Voogd, N. J.; Alvarez de Glasby, B.; Hajdu, E.; Pisera, A. B.; Manconi, R.; Schoenberg, C.; Klautau, M.; Picton, B.; Kelly, M.; Vacelet, J.; Dohrmann, M.; Díaz, M.-C.; Cárdenas, P.; Carballo, J. L.; Rios Lopez, P. (2017). World Porifera database. Accessed at <http://www.marinespecies.org/porifera> on 2017–06–01.
- El-Naggar, M.; Conte, M.; Capon, R. J. *Org. Biomol. Chem.* **2010**, *8*, 407–412.
- Sperry, S.; Crews, P. *Tetrahedron Lett.* **1996**, *37*, 2389–2390.
- Tanaka, Y.; Katayama, T. *Nippon Suisan Gakkaishi* **1976**, *42*, 801–805.
- Aiello, A.; Ciminiello, P.; Fattorusso, E.; Magno, S. *Steroids* **1988**, *52*, 533–542.
- Keyzers, R. A.; Northcote, P. T.; Webb, V. J. *Nat. Prod.* **2002**, *65*, 598–600.
- Davis, R. A.; Mangalindan, G. C.; Bojo, Z. P.; Antemano, R. R.; Rodriguez, N. O.; Concepcion, G. P.; Samson, S. C.; de Guzman, D.; Cruz, L. J.; Tasdemir, D.; Harper, M. K.; Feng, X.; Carter, G. T.; Ireland, C. M. *J. Org. Chem.* **2004**, *69*, 4170–4176.
- Woo, J. K.; Jeon, J. e.; Kim, C. K.; Sim, C. J.; Oh, D. C.; Oh, K. B.; Shin, J. *J. Nat. Prod.* **2013**, *76*, 1380–1383.
- Cardellina, J. H.; Nigh, D.; VanWagenen, B. C. *J. Nat. Prod.* **1986**, *49*, 1065–1067.
- Rasmussen, T.; Jensen, J.; Anthoni, U.; Christophersen, C.; Nielsen, P. H. *J. Nat. Prod.* **1993**, *56*, 1553–1558.
- AlTarabeen, M.; Hassan Aly, A.; Perez Hemphill, C.; Catalina, F.; Rasheed, M.; Wray, V.; Proksch, P. *Z. Naturforsch., C: J. Biosci.* **2015**, *70*, 75–78.
- Gopichand, Y.; Schmitz, F. J. *J. Org. Chem.* **1979**, *44*, 4995–4997.
- Lidgren, G.; Bohlin, L.; Christophersen, C. *J. Nat. Prod.* **1988**, *51*, 1277–1280.
- Marfey, P. *Carlsberg Res. Commun.* **1984**, *49*, 591–596.
- Vijayarathy, S.; Prasad, P.; Fremlin, L. J.; Ratnayake, R.; Salim, A. A.; Khalil, Z.; Capon, R. J. *J. Nat. Prod.* **2016**, *79*, 421–427.
- Siemion, I. Z.; Wieland, T.; Pook, K. H. *Angew. Chem., Int. Ed. Engl.* **1975**, *14*, 702–703.
- Rinehart, K. L.; Kishore, V.; Bible, K. C.; Sakai, R.; Sullins, D. W.; Li, K.-M. *J. Nat. Prod.* **1988**, *51*, 1–21.
- Li, H.; Bowling, J. J.; Fronczek, F. R.; Hong, J.; Jabba, S. V.; Murray, T. F.; Ha, N. C.; Hamann, M. T.; Jung, J. H. *Biochim. Biophys. Acta, Gen. Subj.* **2013**, *1830*, 2591–2599.
- Li, H.; Dang, H. T.; Li, J.; Sim, C. J.; Hong, J.; Kim, D. K.; Jung, J. H. *Biochem. Syst. Ecol.* **2010**, *38*, 1049–1051.
- Calvaresi, M.; Garavelli, M.; Bottoni, A. *Proteins: Struct., Funct., Genet.* **2008**, *73*, 527–538.
- Whitson, E. L.; Ratnayake, A. S.; Bugni, T. S.; Harper, M. K.; Ireland, C. M. *J. Org. Chem.* **2009**, *74*, 1156–1162.
- Mizushima, N. *Genes Dev.* **2007**, *21*, 2861–2873.
- Guo, J. Y.; Chen, H. Y.; Mathew, R.; Fan, J.; Strohecker, A. M.; Karli-Uzunbas, G.; Kamphorst, J. J.; Chen, G.; Lemons, J. M. S.; Karantza, V.; Collier, H. A.; DiPaola, R. S.; Gelinas, C.; Rabinowitz, J. D.; White, E. *Genes Dev.* **2011**, *25*, 460–470.
- Degenhardt, K.; Mathew, R.; Beaudoin, B.; Bray, K.; Anderson, D.; Chen, G.; Mukherjee, C.; Shi, Y.; Gélinas, C.; Fan, Y.; Nelson, D. A.; Jin, S.; White, E. *Cancer Cell* **2006**, *10*, 51–64.
- Klionsky, D. J.; Abdelmohsen, K.; Abe, A.; Abedin, M. J.; Abeliovich, H.; Acevedo Arozena, A.; Adachi, H.; Adams, C. M.; Adams, P. D.; Adeli, K. *Autophagy* **2016**, *12*, 1–222.
- Urban, A.; Eckermann, S.; Fast, B.; Metzger, S.; Gehling, M.; Ziegelbauer, K.; Rübsamen-Waigmann, H.; Freiberg, C. *Appl. Environ. Microbiol.* **2007**, *73*, 6436–6443.
- Mascher, T.; Zimmer, S. L.; Smith, T. A.; Helmann, J. D. *Antimicrob. Agents Chemother.* **2004**, *48*, 2888–2896.
- Brötz, H.; Josten, M.; Wiedemann, I.; Schneider, U.; Götz, F.; Bierbaum, G.; Sahl, H. G. *Mol. Microbiol.* **1998**, *30*, 317–327.
- Ibrahim, S. R. M.; Min, C. C.; Teuscher, F.; Ebel, R.; Kakoschke, C.; Lin, W.; Wray, V.; Edrada-Ebel, R.; Proksch, P. *Bioorg. Med. Chem.* **2010**, *18*, 4947–4956.
- Shang, L.; Chen, S.; Du, F.; Li, S.; Zhao, L.; Wang, X. *Proc. Natl. Acad. Sci. U. S. A.* **2011**, *108*, 4788–4793.
- Patel, J. B.; Cockerill, F. R.; Bradford, P. A.; Eliopoulos, G. M.; Hindler, J. A.; Jenkins, S. G.; Lewis, J. S.; Limbago, B.; Miller, L. A.; Nicolau, D. P.; Powell, M.; Swenson, J. M.; Turnidge, J. D.; Weinstein, M. P.; Zimmer, B. L. *Methods for dilution antimicrobial susceptibility tests for bacteria that grow aerobically. Approved Standard*, 10th ed.; Clinical and Laboratory Standards Institute: USA, 2015; Vol. 35.
- Woodford, N.; Adebisi, A. M. A.; Palepou, M. F. I.; Cookson, B. D. *Antimicrob. Agents Chemother.* **1998**, *42*, 502–508.
- Czugala, M.; Mykhaylyk, O.; Böhrer, P.; Onderka, J.; Stork, B.; Wesselborg, S.; Kruse, F. E.; Plank, C.; Singer, B. B.; Fuchsluger, T. A. *Nanomedicine* **2016**, *11*, 1787–1800.
- Shvets, E.; Fass, E.; Elazar, Z. *Autophagy* **2008**, *4*, 621–628.
- Stülke, J.; Hanschke, R.; Hecker, M. *J. Gen. Microbiol.* **1993**, *139*, 2041–2045.

Publication 3

Manuscript “Daldinone derivatives from the mangrove-derived endophytic fungus *Annulohyphoxylon* sp.”:

Liu Y, Stuhldreier F, Kurtán T, Mándi A, Arumugam S, Lin W, Stork B, Wesselborg S, Weber H, Henrich B, Daletos G, Proksch P.

RSC Advances 7:5381–5393 (2017). doi: 10.1039/C6RA27306H



Cite this: *RSC Adv.*, 2017, 7, 5381

Daldinone derivatives from the mangrove-derived endophytic fungus *Annulohyphoxylon* sp.†

Yang Liu,^{ab} Fabian Stuhldreier,^c Tibor Kurtán,^d Attila Mándi,^d Sathishkumar Arumugam,^e Wenhan Lin,^f Björn Stork,^c Sebastian Wesselborg,^c Horst Weber,^g Birgit Henrich,^h Georgios Daletos^{*a} and Peter Proksch^{*a}

Two new benzo[*h*]fluoranthene metabolites, daldinones H, J (**1** and **3**), and the likewise undescribed artefact, daldinone I (**2**), along with six known compounds (**4**–**9**) were isolated from the endophytic fungus *Annulohyphoxylon* sp. that was obtained from the Mangrove plant *Rhizophora racemosa* collected in Cameroon. The structures of the new compounds were elucidated by 1D and 2D NMR as well as by HRESIMS and ECD spectra analysis. Co-cultivation of this fungus with the actinomycetes *Streptomyces lividans* or with *Streptomyces coelicolor* resulted in an up to 38-fold increase of 1-hydroxy-8-methoxynaphthalene (**9**), while no significant induction was detected when the fungus was co-cultivated either with *Bacillus subtilis* or with *Bacillus cereus*. Compound **2** exhibited strong to moderate cytotoxicity against Ramos and Jurkat J16 cells with IC₅₀ values of 6.6 and 14.1 μM, respectively. Mechanistic studies indicated that compound **2** induces apoptotic cell death caused by induction of intrinsic apoptosis. Moreover, **2** potently blocks autophagy, a potential pro-survival pathway for cancer cells. Feeding experiments with 1,8-dihydroxynaphthalene (DHN) led to an enhanced accumulation of daldinone B (**6**), which supported the proposed biogenetic pathway.

Received 24th November 2016
Accepted 30th December 2016

DOI: 10.1039/c6ra27306h

www.rsc.org/advances

Introduction

Endophytes are microorganisms that colonize asymptotically the intercellular and/or intracellular parts of healthy plants^{1,2} and play an important role in drug discovery.³ In recent years, the increased re-isolation of known substances from fungi has turned the interest of natural product chemists to

hitherto less investigated ecological niches such as Mangrove swamps for bioprospecting of fungi.^{4–6} Mangroves inhabit (sub) tropical coastal regions and are exposed to various stress factors, such as intense light and high salinity followed by tidal range alterations.^{7,8} Endophytic fungi have developed unique metabolic mechanisms, therefore providing nutrients and/or chemical defense to their hosts.⁹ Mangrove-derived endophytic fungi have been shown to produce a plethora of new compounds with some of them showing pronounced biological activities as exemplified by the tetrahydroxanthone derivative phomoxanthone A that was recently isolated by our group from a Mangrove endophyte and showed strong anticancer activity against cisplatin resistant cancer cells in addition to immunostimulant activity.^{6,10}

During our ongoing search for new bioactive secondary metabolites from endophytic fungi,^{11–13} an endophytic fungus was isolated from the Mangrove plant *Rhizophora racemosa*, collected in Cameroon. 18S–28S rDNA and β-tubulin sequencing were used to identify this fungus as a member of the genus of *Annulohyphoxylon*,¹⁴ which we therefore named as *Annulohyphoxylon* sp. CA-2013 isolate YL. *Annulohyphoxylon*, which has been named *Hypoxylon* sect. *Annulata* before, is considered a new genus separated from *Hypoxylon* based on a report of Hsieh.¹⁵ *Annulohyphoxylon* is believed to show the same evolutionary lineage as the genera *Hypoxylon* and *Daldinia*.¹⁶ Previous chemical investigations of taxa of *Annulohyphoxylon* sp. yielded several

^aInstitute of Pharmaceutical Biology and Biotechnology, Heinrich Heine University, Universitätsstrasse 1, D-40225 Duesseldorf, Germany. E-mail: georgios.daletos@uni-duesseldorf.de; proksch@uni-duesseldorf.de

^bKey Laboratory of Marine Drugs, The Ministry of Education of China, School of Medicine and Pharmacy, Ocean University of China, Qingdao 266003, P. R. China

^cInstitute of Molecular Medicine I, Medical Faculty, Heinrich Heine University, Universitätsstrasse 1, D-40225 Duesseldorf, Germany

^dDepartment of Organic Chemistry, University of Debrecen, P. O. B. 20, 400, 4002 Debrecen, Hungary

^eCentre of Advanced Study in Marine Biology, Annamalai University, Parangipettai 608502, Tamilnadu, India

^fState Key Laboratory of Natural and Biomimetic Drugs, Beijing University, Beijing 100191, P. R. China

^gInstitute of Pharmaceutical and Medicinal Chemistry, Heinrich Heine University, Universitätsstrasse 1, D-40225 Duesseldorf, Germany

^hInstitute of Medical Microbiology and Hospital Hygiene, University Clinic of the Heinrich Heine University, D-40225 Duesseldorf, Germany

† Electronic supplementary information (ESI) available: HRESIMS spectra, 1D and 2D NMR spectra of new compounds 1–3, CD calculations for compounds 1 and 3, spectra of co-cultivation experiments, proposed biogenetic pathway cytotoxic effect of compound 2 on Jurkat J16 cells and Ramos cells, and HPLC chromatograms of compounds 1–3 are available. See DOI: 10.1039/c6ra27306h



metabolites including cohaerins A–K,^{15–17} daldinone A,¹⁷ trunca-tone,¹⁸ and truncaquinones A and B.^{17,19}

Subsequent fractionation of the fungal extract following fermentation on solid rice medium afforded two new benzo[*j*]fluoranthene-based metabolites, daldinones H and J (**1** and **3**, respectively), and a hitherto undescribed artefact, daldinone I (**2**) that originated by rapid conversion of **1** during chromatographic isolation. In addition, six known compounds were identified, including daldinone C (**4**), hypoxylonol C (**5**), daldinone B (**6**), 3,4-dihydro-3,4,6,8-trihydroxy-1(*2H*)-naphthalenone (**7**), (*R*)-scytalone (**8**), and 1-hydroxy-8-methoxynaphthalene (**9**) (Fig. 1), which had been previously isolated from members of the order Xylariales. Co-cultivation of *Annulohypoxyton* sp. with the actinomycete *Streptomycetes lividans* or with *Streptomyces coelicolor* resulted in an up to 38-fold increase of **9**. However, when co-culturing the fungus with either *Bacillus subtilis* or with *Bacillus cereus*, no significant induction in the accumulation of fungal metabolites was observed. Compound **2** showed pronounced cytotoxicity against Ramos and Jurkat J16 cell lines with IC₅₀ values of 6.6 and 14.1 μM, respectively, due to induction of intrinsic apoptosis. Moreover, **2** potently blocks autophagy, a potential pro-survival pathway for cancer cells. Feeding of 1,8-dihydroxynaphthalene to the fungal culture resulted in a pronounced increase of daldinones H (**1**) and B (**6**), which corroborated the previously proposed biogenetic pathway.

Results and discussion

The EtOAc extract of the fungus following cultivation on solid rice medium was partitioned between *n*-hexane and 90% aqueous MeOH. The resulting MeOH phase afforded two new benzo[*j*]fluoranthene secondary metabolites (**1** and **3**), and the likewise hitherto undescribed artefact (**2**) that rapidly originated from **1** during chromatographic isolation.

Compound **1** was isolated as a red, amorphous powder. Its molecular formula was established as C₂₀H₁₄O₆ based on the prominent ion peak observed at *m/z* 351.0865 [M + H]⁺ in the HRESIMS spectrum, corresponding to 14 degrees of unsaturation. The ¹H and COSY spectra revealed aromatic signals representative for a 1,2,3-trisubstituted benzene ring at δ_H 6.98 (H-10), 7.64 (H-11), and 7.51 (H-12), two *ortho*-coupled protons at δ_H 6.77 (H-5, *J* = 8.1 Hz) and 7.64 (H-6, *J* = 8.1 Hz), two sets of methylene groups at δ_H 3.39/2.74 (H₂-7), and 3.14/2.94 (H₂-2), as well as an oxymethine proton at δ_H 5.16 (H-1). In the HMBC spectrum of **1**, the correlations from H-5 to C-3a, C-6a, and C-4, from H-6 to C-4 and C-12d, from H-2 to C-1, C-3, C-12c, and C-3a, and from H-1 to C-3, C-12c, and C-12d, suggested the presence of a vermelone²⁰ moiety in the molecule (Fig. 2). The HMBC spectrum verified the presence of a second vermelone subunit as deduced by the correlations observed from H-10 to C-8a, C-9, and C-12, from H-11 to C-9 and C-12a, from H-12 to C-8a, C-10, C-12a, and C-12b, as well as from H-7 to C-6b, C-8, C-12b, and C-8a. The connection of the two substructures at C-6a and C-6b was established on the basis of the HMBC correlation from H-6 to C-6b (Fig. 2). These functionalities accounted for 13 of the 14 degrees of unsaturation, thus leaving only C-12b to C-12c for connection between the two units, rationalizing the remaining degree of unsaturation. Hence, **1** was identified as a new natural product and was named daldinone H.

The relative configuration of the two chirality centers of **1** could not be determined due to the lack of characteristic NOE correlations. For the stereochemical studies, ECD measurement and calculations were carried out, which first required the HPLC separation of **1** from its dehydration product **2**, since **1** was isolated as a 1 : 1 mixture with **2**. Compounds **1** and **2** could be base-line separated using Chiralpack IA column and the HPLC-ECD spectrum of **1** was recorded, which was used for comparison in the ECD calculations. A pure sample of **2** was available and TDDFT-ECD calculation determined its absolute

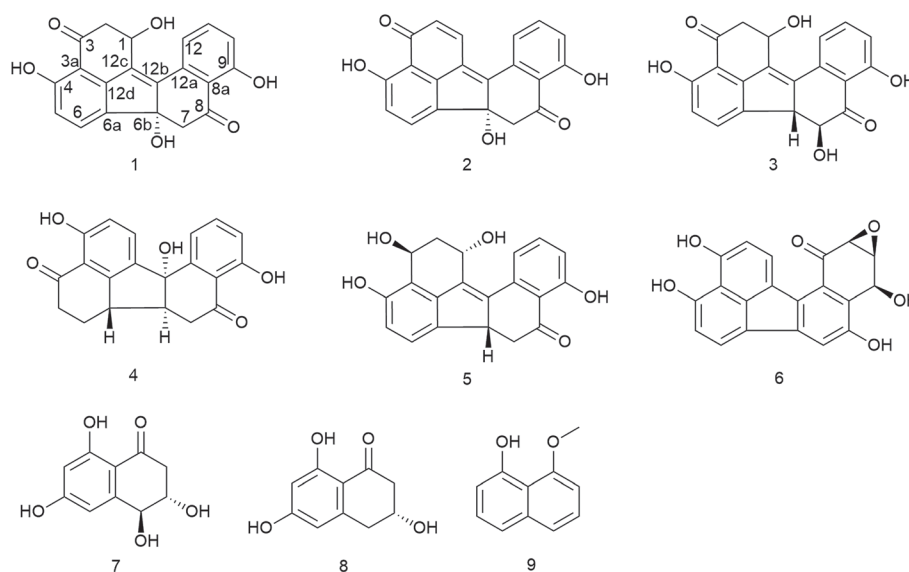


Fig. 1 Structures of isolated compounds from *Annulohypoxyton* sp.



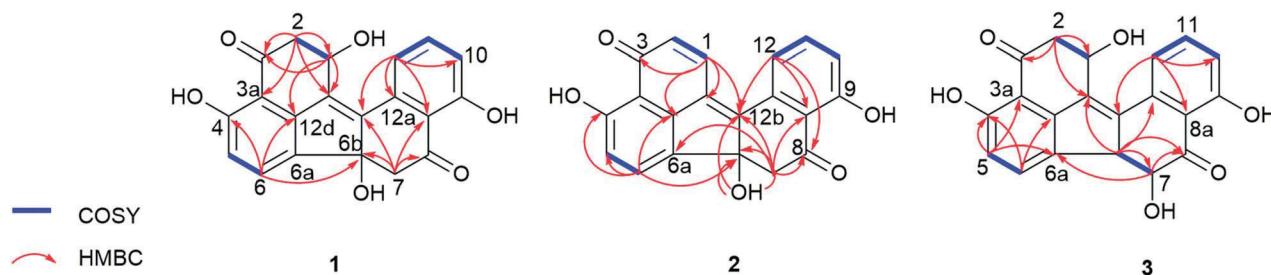


Fig. 2 COSY and selected HMBC correlations of 1–3.

configuration as (6bR), which suggested (6bR) absolute configuration for its precursor 1 as well (*vide infra*).

In order to determine the absolute configuration of 1, the TDDFT-ECD protocol^{21,22} was applied on the (1R,6bR) and (1S,6bR) diastereomers of 1. The Merck Molecular Force Field (MMFF) conformational search produced 5 low-energy conformers for both diastereomers in a 21 kJ mol⁻¹ energy window which were reoptimized at four different DFT levels [B3LYP/6-31G(d) *in vacuo*, B97D/TZVP^{24,25} PCM/MeCN, B3LYP/TZVP PCM/MeCN and CAM-B3LYP/TZVP PCM/MeCN]. The ¹H NMR spectrum of 1 showed a small value of the ³J_{1-H,2-H} (4.9 and 1.9 Hz), which suggested the preferred equatorial orientation of 1-H in solution. The computed B3LYP/6-31G(d) *in vacuo* conformers of (1R,6bR)-1 had preference for the axial orientation of 1-H (see Fig. S9 and Table S1 in the ESI[†]), while those of (1S,6bR)-1 had larger population for the conformers with equatorial 1-H (see Fig. S11 and Table S2 in the ESI[†]). This result would have afforded the assignment of the relative configuration and hence the absolute configuration as (1S,6bR). However, the three solvent model DFT optimizations (B97D/TZVP PCM/MeCN (Fig. 3 and 5), B3LYP/TZVP PCM/MeCN and CAM-B3LYP/TZVP PCM/MeCN) showed that 1-H preferably adopts equatorial orientation in both the (1R,6bR) and the (1S,6bR) diastereomer and thus the correlation of the coupling constant (³J_{1-H,2-H}) with the geometry of the computed conformers could not result in an unambiguous assignment of the relative configuration.

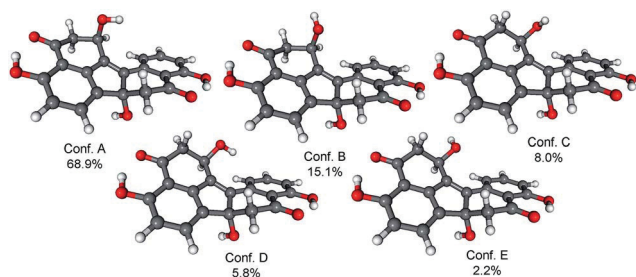


Fig. 3 Structure and population of the low-energy B97D/TZVP PCM/MeCN conformers (>2%) of (1R,6bR)-1 diastereomer. Populations of the same conformers at B3LYP/TZVP PCM/MeCN level are 65.5%, 20.5%, 7.0%, 3.2% and 3.8% (order of last two conformers changed) while at CAM-B3LYP/TZVP PCM/MeCN level are 63.4%, 21.0%, 7.3%, 4.3% and 4.0%.

ECD spectra were computed for the low-energy ($\geq 2\%$) B3LYP/6-31G(d) *in vacuo* (Fig. S10 and S12 of the ESI[†]) and B97D/TZVP PCM/MeCN conformers of (1R,6bR)-1 and (1S,6bR)-1 with various functionals (B3LYP, BH&HLYP and PBE0) and TZVP basis set, and they reproduced well the main features of the experimental spectrum but there was no sufficient difference among the computed ECD spectra of the diastereomers to distinguish them (Fig. 4 and 6). The agreement of the computed ECDs confirmed the configurational assignment of C-6b as (R).

ECD spectra computed for the B3LYP/6-31G(d) *in vacuo* and B97D/TZVP PCM/MeCN conformers performed better over 300 nm for the (1S,6bR) diastereomer, while the two negative Cotton effects (CEs) below 280 nm were reproduced better for the (1R,6bR) diastereomer. ECD spectra were also calculated for B3LYP/TZVP PCM/MeCN and CAM-B3LYP/TZVP^{25,26} PCM/MeCN

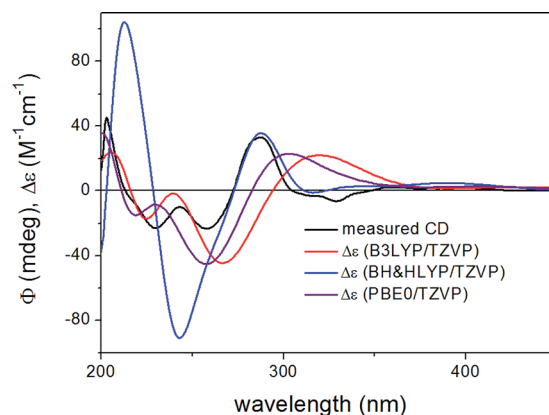


Fig. 4 Experimental ECD spectrum of 1 compared with the Boltzmann-weighted ECD spectra computed for the B97D/TZVP PCM/MeCN low-energy conformers of (1R,6bR)-1 at various levels.

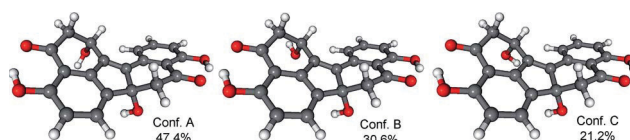


Fig. 5 Structure and population of the low-energy B97D/TZVP PCM/MeCN conformers (>2%) of (1S,6bR)-1 diastereomer. Populations of the same conformers at B3LYP/TZVP PCM/MeCN level are 33.0%, 47.2% and 18.4% (order of first two conformers changed) while at CAM-B3LYP/TZVP PCM/MeCN level are 25.9%, 53.2% and 19.0%.



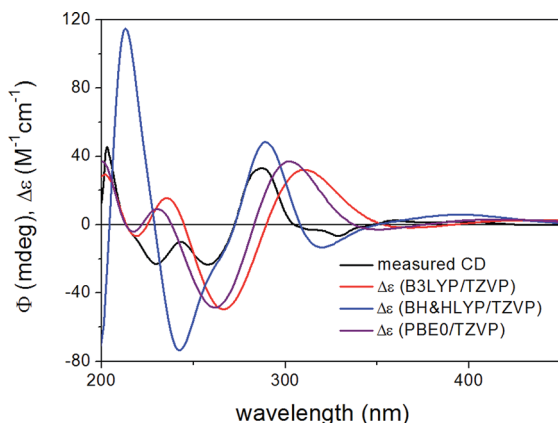


Fig. 6 Experimental ECD spectrum of **1** compared with the Boltzmann-weighted ECD spectra computed for the B97D/TZVP PCM/MeCN low-energy conformers of (1*S*,6*bR*)-**1** at various levels.

conformers (Fig. S13–S16 of the ESI[†]), but these results were found similar to that of the B97D/TZVP PCM/MeCN method and the absolute configuration of C-1 could not be determined unambiguously (Fig. 4 and 6). Moreover, attempts to assign the configuration of C-1 by employing the modified Mosher's method failed to give the corresponding MPA esters, probably due to steric hindrance and/or instability of **1** under reaction conditions.

Compound **2** was isolated as a red, amorphous powder. Its molecular formula was established as C₂₀H₁₂O₅ based on the prominent ion peak observed at *m/z* 333.0756 [M + H]⁺ in the HRESIMS spectrum. The ¹H and ¹³C NMR data of **1** were similar to those of **2**, except for the deshielded signals resonating at δ_H 6.75 (δ_C 133.3, CH-2) and 8.23 (δ_C 134.7, CH-1), indicating that **2** is the dehydration product of **1** bearing an additional C1/2 double bond. In the HMBC spectrum of **2**, the correlations from H-1 to C-12*b*, C-12*c*, C-12*d*, and C-3, as well as from H-2 to C-12*c* and C-3*a* corroborated this assumption (Fig. 2). Notably, **1** was observed to rapidly transform into **2** during the isolation procedure. Since **2** was not detected in the crude fungal extract, it is suggested to be an artefact arising from **1** during the isolation procedure. For compound **2** the name daldinone I is suggested.

The initial MMFF conformational search of the arbitrarily selected (*R*)-**2** resulted in a single conformer in a 21 kJ mol⁻¹ energy window (Fig. 7), which was reoptimized at B3LYP/

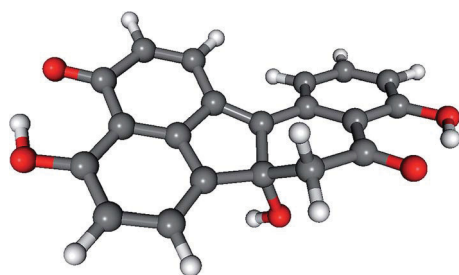


Fig. 7 Structure of the computed conformer of (*R*)-**2** at B3LYP/6-31G(d) *in vacuo* level.

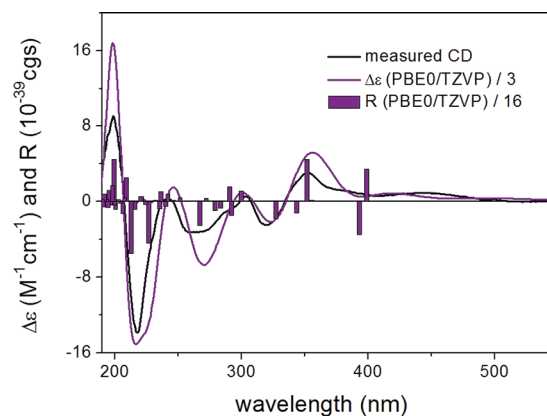


Fig. 8 Experimental ECD spectrum of **2** in MeCN compared with the PBE0/TZVP PCM/MeCN ECD spectrum of the single conformer of (*R*)-**2** computed for the B3LYP/6-31G(d) optimized conformer. Bars represent the rotational strength of conformer A.

6-31G(d) *in vacuo* level followed by ECD calculations at different levels (Fig. 8). The calculated ECD spectra gave excellent agreement with the experimental one indicating (*R*) absolute configuration. Due to the nice agreement and limited conformational freedom, there was no need to use solvent model calculations in this case.

Compound **3** was isolated as a red, amorphous powder and displayed a very similar UV spectrum as **1**. Moreover, the HRESIMS exhibited a prominent ion peak at *m/z* 351.0862 [M + H]⁺, indicating that both compounds shared the same molecular formula (C₂₀H₁₄O₆). Comparison of the ¹H and ¹³C NMR data of **3** to those of **1** revealed close similarity between both compounds, apart from the absence of the methylene group at δ_H 3.39/2.74 (δ_C 50.4, CH₂-7 in **1**) and the presence of two vicinal methine signals at δ_H 4.13 (δ_C 58.7, CH-6*b*) and 3.99 (δ_C 77.7, CH-7) in **3** instead, as supported by the COSY spectrum. The above spectroscopic differences suggested that **3** is a positional isomer of **1** with the hydroxy group (6*b*-OH in **1**) located at C-7. This assumption was further corroborated by the HMBC correlations from H-6*b* to C-12*a*, C-12*c*, C-7, and C-8, as well as from H-7 to C-8 and C-6*a*. In addition, the large coupling

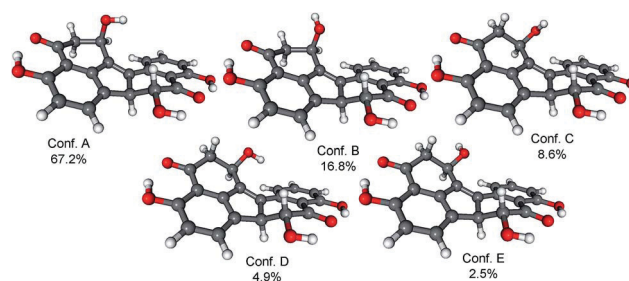


Fig. 9 Structure and population of the low-energy B97D/TZVP PCM/MeCN conformers (>2%) of (1*R*,6*bS*,7*R*)-**3** diastereomer. Populations of the same conformers at B3LYP/TZVP PCM/MeCN level are 63.2%, 22.5%, 7.7%, 2.4% and 4.1% (order of last two conformers changed) while at CAM-B3LYP/TZVP PCM/MeCN level are 61.8%, 22.6%, 8.0%, 3.2% and 4.3%.



constant between H-6b and H-7 ($^3J_{6b,7} = 12.1$ Hz) suggested their *trans*-diaxial relationship. Hence, **3** was identified as a new natural product and was named daldinone J.

Similarly to **1**, the relative configuration of C-1 could not be determined in the lack of characteristic NOE correlations, but a triplet signal for 1-H with 3.7 Hz coupling constant, suggested that 1-H preferably adopts equatorial orientation. The initial MMFF conformational searches were performed for the diastereomeric (1*R*,6*bS*,7*R*)- and (1*S*,6*bS*,7*R*)-**3** yielding 5 conformers for each in a 21 kJ mol⁻¹ energy window. Similarly to the conformational analysis of **1**, the reoptimization of the MMFF conformers was carried at four levels of theory [B3LYP/6-31G(d) *in vacuo*, B97D/TZVP PCM/MeCN, B3LYP/TZVP PCM/MeCN and CAM-B3LYP/TZVP PCM/MeCN] (Fig. 9 and 11). The B3LYP/6-31G(d) *in vacuo* conformers of (1*R*,6*bS*,7*R*)-**3** showed that 1-H adopts preferably axial orientation, while those of (1*S*,6*bS*,7*R*)-**3** had a larger population for conformers with equatorial 1-H (Fig. S32 and S34 of the ESI†). This difference diminished in the solvent model calculations, in which the conformers with equatorial 1-H were identified as the major ones for both diastereomers.

ECD spectra computed for B3LYP/6-31G(d) *in vacuo* (Fig. S33 and S35 of the ESI†) and B97D/TZVP PCM/MeCN reoptimized conformers (Fig. 10 and 12) at various levels were nearly mirror-image to the experimental one for both diastereomers indicating (6*bR*,7*S*) absolute configuration. The C-1 chirality center has minor contribution to the ECD data and thus C-1 diastereomers could not be distinguished by ECD calculations. The large negative specific rotation value of **3** prompted us to run OR calculations for the diastereomers. Similarly to the ECD calculations, the OR calculations of the diastereomers confirmed the (6*bR*,7*S*) absolute configuration but they were not suitable to determine the absolute configuration of C-1. Although both **1** and **3** had (6*bR*) absolute configuration, the geometry of their annulations is different as reflected by the opposite signs of the corresponding CEs. The (6*bR*) absolute configuration of **3** compares well with the reported absolute configuration of hypoxylonol C (**5**),²⁷ which may also suggest (1*S*) absolute configuration for **3**.

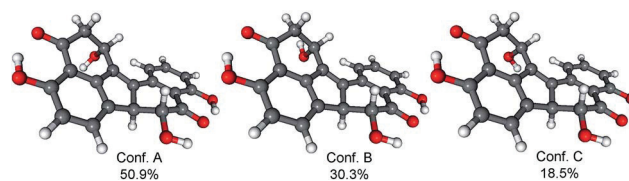


Fig. 11 Structure and population of the low-energy B97D/TZVP PCM/MeCN conformers (>2%) of (1*S*,6*bS*,7*R*)-**3** diastereomer. Populations of the same conformers at B3LYP/TZVP PCM/MeCN level are 37.0%, 45.7% and 16.6% (order of first two conformers changed) while at CAM-B3LYP/TZVP PCM/MeCN level are 30.3%, 51.3% and 17.6%.

The known compounds were identified as daldinone C (**4**),²⁸ hypoxylonol C (**5**),²⁷ daldinone B (**6**),²⁹ 3,4-dihydro-3,4,6,8-trihydroxy-1(2*H*)-naphthalenone (**7**),^{30,31} (R)-scytalone (**8**),^{31,32} and 1-hydroxy-8-methoxynaphthalene (**9**)³³ based on their NMR and MS spectroscopic data and by comparison with the literature.

Co-cultivation of fungi and bacteria has repeatedly been shown to activate silent fungal biogenetic gene clusters, thus either triggering the expression of compounds which are not detected in axenic fungal cultures or enhancing the accumulation of constitutively present metabolites.³⁴ Several attempts were undertaken in this study to influence the pattern of fungal metabolites through co-cultivation of the fungus with bacteria, such as *Bacillus subtilis* 168 trpC2, *Bacillus cereus* T, *Streptomyces lividans* TK24 or *Streptomyces coelicolor* A2(3).^{35,36} Co-cultivation of the fungus with either *S. lividans* or *S. coelicolor* resulted in an up to 38-fold increase in the accumulation of the known compound 1-hydroxy-8-methoxynaphthalene (**9**) as shown by HPLC analysis. On the other hand, when the fungus was co-cultured with *B. subtilis* or with *B. cereus*, no effect on natural product accumulation was observed, hinting at a specificity of the fungal response towards different bacteria (Fig. S40 of the ESI†).

Previously,^{28,37,38} the biogenetic pathway of benzo[*j*]fluoranthene derivatives (compounds **1**, **3**–**6**) was suggested to start with oxidative coupling of 1,8-dihydroxynaphthalene (DHN) and/or 1,3,8-trihydroxynaphthalene (3HN). For an experimental

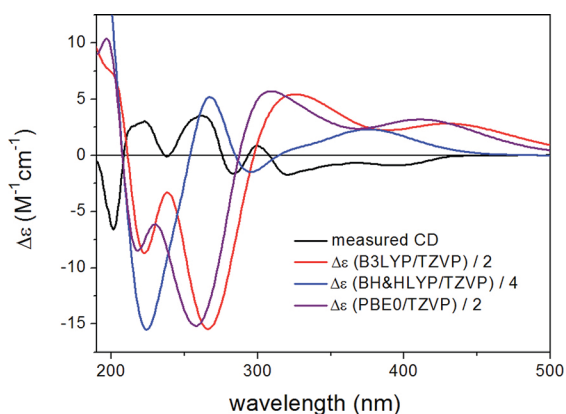


Fig. 10 Experimental ECD spectrum of **3** compared with the Boltzmann-weighted ECD spectra computed for the B97D/TZVP PCM/MeCN low-energy conformers of (1*R*,6*bS*,7*R*)-**3** at various levels.

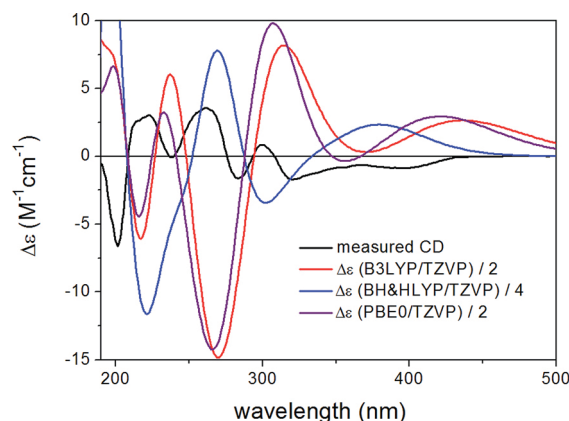


Fig. 12 Experimental ECD spectrum of **3** compared with the Boltzmann-weighted ECD spectra computed for the B97D/TZVP PCM/MeCN low-energy conformers of (1*S*,6*bS*,7*R*)-**3** at various levels.



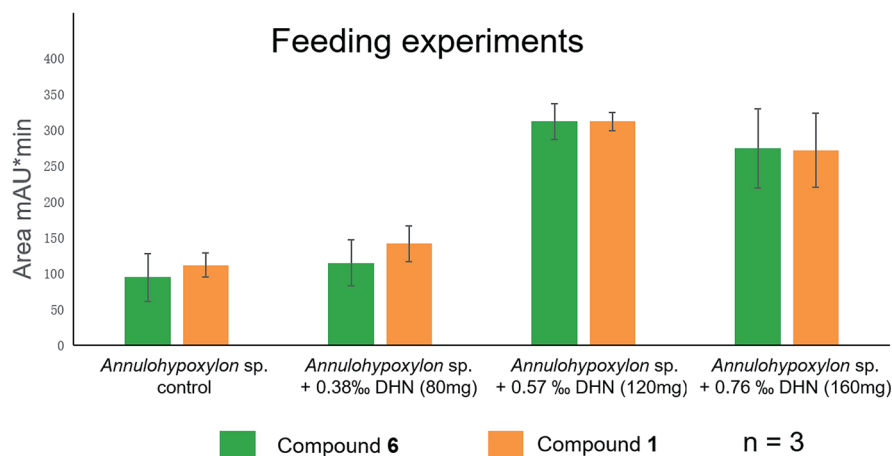


Fig. 13 Feeding experiments of *Annulohypoxyylon* sp. with 1,8-dihydroxynaphthalene (DHN) in three different concentrations 80 mg, 120 mg, and 160 mg. The yield per flask of **1** and **6** is indicated by the corresponding area of UV absorption. Data are means of three independent experiments ($n = 3$).

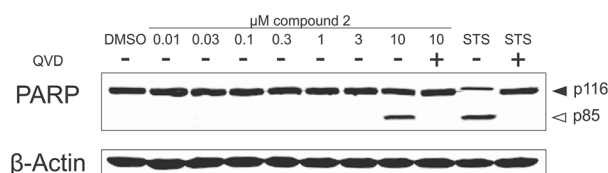
support of the proposed biosynthetic route of the analyzed fungal constituents commercially available 1,8-dihydroxynaphthalene (DHN) was fed to fungal cultures growing on solid rice medium at concentrations of 80 mg, of 120 mg or of 160 mg per flask. Analysis of the resulting crude fungal extracts by HPLC revealed a pronounced increase of the accumulation of compounds **1** and **6** in a dose-dependent manner (Fig. 13). The strongest increase of both compounds was observed in the presence of 120 mg DHN per flask. This induction of **6**, which is the main compound produced by the fungus, is in accordance with the proposed biosynthetic pathway, starting from oxidative coupling of two DHN units (Fig. S41 of the ESI†). Interestingly, the production of **1**, which is assumed to be biosynthesized from two 3HN units was likewise enhanced, suggesting a biochemical equilibrium between DHN and 3HN under catalysis of 3HN-reductases present in the metabolism of the fungus.^{20,39}

The isolated compounds (**2–5**, **7–9**) – apart from **1** and **6**, due to their chemical instability - were investigated for their antibacterial activity toward *Staphylococcus aureus* ATCC 25923, *Acinetobacter baumannii* ATCC BAA747, and *Mycobacterium tuberculosis*, however, none of them showed detectable activity when assayed at an initial dose of 10 μ M. At a same dose, initial

screenings for cytotoxicity of the respective compounds in different cancer cell lines revealed that only compound **2** inhibited the growth of the human leukemia and lymphoma cell lines, Jurkat J16 and Ramos, respectively, in a dose-dependent manner. After 24 h of treatment, the determined IC₅₀ values of compound **2** against Jurkat J16 and Ramos cells were 14.1 and 6.6 μ M, respectively (Fig. S42 of the ESI†). Apparently, Burkitt's lymphoma (Ramos) cells are particularly sensitive toward this compound.

To evaluate the potential contribution of proapoptotic mechanisms of compound **2** with regard to the observed cytotoxicity, we analyzed activation of caspase-3 through two different methods – on the one hand by immunoblotting of the caspase-3 substrate PARP and on the other hand by measuring the fluorescence of the profluorescent caspase-3 substrate Ac-DEVD-AMC. Apoptosis is a programmed form of cell death, which is generally characterized by distinct activation of cysteine-dependent aspartate-directed proteases (caspases), leading to DNA fragmentation and finally to cell death.⁴⁰ First, we detected cleavage of PARP after treatment with compound **2** for 8 h *via* immunoblotting. In both Jurkat J16 and Ramos cells the treatment with 10 μ M of **2** for 8 h lead to an explicit cleavage of PARP, indicating activation of caspases and therefore

A Jurkat J16



B Ramos

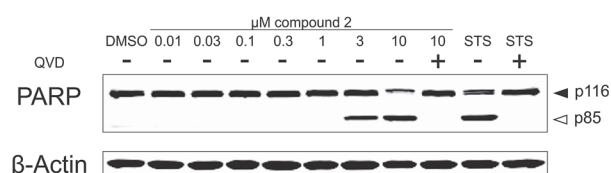


Fig. 14 Compound **2** induces apoptosis. (A) Jurkat J16 cells (acute T cell leukemia cells) and (B) Ramos cells (Burkitt's lymphoma B lymphocytes) were treated with the indicated concentrations of compound **2** in the absence or presence of the caspase inhibitor Q-VD-Oph (10 μ M) for 8 h. Cells treated with staurosporine (STS, 2.5 μ M) were used as positive control for caspase-dependent cleavage of Poly (ADP-ribose) polymerase-1 (PARP). After incubation period cleavage of PARP was determined by Western blot analysis. Solid arrowheads indicate the uncleaved form of PARP, open arrowheads indicate the cleaved form. The expression of β -actin was determined as protein loading control. Shown is the result of a representative blot.



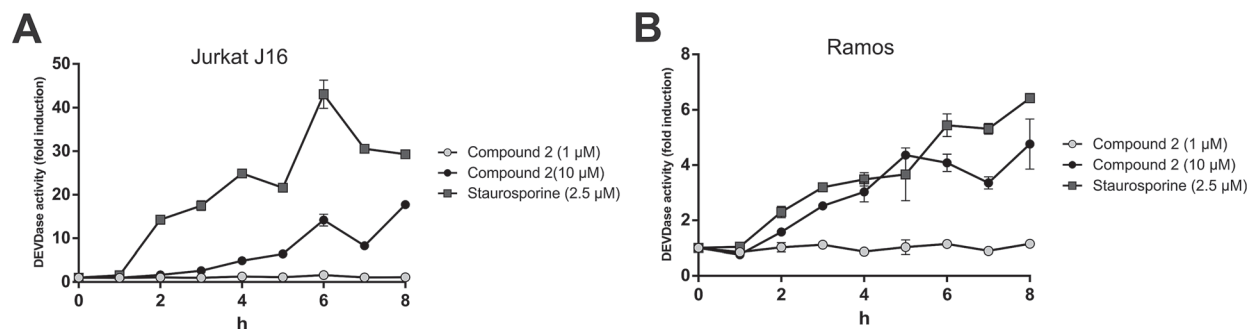


Fig. 15 Compound 2 activates caspase-3 with rapid kinetics. The kinetics of caspase-3 activation in (A) Jurkat J16 cells (acute T cell leukemia cells) and (B) Ramos cells (Burkitt's lymphoma B lymphocytes) after treatment with indicated concentrations of 2 were compared to those of staurosporine (STS, 2.5 μM), a well-established inducer of apoptosis. Caspase-3 activity was measured by the rate of cleavage of the pro-fluorescent caspase-3 substrate Ac-DEVD-AMC. Relative caspase-3 activity in DMSO (0.1% v/v) treated control cells was set to 1. Data shown are the mean \pm SD from a representative experiment performed in triplicate.

induction of apoptosis (Fig. 14). To ensure caspase dependency of the observed cleavage of PARP, the cells were co-incubated with the pan-caspase inhibitor *N*-(2-quinoly)-L-valyl-L-aspartyl-(2,6-difluorophenoxy) methylketone (QVD). This co-incubation entirely abrogates compound 2-induced cleavage of PARP. In the next step, activation of caspase-3 was detected fluoroscopically, to confirm compound 2-related induction of apoptosis. Treatment with 2 at concentrations up to 10 μM leads to cleavage of the profluorescent caspase-3 substrate Ac-DEVD-AMC within a few hours (Fig. 15), indicating once again activation of caspases and induction of apoptosis by compound 2. In Ramos cells, the kinetic of 2-induced activation of caspase-3 appears to be as fast as the kinetic of activation by the extremely potent apoptosis inducer staurosporine.

In order to characterize the proapoptotic effect of 2 more precisely, we performed flow cytometry based analyses with caspase-9 deficient and caspase-9 reconstituted Jurkat cells. The signaling network of induction and execution of apoptosis is highly complex and consists of many regulatory pathways, but the extrinsic (death receptor) pathway and the intrinsic (mitochondrial) pathway are canonically considered as the two core pathways to induce apoptosis. While caspase-8 is the key player of the extrinsic pathway, caspase-9 is the corresponding key player of the intrinsic pathway.⁴⁰ Therefore, experiments with cells lacking these key players can shed light on the pathway triggered by 2 in more detail. To determine caspase-related degradation of DNA by 2, we measured the amount of hypodiploid nuclei after treatment with 2 for 24 h. Comparative experiments in Jurkat cells lacking caspase-9 and in Jurkat cells, reconstituted with caspase-9 revealed that caspase-9 is indispensable for execution of 2-induced apoptosis (Fig. 16). Thus, 2 apparently induces intrinsic, but not extrinsic apoptosis.

Autophagy is a major intracellular catabolic mechanism responsible for the degradation of cytosolic components through lysosomes and plays an important role in cellular homeostasis.⁴¹ The ability to recycle unnecessary or dysfunctional components makes the process of autophagy essential for survival under conditions of starvation. Due to its crucial role regarding pro-survival signaling of fast proliferating cancer

cells, suffering from starvation stress, autophagy is considered as a promising target in anticancer therapy.^{42,43} In order to determine potential effects of 2 regarding regulation of autophagy, we used MEF cells stably expressing mCitrine-hLC3B and analyzed lysosomal degradation of mCitrine-hLC3B upon starvation and treatment with either 2 or with the known autophagy inhibitor bafilomycin A₁ *via* flow cytometry. LC3 is a major component of the double membraned structure called autophagosome, which delivers cytoplasmic components to the lysosomes and gets degraded by the lysosomal degradation system in the course of autophagy. Thereby, degradation of LC3 can be used as an indicator of autophagy. Incubation with 2 almost entirely blocked starvation-induced degradation of LC3, strongly indicating inhibition of autophagy by 2 (Fig. 17). Of note, this effect was not caused by the induction of apoptosis (*e.g. via* the caspase-dependent degradation of autophagy-relevant signaling molecules), since co-treatment with the above mentioned caspase inhibitor QVD did not abolish autophagy inhibition mediated by 2. Along these lines, the apoptosis inducer staurosporine (STS) did not inhibit but rather induced autophagy, further indicating that the induction of apoptosis does not necessarily lead to the inhibition of autophagy (Fig. 17). Taken together, 2 potently inhibits starvation-induced autophagy independently of caspases.

Compound 2 appears to be an interesting candidate for further *in vivo* studies illuminating its usability in anticancer therapy. These subsequent studies could also shed more light on the mechanisms of compound 2-related effects on apoptosis and autophagy.

Experimental section

General experimental procedures

Melting points were measured using a Büchi Melting Point B-540. Optical rotations were determined with a Perkin-Elmer-241 MC polarimeter. ¹H, ¹³C, and 2D NMR spectra were recorded at 25 °C in DMSO-*d*₆ and CH₃OH-*d*₄ on Bruker AVANCE DMX 600 NMR spectrometers. Chemical shifts were referenced to the solvent residual peaks, δ_{H} 2.50 (DMSO-*d*₆) and 3.31 (CH₃OH-*d*₄) ppm for ¹H, and δ_{C} 39.51 (DMSO-*d*₆) and 49.15 (CH₃OH-*d*₄) ppm for ¹³C.



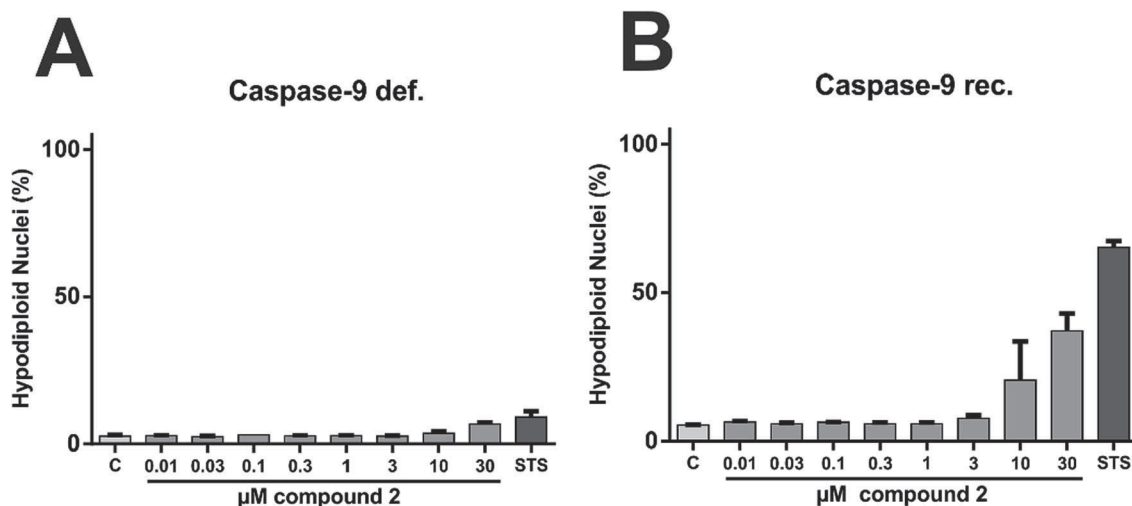


Fig. 16 Compound 2-induced apoptosis is caspase-9 dependent. Induction of apoptosis by 2 in (A) caspase-9 deficient and in (B) caspase-9 reconstituted Jurkat JMR cells (acute T cell leukemia cells) was assessed by flow cytometry to detect apoptotic DNA fragmentation, resulting in hypodiploid nuclei. After incubation period of 24 h cells were processed and measured as described in methods. Cells treated with staurosporine (STS, 2.5 μ M), a well-established inducer of apoptosis, served as positive control. Data shown are the mean \pm SD from a representative experiment performed in triplicate.

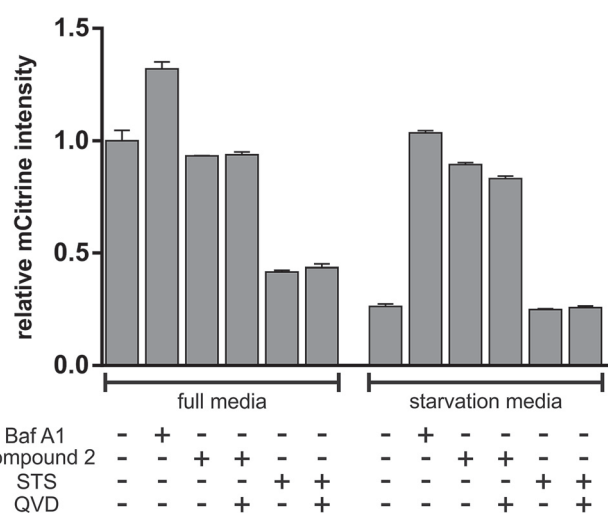


Fig. 17 Compound 2 blocks amino acid starvation-induced autophagy in a caspase-independent manner. MEFs stably expressing mCitrine-hLC3B were cultivated in full medium or starvation medium (EBSS) with 10 μ M compound 2 or 2.5 μ M staurosporine (STS) for 6 h. 10 nM bafilomycin A₁ (Baf A1) served as positive control for inhibition of autophagy and co-treatment with 10 μ M QVD as control for caspase independency. Total cellular mCitrine-hLC3B signals were analyzed by flow cytometry. The median of fluorescence intensity was plotted in a bar diagram. Values are normalized to DMSO (0.1% v/v) treated cells cultivated in full medium (1.0) and represent mean \pm SD.

Mass spectra (ESI) were recorded with a Finnigan LCQ Deca mass spectrometer, and HRMS (ESI) spectra were obtained with a FT-ICR Orbitrap (Thermo-Finnigan) mass spectrometer. Solvents were distilled prior to use and spectral grade solvents were used for spectroscopic measurements. HPLC analysis was performed with a Dionex UltiMate3400 SD with a LPG-3400SD Pump coupled to a photodiode array detector (DAD3000RS);

routine detection was at 235, 254, 280, and 340 nm. The separation column (125 \times 4 mm) was pre-filled with Eurosphere-10 C18 (Knauer, Germany), and the following gradient was used (MeOH, 0.1% HCOOH in H₂O): 0 min (10% MeOH); 5 min (10% MeOH); 35 min (100% MeOH); 45 min (100% MeOH). Semipreparative HPLC was performed using a Merck Hitachi HPLC System (UV detector L-7400; Pump L-7100; Eurosphere-100 C18, 300 \times 8 mm, Knauer, Germany). Column chromatography included LH-20 Sephadex and Merck MN Silica gel 60 M (0.04–0.063 mm). TLC plates with silica gel F254 (Merck, Darmstadt, Germany) were used to monitor fractions; detection was under UV at 254 and 366 nm or by spraying the plates with anisaldehyde reagent followed by heating. Bacterial growth was monitored by measuring the OD₆₀₀ in a Tecan microtiter plate reader (InfiniteM200, Tecan). ECD spectra were recorded on a J-810 spectropolarimeter. HPLC separations of 1 and 2 were performed with a Jasco HPLC system using Chiralpak IA column with 250 mm \times 4.6 mm i.d., 5 μ m (Daicel, Chemical Industries, Ltd.) and *n*-hexane/propan-2-ol eluent at a flow rate of 1.0 mL min⁻¹. HPLC-UV chromatograms were recorded with a Jasco MD-910 multi-wavelength detector. The on-line ECD and UV spectra of 1 were measured simultaneously by stopping the flow at the UV absorption maximum of each peak. The values of the ECD ellipticity (ϕ) were not corrected for the concentration.

Microbial material

The endophytic fungus was isolated from fresh fruits of the Mangrove plant *Rhizophora racemosa* collected in Cameroon in September 2013. The isolation was performed as described before,⁴⁴ and the fungus was identified by using a molecular biological protocol by DNA amplification and sequencing of the 3952 bp of the 18S–28S rDNA region (accession-number KY190099) and 1422 bp of the β tubulin gene (accession



number KY190100)¹⁴ followed by BlastN search in the NCBI-databases. Phylogenetic trees that cover the highest number of homologous sequences in the database were generated. The 18S–28S rDNA sequence from nt 28 – nt 3357 exhibited 64.5% homology to a sequence of respective length of *Xylariaceae* sp. YX28 (e.g. accession number DQ022415), suggesting that the fungus belongs to the class of Xylariales (Fig. S1A of the ESI†). BlastN analysis of part of the rDNA sequence region from nt 2415 – nt 3906 in the unite database⁴⁵ showed a 97.75% homology to *Annulohyphoxylon* sp. (acc-no. JQ747656). Moreover, 1416 bp of the fungal β -tubulin gene revealed 96% homology to *Annulohyphoxylon* sp. (acc-no. KP134522) (see Fig. S1B†) supporting the assumption that the fungus analyzed in this study belongs to the genus of *Annulohydroxylon*. Thus, the fungus was named as *Annulohydroxylon* sp. CA-2013 isolate YL. A voucher strain was kept at one of the authors' laboratory (P.P.). The bacterial strains used for co-cultivation were standard laboratory strains: *Bacillus subtilis* 168 trpC2, *Bacillus cereus* T, *Streptomyces lividans* TK24, and *Streptomyces coelicolor* A2(3).

Fungal fermentation

The fungus was cultivated on solid rice medium in twelve Erlenmeyer flasks. Solid rice medium was prepared by adding demineralized water (110 mL) to rice (100 g) in an Erlenmeyer flask, followed by autoclaving (121 °C, 20 min). The fungus, which nearly covered the whole surface of a petri dish, was inoculated onto this sterile rice medium under the clean bench and was allowed to grow (20 °C) for 25 days.

Co-cultivation experiments of *Annulohyphoxylon* sp. with *B. subtilis* 168 trpC2 and *B. cereus* T

The fungal and bacterial strains were cultivated on solid rice media involving 15 Erlenmeyer flasks (3 flasks for the fungus control, 3 flasks for *B. subtilis* control, 3 flasks for *B. cereus* control, 3 flasks for co-cultivation of the fungus with *B. subtilis*, 3 flasks for co-cultivation of the fungus with *B. cereus*). Each flask (1 L) containing 110 mL of distilled water and 100 g of commercially available milk rice (Milch-Reis, ORYZA) was autoclaved before inoculating the fungus and the bacteria.

B. subtilis and *B. cereus* were grown in lysogeny broth (LB) medium. Overnight cultures of *B. subtilis* and *B. cereus* were used to inoculate prewarmed LB medium (1 : 20), which was then incubated at 37 °C with shaking at 200 rpm to mid exponential growth phase (optical density at 600 nm (OD₆₀₀) of 0.2–0.4). An amount of 10 mL *B. subtilis* (6 flasks) or *B. cereus* (6 flasks) respectively was inoculated to rice medium and the inoculated flasks were kept in an incubator (37 °C) for 4 days. After this preincubation, 5 pieces (1 × 1 cm²) of the fungus growing on malt agar were added to each flask containing *B. subtilis* or *B. cereus*.

Co-cultivation and axenic cultures of the fungus and bacterial control were kept at room temperature (20 °C) until they reached their stationary phase of growth (3 weeks for controls of the fungus and 4 weeks for co-cultivation). Then 500 mL of EtOAc was added to the cultures to stop the growth of cells followed by shaking of the flasks at 150 rpm for 8 h. The cultures

were then left overnight and filtered on the following day using a Büchner funnel. EtOAc was removed by a rotary evaporation. Each extract was then dissolved in 50 mL of MeOH, and 10 μ L of this was injected into the analytical HPLC.

Co-cultivation experiments of *Annulohyphoxylon* sp. with *S. coelicolor* A2(3) and *S. lividans* TK24

Fifteen Erlenmeyer flasks (3 flasks for the fungus control, 3 for co-cultivation of the fungus and *S. coelicolor*, 3 for co-cultivation of the fungus and *S. lividans*, 3 for *S. coelicolor* control, 3 for *S. lividans* control) containing 110 mL of Yeast Malt (YM) medium and 100 g of commercially available milk rice (Milch-Reis, ORYZA) were autoclaved before inoculating the fungus and bacteria. An overnight culture of *S. coelicolor* or of *S. lividans* was used to inoculate prewarmed YM medium (1 : 20), which was then incubated at 30 °C with shaking at 200 rpm to mid exponential growth phase. This preculture was then incubated in fresh YM medium overnight to reach mid exponential growth phase. A volume of 10 mL *S. coelicolor* (6 flasks) and *S. lividans* (6 flasks) respectively was inoculated to rice medium and incubated (30 °C) for 4 days. Then the same process was carried out as described for the experiment of co-cultivation of the fungus with *B. subtilis* or with *B. cereus*.

Feeding experiments with 1,8-dihydroxynaphthalene

Twelve Erlenmeyer flasks containing 90 mL demineralized water and 100 g of commercially available milk rice (Milch-Reis, ORYZA) were autoclaved. Afterwards, different amounts (80 mg, 120 mg, 160 mg) of 1,8-dihydroxynaphthalene (DHN) were dissolved in 20 mL autoclaved water each and added to the autoclaved rice medium by sterile filtration ($n = 3$). Controls were only treated with autoclaved water. Next, the fungus was inoculated onto the medium. Flasks treated with DHN or controls lacking DHN were allowed to grow in an incubator (30 °C) for two weeks.

Cell lines and reagents

Adult lymphoblastic leukemia T cells (Jurkat J16, no. ACC-282) and Burkitt's lymphoma B cells (Ramos, no. ACC-603) were obtained from the German Collection of Microorganisms and Cell Cultures (DSMZ, Germany). Wild-type murine embryonic fibroblasts (MEFs, kindly provided by Xiaodong Wang)⁴⁶ expressing mCitrine-hLC3B were generated by retroviral gene transfer using pMSCVpuro/mCitrine-hLC3B. To generate pMSCVpuro/mCitrine-hLC3B, full-length human MAP1LC3B cDNA was cloned into pMSCVpuro/mCitrine vector (kindly provided by Michael Engelke, University of Göttingen, Germany). Caspase-9-deficient Jurkat JMR cells stably transfected with vector control or caspase-9 were previously described.⁴⁷ All cell lines were grown at 37 °C under humidified air supplemented with 5% CO₂ in RPMI 1640 (Jurkat J16, Jurkat JMR, Jurkat JMR reconstituted with caspase-9, Ramos) or DMEM (mCitrine-hLC3B-MEF) containing 10% fetal calf serum, 1% HEPES, 120 IU mL⁻¹ penicillin, and 120 μ g mL⁻¹ streptomycin. The broad-range caspase inhibitor *N*-(2-quinolyl)-*L*-valyl-*L*-aspartyl-(2,6-difluorophenoxy) methylketone [(QVD), #SML0063], the



autophagy inhibitor bafilomycin A₁ [(Baf A1), #B1793] and the kinase inhibitor staurosporine [(STS), #S5921], used as positive control for induction of apoptosis, were obtained from Sigma-Aldrich. The profluorescent caspase-3 substrate Ac-DEVD-AMC was purchased from Biomol (# ABD-13402).

Determination of cell viability

Jurkat J16 cells and Ramos cells were seeded at a density of 5×10^5 cells per mL and incubated with different concentrations of compound 2 for 24 h. Cells treated with DMSO (0.1% v/v) for 24 h were used as negative control. After incubation for 24 h MTT (3-(4,5-dimethyl-2-thiazolyl)-2,5-diphenyl-2H-tetrazolium bromide; Calbiochem #475989) was added to the cells to a final concentration of 1 mg mL^{-1} , the cells were incubated further for 60 min and then centrifuged at 600 rcf for 5 min. The medium was aspirated and 100 μL DMSO were added to each well to extract the formazan product from the cells. After 25 min of incubation on a shaker at room temperature, the absorbance at 650 nm (reference wavelength) and 570 nm (test wavelength) was measured using a multiplate reader (Synergy Mx, BioTek). Viability and IC₅₀ values (IC₅₀ = half maximal inhibitory concentration) were calculated using Prism 6 (GraphPad Software). Relative viability of DMSO (0.1% v/v) treated control cells was set to 100%.

Western blot analysis

Ramos and Jurkat J16 cells were treated with the indicated concentrations of compound 2. Coincubation with the caspase inhibitor Q-VD-OPh at a concentration of 10 μM was used as proof of caspase-dependency of the observed effects. After incubation time of 24 h, cells were pelletized at 600 rcf at 4 °C for 5 min, washed with PBS and frozen in liquid nitrogen. The cells were lysed in ice-cold lysis buffer [20 mM Tris-HCl, pH 7.5, 150 mM NaCl, 0.5 mM EDTA, 1% Triton X-100, 10 mM NaF, 2.5 mM Na₄P₂O₇, 10 μM Na₂MoO₄, 1 mM Na₃VO₄, protease inhibitors (Sigma #P2714)]. The lysates were cleared from cell debris by centrifugation at 11 000 rcf at 4 °C for 15 min and the total protein concentration was measured by Bradford assay and adjusted to equal concentrations. After loading with Laemmli buffer and heating to 95 °C for 5 min, 25 μg of the protein extract was separated by SDS-PAGE [8% tris-glycine polyacrylamide gel (v/v)] and transferred to a PVDF membrane by Western blotting according to a standard protocol. Analysis of proteins of interest was performed using primary mouse antibodies to poly(ADP-ribose) polymerase-1 (Enzo Life Sciences #BML-SA250) or β -actin (Sigma-Aldrich #A5316) and IRDye800-conjugated secondary antibodies (LI-COR Biosciences #926-32210/11). Signals were detected with an infrared imaging system.

Caspase-3 activity assay

Jurkat J16 cells and Ramos cells were seeded at a density of 1×10^6 cells per mL in 96-well microtiter plates and incubated with different concentrations of compound 2 for the indicated times. Cells treated with DMSO (0.1% v/v) were used as negative control. After incubation period, cells were harvested by

centrifugation at 600 rcf at 4 °C and lysed by incubation with ice-cold lysis buffer (20 mM HEPES, 84 mM KCl, 10 mM MgCl₂, 200 μM EDTA, 200 μM EGTA, 0.5% NP-40, 1 $\mu\text{g mL}^{-1}$ leupeptin, 1 $\mu\text{g mL}^{-1}$ pepstatin, 5 $\mu\text{g mL}^{-1}$ aprotinin) for 10 minutes. After addition of 150 μL reaction buffer (50 mM HEPES, 100 mM NaCl, 10% Sucrose, 0.1% CHAPS, 2 mM CaCl₂, 13.35 mM DTT, 70 μM DEVD-AMC) per well, fluorescence (Ex 360 nm, Em 450 nm) was measured at 37 °C over a time course of 150 min using a multiplate reader (Synergy Mx, BioTek). Caspase activity was determined as the slope of the resulting linear regressions. Data points shown are the mean of triplicates, error bars = SD. Values are normalized to DMSO (0.1% v/v) treated cells (fold change = 1.00).

FACS-based analysis of apoptotic cell death

Caspase-9-deficient Jurkat cells stably transfected with vector control or caspase-9 cDNA were treated with the indicated concentrations of compound 2 for 24 h. Cells treated with DMSO (0.1% v/v) served as negative control and cells treated with the kinase inhibitor staurosporine (2.5 mM) as positive control. After incubation period nuclei were prepared by lysing cells in hypotonic lysis buffer (1% sodium citrate, 0.1% Triton X-100, 50 $\mu\text{g mL}^{-1}$ propidium iodide) at 4 °C overnight. Subsequently, DNA content was analyzed by flow cytometry. Nuclei with a DNA content below that of nuclei of healthy G0/G1 cells were considered as apoptotic.⁴⁸ Data points shown are the mean of triplicates, error bars = SD.

FACS-based analysis of autophagy

MEF cells stably expressing mCitrine-hLC3B were cultured in the indicated medium for 6 h with or without the indicated compounds, harvested with 0.05% trypsin-EDTA, and washed once with phosphate-buffered saline. Subsequently, the intensity of mCitrine fluorescence was analyzed by flow cytometry using FACSDiva software. Reduction of mCitrine-hLC3B compared to medium control indicates autophagy induction.

Extraction and isolation

The crude extract of fungal cultures was subjected to liquid-liquid separation between *n*-hexane and 90% aqueous MeOH. The resulting MeOH fraction (8.2 g) was separated by vacuum liquid chromatography on silica gel, using solvents in a gradient of increasing polarity – *n*-hexane-ethyl acetate-dichloromethane-methanol – to generate 6 fractions. Each fraction was submitted to Sephadex LH-20 and eluted with DCM-MeOH (1 : 1) to remove black pigments. Final purification was carried out by semipreparative HPLC to yield 1 (1 : 1 mixture with 2, 4.2 mg), 2 (14.7 mg), 3 (1.1 mg), 4 (3.2 mg), 5 (4.6 mg), 6 (4.4 mg), 7 (11.2 mg), 8 (20.6 mg), 9 (5.5 mg).

Daldinone H (1)

Red powder; UV [MeOH, photodiode array (PDA)]: $\lambda_{\text{max}} = 200, 242, 292, 397 \text{ nm}$; (6*bR*)-1: $t_{\text{R}} = 7.07 \text{ min}$ on a Chiralpak IA column (hexane/2-propanol 80 : 20); HPLC-ECD {hexane/2-propanol 80 : 20, λ [nm] (ϕ)}. ¹H (600 MHz) and ¹³C (150



Table 1 ^1H and ^{13}C NMR data of compounds 1–3

Position	1^a		2^b		3^a	
	δ_{C} , type ^c	δ_{H} (J in Hz)	δ_{C} , type	δ_{H} (J in Hz)	δ_{C} , type ^c	δ_{H} (J in Hz)
1	63.5, CH	5.16, dd (4.9, 1.9)	134.7, CH	8.23, d (9.8)	63.6, CH	5.77, t (3.7)
2	47.8, CH ₂	3.14, dd (17.2, 4.9); 2.94, dd (17.2, 1.9)	133.3, CH	6.75, d (9.8)	47.2, CH ₂	3.20, dd (17.1, 3.7); 2.96, dd (17.1, 3.7)
3	201.7, C		188.3, C		200.9, C	
3a	114.1, C		113.4, C		112.0, C	
4	160.6, C		159.0, C		158.5, C	
5	115.2, CH	6.77, d (8.1)	114.5, CH	6.93, d (8.1)	114.8, CH	6.78, d (8.3)
6	131.0, CH	7.64, d (8.1)	128.7, CH	7.75, d (8.1)	133.8, CH	7.82, d (8.3)
6a	138.2, C		136.5, C		134.4, C	
6b	84.7, C		84.4, C		58.7, CH	4.13, d (12.1)
7	50.4, CH ₂	3.39, d (16.3); 2.74, d (16.3)	49.3, CH ₂	3.45, d (16.3); 2.97, d (16.3)	77.7, CH	3.99, d (12.1)
8	205.2, C		204.4, C		204.7, C	
8a	115.6, C		114.9, C		113.8, C	
9	163.3, C		162.1, C		162.6, C	
10	119.1, CH	6.98, d (8.0)	120.2, CH	7.15, dd (7.5, 0.5)	118.4, CH	6.95, dd (7.0, 1.0)
11	137.7, CH	7.64, t (8.0)	137.6, CH	7.76, t (7.5)	138.3, CH	7.61, t (7.0)
12	120.3, CH	7.51, d (8.0)	120.7, CH	7.64, dd (7.5, 0.5)	119.0, CH	7.53, dd (7.0, 1.0)
12a	137.9, C		134.6, C		137.2, C	
12b	144.5, C		152.2, C		139.0, C	
12c	134.0, C		127.0, C		136.8, C	
12d	147.0, C		144.5, C		148.1, C	
4-OH				10.65, s		
6b-OH				6.23, s		
9-OH				12.34, s		

^a Measured in CH₃OH-*d*₄ at 600 (^1H) and 150 (^{13}C) MHz. ^b Measured in DMSO-*d*₆ at 600 (^1H) and 150 (^{13}C) MHz. ^c Data extracted from HMBC and HSQC spectra.

MHz) NMR, see Table 1; ESI-MS m/z 351.2 [M + H]⁺, 349.1 [M – H][–]; HRESIMS m/z 351.0865 [M + H]⁺ (calcd for C₂₀H₁₅O₆, 351.0863).

Daldinone I (2)

Red powder; mp 206–207 °C (dec.); [α]_D²⁰ = –154 (*c* 0.35, MeOH); UV [MeOH, photodiode array (PDA)]: λ_{max} = 201, 235, 335, 462 nm; ECD {acetonitrile, λ [nm] ($\Delta\epsilon$)}; ^1H (600 MHz) and ^{13}C (150 MHz) NMR, see Table 1; ESI-MS m/z 333.1 [M + H]⁺, 331.0 [M – H][–]; HRESIMS m/z 333.0756 [M + H]⁺ (calcd for C₂₀H₁₂O₅, 333.0757).

Daldinone J (3)

Red powder; mp 229 °C (dec.); [α]_D²⁰ = –180 (*c* 0.25, MeOH); UV [MeOH, photodiode array (PDA)]: λ_{max} = 201, 242, 292, 398 nm; ECD {acetonitrile, λ [nm] ($\Delta\epsilon$)}; ^1H (600 MHz) and ^{13}C (150 MHz) NMR, see Table 1; ESI-MS m/z 351.3 [M + H]⁺, 349.1 [M – H][–]; HRESIMS m/z 351.0862 [M + H]⁺ (calcd for C₂₀H₁₅O₆, 351.0863).

Computational section

Mixed torsional/low-frequency mode conformational searches were carried out by means of the MacroModel 9.9.223 software using the Merck Molecular Force Field (MMFF) with an implicit solvent model for CHCl₃.⁴⁹ Geometry reoptimizations were carried out at the B3LYP/6-31G(d) level *in vacuo*, B3LYP/TZVP, B97D/TZVP^{23,24} and CAM-B3LYP/TZVP^{25,26} levels with the PCM solvent model for MeCN or MeOH. TDDFT ECD and OR

calculations were run with various functionals (B3LYP, BH&HLYP, CAM-B3LYP, PBE0) and the TZVP basis set as implemented in the Gaussian 09 package with the same or no solvent model as in the preceding DFT optimization step.⁵⁰ ECD spectra were generated as sums of Gaussians with 2100–3000 cm^{–1} widths at half-height (corresponding to *ca.* 15–22 nm at 270 nm), using dipole-velocity-computed rotational strength values.⁵¹ Boltzmann distributions were estimated from the ZPVE-corrected B3LYP/6-31G(d) energies in the gas-phase calculations and from the B3LYP/TZVP, B97D/TZVP and CAM-B3LYP/TZVP energies in the solvated ones. The MOLEKEL software package was used for visualization of the results.⁵²

Acknowledgements

Financial support by the DFG through the GRK 2158 to P. P., B. S. and S. W. is gratefully acknowledged. W. H. L. wants to thank the Ministry of Science and Technology (MOST) to W. H. L. for support. T. K. thanks the Hungarian National Research Foundation (OTKA K105871) for financial support and the National Information Infrastructure Development Institute (NIIFI 10038) for CPU time. The authors are indebted to Prof. R. Kalscheuer (Heinrich-Heine-University, Duesseldorf) for performing anti-bacterial assays.

References

- 1 S. H. Faeth, *Oikos*, 2002, **98**, 25–36.



- 2 D. Wilson, *Oikos*, 1995, **73**, 274–276.
- 3 A. H. Aly, A. Debbab and P. Proksch, *Appl. Microbiol. Biotechnol.*, 2011, **90**, 1829–1845.
- 4 Z. E. Wilson and M. A. Brimble, *Nat. Prod. Rep.*, 2009, **26**, 44–71.
- 5 D. G. I. Kingston, *J. Nat. Prod.*, 2011, **74**, 496–511.
- 6 D. Rönnsberg, A. Debbab, A. Mándi, V. Vasylyeva, P. Böhler, B. Stork, L. Engelke, A. Hamacher, R. Sawadogo, M. Diederich, V. Wray, W. Lin, M. U. Kassack, C. Janiak, S. Scheu, S. Wesselborg, T. Kurtán, A. H. Aly and P. Proksch, *J. Org. Chem.*, 2013, **78**, 12409–12425.
- 7 H. Thatoi, B. C. Behera and R. R. Mishra, *Mycology*, 2013, **4**, 54–71.
- 8 F. Zhu, X. Chen, Y. Yuan, M. Huang, H. Sun and W. Xiang, *Open Nat. Prod. J.*, 2009, **2**, 24–32.
- 9 K. Saikkonen, S. Saari and M. Helander, *Fungal Divers.*, 2010, **41**, 101–113.
- 10 M. Frank, H. Niemann, P. Böhler, B. Stork, S. Wesselborg, W. Lin and P. Proksch, *Curr. Med. Chem.*, 2015, **22**, 3523–3532.
- 11 Y. Liu, V. Wray, M. S. Abdel-Aziz, C. Y. Wang, D. Lai and P. Proksch, *J. Nat. Prod.*, 2014, **77**, 1734–1738.
- 12 Y. Liu, A. Marmann, M. S. Abdel-Aziz, C. Y. Wang, W. E. G. Müller, W. H. Lin, A. Mándi, T. Kurtán, G. Daletos and P. Proksch, *Eur. J. Org. Chem.*, 2015, **12**, 2646–2653.
- 13 Y. Liu, T. Kurtán, C. Y. Wang, W. H. Lin, R. Orfali, W. E. G. Müller, G. Daletos and P. Proksch, *J. Antibiot.*, 2016, **69**, 702–706.
- 14 G. F. Bills, V. Gonzalez-Menendez, J. Martin, G. Platas, J. Fournier, D. Persoh and M. Stadler, *PLoS One*, 2012, **7**, e46687.
- 15 H. M. Hsieh, Y. M. Ju and J. D. Rogers, *Mycologia*, 2005, **97**, 844–865.
- 16 D. N. Quang, M. Stadler, J. Fournier, A. Tomita and T. Hashimoto, *Tetrahedron*, 2006, **62**, 6349–6354.
- 17 F. Surup, K. I. Mohr, R. Jansen and M. Stadler, *Phytochemistry*, 2013, **95**, 252–258.
- 18 D. N. Quang, T. Hashimoto, Y. Nomura, H. Wollweber, V. Hellwig, J. Fournier, M. Stadler and Y. Asakawa, *Phytochemistry*, 2005, **66**, 797–809.
- 19 F. Surup, V. Wiebach, E. Kuhnert and M. Stadler, *Tetrahedron Lett.*, 2016, **57**, 2183–2185.
- 20 J. E. Thompson, S. Fahnestock, L. Farrall, D. Liao, B. Valent and D. B. Jordan, *J. Biol. Chem.*, 2000, **275**, 34867–34872.
- 21 Z. Tian, P. Sun, Y. Yan, Z. Wu, Q. Zheng, S. Zhou, H. Zhang, F. Yu, X. Jia, D. Chen, A. Mándi, T. Kurtán and W. Liu, *Nat. Chem. Biol.*, 2015, **11**, 259–265.
- 22 A. Mándi, I. W. Mudianta, T. Kurtán and M. J. Garson, *J. Nat. Prod.*, 2015, **78**, 2051–2056.
- 23 S. Grimme, *J. Comput. Chem.*, 2006, **27**, 1787–1799.
- 24 P. Sun, D. X. Xu, A. Mándi, T. Kurtán, T. J. Li, B. Schulz and W. Zhang, *J. Org. Chem.*, 2013, **78**, 7030–7047.
- 25 T. Yanai, D. Tew and N. Handy, *Chem. Phys. Lett.*, 2004, **393**, 51–57.
- 26 G. Pescitelli, L. D. Bari and N. Berova, *Chem. Soc. Rev.*, 2011, **40**, 4603–4625.
- 27 M. Fukai, M. Tsukada, K. Miki, T. Suzuki, T. Sugita, K. Kinoshita, K. Takahashi, M. Shiro and K. Koyama, *J. Nat. Prod.*, 2012, **75**, 22–25.
- 28 W. Gu, H. M. Ge, Y. C. Song, H. Ding, H. L. Zhu, X. A. Zhao and R. X. Tan, *J. Nat. Prod.*, 2007, **70**, 114–117.
- 29 L. Du, J. B. King and R. H. Cichewicz, *J. Nat. Prod.*, 2014, **77**, 2454–2458.
- 30 S. Iwasaki, H. Muro, K. Sasaki, S. Woe and S. Okuda, *Tetrahedron Lett.*, 1973, **37**, 3537–3542.
- 31 P. Pittayakhajonwut, P. Sohsomboon, A. Dramaee, R. Suvannakad, S. Lapanun and M. Tantichareon, *Planta Med.*, 2008, **74**, 281–286.
- 32 S. M. Husain, M. A. Schätzle, S. Lüdeke and M. Müller, *Angew. Chem., Int. Ed.*, 2014, **53**, 9806–9811.
- 33 A. K. Nadeau and J. L. Sorensen, *Tetrahedron Lett.*, 2011, **52**, 1697–1699.
- 34 A. Marmann, A. H. Aly, W. Lin, B. Wang and P. Proksch, *Mar. Drugs*, 2014, **12**, 1043–1065.
- 35 H. Chen, G. Daletos, M. S. Abdel-Aziz, D. Thomy, H. Dai, H. Broetz-Oesterhelt, W. Lin and P. Proksch, *Phytochem. Lett.*, 2015, **12**, 35–41.
- 36 A. R. B. Ola, D. Thomy, D. Lai, H. Broetz-Oesterhelt and P. Proksch, *J. Nat. Prod.*, 2013, **76**, 2094–2099.
- 37 E. C. Barnes, J. Jumpathong, S. Lumyong, K. Voigt and C. Hertweck, *Chem.–Eur. J.*, 2016, **22**, 4551–4555.
- 38 Y. L. Zhang, J. Zhang, N. Jiang, Y. H. Lu, L. Wang, S. H. Xu, W. Wang, G. F. Zhang, Q. Xu, H. M. Ge, J. Ma, Y. C. Song and R. X. Tan, *J. Am. Chem. Soc.*, 2011, **133**, 5931–5940.
- 39 W. Fang, S. Ji, N. Jiang, W. Wang, G. Y. Zhao, S. Zhang, H. M. Ge, Q. Xu, A. H. Zhang, Y. L. Zhang, Y. C. Song, J. Zhang and R. X. Tan, *Nat. Commun.*, 2012, **3**, 1039–1048.
- 40 R. C. Taylor, S. P. Cullen and S. J. Martin, *Nat. Rev. Mol. Cell Biol.*, 2008, **9**, 231–241.
- 41 N. Mizushima, *Genes Dev.*, 2007, **21**, 2861–2873.
- 42 K. Degenhardt, R. Mathew, B. Beaudoin, K. Bray, D. Anderson, G. Chen, C. Mukherjee, Y. Shi, C. Gélinas, Y. Fan, D. A. Nelson, S. Jin and E. White, *Cancer Cell*, 2006, **10**, 51–64.
- 43 J. Y. Guo, H. Y. Chen, R. Mathew, J. Fan, A. M. Strohecker, G. Karsli-Uzunbas, J. J. Kamphorst, G. Chen, J. M. Lemons, V. Karantza, H. A. Collier, R. S. Dipaola, C. Gélinas, J. D. Rabinowitz and E. White, *Genes Dev.*, 2011, **25**, 460–470.
- 44 F. B. C. Okoyea, C. S. Nworuc, A. Debbaba, C. O. Esimone and P. Proksch, *Phytochem. Lett.*, 2015, **14**, 51–55.
- 45 U. Köljalg, R. H. Nilsson, K. Abarenkov, L. Tedersoo, A. F. S. Taylor, M. Bahram, S. T. Bates, T. D. Bruns, J. Bengtsson-Palme, T. M. Callaghan, B. Douglas, T. Drenkhan, U. Eberhardt, M. Dueñas, T. Grebenc, G. W. Griffith, M. Hartmann, P. M. Kirk, P. Kohout, E. Larsson, B. D. Lindahl, R. Lücking, M. P. Martín, P. B. Matheny, N. H. Nguyen, T. Niskanen, J. Oja, K. G. Peay, U. Peintner, M. Peterson, K. Pöldmaa, L. Saag, I. Saar, A. Schüßler, J. A. Scott, C. Senés, M. E. Smith, A. Suija, D. L. Taylor, M. T. Telleria, M. Weiß and K. H. Larsson, *Mol. Ecol.*, 2013, **22**, 5271–5277.
- 46 L. Shang, S. Chen, F. Du, S. Li, L. Zhao and X. Wang, *Proc. Natl. Acad. Sci. U. S. A.*, 2011, **108**, 4788–4793.



Paper

- 47 J. Manns, M. Daubrawa, S. Driessen, F. Paasch, N. Hoffmann, A. Löffler, K. Lauber, A. Dieterle, S. Alers, T. Iftner, K. Schulze-Osthoff, B. Stork and S. Wesselborg, *FASEB J.*, 2011, **25**, 3250–3261.
- 48 I. Nicoletti, G. Migliorati, M. C. Pagliacci, F. Grignani and C. J. Riccardi, *Immunol. Methods*, 1991, **139**, 271–279.
- 49 *MacroModel*, Schrödinger, LLC, 2012, <http://www.schrodinger.com/MacroModel>.
- 50 M. J. Frisch, G. W. Trucks, H. B. Schlegel, G. E. Scuseria, M. A. Robb, J. R. Cheeseman, G. Scalmani, V. Barone, B. Mennucci, G. A. Petersson, H. Nakatsuji, M. Caricato, X. Li, H. P. Hratchian, A. F. Izmaylov, J. Bloino, G. Zheng, J. L. Sonnenberg, M. Hada, M. Ehara, K. Toyota, R. Fukuda, J. Hasegawa, M. Ishida, T. Nakajima, Y. Honda, O. Kitao, H. Nakai, T. Vreven, J. A. J. Montgomery, J. E. Peralta, F. Ogliaro, M. Bearpark, J. J. Heyd, E. Brothers, K. N. Kudin, V. N. Staroverov, R. Kobayashi, J. Normand, K. Raghavachari, A. Rendell, J. C. Burant, S. S. Iyengar, J. Tomasi, M. Cossi, N. Rega, J. M. Millam, M. Klene, J. E. Knox, J. B. Cross, V. Bakken, C. Adamo, J. Jaramillo, R. Gomperts, R. E. Stratmann, O. Yazyev, A. J. Austin, R. Cammi, C. Pomelli, J. W. Ochterski, R. L. Martin, K. Morokuma, V. G. Zakrzewski, G. A. Voth, P. Salvador, J. J. Dannenberg, S. Dapprich, A. D. Daniels, O. Farkas, J. B. Foresman, J. V. Ortiz, J. Cioslowski and D. J. Fox, *Gaussian 09, revision B.01*, Gaussian, Inc., Wallingford, CT, 2010.
- 51 P. J. Stephens and N. Harada, *Chirality*, 2010, **22**, 229–233.
- 52 U. Varetto, *MOLEKEL*, v. 5.4, Swiss National Supercomputing Centre, Manno, Switzerland, 2009.



Publication 4

Manuscript “The mycotoxin phomoxanthone A disturbs the form and function of the inner mitochondrial membrane”:

Böhler P*, Stuhldreier F*, Anand R, Kondadi AK, Schlütermann D, Berleth N, Deitersen J, Wallot-Hieke N, Wu W, Frank M, Niemann H, Wesbuer E, Barbian A, Luyten T, Parys JB, Weidtkamp-Peters S, Borchardt A, Reichert AS, Peña-Blanco A, García-Sáez AJ, Itskanov S, van der Blik AM, Proksch P, Wesselborg S*, Stork B*.

** authors contributed equally to the manuscript*

Cell Death & Disease 9:286 (2018). doi: 10.1038/s41419-018-0312-8

ARTICLE

Open Access

The mycotoxin phomoxanthone A disturbs the form and function of the inner mitochondrial membrane

Philip Böhler¹, Fabian Stuhldreier¹, Ruchika Anand², Arun Kumar Kondadi², David Schlütermann¹, Niklas Berleth¹, Jana Deitersen¹, Nora Wallot-Hieke¹, Wenxian Wu¹, Marian Frank³, Hendrik Niemann³, Elisabeth Wesbuer⁴, Andreas Barbian⁴, Tomas Luyten⁵, Jan B. Parys⁵, Stefanie Weidtkamp-Peters⁶, Andrea Borchardt², Andreas S. Reichert², Aida Peña-Blanco⁷, Ana J. García-Sáez⁷, Samuel Itskanov⁸, Alexander M. van der Blik⁸, Peter Proksch³, Sebastian Wesselborg¹ and Björn Stork¹

Abstract

Mitochondria are cellular organelles with crucial functions in the generation and distribution of ATP, the buffering of cytosolic Ca^{2+} and the initiation of apoptosis. Compounds that interfere with these functions are termed mitochondrial toxins, many of which are derived from microbes, such as antimycin A, oligomycin A, and ionomycin. Here, we identify the mycotoxin phomoxanthone A (PXA), derived from the endophytic fungus *Phomopsis longicolla*, as a mitochondrial toxin. We show that PXA elicits a strong release of Ca^{2+} from the mitochondria but not from the ER. In addition, PXA depolarises the mitochondria similarly to protonophoric uncouplers such as CCCP, yet unlike these, it does not increase but rather inhibits cellular respiration and electron transport chain activity. The respiration-dependent mitochondrial network structure rapidly collapses into fragments upon PXA treatment. Surprisingly, this fragmentation is independent from the canonical mitochondrial fission and fusion mediators DRP1 and OPA1, and exclusively affects the inner mitochondrial membrane, leading to cristae disruption, release of pro-apoptotic proteins, and apoptosis. Taken together, our results suggest that PXA is a mitochondrial toxin with a novel mode of action that might prove a useful tool for the study of mitochondrial ion homeostasis and membrane dynamics.

Introduction

Mitochondria are cellular organelles that are crucial to almost all eukaryotic organisms. Among their most important functions are generation and distribution of ATP, buffering of cytosolic Ca^{2+} and, in animal cells, initiation of apoptosis. Disturbance of these or other

functions by mitochondrial toxins can lead to cellular stress and cell death^{1,2}.

Mitochondria produce ATP through oxidative phosphorylation (OXPHOS), which depends on the electron transport chain (ETC) embedded in the inner mitochondrial membrane (IMM). The ETC pumps protons out of the mitochondrial matrix and into the mitochondrial intermembrane space. This generates a proton gradient (ΔpH_m) and, consequently, a membrane potential ($\Delta\Psi_m$) across the IMM. The $\Delta\Psi_m$ is then used to drive the mitochondrial ATP synthase³.

To provide all regions within the cell with sufficient ATP, mitochondria often form a network that constantly undergoes balanced fission and fusion. This allows

Correspondence: Sebastian Wesselborg (sebastian.wesselborg@uni-duesseldorf.de) or Björn Stork (bjoern.stork@uni-duesseldorf.de)

¹Institute of Molecular Medicine I, Medical Faculty, Heinrich Heine University Düsseldorf, 40225 Düsseldorf, Germany

²Institute of Biochemistry and Molecular Biology I, Medical Faculty, Heinrich Heine University Düsseldorf, 40225 Düsseldorf, Germany

Full list of author information is available at the end of the article

Philip Böhler, Fabian Stuhldreier, Sebastian Wesselborg, Björn Stork contributed equally to this work.

Edited by G. Raschella

© The Author(s) 2018



Open Access This article is licensed under a Creative Commons Attribution 4.0 International License, which permits use, sharing, adaptation, distribution and reproduction in any medium or format, as long as you give appropriate credit to the original author(s) and the source, provide a link to the Creative Commons license, and indicate if changes were made. The images or other third party material in this article are included in the article's Creative Commons license, unless indicated otherwise in a credit line to the material. If material is not included in the article's Creative Commons license and your intended use is not permitted by statutory regulation or exceeds the permitted use, you will need to obtain permission directly from the copyright holder. To view a copy of this license, visit <http://creativecommons.org/licenses/by/4.0/>.

remodelling of the network as well as removal and recycling of damaged mitochondria through mitophagy^{1,4,5}. Excessive fission can be triggered by mitochondrial toxins that cause loss of $\Delta\Psi_m$, such as the protonophore carbonyl cyanide *m*-chlorophenyl hydrazone (CCCP)⁶.

The $\Delta\Psi_m$ also plays a role in the mitochondrial buffering of cytosolic Ca^{2+} . Normally, the cytosol of a typical animal cell contains only a very low Ca^{2+} concentration ($[\text{Ca}^{2+}]_{\text{cyt}}$, $\sim 0.1 \mu\text{M}$), whereas the concentration of Ca^{2+} within the endoplasmic reticulum ($[\text{Ca}^{2+}]_{\text{ER}}$, $> 100 \mu\text{M}$) or outside the cell ($[\text{Ca}^{2+}]_{\text{ext}}$, $> 1000 \mu\text{M}$) is up to 10,000-fold higher². In response to certain stimuli, Ca^{2+} channels in the ER and/or the plasma membrane open to release Ca^{2+} into the cytosol as a second messenger. Mitochondria contribute to removal of cytosolic Ca^{2+} by uptake into their matrix via $\Delta\Psi_m$ -driven Ca^{2+} transporters. After that, a slow, regulated efflux moves the Ca^{2+} out of the matrix and into the cristae, which are folds in the IMM, from where it is slowly released and shuttled back to the ER^{2,7-9}. A separate mechanism through which Ca^{2+} can cross the IMM is the mitochondrial permeability transition pore (mPTP), which can open irreversibly in response to severe mitochondrial stress. The mPTP directly connects the mitochondrial matrix with the cytosol to allow the free exchange of molecules up to 1.5 kDa in size, including Ca^{2+} . Irreversible mPTP opening leads to release of mitochondrial Ca^{2+} , loss of $\Delta\Psi_m$, swelling of the matrix and eventually mitochondrial outer membrane permeabilisation (MOMP)^{10,11}.

In animal cells, MOMP initiates apoptosis. Several proteins normally contained in the cristae attain a pro-apoptotic function if they pass the outer mitochondrial membrane (OMM) and are released into the cytosol. Among these proteins are cytochrome *c* (CYCS), SMAC (DIABLO) and OMI (HTRA2). Cytosolic CYCS becomes part of the caspase-activating apoptosome complex, while DIABLO and HTRA2 bind and inhibit the inhibitor of apoptosis proteins (IAPs), thus attenuating their inhibition of caspases¹. MOMP can be caused either passively through rupture of the OMM, such as triggered by the mPTP, or actively through the formation of pores in the OMM by the pro-apoptotic proteins BAK and BAX, which can be induced in response to severe cellular stress¹².

A variety of mitochondrial toxins with different effects and molecular targets is known today¹³. Several of these toxins are natural products, such as the *Streptomyces*-derived ETC inhibitor antimycin A and the ATP synthase inhibitor oligomycin A.

Phomoxanthone A and B (PXA and PXB) are natural products named after the fungus *Phomopsis*, from which they were first isolated, and after their xanthonoid structure (Fig. S1). PXA is a homodimer of two acetylated tetrahydroxanthonones symmetrically linked at C-4,4',

whereas PXB is structurally almost identical but asymmetrically linked at C-2,4'. Both possess antibiotic activity against diverse organisms from all biological kingdoms. Originally described in 2001, PXA and PXB were tested against the protozoan *Plasmodium falciparum*, the Gram-positive *Mycobacterium tuberculosis*, and three animal cell lines. In all of these organisms, both PXA and PXB showed significant cytotoxic activity, with PXA being more toxic in every case¹⁴. A later study in different organisms produced similar results, showing that PXA inhibits the growth of the Gram-positive *Bacillus megaterium*, the alga *Chlorella fusca*, and the fungus *Ustilago violacea*¹⁵.

We previously showed that PXA induces apoptosis in human cancer cell lines. Signs of apoptosis were observed as early as after 4 h of treatment with low micromolar doses of PXA^{16,17}. However, the mechanism by which PXA causes apoptosis or cytotoxicity in general has never before been investigated.

The aim of this study was to elucidate the mechanism through which PXA exerts its toxicity. Following our initial results, we hypothesised that PXA directly affects the mitochondria and thus investigated its effects on the ETC, $\Delta\Psi_m$, ATP production, Ca^{2+} buffering, and mitochondrial morphology. It appears that PXA is a mitochondrial toxin that specifically affects the IMM, leading to loss of $\Delta\Psi_m$, ETC inhibition, Ca^{2+} efflux, mitochondrial fragmentation, cristae disruption, and finally to the release of mitochondrial pro-apoptotic factors.

Results

PXA induces Ca^{2+} release from an intracellular store

To determine how PXA induces apoptosis, we analysed its effect on cellular Ca^{2+} levels since ionic imbalance can be an apoptotic trigger. Treatment of Ramos cells with PXA resulted in a strong, steady increase of $[\text{Ca}^{2+}]_{\text{cyt}}$ (Fig. 1a). Interestingly, there was a delay of about 2–5 min between addition of PXA and increase in $[\text{Ca}^{2+}]_{\text{cyt}}$. Since this pattern of Ca^{2+} release is similar to that caused by the tyrosine phosphatase inhibitor pervanadate (VO_4^{3-}) (Fig. S2a), and since tyrosine phosphatase inhibition can induce apoptosis, we tested the effect of PXA on tyrosine phosphorylation. However, in contrast to pervanadate, we could not detect any effect (Fig. S2b). In a broader picture, PXA had no inhibitory effect on any of 141 protein kinases against which we tested it (Table S1).

We next tried to determine the origin of the released Ca^{2+} . Since PXA increases $[\text{Ca}^{2+}]_{\text{cyt}}$ even in the absence of extracellular Ca^{2+} , we tested if it releases Ca^{2+} from the ER. Using thapsigargin, which causes a net efflux of Ca^{2+} from the ER, we could induce an increase in $[\text{Ca}^{2+}]_{\text{cyt}}$ even after PXA-inducible Ca^{2+} stores were depleted

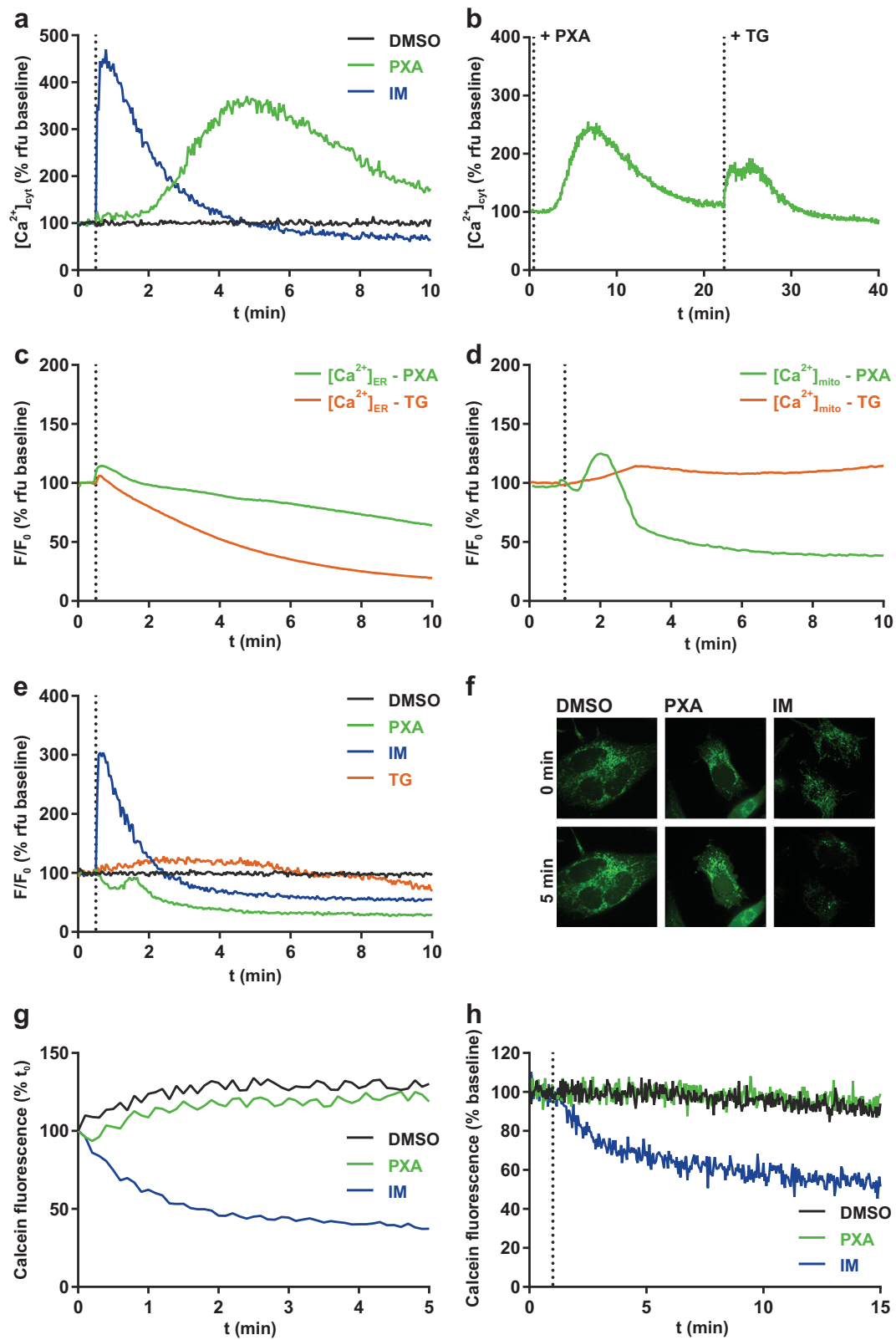


Fig. 1 (See legend on next page.)

Fig. 1 PXA causes an increase of $[Ca^{2+}]_{cyt}$ and a release of $[Ca^{2+}]_{mito}$ but not $[Ca^{2+}]_{ER}$. **a** Live measurement of the effect of PXA (10 μ M) on $[Ca^{2+}]_{cyt}$ in Ramos cells, where DMSO (0.1% v/v) was used as vehicle control and ionomycin (IM; 2 μ M) was used as positive control, and **b** live measurement of $[Ca^{2+}]_{cyt}$ after PXA followed by thapsigargin (TG; 10 μ M). Measurements were performed by flow cytometry using the Ca^{2+} -sensitive fluorescent probe Fluo-4-AM (Ex 488 nm, Em 530 \pm 30 nm) in the absence of extracellular Ca^{2+} by maintaining the cells in Krebs-Ringer buffer containing 0.5 mM EGTA during measurement. **c, d** Comparison of the effect of PXA (10 μ M) and thapsigargin (TG; 1 μ M) on either $[Ca^{2+}]_{ER}$ or $[Ca^{2+}]_{mito}$ as measured by the Ca^{2+} -sensitive fluorescent protein CEPIA targeted to the respective organelle in HeLa cells. All traces were normalised (F/F_0) where F_0 is the starting fluorescence of each trace. **e** Comparison of the effect of PXA (10 μ M), ionomycin (IM; 2 μ M), and thapsigargin (TG; 1 μ M) on $[Ca^{2+}]_{mito}$ in Ramos cells stably transfected with the Ca^{2+} -sensitive ratiometric fluorescent protein mito-Pericam. DMSO (0.1% v/v) was used as vehicle control. F/F_0 is the ratio of fluorescence with excitation at 488 nm (high $[Ca^{2+}]$) to 405 nm (low $[Ca^{2+}]$). **f, g** Live imaging and quantification of the effect of PXA (10 μ M) on mPTP opening in HeLa cells as measured by mitochondrial calcein fluorescence using the calcein/cobalt quenching method. DMSO (0.1% v/v) was used as vehicle control and ionomycin (IM; 2 μ M) was used as positive control. Mitochondrial calcein fluorescence was quantified. **h** Additional live measurement of the effect of PXA on mPTP opening in Ramos cells by the calcein/cobalt quenching method using flow cytometry

(Fig. 1b), suggesting that the Ca^{2+} released by PXA at least partially originates from a source other than the ER.

PXA induces Ca^{2+} release mainly from the mitochondria

To quantify the effect of PXA on Ca^{2+} stores, we used HeLa cells expressing CEPIA Ca^{2+} probes targeted to either the ER or the mitochondria. Although PXA provoked some Ca^{2+} release from the ER, it was much slower and weaker than that evoked by thapsigargin (Fig. 1c). Mitochondria, however, were quickly and severely depleted (Fig. 1d). This effect of PXA on mitochondrial Ca^{2+} was confirmed in Ramos cells, making use of the Ca^{2+} probe Pericam (Fig. 1e).

Mitochondrial Ca^{2+} release caused by PXA is independent from the mPTP

Large-scale Ca^{2+} efflux from the mitochondria can result from persistent opening of the mPTP. We thus tested whether PXA induces mPTP opening by using the cobalt/calcein method, comparing PXA to the mPTP inducer ionomycin (IM). While IM caused a strong decrease in mitochondrial calcein fluorescence as expected, PXA had no observable effect (Fig. 1f, g; Supplementary Movies S1–S3). Similar results were obtained by further live measurement using flow cytometry (Fig. 1h). In addition, we tested whether the mPTP inhibitor cyclosporin A (CsA) can prevent the mitochondrial Ca^{2+} release caused by PXA. We measured mitochondrial Ca^{2+} retention capacity in isolated mitochondria, comparing PXA to IM and CCCP. This was done in either normal isolated mitochondria or mitochondria loaded with Ca^{2+} , and in the presence of either CsA or its derivative cyclosporin H (CsH), which does not affect the mPTP (Fig. 2)¹⁸. While PXA caused a decrease in calcium green fluorescence, indicating Ca^{2+} release, under every condition, i.e., regardless of Ca^{2+} loading and also in the presence of CsA, IM had an observable effect only in loaded mitochondria, but also regardless of CsA. On the other hand, CCCP caused a release of Ca^{2+} only in the presence of CsH but not CsA, indicating that CCCP-induced Ca^{2+} release does indeed depend on the mPTP, unlike that

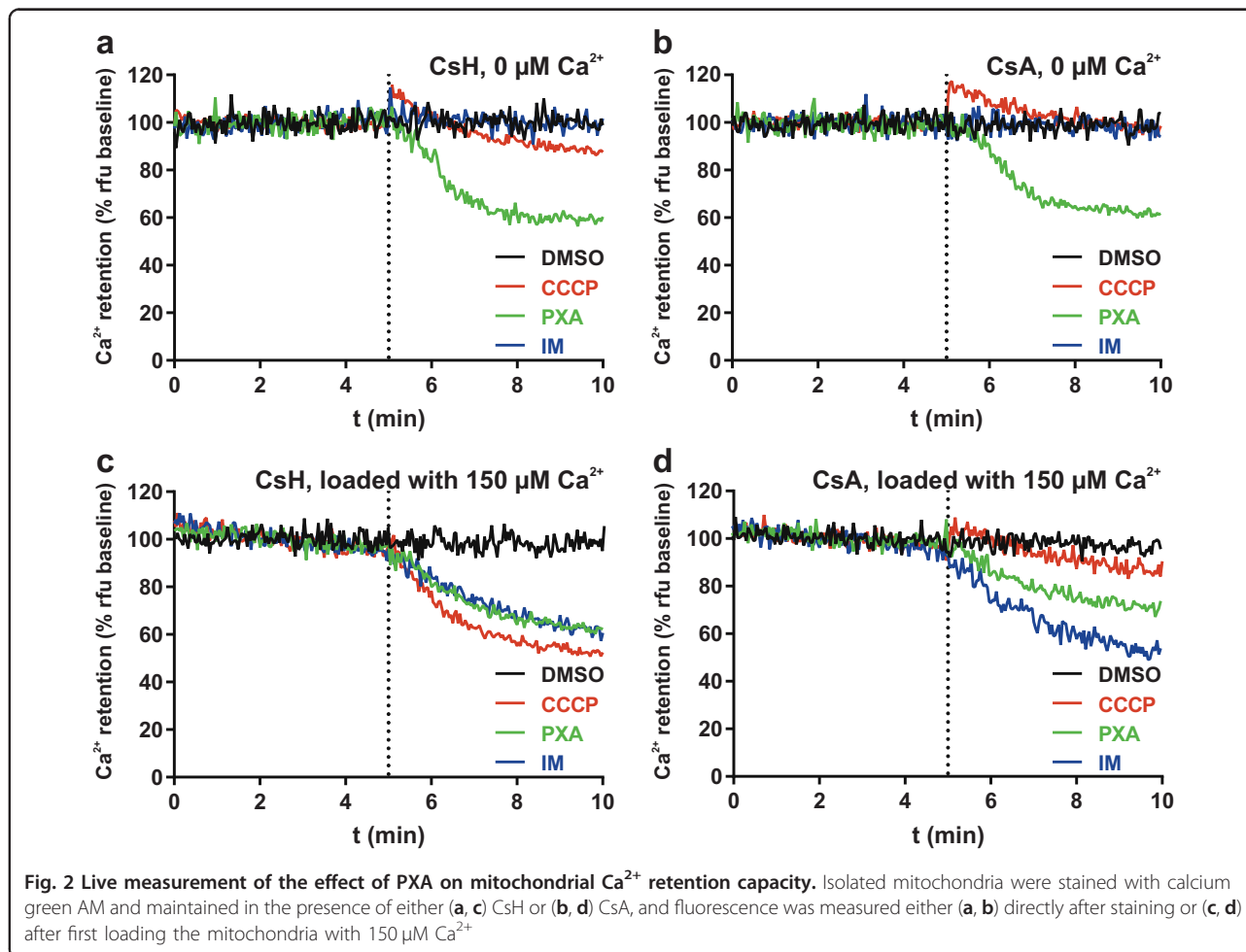
induced by PXA. Taken together, these results indicate that PXA causes mitochondrial Ca^{2+} release largely independent from the mPTP.

PXA depolarises the mitochondria but does not uncouple cellular respiration

A change in $[Ca^{2+}]_{mito}$ likely correlates with changes in other mitochondrial ion gradients. Uptake of Ca^{2+} into the mitochondrial matrix is driven by $\Delta\Psi_m$. We thus analysed the effect of PXA on $\Delta\Psi_m$. Indeed, PXA caused immediate mitochondrial depolarisation similar to CCCP, both in whole cells and isolated mitochondria (Fig. 3a, b). The EC_{50} for PXA-induced loss of $\Delta\Psi_m$ in Ramos cells was determined to be $1.1 \pm 0.3 \mu$ M (Fig. S3). The key contributor to $\Delta\Psi_m$ is ΔpH_m , which is maintained via cellular respiration by consumption of O_2 . If the PXA-induced loss of $\Delta\Psi_m$ was caused by loss of ΔpH_m downstream of the ETC, as in case of CCCP, it would be accompanied by an increase in respiration to compensate for the loss. Therefore, we measured cellular O_2 consumption upon increasing concentrations of either PXA or CCCP. As expected, CCCP caused a dose-dependent increase in O_2 consumption. However, in contrast to CCCP, PXA caused no increase but rather a slight decrease in O_2 consumption (Fig. 3c). An overview of the kinetics of the effects of PXA on $[Ca^{2+}]_{cyt}$, $[Ca^{2+}]_{mito}$, O_2 consumption and $\Delta\Psi_m$ is presented in Fig. 3d.

PXA inhibits cellular respiration by disrupting the electron transport chain

Since PXA had a moderate inhibitory effect on cellular O_2 consumption under basal conditions, we next measured O_2 consumption after the respiration rate was first increased by CCCP. Here, treatment with PXA caused a strong decrease in O_2 consumption to levels below baseline (Fig. 4a). It thus appeared likely that PXA, unlike CCCP, is not an inducer but rather an inhibitor of cellular respiration and of the ETC. We, therefore, compared PXA to known ETC inhibitors: rotenone (complex I), thenoyltrifluoroacetone (TTFA; complex II), antimycin A (complex III), sodium azide (NaN_3 ; complex IV) and



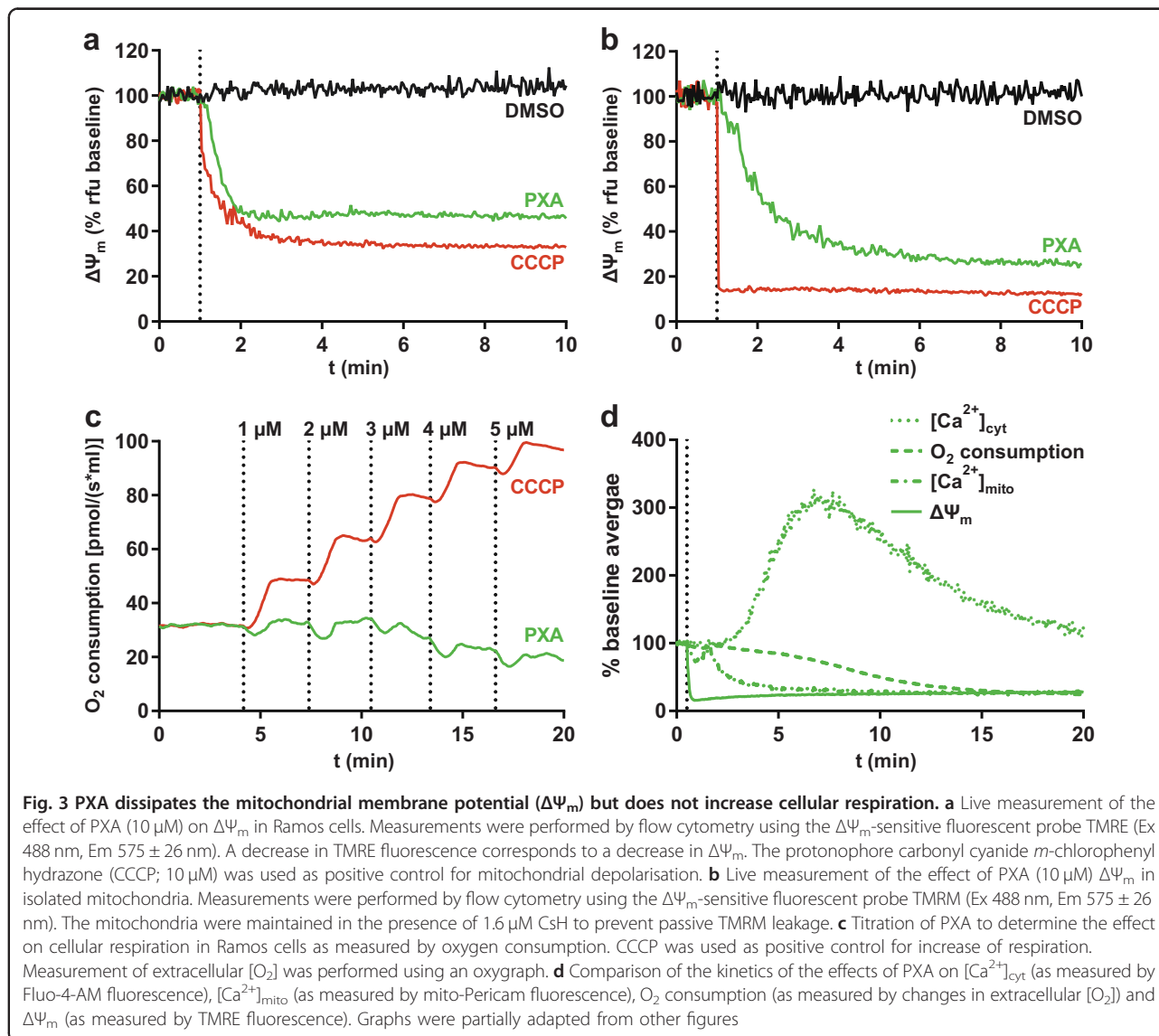
oligomycin A (complex V / ATP synthase). In an O_2 consumption assay, PXA caused a strong decrease in cellular respiration, both after CCCP treatment and under basal conditions, similar to that caused by rotenone, antimycin A and azide (Fig. 4b). Oligomycin A expectedly inhibited respiration under basal conditions but not after CCCP treatment since CCCP uncouples respiration from ATP synthesis. TTFA did not have a significant effect, probably because complex II is not involved in respiration if complex I substrates are available¹⁹.

Since a functional ETC is required for ATP synthesis by OXPHOS, we also compared PXA to known ETC inhibitors in this context. Indeed, PXA as well as all tested ETC inhibitors strongly reduced cellular ATP levels if galactose was the only available sugar and ATP had to be synthesised via OXPHOS instead of glycolysis (Fig. 4c). Thus assuming that PXA targets the ETC, we tried to determine if it specifically inhibits one of the ETC complexes. This experiment was performed in permeabilized cells, comparing PXA to rotenone. Succinate, which induces complex II-dependent respiration only if complex I is inhibited, alleviated rotenone-induced inhibition of O_2

consumption but had only a marginal effect in PXA-treated cells. In contrast, duroquinol, which induces complex III-dependent respiration, increased O_2 consumption in both PXA-treated as well as rotenone-treated cells back to levels before inhibition (Fig. 4d). These data suggest that PXA might either affect both complex I and II or the shuttling of electrons between complex I/II and III.

Comparison of PXA with other ETC inhibitors

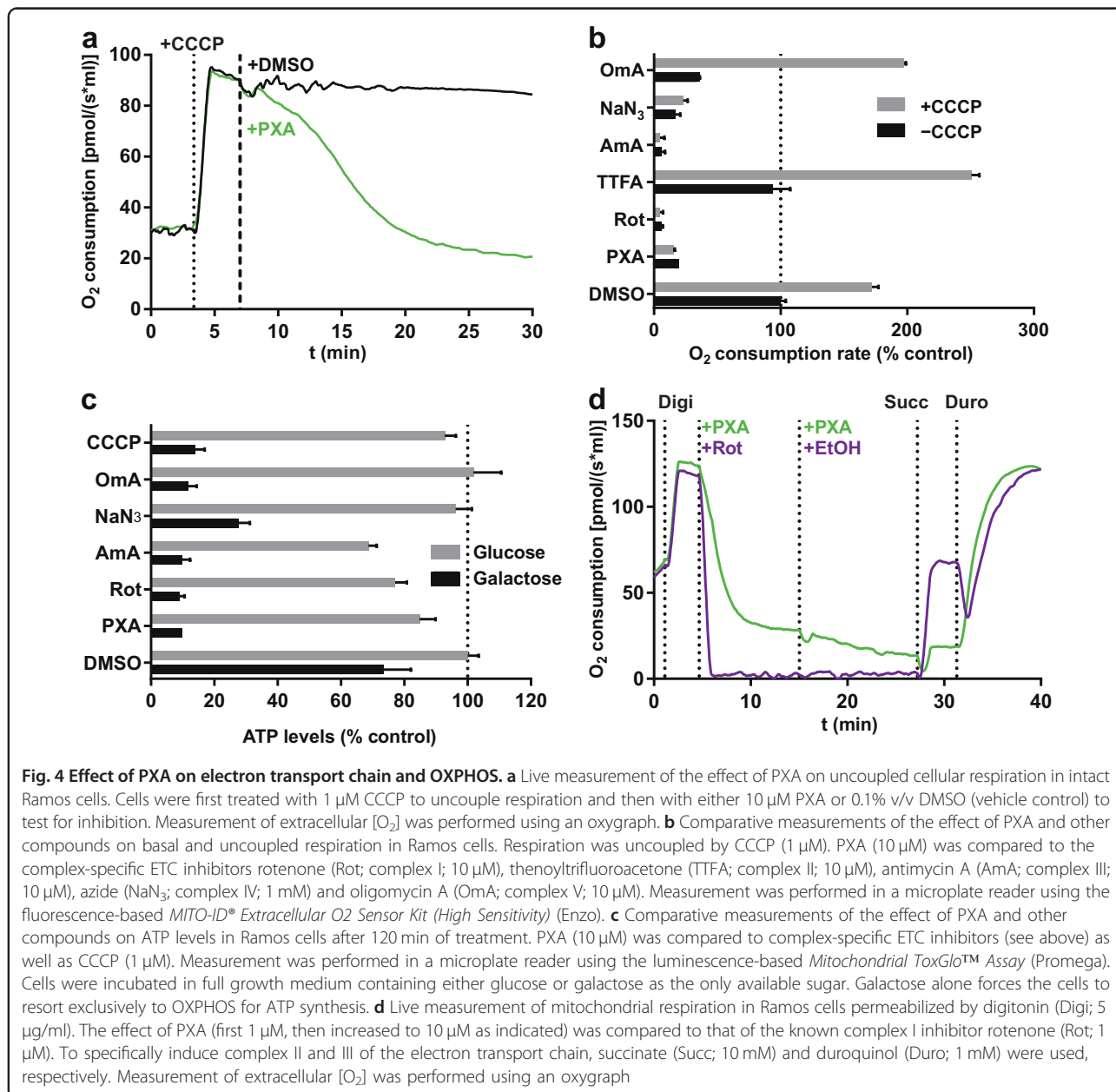
While PXA inhibits the ETC as well as ATP synthesis, it differs from the other ETC inhibitors used in this study concerning its effects on Ca^{2+} and $\Delta\Psi_m$. Unlike PXA, neither CCCP nor any of the tested ETC inhibitors with the exception of antimycin A caused a noticeable release of Ca^{2+} (Fig. S4a), and that caused by antimycin A was much weaker and had an earlier but slower onset than the one caused by PXA. Similarly, while both CCCP and PXA induced a strong and immediate decrease in $\Delta\Psi_m$, none of the other ETC inhibitors except antimycin A had any effect on $\Delta\Psi_m$, and that of antimycin A was much slower and weaker (Fig. S4b). Since we previously



showed that PXA is cytotoxic and induces apoptosis, we also compared it to CCCP, ETC inhibitors, IM (control for Ca^{2+} release) and staurosporine (control for cytotoxicity/apoptosis) in these regards. PXA, staurosporine and CCCP strongly induced apoptosis, while the ETC inhibitors and IM were much weaker inducers in Ramos cells and did not noticeably induce apoptosis at all in Jurkat cells (Fig. 5a, b). Dependency on OXPHOS for ATP synthesis, which considerably increased the toxicity of the ETC inhibitors, appeared to have no effect on the toxicity of PXA or staurosporine (Fig. 5c, d). These observations indicate that PXA probably causes cytotoxicity in general and apoptosis in particular not via its effects on the ETC, $\Delta\Psi_m$, or $[\text{Ca}^{2+}]_{\text{mito}}$, but rather that all of these events might have a common cause further upstream.

PXA causes irreversible cleavage of OPA1 mediated by OMA1 but not YME1L1

Several stress conditions including loss of $\Delta\Psi_m$ and low levels of ATP can induce cleavage of the IMM fusion regulator OPA1 by the protease OMA1 (ref. 20). Additionally, OPA1 is also cleaved by the protease YME1L1, resulting in fragments of different size. We treated MEF cells deficient for either one or both of these proteases with either PXA or CCCP. We observed that PXA, like CCCP, caused stress-induced OPA1 cleavage that was dependent on OMA1, whereas expression of YME1L1 did not have any visible effect on PXA-induced OPA1 cleavage (Fig. 6a). Similarly to their effect in MEF cells, PXA and CCCP-induced cleavage of OPA1 in Ramos and Jurkat cells within minutes. Interestingly, and unlike CCCP, removal of PXA did not enable recovery of the

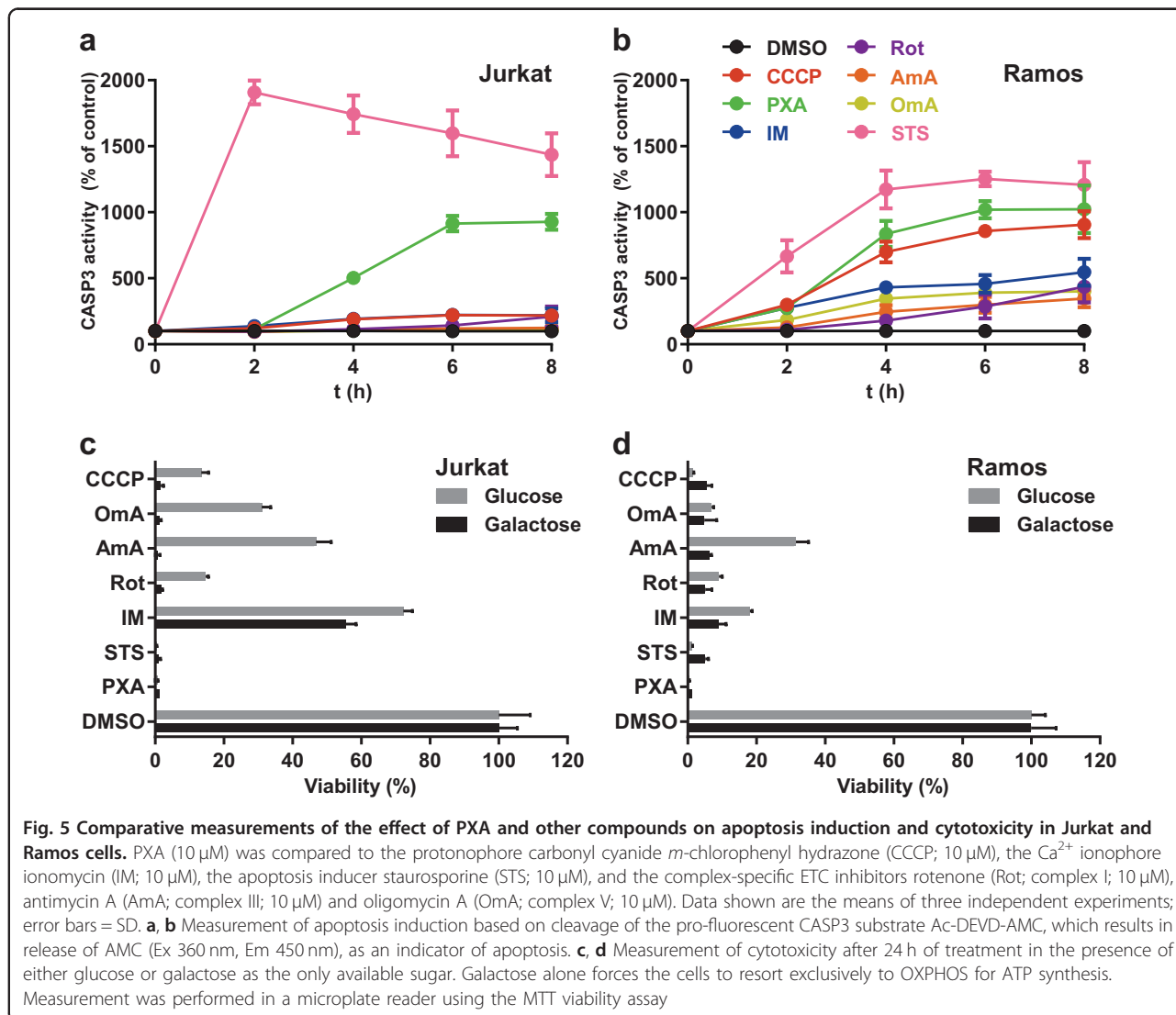


long OPA1 forms (Fig. 6b). This prompted us to also investigate the effects of removal of PXA on cytotoxicity. Indeed, though PXA was about fivefold less toxic if removed after a few minutes, it still irreversibly primed the cells for death (Fig. 6c). It, thus, appears that at least some of the effects of PXA on the cells are irreversible.

PXA induces fragmentation of the inner but not of the outer mitochondrial membrane independently of OMA1, OPA1 and DRP1

Excessive processing of OPA1 by OMA1 changes mitochondrial cristae morphology, resulting in the release of pro-apoptotic factors such as CYCS and SMAC. We,

therefore, investigated the effects of PXA on SMAC localisation and on recruitment of BAX to the OMM. We observed that PXA indeed induced recruitment of GFP-BAX to the mitochondria, with concurrent release of SMAC-mCherry into the cytosol, within about 2–3 h (Fig. 7a and Supplementary Movie S4; quantification shown in Fig. S5). OPA1 processing by OMA1 also prevents IMM fusion and, if excessive, results in mitochondrial fragmentation. Intriguingly, PXA caused rapid fragmentation of the mitochondrial network within minutes (Fig. 7b), and independent of the cells' OMA1 or YME1L1 status (Fig. 7c, left panels; Supplementary Movies S5–S7). The persistence of PXA-induced

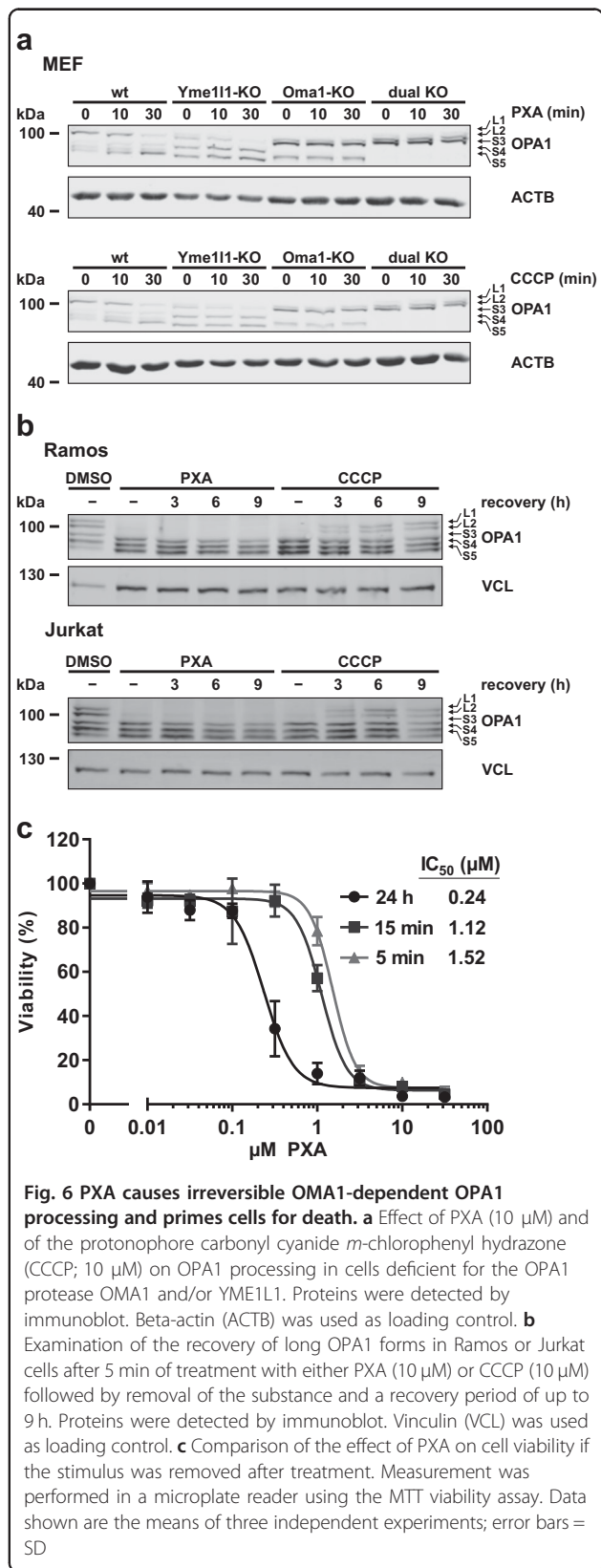


mitochondrial fragmentation in OMA1-YME1L1 DKO cells indicates that this process is independent of OPA1 cleavage.

Mitochondrial fission is also regulated by the dynamin DRP1, which mediates OMM fission. We, thus, tested the effect of PXA on the mitochondrial morphology in DRP1-deficient MEF cells. Again, fragmentation was observed within minutes after treatment (Fig. 7c, right panel; Supplementary Movie S8). We next used dual staining of both the matrix (via HSP60) as well as the OMM (via TOMM20) to determine whether both or only one of these structures are affected by PXA. CCCP was used as a positive control for fragmentation. As expected, CCCP could not induce fragmentation in DRP1-KO cells, and in WT cells it induced fragmentation of both the IMM and OMM together (Fig. 8a, b). In contrast, in the WT cells treated with PXA, fragmentation was much stronger and resulted in smaller fragments. More intriguingly, in

DRP1-KO cells treated with PXA, only the matrix appeared to have fragmented, whereas the OMM appeared to have shrunken around the matrix fragments but otherwise remained connected (Fig. 8a, b). This effect could also be observed in cells deficient for both DRP1 and OPA1 (Fig. S6) demonstrating that PXA acts independently of canonical regulators of mitochondrial fission. Finally, a close examination of the mitochondrial ultrastructure by transmission electron microscopy (TEM) revealed that PXA causes OMA1-independent disruption of mitochondrial matrix morphology, complete loss of cristae, and condensation of IMM structures at the OMM (Fig. 8c).

Taken together, our results show that PXA disturbs mitochondrial form and function in several ways. Some effects, such as the rapid inhibition of both $\Delta\Psi_m$ and the ETC at the same time, the delayed release of mitochondrial Ca^{2+} , and the fragmentation of the inner but not the



outer mitochondrial membrane, are unique and indicate a mode of action that is distinct from all other compounds to which it was compared in this study.

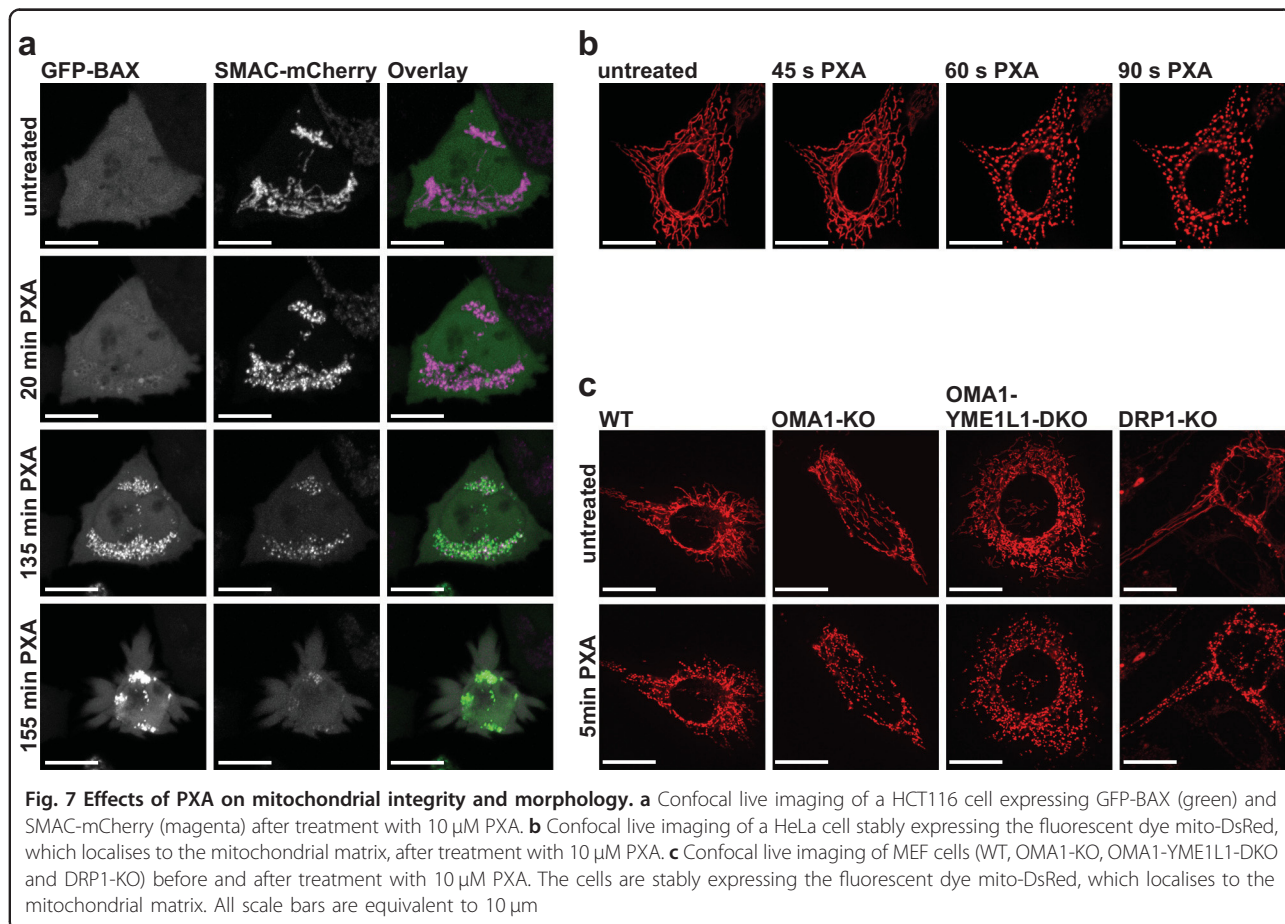
Discussion

The mycotoxin PXA is a toxic natural product whose mechanism of action has so far remained elusive. We provide evidence that PXA disrupts mitochondrial function and causes IMM fragmentation and cristae disruption independently of DRP1 and OPA1, leading to the release of pro-apoptotic factors and ultimately to apoptosis.

PXA, just like CCCP, dissipates $\Delta\Psi_m$ within seconds. In the case of CCCP, respiration increases to compensate this, whereas PXA has the opposite effect and blocks respiration. Conversely, respiration is also blocked by ETC inhibitors, yet in contrast to PXA, these do not strongly affect $\Delta\Psi_m$. This suggests an entirely different mode of action for PXA. Additionally, unlike any of these compounds, PXA causes a strong mitochondrial release of Ca^{2+} and rapid fragmentation of the IMM but not the OMM.

Release of mitochondrial Ca^{2+} and loss of $\Delta\Psi_m$ can be results of persistent mPTP opening, yet we showed that PXA does not strongly affect the mPTP. Since mitochondrial ion gradients are interdependent through various antiporters that are generally linked to $\Delta\Psi_m$ (ref. ²), one might assume that loss of $\Delta\Psi_m$ disturbs these gradients sufficiently to induce a net Ca^{2+} efflux from the mitochondria. For CCCP, contradictory results have been reported—in some cases it caused Ca^{2+} release²¹, in some cases it did not²². We observed no effect of CCCP and most ETC inhibitors on $[\text{Ca}^{2+}]_{\text{cyt}}$, and in fact both ETC-deficient (ρ^0) mitochondria²³ and depolarised mitochondria²⁴ can still facilitate a net uptake of Ca^{2+} . It, thus, appears that the mitochondrial Ca^{2+} release induced by PXA is not necessarily a result of its effects on the ETC and $\Delta\Psi_m$, but rather that all of these effects might have a common cause.

The delay between addition of PXA and the first observable increase in $[\text{Ca}^{2+}]_{\text{cyt}}$ and decrease in $[\text{Ca}^{2+}]_{\text{mito}}$ contrasts with the immediate change in $\Delta\Psi_m$ (Fig. 3d). This discrepancy could possibly be explained by the hypothesis that mitochondria release Ca^{2+} mainly into the cristae, and that the cristae junctions may function as bottlenecks for mitochondrial Ca^{2+} transport^{8,25}. Cristae junctions are regulated by OPA1, which is cleaved by OMA1 in response to mitochondrial stress, leading to cristae disruption²⁶. We not only showed that OPA1 is irreversibly cleaved by OMA1 upon PXA treatment, but that PXA also causes cristae disruption independently of OMA1. Thus, PXA-induced cristae disruption might cause the release of Ca^{2+} from the cristae and thus eventually into the cytosol. In addition, irreversible cristae



disruption could well be a sufficient condition for the release of pro-apoptotic factors and thus the induction of apoptosis^{26–28}.

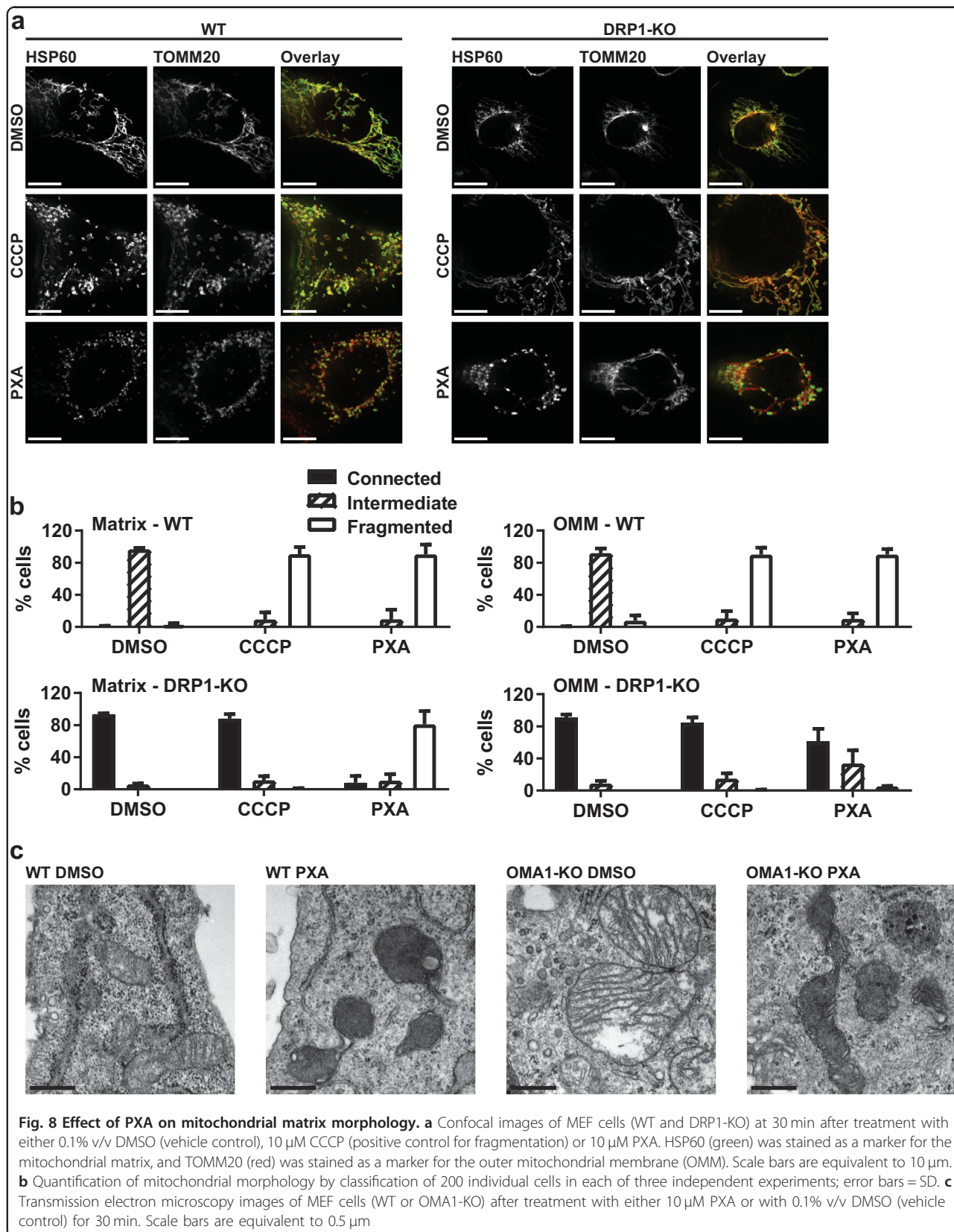
OPA1 also affects the fragmentation of mitochondrial network structures, which can be induced by PXA as well as CCCP. In the case of CCCP, this is commonly explained by the excessive activation of DRP1 after increased OPA1 processing by OMA1, which in turn is a response to several kinds of cellular stress including impaired ATP production and loss of $\Delta\Psi_m$ (ref. 4,6,20,29–32). Since PXA dissipates $\Delta\Psi_m$, inhibits ATP production and consequently induces OMA1-mediated OPA1 cleavage, one might assume that it induces fragmentation via the same mechanism, yet we observed PXA-induced fragmentation events that were independent of DRP1, OMA1 and even OPA1.

Mitochondrial fragmentation independent of DRP1 is an unusual phenomenon but has been reported in cells undergoing apoptosis after pro-apoptotic factors had already been released^{33,34}. In the case of PXA, however, fragmentation occurs within minutes after treatment, whereas pro-apoptotic factors are released only after several hours. In addition, whereas both the OMM and

IMM are divided together during DRP1-dependent fragmentation, PXA can cause exclusive fragmentation of the IMM while the OMM remains intact. This is surprising since no active mechanism for exclusive IMM fission is known in higher eukaryotes, and there are only few reports documenting this phenomenon^{6,35,36}.

The OMA1-processed short OPA1 forms play a role in IMM fission and cristae morphology^{5,29,35}. However, since PXA-induced IMM fragmentation and cristae disruption are independent of both OMA1 and OPA1, this implies that OPA1 may well be an IMM fission regulator but not necessarily a fission executor. It has been recently proposed that OPA1 is dispensable for cristae junction biogenesis but may still be required for cristae junction remodelling³⁷. Our results suggest that excessive OPA1 processing may be sufficient but not necessary for inner membrane remodelling and cristae disruption and for the consequent release of pro-apoptotic factors.

The independence of PXA-induced IMM fragmentation from DRP1, OMA1 and OPA1, as well as its very fast onset, suggest that it might not depend on the fission/fusion machinery at all, but could work via a completely separate mechanism. Since no such mechanism is known



in higher eukaryotes, any attempt at explaining this effect remains speculative. One explanation could be a change in IMM fluidity or matrix architecture, causing an immediate and strong retraction of the IMM. This could result from interference with the tethering of IMM and OMM at mitochondrial contact sites. If this is the case, a possible mechanistic target of PXA could be the mitochondrial phospholipid cardiolipin, which is present almost exclusively in the IMM and especially at mitochondrial contact sites^{38,39}. Cardiolipin serves as a membrane anchor for many proteins that are implicated in mitochondrial contact site formation, mitochondrial ultrastructure and the ETC, such as MIC27 (APOOL)^{40,41}, F₁F₀ ATP synthase^{41,42}, CYCS⁴¹, and ETC complexes III and IV^{41,43,44}. A disruptive interaction between PXA and either cardiolipin or cardiolipin-binding proteins might thus explain several of the effects induced by PXA.

In summary, we identified PXA as a mitochondrial toxin with a mode of action distinct from known ETC inhibitors, OXPHOS uncouplers, and ionophores. Its effects, such as the rapid inhibition of both ETC and $\Delta\Psi_m$, the release of mitochondrial Ca²⁺, and the induction of DRP1- and OPA1-independent cristae disruption and fission of the inner but not the outer mitochondrial membrane, might render it a useful tool in studying these phenomena. Further studies may reveal the molecular target of PXA and the mechanisms through which it induces mitochondrial Ca²⁺ release and IMM fission.

Material and methods

Cell lines and cell culture

Jurkat cells were obtained from DSMZ (#ACC-282). Ramos cells were kindly provided by Michael Engelke (Institute of Cellular and Molecular Immunology, University Hospital Göttingen, Göttingen, Germany). HeLa cells stably expressing mito-DsRed were kindly provided by Aviva M. Tolkovsky (Department of Clinical Neurosciences, University of Cambridge, England, UK) and have been described previously⁴⁵. MEF cells deficient for OMA1 and/or YME1L1 as well as the corresponding wild-type cells were generated by Ruchika Anand and kindly provided by Thomas Langer (Institute for Genetics, University of Cologne, Germany) and have been described previously²⁹. MEF cells deficient for DRP1 as well as the corresponding wild-type cells used for live imaging were kindly provided by Hiromi Sesaki (Department of Cell Biology, Johns Hopkins University, Baltimore, MD, USA) and have been described previously³³. MEF cells deficient for DRP1 used for imaging of fixed cells were generated using the CRISPR/Cas9 system as described previously⁴⁶. The DNA target sequence for the guide RNA was 5'-CAGTGGGAAGAGCTCAGTGC-3'. HCT116 cells were kindly provided by Frank Essmann (Interfaculty Institute of Biochemistry, Eberhard Karls University Tübingen,

Germany). Transient expression of SMAC-mCherry and GFP-BAX was achieved by lipofection at 70–80% confluence using Lipofectamine 2000 (Life Technologies, Darmstadt, Germany). Cells were incubated with 0.15 μ l Lipofectamine 2000, 50 ng pcDNA3-Smac(1-60)mCherry (Addgene ID 40880; this plasmid was kindly provided by Stephen Tait (Beatson Institute, University of Glasgow, Scotland, UK) and has been described previously⁴⁷), and 50 ng pGFP-Bax (kindly provided by Nathan R. Brady, Department of Molecular Microbiology and Immunology, Johns Hopkins University, Baltimore, MD, USA) per well in glass bottom 8-well chambers (Ibidi, Planegg, Germany) for 16 h. HeLa cells used for Ca²⁺ measurements were cultured in Dulbecco's modified Eagle's medium supplemented with 10% fetal calf serum (FCS) and 4 mM L-glutamine, 100 U/ml penicillin and 100 μ g/ml streptomycin at 37 °C and 5% CO₂. They were authenticated using autosomal STR profiling performed by the University of Arizona Genetics Core and they fully matched the DNA fingerprint present in reference databases. Cell lines stably expressing either mito-DsRed (except HeLa; see above) or ratiometric mito-Pericam were generated by retroviral transfection using the Platinum-E (Plat-E) packaging cell line (kindly provided by Toshio Kitamura, Institute of Medical Science, University of Tokyo, Japan) and the retroviral vectors pMSCVpuro-mito-DsRed1 (Addgene ID 87379) or pMSCVpuro-mito-Pericam (Addgene ID 87381). The medium used for the cultivation of Jurkat cells and Ramos cells was RPMI 1640 medium, and the medium used for cultivation of HCT116 cells was McCoy's 5A medium. All other cells were cultivated in high-glucose Dulbecco's Modified Eagle's medium (DMEM). All media were supplemented with 10% FCS, 100 U/ml penicillin, and 100 μ g/ml streptomycin. All cell lines were maintained at 37 °C and 5% CO₂ in a humidity-saturated atmosphere.

Reagents

Phomoxanthone A was isolated and purified as described previously¹⁶. We found that PXA becomes unstable if dissolved in dimethyl sulfoxide (DMSO) and readily isomerises into the essentially non-toxic compound dicerandrol C (data not shown), in a process similar to the one previously described for the structurally related secalonic acids⁴⁸. However, PXA is barely soluble in EtOH and not soluble in H₂O. Therefore, PXA was prepared in small lyophilised aliquots and only dissolved in DMSO immediately before usage.

The tyrosine phosphatase inhibitor pervanadate (VO₄³⁻) was freshly prepared by mixing 30 mM sodium orthovanadate with 60 mM H₂O₂ in phosphate-buffered saline (PBS) and incubating at room temperature (RT) in the dark for 10 min; sodium orthovanadate was purchased from Sigma (Munich, Germany), #450243; IM from

Sigma, #I9657; thapsigargin (TG) from Sigma, #T9033; carbonyl cyanide *m*-chlorophenyl hydrazone (CCCP) from Sigma, #C2759; rotenone from Sigma, #45656; the-noyltrifluoroacetone (TTFA) from Sigma, #88300; anti-mycin A from Sigma, #A8674; sodium azide (NaN₃) from Sigma, #S2002; oligomycin A from Toronto Research Chemicals (Toronto, Canada), #O532970; staurosporine (STS) from LC Laboratories (Woburn, MA, USA), #9300. All cell culture reagents were purchased from Life Technologies, and all other reagents where no manufacturer is explicitly mentioned were purchased from Carl Roth GmbH (Karlsruhe, Germany).

Replicates and statistical analysis

Experiments were replicated at least three times, and representative data are shown. Error bars indicate standard deviation. All statistical analysis was performed using Prism v7.01 (GraphPad Software, La Jolla, CA, USA).

In vitro kinase activity screening

The effect of PXA on the activity of 141 protein kinases was assessed by the International Centre for Kinase Profiling (Dundee, Scotland, UK) using a radioactive filter binding assay with ³³P ATP^{49,50}.

Live measurement of [Ca²⁺]_{cyt} by Fluo-4-AM

Cells were stained by incubation in growth medium containing 1 μM Fluo-4-AM (Life Technologies; #F14201), 0.005% w/v Pluronic F-127 (Sigma, #540025), 10 mM HEPES and 5% v/v FCS at 30 °C. After 25 min, an equal volume of full growth medium was added, the temperature was increased to 37 °C, and the cells were incubated for another 10 min. After that, the cells were washed and resuspended in Krebs-Ringer buffer (10 mM HEPES pH 7.0, 140 mM NaCl, 4 mM KCl, 1 mM MgCl₂, 10 mM glucose) supplemented with 1 mM CaCl₂. The cells were kept at RT in the dark until measurement. Just before measurement, the cells were washed and resuspended in Krebs-Ringer buffer supplemented with 0.5 mM EGTA. Fluo-4-AM fluorescence was measured live using an LSRFortessa flow cytometer (BD, Franklin Lakes, NJ, USA) recording fluorescence in the FITC channel (Ex 488 nm, Em 530 ± 30 nm). For each sample, after at least 30 s of baseline measurement, the stimulus was added and measurement was continued for at least 10 min.

Live measurement of [Ca²⁺]_{mito} and [Ca²⁺]_{ER} by CEPIA

Measurements of [Ca²⁺]_{mito} and [Ca²⁺]_{ER} in HeLa single cells were performed as described previously^{51,52}, using the genetically-encoded Ca²⁺ indicators CEPIA3mt (Addgene ID 58219) and G-CEPIA1er (Addgene ID 58215), respectively, which were developed by Dr. M. Iino (The University of Tokyo, Japan)⁵³. The constructs were

introduced into HeLa cells utilising the X-tremeGENE HP DNA transfection reagent (Roche, Mannheim, Germany) according to the manufacturer's protocol. The [Ca²⁺] measurements were performed 48 h after transfection using a Zeiss Axio Observer Z1 Inverted Microscope equipped with a 20 × air objective and a high-speed digital camera (Axiocam Hsm, Zeiss, Jena, Germany). Changes in fluorescence were monitored in the GFP channel (Ex 480 nm, Em 520 nm). Extracellular Ca²⁺ was chelated with 3 mM EGTA, and PXA (10 μM) or thapsigargin (1 μM) were added as indicated on the figures. All traces were normalised (F/F_0) where F_0 is the starting fluorescence of each trace.

Live measurement of [Ca²⁺]_{mito} by ratiometric mito-Pericam

Ramos cells stably transfected with ratiometric mito-Pericam as described above were used for this measurement. Ratiometric mito-Pericam is a Ca²⁺-sensitive fluorescent protein and was described previously^{54,55}. An increase in [Ca²⁺] causes a shift of the Pericam excitation maximum from ~410 to ~495 nm while the emission peak remains at ~515 nm. Pericam fluorescence was measured live using an LSRFortessa flow cytometer recording fluorescence in both the FITC channel (Ex 488 nm, Em 530 ± 30 nm) and the AmCyan channel (Ex 405 nm, Em 525 ± 50 nm). For each sample, after at least 30 s of baseline measurement, the stimulus was added and measurement was continued for at least 10 min. The ratio of fluorescence with excitation at 488 to 405 nm was calculated.

Live measurement of mPTP opening by cobalt-calcein assay

This method was adapted from previously published protocols^{10,18,56}. The cells were stained by incubation in Krebs-Ringer buffer supplemented with 1 mM CaCl₂, 1 mM CoCl₂, and 1 μM calcein-AM (Life Technologies, #65-0853-78) at 37 °C for 30 min. After that, the cells were washed and maintained in Krebs-Ringer buffer supplemented with 1 mM CaCl₂ and 1.6 μM cyclosporin H (CsH) to prevent passive efflux of calcein. For live measurement by confocal microscopy, imaging and quantification were performed using a Perkin Elmer Spinning Disc microscope with a 60 × objective (oil-immersion and NA = 1.49) at an excitation wavelength of 488 nm. The videos were obtained at 1000 × 1000 pixel resolution with a Hamamatsu C9100 camera. Additional live measurement by flow cytometry was performed using an LSRFortessa flow cytometer recording fluorescence in the FITC channel (Ex 488 nm, Em 530 ± 30 nm). For each sample, after at least 30 s of baseline measurement, the stimulus was added and measurement was continued for at least 10 min.

Isolation of live mitochondria

Adherent cells were harvested by a cell scraper. All cells were pelleted by centrifugation at 600 rcf, resuspended in ice-cold mitochondria isolation buffer (210 mM mannitol, 70 mM sucrose, 1 mM K₂EDTA, 20 mM HEPES), and passed through a 23 G needle ten times. The resulting suspension was centrifuged at 600 rcf and the supernatant was transferred to a new tube and centrifuged at 6500 rcf and 4 °C for 15 min. The resulting mitochondrial pellet was resuspended in sodium-free mitochondrial respiration buffer MiR05 (0.5 mM EGTA, 3 mM MgCl₂, 60 mM lactobionic acid, 20 mM taurine, 10 mM KH₂PO₄, 20 mM HEPES, 110 mM D-sucrose, 0.1% w/v fatty-acid-free bovine serum albumin [BSA]) supplemented with 10 mM succinate and 5 mM malate.

Live measurement of mitochondrial Ca²⁺ retention capacity by calcium green

Live mitochondria isolated as described above were stained by incubation in MiR05 buffer supplemented with 10 mM succinate, 5 mM malate, and 1 μM calcium green AM (Life Technologies, #C3012) for 20 min on a shaker at 37 °C. Before measurement, the mitochondria were pelleted at 6500 rcf for 5 min, washed and resuspended in MiR05 supplemented with 10 mM succinate, 5 mM malate, and 5 μM of either CsH or CsA. In experiments where the mitochondria were loaded with Ca²⁺ before measurement, this was achieved by incubation in MiR05 additionally supplemented with 150 μM CaCl₂ on a shaker at 37 °C for 10 min after the first washing step and followed by a second washing step.

Measurement of mitochondrial membrane potential by TMRE and TMRM

For measurement in whole cells, the cells were stained by incubation in full growth medium containing 100 nM tetramethylrhodamine ethyl ester (TMRE; AAT Bioquest, Sunnyvale, CA, USA; #22220) and 10 mM HEPES at 37 °C in the dark for 15 min. After that, the cells were washed and resuspended in full growth medium containing 10 mM HEPES and were incubated at 37 °C in the dark for another 15 min. The cells were maintained at these conditions until measurement. For measurement in live mitochondria, these were isolated as described above, resuspended in sodium-free mitochondrial respiration buffer MiR05 supplemented with 10 mM succinate, 5 mM malat, and 1 mM ADP, stained with 50 nM tetramethylrhodamine methyl ester (TMRM; Life Technologies, #T668) at 37 °C for 15 min, and washed and resuspended in MiR05 additionally supplemented with 1.6 μM cyclosporin H (CsH) to prevent passive TMRM leakage. For live measurement, TMRE or TMRM fluorescence was measured using an LSRFortessa flow cytometer recording fluorescence in the PE channel (Ex 488 nm, Em 575 ± 26 nm). For each sample, after at least 30 s

of baseline measurement, the stimulus was added and measurement was continued for at least 10 min. For the titration of the EC₅₀ for mitochondrial depolarisation, TMRE fluorescence was measured using a Synergy Mx microplate reader (BioTek, Bad Friedrichshall, Germany) recording fluorescence at Ex 549 ± 9 nm, Em 575 ± 9 nm. TMRE fluorescence was measured right before and 10 min after addition of PXA. EC₅₀ values were calculated using Prism v7.01.

Live O₂ respirometry measurements

This method was adapted from previously published protocols^{19,57}. All measurements were performed using an OROBOROS Oxygraph-2k (Oroboros Instruments, Innsbruck, Austria). For measurement of total cellular respiration, intact cells (2 × 10⁶ cells/ml) were used and maintained in full growth medium supplemented with 20 mM HEPES during measurement. For direct measurement of mitochondrial respiration, digitonin-permeabilised cells (2 × 10⁶ cells/ml) were used and maintained in mitochondrial respiration buffer MiR05 during measurement. To induce respiration, 10 mM glutamate, 5 mM malate, 1 mM ADP, and 5 μg/ml digitonin were added. The following complex-specific ETC inducers were used: For complex II, 10 mM succinate (from Sigma, #S3674); for complex III, 1 mM tetramethylhydroquinone / duroquinol (from TCI Germany, Eschborn, Germany; #T0822); for complex IV, 50 μM tetramethyl-*p*-phenylenediamine (TMPD; from Sigma, #87890) supplemented with 200 μM ascorbate.

Fluorimetric O₂ consumption assay

This measurement was performed using the *MITO-ID[®] Extracellular O₂ Sensor Kit (High Sensitivity)* (Enzo Life Sciences, Lörrach, Germany; #51045) according to manufacturer's instructions. Fluorescence was measured using a Synergy Mx microplate reader (Ex 340–400 nm, Em 630–680 nm; time-resolved fluorescence, delay time 30 μs, integration time 100 μs).

Measurement of cellular ATP levels

This measurement was performed using the *Mitochondrial ToxGlo[™] Assay* (Promega, Mannheim, Germany; #G8000) according to manufacturer's instructions. Since most cancer cells prefer ATP synthesis by glycolysis over OXPHOS if glucose is present, this experiment was conducted in the presence of either glucose or galactose as the only available sugar, the latter of which reduces the net ATP yield of glycolysis to zero and forces the cells to resort to OXPHOS for ATP production^{58,59}.

Fluorimetric caspase-3 activity assay

Caspase-3 activity was measured as described previously⁶⁰. Briefly, cells were harvested by centrifugation at

600 rcf and lysed with 50 μ l of ice-cold lysis buffer (20 mM HEPES, 84 mM KCl, 10 mM, MgCl₂, 200 μ M EDTA, 200 μ M EGTA, 0.5% NP-40, 1 μ g/ml leupeptin, 1 μ g/ml pepstatin, 5 μ g/ml aprotinin) on ice for 10 min. Cell lysates were transferred to a black flat-bottom microplate and mixed with 150 μ l of ice-cold reaction buffer (50 mM HEPES, 100 mM NaCl, 10% sucrose, 0.1% CHAPS, 2 mM CaCl₂, 13.35 mM DTT, 70 μ M Ac-DEVD-AMC). The kinetics of AMC release were monitored by measuring AMC fluorescence intensity (Ex 360 nm, Em 450 nm) at 37 °C in intervals of 2 min over a time course of 150 min, using a Synergy Mx microplate reader. The slope of the linear range of the fluorescence curves (Δ rfu/min) was considered as corresponding to caspase-3 activity.

Measurement of cell viability by MTT assay

Cell viability was determined by the ability to convert the yellow MTT substrate (Roth, #4022) into a blue formazan product. MTT solution (5 mg/ml MTT in PBS) was added to cells to a final concentration of 1 mg/ml, and the cells were then incubated at 37 °C for 60 min and pelleted at 600 rcf. The supernatant was discarded and replaced with DMSO. After the formazan crystals were fully dissolved, absorption was measured (test wavelength 570 nm, reference wavelength 650 nm). Reference absorbance was subtracted from test absorbance. Cell-free medium samples were considered as having 0% viability and the average of the control samples was considered as having 100% viability. IC₅₀ values were calculated using Prism v7.01.

Immunoblotting

Cells were harvested by centrifugation at 11,000 rcf in 4 °C for 10 s, quick-frozen in liquid nitrogen, thawed on ice, incubated in lysis buffer (20 mM Tris-HCl, 150 mM NaCl, 1% v/v Triton X-100, 0.5 mM EDTA, 1 mM Na₃VO₄, 10 mM NaF, 2.5 mM Na₄P₂O₇, 0.5% sodium deoxycholate, protease inhibitor (Sigma, #P2714)) for 30 min and vortexed repeatedly. The cell lysates were then cleared from cell debris by centrifugation at 20,000 rcf for 15 min. Sodium dodecyl sulfate-polyacrylamide gel electrophoresis and western blot were performed according to standard protocol. The antibodies used for protein detection were mouse anti-phospho-tyrosine (Merck-Millipore, Darmstadt, Germany; clone 4G10, #05-1050); rabbit anti-OPA1 (described previously³⁷); mouse anti-ACTB (Sigma; clone AC-74, #A5316); and mouse anti-VCL (Sigma; clone hVIN-1, #V9131).

Confocal microscopy

Live imaging of HCT116 cells transiently expressing GFP-BAX and SMAC-mCherry was performed using a Zeiss LSM 710 ConfoCor3 microscope (Carl Zeiss, Jena, Germany) with a C-Apochromat \times 40 N.A. 1.2 water

immersion objective (Zeiss). Excitation light came from argon ion (488 nm) and DPSS (561 nm) lasers. The cells were maintained in full growth medium at 37 °C and 5% CO₂ during imaging. Images were recorded every 5 min and were processed with Fiji⁶¹. For each time frame, the standard deviation (SD) of the fluorescence intensity was measured for each channel. A low SD was considered as corresponding to homogenous distribution, whereas a high SD was considered as corresponding to accumulation.

Live imaging of HeLa cells stably expressing mito-DsRed was performed using a Cell Observer SD Dual Cam spinning disc confocal microscope (Zeiss) equipped with a C-Apochromat 63 \times , N.A. of 1.45 oil-immersion objective. Excitation light came from an argon ion (488 nm) and DPSS (561 nm) laser. The cells were maintained in full growth medium supplemented with 10 mM HEPES at 37 °C during imaging. Images were recorded every 5 s.

Live imaging of MEF cells stably expressing mito-DsRed was performed using a Perkin Elmer Spinning Disc microscope with a 60 \times objective (oil-immersion and NA = 1.49) at an excitation wavelength of 561 nm. The videos were obtained at 1000 \times 1000 pixel resolution with a Hamamatsu C9100 camera. The cells were maintained in full growth medium supplemented with 10 mM HEPES at 37 °C during imaging.

For imaging of fixed HeLa and MEF cells, the cells were seeded on glass coverslips and grown to 60–90% confluence prior to experiments. Cells were treated with either 10 μ M PXA, 10 μ M CCCP or 0.1% v/v DMSO for 30 min, and were fixed by incubation with pre-warmed 4% paraformaldehyde in PBS at 37 °C for 10 min. Coverslips were then washed once with PBS, followed by incubation with PBS supplemented with 0.5% Triton X-100 for 10 min at RT. The coverslips were washed three times for 3–5 min with PBS supplemented with 0.2% Tween-20 (PBS-T). The coverslips were then incubated at RT for 30 min with blocking buffer (PBS-T supplemented with 0.2% fish gelatin and 5% goat serum) in a humidified box, followed by 1 h incubation with primary antibodies (anti-HSP60 clone N-20, #sc-1052 and anti-TOMM20 clone FL-145, #sc-11415 both from Santa Cruz, Dallas, TX, USA) diluted in blocking buffer. The coverslips were then washed three times with PBS-T, and incubated with blocking buffer for 30 min before adding secondary antibodies (Alexa Fluor 488-labelled donkey anti-goat and Alexa Fluor 594-labelled donkey anti-rabbit). Immunofluorescence images were acquired with a Marianas spinning disc confocal microscope (Intelligent Imaging Innovations, Denver, CO, USA).

Transmission electron microscopy

TEM samples were fixed for a minimum of 4 h in 2.5% v/v glutaraldehyde (GA) and 4% w/v paraformaldehyde

(PFA) in 0.1 M cacodylate buffer (pH 7.4) at 4 °C. Then, samples were incubated in 1% osmium tetroxide in 0.1 M cacodylate buffer for 2 h. Dehydration was achieved using acetone (50%, 70%, 90% and 100%) and block contrast was applied (1% phosphotungstic acid/0.5% uranylacetate in 70% acetone). A SPURR embedding kit (Serva, Heidelberg, Germany) was used to embed samples, which were polymerised overnight at 70 °C, before cutting into 80 nm sections using an Ultracut EM UC7 (Leica, Wetzlar, Germany). Images were captured using an H600 TEM (Hitachi, Tokyo, Japan) at 75 kV.

Acknowledgements

We thank Michael Engelke for providing Ramos B lymphocytes, Hiromi Sesaki for providing wild-type and DRP1-KO MEFs, Frank Essmann for providing HCT116 cells, and Aviva M. Tolkovsky for providing mito-DsRed-expressing HeLa cells. We are furthermore indebted to Thomas Langer for providing wild-type, OMA1-KO, YME1L1 KO and OMA1/YME1L1 DKO MEFs. We thank Stephen Tait for providing the plasmid pcDNA3-Smac(1-60)mCherry, Nathan R. Brady for providing the plasmid pGFP-Bax, and Toshio Kitamura for providing Plat-E cells. This study was supported by the Deutsche Forschungsgemeinschaft STO 864/3-1, STO 864/4-1, STO 864/5-1 (to B.S.), GRK 2158 (to P.P., to S.W. and to B.S.), and SFB 974 Project B09 (to A.S.R.), the Research Committee of the Medical Faculty of the Heinrich Heine University Düsseldorf 22/2015 (to B.S.) and 02/2015 (to A.S.R. and R.A.) and 37/2015 (to A.K.K.), and the Düsseldorf School of Oncology (to S.W. and B.S.; funded by the Comprehensive Cancer Centre Düsseldorf/Deutsche Krebshilfe and the Medical Faculty of the Heinrich Heine University Düsseldorf).

Author details

¹Institute of Molecular Medicine I, Medical Faculty, Heinrich Heine University Düsseldorf, 40225 Düsseldorf, Germany. ²Institute of Biochemistry and Molecular Biology I, Medical Faculty, Heinrich Heine University Düsseldorf, 40225 Düsseldorf, Germany. ³Institute of Pharmaceutical Biology and Biotechnology, Faculty of Mathematics and Natural Sciences, Heinrich Heine University Düsseldorf, 40225 Düsseldorf, Germany. ⁴Institute of Anatomy I, Medical Faculty, Heinrich Heine University Düsseldorf, 40225 Düsseldorf, Germany. ⁵Laboratory of Molecular and Cellular Signaling, Department of Cellular and Molecular Medicine, KU Leuven, 3000 Leuven, Belgium. ⁶Center for Advanced Imaging, Faculty of Mathematics and Natural Sciences, Heinrich Heine University Düsseldorf, 40225 Düsseldorf, Germany. ⁷Interfaculty Institute of Biochemistry, Eberhard Karls University Tübingen, 72076 Tübingen, Germany. ⁸Department of Biological Chemistry, David Geffen School of Medicine at UCLA, Los Angeles, CA 90095, USA

Conflict of interest

The authors declare that they have no conflict of interest.

Publisher's note

Springer Nature remains neutral with regard to jurisdictional claims in published maps and institutional affiliations.

Supplementary Information accompanies this paper at (<https://doi.org/10.1038/s41419-018-0312-8>).

Received: 1 December 2017 Accepted: 4 January 2018

Published online: 19 February 2018

References

- Vyas, S., Zaganjor, E. & Haigis, M. C. Mitochondria and Cancer. *Cell* **166**, 555–566 (2016).
- Rizzuto, R., De Stefani, D., Raffaello, A. & Mammucari, C. Mitochondria as sensors and regulators of calcium signalling. *Nat. Rev. Mol. Cell Biol.* **13**, 566–578 (2012).
- Nunnari, J. & Suomalainen, A. Mitochondria: in sickness and in health. *Cell* **148**, 1145–1159 (2012).
- Mishra, P. & Chan, D. C. Metabolic regulation of mitochondrial dynamics. *J. Cell Biol.* **212**, 379–387 (2016).
- Youle, R. J. & van der Bliek, A. M. Mitochondrial fission, fusion, and stress. *Science* **337**, 1062–1065 (2012).
- van der Bliek, A. M., Shen, Q., Kawajiri, S. Mechanisms of mitochondrial fission and fusion. *Cold Spring Harb. Perspect. Biol.* **5**, a011072 (2013).
- Demaurex, N., Poburko, D. & Frieden, M. Regulation of plasma membrane calcium fluxes by mitochondria. *Biochim. Biophys. Acta* **1787**, 1383–1394 (2009).
- Palty, R. et al. NCLX is an essential component of mitochondrial Na⁺/Ca²⁺ exchange. *Proc. Natl Acad. Sci. USA* **107**, 436–441 (2010).
- Jiang, D., Zhao, L. & Clapham, D. E. Genome-wide RNAi screen identifies Letm1 as a mitochondrial Ca²⁺/H⁺ antiporter. *Science* **326**, 144–147 (2009).
- Bonora, M. et al. Comprehensive analysis of mitochondrial permeability transition pore activity in living cells using fluorescence-imaging-based techniques. *Nat. Protoc.* **11**, 1067–1080 (2016).
- Rao, V. K., Carlson, E. A. & Yan, S. S. Mitochondrial permeability transition pore is a potential drug target for neurodegeneration. *Biochim. Biophys. Acta* **1842**, 1267–1272 (2014).
- Chipuk, J. E. & Green, D. R. Dissecting p53-dependent apoptosis. *Cell Death Differ.* **13**, 994–1002 (2006).
- Wallace, K. B. & Starkov, A. A. Mitochondrial targets of drug toxicity. *Annu. Rev. Pharmacol. Toxicol.* **40**, 353–388 (2000).
- Isaka, M. et al. Phomoxanthones A and B, novel xanthone dimers from the endophytic fungus *Phomopsis* Species. *J. Nat. Prod.* **64**, 1015–1018 (2001).
- Elsässer, B. et al. X-ray structure determination, absolute configuration and biological activity of phomoxanthone A. *Eur. J. Org. Chem.* **2005**, 4563–4570 (2005).
- Rönsberg, D. et al. Pro-apoptotic and immunostimulatory tetrahydroxanthone dimers from the endophytic fungus *Phomopsis longicolla*. *J. Org. Chem.* **78**, 12409–12425 (2013).
- Frank, M. et al. Phomoxanthone A - from mangrove forests to anticancer therapy. *Curr. Med. Chem.* **22**, 3523–3532 (2015).
- Petronilli, V. et al. Transient and long-lasting openings of the mitochondrial permeability transition pore can be monitored directly in intact cells by changes in mitochondrial calcein fluorescence. *Biophys. J.* **76**, 725–734 (1999).
- Salabei, J. K., Gibb, A. A. & Hill, B. G. Comprehensive measurement of respiratory activity in permeabilized cells using extracellular flux analysis. *Nat. Protoc.* **9**, 421–438 (2014).
- Baker, M. J. et al. Stress-induced OMA1 activation and autocatalytic turnover regulate OPA1-dependent mitochondrial dynamics. *EMBO J.* **33**, 578–593 (2014).
- de la Fuente, S., Fonteriz, R. I., de la Cruz, P. J., Montero, M. & Alvarez, J. Mitochondrial free [Ca²⁺] dynamics measured with a novel low-Ca(2+) affinity aequorin probe. *Biochem. J.* **445**, 371–376 (2012).
- Hoth, M., Fanger, C. M. & Lewis, R. S. Mitochondrial regulation of store-operated calcium signaling in T lymphocytes. *J. Cell Biol.* **137**, 633–648 (1997).
- de Andrade, P. B. et al. Diabetes-associated mitochondrial DNA mutation A3243G impairs cellular metabolic pathways necessary for beta cell function. *Diabetologia* **49**, 1816–1826 (2006).
- Trenker, M., Malli, R., Fertschaj, I., Levak-Frank, S. & Graier, W. F. Uncoupling proteins 2 and 3 are fundamental for mitochondrial Ca²⁺ uniport. *Nat. Cell Biol.* **9**, 445–452 (2007).
- Fülöp, L., Szanda, G., Eryedi, B., Várnai, P. & Spät, A. The effect of OPA1 on mitochondrial Ca²⁺ signaling. *PLoS ONE* **6**, e25199 (2011).
- MacVicar, T. & Langer, T. OPA1 processing in cell death and disease - the long and short of it. *J. Cell Sci.* **129**, 2297–2306 (2016).
- Zick, M., Rabl, R. & Reichert, A. S. Cristae formation-linking ultrastructure and function of mitochondria. *Biochim. Biophys. Acta* **1793**, 5–19 (2009).
- Scorrano, L. et al. A distinct pathway remodels mitochondrial cristae and mobilizes cytochrome c during apoptosis. *Dev. Cell* **2**, 55–67 (2002).
- Anand, R. et al. The i-AAA protease YME1L and OMA1 cleave OPA1 to balance mitochondrial fusion and fission. *J. Cell Biol.* **204**, 919–929 (2014).
- Head, B., Griparic, L., Amiri, M., Gandre-Babbe, S. & van der Bliek, A. M. Inducible proteolytic inactivation of OPA1 mediated by the OMA1 protease in mammalian cells. *J. Cell Biol.* **187**, 959–966 (2009).
- Ishihara, N., Fujita, Y., Oka, T. & Mihara, K. Regulation of mitochondrial morphology through proteolytic cleavage of OPA1. *EMBO J.* **25**, 2966–2977 (2006).

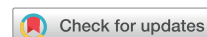
32. Duvezin-Caubet, S. et al. Proteolytic processing of OPA1 links mitochondrial dysfunction to alterations in mitochondrial morphology. *J. Biol. Chem.* **281**, 37972–37979 (2006).
33. Wakabayashi, J. et al. The dynamin-related GTPase Drp1 is required for embryonic and brain development in mice. *J. Cell Biol.* **186**, 805–816 (2009).
34. Ishihara, N. et al. Mitochondrial fission factor Drp1 is essential for embryonic development and synapse formation in mice. *Nat. Cell Biol.* **11**, 958–966 (2009).
35. Suen, D. F., Norris, K. L. & Youle, R. J. Mitochondrial dynamics and apoptosis. *Genes Dev.* **22**, 1577–1590 (2008).
36. Labrousse, A. M., Zappaterra, M. D., Rube, D. A. & van der Bliek, A. M. *C. elegans* dynamin-related protein DRP-1 controls severing of the mitochondrial outer membrane. *Mol. Cell* **4**, 815–826 (1999).
37. Barrera, M., Koob, S., Dikov, D., Vogel, F. & Reichert, A. S. OPA1 functionally interacts with MIC60 but is dispensable for crista junction formation. *FEBS Lett.* **590**, 3309–3322 (2016).
38. van Meer, G. & de Kroon, A. I. Lipid map of the mammalian cell. *J. Cell Sci.* **124**, 5–8 (2011). (Pt 1).
39. Ardail, D. et al. Mitochondrial contact sites. Lipid composition and dynamics. *J. Biol. Chem.* **265**, 18797–18802 (1990).
40. Weber, T. A. et al. APOOL is a cardiolipin-binding constituent of the Mitofilin/MINOS protein complex determining cristae morphology in mammalian mitochondria. *PLoS ONE* **8**, e63683 (2013).
41. Planas-Iglesias, J. et al. Cardiolipin interactions with proteins. *Biophys. J.* **109**, 1282–1294 (2015).
42. Acehan, D. et al. Cardiolipin affects the supramolecular organization of ATP synthase in mitochondria. *Biophys. J.* **100**, 2184–2192 (2011).
43. Pfeiffer, K. et al. Cardiolipin stabilizes respiratory chain supercomplexes. *J. Biol. Chem.* **278**, 52873–52880 (2003).
44. Zhang, M., Mileykovskaya, E. & Dowhan, W. Gluing the respiratory chain together. Cardiolipin is required for supercomplex formation in the inner mitochondrial membrane. *J. Biol. Chem.* **277**, 43553–43556 (2002).
45. Bampton, E. T. W., Goemans, C. G., Niranjani, D., Mizushima, N. & Tolkovsky, A. M. The dynamics of autophagy visualised in live cells: from autophagosome formation to fusion with endo/lysosomes. *Autophagy* **1**, 23–36 (2014).
46. Ran, F. A. et al. Genome engineering using the CRISPR-Cas9 system. *Nat. Protoc.* **8**, 2281–2308 (2013).
47. Tait, S. W. et al. Resistance to caspase-independent cell death requires persistence of intact mitochondria. *Dev. Cell* **18**, 802–813 (2010).
48. Qin, T., Iwata, T., Ransom, T. T., Beutler, J. A. & Porco, J. A. Jr. Syntheses of dimeric tetrahydroxanthones with varied linkages: Investigation of “Shape-shifting” properties. *J. Am. Chem. Soc.* **137**, 15225–15233 (2015).
49. Hastie, C. J., McLauchlan, H. J. & Cohen, P. Assay of protein kinases using radiolabeled ATP: a protocol. *Nat. Protoc.* **1**, 968–971 (2006).
50. Bain, J. et al. The selectivity of protein kinase inhibitors: a further update. *Biochem. J.* **408**, 297–315 (2007).
51. Vervloessem, T., Ivanova, H., Luyten, T., Parys, J. B., Bultynck, G. The selective Bcl-2 inhibitor venetoclax, a BH3 mimetic, does not dysregulate intracellular Ca²⁺ signaling. *Biochim. Biophys. Acta* **1864**, 968–976 (2017).
52. Bittremieux, M. et al. DPB162-AE, an inhibitor of store-operated Ca²⁺ entry, can deplete the endoplasmic reticulum Ca²⁺ store. *Cell Calcium* **62**, 60–70 (2017).
53. Suzuki, J. et al. Imaging intraorganellar Ca²⁺ at subcellular resolution using CEPIA. *Nat. Commun.* **5**, 4153 (2014).
54. Nagai, T., Sawano, A., Park, E. S. & Miyawaki, A. Circularly permuted green fluorescent proteins engineered to sense Ca²⁺. *Proc. Natl Acad. Sci. USA* **98**, 3197–3202 (2001).
55. Filippin, L. et al. Improved strategies for the delivery of GFP-based Ca²⁺ sensors into the mitochondrial matrix. *Cell Calcium* **37**, 129–136 (2005).
56. Petronilli, V., Penzo, D., Scorrano, L., Bernardi, P. & Di Lisa, F. The mitochondrial permeability transition, release of cytochrome c and cell death. Correlation with the duration of pore openings in situ. *J. Biol. Chem.* **276**, 12030–12034 (2001).
57. Kuznetsov, A. V. et al. Analysis of mitochondrial function in situ permeabilized muscle fibers, tissues and cells. *Nat. Protoc.* **3**, 965–976 (2008).
58. Warburg, O. On the origin of cancer cells. *Science* **123**, 309–314 (1956).
59. Marroquin, L. D., Hynes, J., Dykens, J. A., Jamieson, J. D. & Will, Y. Circumventing the Crabtree effect: replacing media glucose with galactose increases susceptibility of HepG2 cells to mitochondrial toxicants. *Toxicol. Sci.* **97**, 539–547 (2007).
60. Czugala, M. et al. Efficient and safe gene delivery to human corneal endothelium using magnetic nanoparticles. *Nanomedicine (Lond.)* **11**, 1787–1800 (2016).
61. Schindelin, J. et al. Fiji: an open-source platform for biological-image analysis. *Nat. Methods* **9**, 676–682 (2012).

Publication 5

Manuscript “Dithiodiketopiperazine derivatives from endophytic fungi *Trichoderma harzianum* and *Epicoccum nigrum*”:

Harwoko H, Daletos G, Stuhldreier E, Lee J, Wesselborg S, Feldbrügge M, Müller WEG, Kalscheuer R, Ancheeva E, Proksch P.

Natural Product Research (2019). doi: 10.1080/14786419.2019.1627348



Dithiodiketopiperazine derivatives from endophytic fungi *Trichoderma harzianum* and *Epicoccum nigrum*

Harwoko Harwoko^{a,b} , Georgios Daletos^a , Fabian Stuhldreier^c, Jungho Lee^{d,e}, Sebastian Wesselborg^c, Michael Feldbrügge^{d,e}, Werner E. G. Müller^f, Rainer Kalscheuer^a , Elena Ancheeva^a  and Peter Proksch^a

^aInstitute of Pharmaceutical Biology and Biotechnology, Heinrich Heine University, Universitaetsstrasse 1, Geb. 26.23, Duesseldorf, Germany; ^bDepartment of Pharmacy, Faculty of Health Sciences, Universitas Jenderal Soedirman, Jalan dr. Soeparno Karangwangkal, Purwokerto, Indonesia; ^cInstitute of Molecular Medicine I, Medical Faculty, Heinrich Heine University, Universitaetsstrasse 1, Geb. 23.12, Duesseldorf, Germany; ^dInstitute for Microbiology, Heinrich Heine University, Universitaetsstrasse 1, Geb. 26.12, Duesseldorf, Germany; ^eBioeconomy Science Center (BioSC), c/o Forschungszentrum Juelich, Juelich, Germany; ^fInstitute of Physiological Chemistry, Universitaetsmedizin der Johannes Gutenberg-Universitaet Mainz, Mainz, Germany

ABSTRACT

A new epidithiodiketopiperazine (ETP), pretrichodermamide G (**1**), along with three known (epi)dithiodiketopiperazines (**2-4**) were isolated from cultures of *Trichoderma harzianum* and *Epicoccum nigrum*, endophytic fungi associated with medicinal plants *Zingiber officinale* and *Salix* sp., respectively. The structure of the new compound (**1**) was established on the basis of spectroscopic data, including 1D/2D NMR and HRESIMS. The isolated compounds were investigated for their antifungal, antibacterial and cytotoxic potential against a panel of microorganisms and cell lines. Pretrichodermamide A (**2**) displayed antimicrobial activity towards the plant pathogenic fungus *Ustilago maydis* and the human pathogenic bacterium *Mycobacterium tuberculosis* with MIC values of 1 mg/mL (2 mM) and 25 µg/mL (50 µM), respectively. Meanwhile, epicorazine A (**3**) exhibited strong to moderate cytotoxicity against L5178Y, Ramos, and Jurkat J16 cell lines with IC₅₀ values ranging from 1.3 to 28 µM. Further mechanistic studies indicated that **3** induces apoptotic cell death.

ARTICLE HISTORY

Received 12 February 2019
Accepted 25 May 2019

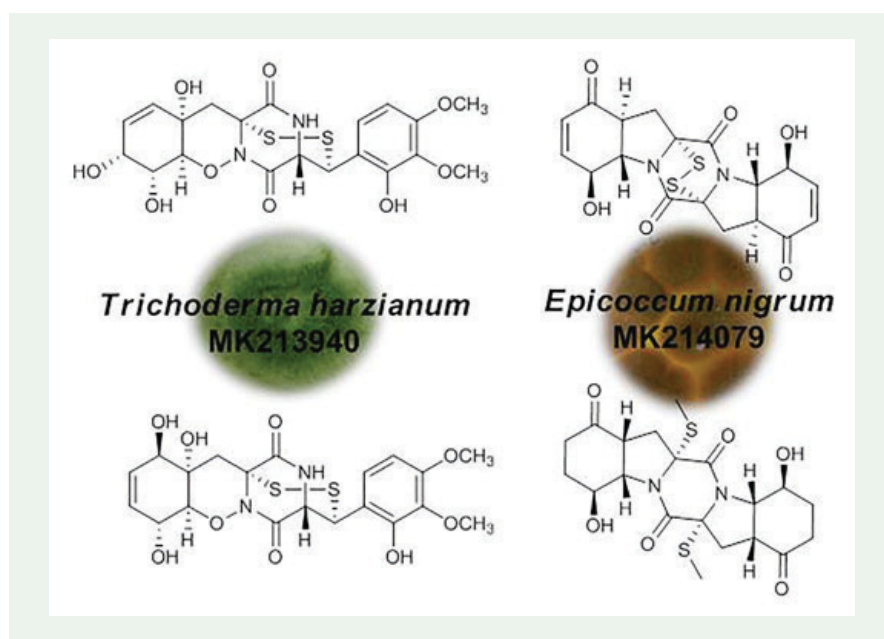
KEYWORDS

Trichoderma harzianum;
Epicoccum nigrum;
epidithiodiketopiperazine;
endophytic fungi;
antimicrobial activity;
cytotoxicity; apoptosis

CONTACT Prof. Dr. Peter Proksch  proksch@uni-duesseldorf.de; Dr. Elena Ancheeva  elena.ancheeva@uni-duesseldorf.de

 Supplemental data for this article can be accessed at <https://doi.org/10.1080/14786419.2019.1627348>.

© 2019 Informa UK Limited, trading as Taylor & Francis Group



1. Introduction

Microorganisms residing in plant tissues without causing any apparent symptoms, namely endophytes, are important resources for the discovery of biologically active compounds with promising agricultural and pharmaceutical applications (Aly et al. 2011). Moreover, endophytes possess the advantage of large-scale production of diverse bioactive metabolites and potential drug leads (Aly et al. 2010) which is not always possible in plants. *Trichoderma* species are recognized as mycoparasites and are widely used in agriculture as biofungicides and bioremediation agents (Błaszczyk et al. 2014; Zeilinger et al. 2016; Ghorbanpour et al. 2018). Similarly, *Epicoccum nigrum* (synonym *E. purpurascens*), which can parasitize the mycelium of fungal pathogens of crops, is used as a biocontrol agent (Madrigal et al. 1991; Koutb and Ali 2010). Diverse bioactive compounds including diketopiperazine alkaloids and various terpenoids were currently reported from these two biocontrol fungi (Wang et al. 2010; Yamazaki et al. 2015a, 2015b; Perveen et al. 2017; Fang et al. 2018; Han et al. 2018; Liang et al. 2019). Moreover, *T. harzianum* was shown to be tolerant towards the heavy metals cadmium and mercury, thus underlying its potential role in the detoxification of environmental pollutants (Faedda et al. 2012).

In the course of our screening for new and bioactive compounds from endophytes associated with medicinal plants, we investigated two endophytic fungal strains, *T. harzianum* MK213940 and *E. nigrum* MK214079 which were isolated from healthy leaves of *Zingiber officinale* (Zingiberaceae) and *Salix* sp. (Salicaceae), respectively. Ginger rhizome is traditionally used as antiemetic and its crude extract and various constituents were shown to exhibit antitumor, immunomodulatory, antiviral, and antimicrobial effects (Chrubasik et al. 2005). Interestingly, the ginger endophyte *T. harzianum* was found to be highly active against common fungal and bacterial pathogens associated with Zingiberaceae crops (Rajan et al. 2002). The second fungus investigated in this study, *E. nigrum* was isolated from willow leaves collected in Russia. *Salix*

sp. (Salicaceae) have been profoundly associated with the discovery of salicylic acid and derivatives exhibiting antiinflammatory, antirheumatic, antipyretic, analgesic, and antiseptic effects (Barnes et al. 2002).

In our previous reports we described a new cytochalasin with potent cytotoxicity, isolated from *T. harzianum* that was obtained from *Cola nitida* leaves (Chen et al. 2015). In addition, *E. nigrum* isolated from leaves of *Mentha suaveolens* Ehr. produced new polyketides that showed *in vitro* inhibitory activity against a panel of protein kinases and histone deacetylases (El Amrani et al. 2014). Herein, we investigated the chemical profiles of new isolates of these fungi. HPLC-DAD and LC-MS analyses of their crude extracts showed that both fungi are able to accumulate a rare fungal secondary metabolites class, epidithiodiketopiperazines (ETPs). These natural products are characterized by an internal disulfide linkage across the diketopiperazine ring (Guimarães et al. 2010). Examples of diketopiperazines (DKPs) that have been previously isolated from fungi belonging to the genus *Trichoderma* or *Epicoccum*, include gliovirin, pretrichodermamide A, trichodermamides A and B, five halogenated ETPs, epicoccins E-T, and epicorazines A and B displaying a wide range of biological activities (Deffieux et al., 1978a, 1978b, Garo et al. 2003; Seephonkai et al. 2006; Guo et al. 2009; Wang et al. 2010; Yamazaki et al. 2015a, 2015b). To date, only eighteen DKP derivatives have been previously reported possessing a rare 1,2-oxazadecaline core (Yokose et al. 1984; Orfali et al. 2015; Yamazaki et al. 2015a, 2015b; Kajula et al. 2016; Yurchenko et al. 2016). In this study, chemical investigation of *T. harzianum* and *E. nigrum* resulted in the isolation of a new ETP (**1**), along with three known derivatives (**2-4**). The structure of the new compound **1** was unequivocally deduced by NMR spectroscopic analysis and mass spectrometry, as well as by comparison with the literature. Antifungal, antibacterial and cytotoxic assays results of **1-4** are likewise reported.

2. Results and discussion

Four dithiodiketopiperazines from two endophytes were isolated and identified in this study. Among them, a new ETP derivative (**1**) together with pretrichodermamide A (**2**) were isolated from the endophytic fungus *T. harzianum* and two known bioactive secondary metabolites, epicorazine A (**3**) and ent-epicoccin G (**4**) were obtained from the culture of *E. nigrum* (Deffieux et al. 1978a; Seephonkai et al. 2006; Wang et al. 2010). Structures of these compounds are shown in Figure 1. To obtain these compounds, the EtOAc extracts of the aforementioned fungi were partitioned against *n*-hexane and 10% MeOH and the MeOH phases were further separated by VLC, following by size-exclusion chromatography over Sephadex LH-20. As a final purification step, semi-preparative HPLC was applied to afford compounds **1-4**.

Compound **1** was isolated as yellow solid. Its molecular formula was established by HRESIMS as C₂₀H₂₂N₂O₉S₂ (11 degrees of unsaturation) on the basis of the protonated molecular ion peak at *m/z* 499.0839 [M + H]⁺. The ¹H and ¹³C NMR data of **1** (Table S1) were similar to those of pretrichodermamides D or E, secondary metabolites biosynthesized by the marine algae-derived fungus *Penicillium* sp. (Yurchenko et al. 2016). Accordingly, the ¹H and ¹³C NMR spectra of **1** showed the signals of two methoxy groups (δ_{H} 3.78/3.67; δ_{C} 55.5/60.0), one phenolic hydroxy proton (δ_{H} 9.47), and two

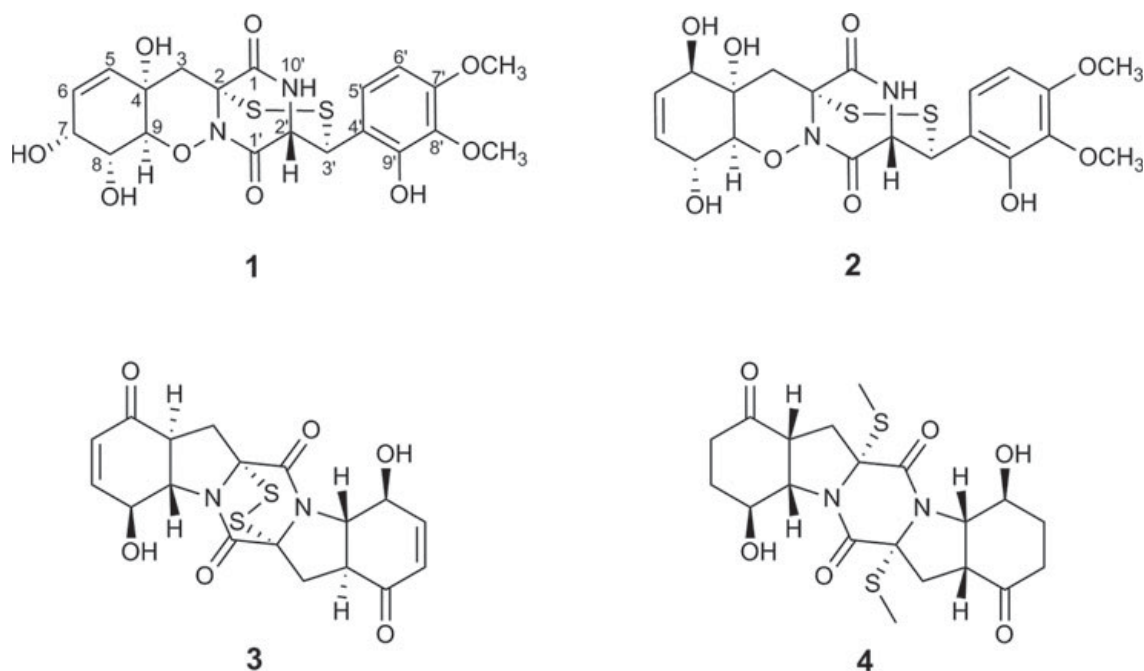


Figure 1. Dithiodiketopiperazines produced by the endophytic fungi *Trichoderma harzianum* (1-2) and *Epicoccum nigrum* (3-4).

ortho coupled aromatic methines (δ_{H} 7.43/6.55, $J = 8.8$ Hz; δ_{C} 122.6/103.1) (Yurchenko et al. 2016). Observed HMBC correlations arising from the aromatic proton H-5' to C-7' (δ_{C} 153.1) and C-9' (δ_{C} 147.6) and from H-6' to C-4' (δ_{C} 116.2) and C-8' (δ_{C} 136.0) suggested the presence of a tetrasubstituted benzene ring, in which 7'-OMe and 8'-OMe groups are attached to the respective carbons. Further correlations from 9'-OH to C-4', C-8' and C-9' confirmed a 2,3-dimethoxyphenol unit in **1**.

A series of ^1H - ^1H COSY cross-peaks established a spin system starting from H-5 (δ_{H} 5.53) and extending till H-9 (δ_{H} 4.13). Moreover, HMBC correlations from H-5 and H-9 to the oxygenated sp^3 carbon C-4 (δ_{C} 66.8) indicated the presence of a cyclohexene ring in the structure of **1**, bearing a double bond at C-5/C-6 and four oxygenated carbons, as in the corresponding ring of the known pretrichodermamide D. These signals were indicative of an oxazine-cyclohexene moiety, identical to that observed for **2** and pretrichodermamide D (Yurchenko et al. 2016), as confirmed by the HMBC correlations from H₂-3 (δ_{H} 2.10, 2.36) to C-4 (δ_{C} 70.8), C-5 (δ_{C} 133.4), and C-9 (δ_{C} 82.2), from 4-OH (δ_{H} 5.27) to C-3 (δ_{C} 37.9), C-4, and C-9, from H-5 to C-7 (δ_{C} 65.8) and C-9, from H-6 to C-4 and C-8 (δ_{C} 66.3) (Figure S1). The ^1H - ^1H COSY correlation between H-2' (δ_{H} 4.37) and NH-10' amino group (δ_{H} 8.97) in addition to HMBC correlations from NH-10' to C-1' (δ_{C} 164.8) and C-2 (δ_{C} 68.0), and the remaining two sulfur atoms in the molecular formula of **1**, suggested the presence of a 6-6-6-7 epidithiodiketopiperazine skeleton similar to that of its derivatives, pretrichodermamides A-F (Orfali et al. 2015; Yurchenko et al. 2016).

The relative configuration of stereogenic centers in **1** was deduced to be the same as in the closely related natural product, pretrichodermamide D based on the identical values of observed chemical shifts at positions CH5 – CH9 ($\Delta\delta_{\text{H}} < 0.05$ ppm; $\Delta\delta_{\text{C}} < 0.5$ ppm), and ^1H – ^1H coupling constants patterns of H₇₋₈ (4.8 Hz) and H₈₋₉ (8.8 Hz) and H_{2'-3'} (2.1 Hz) (Seephonkai et al. 2006; Orfali et al. 2015; Yurchenko et al. 2016).

Moreover, the ROESY correlations of H-9 with 4-OH, 7-OH, and 8-OH (Figure S1) supported this structural assignment, as observed for **2** and pretrichodermamide D. Considering the common biosynthetic origin of **1** and other pretrichodermamides and its negative optical rotation value, the absolute configuration of **1** is suggested to be the same as for pretrichodermamide D (Orfali et al. 2015; Yurchenko et al. 2016). On the basis of the above data, **1** was determined as a new 1,2-oxazadecaline epidithiodiketopiperazine, N-demethyl derivative of pretrichodermamide D, and the trivial name pretrichodermamide G is proposed for this natural product (Orfali et al. 2015; Yurchenko et al. 2016).

The structures of pretrichodermamide A (**2**), epicorazine A (**3**) and ent-epicoccin G (**4**) were identified by NMR and ESI-MS data and by comparison with the literature (Deffieux et al. 1978a; Seephonkai et al. 2006; Wang et al. 2010). Compounds **1** and **2** are rare derivatives of ETPs as the disulfide bond is connected between the α - and β -positions of two amino acid residues, similar to gliovirin (Yamazaki et al. 2015a, 2015b). Interestingly, compound **2** was previously isolated from the same genus, *Trichoderma* sp., associated with bamboo leaves and red algae collected in Northeast Thailand and Palau, respectively (Seephonkai et al. 2006; Yamazaki et al. 2015a, 2015b). Compounds **3** and **4** feature symmetrical DKP scaffolds, but only compound **4** possesses free thiomethyl groups among these derivatives.

DKPs **1-4** were subjected to antifungal and antibacterial assays against the phytopathogenic fungus *Ustilago maydis* and a panel of human pathogenic bacteria. Remarkably, pretrichodermamide A (**2**) selectively inhibited the growth of *U. maydis* with an MIC value of 1 mg/mL compared with that of the positive controls nystatin (MIC = 0.02 mg/mL) and nourseothricin (MIC = 2 mg/mL), as shown in Table S2. The latter compound is extensively used as a selection marker to generate transgenic fungal strains (Brachmann et al. 2004). *U. maydis* has been used as a model phytopathogenic fungus, which can infect only *Zea mays* and its progenitor plant (teosinte) causes corn smut, resulting in stunted growth and crop yield losses (Vollmeister et al. 2012; Mueller et al. 2016). Only pretrichodermamide A (**2**) and epicorazine A (**3**) displayed potential inhibitory effects against *U. maydis*, showing zones of inhibition of 15 and 10 mm at 100 μ g/disk, respectively. Meanwhile, nystatin 10 mg/mL and nourseothricin 20 mg/mL displayed inhibition diameters of 29 and 14 mm, respectively (Figure S9). To the best of our knowledge, the growth inhibitory activity of pretrichodermamide A (**2**) and epicorazine A (**3**) against *U. maydis* are reported in this study for the first time. In addition, pretrichodermamide A (**2**) exhibited moderate antitubercular (MIC = 25 μ g/mL) and weak cytotoxic activities, consistent with earlier reports (Seephonkai et al. 2006; Zhou et al. 2013). A further dithiodiketopiperazine related to pretrichodermamide A (**2**), peniciadametizine B, isolated from *Penicillium adametzioides* was reported to display antifungal activity against *Alternaria brassicae* (Liu et al. 2015). Several strains of *T. harzianum* are well-known producers for antifungal metabolites such as isoharzianic acid, harzianopyridone, and trichoharzianol (Vinale et al. 2014; Ahluwalia et al. 2015; Jeerapong et al. 2015).

The initial screening for cytotoxicity of the isolated compounds (**1-4**) indicated that only epicorazine A (**3**) had potent cytotoxic activity against the mouse lymphoma cell line (L5178Y) with IC_{50} value of 1.3 μ M, as well as moderate cytotoxicity against human

lymphoma (Ramos) and leukemia (Jurkat J16) cell lines with IC_{50} values of 28 and $20\ \mu\text{M}$, respectively (Table S3). On the other hand, the new compound **1** and its derivatives pretrichodermamide A (**2**) and ent-epicoccin G (**4**) showed no cytotoxic activity when assayed at doses of $20\text{--}30\ \mu\text{M}$. Similarly, previous cytotoxicity assays for related compounds, i.e. pretrichodermamides A-F and epicoccins A-T indicated weak cytotoxicities (Guo et al. 2009; Wang et al. 2010; Orfali et al. 2015; Yurchenko et al. 2016). The presence of a chlorine atom in several DKP related natural products such as N-methyl-pretrichodermamide B, trichodermamide B, chlorotrithiobrevamide, and chloro-ETP (DC1149B) was found to play a vital role for their cytotoxicity (Garo et al. 2003; Orfali et al. 2015; Yamazaki et al. 2015a, 2015b; Jans et al. 2017). Hence, the chlorohydrin moiety might be precursor to a reactive epoxide in the active form of those derivatives (Garo et al. 2003). In consequence, the replacement of this reactive moiety in case of pretrichodermamides A-F or trichodermamides A and C by a trans vicinal diol eliminates their cytotoxic activity (Orfali et al. 2015; Yurchenko et al. 2016; Jans et al. 2017).

The strong cytotoxic properties of epicorazine A (**3**) have been previously described in the literature, however none of the former studies provided insights into the mechanism of action of this dithiodiketopiperazine (Kleinwächter et al. 2001; Kong et al. 2014; Bingui et al. 2015). In this study, we investigated the influence of **3** on apoptosis, the programmed cell death which is generally characterized by membrane blebbing and DNA fragmentation leading to cell death. Cysteine-dependent aspartate-directed proteases (caspases) are the key regulators for inducing apoptosis through intrinsic (mitochondrial) or extrinsic (death receptor) pathways (Taylor et al. 2008). Accordingly, in order to estimate the potential contribution of pro-apoptotic mechanisms for the cytotoxicity of epicorazine A (**3**), we analyzed activation of caspase-3 through two different methods: first by immunoblotting for the cleavage of the caspase-3 substrate poly (ADP-ribose) polymerase-1 (PARP-1) and second by measuring the fluorescence of the pro-fluorescent caspase-3 substrate Ac-DEVD-AMC.

Western blot experiments revealed cleavage of the caspase-3-substrate PARP after treatment with epicorazine A (**3**) in both Ramos and Jurkat J16 cell lines, indicating activation of caspase-3 and thus induction of apoptosis. Furthermore, we performed co-incubation with the pan-caspase inhibitor N-(2-quinoly)l-L-valyl-L-aspartyl-(2,6-difluorophenoxy) methylketone (QVD) to prove caspase dependency of the observed cleavage of PARP (Figure S10). QVD completely blocked cleavage of PARP after treatment with epicorazine A (**3**) at concentrations up to $30\ \mu\text{M}$, demonstrating a causative role of caspases and thereby occurrence of apoptosis. Briefly, epicorazine A (**3**) has the potential to induce apoptosis, even though high doses and long incubation periods are needed to kill the tested cancer cells. Thereby, epicorazine A (**3**) and its congeners (epicorazines B-C) have potential therapeutic value for targeting cancer cell (Kleinwächter et al. 2001; Vigushin et al. 2004).

3. Conclusion

Chemical investigation of two endophytic fungi *T. harzianum* and *E. nigrum* resulted in the isolation and characterization of the new pretrichodermamide G (**1**) along with

three known derivatives (**2-4**). Among these dithiodiketopiperazines, **2** exhibited selective antifungal activity against *U. maydis*, whereas **3** revealed potent cytotoxicity through apoptotic cell death. Structure of cyclohexene unit in **2** (substitution pattern and/or location of double bond) is important for the selective antifungal activity of this metabolite (**2** vs **1**), while the presence of α,β -unsaturated carbonyl moiety in **3** is likely to be responsible for its cytotoxicity as the contribution of this functionality to the cytotoxic properties of structurally distinct compounds is well described in the literature (Amslinger 2010; Nakayachi et al. 2004).

Acknowledgments

HH thanks the German Academic Exchange Service (DAAD) for a doctoral scholarship. The authors are grateful to Profs. H. Brötz-Oesterhelt (Eberhard Karls University Tuebingen) and M.U. Kassack (Heinrich Heine University Duesseldorf) for performing antibacterial and cytotoxicity screenings, respectively.

Disclosure statement

No potential conflict of interest was reported by the authors.

Funding

This work was supported by grants from the Deutsche Forschungsgemeinschaft (DFG) GRK 2158 (to PP, RK and SW), the Manchot Foundation (to PP), the DAAD (BALIPEND project number 16GW0107K; to PP), the BMBF (BALIPEND project number 16GW0107K; to PP) and the Bioeconomy Science Center (NRW strategiejektorjekt BioSC number 313/323-400-002 13; to MF).

ORCID

Harwoko Harwoko  <http://orcid.org/0000-0002-4111-7147>

Georgios Daletos  <http://orcid.org/0000-0002-1636-6424>

Rainer Kalscheuer  <http://orcid.org/0000-0002-3378-2067>

Elena Ancheeva  <http://orcid.org/0000-0002-2440-4427>

References

- Ahluwalia V, Kumar J, Rana VS, Sati OP, Walia S. 2015. Comparative evaluation of two *Trichoderma harzianum* strains for major secondary metabolite production and antifungal activity. *Nat Prod Res.* 29(10):914–920.
- Aly AH, Debbab A, Kjer J, Proksch P. 2010. Fungal endophytes from higher plants: a prolific source of phytochemicals and other bioactive natural products. *Fungal Divers.* 41(1):1–16.
- Aly AH, Debbab A, Proksch P. 2011. Fungal endophytes: unique plant inhabitants with great promises. *Appl Microbiol Biotechnol.* 90(6):1829–1845.
- Amslinger S. 2010. The tunable functionality of alpha, beta-unsaturated carbonyl compounds enables their differential application in biological systems. *Chem Med Chem.* 5(3):351–356.
- Barnes J, Anderson LA, Phillipson JD. 2002. *Herbal medicines: a guide for healthcare professionals*. 2nd ed. London: Pharmaceutical Press.
- Bingui W, Linghong M, Caiguo H, Xiaoming L. 2015. Thio-diketopiperazine compound and its preparation method and application as antitumor agent. *Faming Zhuanli Shenqing*, 8pp. CN 104804020A, 20150729, Patent written in Chinese Application: CN 2014 – 10042650.

- Błaszczak L, Siwulski M, Sobieralski K, Lisiecka J, Jędrzycka M. 2014. *Trichoderma* spp. – application and prospects for use in organic farming and industry. *J Plant Prot Res.* 54(4):309–317.
- Brachmann A, König J, Julius C, Feldbrügge M. 2004. A reverse genetic approach for generating gene replacement mutants in *Ustilago maydis*. *Mol Genet Genomics.* 272(2):216–226.
- Chen H, Daletos G, Okoye F, Lai D, Dai H, Proksch P. 2015. A new cytotoxic cytochalasin from the endophytic fungus *Trichoderma harzianum*. *Nat Prod Commun.* 10(4):585–587.
- Chrubasik S, Pittler MH, Roufogalis BD. 2005. Zingiberis rhizoma: a comprehensive review on the ginger effect and efficacy profiles. *Phytomedicine.* 12(9):684–701.
- Deffieux G, Baute MA, Baute R, Filleau MJ. 1978a. New antibiotics from the fungus *Epicoccum nigrum*. II. Epicorazine A: structure elucidation and absolute configuration. *J Antibiot.* 31(11):1102–1105.
- Deffieux G, Filleau, M-J, Baute, R. 1978b. New antibiotics from the fungus *Epicoccum nigrum*. III. Epicorazine B: Structure elucidation and absolute configuration. *J Antibiot.* 31(11):1106–1109.
- El Amrani M, Lai D, Debbab A, Aly AH, Siems K, Seidel C, Schnekenburger M, Gaigneaux A, Diederich M, Feger D, et al. 2014. Protein kinase and HDAC inhibitors from the endophytic fungus *Epicoccum nigrum*. *J Nat Prod.* 77(1):49–56.
- Faedda R, Puglisi I, Sanzaro V, Petrone G, Cacciola SO. 2012. Expression of genes of *Trichoderma harzianum* in response to the presence of cadmium in the substrate. *Nat Prod Res.* 26(24):2301–2308.
- Fang ST, Wang YJ, Ma XY, Yin XL, Ji NY. 2018. Two new sesquiterpenoids from the marine-sediment-derived fungus *Trichoderma harzianum* P1-4. *Nat Prod Res.* 1–7.
- Garo E, Starks CM, Jensen PR, Fenical W, Lobkovsky E, Clardy J. 2003. Trichodermamides A and B, cytotoxic modified dipeptides from the marine-derived fungus *Trichoderma virens*. *J Nat Prod.* 66(3):423–426.
- Ghorbanpour M, Omidvari M, Abbaszadeh-Dahaji P, Omidvar R, Kariman K. 2018. Mechanisms underlying the protective effects of beneficial fungi against plant diseases. *Biol Control.* 117:147–157.
- Guimarães DO, Borges WS, Vieira NJ, de Oliveira LF, da Silva C, Lopes NP, Dias LG, Durán-Patrón R, Collado IG, Pupo MT. 2010. Diketopiperazines produced by endophytic fungi found in association with two Asteraceae species. *Phytochemistry.* 71(11–12):1423–1429.
- Guo H, Sun B, Gao H, Chen X, Liu S, Yao X, Liu X, Che Y. 2009. Diketopiperazines from the *Cordyceps*-colonizing fungus *Epicoccum nigrum*. *J Nat Prod.* 72(12):2115–2119.
- Han MJ, Qin D, Ye TT, Yan X, Wang JQ, Duan XX, Dong JY. 2018. An endophytic fungus from *Trichoderma harzianum* SWUKD3.1610 that produces nigranoic acid and its analogues. *Nat Prod Res.*:1–9.
- Jans PE, Mfuh AM, Arman HD, Shaffer CV, Larionov OV, Mooberry SL. 2017. Cytotoxicity and mechanism of action of the marine-derived fungal metabolite trichodermamide B and synthetic analogues. *J Nat Prod.* 80(3):676–683.
- Jeerapong C, Phupong W, Bangrak P, Intana W, Tuchinda P. 2015. Trichoharzianol, a new antifungal from *Trichoderma harzianum* F031. *J Agric Food Chem.* 63(14):3704–3708.
- Kajula M, Ward JM, Turpeinen A, Tejesvi MV, Hokkanen J, Tolonen A, Häkkänen H, Picart P, Ihalainen J, Sahl H-G, et al. 2016. Bridged epipolythiodiketopiperazines from *Penicillium raciborskii*, an endophytic fungus of *Rhododendron tomentosum* Harmaja. *J Nat Prod.* 79(4):685–690.
- Kleinwächter P, Dahse HM, Luhmann U, Schlegel B, Dornberger K. 2001. Epicorazine C, an antimicrobial metabolite from *Stereum hirsutum* HKI 0195. *J Antibiot.* 54(6):521–525.
- Kong F, Wang Y, Liu P, Dong T, Zhu W. 2014. Thiodiketopiperazines from the marine-derived fungus *Phoma* sp. OUCMDZ-1847. *J Nat Prod.* 77(1):132–137.
- Koutb M, Ali EH. 2010. Potential of *Epicoccum purpurascens* strain 5615 AUMC as a biocontrol agent of *Pythium irregulare* root rot in three leguminous plants. *Mycobiology.* 38(4):286–294.
- Liang XR, Ma XY, Ji NY. 2019. Trichosordarin A, a norditerpene glycoside from the marine-derived fungus *Trichoderma harzianum* R5. *Nat Prod Res.* 1–6.
- Liu Y, Mándi A, Li XM, Meng LH, Kurtán T, Wang BG. 2015. Peniciadametizine A, a dithiodiketopiperazine with a unique spiro[furan-2,7'-pyrazino[1,2-b][1,2]oxazine] skeleton, and a related

- analogue, peniciadametizine B, from the marine sponge-derived fungus *Penicillium adametzioides*. *Mar Drugs*. 13(6):3640–3652.
- Madrigal C, Tadeo JL, Melgarejo P. 1991. Relationship between flavipin production by *Epicoccum nigrum* and antagonism against *Monilinia laxa*. *Mycol Res*. 95(12):1375–1381.
- Mueller DS, Wise KA, Sisson AJ, Allen TW, Bergstrom GC, Bosley DB, Bradley CA, Broders KD, Byamukama E, Chilvers MI, et al. 2016. Corn yield loss estimates due to diseases in the United States and Ontario, Canada from 2012 to 2015. *Plant Health Prog*. 17(3):211–222.
- Nakayachi T, Yasumoto E, Nakano K, Morshed S, Hashimoto K, Kikuchi H, Nishikawa H, Kawase M, Sakagami H. 2004. Structure-activity relationships of α,β -unsaturated ketones as assessed by their cytotoxicity against oral tumor cells. *Anticancer Res*. 24:737–742.
- Orfali RS, Aly AH, Ebrahim W, Abdel-Aziz MS, Müller WEG, Lin W, Daletos G, Proksch P. 2015. Pretrichodermamide C and N-methylpretrichodermamide B, two new cytotoxic epidithiodiketopiperazines from hyper saline lake derived *Penicillium* sp. *Phytochem Lett*. 11:168–172.
- Perveen I, Raza MA, Iqbal T, Naz I, Sehar S, Ahmed S. 2017. Isolation of anticancer and antimicrobial metabolites from *Epicoccum nigrum*; endophyte of *Ferula sumbul*. *Microb Pathog*. 110: 214–224.
- Rajan PP, Gupta SR, Sarma YR, Jackson GVH. 2002. Diseases of ginger and their control with *Trichoderma harzianum*. *Indian Phytopathol*. 55(2):173.
- Seephonkai P, Kongsaree P, Prabpai S, Isaka M, Thebtaranonth Y. 2006. Transformation of an irregularly bridged epidithiodiketopiperazine to trichodermamide A. *Org Lett*. 8(14): 3073–3075.
- Taylor RC, Cullen SP, Martin SJ. 2008. Apoptosis: controlled demolition at the cellular level. *Nat Rev Mol Cell Biol*. 9(3):231–241.
- Vigushin DM, Mirsaidi N, Brooke G, Sun C, Pace P, Inman L, Moody CJ, Coombes RC. 2004. Gliotoxin is a dual inhibitor of farnesyltransferase and geranylgeranyltransferase I with antitumor activity against breast cancer *in vivo*. *Med Oncol*. 21(1):21–30.
- Vinale F, Manganiello G, Nigro M, Mazzei P, Piccolo A, Pascale A, Ruocco M, Marra R, Lombardi N, Lanzuise S, et al. 2014. A novel fungal metabolite with beneficial properties for agricultural applications. *Molecules*. 19(7):9760–9772.
- Vollmeister E, Schipper K, Baumann S, Haag C, Pohlmann T, Stock J, Feldbrügge M. 2012. Fungal development of the plant pathogen *Ustilago maydis*. *FEMS Microbiol Rev*. 36(1):59–77.
- Wang JM, Ding GZ, Fang L, Dai JG, Yu SS, Wang YH, Chen XG, Ma SG, Qu J, Xu S, et al. 2010. Thiodiketopiperazines produced by the endophytic fungus *Epicoccum nigrum*. *J Nat Prod*. 73(7):1240–1249.
- Yamazaki H, Rotinsulu H, Narita R, Takahashi R, Namikoshi M. 2015a. Induced production of halogenated epidithiodiketopiperazines by a marine-derived *Trichoderma cf. brevicompactum* with sodium halides. *J Nat Prod*. 78(10):2319–2321.
- Yamazaki H, Takahashi O, Murakami K, Namikoshi M. 2015b. Induced production of a new unprecedented epitridithiodiketopiperazine, chlorotrithiobrevamide, by a culture of the marine-derived *Trichoderma cf. brevicompactum* with dimethyl sulfoxide. *Tetrahedron Lett*. 56(45): 6262–6265.
- Yokose K, Nakayama N, Miyamoto C, Furumai T, Maruyama HB, Stipanovic RD, Howell CR. 1984. Structure of FA-2097, a new member of the dioxopiperazine antibiotics. *J Antibiot*. 37(6): 667–669.
- Yurchenko AN, Smetanina OF, Ivanets EV, Kalinovskiy AI, Khudyakova YV, Kirichuk NN, Popov RS, Bokemeyer C, von Amsberg G, Chingizova EA, et al. 2016. Pretrichodermamides D–F from a marine algicolous fungus *Penicillium* sp. *KMM 4672*. *Mar Drugs*. 14(7):1–9.
- Zeilinger S, Gruber S, Bansal R, Mukherjee PK. 2016. Secondary metabolism in *Trichoderma* – chemistry meets genomics. *Fungal Biol Rev*. 30(2):74–90.
- Zhou Y, Debbab A, Mándi A, Wray V, Schulz B, Müller WEG, Kassack M, Lin WH, Kurtán T, Proksch P, et al. 2013. Alkaloids from the sponge-associated fungus *Aspergillus* sp. *Eur J Org Chem*. 2013(5):894–906.

Publication 6


Manuscript “First Results from a Screening of 300 Naturally Occurring Compounds: 4,6-dibromo-2-(2',4'-dibromophenoxy)phenol, 4,5,6-tribromo-2-(2',4'-dibromophenoxy)phenol, and 5-epi-nakijinone Q as Substances with the Potential for Anticancer Therapy”:

Mayer S, Prechtel M, Liebfried P, Cadeddu RP, Stuhldreier E, Kohl M, Wenzel F, Stork B, Wesselborg S, Proksch P, Germing U, Haas R, Jäger P.

Marine Drugs 17:521 (2019). doi: 10.3390/md17090521

Article

First Results from a Screening of 300 Naturally Occurring Compounds: 4,6-dibromo-2-(2',4'-dibromophenoxy)phenol, 4,5,6-tribromo-2-(2',4'-dibromophenoxy)phenol, and 5-epi-nakijinone Q as Substances with the Potential for Anticancer Therapy

Saskia Mayer ^{1,†}, Marie Prechtel ^{1,†}, Pia Liebfried ^{2,†}, Ron-Patrick Cadeddu ² , Fabian Stuhldreier ³ , Matthias Kohl ¹ , Folker Wenzel ¹, Björn Stork ³ , Sebastian Wesselborg ³, Peter Proksch ⁴, Ulrich Germing ², Rainer Haas ² and Paul Jäger ^{2,*} 

¹ Faculty Medical and Life Sciences, Campus Villingen-Schwenningen, Hochschule Furtwangen University, 78120 Furtwangen, Germany

² Department of Hematology, Oncology and Clinical Immunology, University Hospital Düsseldorf, 40225 Düsseldorf, Germany

³ Institute for Molecular Medicine I, University Hospital Düsseldorf, 40225 Düsseldorf, Germany

⁴ Institute of Pharmaceutical Biology and Biotechnology, Heinrich Heine University, 40225 Düsseldorf, Germany

* Correspondence: PaulSebastian.Jaeger@med.uni-duesseldorf.de; Tel.: +49-2118117786

† These authors contributed equally to this work.

Received: 24 August 2019; Accepted: 2 September 2019; Published: 5 September 2019



Abstract: There is a variety of antineoplastic drugs that are based on natural compounds from ecological niches with high evolutionary pressure. We used two cell lines (Jurkat J16 and Ramos) in a screening to assess 300 different naturally occurring compounds with regard to their antineoplastic activity. The results of the compounds 4,6-dibromo-2-(2',4'-dibromophenoxy)phenol (P01F03), 4,5,6-tribromo-2-(2',4'-dibromophenoxy)phenol (P01F08), and 5-epi-nakijinone Q (P03F03) prompted us to perform further research. Using viability and apoptosis assays on the cell lines of primary human leukemic and normal hematopoietic cells, we found that P01F08 induced apoptosis in the cell lines at IC₅₀ values between 1.61 and 2.95 μ M after 72 h. IC₅₀ values of peripheral blood mononuclear cells (PBMNCs) from healthy donors were higher, demonstrating that the cytotoxicity in the cell lines reached 50%, while normal PBMNCs were hardly affected. The colony-forming unit assay showed that the hematopoietic progenitor cells were not significantly affected in their growth by P01F08 at a concentration of 3 μ M. P01F08 showed a 3.2-fold lower IC₅₀ value in primary leukemic cells [acute myeloid leukemia (AML)] compared to the PBMNC of healthy donors. We could confirm the antineoplastic effect of 5-epi-nakijinone Q (P03F03) on the cell lines via the induction of apoptosis but noted a similarly strong cytotoxic effect on normal PBMNCs.

Keywords: marine sponge derived natural products; polybrominated diphenyl ethers; sesquiterpene aminoquinone; bioactive natural products; cytotoxic activity; apoptosis; peripheral blood mononuclear cells; primary leukemic cells; acute myeloid leukemia; drug leads

1. Introduction

According to recent estimates, more than 8.9 million people die of cancer worldwide every year [1]. Independent of the type of cancer, our general understanding of the processes underlying cancer is that

the malignant transformation within the cell of origin is accompanied by multiple genetic alterations and mutations. The latter are caused by a variety of environmental and lifestyle factors such as smoking or nutrition habits, viruses, and aging, which are generally associated with increasing genetic instability [2]. The systemic treatment of patients with cancer still largely relies on cytostatic agents also affecting normal cells to some extent. As a result, side effects are encountered, causing morbidity with substantial impact on the quality of life [3]. Cytotoxic drugs are often modified compounds derived from natural products. For example, Vinca alkaloids represent compounds from the Madagascar periwinkle plant [4], while Taxol is retrieved from the bark of the western yew [5].

With a better understanding of the molecular mechanisms underlying cancer, new types of targeted therapies have emerged. Nowadays, targeted therapies based on molecularly designed small molecules are on the rise. For instance, the tyrosine kinase inhibitor Imatinib was developed to target the fusion gene BCR-ABL, which is constitutively activated in chronic myeloid leukemia (CML). This kind of molecular precision therapy was extremely successful, providing long term hematological and molecular remissions for patients with CML without significant toxicity [6]. An example for a targeted therapy rooted in a natural compound is Midostaurin. It is a semi-synthetic derivative of the structurally related Staurosporine, which was first isolated from the soil-derived actinobacteria *Streptomyces staurosporeus*. Midostaurin resulted from a drug discovery effort to improve the protein kinase C inhibitory activity of Staurosporine [7] and targets constitutively activated mutant FMS-like tyrosine kinase-3 (FLT3), which is expressed in a subpopulation of patients with acute myeloid leukemia (AML) [8]. The search for new naturally occurring compounds with potential antineoplastic activity starts in ecological niches with high evolutionary pressure. For example, bioactive metabolites of marine organisms are particularly efficient in their protection, adaptation, and survival within the specific ecosystem of the sea. Sponges mainly rely on chemical defense mechanisms, allowing successful competition for space and resources [9]. Interestingly, marine compounds interfere with signaling pathways relevant for malignant cells such as those involved in cell death and inflammatory processes [10]. These organisms therefore represent a rich but sparsely exploited source of compounds with a high degree of structural and anti-neoplastic properties [11].

Based on the results of a screening of 300 natural compounds (P01-P05, B-G, 02-11) contained within the biobank of the Institute of Pharmaceutical Biology and Biotechnology at the Heinrich Heine University Düsseldorf on the cell lines Jurkat (T cell leukemia) and Ramos (B cell lymphoma), we chose three different compounds, i.e., 4,6-dibromo-2-(2',4'-dibromophenoxy)phenol (P01F03), 4,5,6-tribromo-2-(2',4'-dibromophenoxy)phenol (P01F08), and 5-epi-nakijinone Q (P03F03). They were selected because they showed strong antiproliferative activity on cell lines and are somewhat incompletely characterized in the literature. The polybrominated diphenyl ether derivatives P01F03 (Figure 1A) and P01F08 (Figure 1B) were isolated from the marine sponge *Dysidea* sp. [12], while P03F03 (Figure 1C) was derived from the sponge *Dactylospongia metachromia* [13]. Going beyond the cell line models, we further investigated these compounds using primary malignant cells obtained from patients with myeloid stem cell disorder. With the perspective to use them for the treatment of patients with leukemia, it was mandatory to assess the natural compounds with regard to their potential cytotoxic side effects on healthy human peripheral blood mononuclear cells using suspension culture and colony-forming unit assays. Our results demonstrated sufficient antineoplastic activity for all three natural compounds without undue toxicity of the two polybrominated diphenyls as far as the normal blood and the progenitor cells are concerned. Further studies concentrating on other types of human leukemia and more elaborate assays such as long-term culture initiating cell assays for determining hematopoietic toxicity may help to pave the way towards clinical application.

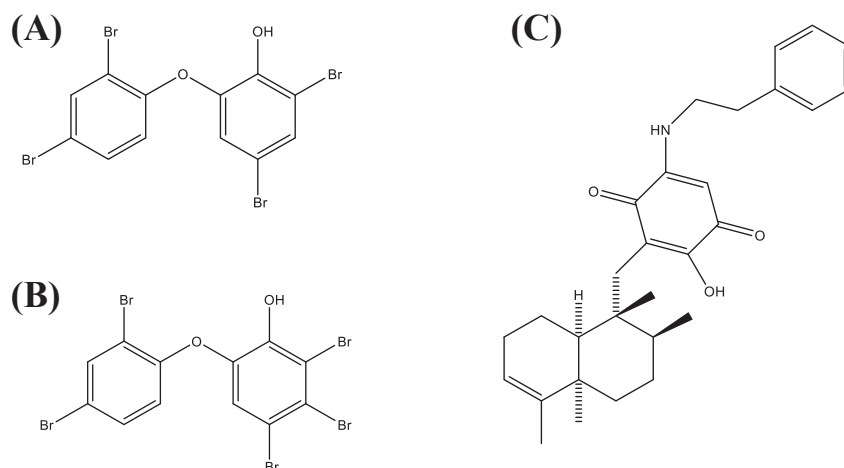


Figure 1. Structural formula of (A) 4,6-dibromo-2-(2',4'-dibromophenoxy)phenol (P01F03), (B) 4,5,6-tribromo-2-(2',4'-dibromophenoxy)phenol (P01F08), and (C) 5-epi-Nakijinone Q (P03F03) (all provided by the Institute of Pharmaceutical Biology and Biotechnology, Heinrich Heine University, Düsseldorf, Germany).

2. Methods

2.1. Compounds

P01F03, P01F08, and P03F03 were obtained from the compound library of the Institute for Pharmaceutical Biology and Biotechnology of the Heinrich Heine University Düsseldorf freshly prepared and dissolved in DMSO. Until use for the assays, they were kept at $-20\text{ }^{\circ}\text{C}$ in a temperature-controlled refrigerator.

2.2. Cell Line Culturing Conditions

Jurkat J16 (acute T cell leukemia cells), Ramos (Burkitt's lymphoma B lymphocytes), HL-60 (acute promyelocytic leukemia cells), and THP-1 (acute monocytic leukemia cells) (each 2×10^6 cells plated) were cultivated in T75 cm^2 culture flasks in RPMI-1640 medium supplemented with 10% fetal bovine serum (FBS) and 1% penicillin/streptomycin/L-glutamine (PSG) (all from Sigma-Aldrich Chemie GmbH, Taufkirchen, Germany) in a humidified atmosphere of 5% CO_2 at $37\text{ }^{\circ}\text{C}$. In accordance with the manufacturer's recommendation, no growth factors were added to the culture medium of cell lines (all purchased from DMSZ, Braunschweig, Germany). The cell density was determined using a Neubauer chamber slide.

2.3. Patients' Samples and Healthy Controls

In this work, peripheral blood samples (PB) from a total of 6 patients (median age: 67 years, range: 40–74 years) covering two AML common subtypes according to the World Health Organization (WHO) classification with a median peripheral blast count of 54% (range: 18–92%) were included. Samples were obtained at diagnosis at the Department of Hematology, Oncology and Clinical Immunology, of the University Hospital Düsseldorf. Patients' characteristics with hematological parameters are given in Table 1. Control samples were derived from 9 healthy individuals undergoing apheresis of enriched peripheral blood mononuclear cells as donors for allogeneic stem cell transplantation. The aliquots were provided from the Institute of Transplantation Diagnostics and Cell Therapeutics of the University Hospital Düsseldorf. The study was approved by the local ethical review committee (study number: 5944R; registration ID: 2017044215), and all patients gave written informed consent.

Table 1. Patient demographics and clinical characteristics.

Characteristic	No.	%
No.	6	
Median age, years	67	
Range		40–74
Sex		
Male	2	33.3
Female	4	66.7
AML		
WHO		
With recurrent genetic abnormalities	4	66.7
MDS-related changes	2	33.3
Karyotype		
Normal	5	84.3
Aberrant	1	16.7
Molecular/genetic risk		
Favorable	3	50
Intermediate	1	16.7
Adverse	2	33.3
Median blasts BM, %	75	
Range		50–99
Median ANC, $\times 10^9/L$	2.119	
Range		0.189–5.248
Median Hb, g/dL	8.2	
Range		4.3–9.6
Median plts, $\times 10^9/L$	59.0	
Range		12.0–168.0
Median blasts PB, %	54	
Range		18–92

Abbreviations: AML, acute myeloid leukemia; ANC, absolute neutrophil count; BM, bone marrow; Hb, haemoglobin; MDS, myelodysplastic syndrome; No., number; NOS, not otherwise specified; PB, peripheral blood; WHO, World Health Organization. Molecular and genetic risk was classified according to the European Leukemia Net (ELN) 2017 criteria.

2.4. Isolation and Cultivation of Mononuclear Cells and CD34+ Cells

Mononuclear cells were obtained from peripheral blood (PB) or apheresis products (AP) following density gradient separation. An interim step lysis of remaining erythrocytes with hypotonic 0.83% ammonium chloride was performed. CD34+ cells were positively selected from PB or AP-derived mononuclear cells (MNC) by immunomagnetic cell separation (Miltenyi Biotec, Bergisch-Gladbach, Germany) as published (Schroeder 2009).

The cells were cultivated with a cell density of 100–1000 cells/ μL in T75 cm² culture flasks in RPMI-1640 medium supplemented with 10% FBS and 1% PSG in a humidified atmosphere of 5% CO₂ at 37 °C. The cell density was determined using a Neubauer chamber slide. To sufficiently maintain healthy and patient MNCs and CD34+ cells in culture, the RPMI medium contained Interleukin 3 (IL-3), IL-6, stem cell factor (SCF), and FLT3-ligand (all 10 ng/mL, PreproTech GmbH, Hamburg, Germany).

2.5. 3-(4,5-dimethylthiazol-2-yl)-2,5-diphenyltetrazolium bromide (MTT) Assay

Cell viability was determined by the MTT assay. It is a colorimetric method based on the ability of cells to convert the yellow MTT 3-(4,5-dimethylthiazol-2-yl)-2,5-diphenyltetrazolium bromide substrate into a blue formazan product. This reduction is NAD(P)H-dependent and, as a result, the absorbance of the purple dye is proportional to the number of viable cells.

For cell lines, 50 μL of cell suspension was added in each well of a 96-well plate. The cell density was 1×10^6 cells/mL for an incubation time of 24 h and 0.25×10^6 cells/mL for an incubation time of 72 h. Since primary cells of patients with a hematological neoplasia have a lower proliferation

rate than cell lines, 125 μL of cell suspension were used with a cell density of 6×10^5 cells/mL for an incubation time of 72 h. The two-fold concentrated compound-dilution was added (cell lines: 50 μL , MNC: 125 μL) so that the final volume in each well amounted to 100 μL /250 μL . All samples were tested in triplicates. DMSO (0.1% *v/v*), staurosporine (STS, 10 μM) (both diluted in RPMI medium), and medium were used as controls. After a 24 or 72 h incubation in a humidified atmosphere of 5% CO_2 at 37 $^\circ\text{C}$, 20 μL MTT solution (dissolved in ddH₂O, 5 mg/mL, sterile-filtered) were added and incubated for another hour. MNCs of patient samples had a lower metabolic rate. These samples, therefore, were incubated for two hours with MTT solution. The cells were then centrifuged at $600\times g$ and 4 $^\circ\text{C}$ for 5 min, and the supernatant was removed. DMSO (cell lines: 100 μL ; MNCs: 70–90 μL) was added, and the cells were incubated in the dark at room temperature for 20–30 min on a rocking platform. When the crystals dissolved, the samples were transferred to a 96-well plate with a flat bottom, and the absorbance was measured in a plate reader using a wavelength of 570 nm and a reference wavelength of 650 nm. The mean values of the staurosporine controls were subtracted from all other values, since a relative viability of 0% could be assumed here. The relative viability of the cells incubated with DMSO was set to 100%. For the remaining absorption values, a relative viability was determined. These relative viability values were calculated with the software Prism via a non-linear regression analysis, and the IC₅₀ value was calculated. The mean inhibitory concentration (IC₅₀) is the concentration of an inhibitor at which half-maximum inhibition is observed. All IC₅₀ values are given with the 95% confidence interval.

2.6. Propidium Iodide (PI) Uptake

The propidium iodide (PI) uptake assay is a method for detecting cell death. Therefore, the plasma membrane integrity is determined via the uptake of propidium iodide (PI). It is a small fluorescent molecule that binds to DNA. It cannot passively pass into cells that have an intact plasma membrane, as is the case for viable or early apoptotic cells. As a result, only a defective plasma membrane allows the uptake of PI. The method does not differentiate between late apoptotic and necrotic cells, as the plasma membranes become permeable in both scenarios. Accordingly, every sample was additionally incubated with the broad-range caspase inhibitor Q-VD-OPh (QVD; 1:1000), which inhibits apoptosis. With the assemblage of the data of each sample with and without QVD, apoptosis and necrosis could be distinguished.

Subsequently, 50 μL cell suspensions were added in each well of a 96-well plate. The cell density was 1×10^6 cells/mL for incubation times of 24 h and 72 h. Then, 50 μL of the two-fold concentrated compound dilution was added so that the final concentration per compound was 10 μM and the volume in each well amounted to 100 μL . All samples were tested in triplicates. After the incubation time, the plate was centrifuged at $800\times g$ and 4 $^\circ\text{C}$ for 5 min. After, the supernatant was removed and 150 μL of PI solution (0.01 mg/mL in PBS) was added. Subsequently, the plate was incubated in the dark at RT for 15 min. After that, every sample (10,000 cells) was measured by flow cytometry.

2.7. DEVDase Assay for the Fluorometric Analysis of Caspase-3-Activity

This assay serves for determination of the apoptosis rate. Caspase-3 is activated in the course of apoptosis. To determine the apoptosis rate, the synthetic fluorophore-tagged substrate of caspase-3 (Ac-DEVD-AMC) is added. It is cleaved by activated caspase-3, which leads to the release of the fluorophore AMC (7-amido-4-methylcoumarin). As a result, the measured fluorescence is directly proportional to the DEVDase activity.

For this assay, 1×10^5 cells per well were seeded in a 96-well plate. For determining kinetics of the caspase-3 activity over 8 h, every 2 h, the compound dilution was added to a part of the wells. At the end, the caspase-3 activity was measured after a treatment for 2, 4, 6, and 8 h of incubation. The final volume in each well reached 100 μL , and the samples were tested in triplicates. After 8 h of incubation, the cells were centrifuged at $800\times g$ and 4 $^\circ\text{C}$ for 5 min, the supernatant was removed, and the cells were frozen at -80°C . During the following steps, the cells were kept

on ice. At first, the cells were thawed on ice, and 50 μ L lysis buffer (20 mM HEPES, 84 mM KCl, 10 mM $MgCl_2$, 200 μ M EDTA, 200 μ M ethylene glycol-bis(2-aminoethylether)-N,N,N',N'-tetraacetic acid (EGTA), 0.5% nonyl phenoxy polyethoxyethanol NP-40) containing the protease inhibitors leupeptin, aprotinin, and pepstatin were added to each well. Subsequently, the cells were incubated on ice for 10 min. Then, 40 μ L of the sample were transferred in a new black 96-well plate with a flat bottom, and 150 μ L reaction buffer (50 mM HEPES, 100 mM NaCl, 10% Sucrose, 0.1% 3-[(3-Cholamidopropyl)dimethylammonio]-1-propanesulfonate hydrate (CHAPS), 2 mM $CaCl_2$) including the substrate Ac-DEVD-AMC were added. Finally, the fluorescence was measured every 2 min for 2.5 h at 37 °C with an excitation of 360 nm and an emission of 450 nm. To evaluate this assay, the linear rise of the fluorescence was determined. The mean of the control samples "DMSO" was set as "1".

2.8. Semisolid Clonogenic Assays

To assess colony-forming capacity of healthy CD34+ hematopoietic stem and progenitor cells (HSPC) after incubation with compound P01F08, colony forming unit assays (CFU) were performed. Therefore, 1×10^5 MNC were incubated for 24 and 72 h on a 96-well plate with P01F08 in 4 different concentrations (0.3, 1, 3, 10 μ M) and under previously mentioned cell culture conditions. Incubations with medium only, DMSO (0.1% *v/v*), and staurosporine (STS, 10 μ M) were used as controls.

After incubation, viable cells were determined by the CASY cell counter. Then, 50,000 viable cells were seeded in semisolid ready-to-use methylcellulose growth medium (MethoCult H4436; Stem Cell Technologies, Vancouver, BC, Canada) in a 24-well plate and incubated for 14 days at 37 °C and 5% CO_2 under humidified conditions. Subsequently, the colonies were counted and differentiated in red precursors (colony-forming unit-erythroid, CFU-E; burst-forming unit-erythroid, BFU-E), white precursors (colony-forming unit-granulocyte, -monocyte, CFU-GM; colony-forming unit-granulocyte; CFU-G; colony-forming unit-monocyte, CFU-M) and colony-forming unit-granulocyte, -erythrocyte, -monocyte, -megakaryocyte (CFU-GEMM) by light microscopy (Axiovert 25 microscope Zeiss, Jena, Germany).

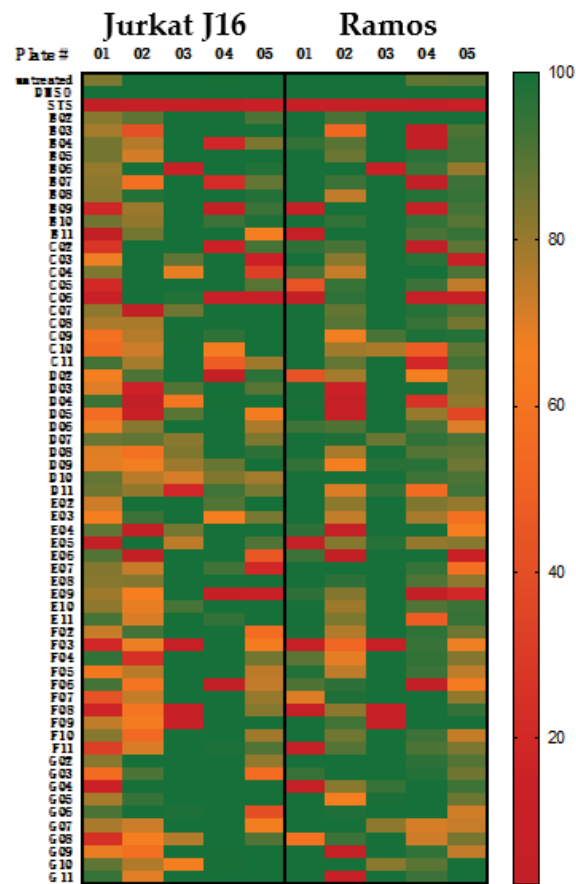
2.9. Statistical Analyses

Statistical analyses were performed using Prism 5.01 (GraphPad Software Inc., La Jolla, CA, USA) and Microsoft Excel 2016 (Microsoft Inc., Redmont, WA, USA) with details given in the respective figure legend. Significance of MTT and DEVDase assays was determined using Welch's t-tests of the peripheral blood mononuclear cells (PBMNCs) against the cell lines and the AML cells. For PI uptake and CFU assays, the significance between treated against untreated as well as DMSO control against treated groups was tested. The significance is indicated by asterisks in the figures (no star: *p*-value > 0.05, *: *p*-value \leq 0.05, **: *p*-value \leq 0.01, ***: *p*-values \leq 0.001).

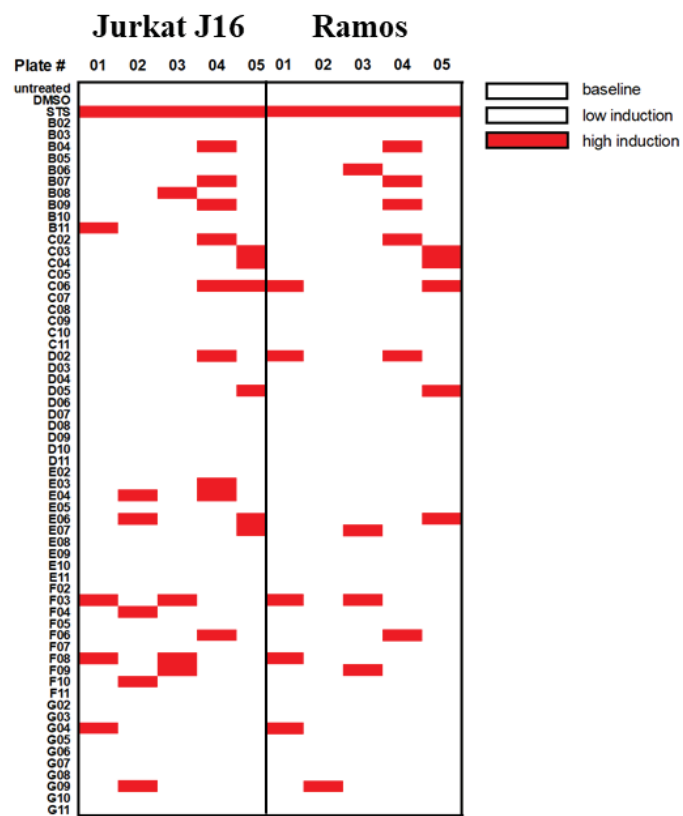
3. Results

3.1. Cytotoxicity Screening of 300 Natural Compounds

In order to identify a natural compound that might have an antineoplastic effect, 300 natural compounds (P01-P05, B-G, 02-11; Figure 2) were first examined during an initial screening process to determine whether cytotoxicity and apoptosis in the cell lines Jurkat J16 and Ramos could be observed (Figure 2). The screening was performed using MTT assay (Figure 2A) and caspase-3 assay (Figure 2B) with a final concentration of 10 μ M of each compound per well. Cytotoxicity could be shown in several natural compounds (Figure 2C). Following literature research, three compounds of marine origin emerged as promising candidates for further research [4,6-dibromo-2-(2',4'-dibromophenoxy)phenol (P01F03), 4,5,6-tribromo-2-(2',4'-dibromophenoxy)phenol (P01F08), and 5-epi-nakijinone Q (P03F03)].



(A)



(B)

Figure 2. Cont.

Code	Name	Code	Name
P01B09	Phomoxanthone A	P03F03	5-epi-Nakijiquinone Q
P01B11	Helenalin	P03F09	Luffariellolid
P01C06	Manzamine A	P04B03	Altersolanol C
P01E05	(+) Aeropylsinin-1	P04B04	Pyrocidine D
P01F03	4,6-dibromo-2-(2',4'-dibromophenoxy)phenol	P04B07	Beauvericin
P01F07	3,5-Dibromo-2-hydroxy-4-methoxyphenylacetonitril	P04B09	Cochliodinol
P01F08	4,5,6-tribromo-2-(2',4'-dibromophenoxy)phenol	P04C02	Enniatin B1
P01G04	Enniatin B	P04C06	Hexaprenylhydroquinone
P01G08	(-) Matairesinol	P04C10	Manzamine J N-Oxid
P02B03	(-) Arctigenin	P04D02	Pyrenocine A
P02D04	Altersolanol A	P04F06	Secalonic acid F
P02D05	Isofistularin 3	P05C03	diaporthins B
P02E04	Aranorosin	P05C04	daldinone I
P02E06	Enniatin A1	P05C06	Tylophorinine
P03B06	8-O-manzamine A	P05E07	Beauvericin J

(C)

Figure 2. Cytotoxic effect (A) and apoptosis induction (B) of 300 natural compounds on Jurkat J16 and Ramos. Compound codes are composed of Plate # (columns P01-P05) and individual well labeling (row B02-G11). (A) MTT assay after 72 h of incubation with 10 μ M of each compound. Untreated, staurosporine treated (STS, 10 μ M) and DMSO treated (0.1% *v/v*) cells were used as control. Viability is indicated by color scale ranging from green (100% viability) to red (0% viability). Viability was calculated from DMSO control. (B) Measurement of caspase-3 activation after treatment with different natural compounds (10 μ M) for 8 h. Fold induction was calculated by the DMSO control. (C) Compounds that were shown to be cytotoxic in our screening (compound code with corresponding name). Further names can be provided on request.

3.2. Cytotoxicity on Cell Lines Jurkat J16, Ramos, HL-60, THP-1, and Healthy PBMNCs

Initially, the compounds were further tested in Jurkat J16 and Ramos cells by performing repeated MTT assays as well as in the two acute myeloid leukemia cell lines HL-60 and THP-1. In addition to the anti-proliferative effect of the compounds on cancer cell lines, it was essential to investigate how the compounds affect healthy cells to identify a possible therapeutic window. The cells were incubated for 24 h or 72 h with eight different concentrations ranging from 0.01 μ M to 30 μ M of the respective compounds. As negative control, DMSO (0.1% *v/v*) was used. Staurosporine (10 μ M), an indolocarbazole representing a strong inducer of apoptosis, was used as positive control. Following exposure, viability was determined using the MTT assay, while the corresponding IC₅₀ values were calculated.

We observed a clear time and concentration dependent decline in viability for all three compounds. P01F03 did not cause sufficient cytotoxicity in PBMNCs, Jurkat J16 cells, HL-60 cells, and THP-1 cells to obtain an IC₅₀ value after 24 h incubation. After 72 h incubation, viability of all cells decreased with IC₅₀ values ranging from 1.81 μ M to 31.4 μ M (Figure 3A) with significant differences between PBMNCs and the lymphatic cell lines.

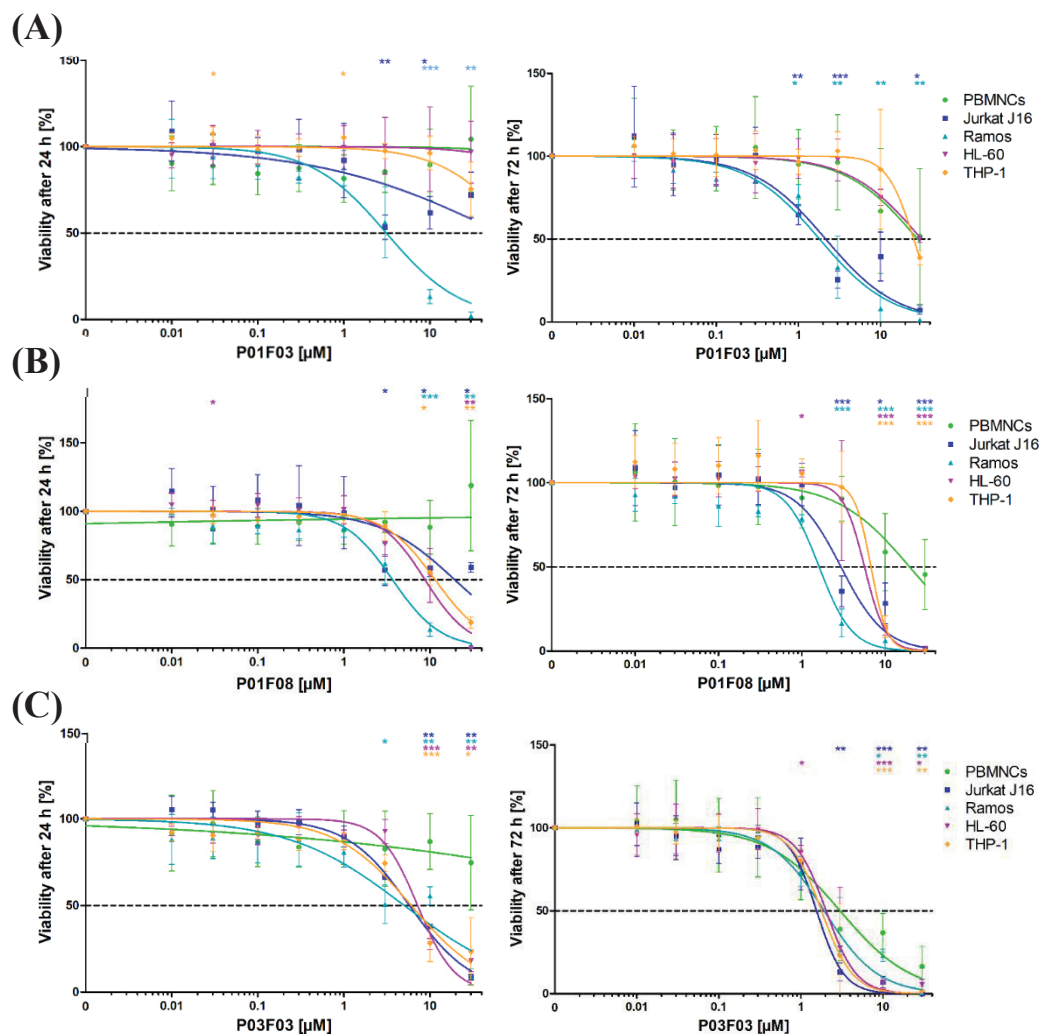


Figure 3. Cytotoxicity in cell lines Jurkat J16, Ramos, HL-60, and THP-1 and on healthy peripheral blood mononuclear cells (PBMNCs). MTT assay (viability) of Jurkat J16, Ramos, HL-60, and THP-1 and healthy PBMNCs after 24 h and 72 h of incubation with the compounds. (A) 4,6-dibromo-2-(2',4'-dibromophenoxy)phenol (P01F03); (B) 4,5,6-tribromo-2-(2',4'-dibromophenoxy)phenol (P01F08); and (C) 5-epi-Nakijinone Q (P03F03). The data are shown as mean \pm SD of three individual experiments in cell lines (Jurkat J16, Ramos, HL-60, THP-1), five individual experiments in PBMNCs after 24 h incubation, and nine individual experiments in PBMNCs after 72 h incubation. All experiments were performed in triplicates. The values are normalized to staurosporine (STS, 10 μ M) and DMSO (0.1% *v/v*). Welch's t-test was used to detect statistically significant differences between PBMNCs and cell lines. Statistical significance was established at asterisks displaying *p*-values * *p* < 0.05, ** *p* < 0.01, *** *p* < 0.001.

After incubation with P01F08 for 24 h, only the PBMNCs were hardly effected. IC₅₀ values for all cell lines ranged from 3.68 to 19.38 μ M. After 72 h incubation with P01F08, the PBMNCs reached an IC₅₀ value of 19.62 μ M while the cell lines ranged from 1.61 to 6.74 μ M (Figure 3B). In the higher concentrations of 3, 10, and 30 μ M, a significant difference between the effect on PBMNCs and all cell lines was observed.

P03F03 showed overall higher cytotoxic effects. IC₅₀ values ranging from 5.04 to 7.18 μ M were found for the cell lines, while PBMNCs viability did not decline under 50% after 24 h incubation. In contrast, all cell viability was strongly affected after 72 h incubation with P03F03. IC₅₀ values ranged from 1.56 to 3.01 μ M (Figure 3C). Because of the equally strong effect of P03F03 on the healthy

PBMNCs, a greater therapeutical window for this compound was not expected. The exact IC₅₀ values with the corresponding 95% confidence interval are shown in Table 2.

Table 2. Mean IC₅₀ values (with 95% confidence intervals) of Melphalan in four different cell lines and AML patient samples and PBMNCs from healthy donors compared to the compounds P01F03, P01F08, and P03F03 (Melphalan values are from Strese et al., 2017).

Cells	Melphalan IC ₅₀ (μM)	P01F03 IC ₅₀ (μM)	P01F08 IC ₅₀ (μM)	P03F03 IC ₅₀ (μM)
MV4-11	1.7 (1.4–2.0)			
HL-60	6.1 (5.5–6.9)	31.4 (21.38–46.11)	5.65 (4.25–7.52)	2.03 (1.54–2.69)
Kasumi	3.8 (3.3–4.5)			
KG1-A	8.6 (7.1–10)			
THP-1		25.26 (19.92–32.03)	6.74 (3.88–11.71)	1.79 (1.44–2.22)
Jurkat J16		2.15 (1.267–3.630)	2.95 (2.08–4.18)	1.56 (1.27–1.91)
Ramos		1.81 (1.35–2.42)	1.61 (1.30–1.99)	1.92 (1.55–2.39)
Patients	5.5 (4.7–6.5)	19.22 (9.36–39.44)	6.22 (4.55–8.50)	2.32 (1.47–3.67)
PBMNC	9.7 (5.0–19)	28.15 (16.58–47.78)	19.62 (13.28–28.98)	3.01 (2.18–4.16)

3.3. Induction of Apoptosis in Ramos and Jurkat J16 Cells in Comparison to Healthy PBMNCs

In addition, cytotoxicity was assessed by the PI uptake assay using culture medium and DMSO as negative controls, while staurosporine (STS, 10 μM) was used as positive control [14]. This is a measurement in which the proportion of dead cells can be evaluated. In principle, this method cannot discriminate between late apoptosis and necrosis. However, in order to measure apoptotic activity, the cells were incubated with and without the multi caspase inhibitor QVD [15]. As a result, a statement about the potential induction of apoptosis could be made. The PI uptake was measured for the cell lines Jurkat J16 and Ramos with the two incubation times, 24 h and 72 h.

After 24 h of incubation, a difference in the PI uptake of the cells exposed to the compounds only and those co-incubated with QVD could be noticed. In Jurkat J16 cells, this effect was less pronounced than in Ramos cells (Figure 4A,B). There was a difference in PI uptake in cells exposed to the natural compounds without QVD in P01F08 and a significant difference in P01F03 and P03F03 after 24 h of incubation. These findings indicated that the compounds acted, at least partially, via the induction of apoptosis.

After 24 h of incubation, a clear and significant difference between the samples P01F03 and P01F03 + QVD ($p = 0.0079$) and P03F03 and P03F03 + QVD ($p < 0.0004$) could be observed.

After 72 h, a significant difference between the DMSO control and the treated groups could be obtained. However, at this time, 78.4% of the Jurkat J16 cells treated with P01F03 incorporated PI, irrespective of the presence of QVD (also 78.4%). Similarly, Jurkat J16 cells incubated with P01F08 reached a PI uptake of 83.4% without QVD and 81.5% with QVD (Figure 4A). In Ramos cells (Figure 4B), the PI uptake showed a greater difference in the presence of QVD after 72 h. Without QVD, 98.6% of Ramos cells treated with P01F03 incorporated PI; in the presence of QVD, 51.5% of the cells incorporated PI. For P01F08, the PI uptake sunk from 98.2% without QVD to 50.4% with QVD. For P03F03, the difference was slightly smaller (90.6% PI uptake without QVD, 57% PI uptake with QVD). All compounds showed a significant difference in co-exposure with QVD (P01F03: $p = 0.0005$; P01F08: $p = 0.0002$; P03F03: $p = 0.0035$).

The high degree of PI uptake following the exposure of the cells to the compounds confirmed the cytotoxicity of the compounds and was in line with the results of the MTT assay. Furthermore, the co-exposure with QVD in our preliminary experiments gave rise to the hypothesis that the compounds acted via the induction of apoptosis. To confirm the apoptosis inducing ability of P01F08, which turned out to have a therapeutic gap (Section 3.2), we used the DEVDase assay for measurement of the caspase-3 activity as an indicator for apoptosis.

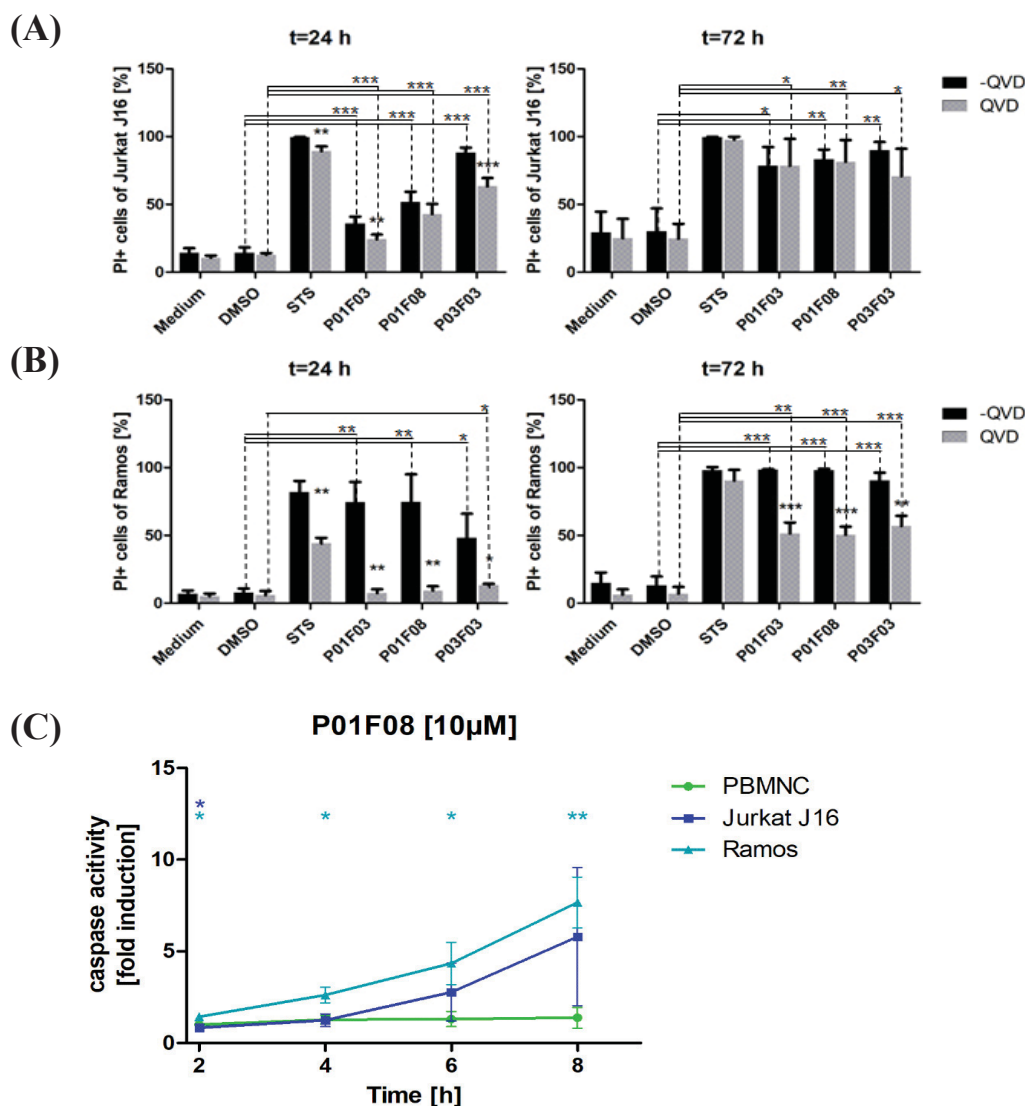


Figure 4. Propidium iodide (PI) uptake in the cell lines (A) Jurkat J16 and (B) Ramos with and without caspase inhibitor Q-VD-Oph (QVD) with 10 μ M of each compound and incubation times of 24 h and 72 h. The results are shown as mean \pm SD of three independent experiments, which were performed in triplicates. Welch's t-test was used to detect statistically significant differences. Significance between treated and untreated groups is indicated with asterisks above the columns. Significance between DMSO and different cells is shown with asterisks on lines above displaying p -values * $p < 0.05$, ** $p < 0.01$, *** $p < 0.001$. (C) Kinetics of caspase-3 activity in PBMNCs and in cell lines Jurkat J16 and Ramos after the stimulation for up to 8 h with 4,5,6-tribromo-2-(2',4'-dibromophenoxy)phenol (P01F08). The results are shown as mean \pm SD of triplicates. The values are normalized to DMSO. Welch's t-test was used to detect statistically significant differences between PBMNCs and cell lines and are established at asterisks displaying p -values * $p < 0.05$, ** $p < 0.01$, *** $p < 0.001$.

In preliminary experiments with staurosporine, strong apoptosis was induced in all cell types (data not shown). Following exposure of Jurkat J16 and Ramos cells (Figure 4C) to P01F08 in three independent experiments, a rise of caspase-3 activity could be observed. The increase was not as high as observed in the cells exposed to STS. Still, P01F08 exerted a caspase-3 activity, which increased as a function of the time of exposure (2 h vs. 8 h: Ramos $p = 0.0154$; Jurkat $p = 0.15$). The caspase-3 activity of P01F08 was also determined for the PBMNCs by the DEVDase assay. Following exposure to P01F08, there was no stringent increase in caspase-3 activity compared to the malignant counterparts (Figure 4C). In line with the preliminary results (Section 3.2), no significant caspase activity in PBMNCs

was observed, even after eight hours of testing. The different effects were particularly clear for Ramos, and significant differences between Ramos cells and healthy PBMNCs at all times could be observed (2 h: $p = 0.0112$; 4 h: $p = 0.0161$; 6 h: $p = 0.0354$; 8 h: $p = 0.0091$) while for Jurkat cells, a statistically significant difference could only be observed after 2 h ($p = 0.038$) (Figure 4C).

3.4. Differentiation Capacity of Healthy PBMNCs Following Exposure to P01F08

In our preliminary results, P01F08 stood out as a promising apoptosis inducing compound that might open a therapeutic window. In a next step, PBMNCs enriched for HSPCs were incubated with compound P01F08 for 24 h and 72 h before they were plated in a CFU assay to investigate the proliferation and the differentiation of clonogenic progenitor cells (red precursor, white precursor, CFU-GEMM). For both incubation times, a clear decrease in the number of colony-forming cells was observed at a concentration of 10 μM . In fact, the cells that were incubated for 72 h with 10 μM of the compound showed a reduction of 94.0% of total colonies compared to the DMSO control (number of total colonies DMSO 74.5 vs. P01F08 10 μM 4.5; $p = 0.0199$) and the other concentration (3 μM : $p < 0.0001$; 0.3 μM : $p = 0.0016$). At concentrations of 0.3, 1, and 3 μM , the proliferation and the differentiation were hardly affected, independent of the incubation time (Figure 5).

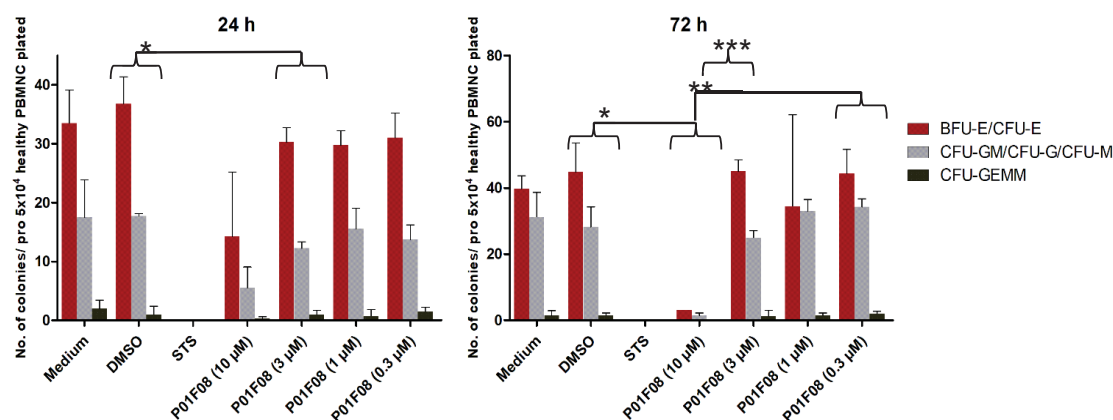


Figure 5. Colony forming units (CFU) assay with PBMNCs after 24 h and 72 h of treatment with 4,5,6-tribromo-2-(2',4'-dibromophenoxy)phenol (P01F08) in different concentrations. The bars represent the mean \pm SD of two patient samples performed in duplicates. Colonies were differentiated in red precursors (colony-forming unit-erythroid, CFU-E; burst-forming unit-erythroid, BFU-E), white precursors (colony-forming unit-granulocyte, -monocyte, CFU-GM; colony-forming unit-granulocyte; CFU-G; colony-forming unit-monocyte, CFU-M), and colony-forming unit-granulocyte, -erythrocyte, -monocyte, -megakaryocyte (CFU-GEMM) by light microscopy. Welch's t-test was used to detect statistically significant differences between all colonies of DMSO and the different concentration of P01F08. Statistical significance was established at asterisks display p -values * $p < 0.05$, ** $p < 0.01$, *** $p < 0.001$, **** $p < 0.0001$.

3.5. Cytotoxicity on Primary Malignant Cells Obtained from Patients with AML

With proven efficacy on myeloid cell lines (Section 3.2), we were interested in the effect of the compounds on primary patient cells. Blood samples were obtained with written informed consent of six patients with an untreated AML and blast excess in the peripheral blood (Table 1). The mononuclear cells were obtained using a density gradient centrifugation. For determination of viability, MTT assays were performed.

Following incubation of AML patients' cells with P01F03, an IC50 value of 19.22 μM (9.36–39.44 μM) was reached. The IC50 value of P01F08 on primary malignant cells amounted to 6.22 μM (4.55–8.50 μM), and P03F03 showed an IC50 value of 2.32 μM (1.47–3.67 μM). Comparing the IC50 values of the healthy PBMNCs with the IC50 values of the AML patients, P01F03 showed a difference of 8.93 μM . This corresponded to 1.5-fold lower toxicity in healthy PBMNC compared to primary AML cells.

However, there was no statistical significance. P01F08 exhibited a difference of 13.4 μM and therefore corresponded to a 3.2-fold higher affection of primary malignant cells compared to healthy counterparts. At higher concentrations of 10 μM and 30 μM , P01F08 and P03F03 showed clear and significant differences in cytotoxicity between primary AML cells and the healthy counterparts (P01F08: 10 μM : $p = 0.0014$, 30 μM : $p = 0.0003$; P03F03: 10 μM : $p < 0.0001$, 30 μM : $p = 0.0196$). However, the IC₅₀ value of P03F03 only differed by 0.7 μM in healthy PBMNCs to the cytotoxicity in AML cells (Figure 6).

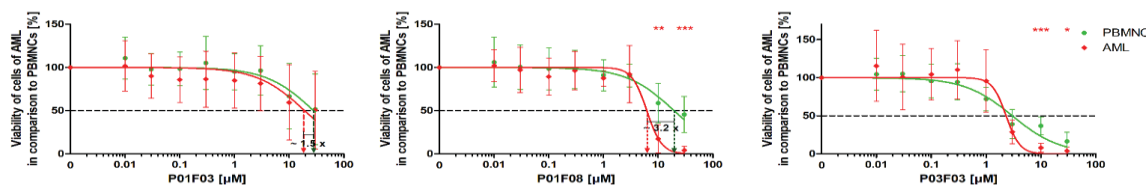


Figure 6. Cytotoxicity on primary malignant cells obtained from patients with AML. MTT assays (viability) of cells from patients with acute myeloid leukemia ($n = 6$) in comparison to cells from healthy donors ($n = 9$), as previously shown in Figure 3, after 72 h of incubation with compounds 4,6-dibromo-2-(2',4'-dibromophenoxy)phenol (P01F03), 4,5,6-tribromo-2-(2',4'-dibromophenoxy)phenol (P01F08), and 5-epi-Nakijinone Q (P03F03). The results are shown as mean \pm SD of the experiments performed in triplicates. The values are normalized to staurosporine (STS, 10 μM) and DMSO (0.1% *v/v*). Welch's *t*-test was used to detect statistically significant differences between healthy PBMNCs and AML cells. Statistical significance was established at asterisks display *p*-values * $p < 0.05$, ** $p < 0.01$, *** $p < 0.001$.

4. Discussion

Following an extensive screening of 300 natural compounds contained within a natural product library established at the Institute of Pharmaceutical Biology and Biotechnology, Heinrich Heine University Düsseldorf, we focused on three candidate compounds because they had a clear-cut, dose-dependent antineoplastic effect on two model cell lines, Jurkat (T-cell) and Ramos (B-cell). In further tests, the IC₅₀ values of the compounds for Jurkat J16 and Ramos cells following 72 h of incubation varied between 1.61 and 2.95 μM . Jurkat J16 cells had a higher proliferation rate than Ramos cells. According to the German Collection of Microorganisms and Cell Culture, the doubling time for Ramos cells is about 48 h [16] and for Jurkat about 25–35 h [17]. Ramos cells were more affected than Jurkat cells after 24 h. This could be an indicator for the underlying mechanism. Potentially, the compounds need to be enriched in the cells before apoptosis is induced. In cells with lower proliferation rates, this would lead to a higher cytotoxicity after a short period of time. It is interesting to note that, unlike other cytotoxic drugs, the effect of the compounds after 24 h did not inevitably depend on the cumulative population doubling (CPD). In the used cell lines, the effect was more pronounced in slower proliferating cell lines (Jurkat J16 and THP-1) after 24 h. This suggested a cytostatic effect independent of the cell division rate.

Compared to the IC₅₀ values of Jurkat J16 and Ramos cells, the IC₅₀ values observed for PBMNCs obtained from healthy donors were significantly higher. In other words, while the cytotoxicity in the cell lines already reached 50%, normal PBMNCs were unaffected. These findings implied that normal blood cells were less susceptible to the toxic effects of the compounds.

When investigating apoptosis induction by PI uptake with the usage of QVD, a clear trend could be shown. As QVD is an apoptosis inhibitor, cells that die from necrosis would have a higher intake in PI than cells that die apoptotic. The significant differences between the PI uptake in Jurkat J16 and Ramos cells that were treated with or without QVD suggested that the compounds induced apoptosis. It was noticeable that the compounds had a lower effect on Jurkat J16 cells than on Ramos cells after 24 h of incubation. When comparing the results from the MTT assays and the results of PI uptake, a relationship was recognizable. For example, after 24 h of incubation with 10 μM P01F03, about 38% of the Jurkat J16 cells died according to the MTT assay. The PI uptake also showed 36% of PI uptake in

cells without QVD. The differences between Jurkat and Ramos cells could therefore be attributed to the reasons mentioned above. Keeping in mind that the compounds might have needed to be enriched first, the incubation time of 24 h was not long enough for the compounds to accumulate in the cells in a way that apoptosis was induced. The lower CPD of Ramos cells might have enabled the compounds to enrich in one cell enough for apoptosis induction. After 72 h of incubation, the gap between cells treated with QVD and cells without co-incubation with QVD closed. Because of the longer incubation time, the cells may have undergone apoptosis despite the protective effects of QVD and reached the stage of secondary necrosis.

Because the difference in induced cytotoxicity between PBMNCs and lymphatic and myeloid cell lines was highest for P01F08, this compound was analyzed in further tests. The results of the PI uptake were supported by a DEVDase assay showing that the lymphatic cell lines Jurkat J16 and Ramos had higher caspase-3 activity than healthy PBMNCs. Keeping in mind that the healthy PBMNCs showed no decrease in viability in the MTT assays after 24 h, the results of the DEVDase assay can be explained. There was hardly any caspase-3 activity, even after 8 h of incubation with P01F08. This might have been due to the lack of cell toxicity after a short incubation time.

Moreover, the results of our colony-forming unit assays showed that even the sensitive hematopoietic progenitor cells were not significantly affected in their growth by P01F08 at a concentration of 3 μM . This difference could be relevant, as it reflects a potential therapeutic window permitting the use of these substances for the development of antineoplastic drugs for the treatment of patients with hematological malignancies. We also included the myeloid derived cell lines HL-60 and THP-1 in our analysis and found that the results obtained were at least partially similar to those observed with the T- and the B-cell derived cell lines. Considering the potential pitfalls associated with the use of cell lines kept in culture for a long time, we extended our experiments using freshly prepared leukemic cells from patients with acute myeloid leukemia. Based on the samples of six different and newly diagnosed patients with AML, prior to therapy, we examined their leukemic blasts excess in the peripheral blood. Compared to the IC50 values of healthy donors, we found that the IC50 values were even smaller, thereby pronouncing the gap between normal and malignant cells. In particular, P01F08 showed a 3.2-fold lower IC50 value in primary leukemic cells (6.22 μM ; 4.55–8.50 μM) compared to the PBMNC of healthy donors (19.62 μM ; 13.28–28.98 μM). Considering the fact that primary malignant cells behave substantially differently from most cell lines, our findings demonstrate, for the first time, the therapeutic relevance of these compounds for patients with AML [18]. Differently from us, Li et al. investigated the effect of cytostatic agents on mesenchymal stem cells, on healthy PBMNCs, and on the acute promyelocytic leukemic cell line NB-4. For the cytostatic drug Paclitaxel, there were significantly higher differences between the leukemic cell line (IC50: 0.223×10^{-7} mol/L, ± 0.001) and the healthy PBMNCs (IC50: 56.2×10^{-7} mol/L, ± 0.8). Of note, paclitaxel is rarely used in patients with hematological malignancies for whom cytarabine and cyclophosphamide are major components within most of the treatment protocols. These two drugs show similar IC50 values compared to P01F08 (Table 3) [19].

Table 3. Chemosensitivity of NB-4 cells and PBMNCs [IC50(10^7 mol/L)]. The results represent the mean \pm SEM of triplicate cultures of one representative experiment. NB-4 cell, acute promyelocytic leukemia cell line (adapted from Li et al., 2004).

Agent	NB-4 Cell	PBMNC	Factor (PBMNC/NB-4 Cell)
Cytarabine	29.2 \pm 3.9	46.3 \pm 7.4	1.58
Busulphan	390 \pm 28	154 \pm 43	0.39
Cyclophosphamide	4900 \pm 210	12,600 \pm 800	2.57

Strese et al. conducted a study comparing the effects of Melflufen and Melphalan on different leukemic cell lines, including primary AML cells, with the effects on healthy PBMNCs. Melflufen showed a 7.5-fold higher IC50 value on healthy PBMNCs compared to primary AML

cells, whereas Melphalan showed a 1.8-fold higher IC₅₀ value on PBMNCs. In contrast to Melflufen, Melphalan is a classical alkylating cytostatic drug that is used in hematological malignancies as a conditioning regimen before blood stem cell transplantation or at a lower dose with palliative intention. Therefore, Melphalan is well suited to compare its IC₅₀ values with those of P01F08 (Table 2) [20], keeping in mind that different cytotoxicity tests were used in the two studies {MTT vs. FMCA (fluorometric microculture cytotoxicity assay), Strese et al. vs. XTT 2,3-bis(2-methoxy-4-nitro-5-sulphophenyl)-5-[(phenylamino) carbonyl]-2H-tetrazolium hydroxide, Li et al.}.

There are little data on some derivatives of the polybrominated diphenyl ethers. For instance, PANC-1 cells were exposed to the derivatives 3,4,5-tribromo-2-(2',4'-dibromophenoxy)-phenol and 3,5-dibromo-2-(2',4'-dibromophenoxy)-phenol, respectively. Under glucose-starved conditions, IC₅₀ values of 2.1 and 3.8 µM were observed. Using similar culture conditions, no anti-proliferative activity was observed up to a concentration of 30 µM. In the search for the mechanisms underlying the anti-proliferative effect, the authors assumed that 3,4,5-tribromo-2-(2',4'-dibromophenoxy)-phenol inhibited complex II in the mitochondrial electron transport chain [21] potentially favoring apoptosis. This view would be in line with our findings showing apoptosis as a prominent mechanism for the toxic effect observed in our cells independent of their origin. The story is different as far as P03F03 is concerned. It can be isolated from the sponge *Dactylosporgia metachromia*, which is a part of the genus *Dactylosporgia*, a source of bioactive secondary metabolites. These compounds are interesting, as their biological activities include antitumor, anti-inflammatory, and antiviral activities. The species was originally described as *Hippospongia metachromia* by De Laubenfels in 1954 [13]. Using the MTT assay with L5178Y mouse lymphoma cells as the target, P03F03 was cytotoxic with an IC₅₀ value of 1.1 µM. When tested against 16 protein kinases involved in the regulation of tumor growth and metastasis, P03F03 inhibited anaplastic lymphoma kinase (ALK), focal adhesion kinase (FAK), insulin like growth factor (IGF11-R), proto-oncogene SRC, and vascular endothelial growth factor (VEGF-R2 R2) [13]. Other compounds with a nakijiquinone core structure, such as P03F03, have been isolated from *Spongia* sp., *Dactylosporgia elegans*, *Smenospongia* sp., and *Hippospongia* sp. These compounds have received great attention, as they have a wide range of biological activities, such as cytotoxic, anti-microbial, and inhibitory activity against the tyrosine kinase epidermal growth factor receptor (EGFR) and protein kinase C [13]. Similar to the published results, our findings confirm the anti-neoplastic effect of the compound on Jurkat J16 and Ramos cell lines via the induction of apoptosis. Still, we found that this compound was also cytotoxic for healthy PBMNCs, as reflected by the similar IC₅₀ values. In our view, this natural compound in its present form without structural modifications is not suitable for further drug development.

Based on a large library of natural compounds with antineoplastic activity, we propose a stepwise approach using a variety of different methods to assess the therapeutic potential of candidate compounds. Particular emphasis is laid on the use of primary human cells—both normal and malignant—to come as close as possible to the true in vivo situation, avoiding inherent artifacts related to the use of cell lines.

Author Contributions: Conception and design: R.H., P.J., P.L., P.P., B.S., S.W. and F.S. Provision of patients' samples: R.H., P.J. and U.G. Experiments, collection and assembly of data: S.M., M.P., P.L., F.S., and P.J. Data analysis and interpretation: S.M., M.P., P.L., R.H., M.K., P.P. and P.J. Induction training and consulting: R.-P.C., P.L., F.S., P.J. and B.S. Manuscript writing: R.H., M.P., S.M., S.W., B.S. and P.J. Final approval of the manuscript: all authors.

Funding: This research received no external funding.

Acknowledgments: This work was supported by the Leukämie Lymphom Liga e. V., Düsseldorf, Germany and by the RTG 2158 of the Deutsche Forschungsgemeinschaft (to B.S., P.P. and S.W.). P.P. also wants to thank the Manchot Foundation for support.

Conflicts of Interest: The authors declare no conflict of interest.

References

1. Global Burden of Disease Cancer Collaboration; Fitzmaurice, C.; Akinyemiju, T.F.; Al Lami, F.H.; Alam, T.; Alizadeh-Navaei, R.; Allen, C.; Alsharif, U.; Alvis-Guzman, N.; Amini, E.; et al. Global, Regional, and National Cancer Incidence, Mortality, Years of Life Lost, Years Lived with Disability, and Disability-Adjusted Life-Years for 29 Cancer Groups, 1990 to 2016: A Systematic Analysis for the Global Burden of Disease Study. *JAMA Oncol.* **2018**, *4*, 1553–1568.
2. Blackadar, C.B. Historical review of the causes of cancer. *World J. Clin. Oncol.* **2016**, *7*, 54–86. [[CrossRef](#)]
3. Brown, S.A.; Sandhu, N.; Herrmann, J. Systems biology approaches to adverse drug effects: The example of cardio-oncology. *Nat. Rev. Clin. Oncol.* **2015**, *12*, 718–731. [[CrossRef](#)]
4. Moudi, M.; Go, R.; Yien, C.Y.S.; Nazre, M. Vinca alkaloids. *Int. J. Prev. Med.* **2013**, *4*, 1231–1235.
5. Slichenmyer, W.J.; Von Hoff, D.D. New natural products in cancer chemotherapy. *J. Clin. Pharmacol.* **1990**, *30*, 770–788. [[CrossRef](#)]
6. O'Brien, S.G.; Guilhot, F.; Larson, R.A.; Gathmann, I.; Baccarani, M.; Cervantes, F.; Cornelissen, J.J.; Fischer, T.; Hochhaus, A.; Hughes, T.; et al. Imatinib compared with interferon and low-dose cytarabine for newly diagnosed chronic-phase chronic myeloid leukemia. *N. Engl. J. Med.* **2003**, *348*, 994–1004. [[CrossRef](#)]
7. Manley, P.W.; Weisberg, E.; Sattler, M.; Griffin, J.D. Midostaurin, a Natural Product-Derived Kinase Inhibitor Recently Approved for the Treatment of Hematological Malignancies. *Biochemistry* **2018**, *57*, 477–478. [[CrossRef](#)]
8. Stone, R.M.; Mandrekar, S.J.; Sanford, B.L.; Laumann, K.; Geyer, S.; Bloomfield, C.D.; Thiede, C.; Prior, T.W.; Döhner, K.; Marcucci, G. Midostaurin plus Chemotherapy for Acute Myeloid Leukemia with a FLT3 Mutation. *N. Engl. J. Med.* **2017**, *377*, 454–464. [[CrossRef](#)]
9. Newman, D.J.; Cragg, G.M. Natural Products as Sources of New Drugs from 1981 to 2014. *J. Nat. Prod.* **2016**, *79*, 629–661. [[CrossRef](#)]
10. Schnekenburger, M.; Dicato, M.; Diederich, M. Epigenetic modulators from “The Big Blue”: A treasure to fight against cancer. *Cancer Lett.* **2014**, *351*, 182–197. [[CrossRef](#)]
11. Cragg, G.M.; Newman, D.J. Natural products: A continuing source of novel drug leads. *Biochim. Biophys. Acta* **2013**, *1830*, 3670–3695. [[CrossRef](#)]
12. Fu, X.; Schmitz, F.J. New brominated diphenyl ether from an unidentified species of *Dysidea* sponge. ¹³C NMR data for some brominated diphenyl ethers. *J. Nat. Prod.* **1996**, *59*, 1102–1103. [[CrossRef](#)]
13. Daletos, G.; de Voogd, N.J.; Müller, W.E.G.; Wray, V.; Lin, W.; Feger, D.; Kubbutat, M.; Aly, A.H.; Proksch, P. Cytotoxic and protein kinase inhibiting nakijiquinones and nakijiquinols from the sponge *Dactylospongia metachromia*. *J. Nat. Prod.* **2014**, *77*, 218–226. [[CrossRef](#)]
14. Crowley, L.; Scott, A.P.; Marfell, B.J.; Boughaba, J.A.; Chojnowski, G.; Waterhouse, N.J. Measuring Cell Death by Propidium Iodide Uptake and Flow Cytometry. *Cold Spring Harb. Protoc.* **2016**, *7*, pdb-prot087163. [[CrossRef](#)]
15. Caserta, T.M.; Smith, A.N.; Gultice, A.D.; Reedy, M.A.; Brown, T.L. Q-VD-OPh, a broad spectrum caspase inhibitor with potent antiapoptotic properties. *Apoptosis* **2003**, *8*, S345–S352. [[CrossRef](#)]
16. Leibniz Institute RAMOS. German Collection of Microorganisms and Cell Cultures GmbH. Available online: <https://www.dsmz.de/collection/catalogue/details/culture/ACC-603> (accessed on 2 September 2019).
17. Leibniz Institute JURKAT. German Collection of Microorganisms and Cell Cultures GmbH. Available online: <https://www.dsmz.de/collection/catalogue/details/culture/ACC-282> (accessed on 2 September 2019).
18. Briske-Anderson, M.J.; Finley, J.W.; Newman, S.M. The influence of culture time and passage number on the morphological and physiological development of Caco-2 cells. *Proc. Soc. Exp. Biol. Med.* **1997**, *214*, S248–S257. [[CrossRef](#)]
19. Li, J.; Law, H.K.W.; Lau, Y.L.; Chan, G.C.F. Differential damage and recovery of human mesenchymal stem cells after exposure to chemotherapeutic agents. *Br. J. Haematol.* **2004**, *127*, S326–S334. [[CrossRef](#)]

20. Strese, S.; Saadia, H.B.; Velandar, E.; Haglund, C.; Höglund, M.; Larsson, R.; Gullbo, J. In vitro and in vivo anti-leukemic activity of the peptidase-potentiated alkylator melflufen in acute myeloid leukemia. *Oncotarget* **2017**, *8*, S6341–S6352. [[CrossRef](#)]
21. Arai, M.; Shin, D.; Kamiya, K.; Ishida, R.; Setiawan, A.; Kotoku, N.; Kobayashi, M. Marine spongean polybrominated diphenyl ethers, selective growth inhibitors against the cancer cells adapted to glucose starvation, inhibits mitochondrial complex II. *J. Nat. Med.* **2017**, *71*, 44–49. [[CrossRef](#)]



© 2019 by the authors. Licensee MDPI, Basel, Switzerland. This article is an open access article distributed under the terms and conditions of the Creative Commons Attribution (CC BY) license (<http://creativecommons.org/licenses/by/4.0/>).

Publication 7

Manuscript “Novel meriolin derivatives as rapid apoptosis inducers”:

Drießen D, Stuhldreier E, Frank A, Stark H, Wesselborg S, Stork B, Müller TJJ.

Bioorganic & Medicinal Chemistry 27:3463–3468 (2019). doi: 10.1016/j.bmc.2019.06.029



Novel meriolin derivatives as rapid apoptosis inducers

Daniel Drießen^a, Fabian Stuhldreier^b, Annika Frank^c, Holger Stark^c, Sebastian Wesselborg^b, Björn Stork^b, Thomas J.J. Müller^{a,*}

^a Institut für Organische Chemie und Makromolekulare Chemie, Heinrich-Heine-Universität Düsseldorf, Universitätsstraße 1, D-40225 Düsseldorf, Germany

^b Institut für Molekulare Medizin I, Heinrich-Heine-Universität Düsseldorf, Universitätsstraße 1, D-40225 Düsseldorf, Germany

^c Institut für Pharmazeutische und Medizinische Chemie, Heinrich-Heine-Universität Düsseldorf, Universitätsstraße 1, D-40225 Düsseldorf, Germany

ARTICLE INFO

This work is dedicated to Prof. Dr. Peter Prosch on the occasion of his 65th birthday.

Keywords:

Synthetic methods
One-pot reaction
Masuda borylation-Suzuki coupling
Meriolin
Apoptosis
Sphingosine kinase 2

ABSTRACT

3-(Hetero)aryl substituted 7-azaindoles possessing multikinase inhibitor activity are readily accessed in a one-pot Masuda borylation-Suzuki coupling sequence. Several promising derivatives were identified as apoptosis inducers and, emphasizing the multikinase inhibition potential, as sphingosine kinase 2 inhibitors. Our measurements provide additional insights into the structure-activity relationship of meriolin derivatives, suggesting derivatives bearing a pyridine moiety with amino groups in 2-position as most active anticancer compounds and thus as highly promising candidates for future *in vivo* studies.

1. Introduction

A variety of marine compounds consists of indole or 7-azaindole core elements¹ and quite some have revealed interesting biological and pharmacological activity. Meridianins originate from the ascidian *Aplidium meridianum*, while variolins were first isolated from the antarctic sponge *Kirkpatrickia variolosa*.^{2,3} In comparison to meridianins and variolins (Fig. 1) meriolins can be considered to be truncated hybrid derivatives combining structural motifs of both classes.⁴ Quite early 3-(hetero)aryl substituted 7-azaindoles have therefore become a lead structure for the development of kinase inhibitors.

Indeed, meriolins have been reported to strongly inhibit various protein kinases.^{5,6} This finding correlates excellently with the ability of 7-azaindoles to bind to the hinge region of kinases. In some cases, also ligands with kinase domains of signaling cascade proteins (e.g. PDK1) were successfully cocrystallized.⁷ Further studies also indicated a high potential of meriolins in the treatment of neurodegenerative diseases, bipolar disorders, strokes, cancer, and chronic inflammations.⁶

Multikinase inhibitors are well-known inducers of apoptotic cell death.^{8–10} For application in therapeutic context initiating apoptosis is much more favorable than induction of necrosis as apoptosis does not harm the host by causing inflammatory reactions.¹¹ The major effectors of the highly regulated apoptotic signaling network are cysteinyl-aspartate specific proteases (caspases) including the most potent

executioner of apoptosis, caspase-3.¹¹ Besides caspases several interconnected kinase-driven signaling pathways are involved in the regulation of apoptosis. Since many of these signaling cascades negatively regulate apoptosis in cancer cells, inhibition of kinases is a reasonable approach for anticancer therapy.¹² Particularly in treatment of acute leukemias targeting kinases seems to be a valid strategy as demonstrated by the recent approval of the multitargeted kinase inhibitor midostaurin for acute myeloid leukemia.¹³ Furthermore, also lymphomas are reported to be most vulnerable to multikinase inhibition.¹⁴ Interestingly, multiple kinases which were reported to be inhibited by meriolin derivatives⁵ are heavily linked to downregulation of apoptosis in cancer cells, for instance GSK3 or CDK7.^{15–17} Summing up, meriolin derivatives appear to be promising candidates for induction of apoptosis in leukemia and lymphoma cells.

The sphingosine kinases 1 and 2 (SK1, SK2) are important regulators of the sphingolipid metabolism.¹⁸ By fine-tuning the levels of sphingosine-1-phosphate (through phosphorylation of sphingosine) the enzymes are involved in cell proliferation and apoptosis and hence connected to cancerous diseases. Recent research even reported on the connection between SK2 inhibition and induction of caspase-3 cleavage in TRAIL resistant cancer cells.¹⁹

As a consequence, rational design of meriolins as kinase inhibitors by a reliable, modular methodology is highly desirable. First syntheses of meriolins reported longest linear sequences of four steps, however,

* Corresponding author.

E-mail address: ThomasJJ.Mueller@hhu.de (T.J.J. Müller).

<https://doi.org/10.1016/j.bmc.2019.06.029>

Received 29 March 2019; Received in revised form 28 May 2019; Accepted 18 June 2019

Available online 19 June 2019

0968-0896/© 2019 Elsevier Ltd. All rights reserved.

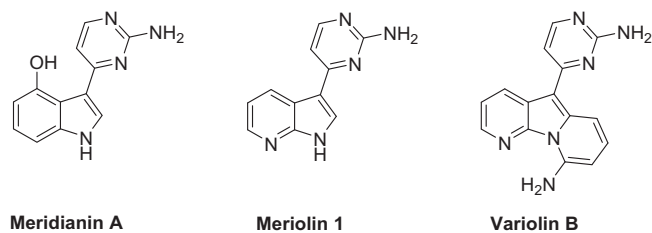
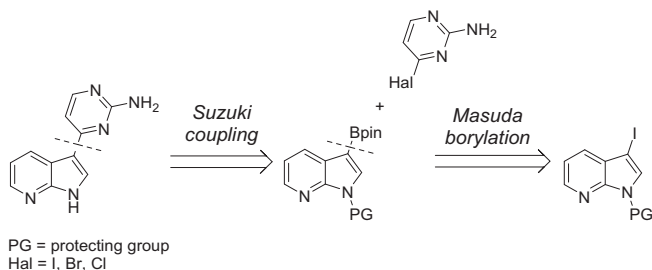


Fig. 1. Natural products meridianin A and variolin B with high bioactivity and meriolin 1 as a structural hybrid.



Scheme 1. Retrosynthetic analysis of meriolin 1.

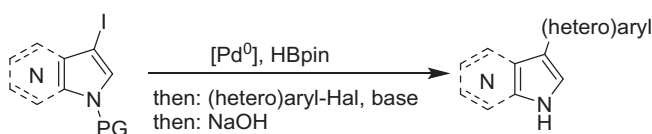
resulting in low overall yields.^{20,21} Based upon the availability and accessibility of (hetero)aryl halides, the retrosynthetic analysis of meriolins suggests Suzuki-Miyaura-coupling²² as a reliable, versatile terminal key step for the formation of the desired compounds (Scheme 1).

Pinacolyl boronates are stable to moisture, light, can be stored at room temperature and can be obtained by Masuda borylation upon reacting an (hetero)aryl halide in the presence of pinacol borane, triethylamine and a palladium catalyst.²³ In comparison to the related Miyaura borylation²⁴ with B_2pin_2 the Masuda reaction represents a more atom-economical approach. Most favorably, both catalytic processes, borylation and (hetero)arylation can be concatenated in a one-pot fashion, i.e. in the sense of a one-pot Masuda borylation-Suzuki (hetero)arylation (MBSA) sequence.

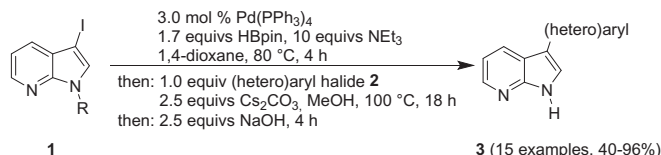
First examples of MBSA were reported on the synthesis of biaryls,²⁵ but it was not before 2011 when we came up with a general MBSA sequence employing heterocyclic halides as substrates, which were successfully applied to concise total syntheses of several marine alkaloids^{26–28} and kinase inhibitors (Scheme 2).⁷

Besides the highly practical nature of one-pot processes, where all transformations are conducted in a consecutive or sequential fashion, the MBSA synthesis of bi(hetero)aryls starting from two different (hetero)aryl halides can be considered as a sequentially Pd-catalyzed process.²⁹ Most characteristically, the initial catalyst also will catalyze the subsequent reaction(s) without further addition of catalyst loading.

Herein we report an optimized MBSA sequence for the synthesis of novel meriolin derivatives that have previously been identified to be potent inhibitors of PDK1.⁷ Various 3-pyrimidyl and 3-pyridyl substituted 7-azaindoles as key pharmacophores, in particular with amino substituents on the azine moieties, were screened with respect to their apoptosis inducing potential and to establish first structure-activity relationships (SAR). In addition, the inhibition of sphingosine kinases 1 and 2 (SK1, SK2) was assessed by initial screening studies.



Scheme 2. Masuda borylation-Suzuki coupling (MBSA) sequence in a one-pot fashion.



Scheme 3. MBSA one-pot synthesis of meriolin derivatives 3.

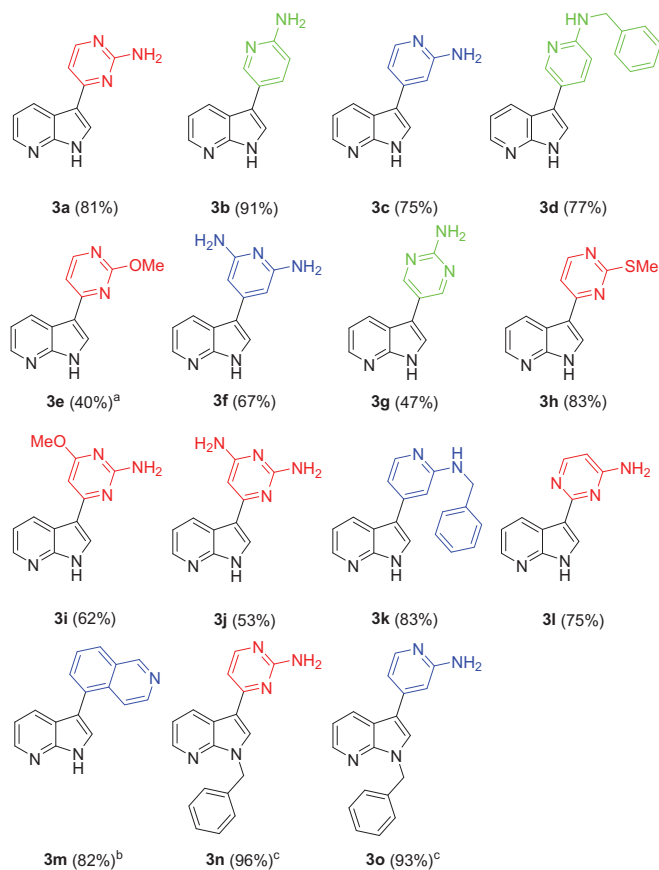


Fig. 2. Scope of MBSA one-pot synthesis of meriolin derivatives 3 (isolated yields are given in parentheses; color code for halides 2: red = chloride, blue = bromide, green = iodide). ^aSecond regioisomer was formed. ^bDME/water was used in the Suzuki coupling step. ^cNo deprotection after Suzuki coupling step.

2. Results and discussion

2.1. Masuda borylation-Suzuki coupling sequence

Based upon our experience in applying the MBSA sequence to the synthesis of marine natural products and analogues, we first established, starting from *N*-protected 3-iodo-7-azaindole 1 and equi-toichiometric amounts of (hetero)aryl halides 2, an optimized protocol for efficiently preparing meriolin derivatives 3 (Scheme 3, Fig. 2).^{26–28}

The *N*-protected 7-azaindoles 1 were prepared in quantitative yields using a one-pot protocol of iodination followed by subsequent protection in dimethylformamide under basic conditions.²⁸ A change from *N*-Boc protected 7-azaindoles to a tosyl protection group was chosen to provide a more stable reagent with respect to the reaction conditions. In comparison to our initial protocol by raising the amount of pinacol borane dehydrohalogenation of the starting material can be efficiently suppressed. Also increasing the excess of triethylamine in the Masuda borylation step turned out to be favorable.²³ With a reaction time of 4 h in 1,4-dioxane conversion to the corresponding pinacolyl ester is essentially quantitative, according to its yields, if isolated. Excessive

pinacol borane is efficiently scavenged by the addition of methanol after completion of the Masuda borylation. The addition of cesium carbonate and (hetero)aryl halide is sufficient to facilitate the Suzuki coupling. In comparison to *Boc*-protected (7-aza)indoles the tosyl protecting group remains intact during the Suzuki arylation step. The concurrent deprotection by the alcoholic carbonate solution can be suppressed.³⁰ The catalytic system obviously remains stable to give a full conversion to the protected meriolin derivatives. Finally, by addition of sodium hydroxide to the reaction mixture deprotection of the tosyl group gives rise to the isolation of meriolin derivatives **3** in good to excellent yields. In essence, a single and simple catalyst system sequentially catalyzes both borylation and (hetero)arylation, and finally, the tosyl group can be selectively cleaved by addition of sodium hydroxide. It is noteworthy to mention that all compounds can be uneventfully isolated by a single simple flash chromatography.

2.2. Biological activity

The class of meriolins is known to act highly cytotoxic in cancer cells.³¹ In order to characterize their cytotoxicity profile we measured cell viability of leukemia and lymphoma cells after treatment with several novel meriolin derivatives **3** using the resazurin reduction assay. Out of 13 tested meriolins **3**, 6 exhibited pronounced cytotoxicity against the tested cancer cell lines with IC_{50} values ranging from 0.06 to 6 μ M (Fig. 3, Table 1). The remaining meriolins **3** possessed low cytotoxicity ($IC_{50} > 10 \mu$ M) or were inactive in the tested concentration range up to 30 μ M (data not shown). Meriolin derivative **3f** demonstrated the highest potency in both cell lines, as reflected by its remarkably low IC_{50} values. Compared to meriolin **1**, compound **3f** showed up to 50-fold increased cytotoxicity. The high quantity of tested meriolin derivatives provides insight into their structure-activity relationship. The amino group in 2-position of the azine moiety seems to be crucial for the cytotoxic efficacy since the vast majority of tested meriolin derivatives lacking this group failed to potentially induce cytotoxicity (**3e**, **3g**, **3h**, **3m**). In addition, meriolin derivatives carrying a pyridine substituent are apparently more cytotoxic than derivatives

with a pyrimidine substituent (see **3a/j** vs. **3c/f**). Comparing the cytotoxicity of compounds **3a** and **3j**, a second amino group at the azine in *meta*-orientation seems to further increase the compound's effect (Fig. 3).

In order to determine whether the observed cytotoxicity of compounds **3a**, **3c**, **3d**, **3f**, **3i** and **3j** is related to induction of apoptosis we performed fluorimetric caspase-3 activity assays. Measuring activation of caspase-3 by using two concentrations per selected compound with regard to their cytotoxicity profile, we showed that all six compounds distinctly induce apoptosis within 3–4 h (Fig. 4). Of note, compound **3f** caused even higher activation of caspase-3 in Ramos cells than the multikinase inhibitor staurosporine (STS; used as positive control), although STS was applied in a considerably higher concentration (2.5 μ M vs. 0.1 μ M). To further verify rapid induction of apoptosis, we detected cleavage of the caspase-3 substrate PARP1 via immunoblotting (Fig. 4). Again, every compound of the mentioned subset induced apoptosis within a few hours, in line with the results of the caspase-3 activity assay.

In order to improve multikinase inhibitor abilities of the compounds biological activities, selected compounds were evaluated by screening against sphingosine kinase 1 and 2. The selected compounds **3a**, **3c** and **3f** showed clear preference for SK2 in a screening at 10 μ M. Compound **3c** was the least active compound with $10\% \pm 5\%$ and $39\% \pm 5\%$ inhibition of SK1 and SK2, respectively. Compounds **3a** and **3f** showed pronounced inhibition of SK2 with $72\% \pm 3\%$ and $87\% \pm 7\%$, respectively, while SK1 inhibition was only moderate ($10\% \pm 4\%$ and $18\% \pm 1\%$, respectively).

All tested compounds showed a marked inhibition of SK2 and weak action on SK1. It has to be noted that the compounds showed fluorescence quenching that may influence the assay results. Having the similar assay conditions for both isoenzymes, the selectivities on SK2 for **3a** and **3f** are clearly based on biological activity and not on physicochemical properties. The SK2 is known as a target involved in cell proliferation and apoptosis. As recently reported inhibition of SK2 led to TRAIL-dependent caspase-3 cleavage and was able to overcome TRAIL resistance in non-small cell lung cancer cells.¹⁹ Collectively, the

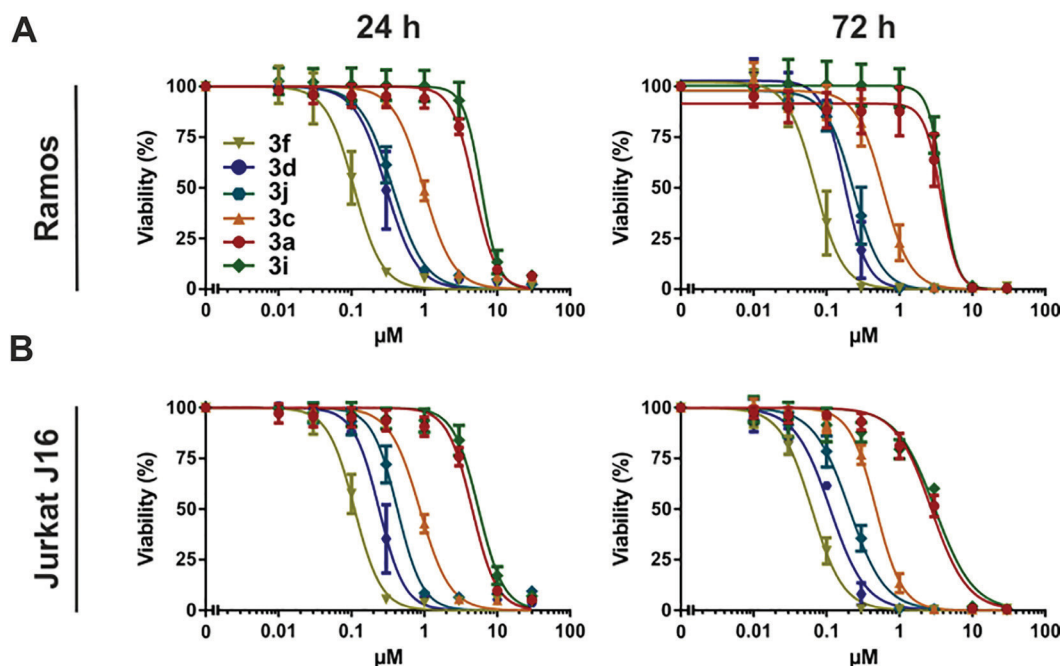


Fig. 3. Selected meriolin derivatives **3** exhibit pronounced cytotoxicity on human lymphoma and leukemia cell lines. (A) Ramos (Burkitt's lymphoma) and (B) Jurkat J16 (acute T-cell leukemia) cells were incubated with escalating concentrations of meriolin derivatives **3** for 24 or 72 h. After incubation, cell viability was determined by resazurin reduction assay as described in methods. Relative viability of DMSO (0.1% v/v)-treated control cells was set to 100%. Data points shown are the mean of three independent experiments, error bars = SD. IC_{50} values (IC_{50} = half maximal inhibitory concentration) were calculated via nonlinear regression curve fitting using Prism 6 (GraphPad Software).

Table 1

Cytotoxicity of meriolin derivatives **3** towards leukemia and lymphoma cells as determined by resazurin reduction assay. IC₅₀ expressed as mean from three independent experiments. Bracketed values indicate 95% confidence intervals.

compound	Ramos 24 h	Ramos 72 h	Jurkat J16 24 h	Jurkat J16 72 h
3a	4.80 μ M [4.28–5.37]	3.73 μ M [2.63–5.28]	4.53 μ M [4.00–5.13]	2.74 μ M [2.42–3.11]
3c	0.97 μ M [0.91–1.05]	0.60 μ M [0.50–0.71]	0.87 μ M [0.81–0.93]	0.48 μ M [0.44–0.51]
3d	0.30 μ M [0.26–0.34]	0.18 μ M [0.16–0.20]	0.24 μ M [0.21–0.27]	0.11 μ M [0.10–0.13]
3f	0.11 μ M [0.10–0.11]	0.07 μ M [0.06–0.08]	0.11 μ M [0.10–0.11]	0.06 μ M [0.06–0.07]
3i	6.04 μ M [5.15–7.08]	3.90 μ M [2.67–5.72]	5.56 μ M [4.93–6.26]	3.08 μ M [2.51–3.78]
3j	0.37 μ M [0.34–0.40]	0.24 μ M [0.21–0.27]	0.43 μ M [0.37–0.49]	0.21 μ M [0.19–0.23]

presented data support the pharmacological activity observed in cell viability assays and serve as additional argument for the proof of concept of the presented compounds on multi-kinase inhibition.

3. Conclusions

The MBSA sequence is a concise and reliable methodology for easily accessing a broad spectrum of novel active agents in a one-pot fashion. Moreover, a modular diversity oriented synthesis can be readily achieved by simply varying the halides. A particular advantage is the sequentially Pd-catalyzed process, which is highly catalyst economical. This methodological tool is currently applied in various concise total syntheses of natural products and bioactive compounds. Here, we used the methodology for generating several new inducers of apoptotic cell death in cancer cells. In particular, **3f** showed a great potential as a valuable lead compound for future anticancer studies.

4. Experimental section

4.1. Synthesis of **1a**²⁸

7-Azaindole (3.54 g, 30.0 mmol) and potassium hydroxide (4.96 g, 75.0 mmol) were dissolved in DMF (55.0 mL). A solution of iodine (7.63 g, 30.3 mmol) in DMF (55.0 mL) was added dropwise to the solution at room temp and the resulting mixture was stirred for 30 min. After addition of a second portion of potassium hydroxide (4.96 g, 75.0 mmol) the mixture was stirred at room temp for 10 min before a solution of *p*-toluene sulfonyl chloride (12.14 g, 63.0 mmol) in DMF (55.0 mL) was added dropwise. The resulting mixture was stirred at room temp for 3 h. After complete conversion (monitored by TLC) the reaction mixture was poured onto ice water (200 mL) and stored in the refrigerator overnight. The resulting yellow precipitate was filtrated, washed with ice water (50.0 mL) and dried *in vacuo* to give the desired product **1a** (11.74 g, 98%) as a light yellow solid (for full analytical details, see the Supporting Information).

4.2. General procedure MBSA (Compound **3f**)

The 7-azaindole **1a** (1.00 mmol, 398 mg) and tetrakis(triphenylphosphane)palladium(0) (35.0 mg, 0.03 mmol) were placed in a dry screw-cap vessel with a magnetic stir bar. After evacuating and refilling with argon for three times dry 1,4-dioxane (5.0 mL) was added and the resulting mixture was degassed with argon for 10 min. Dry triethylamine (1.40 mL, 10.0 mmol) and 4,4,5,5-tetramethyl-1,3,2-dioxaborolane (0.25 mL, 1.70 mmol) were successively added. Then the reaction mixture was stirred in a preheated oil bath at 80 °C for 4 h. The mixture was cooled to room temp (water bath). Dry methanol (5.0 mL) was added and the mixture was stirred at room temp for 10 min. After the addition of 2,6-diamino-4-bromopyridine (**2f**) (1.00 mmol, 129 mg) and cesium carbonate (823 mg, 2.50 mmol) the mixture was stirred in a preheated oil bath at 100 °C for 18 h. After the Suzuki coupling was completed the mixture was cooled to room temp (water bath). Sodium hydroxide (100 mg, 2.50 mmol) was added and the reaction was stirred at 100 °C for 4 h. Then, after cooling to room temp (water bath), the

solvents were removed *in vacuo* and the residue was absorbed onto Celite®. After purification by chromatography on silica gel (dichloromethane/methanol/ aqueous ammonia, see Supporting Information) and after drying *in vacuo* at 80 °C for 18 h compound **3f** (151 mg, 67%) was obtained as an orange solid. ¹H NMR (DMSO-*d*₆, 300 MHz): δ = 5.33 (bs, 4H), 6.05 (s, 2H), 7.15 (dd, *J* = 4.7, 7.9 Hz, 1H), 7.74 (d, *J* = 2.5 Hz, 1H), 8.14–8.44 (m, 2H), 11.88 (s, 1H); ¹³C NMR (DMSO-*d*₆, 75 MHz): δ = 93.1, 113.6, 115.9, 117.3, 124.0, 127.7, 142.9, 144.3, 149.0, 159.2; EI MS (*m/z* (%)): 226 (14) [M + H⁺], 225 (100) [M⁺], 198 (21) [C₁₁H₁₀N₄⁺], 170 (7) [C₁₀H₈N₃⁺], 155 (4) [C₁₀H₇N₂⁺], 118 (5) [C₇H₆N₂⁺]; Anal. calcd. for C₁₂H₁₁N₄ (225.25): C 63.99, H 4.92, N 31.09; Found: C 63.89, H 4.88, N 30.80. (For full experimental and analytical details, see Supporting Information).

4.3. Cell lines and reagents

Adult lymphoblastic leukemia T cells (Jurkat J16, no. ACC-282) and Burkitt's lymphoma B cells (Ramos, no. ACC-603) were obtained from the German Collection of Microorganisms and Cell Cultures (DSMZ, Germany). Both cell lines were routinely cultured in RPMI 1640 media supplemented with 10% FCS, 120 IU/ml penicillin, and 120 μ g/ml streptomycin. Resazurin sodium salt and Q-VD-Oph hydrate (QVD) were purchased from Sigma Aldrich Life Science (Darmstadt, Germany), staurosporine (STS) from LC Laboratories (Woburn, MA, USA) and Ac-DEVD-AMC from Biomol (Hamburg, Germany). The antibodies used for immunoblotting were mouse anti-PARP1 (Enzo Life Sciences, New York, NY, USA; #BML-SA250) and mouse anti-GAPDH (Abcam, Cambridge, United Kingdom; #ab8245).

4.4. Resazurin reduction assay

Cell viability was evaluated using the resazurin reduction assay. In viable cells the non-fluorescent dye resazurin gets reduced to highly fluorescent resorufin.³² Therefore resorufin fluorescence can serve as a measure for metabolic activity. For viability testings, Ramos and Jurkat J16 cells were seeded in a density of 0.5 \times 10⁶ cells/mL and treated with the compounds of interest for the indicated time. Resazurin (40 μ M) was added 3 h prior to end of incubation time. Finally, the fluorescence of resorufin (excitation: 535 nm, emission: 590 nm) was measured using a microplate spectrophotometer. Viability of control cells (0.1% DMSO) was set to 100%.

4.5. Immunoblotting

Immunoblotting was performed according to standard protocol as described earlier.³³ Signals were detected using IRDye800- or IRDye680- conjugated secondary antibodies and an infrared imaging system (LI-COR Biosciences, Lincoln, NE, USA).

4.6. Fluorimetric caspase-3 activity assay

Activation of caspase-3 was detected as described previously.³³ Briefly, cells plated in 96-well microtiter plates were lysed in caspase assay buffer (20 mM HEPES, 84 mM KCl, 10 mM MgCl₂, 200 μ M EDTA,

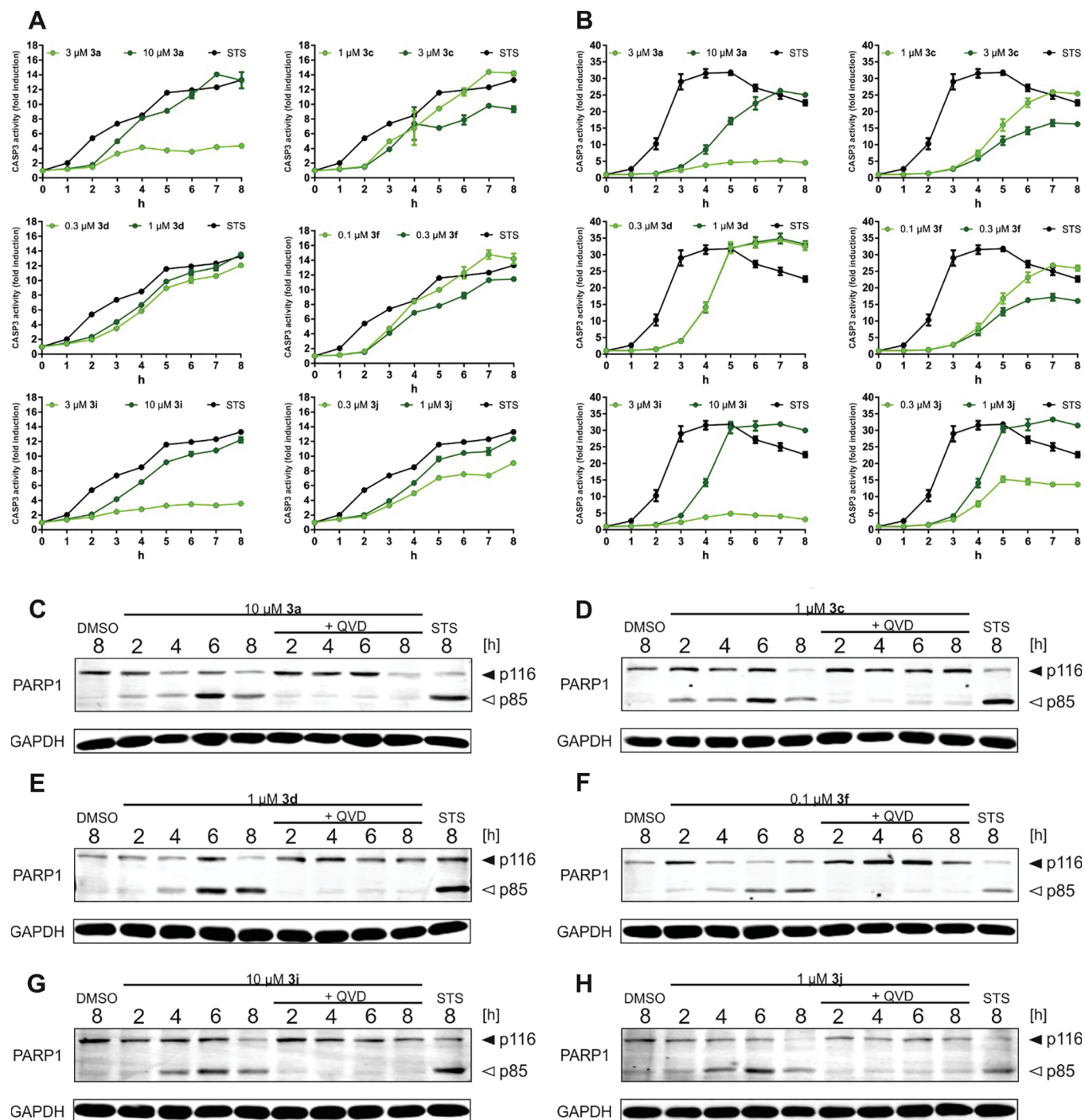


Fig. 4. A subset of meriolin derivatives **3** induces apoptosis in rapid kinetics. (A) Ramos or (B) Jurkat J16 cells were treated with the indicated meriolin derivatives **3** for up to 8 h. After a lysis step, the pro-fluorescent caspase-3 substrate Ac-DEVD-AMC was added. Increase in fluorescence of AMC was measured at 37 °C for at least 60 min using a microplate spectrophotometer and reflects caspase-3 activity. The multitkinase inhibitor staurosporine (STS, 2.5 μM) served as positive control for caspase-3 activation. Curves for STS are reused in corresponding diagrams. Ramos cells were treated with (C) **3a**, (D) **3c**, (E) **3d**, (F) **3f**, (G) **3i**, or (H) **3j** in defined concentrations (selected on the basis of initial cytotoxicity testings) for 2–8 h. Subsequently, cells were harvested, lysed and deployed for immunoblotting against the caspase-3 substrate PARP1. Expression of GAPDH was used as protein loading control. Co-treatment with the broad-spectrum caspase inhibitor Q-VD-OPh (QVD, 10 μM) was conducted in order to confirm caspase dependency of PARP1 cleavage. The uncleaved form of PARP (p116) is indicated by filled arrowheads, the cleaved form (p85) by open arrowheads. STS (2.5 μM) served as positive control.

200 μM EGTA, 0.5% NP-40, 1 μg/mL leupeptin, 1 μg/mL pepstatin, 5 μg/mL aprotinin) after the indicated incubation time. Subsequently, reaction buffer containing the pro-fluorescent caspase-3 substrate Ac-DEVD-AMC was added. In the final step, increase in AMC fluorescence, indicating caspase-3 activity, was measured over a period of at least 60 min.

4.7. Sphingosine kinase inhibition assays

The inhibition of the sphingosine kinase was measured as reported previously^{18a} with minor changes. Briefly, the compounds of interest (10 μM) were incubated with sphingosine kinase (SK) 1 or 2 (0.5 U/mL or 0.1 U/mL final concentration, respectively) for 15 min. Then 5 μM

sphingosine and ATP (final concentration, assay volume of 10 μ L) were added and incubated for 30 or 60 min (SK1 and 2, respectively) at room temperature. Afterwards the detection reagent (BellBrook Labs) was added and incubated for 60 min in the dark. The buffer contained 50 mM HEPES (pH 7.5), 4 mM $MgCl_2$, 100 μ M sodium orthovanadate, 1 mM dithiothreitol, 0.01% Brij 35 and 2 mM egtazic acid. Assays were performed in triplicates in two independent experiments (**3a** and **3c** at SK1 with $n = 1$). Relative fluorescence intensity of the compounds was calculated relative to specific fluorescence intensity (total fluorescence intensity minus blank was set to 100%). Inhibition values are derived by calculating 100 minus relative fluorescence intensity. Values are reported as global means of all replicates with standard error of mean.

Acknowledgement

The authors cordially thank the GRK 2158 (Deutsche Forschungsgemeinschaft) for financial support.

References

1. a) Lebar MD, Baker BJ. *Aust J Chem.* 2010;63:862–866
b) Seldes AM, Brasco MFR, Franco LH, Palermo JA. *Nat Prod Res.* 2007;21:555–563
c) Franco LH, Bal de Kier Joffé E, Puricelli L, Tatian M, Seldes AM, Palermo JA. *J Nat Prod.* 1998;61:1130–1132.
2. a) Gompel M, Loest M, bal de Kier Joffé E, Puricelli L, Hernandez Franco L, Palermo JA, Meijer L. *Bioorg Med Chem Lett.* 2004;14:1703–1707
b) Fresneda PM, Molina P, Delgado S, Bleda JA. *Tetrahedron Lett.* 2000;41:4777–4780
c) Jiang B, Yang C-G. *Heterocycles.* 2000;53:1489–1498
d) Franco LH, Palermo JA. *Chem Pharm Bull.* 2003;51:975–977.
3. a) Perry NB, Ettouati L, Litaudon M, et al. *Tetrahedron.* 1994;50:3987–3992
b) Trimurtulu G, Faulkner DJ, Perry NB, et al. *Tetrahedron.* 1994;50:3993–4000
c) Anderson RJ, Morris JC. *Tetrahedron Lett.* 2001;42:8697–8699.
4. Walker SR, Carter EJ, Huff BC, Morris JC. *Chem Rev.* 2009;109:3080–3098.
5. a) Bettayeb K, Tirado OM, Marionneau-Lambot S, et al. *Cancer Res.* 2007;67:8325–8334
b) Echalié A, Bettayeb K, Ferandin Y, et al. *J Med Chem.* 2008;51:737–751
c) Hammond M, Washburn DG, Hoang HT, Thompson, et al. *Bioorg Med Chem Lett.* 2009;19:4441–4445
d) Hong S, Lee S, Kim B, Lee H, Hong S, Hong S. *Bioorg Med Chem Lett.* 2010;20:7212–7215
e) Nanos-Webb A, Jabbour NA, Multani AS, et al. *Brest Cancer Res Treat.* 2012;132:575–588
f) Jarry M, Lecointre C, Malleval C, et al. *Neuro-Oncol.* 2014;16:1484–1498
g) Singh U, Chashoo G, Khan SU, et al. *J. Med. Chem.* 2017;60:9470–9489
h) Alexander A, Karaks C, Chen X, et al. *Oncotarget.* 2017;8:14897–14911.
6. a) Eldar-Finkelman H. *Trends Mol Med.* 2002;8:126–132
b) Dorronsoro I, Castro A, Martinez A. *Expert Opin Ther Pat.* 2002;2:1527–1536
c) Zhang H-C, Ye H, Conway BR, et al. *Bioorg Med Chem Lett.* 2004;14:3245–3250.
7. Wucherer-Plietker M, Merkul E, Müller TJJ, et al. *Bioorg Med Chem Lett.* 2016;26:3073–3080.
8. Llobet D, Eritja N, Yeramian A, et al. *Eur J Cancer.* 2010;46:836–850.
9. Zhang L, Wang H, Li W, Zhong J, Yu R. *Oncotarget.* 2017;8:3289–3303.
10. Tai WT, Cheng AL, Shiau CW, et al. *Mol Cancer Ther.* 2012;11:452–463.
11. Taylor RC, Cullen SP, Martin SJ. *Nat Rev Mol Cell Biol.* 2008;9:231–241.
12. Gross S, Rahal R, Stransky N, Lengauer C, Hoeflich KP. *J Clin Invest.* 2015;125:1780–1789.
13. Stone RM, Mandrekar SJ, Sanford BL, et al. *J Med.* 2017;377:454–464.
14. Roders N, Herr F, Ambrose G, et al. *Front Immunol.* 2018;24:787.
15. Mohapatra S, Chu B, Zhao X, Djeu J, Cheng JQ, Pledger WJ. *Int J Biochem Cell Biol.* 2009;41:595–602.
16. Maccallum DE, Melville J, Frame S, et al. *Cancer Res.* 2005;65:5399–5408.
17. Mirlashari MR, Randen I, Kjeldsen-Kragh J. *Leuk Res.* 2012;36:499–508.
18. a) Vogt D, Weber J, Ihlefeld K, Brüggerhoff A, Proschak E, Stark H. *Bioorg Med Chem.* 2014;22:5324–5367
b) Vogt D, Stark H. *Med Res Rev.* 2017;37:3–51.
19. Yiang J, Yang C, Zhang S, et al. *Cancer Biol Ther.* 2015;16:1194–1204.
20. Anderson RJ, Hill JB, Morris JC. *J Org Chem.* 2005;70:6204–6212.
21. Fresneda PM, Molina P, Bleda JA. *Tetrahedron.* 2001;57:2355–2363.
22. a) Miyaura N, Yanagi T, Suzuki A. *Synth Commun.* 1981;11:513–519
b) Miyaura N, Suzuki A. *Chem Rev.* 1995;95:2457–2483
c) Suzuki A. *Chem Commun.* 2005;38:4759–4763.
23. a) Murata M, Watanabe S, Masuda Y. *J Org Chem.* 1997;62:6458–6459
b) Murata M, Oyama T, Watanabe S, Masuda Y. *J Org Chem.* 2000;65:164–168
c) Lam KC, Marder TB, Lin Z. *Organometallics.* 2010;29:1849–1857.
24. Ishiyama T, Murata M, Miyaura N. *J Org Chem.* 1995;60:7508–7510.
25. a) Baudoín O, Guénard D, Guéritte F. *J Org Chem.* 2000;65:9268–9271
b) Baudoín O, Cesario M, Guénard D, Guéritte F. *J Org Chem.* 2002;67:1199–1207
c) Penhoat M, Levacher V, Dupas G. *J Org Chem.* 2003;68:9517–9520
d) Broutin P-E, Cjerna I, Campaniello M, Frédéric Leroux F, Colobert. *Org Lett.* 2004;6:4419–4422
e) Abreu AS, Ferreira PMT, Queiroz M-JRP, Ferreira ICFR, Calhelha RC, Estevinho LM. *Eur J Org Chem.* 2005;14:2951–2957.
26. Merkul E, Schäfer E, Müller TJJ. *Org Biomol Chem.* 2011;9:3139–3141.
27. Tasch BOA, Merkul E, Müller TJJ. *Eur J Org Chem.* 2011;24:4532–4535.
28. Tasch BOA, Antovic D, Merkul E, Müller TJJ. *Eur J Org Chem.* 2013;21:4564–4569.
29. a) For reviews, see Müller TJJ. *Top Organomet Chem.* 2006;19:149–205
b) Lessing T, Müller TJJ. *Appl Sci.* 2015;5:1803–1836.
30. Huang S, Li R, Connolly PJ, Emanuel S, Middleton SA. *Bioorg Med Chem Lett.* 2006;16:4818–4821.
31. Jarry M, Lecointre C, Malleval C, et al. *Neuro-Oncology.* 2014;16:1484–1498.
32. O'Brien J, Wilson I, Orton T, Pognan F. *Eur J Biochem.* 2000;267:5421–5426.
33. Böhler P, Stuhldreier F, Anand R, et al. *Cell Death Dis.* 2018;9:286.

Publication 8

Manuscript “Azaphilone pigments and macrodiolides from the coprophilous fungus *Coniella fragariae*”:

Yu H, Sperlich J, Höfert SP, Janiak C, Teusch N, Stuhldreier F, Wesselborg S, Wang C, Kassack MU, Dai H, Liu Z, Proksch P.

Fitoterapia 137:104249 (2019). doi: 10.1016/j.fitote.2019.104249



Azaphilone pigments and macrodiolides from the coprophilous fungus *Coniella fragariae*



Haiqian Yu^a, Julia Sperlich^b, Simon-Patrick Höfert^c, Christoph Janiak^c, Nicole Teusch^{b,d}, Fabian Stuhldreier^e, Sebastian Wesselborg^e, Chenyin Wang^f, Matthias U. Kassack^f, Haofu Dai^g, Zhen Liu^{a,*}, Peter Proksch^{a,*}

^a Institute of Pharmaceutical Biology and Biotechnology, Heinrich-Heine-Universität Düsseldorf, Universitätsstrasse 1, 40225 Düsseldorf, Germany

^b Bio-Pharmaceutical Chemistry and Molecular Pharmacology, Faculty of Applied Natural Sciences, Technische Hochschule Köln, Chempark, 51368 Leverkusen, Germany

^c Institute of Inorganic and Structural Chemistry, Heinrich-Heine-Universität Düsseldorf, Universitätsstrasse 1, 40225 Düsseldorf, Germany

^d Department of Biomedical Sciences, Faculty of Human Sciences, University of Osnabrueck, Barbarastrasse 22, 49076 Osnabrueck, Germany

^e Institute for Molecular Medicine I, Medical Faculty, Heinrich-Heine-Universität Düsseldorf, Universitätsstrasse 1, 40225 Düsseldorf, Germany

^f Institute of Pharmaceutical and Medicinal Chemistry, Heinrich-Heine-Universität Düsseldorf, Universitätsstrasse 1, 40225 Düsseldorf, Germany

^g Key Laboratory of Biology and Genetic Resources of Tropical Crops, Ministry of Agriculture, Institute of Tropical Bioscience and Biotechnology, Chinese Academy of Tropical Agricultural Sciences, Haikou 571101, China

ARTICLE INFO

Keywords:

Coniella fragariae
Azaphilones
Pyrenophorin
Cytotoxicity

ABSTRACT

Two azaphilone pigments (1 and 2), two dihydrobenzofurans (3 and 4), two macrodiolides (5 and 6), and a dimeric alkyl aromatic constituent (7) were isolated from the goose dung-derived fungus *Coniella fragariae*. Compounds 1–3 proved to be new natural products. Coniellins H and I (1 and 2) feature a tetracyclic core and an aldehyde group at C-5, which is unusual for azaphilone derivatives. The X-ray structure of pyrenophorin (5) is reported for the first time. Pyrenophorin (5) showed strong cytotoxicity against several cancer cell lines with IC₅₀ values ranging from 0.07 to 7.8 μM.

1. Introduction

Secondary metabolites of fungi are known for their high structural diversity and pronounced biological activities [1]. Azaphilones as a large group of fungal pigments assembled via the polyketide pathway are found in numerous species of fungi including the genera *Penicillium*, *Aspergillus*, *Talaromyces*, *Chaetomium*, and *Monascus* [2,3]. The structures of azaphilones are based on a highly oxygenated pyranoquinone bi- or tri-cyclic core, which is responsible for their red or yellow colors [2,3]. Several azaphilones have been reported to show pronounced bioactivities. Peyronellone B exhibited a strong hypoxia-protective effect [4]. Penicilone B displayed potent antibacterial activity against two strains of methicillin-resistant *Staphylococcus aureus* with MIC values of 3.13 μg/mL [5]. *epi*-Isochromophilone II showed strong cytotoxicity against three renal carcinoma cell lines ACHN, 786-O and OS-RC-2 with IC₅₀ values of 4.4, 3.0 and 3.9 μM [6].

In our previous study, a series of new azaphilones was isolated from the goose dung-derived fungus *Coniella fragariae* [7]. Fungi of the genus *Coniella* (syn. *Piliidiella* and *Schizoparme*) are generally known as plant-pathogenic fungi [8]. However, chemical investigations of these fungi

have rarely been conducted. In continuation of our previous study on *C. fragariae*, we report now two new azaphilone pigments, coniellins H (1) and I (2), and a new dihydrobenzofuran, conielldihydrobenzofuran (3) as well as four known compounds including a further dihydrobenzofuran (4), two macrodiolides (5 and 6) and a dimeric alkyl aromatic constituent (7) (Fig. 1). The structure elucidation of the new compounds and their cytotoxic activities are discussed in this paper.

2. Results and discussion

The molecular formula of 1 was determined as C₂₃H₂₈O₇ based on the HRMS data, indicating 10 degrees of unsaturation. The ¹³C NMR data of 1 (Table 1) combined with HSQC data indicated the presence of three carbonyls at δ_C 204.7 (C-13), 196.6 (C-6) and 191.1 (C-10), an ester carbonyl at δ_C 169.0 (C-21), and four olefinic carbons at δ_C 170.3 (C-3), 99.0 (C-4), 154.9 (C-4a) and 115.1 (C-5), accounting for 6 degrees of unsaturation. Thus, compound 1 was suggested to be a tetracyclic natural product. The HMBC correlations from Me-11 (δ_H 2.16) to C-3 and C-4, from H-4 (δ_H 7.24) to C-5, C-4a and C-8a, from H-10 (δ_H 10.06) to C-4a and C-5, from Me-9 (δ_H 1.35) to C-6, C-7 and C-8, from

* Corresponding authors.

E-mail address: zhenfeizi0@sina.com (Z. Liu).

<https://doi.org/10.1016/j.fitote.2019.104249>

Received 21 May 2019

Available online 25 June 2019

0367-326X/© 2019 Elsevier B.V. All rights reserved.

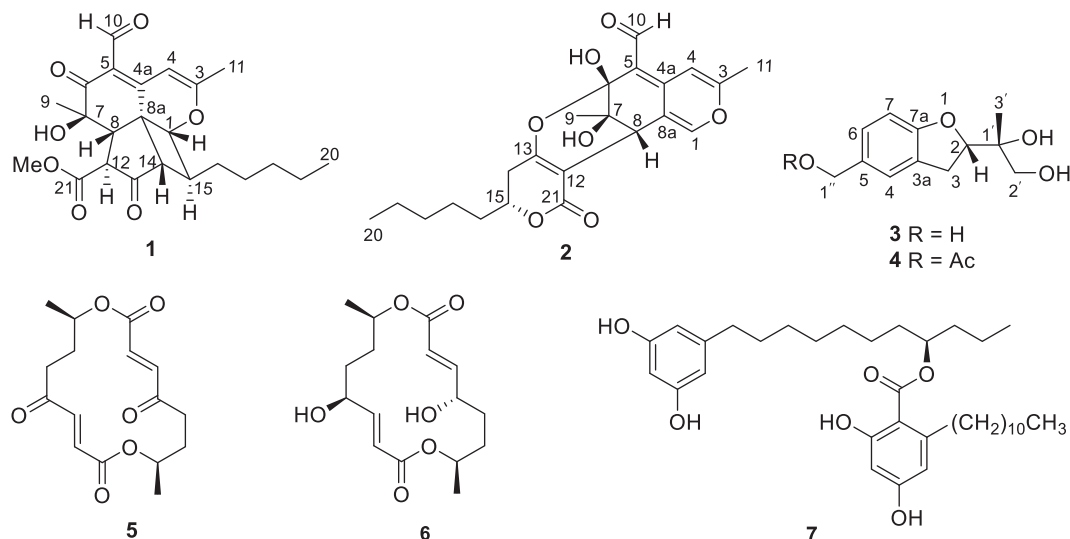


Fig. 1. Structures of isolated compounds.

Table 1
¹H and ¹³C NMR Data of Compounds 1 and 2.

Position	1 ^a		2 ^b	
	δ_c , type	δ_H , (J in Hz)	δ_c , type	δ_H , (J in Hz)
1	80.6, CH	4.86, d (4.8)	146.8, CH	7.47, s
3	170.3, C		160.9, C	
4	99.0, CH	7.24, s	101.2, CH	6.77, s
4a	154.9, C		147.8, C	
5	115.1, C		111.4, C	
6	196.6, C		104.1, C	
7	74.1, C		67.4, C	
8	50.5, CH	3.51, d (11.2)	39.3, CH	3.69, s
8a	42.0, C		121.6, C	
9	21.6, CH ₃	1.35, s	19.3, CH ₃	1.36, s
10	191.1, CH	10.06, s	188.5, CH	9.94, s
11	22.1, CH ₃	2.16, s	20.0, CH ₃	2.24, s
12	58.7, CH	3.13, dd (11.2, 1.2)	102.7, C	
13	204.7, C		164.6, C	
14	63.5, CH	3.00, dd (8.9, 1.2)	31.6, CH ₂	2.46, ddd (17.0, 11.1, 1.3)
15	43.3, CH	3.09, m	75.5, CH	4.25, m
16	28.4, CH ₂	1.63, m	34.7, CH ₂	1.75, m
17	25.9, CH ₂	1.55, m		1.57, m
18	31.5, CH ₂	1.27, m	24.5, CH ₂	1.45, m
19	22.4, CH ₂	1.29, m		1.34, m
20	14.0, CH ₃	0.89, t (7.0)	31.4, CH ₂	1.27, m
21	169.0, C		22.4, CH ₂	1.29, m
6-OH			13.9, CH ₃	0.87, t (7.0)
21-OMe	53.3, CH ₃	3.83, s	166.0, C	
				9.01, s

^a Recorded at 300 MHz (¹H) and 75 MHz (¹³C) in CDCl₃.^b Recorded at 600 MHz (¹H) and 150 MHz (¹³C) in CDCl₃.

H-8 (δ_H 3.51) to C-6, C-4a and C-1, and from H-1 (δ_H 4.86) to C-3 and C-8 indicated the presence of a pyranoquinone bicyclic ring, in which two methyl groups are attached to C-3 and C-7 and an aldehyde group is connected to C-5. A third cyclopentanone ring was established from the COSY correlation between H-8 and H-12 (δ_H 3.13) together with the HMBC correlations from H-12 to C-13, and from H-14 (δ_H 3.00) to C-13, C-8 and C-4a. The HMBC correlations from H-8, H-12 and a methoxy group (δ_H 3.83) to C-21 confirmed the attachment of a methoxycarbonyl group to C-12. The remaining signals accounted for a *n*-hexanyl side chain from C-15 to C-20 based on the COSY correlations

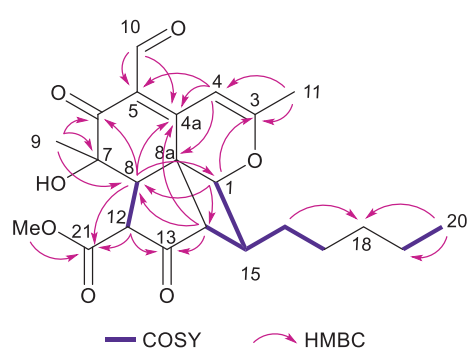


Fig. 2. COSY and key HMBC correlations of compound 1.

between H-15/H_{ab}-16/H_{ab}-17 and between H_{ab}-19 and Me-20 as well as on the HMBC correlations from H_{ab}-16 to Me-18 and from Me-20 to C-18 and C-19. In addition, the COSY correlations between H-14/H-15/H-1 and the HMBC correlation from H-1 to C-14 indicated the presence of a fourth cyclobutane ring. Thus, the planar structure of 1 was elucidated as shown (Fig. 2), representing a new tetracyclic azaphilone derivative, for which the trivial name coniellin H is proposed.

The NOE correlations between H-14/H-1, H-1/H-8, H-8/H-14 suggested that these protons were proximate in space (Fig. 3). The large coupling constant (11.2 Hz) between H-8 and H-12 indicated that these two protons are oriented on the opposite sides of the cyclopentanone ring. In addition, the NOE correlations from Me-9 to both H-8 and H-12

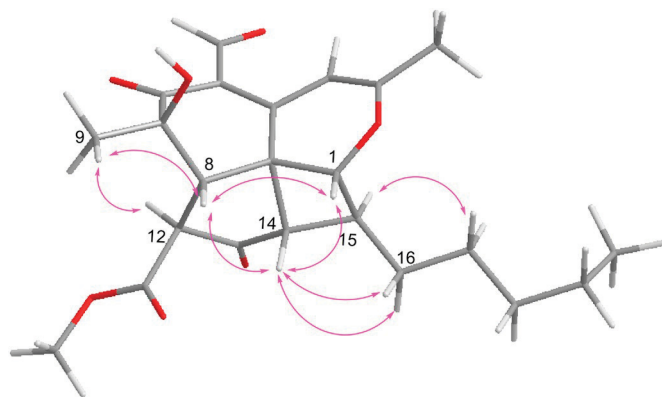


Fig. 3. Key ROESY correlations of compound 1.

Table 2
¹H and ¹³C NMR Data of Compound 3.^a

Position	δ_c , type	δ_{Hb} (J in Hz)
2	85.7, CH	4.81, dd (9.6, 8.3)
3	30.2, CH ₂	3.26, dd (16.0, 8.3) 3.20, dd (16.0, 9.6)
3a	127.4, C	
4	124.4, CH	7.21, d (1.8)
5	133.5, C	
6	127.5, CH	7.10, dd (8.1, 1.8)
7	109.0, CH	6.74, d (8.1)
7a	159.0, C	
1'	73.6, C	
2'	67.0, CH ₂	3.78, d (11.0) 3.54, d (11.0)
3'	19.3, CH ₃	1.20, s
1''	65.3, CH ₂	4.60, s

^a recorded at 600 MHz (¹H) and 150 MHz (¹³C) in CDCl₃.

assigned Me-9 on the α -face of the cyclohexenone ring. Furthermore, H-14 exhibited NOE correlations to H_{ab}-16 whereas H-15 showed NOE correlations to H_{ab}-17, indicating opposite orientation between H-14 and H-15. The absolute configuration at C-7, C-8, and C-12 in **1** is suggested to be identical to that of the previously reported coniellin A (Fig. 8) based on the close biogenetic relationship of both compounds [7]. Thus, the stereochemistry of **1** was determined as shown.

Coniellin I (**2**) had the molecular formula C₂₂H₂₆O₇ as determined by the HRMS data, corresponding to ten degrees of unsaturation. The ¹H and ¹³C NMR data of **2** (Table 2) were similar to those of **1**, suggesting structural similarity between both compounds. For instance, the correlations in the HMBC spectrum of **2** from Me-11 (δ_H 2.24) to C-3 and C-4, from H-4 (δ_H 6.77) to C-5 and C-8a, from H-10 (δ_H 9.94) to C-5 and C-6, from 6-OH (δ_H 9.01) to C-5, C-6 and C-7, from Me-9 (δ_H 1.36) to C-6, C-7 and C-8, from H-8 (δ_H 3.69) to C-4a, C-8a and C-1, and from H-1 (δ_H 7.47) to C-3, C-4a, C-8a and C-8 established a pyranoquinone bicyclic ring similar to that in **1** except for the presence of a double bond at C-1/C-8a and a hydroxy group at C-6 in **2**. A third α,β -unsaturated δ -lactone ring was deduced from the COSY correlation between H-15/H_{ab}-14 as well as from the HMBC correlations from H-8 to C-12, C-13 and C-21, from H_{ab}-14 to C-12 and C-13, and from H-15 to C-21. The COSY correlations between H-15/H_{ab}-16/H_{ab}-17/H_{ab}-18 and between H_{ab}-19 and Me-20 along with the HMBC correlations from Me-20 to C-18 and C-19 indicated the attachment of a *n*-pentanyl side chain at C-15. The above NMR data accounted for nine degrees of unsaturation, suggesting the presence of a fourth ring in **2**. Based on the chemical shifts of C-6 (δ_C 104.1) and C-13 (δ_C 164.6) and the molecular formula of **2**, an ether bridge between C-6 and C-13 was suggested. Thus, the planar structure of **2** was elucidated as shown (Fig. 4).

The relative configuration of **2** was determined by NOE correlations and coupling constants. In the ROESY spectrum, Me-19 exhibited

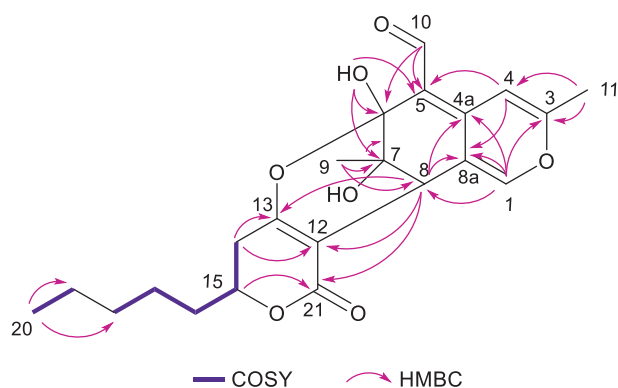


Fig. 4. COSY and key HMBC correlations of compound **2**.

correlations to 6-OH, H-8 and H_b-14 (δ_H 2.32), indicating that 6-OH and H-8 were on the same side and Me-9 was on the α -face of the cyclohexene ring whereas 7-OH was on the opposite side (Fig. 5). In addition, the NOE correlation from H-15 to H_b-14 and H_b-16 (δ_H 1.57) together with the coupling constants between H-15 to H_{ab}-14 ($^2J_{H-15/Ha-14} = 11.1$ Hz, $^2J_{H-15/Hb-14} = 4.2$ Hz) suggested that H-15 and H_b-14 were on the same side of the lactone ring whereas H_a-14 was on the opposite side. Based on the biogenetic relationship between **2** and coniellin A (Fig. 8), whose absolute configuration has been determined by ECD calculations [7], compound **2** is suggested to share the same absolute configuration at C-7 and C-8. Accordingly, the absolute configuration of **2** was assigned as 6*R*,7*R*,8*R*,15*R*.

The molecular formula of **3** was established as C₁₂H₁₆O₄, suggesting five degrees of unsaturation. The ¹³C NMR spectrum of **3** (Table 2) showed six olefinic carbons at δ_C 127.4 (C-3a), 124.4 (C-4), 133.5 (C-5), 127.5 (C-6), 109.0 (C-7) and 159.0 (C-7a), three methylene groups at δ_C 30.2 (C-3), 67.0 (C-2') and 65.3 (C-1''), an oxygenated methine at δ_C 85.7 (C-2), a non-protonated carbon at δ_C 73.6 (C-1'), and a methyl group at δ_C 19.3 (C-3'). An ABX benzene ring system was detected at δ_H 7.21 (d, $J = 1.8$ Hz, 1H, H-4), 7.10 (dd, $J = 8.1, 1.8$ Hz, 1H, H-6), 6.74 (d, $J = 8.1$ Hz, 1H, H-7). A dihydrobenzofuran bicyclic core was established by the COSY correlations between H-2/H_{ab}-3, and H-6/H-7 in addition to the HMBC correlations from H-2 to H-7a, from H_{ab}-3 to C-3a and C-7a, from H-4 to C-3, C-6 and C-7a, from H-6 to C-4 and C-7a, and from H-7 to C-3a and C-5. Furthermore, the HMBC correlations from Me-3' to C-2, C-1' and C-2', from H_{ab}-2' to C-2, C-1' and C-3', and from H_{ab}-1'' to C-4, C-5 and C-6 indicated the attachment of a 1,2-dihydroxyisopropyl group and a hydroxymethyl group at C-2 and C-5, respectively. Thus, the planar structure of **3** was elucidated as shown (Fig. 6), for which the trivial name conielldihydrobenzofuran is proposed.

The absolute configuration of **3** was suggested to be (2*S*,1'*R*) by comparison of its ¹³C NMR data and optical rotation (Table 3) with those of (2*R*,1'*S*)-, (2*S*,1'*R*)-, (2*R*,1'*R*)-, and (2*S*,1'*S*)-2,3-dihydro-2-(1',2'-dihydroxy-1'-methyl-ethyl)-6-methoxybenzofuran [9,10].

The four known compounds were identified as 5-(1''-acetyloxymethylene)-2-(1,2-dihydroxyisopropyl)-2,3-dihydrobenzofuran (**4**) [11], pyrenophorin (**5**) [12], pyrenophorol (**6**) [13], and 15-dehydroxyintegricin B (**7**) [14] based on their NMR and MS data as well as by comparison with the literature. Here, the absolute configuration of the C₂-symmetric ring in pyrenophorin (**5**) with *R*-configuration at C-6 and the symmetry-related C-6' is reported for the first time using X-ray analysis (Fig. 7).

All isolated compounds (**1**–**7**) were tested for their cytotoxicity against the MDA-MB-231 human breast cancer cell line (Table 4). Only pyrenophorin (**5**) showed cytotoxicity with an IC₅₀ value of 7.8 μ M. Pyrenophorin (**5**) as well as the analogue pyrenophorol (**6**) were further tested against additional cell lines (Table 3). Pyrenophorin (**5**) showed significant cytotoxicity against A2780 *cis*-platin sensitive and *cis*-platin resistant cells, Ramos cells, and against Jurkat J16 cells with IC₅₀ values of 0.5, 0.9, 0.6, and 0.07 μ M, respectively. Pyrenophorol (**6**) in contrast was inactive. Comparison of the structures of pyrenophorin (**5**) and pyrenophorol (**6**) indicated the importance of the α,β -unsaturated ketone unit of **5** for cytotoxicity.

Coniellins H and I (**1** and **2**) feature a tetracyclic core and an aldehyde group at C-5, which is unusual for azaphilone derivatives. A proposed biosynthetic pathway is shown in Fig. 8. The azaphilone intermediate A is formed through esterification of a β -ketoacid (from the FAS pathway) to the polyketide chromophore (from the PKS pathway) followed by a C-8/C-12 Knoevenagel cyclization and reduction [15]. Hydrolysis of intermediate A gives the lactone ring-opened product B. From the intermediate B, coniellin H (**1**) is obtained by elimination of 15-OH, [2 + 2]cycloaddition and methylation. The second branch of the pathway from intermediate B to dihydropyrone C is suggested to be catalysed by type III PKS [16]. Then attack of OH-13 to the carbonyl at C-6 affords the hemiketal group of coniellin H (**2**).

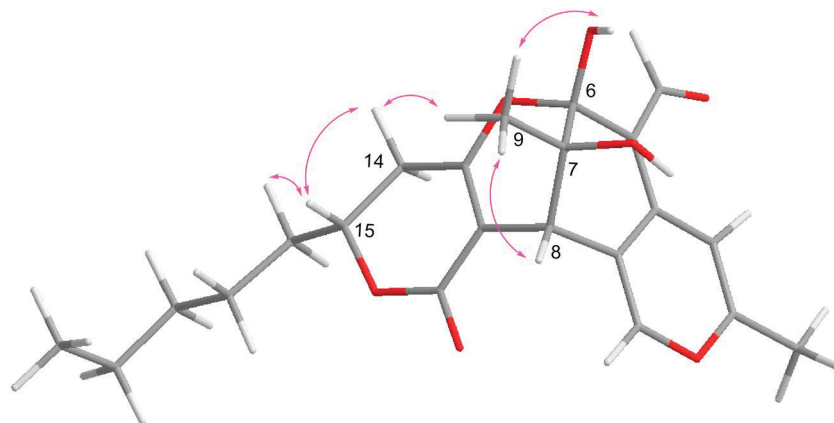


Fig. 5. Key ROESY correlations of compound 2.

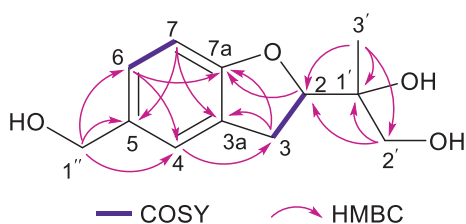


Fig. 6. COSY and key HMBC correlations of compound 3.

Table 3
Comparison of ^{13}C NMR data in CDCl_3 and optical rotation in CHCl_3 .

	3	2R,1'S	2S,1'R	2R,1'R	2S,1'S
C-2	85.7	86.13		88.60	
C-1'	73.6	73.76		73.17	
C-2'	67.0	66.96		68.73	
$[\alpha]$ in CHCl_3	+17	-27.6	+27.9	-21.2	+20.3

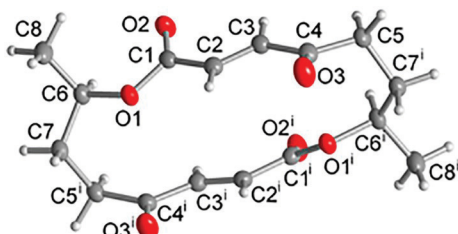


Fig. 7. Molecular structure of compound 5; the ring lies on the special position around a twofold proper rotation axis (C_2) (symmetry code: $-x + 1, -y + 1, z$).

Table 4
Cytotoxicity (IC_{50} , μM) of pyrenophorin (5) and pyrenophorol (6).

	MDA-MB-231	<i>cis</i> -platin sensitive A2780	<i>cis</i> -platin resistant A2780	Ramos	Jurkat J16
Pyrenophorin (5)	7.8	0.5	0.9	0.6	0.07
Pyrenophorol (6)	> 100	> 100	> 100	> 100	> 100
STS ^a	0.039	–	–	0.037	0.059
cDDP ^b	–	2.1	11.1	–	–

^a Staurosporin as positive control.

^b *cis*-Diammindichloridoplatin as positive control.

3. Experimental section

3.1. General experimental procedures

^1D and ^2D NMR spectra were recorded with Bruker Avance III 300 or 600 spectrometers. Mass spectra were obtained by a LC-MS HP1100 Agilent Finnigan LCQ Deca XP Thermoquest and HRESIMS data were recorded on a Bruker Daltonics UHR-QTOF Maxis 4G mass spectrometer. Optical rotations were measured with a JASCO P-2000 polarimeter. HPLC analysis was performed using a Dionex UltiMate-3400SD system coupled with a LPG-3400SD Pump, a photodiode array detector (DAD3000RS) and a Knauer Eurospher C_{18} analytical column (125×4 mm, $5 \mu\text{m}$). Semi-preparative HPLC was performed with a Lachrom-Merck Hitachi system (UV detector L-7400, pump L-7100, 300×8 mm Knauer Eurospher-100 C_{18} column). Column chromatography was carried out using Sephadex LH-20, Merck MN Silica gel 60 M or LiChroprep RP-18 as stationary phases. Plates precoated with Merck silica gel F254 were used for TLC with detection under 254 and 365 nm followed by spraying with anisaldehyde reagent.

3.2. Identification, cultivation and isolation

In September 2016, goose (*Anser anser*) dung was collected at the North Sea coast close to Garding, Germany. The fungus was identified as *C. fragariae* (GenBank No. [KJ710465.1](https://www.ncbi.nlm.nih.gov/nuccore/KJ710465.1)) by DNA amplification and sequencing of its ITS region [17]. The fungus was fermented on rice medium in 50 Erlenmeyer flasks (each containing 100 g of rice and 110 mL of demineralized water, autoclaved at 121°C for 20 min) for two weeks at 20°C under static conditions. 500 mL EtOAc were added to each flask to terminate fermentation followed by shaking for 8 h at 150 rpm. 52 g EtOAc crude extract was divided into a *n*-hexane fraction and a MeOH fraction (27 g) by liquid-liquid separation. The MeOH fraction was separated by vacuum liquid chromatography on a RP-18 column (60×200 mm) using a solvent gradient (from 100% H_2O to 100% MeOH) to give seven fractions (Fr.1 to Fr.7). Compound 5 (100 mg) was obtained from Fr.1 (4.1 g) as needle crystals. The rest of Fr.1 was fractionated on a silica gel column (30×600 mm) eluted with a gradient of CH_2Cl_2 and MeOH (1:0 to 8:2) to give 6 subfractions (Fr.1.1 to Fr.1.6). Fr.1.2 was purified by semipreparative HPLC using 30% MeOH- H_2O to afford 6 (4.8 mg). Fr.1.5 was separated by semipreparative HPLC using 25% MeOH- H_2O to give 3 (5.1 mg) and 4 (4.7 mg). Fr.2 (0.6 g) was subjected to a Sephadex LH-20 column (20×1000 mm) with MeOH as mobile phase, followed by separation using semipreparative HPLC to give 2 (5.8 mg). Fr.4 (0.9 g) was fractionated on a silica gel column (30×300 mm) with *n*-hexane and EtOAc as mobile phase to give three subfractions (Fr.4.1 to Fr.4.3). Fr.4.3 was separated by semipreparative HPLC using 50% MeOH- H_2O to afford 1 (5.0 mg). Fr.6 (2.6 g) was subjected to a silica column

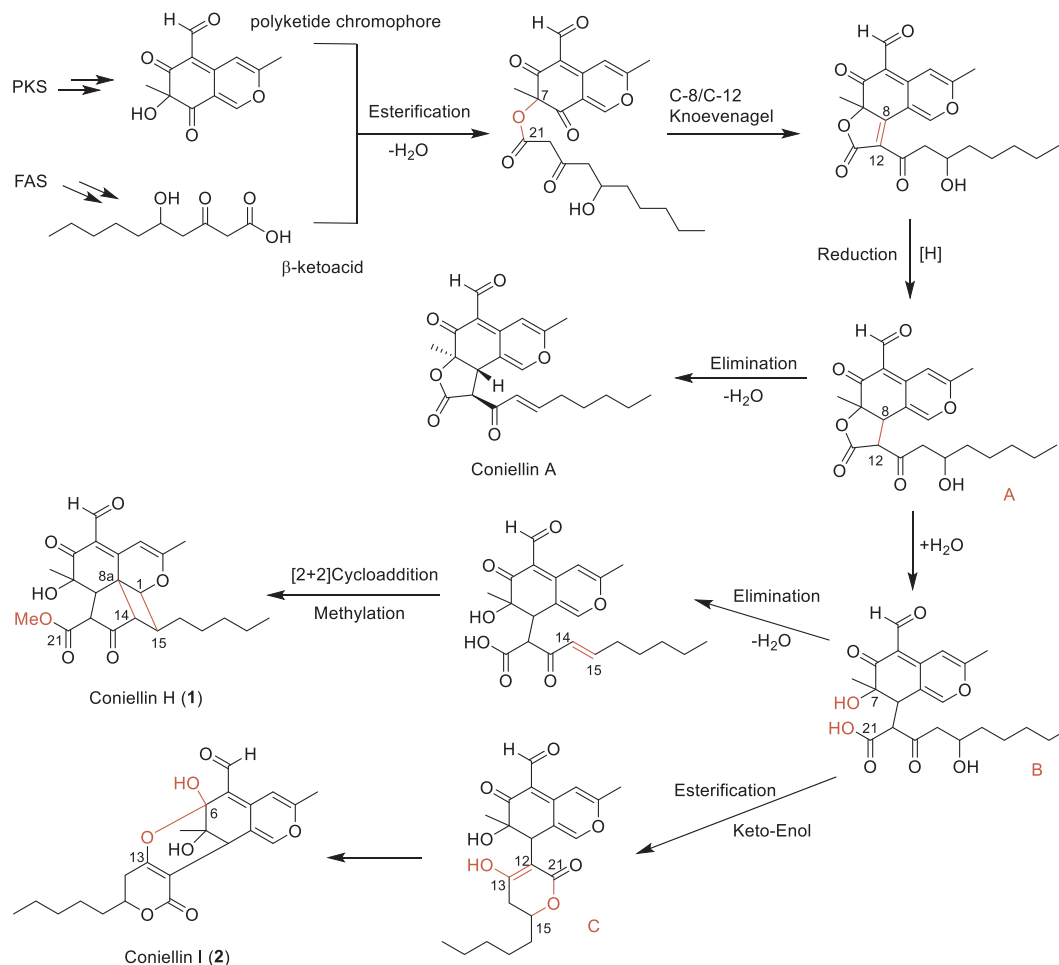


Fig. 8. Proposed biosynthetic pathway for compounds 1 and 2.

(30 × 600 mm) using a gradient of *n*-hexane and EtOAc, followed by purification with semipreparative HPLC using 80% MeOH-H₂O to give 7 (3.2 mg).

Coniellin H (1): brown amorphous solid; $[\alpha]_{20D} +413$ (c 0.1, CHCl₃); UV (MeOH) λ_{\max} 258, 384 nm; ¹H and ¹³C NMR data, Table 1; HRESIMS *m/z* 417.1905 [M + H]⁺ (calcd for C₂₃H₂₉O₇, 417.1908).

Coniellin I (2): brown amorphous solid; $[\alpha]_{20D} -482$ (c 0.1, CHCl₃); UV (MeOH) λ_{\max} 259, 384 nm; ¹H and ¹³C NMR data, Table 1; HRESIMS *m/z* 403.1794 [M + H]⁺ (calcd for C₂₂H₂₇O₇, 403.1757).

Coniellidihydrobenzofuran (3): colorless powder; $[\alpha]_{20D} +17$ (c 0.1, CHCl₃); UV (MeOH) λ_{\max} 230, 283 nm; ¹H and ¹³C NMR data, Tables 2; HRESIMS *m/z* 247.0941 [M + Na]⁺ (calcd for C₁₂H₁₆NaO₄, 247.0941).

3.3. X-ray crystallographic analysis of compound 5

Data Collection: compound 5 was measured with a Bruker Kappa APEX2 CCD diffractometer with a microfocus tube using Cu K α radiation ($\lambda = 0.71073$ Å). For data collection APEX2, for cell refinement and data reduction SAINT [18], and for experimental absorption correction SADABS were used [19]. The structure was solved by intrinsic phasing using SHELXT [20], refinement was done by full-matrix least-squares on F^2 using SHELXL-2016/6 [21]. The hydrogen atoms were positioned geometrically (with C-H = 0.95 Å for aromatic and aliphatic CH, 1.00 Å for tertiary CH, 0.99 Å for CH₂ and 0.98 Å for CH₃) and refined using riding models (AFIX 43, 13, 23, 137, respectively), with $U_{\text{iso}}(\text{H}) = 1.2U_{\text{eq}}(\text{CH}, \text{CH}_2)$ and $1.5U_{\text{eq}}(\text{CH}_3)$.

The absolute structure of 5 was solved using anomalous dispersion

from Cu K α , resulting in a Flack parameter of $x = 0.12$ [4] using Parsons quotient method [22,23].

All graphics were drawn using DIAMOND [24]. The analyses of hydrogen bonds (inter- and intramolecular) as well as π - π and CH- π interactions were done using PLATON for Windows [25–28]. The structural data has been deposited in the Cambridge Crystallographic Data Center (CCDC No. 1914503).

Crystal Data of 5: C₁₆H₂₀O₆, *M* = 308.32, orthorhombic system, space group *P*2₁2₁2, *a* = 9.8268(14) Å, *b* = 15.824(2) Å, *c* = 5.1127(7) Å, *V* = 795.0(2) Å³, *Z* = 2, *D*_{calc} = 1.288 g/cm³, crystal size 0.26 × 0.10 × 0.10 mm, $\mu(\text{Cu K}\alpha) = 0.82 \text{ mm}^{-1}$, $5.3^\circ < \theta < 66.5^\circ$, *N*_t = 5254, *N* = 1383 (*R*_{int} = 0.025), *R*₁ = 0.026, *wR*₂ = 0.067, *S* = 1.08, Flack parameter = 0.12(4).

3.4. Cytotoxicity assay

Cytotoxicity tests using the human breast cancer cell line MDAMB-231, the cisplatin sensitive and resistant human ovarian cancer cell line A2780, the adult lymphoblastic leukemia T cells Jurkat J16, or Burkitt's lymphoma B cells (Ramos) were carried out as described before [7,29].

Acknowledgment

P.P. and S.W. want to thank the DFG (GRK 2158) and the Manchot Foundation for support.

Appendix A. Supplementary data

Supplementary data to this article can be found online at <https://doi.org/10.1016/j.fitote.2019.104249>.

References

- [1] G.F. Bills, J.B. Gloer, Biologically active secondary metabolites from the fungi, *Microbiol. Spectrum* 4 (2016) 1–32.
- [2] N. Osmanova, W. Schultze, N. Ayoub, Azaphilones: a class of fungal metabolites with diverse biological activities, *Phytochem. Rev.* 9 (2010) 315–342.
- [3] J.M. Gao, S.X. Yang, J.C. Qin, Azaphilones: chemistry and biology, *Chem. Rev.* 113 (2013) 4755–4811.
- [4] T.X. Li, R.H. Liu, X.B. Wang, J. Luo, J.G. Luo, L.Y. Kong, M.H. Yang, Hypoxia-protective azaphilone adducts from *Peyronellaea glomerata*, *J. Nat. Prod.* 81 (2018) 1148–1153.
- [5] W.X. Wang, S. Kusari, M. Spittler, H. Laatsch, C. Golz, C. Strohmman, P. Kusari, O. Kayser, Antibacterial azaphilones from an endophytic fungus, *Colletotrichum* sp. BS4, *J. Nat. Prod.* 79 (2016) 704–710.
- [6] X. Luo, X. Lin, H. Tao, J. Wang, J. Li, B. Yang, X. Zhou, Y. Liu, Isochromophilones A-F, cytotoxic chloroazaphilones from the marine mangrove endophytic fungus *Diaporthe* sp. SCSIO 41011, *J. Nat. Prod.* 81 (2018) 934–941.
- [7] H. Yu, J. Sperlich, A. Mandi, T. Kurtan, H. Dai, N. Teusch, Z.Y. Guo, K. Zou, Z. Liu, P. Proksch, Azaphilone derivatives from the fungus *Coniella fragariae* inhibit NF- κ B activation and reduce tumor cell migration, *J. Nat. Prod.* 81 (2018) 2493–2500.
- [8] L.V. Alvarez, J.Z. Groenewald, P.W. Crous, Revising the *Schizoparmaceae*: *Coniella* and its synonyms *Pilidiella* and *Schizoparme*, *Stud. Mycol.* 85 (2016) 1–34.
- [9] R. Tovar-Miranda, R. Cortes-Garcia, N.F. Santos-Sanchez, P. Joseph-Nathan, Isolation, total synthesis, and relative stereochemistry of a dihydrofurocoumarin from *Dorstenia contrajerva*, *J. Nat. Prod.* 61 (1998) 1216–1220.
- [10] R. Tovar-Miranda, R. Cortes-Garcia, P. Joseph-Nathan, Synthesis and absolute configuration of the four possible stereoisomers of prandiol, *Tetrahedron Asymmetry* 13 (2002) 1147–1152.
- [11] J.H. Ding, T. Feng, Z.H. Li, L. Li, J.K. Liu, Twelve new compounds from the basidiomycete *Boreostereum vibrans*, *Nat. Prod. Bioprospect.* 2 (2012) 200–205.
- [12] M.A. Kastanias, M. Chrysayi-Tokousbalides, Bioactivity of the fungal metabolite (8R,16R)-(-)-pyrenophorin on graminaceous plants, *J. Agric. Food Chem.* 53 (2005) 5943–5947.
- [13] W. Zhang, K. Krohn, H. Egold, S. Draeger, B. Schulz, Diversity of antimicrobial pyrenophorol derivatives from an endophytic fungus, *Phoma* sp, *Eur. J. Org. Chem.* (2008) 4320–4328.
- [14] H.L. Liu, X.Y. Huang, J. Li, G.R. Xin, Y.W. Guo, Absolute configurations of integracins A, B, and 15'-dehydroxy-integracin B, *Chirality* 24 (2012) 459–462.
- [15] W. Chen, R. Chen, Q. Liu, Y. He, K. He, X. Ding, L. Kang, X. Guo, N. Xie, Y. Zhou, Y. Lu, R.J. Cox, I. Molnar, M. Li, Y. Shao, F. Chen, Orange, red, yellow: biosynthesis of azaphilone pigments in *Monascus* fungi, *Chem. Sci.* 8 (2017) 4917–4925.
- [16] T. Aizawa, S.Y. Kim, S. Takahashi, M. Koshita, M. Tani, Y. Futamura, H. Osada, N. Funa, Alkyldihydropyrone, new polyketides synthesized by a type III polyketide synthase from *Streptomyces reveromyceticus*, *J. Antibiot.* 67 (2014) 819–823.
- [17] J. Kjer, A. Debbab, A.H. Aly, P. Proksch, Methods for isolation of marine-derived endophytic fungi and their bioactive secondary products, *Nat. Protoc.* 5 (2010) 479–490.
- [18] Apex2, Data Collection Program for the CCD Area-detector System; SAINT, Data Reduction and Frame Integration Program for the CCD Area-detector System, Bruker Analytical X-ray Systems, Madison, WI, USA, 1997–2012.
- [19] G.M. Sheldrick, SADABS: Area-Detector Absorption Correction, University of Goettingen, Germany, 1996.
- [20] G.M. Sheldrick, SHELXT - integrated space-group and crystal-structure determination, *Acta Crystallogr. A.* 71 (2015) 3–8.
- [21] G.M. Sheldrick, Crystal structure refinement with SHELXL, *Acta Crystallogr. C.* 71 (2015) 3–8.
- [22] H.D. Flack, G. Bernardinelli, Absolute structure and absolute configuration, *Acta Crystallogr. A.* 55 (1999) 908–915.
- [23] H.D. Flack, On enantiomorph-polarity estimation, *Acta Crystallogr. A.* 39 (1983) 876–881.
- [24] K. Brandenburg, Diamond (Version 3.2), Crystal and Molecular Structure Visualization, Bonn, Germany (2009).
- [25] A.L. Spek, Structure validation in chemical crystallography, *Acta Crystallogr. D.* 65 (2009) 148–155.
- [26] A.L. Spek, Single-crystal structure validation with the program PLATON, *J. Appl. Crystallogr.* 36 (2003) 7–13.
- [27] A.L. Spek, PLATON - a Multipurpose Crystallographic Tool, Utrecht University, Utrecht, The Netherlands, 2008.
- [28] L.J. Farrugia, Windows Implementation, Version 40608, University of Glasgow, Scotland, 2008.
- [29] A. Mokhlesi, F. Stuhldreier, K.W. Wex, A. Berscheid, R. Hartmann, N. Rehberg, P. Sureechatchaiyan, C. Chaidir, M.U. Kassack, R. Kalscheuer, H. Brötz-Oesterheld, S. Wesselborg, B. Stork, G. Daletos, P. Proksch, Cyclic cystine-bridged peptides from the marine sponge *Clathria basilana* induce apoptosis in tumor cells and depolarize the bacterial cytoplasmic membrane, *J. Nat. Prod.* 80 (2017) 2941–2952.

Publication 9

Manuscript “Sesterterpenes and macrolide derivatives from the endophytic fungus *Aplosporella javeedii*”:

Gao Y, Stuhldreier F, Schmitt L, Wesselborg S, Wang L, Müller WEG, Kalscheuer R, Guo Z, Zou K, Liu Z, Proksch P.

Fitoterapia 146:104652 (2020). doi: 10.1016/j.fitote.2020.104652



Sesterterpenes and macrolide derivatives from the endophytic fungus *Aplosporella javeedii*



Ying Gao^a, Fabian Stuhldreier^b, Laura Schmitt^b, Sebastian Wesselborg^b, Lin Wang^a, Werner E.G. Müller^c, Rainer Kalscheuer^a, Zhiyong Guo^d, Kun Zou^d, Zhen Liu^{a,*}, Peter Proksch^{a,d,*}

^a Institute of Pharmaceutical Biology and Biotechnology, Heinrich Heine University Düsseldorf, Universitätsstrasse 1, 40225 Düsseldorf, Germany

^b Institute of Molecular Medicine I, Medical Faculty, Heinrich Heine University Düsseldorf, Universitätsstrasse 1, 40225 Düsseldorf, Germany

^c Institute of Physiological Chemistry, Universitätsmedizin der Johannes Gutenberg-Universität Mainz, 55128 Mainz, Germany

^d Hubei Key Laboratory of Natural Products Research and Development, College of Biological and Pharmaceutical Sciences, China Three Gorges University, Yichang 443002, China

ARTICLE INFO

Keywords:

Aplosporella javeedii
Sesterterpenes
Macrolides
Cytotoxicity
Antibacterial activity
Pro-apoptotic activity

ABSTRACT

Five sesterterpenes (1–5) including two new compounds (1 and 2), as well as a new (6) and a known macrolide (7) were isolated from the endophytic fungus *Aplosporella javeedii*. The structures of the new compounds were elucidated by analysis of their 1D and 2D NMR and HRMS data as well as by comparison with the literature. Compound 4 and its acetyl derivatives 4a, 4b, 4c which were prepared by acetylation of 4 exhibited moderate cytotoxicity against the mouse lymphoma cell line L5178Y with IC₅₀ values ranging from 6.2 to 12.8 μM, respectively. Moreover, 4a and 4c exhibited also cytotoxicity against human leukemia (Jurkat J16) and lymphoma (Ramos) cell lines. Compound 7 showed strong cytotoxicity against the L5178Y cell line, as well as against human Jurkat J16 and Ramos cells with IC₅₀ values of 0.4, 5.8, and 4.4 μM, respectively. Mechanistic studies indicated that 7 induces apoptotic cell death. In addition, compounds 3, 4 and 7 showed low antibacterial activities against *Mycobacterium tuberculosis* H37Rv and compound 6 against *Staphylococcus aureus*, respectively, with MICs of 100 μM. Preliminary structure-activity relationships are discussed.

1. Introduction

Endophytic fungi are an important source of new natural products with some of them showing pronounced biological activities and even exhibiting new modes of action [1–5]. Recent examples from our group include the mitochondrial toxin phomoxanthone A that disturbs the inner mitochondrial membrane within seconds and shows strong anticancer activity [6,7], as well as the unusual chlorinated flavonoid chlorflavonin that shows strong antimycobacterial activity [8]. In the search for new natural products from fungal endophytes ecologically unique and less investigated habitats such as Mangrove swamps [9] or newly discovered fungal species that have not been analyzed previously with regard to their secondary constituents are of special importance. During our ongoing studies on bioactive natural products from endophytic fungi [10–13], we isolated the endophyte *Aplosporella javeedii* from stem tissue of *Orychophragmus violaceus* (L.) O. E. Schul (Brassicaceae) collected in Beijing. This fungus was first described in 2013 [14], and has up to now hardly been studied with regard to its chemical

constituents. A first investigation of this fungus yielded a series of new antifungal polyketide derivatives with some of them showing pronounced activity against *Candida albicans* [15]. In continuation of our study on *A. javeedii*, we report now five sesterterpenes (1–5) including two new compounds (1 and 2) as well as a new (6) and a known macrolide derivative (7) and their antibacterial and cytotoxic activities (Fig. 1).

2. Results and discussion

Compound 1 was isolated as colorless oil. The molecular formula of 1 was established as C₂₅H₄₀O₄ based on the HRESIMS data, indicating six degrees of unsaturation. The ¹³C NMR spectrum of 1 displayed the presence of 25 carbons including one ketone carbonyl (δ_C 212.0, C-18), six olefinic carbons, three oxygenated carbons, three aliphatic methines, six methylenes, five methyls, and one aliphatic quaternary carbon, accounting for four degrees of unsaturation. Thus, compound 1 was suggested to be bicyclic. The ¹H and ¹³C NMR data of 1 (Table 1)

* Corresponding authors at: Institute of Pharmaceutical Biology and Biotechnology, Heinrich Heine University Düsseldorf, Universitätsstrasse 1, 40225 Düsseldorf, Germany.

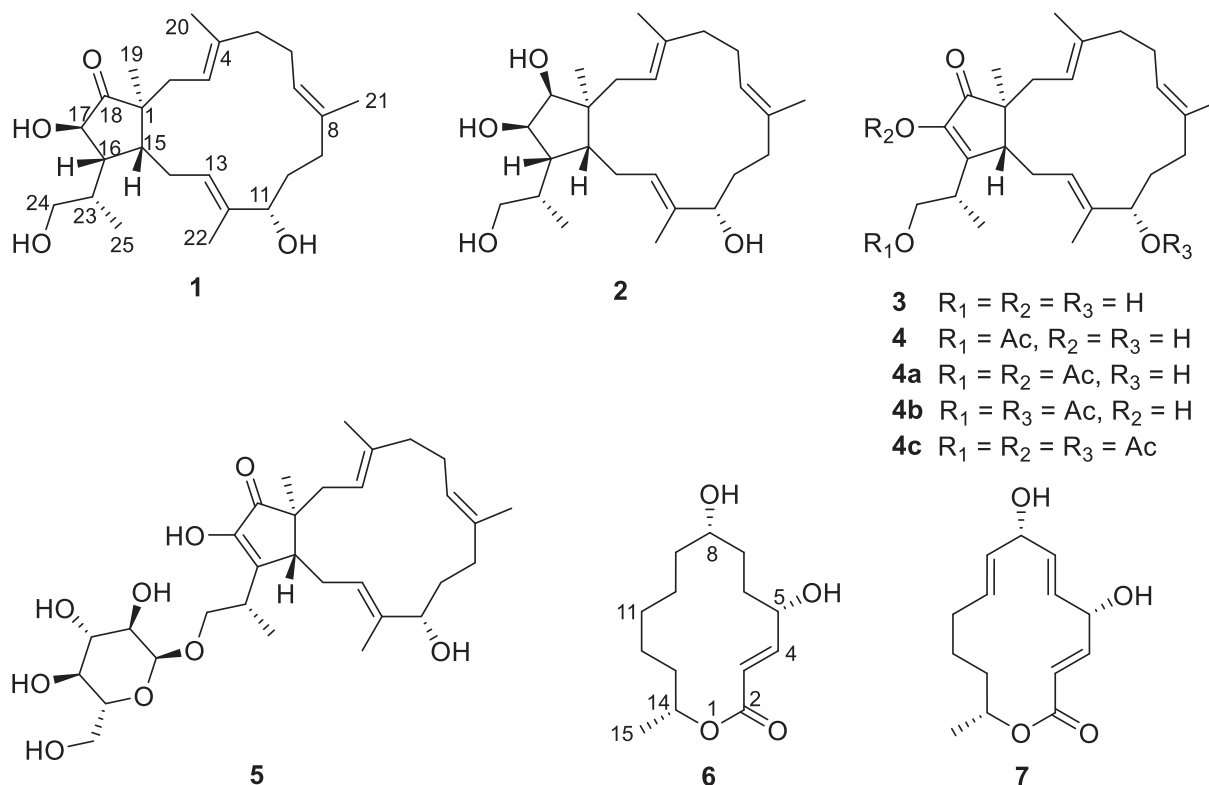
E-mail addresses: zhenfeizi0@sina.com (Z. Liu), proksch@uni-duesseldorf.com (P. Proksch).

<https://doi.org/10.1016/j.fitote.2020.104652>

Received 1 April 2020; Received in revised form 28 May 2020; Accepted 29 May 2020

Available online 06 June 2020

0367-326X/ © 2020 Elsevier B.V. All rights reserved.

Fig. 1. Structures of isolated compounds from *A. javeedii*.Table 1
 1H and ^{13}C NMR Data for compounds 1 and 2.

Position	1 ^a		2 ^a	
	δ_C , type	δ_H (J in Hz)	δ_C , type ^b	δ_H (J in Hz)
1	52.3, C		48.9, C	
2	37.0, CH ₂	2.14, m, 2.08, m	33.8, CH ₂	2.30, dd (13.9, 9.0), 1.99, m
3	122.5, CH	5.25, t (7.8)	124.8, CH	5.26, t (8.1)
4	138.8, C		136.4, C	
5	41.1, CH ₂	2.16, m, 2.11, m	40.8, CH ₂	2.13, m, 2.07, m
6	24.7, CH ₂	2.22, m	24.8, CH ₂	2.16, m
7	125.3, CH	5.19, m	126.1, CH	5.16, m
8	133.9, C		133.4, C	
9	36.0, CH ₂	2.06, m, 1.82, m	36.1, CH ₂	2.01, m, 1.84, m
10	31.2, CH ₂	1.77, m, 1.62, m	31.1, CH ₂	1.79, m, 1.59, m
11	77.5, CH	3.90, dd (9.9, 4.4)	77.6, CH	3.84, dd (10.7, 3.9)
12	136.5, C		134.4, C	
13	132.1, CH	5.18, m	132.9, CH	5.13, m
14	25.3, CH ₂	2.25, m, 2.14, m	24.9, CH ₂	2.04, m, 1.93, m
15	43.0, CH	2.29, m	44.8, CH	1.96, m
16	46.7, CH	2.06, m	50.3, CH	2.06, m
17	77.6, CH	4.07, d (13.1)	74.2, CH	3.87, dd (8.0, 6.7)
18	212.0, C		80.7, CH	3.59, d (6.8)
19	19.0, CH ₃	1.01, s	21.8, CH ₃	1.04, s
20	15.9, CH ₃	1.66, s	15.8, CH ₃	1.64, s
21	15.6, CH ₃	1.64, s	15.0, CH ₃	1.62, s
22	10.8, CH ₃	1.57, s	10.8, CH ₃	1.56, s
23	37.3, CH	2.00, m	36.6, CH	1.81, m
24	67.3, CH ₂	3.61, dd (10.5, 4.4), 3.41, dd (10.5, 6.6)	67.6, CH ₂	3.56, dd (10.5, 3.9) 3.23, dd (10.5, 7.5) 1.14, d (6.6)
25	15.7, CH ₃	1.20, d (6.7)	15.9, CH ₃	1.14, d (6.6)

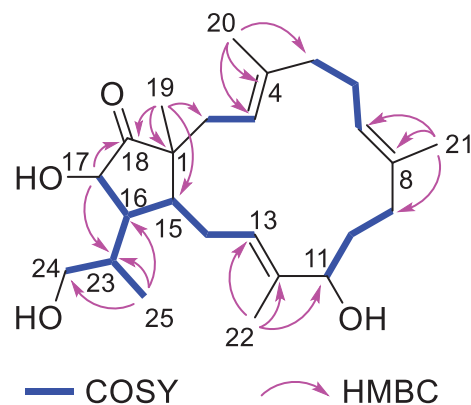
^a Recorded at 600 MHz (1H) and 150 MHz (^{13}C) in CD₃OD.^b Data extracted from HSQC and HMBC spectra.

Fig. 2. Key COSY and HMBC correlations for compound 1.

were similar to those of the co-isolated known bicyclic sesterterpene, (–)-terpestacin (3) [16,17]. Compound 1 differed from 3, however, by the presence of two additional protons at δ_H 4.07 (H-17) and 2.06 (H-16). The observed COSY correlations between H-17/H-16, H-16/H-15 (δ_H 2.29), along with the HMBC correlations from H-17 to C-18 and C-23 (δ_C 37.3), and from Me-25 to C-16 (δ_C 46.7), C-23, and C-24 (δ_C 67.3), indicated the disappearance of the double bond at C-16/C-17 of 3 in compound 1 (Fig. 2). Detailed analysis of the 2D NMR spectra of 1 revealed that the remaining substructure of 1 was identical to that of 3. Thus, compound 1 was identified as a 16,17-dihydro-(–)-terpestacin derivative, for which the trivial name terpestacin B is proposed. The three double bonds in 1 were *E*-configured as evident from the NOE correlations between H-3 (δ_H 5.25)/H-5b (δ_H 2.11), Me-20 (δ_H 1.66)/H-2b (δ_H 2.08), H-7 (δ_H 5.19)/H-9b (δ_H 1.82), Me-21 (δ_H 1.64)/H-6 (δ_H 2.22), H-13 (δ_H 5.18)/H-11 (δ_H 3.90), and Me-22 (δ_H 1.57)/H-14b (δ_H 2.14). The large coupling constant (13.2 Hz) between H-17 and H-16 indicated their *trans* orientation. The ROESY correlations between H-17/H-14b, H-14b/Me-22, Me-22/Me-19, Me-19/H-14b suggested that

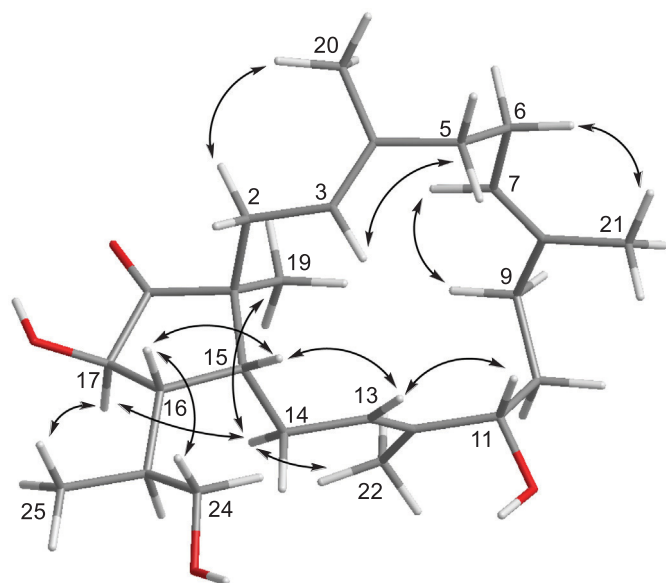


Fig. 3. Key ROESY correlations for compound 1.

these substituents were on the same face of the ring, whereas the ROESY relationship between H-16/H-15, H-15/H-13, H-13/H-11 indicated that these protons were on the opposite side of the ring (Fig. 3). Thus, the relative configuration of compound 1 was assigned as 1*S**, 11*S**, 15*R**, 16*R**, 17*R**, 23*S**. Considering the close biogenetic relationship between 1 and 3, the absolute configuration of 1 may be tentatively assigned as 1*S*, 11*S*, 15*R*, 23*S* which is identical to that of 3 for which the absolute configuration had been earlier confirmed by X-ray crystallographic analysis [18] and total enantioselective synthesis [19–22].

On the basis of the HRESIMS data, the molecular formula of compound 2 was determined as C₂₅H₄₂O₄, containing two additional protons when compared to 1. The NMR data (Table 1) of 2 were similar to those of 1 except for the replacement of the ketone moiety by an additional oxygenated methine (δ_C 80.7 and δ_H 3.59, CH-18) in 2. The location of this additional methine at C-18 was confirmed by the COSY correlations between H-18/H-17 (δ_H 3.87), H-17/H-16 (δ_H 2.06), H-16/H-23 (δ_H 1.81), and H-23/Me-25 (δ_H 1.14) in addition to the HMBC correlations from H-18 to C-2 (δ_C 33.8), C-15 (δ_C 44.8), C-16 (δ_C 50.3) and C-19 (δ_C 21.8). The remaining substructure of 2 was determined to be identical to that of 1 by analysis the 2D NMR data of 2. Thus, the structure of compound 2 was elucidated as shown, for which the trivial name terpestacin C is proposed. In the ROESY spectrum of 2, H-18 exhibited correlations to H-17 and Me-19 (δ_H 1.04), indicating that those protons have the same orientation. Based on the similar NOE correlations and the biogenetic relationship to the known compound 3, the relative configuration of 2 was assigned as 1*S**, 11*S**, 15*R**, 16*R**, 17*R**, 18*S**, 23*S**. Based on the close biogenetic relationship of both compounds the relative configuration of 2 probably matches its absolute configuration like in the case of 1.

The molecular formula of compound 6 was established as C₁₄H₂₄O₄ by HRESIMS, indicating three degrees of unsaturation. The ¹³C NMR spectra of 6 exhibited one ester carbonyl carbon at δ_C 168.7 (C-2), two olefinic carbons at δ_C 152.7 (C-4) and 121.4 (C-3), three oxygenated carbons at δ_C 71.9 (C-14), 71.0 (C-5), and 70.1 (C-8), and one methyl group at δ_C 20.7 (C-15) in addition to seven aliphatic methylenes (Table 2). Detailed analysis of the 2D NMR spectra indicated that 6 was similar to the co-isolated known compound mutolide (7) [23,24] as well as to the previously reported macrolide, pestalotioprolide C [10]. This was further confirmed by the COSY correlations between H-3/H-4, H-4/H-5, H-5/H₂-6, H₂-6/H₂-7, H₂-7/H-8, H-8/H₂-9, H₂-10/H₂-11, H₂-12/H₂-13, H₂-13/H-14, H-14/Me-15, along with key HMBC

Table 2
¹H and ¹³C NMR Data for compound 6.^a

position	δ_C , type	δ_H (J in Hz)
2	168.7, C	
3	121.4, CH	6.03, dd (15.8, 1.5)
4	152.7, CH	6.93, dd (15.8, 5.4)
5	71.0, CH	4.48, m
6	31.9, CH ₂	1.89, ddt (14.7, 9.5, 2.7), 1.81, dddd (14.7, 8.2, 6.0, 2.5)
7	31.1, CH ₂	1.69, m, 1.30, m
8	70.1, CH	3.45, m
9	35.5, CH ₂	1.45, m, 1.32, m
10	25.1, CH ₂	1.49, m, 1.32, m
11	27.0, CH ₂	1.25, m
12	24.4, CH ₂	1.56, m, 1.23, m
13	35.2, CH ₂	1.66, m
14	71.9, CH	5.00, dqd (8.2, 6.3, 4.6)
15	20.7, CH ₃	1.28, d (6.3)

^a Recorded at 600 MHz (¹H) and 150 MHz (¹³C) in CD₃OD.

correlations from H-8 to C-10, from H₂-13 to C-11, and from H-3, H-4, and H-14 to C-2. Thus, compound 6 was identified as 6,7,9,10-tetrahydromutolide. The large coupling constant (15.8 Hz) between H-3 and H-4 indicated *E* configuration for the double bond. The relative configuration at C-5, 8, and 14 of 6 cannot be directly deduced from the ROESY spectrum due to the flexibility of the macrocyclic ring and overlapping signals in the ¹H NMR spectrum. The absolute configuration of mutolide (7) had been determined as 5*S*, 8*S*, and 14*R* by X-ray analysis [23]. 6,7,9,10-Tetrahydromutolide (6) is suggested to share the same configuration at C-5, 8, and 14 as 7 due to their close biogenetic relationship.

The remaining compounds were identified as the known sesterterpenes, fusaproliferin (4) [25,26] and 24- α -D-glucosyl(-)-terpestacin (5) [27]. All sesterterpenes (1–5) isolated in this study exhibited the same skeleton. Terpestacin (3) had been first isolated from *Arthrinium* sp. [16] and showed anti-HIV [16], anti-angiogenic [28], anti-cancer [29,30], as well as anti-fungal [25] activities. Fusaproliferin (4) is an acetic acid ester of terpestacin and is known for its phytotoxic [31] and anti-cancer activity [32].

All isolated compounds (1–7) were tested for their antibacterial activities against *Mycobacterium tuberculosis* H37Rv, *Staphylococcus aureus* ATCC 29213 and *Acinetobacter baumannii* BAA1605. Compounds 3, 4 and 7 showed low antibacterial activities against *M. tuberculosis* and compound 6 against *S. aureus*, respectively, with MICs of 100 μ M. All other compounds were not active in these assays. All isolated compounds were also tested for their cytotoxicity against the mouse lymphoma cell line L5178Y as well as against human leukemia (Jurkat J16) and lymphoma (Ramos) cell lines (Table 3). Fusaproliferin (4)

Table 3
Cytotoxicity (IC₅₀, μ M) of isolated and semisynthetically derived compounds against L5178Y, Ramos and Jurkat J16 cell lines.

Compound	L5178Y ^a 72 h	Ramos ^b 24 h	Ramos 72 h	Jurkat J16 ^b 24 h	Jurkat J16 72 h
1	- ^c	> 20	> 20	16.5	16.5
2	-	14.8	19.4	> 20	> 20
3	-	-	-	-	-
4	10.8	12.1	10.4	> 20	13.4
4a	6.2	15.3	12.6	18.2	13.2
4b	12.8	> 20	4.8	> 20	10.5
4c	11.0	12.0	4.6	18.1	15.9
5	-	-	-	-	-
6	-	-	-	-	-
7	0.4	4.4	0.8	5.8	1.4

^a Kahalalide F (IC₅₀ = 4.3 μ M) was used as positive control.

^b Staurosporine (STS, IC₅₀ = 2.5 μ M) was used as positive control.

^c Not active.

exhibited cytotoxicity with an IC_{50} value of 10.8 μM against the L5178Y cell line after 72 h of incubation, whereas (–)-terpestacin (**3**) was inactive in comparison. The presence of an acetyl function in fusaproliferin (**4**) thus increases the cytotoxicity compared to the hydroxyl analogue **3**. Based on this result the diacetyl derivatives **4a** and **4b** and the triacetyl derivative **4c** of fusaproliferin (**4**) were prepared by acetylation of **4**. Compounds **4a**, **4b**, **4c** exhibited IC_{50} values of 6.2, 12.8, and 11.0 μM against the L5178Y cell line after 72 h of incubation, respectively. Whereas **4b** and **4c** were almost equipotent to the parent compound fusaproliferin (**4**), acetylation of the hydroxy group at C-17 increased the cytotoxicity of **4a** compared to **4** against the L5178Y cell line. In the human lymphoma (Ramos) cell line, compounds **2**, **4**, **4a**, and **4c** exhibited IC_{50} values of 14.8, 12.1, 15.3, and 12.0 μM after 24 h of incubation, respectively, whereas compounds **1**, **4a**, and **4c** showed cytotoxicity against the human leukemia (Jurkat J16) cell line with IC_{50} values of 16.5, 18.2, and 18.1 μM after 24 h of incubation, respectively. Thus, **4a** and **4c** showed cytotoxicity against both human cell lines, whereas **4b** was inactive ($IC_{50} > 20 \mu\text{M}$) against both cell lines in comparison.

The macrolide mutolide (**7**) displayed strong cytotoxicity against the L5178Y cell line with an IC_{50} value of 0.4 μM after 72 h of incubation, which was ten times lower than that of the positive control kahalalide F (IC_{50} 4.3 μM), whereas compound **6** was inactive in comparison. The absence of double bonds at $\Delta^{6,7}$ and $\Delta^{9,10}$ in the 14-membered ring of **6** apparently leads to a complete loss of cytotoxicity compared to **7**. Mutolide (**7**) showed also significant cytotoxicity against the human leukemia (Jurkat J16) and lymphoma (Ramos) cell lines. After 24 h incubation, the IC_{50} values of mutolide (**7**) against Jurkat J16 and Ramos cells were 5.8 and 4.4 μM , respectively whereas after 72 h of incubation these values dropped to 1.4 and 0.8 μM respectively. Mutolide (**7**) has been reported as an anti-inflammatory compound which exerts its anti-inflammatory effect via NF- κB inhibition [24]. The compound, however, showed also pro-apoptotic activity in this study. Apoptosis is the process of programmed cell death which leads to the elimination of damaged cells. Dysregulation of apoptosis is a significant factor in many human diseases such as cancer [33,34]. In order to evaluate the pro-apoptotic mechanism of mutolide (**7**), we performed an immunoblot analysis for the cleavage of the caspase-substrate poly (ADP-ribose) polymerase-1 (PARP-1) [11]. Caspases are cysteine-dependent aspartate-directed proteases and act as central executioners of the apoptotic machinery. During apoptosis PARP1 is cleaved upon activation of effector caspases such as caspase-3 that comprises a point of convergence of extrinsic and intrinsic apoptosis pathways [34]. In the Western blot experiment in the Ramos cell line, treatment of cells with 10 μM mutolide (**7**) for 2–8 h lead to an explicit cleavage of PARP-1, indicating the activation of caspase-3 and induction of apoptosis (Fig. 4). Furthermore, processing of the fluorogenic caspase-3 substrate Ac-DEVD-AMC was detected, which can identify and quantify caspase-3 activity in apoptotic cells. After treatment with mutolide (**7**) at concentrations up to 10 μM cleavage of Ac-DEVD-AMC was observed within a few hours, which is an additional proof for

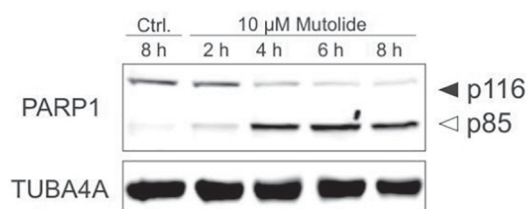


Fig. 4. Mutolide (**7**) induces apoptosis in Ramos cell line (Burkitt's lymphoma B lymphocytes). After incubation for 2–8 h, cleavage of PARP was determined by Western blot analysis. Solid arrowheads indicate the uncleaved form of PARP, open arrowheads indicate the cleaved form. The expression of TUBA4A was determined as protein loading control. Negative control (Ctrl.) was 0.1% DMSO.

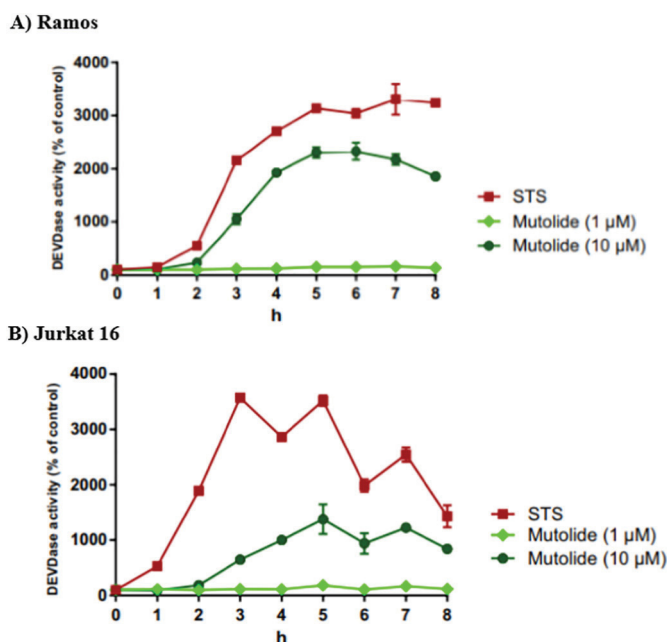


Fig. 5. The kinetics of caspase-3 activation in (A) Ramos cells (Burkitt's lymphoma B lymphocytes) and (B) Jurkat J16 cells (acute T cell leukemia cells) after treatment with indicated concentrations of mutolide (**7**). Caspase-3 activity was measured by the rate of cleavage of Ac-DEVD-AMC. Cells treated with staurosporine (STS, $IC_{50} = 2.5 \mu\text{M}$) were used as positive control. Cells treated with 0.1% DMSO were used as negative control and set to 0. Data shown are the mean \pm SD from a representative experiment performed in triplicate.

mutolide (**7**)-induced apoptosis (Fig. 5). Mutolide (**7**) is thus of interest for further studies on anticancer activity.

3. Experimental section

3.1. General experimental procedures

Optical rotations were measured using a Perkin-Elmer-241 MC polarimeter. ^1H , ^{13}C and 2D NMR spectra were recorded at 25 $^\circ\text{C}$ in CD_3OD on a Bruker ARX 600 NMR spectrometer. Chemical shifts were referenced to the solvent residual peaks. Mass spectra (ESI) were measured on a Finnigan LCQ Deca XP Thermoquest mass spectrometer (Bremen, Germany). HRESIMS data were recorded with a UHR-QTOF maxis 4G (Bruker Daltonics) mass spectrometer. HPLC analysis was performed with a Dionex Ultimate-3400SD system with a LPG-3400SD pump and a photodiode array detector (DAD 3000RS), using the routine detection channels at 235, 254, 280 and 340 nm. The analytical HPLC column (125 \times 4 mm) was prefilled with Eurosphere-10 C_{18} (Knauer, Germany). Semi-preparative HPLC was carried out on a Merck Hitachi HPLC system (UV detector L7400; pump L7100; Eurosphere-100 C_{18} , 300 \times 8 mm, Knauer, Germany). TLC plates precoated with silica gel F $_{254}$ (Merck, Germany) were used for analysis of fractions under 254 and 366 nm or after spraying the plates with anisaldehyde reagent followed by heating. Merck MN silica gel 60 M (0.04–0.063 mm) or Sephadex LH-20 were used for column chromatography. Distilled or spectral grade solvents were used for column chromatography and spectroscopic measurements, respectively.

3.2. Fungal material and identification

The endophytic fungus was isolated from fresh, healthy stem tissue of *Orychophragmus violaceus* (L.) O. E. Schul (Brassicaceae), which was collected in April 2018 in Beijing, P.R. China. The isolation of the fungal strain was achieved according to a standard procedure as described before [35]. It was identified as *Aplosporella javeedii* according

to DNA amplification and sequencing of the ITS region with the GenBank accession number MN720704. The fungal strain (ID code ZGB-B) is kept in the Institute of Pharmaceutical Biology and Biotechnology, Heinrich-Heine University, Duesseldorf, Germany.

3.3. Cultivation, extraction and isolation

The fungus was cultivated in ten 1 L Erlenmeyer flasks on solid rice medium (100 g rice and 110 mL demineralized water). After autoclaving at 121 °C for 20 min and cooling down to room temperature, the fungal strain was added. After growing for around 20 days, the fungal cultures were extracted with 800 mL EtOAc each which resulted in a brown extract (10.5 g). Silica gel vacuum liquid chromatography (VLC) was used for the separation of the crude extract. Using solvents of increasing polarity (*n*-hexane, EtOAc, CH₂Cl₂, and MeOH), 12 fractions (V1 to V12) were obtained in total. Fraction V4 (1.1 g) was separated on a silica gel column with a *n*-hexane-EtOAc gradient (20:1 to 0:100), affording ten subfractions. Subfraction V4-S4 (165.5 mg) was purified by semi-preparative HPLC using MeOH-H₂O (70:30 to 95:5) to give **4** (56.6 mg). Fraction V5 (235.9 mg) was subjected to a Sephadex LH-20 column using CH₂Cl₂-MeOH (1:1) as eluent to obtain seven subfractions. Subfraction V5-S2 (48.8 mg) was purified by semi-preparative HPLC using MeOH-H₂O (70:30 to 93:7) to give **3** (8.7 mg). Fraction V6 (261.4 mg) was separated on a Sephadex LH-20 column using CH₂Cl₂-MeOH (1:1) as eluent to obtain six subfractions. Subfraction V6-S3 (88.6 mg) was purified by semi-preparative HPLC using MeOH-H₂O (30:70 to 55:45) to give **1** (1.8 mg), **6** (3.0 mg), and **7** (2.5 mg). Fractions V7 (206.4 mg) and V8 (100.2 mg) were combined and applied to a Sephadex LH-20 column with CH₂Cl₂-MeOH (1:1) as eluent, followed by purification using semi-preparative HPLC with MeOH-H₂O (40:60) as mobile phase to give **2** (3.7 mg). Fraction V9 (1.0 g) was separated on a Sephadex LH-20 column using CH₂Cl₂-MeOH (1:1) to give six subfractions. Subfraction V9-S3 (102.8 mg) was subjected to a silica gel column with a CH₂Cl₂-MeOH gradient (20:1 to 0:100), followed by purification using semi-preparative HPLC with MeOH-H₂O (75:25) as mobile phase to afford **5** (2.0 mg).

Terpestacin B (**1**): Colorless oil; [α]_D²⁰ – 68 (c 0.2, MeOH); UV (MeOH) λ_{\max} 201 nm; ¹H and ¹³C NMR data, see Table 1; HRESIMS [M + Na]⁺ *m/z* 427.2821 (calcd for C₂₅H₄₀O₄Na 427.2819).

Terpestacin C (**2**): Colorless oil; [α]_D²⁰ – 537 (c 0.2, MeOH); UV (MeOH) λ_{\max} 201 nm; ¹H and ¹³C NMR data, see Table 1; HRESIMS [M + Na]⁺ *m/z* 429.2982 (calcd for C₂₅H₄₂O₄Na 429.2975).

6,7,9,10-Tetrahydromutolide (**6**): Colorless powder; [α]_D²⁰ – 29 (c 0.2, MeOH); UV (MeOH) λ_{\max} 212 nm; ¹H and ¹³C NMR data, see Table 2; HRESIMS [M + Na]⁺ *m/z* 279.1570 (calcd for C₁₄H₂₄O₄Na 279.1567).

3.4. Acylation of compound 4

To compound **4** (14.7 mg) was added acetic anhydride (1 mL) followed by stirring overnight at room temperature. Then the mixture was washed with nanopure water (1 mL). The organic layer was evaporated under vacuum and gave a colorless oil. The resulting oil was separated by semi-preparative HPLC using MeCN-H₂O (50:50 to 85:15) to give **4** (0.7 mg, residual), **4a** (3.1 mg), **4b** (1.5 mg), and **4c** (4.7 mg). The structures of the semisynthetic compounds **4a**, **4b** and **4c** were elucidated by interpretation of their NMR and MS spectra and by comparison with the spectra of the parent compound **4**.

Compound **4a**: Colorless oil; [α]_D²⁰ – 17 (c 0.2, MeOH); UV (MeOH) λ_{\max} 202 and 236 nm; ESIMS [M-H₂O + H]⁺ *m/z* 469.3, [2 M + Na]⁺ *m/z* 995.5; ¹H NMR (600 MHz, CD₃OD) δ 5.39 (m, 1H), 5.32 (dd, *J* = 10.4, 5.0 Hz, 1H), 5.17 (m, 1H), 4.20 (dd, *J* = 10.8, 6.4 Hz, 1H), 4.17 (dd, *J* = 10.8, 8.1 Hz, 1H), 3.99 (dd, *J* = 9.7, 4.1 Hz, 1H), 2.99 (m, 1H), 2.92 (dd, *J* = 11.0, 2.4 Hz, 1H), 2.48 (m, 1H), 2.35–2.28 (m, 3H), 2.25 (s, 3H), 2.17–2.04 (m, 4H), 2.00 (s, 3H), 1.86–1.75 (m, 3H), 1.65 (s, 6H), 1.58 (s, 3H), 1.27 (d, *J* = 7.1 Hz, 3H),

1.02 (s, 3H).

Compound **4b**: Colorless oil; [α]_D²⁰ – 35 (c 0.2, MeOH); UV (MeOH) λ_{\max} 201 and 263 nm; ESIMS [M + Na]⁺ *m/z* 509.5; ¹H NMR (600 MHz, CD₃OD) δ 5.53 (m, 1H), 5.33 (dd, *J* = 10.5, 5.0 Hz, 1H), 5.23–5.20 (m, 1H), 5.19 (dd, *J* = 10.3, 3.8 Hz, 1H), 4.30 (dd, *J* = 10.4, 8.1 Hz, 1H), 4.25 (dd, *J* = 10.4, 6.7 Hz, 1H), 2.80 (m, 1H), 2.73 (dd, *J* = 11.3, 2.3 Hz, 1H), 2.42 (m, 1H), 2.37–2.29 (m, 3H), 2.17–2.07 (m, 3H), 2.00 (s, 3H), 1.99 (s, 3H), 1.95 (ddd, *J* = 18.0, 11.4, 7.7 Hz, 1H), 1.86–1.82 (m, 1H), 1.78–1.75 (m, 1H), 1.70 (dd, *J* = 13.7, 4.8 Hz, 1H), 1.66 (s, 3H), 1.65 (s, 3H), 1.59 (s, 3H), 1.29 (d, *J* = 7.1 Hz, 3H), 0.96 (s, 3H).

Compound **4c**: Colorless oil; [α]_D²⁰ – 41 (c 0.2, MeOH); UV (MeOH) λ_{\max} 205 and 236 nm; ESIMS [M + Na]⁺ *m/z* 551.5; ¹H NMR (600 MHz, CD₃OD) δ 5.53 (m, 1H), 5.34 (dd, *J* = 10.3, 5.4 Hz, 1H), 5.21 (m, 1H), 5.19 (dd, *J* = 10.2, 4.0 Hz, 1H), 4.20 (dd, *J* = 10.8, 6.3 Hz, 1H), 4.15 (dd, *J* = 10.8, 8.2 Hz, 1H), 2.98 (m, 1H), 2.93 (dd, *J* = 11.0, 2.5 Hz, 1H), 2.47 (m, 1H), 2.37–2.28 (m, 3H), 2.25 (s, 3H), 2.19–2.06 (m, 4H), 2.00 (s, 3H), 1.99 (s, 3H), 1.88–1.82 (m, 2H), 1.79–1.76 (m, 1H), 1.67 (s, 3H), 1.66 (s, 3H), 1.61 (s, 3H), 1.25 (d, *J* = 7.1 Hz, 3H), 1.01 (s, 3H).

3.5. Cytotoxicity and apoptosis assays

The cytotoxicity against the L5178Y mouse lymphoma cell line (European Collection of Authenticated Cell Cultures, Catalogue No. 87111908) was tested using the MTT method as described previously [36]. Kahalalide F was used as positive control (IC₅₀ 4.3 μ M) and media with 0.1% DMSO were used as negative control. The cytotoxicity against adult lymphoblastic leukemia T cells (Jurkat J16, No. ACC-282) and Burkitt's lymphoma B cells (Ramos, No. ACC-603) was tested as described previously [11]. The protein kinase inhibitor staurosporine (STS, #S5921) was used as positive control for apoptosis, while media with 0.1% DMSO were used as negative control. Activation of caspase-3 as a hallmark of apoptosis was determined as described earlier. Briefly, fluorescence of the pro-fluorescent caspase-3 substrate Ac-DEVD-AMC (Biomol, #ABD-13402) was measured via microplate spectrophotometer and served as an indirect measure of apoptotic cell death [37]. All experiments were carried out in triplicate.

3.6. Antibacterial assay

The antibacterial assay was performed with the broth microdilution method following the recommendation of the Clinical and Laboratory Standards Institute (CLSI) [38]. The antibacterial activity was evaluated by calculating the MIC against a panel of Gram positive and negative bacterial strains including *Mycobacterium tuberculosis* H37Rv, *Staphylococcus aureus* ATCC 29213, and *Acinetobacter baumannii* BAA1605. MICs of 50–100 μ M are considered to reflect a weak activity, whereas MIC > 100 μ M is considered inactive.

Acknowledgments

This study was supported by the Deutsche Forschungsgemeinschaft (DFG, German Research Foundation) – project number 270650915 / GRK 2158 (to P.P., S.W. and R.K.). P.P. also wants to thank the Jürgen Manchot Foundation for support. W.L. wishes to thank the China Scholarship Council, the Ministry of Education of China, for a doctoral scholarship.

Appendix A. Supplementary data

Supplementary data to this article can be found online at <https://doi.org/10.1016/j.fitote.2020.104652>.

References

- [1] A.H. Aly, A. Debbab, P. Proksch, Fungal endophytes: unique plant inhabitants with great promises, *Appl. Microbiol. Biotechnol.* 90 (2011) 1829–1845.
- [2] A.H. Aly, A. Debbab, J. Kjer, P. Proksch, Fungal endophytes from higher plants: a prolific source of phytochemicals and other bioactive natural products, *Fungal Divers.* 41 (2010) 1–16.
- [3] F. Uzma, C.D. Mohan, A. Hashem, et al., Endophytic fungi—alternative sources of cytotoxic compounds: a review, *Front. Pharmacol.* 9 (2018) 309.
- [4] S. Gouda, G. Das, S.K. Sen, H.S. Shin, J.K. Patra, Endophytes: a treasure house of bioactive compounds of medicinal importance, *Front. Microbiol.* 7 (2016) 1538.
- [5] A.H. Aly, A. Debbab, P. Proksch, Fungal endophytes—secret producers of bioactive plant metabolites, *Die Pharmazie* 68 (2013) 499–505.
- [6] P. Böhler, F. Stuhldreier, R. Anand, et al., The mycotoxin phomoxanthone a disturbs the form and function of the inner mitochondrial membrane, *Cell Death Dis.* 9 (2018) 286.
- [7] C. Wang, L. Engelke, D. Bickel, et al., The tetrahydroxanthone-dimer phomoxanthone a is a strong inducer of apoptosis in cisplatin-resistant solid cancer cells, *Bioorg. Med. Chem.* 27 (2019) 115044.
- [8] N. Rehberg, H.S. Akone, T.R. Joerger, et al., Chlorflavonin targets acetohydroxyacid synthase catalytic subunit IlvB1 for synergistic killing of *Mycobacterium tuberculosis*, *ACS Infect. Dis.* 4 (2018) 123–134.
- [9] E. Ancheeva, G. Daletos, P. Proksch, Lead compounds from mangrove-associated microorganisms, *Mar. Drugs* 16 (2018) 319.
- [10] S. Liu, H. Dai, G. Makhloufi, et al., Cytotoxic 14-membered macrolides from a mangrove-derived endophytic fungus, *Pestalotiopsis microspora*, *J. Nat. Prod.* 79 (2016) 2332–2340.
- [11] H. Harwoko, G. Daletos, F. Stuhldreier, et al., Dithiodiketopiperazine derivatives from endophytic fungi *Trichoderma harzianum* and *Epicoccum nigrum*, *Nat. Prod. Res.* (2019) 1–9.
- [12] S. Liu, Y. Zhao, C. Heering, et al., Sesquiterpenoids from the endophytic fungus *Rhinocladiella similis*, *J. Nat. Prod.* 82 (2019) 1055–1062.
- [13] Y. Liu, F. Stuhldreier, et al., Daldinone derivatives from the mangrove-derived endophytic fungus *Annulohyphoxylon* sp, *RSC Adv.* 7 (2017) 5381–5393.
- [14] F. Jami, B. Slippers, M.J. Wingfield, M. Gryzenhout, *Botryosphaeriaceae* species overlap on four unrelated, native south African hosts, *Fungal Biol.* 118 (2014) 168–179.
- [15] Y. Gao, et al., Antifungal polyketide derivatives from the endophytic fungus *Aplosporella javeedii*, *Bioorg. Med. Chem.* 28 (2020) 115456.
- [16] M. Oka, S. Iimura, O. Tenmyo, et al., Terpestacin, a new syncytium formation inhibitor from *Arthrinium* sp, *J. Antibiot.* 46 (1993) 367–373.
- [17] S. Iimura, M. Oka, Y. Narita, et al., Terpestacin, a novel syncytium formation inhibitor, isolated from *Arthrinium* species, *Tetrahedron Lett.* 34 (1993) 493–496.
- [18] M. Oka, S. Iimura, Y. Narita, et al., Stereochemistry and biosynthesis of terpestacin, a new syncytium formation inhibitor, *J. Organomet. Chem.* 58 (1993) 1875–1881.
- [19] J. Chan, T.F. Jamison, Enantioselective synthesis of (–)-terpestacin and structural revision of siccanol using catalytic stereoselective fragment couplings and macrocyclizations, *J. Am. Chem. Soc.* 126 (2004) 10682–10691.
- [20] G.O. Berger, M.A. Tius, Terpestacin core structure: control of stereochemistry, *Org. Lett.* 7 (2005) 5011–5013.
- [21] G.O. Berger, M.A. Tius, Total synthesis of (±)-terpestacin and (±)-11-*epi*-terpestacin, *J. Organomet. Chem.* 72 (2007) 6473–6480.
- [22] A.G. Myers, M. Siu, F. Ren, Enantioselective synthesis of (–)-terpestacin and (–)-fusaproliferin: clarification of optical rotational measurements and absolute configurational assignments establishes a homochiral structural series, *J. Am. Chem. Soc.* 124 (2002) 4230–4232.
- [23] H.B. Bode, M. Walker, A. Zeeck, Structure and biosynthesis of mutolide, a novel macrolide from a UV mutant of the fungus F-24707, *Eur. J. Org. Chem.* (8) (2000) 1451–1456.
- [24] M. Shah, S.K. Deshmukh, S.A. Verekar, et al., Anti-inflammatory properties of mutolide isolated from the fungus *Lepidosphaeria* species (PM0651419), *SpringerPlus.* 4 (2015) 706.
- [25] A. Cimmino, S. Sarrocco, M. Masi, et al., Fusaproliferin, terpestacin and their derivatives display variable allelopathic activity against some ascomycetous fungi, *Chem. Biodivers.* 13 (2016) 1593–1600.
- [26] A. Santini, A. Ritieni, V. Fogliano, et al., Structure and absolute stereochemistry of fusaproliferin, a toxic metabolite from *Fusarium proliferatum*, *J. Nat. Prod.* 59 (1996) 109–112.
- [27] D.L. Guo, M. Zhao, S.J. Xiao, et al., Two new diketopiperazines and a new glucosyl sesterterpene from *Alternaria alternata*, an endophytic fungi from *Ceratostigma griffithii*, *Phytochem. Lett.* 14 (2015) 260–264.
- [28] H.J. Jung, H.B. Lee, C.J. Kim, et al., Anti-angiogenic activity of terpestacin, a bicyclo sesterterpene from *Embellisia chlangospora*, *J. Antibiot.* 56 (2003) 492–496.
- [29] H.J. Jung, J.S. Shim, J. Lee, et al., Terpestacin inhibits tumor angiogenesis by targeting UQCRB of mitochondrial complex III and suppressing hypoxia-induced reactive oxygen species production and cellular oxygen sensing, *J. Biol. Chem.* 285 (2010) 11584–11595.
- [30] K.C. Park, S.H. Choi, Effects of endostatin and a new drug terpestacin against human neuroblastoma xenograft and cell lines, *Pediatr. Surg. Int.* 29 (2013) 1327–1340.
- [31] A. Santini, G. Meca, S. Uhlig, et al., Fusaproliferin, beauvericin and enniatins: occurrence in food—a review, *World Mycotoxin J.* 5 (2012) 71–81.
- [32] N. Hoque, C.M. Hasan, M.S. Rana, et al., Fusaproliferin, a fungal phytotoxin shows rapid and potent cytotoxicity against pancreatic cancer cell lines, *Molecules.* 23 (2018) 3288.
- [33] S. Elmore, Apoptosis: a review of programmed cell death, *Toxicol. Pathol.* 35 (2007) 495–516.
- [34] R.S. Wong, Apoptosis in cancer: from pathogenesis to treatment, *J. Exp. Clin. Cancer Res.* 30 (2011) 87.
- [35] A. Debbab, A.H. Aly, et al., Bioactive metabolites from the endophytic fungus *Stemphylium globuliferum* isolated from *Mentha pulegium*, *J. Nat. Prod.* 72 (2009) 626–631.
- [36] M. Ashour, R.A. Edrada, R. Ebel, et al., Kahalalide derivatives from the Indian sacoglossan mollusk *Elysia grandifolia*, *J. Nat. Prod.* 69 (2006) 1547–1553.
- [37] J. Manns, M. Daubrawa, S. Driessen, et al., Triggering of a Novel Intrinsic Apoptosis Pathway by the Kinase Inhibitor Staurosporine: Activation of Caspase-9 in the Absence of Apaf-1, 25 (2011), pp. 3250–3261.
- [38] CLSI, Methods for Dilution Antimicrobial Susceptibility Tests for Bacteria that Grow Aerobically. 11th Ed. CLSI Standard M07, Clinical and Laboratory Standards Institute, Wayne, PA, 2018.

Publication 10

Manuscript “Didymellanosine, a new decahydrofluorene analogue, and ascolactone C from *Didymella* sp. IEA-3B.1, an endophyte of *Terminalia catappa*”:

Ariantari NP, Ancheeva E, Frank M, Stuhldreier E, Meier D, Gröner Y, Reimche I, Teusch N, Wesselborg S, Müller WEG, Kalscheuer R, Liu Z, Proksch P

RSC Advances 10:7232–7240 (2020). doi: 10.1039/c9ra10685e


 Cite this: *RSC Adv.*, 2020, **10**, 7232

Didymellanosine, a new decahydrofluorene analogue, and ascolactone C from *Didymella* sp. IEA-3B.1, an endophyte of *Terminalia catappa*†

 Ni P. Ariantari,^{ab} Elena Ancheeva,^a Marian Frank,^a Fabian Stuhldreier,^c Dieter Meier,^a Yvonne Gröner,^a Irene Reimche,^d Nicole Teusch,^d Sebastian Wesselborg,^c Werner E. G. Müller,^e Rainer Kalscheuer,^a Zhen Liu^{*a} and Peter Proksch^{*af}

Didymellanosine (**1**), the first analogue of the decahydrofluorene-class of natural products bearing a 13-membered macrocyclic alkaloid conjugated with adenosine, and a new benzolactone derivative, ascolactone C (**4**) along with eight known compounds (**2**, **3**, **5–10**), were isolated from a solid rice fermentation of the endophytic fungus *Didymella* sp. IEA-3B.1 derived from the host plant *Terminalia catappa*. In addition, ascochitamine (**11**) was obtained when (NH₄)₂SO₄ was added to rice medium and is reported here for the first time as a natural product. Didymellanosine (**1**) displayed strong activity against the murine lymphoma cell line L5178Y, Burkitt's lymphoma B cells (Ramos) and adult lymphoblastic leukemia T cells (Jurkat J16), with IC₅₀ values of 2.0, 3.3 and 4.4 μM, respectively. When subjected to a NFκB inhibition assay, didymellanosine (**1**) moderately blocked NFκB activation in the triple-negative breast cancer cell line MDA-MB 231. In an antimicrobial assay, ascomylactam C (**3**) was the most active compound when tested against a panel of Gram-positive bacteria including drug-resistant strains with MICs of 3.1–6.3 μM, while **1** revealed weaker activity. Interestingly, both compounds were also found active against Gram-negative *Acinetobacter baumannii* with MICs of 3.1 μM, in the presence of a sublethal concentration (0.1 μM) of colistin.

 Received 18th December 2019
 Accepted 11th February 2020

DOI: 10.1039/c9ra10685e

rsc.li/rsc-advances

Introduction

Endophytic fungi are microorganisms which reside in inner tissues of host plants, that represent a notable reservoir for a wide array of biologically active molecules.^{1,2} These metabolites provide natural product pharmacophores which are of importance for the discovery of molecules for pharmaceutical and agricultural purposes.^{1,3} Examples of bioactive natural products derived from fungal endophytes include the

insecticidal compound nodulisporic acid A,⁴ and a number of potent anti-HIV compounds such as altertoxins I–III and V.⁵ Moreover, the isolation of remarkable anticancer agents from endophytes, especially those that were originally obtained from host plants, such as paclitaxel,⁶ podophyllotoxin,⁷ and camptothecin,⁸ point to their potential as alternative sources of pharmaceutically valuable metabolites.

In our search for bioactive metabolites from endophytes, we investigated *Didymella* sp. IEA-3B.1, a fungus isolated from leaves of *Terminalia catappa* (Combretaceae) from Bali, Indonesia. Species of the genus *Didymella* have been identified as teleomorphs of numerous important plant pathogens formerly only known from their corresponding anamorphs. Examples within the family Didymellaceae include several environmentally relevant species of *Ascochyta*,^{9,10} and *Phoma*.^{11,12} Literature survey of the genus *Didymella* revealed the occurrence of the phytotoxin pinolidoxin,¹⁰ tricycloalternarene derivatives,¹³ and desmethylchlorodiaportintone, a dichloroisocoumarin that showed significant inhibition of NO production.¹⁴ Another recent study on this genus afforded five compounds of the decahydrofluorene-class, including cytotoxic ascomylactams A–C, along with phomapyrrolidones A and C.¹⁵ In the present study, we describe the isolation and structure elucidation of two newly discovered metabolites (**1** and **4**) from a solid rice fermentation of *Didymella* sp. IEA-3B.1, and of ascochitamine

^aInstitute of Pharmaceutical Biology and Biotechnology, Heinrich Heine University Düsseldorf, Universitätsstrasse 1, 40225 Düsseldorf, Germany. E-mail: zhenfeizi0@sina.com; proksch@uni-duesseldorf.de

^bDepartment of Pharmacy, Faculty of Mathematics and Natural Sciences, Udayana University, 80361 Bali, Indonesia

^cInstitute of Molecular Medicine I, Medical Faculty, Heinrich Heine University Düsseldorf, Universitätsstrasse 1, 40225 Düsseldorf, Germany

^dDepartment of Biomedical Sciences, Institute of Health Research and Education, University of Osnabrück, Germany

^eInstitute for Physiological Chemistry, University Medical Center of the Johannes Gutenberg University Mainz, Duesbergweg 6, 55128 Mainz, Germany

^fHubei Key Laboratory of Natural Products Research and Development, College of Biological and Pharmaceutical Sciences, China Three Gorges University, Yichang 443002, People's Republic of China

† Electronic supplementary information (ESI) available: MS, 1D and 2D NMR spectra of compounds **1**, **4** and **11**. See DOI: 10.1039/c9ra10685e



(11) obtained from a fungal fermentation on solid rice medium following addition of $(\text{NH}_4)_2\text{SO}_4$, as well as the results of cytotoxicity, NF κ B inhibition and antimicrobial assays conducted with the isolated compounds.

Results and discussion

Chromatographic workup of the EtOAc extract of the fungal endophyte *Didymella* sp. cultured on solid rice medium, yielded two new natural products, didymellanosine (1) and ascolactone C (4), together with eight known compounds, phomapyrrolidone A (2),^{15,16} ascolactam C (3),¹⁵ (9*S*,11*R*)-(+)-ascosalitoxin (5),¹⁷ ascochitine (6),^{18,19} fusarimine (7),²⁰ 3,6,8-trihydroxy-3-methyl-3,4-dihydroisocoumarin (8),²¹ 3-methoxy-6,8-dihydroxy-3-methyl-3,4-dihydro-isocoumarin (9),²¹ and 6,8-dihydroxy-3-methyl-isocoumarin (10)²² (Fig. 1). The known compounds were identified by comparison of their NMR and MS data, as well as their specific optical rotations with data reported in the literature.

Didymellanosine (1) was isolated as a white, amorphous solid. The molecular formula of 1 was established as $\text{C}_{44}\text{H}_{54}\text{N}_6\text{O}_8$ from the HRESIMS data, accounting for twenty-one degrees of unsaturation. The planar structure of 1 was deduced by detailed analysis of 1D and 2D NMR spectra, as well as by comparison of its NMR data to those of reported structurally related alkaloids.^{15,16,23} The ^1H and ^{13}C NMR spectra of 1 (Table 1) aided by HSQC revealed signals of six methyl groups, four methylenes and twenty-one methines, including six aromatic methines at δ_{H} 8.47 (H-43), 8.20 (H-39), 7.10 (H-30 and H-34), 6.97 (H-33) and 6.71 (H-31), as well as thirteen quaternary

carbons (eleven sp^2 and two sp^3). The consecutive COSY correlations (Fig. 2) observed from H-7 through H-16, and between H-1/H-20, H-7/H-15, H-8/H-13, H-10/Me-24, and H-14/Me-25, together with the HMBC correlations from Me-20 to C-1, C-2 and C-5, from Me-21 to C-1, C-2 and C-3, from Me-22 to C-3, C-4, C-5, and C-16, and from Me-23 to C-5, C-6 and C-7, indicated the presence of a 5/6/5/6 tetracyclic system with six methyl groups at C-1, C-2, C-4, C-6, C-10 and C-12. The COSY correlations between H-30/H-31, H-33/H-34 along with the HMBC correlations from H-30 and H-34 to C-32, and from H-31 and H-33 to C-29 confirmed the presence of a *para*-substituted benzene ring in 1. Moreover, the NH signal resonating at δ_{H} 7.70 (H-35) showed HMBC correlations to C-18, C-26, C-27 and to a carbonyl C-19, while H-26 showed HMBC correlations to C-18, C-19, and C-27, suggesting the presence of a γ -lactam ring, which was further connected to the benzene ring through a methylene group, as evident from the HMBC correlations from H₂-28 to C-26, C-27, C-29 and C-30, and from 27-OH to C-27 and C-28. Additional HMBC correlations from H-15 to C-32, from H-16 and H-26 to C-17, and from 17-OH (δ_{H} 11.44) to C-16, C-17 and C-18 indicated an ether bridge between C-15 and C-32 and the linkage of lactam ring and tetracyclic core through C-17. Thus, a macrocyclic decahydrofluorene skeleton similar to 3 was established for 1. The attachment of an additional adenosine moiety at C-26 was deduced by the spin systems from H-46 to H₂-50 and between H-26 and NH-36, the HMBC correlations from H-46 to C-41 and C-43, from H-43 to C-41 and C-45, from H-39 to C-37 and C-41, from NH-36 to C-37 and C-45, and from H-26 to C-37, along with the molecular formula of 1. Thus, the planar structure of 1 was elucidated as shown (Fig. 2).

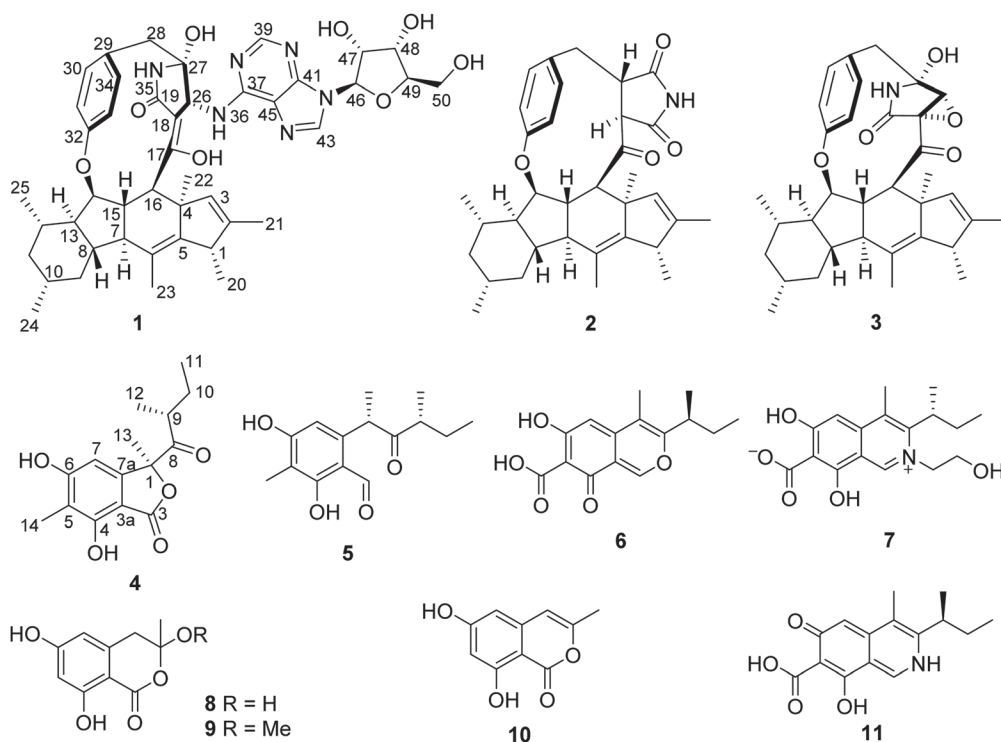


Fig. 1 Compounds isolated from *Didymella* sp. IEA-3B.1.



Table 1 ^1H and ^{13}C NMR data for compound 1^a

No.	δ_{C} , type	δ_{H} (J in Hz)	No.	δ_{C} , type	δ_{H} (J in Hz)
1	43.5, CH	2.68, q (7.1)	27	85.7, C	
2	138.0, C		28	46.0, CH ₂	2.94, d (12.5); 2.88, d (12.5)
3	131.3, CH	4.44, s	29	128.9, C	
4	52.6, C		30	130.6, CH	7.10, d (8.4)
5	144.7, C		31	119.4, CH	6.97, dd (8.4, 2.2)
6	125.5, C		32	157.3, C	
7	46.9, CH	1.95, t (12.0)	33	122.0, CH	6.71, dd (8.4, 2.2)
8	42.7, CH	1.54, m	34	129.9, CH	7.11, d (8.4)
9	39.6, CH ₂	2.08, d (12.2); 0.72, m	35		7.70, s
10	31.8, CH	1.52, m	36		7.46, d (5.1)
11	44.7, CH ₂	1.74, m; 0.68, m	37	152.2, C	
12	30.9, CH	1.79, m	39	150.8, CH	8.20, s
13	56.3, CH	1.16, m	41	147.8, C	
14	87.0, CH	4.52, dd (8.1, 5.2)	43	140.4, CH	8.47, s
15	52.3, CH	1.97, m	45	119.8, C	
16	46.2, CH	3.49, d (7.2)	46	87.9, CH	5.89, d (5.2)
17	163.6, C		47	73.7, CH	4.48, q (5.4)
18	106.6, C		48	70.0, CH	4.13, q (4.6)
19	169.6, C		49	85.3, CH	3.94, q (3.9)
20	18.4, CH ₃	0.80, d (7.1)	50	61.1, CH ₂	3.68, ddd (12.0, 4.7, 4.2); 3.52, ddd (12.0, 6.3, 3.8)
21	12.3, CH ₃	0.40, s	17-OH		11.44, s
22	27.6, CH ₃	0.95, s	27-OH		6.62, s
23	15.3, CH ₃	1.73, s	47-OH		5.47, d (6.0)
24	22.4, CH ₃	0.92, d (6.5)	48-OH		5.18, d (5.1)
25	19.9, CH ₃	1.07, d (6.1)	50-OH		5.16, t (5.5)
26	55.5, CH	4.11, d (5.1)			

^a Recorded at 600 MHz (^1H) and 125 MHz (^{13}C) in DMSO- d_6 .

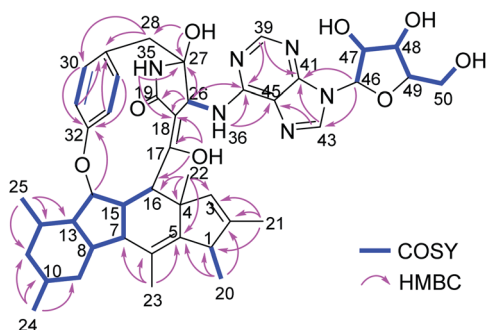


Fig. 2 COSY and key HMBC correlations of compound 1.

Compound 1 shares a similar partial structure with embellicine B,²³ and ascomylactam A,¹⁵ except for the presence of an adenine unit in 1 instead of hydroxy or methoxy groups in the former compounds.

The relative configuration of 1 was deduced through analysis of the NOESY spectrum of 1 and by comparison with those of ascomylactams A and C (3),¹⁵ (Fig. 3). The NOE correlations between H-16/H-14, H-14/H-13, H-13/H-7, H-7/Me-22, Me-22/H-16, H-16/H-31, H-31/Me-25, Me-25/H-14, H-14/H-31, Me-25/H-11b, H-11b/H-13 and H-11b/Me-24 suggested these protons to be on the same side of the molecule, whereas NOEs observed for H-1/OH-17, OH-17/H-15, H-15/H-8, H-8/H-12, H-12/H-10, OH-17/H-26, H-26/H-33, and H-33/H-15 indicated them to be on

the opposite side. In addition, the NOE correlations between H-26/H-34, H-26/H-33, H-33/H-15, and between NH-35/H-30, H-31/H-14, H-31/Me-25, OH-27/NH-36 indicated restricted rotation of the benzene ring and its parallel orientation to the γ -lactam ring, the same as reported for ascomylactams A and C (3).¹⁵

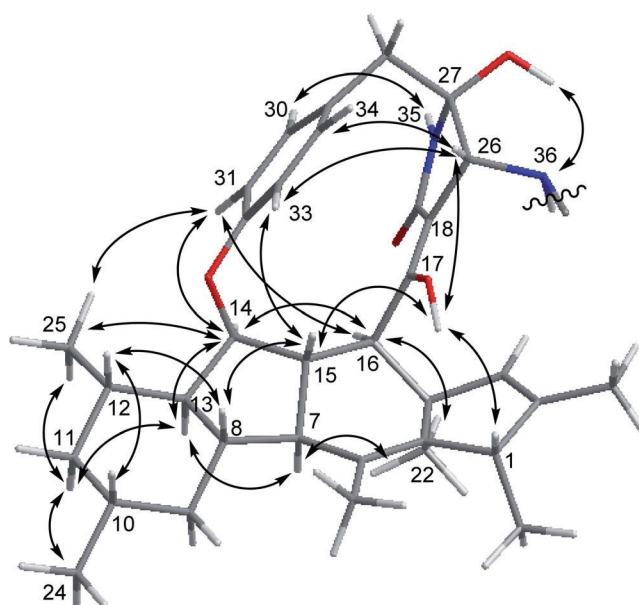


Fig. 3 Key NOE correlations of compound 1.



Moreover, the relative configuration of the adenosine moiety was elucidated by the NOE correlations between H-46/H-49, H-46/OH-47, and H-49/OH-48, as well as by comparison of the chemical shifts and coupling constants with literature data.^{24,25} Thus, the structure of compound **1** was determined as shown, representing the first example within decahydrofluorene-type alkaloids bearing a 13-membered macrocyclic skeleton conjugated with an adenosine moiety.

Ascolactone C (**4**), was obtained as a white, amorphous solid. Its HRESIMS spectrum exhibited a prominent pseudomolecular ion peak at m/z 279.1226 $[M + H]^+$, which was attributed to the molecular formula $C_{15}H_{18}O_5$, corresponding to 7 degrees of unsaturation. Inspection of the 1H NMR data of **4** (Table 2) revealed resonances of one aromatic singlet, four methyl groups, one set of methylene protons and one methine. The aromatic proton which appeared at δ_H 6.58 (H-7), exhibited HMBC correlations to C-3a, C-5 and C-6, while the aromatic methyl singlet at δ_H 2.09 (Me-14) showed HMBC correlations to C-4, C-5 and C-6, suggesting the presence of a penta-substituted benzene ring bearing a methyl substituent at the *meta*-position (Fig. 4). The COSY correlations between Me-11/H₂-10/H-9/Me-12, along with the HMBC correlations from H-9, H₂-10 and Me-12 to a ketone carbonyl at δ_C 210.8 (C-8), allowed the establishment of 2-methyl-1-oxobutyl moiety. The HMBC correlations from Me-13 (δ_H 1.67) to C-1, C-7a and C-8, and from H-7 to C-1, confirmed the connection of 2-methyl-1-oxobutyl moiety to the aromatic ring through C-1. Moreover, the weak HMBC correlation detected from H-7 and to the carbonyl C-3, together with the chemical shift of C-1 (δ_C 90.7) and the remaining one degree of unsaturation, indicated the presence of a γ -lactone fused to the benzene ring, thus forming the benzolactone skeleton. In addition, two hydroxy groups were deduced at C-4 and C-6 of the benzene ring based on the chemical shifts of C-4 and C-6 and the molecular formula of **4**. Accordingly, the planar structure of **4** was established as shown (Fig. 4). Compound **4** is structurally related to ascolactones A

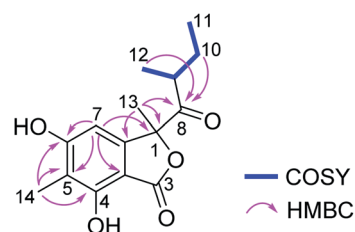


Fig. 4 COSY and key HMBC correlations of compound **4**.

and B, except for the replacement of the carboxy group at C-5 by a methyl group in **4**.¹⁹ The absolute configuration of the latter two compounds was determined by TDDFT-ECD calculations and chemical reactions. The absolute configuration of **4** was concluded to be the same as that of ascolactone B (1*S*,9*R*) on the basis of a good agreement of the 1H NMR data with regard to resonances of the side chain (δ_H 0.49, 1.06 for Me-11,12 in ascolactone A compared to δ_H 0.85, 0.78 for Me-11,12 in ascolactone B), as well as based on similar negative values of their specific optical rotations.¹⁹

In an attempt to influence the metabolite pattern of the fungus *Didymella* sp. IEA-3B.1, the strain was subjected to further fermentation in presence of 3.5 g $(NH_4)_2SO_4$ that had been added to solid rice medium. HPLC analysis of the extracts resulting from fungal fermentation on rice with and without addition of $(NH_4)_2SO_4$, revealed distinct differences of the metabolite profiles between these two cultures (Fig. S1†). The production of the main fungal metabolite during fermentation on solid rice medium, ascochitine (**6**), an azaphilone contributing to the green color of this culture, dramatically decreased when $(NH_4)_2SO_4$ was added to rice medium, thus resulting in a white coloration of the fungal culture in the presence of $(NH_4)_2SO_4$ (Fig. S2†). Similarly, isocoumarins (**8–10**) and decahydrofluorene analogues (**1–3**) were significantly down-regulated in the salt containing culture. In contrast, compound **11** was only detected in the presence of $(NH_4)_2SO_4$. The 1H NMR data of **11** were similar to those of ascochitine (**6**) and fusarimine (**7**), two azaphilone derivatives co-isolated in this study. Detailed investigation of HRESIMS and 2D NMR data of **11** identified it as the previously reported synthetic compound, ascochitamine, which was prepared by adding NH_3 or NH_4OH to ascochitine (**6**).²⁶ The formation of nitrogen containing azaphilones through substitution of the pyrane oxygen by nitrogen derived from endogenous ammonia or exogenous amino acids during fungal fermentation is well known.^{27,28} The different pH values and nitrogen sources [$(NH_4)_2SO_4$, $NaNO_3$ and peptone], in the culture medium of *Monascus anka* have been shown to affect the composition and color of *Monascus* pigments as well.²⁹ Therefore, the accumulation of ascochitamine (**11**) in this study is presumably due to the fungal response to the presence of ammonium present in the culture medium containing $(NH_4)_2SO_4$. This result also provided further evidence of the effects of media composition (*e.g.* addition of salts) on the profile of azaphilone pigments, as we reported recently for bulgariolactone D isolated from a mistletoe-associated fungus, *Bulgaria inquinans*, cultured on

Table 2 1H and ^{13}C NMR data for compound **4**^a

Position	δ_C , type ^b	δ_H (J in Hz)
1	90.7, C	
3	160.7, C	
3a	102.8, C	
4	156.2, C	
5	112.7, C	
6	163.7, C	
7	101.3, CH	6.58, s
7a	149.0, C	
8	210.8, C	
9	42.2, CH	2.83, m
10	26.6, CH ₂	1.71, ddd (14.0, 7.4, 6.7) 1.36, ddd (14.0, 7.4, 6.7)
11	11.7, CH ₃	0.87, t (7.4)
12	16.7, CH ₃	0.79, d (6.8)
13	23.4, CH ₃	1.67, s
14	7.7, CH ₃	2.09, s

^a Recorded at 600 MHz (1H) and 150 MHz (^{13}C). ^b Data were extracted from HSQC and HMBC.



solid Czapek medium containing different salt mixtures (MgSO₄, NaNO₃ and NaCl).³⁰

All isolated compounds were investigated for their cytotoxicity towards the murine lymphoma cell line L5178Y. Compound **1** showed pronounced activity with an IC₅₀ value of 2.0 μM, even more active than that of the positive control, kahalalide F (IC₅₀ 4.3 μM), while the remaining compounds were inactive. Furthermore, **1** was also active when assayed against two human cancer cell lines, Burkitt's lymphoma B cells (Ramos) and the adult lymphoblastic leukemia T cells (Jurkat J16) with IC₅₀ values of 3.3 and 4.4 μM, respectively (Table 3). As a counter screen for general toxicity, **1** was assayed against non-malignant human fetal lung fibroblast MRC5 cells which resulted in an IC₅₀ value of merely 21.2 μM. Thus, **1** is approximately 5–6 times more active against the tested cancer cell lines than against MRC5 cells, indicating moderate selectivity of **1** for cancer cells.

Furthermore, we evaluated the impact of compound **1** on NFκB activity. For NFκB inhibition study, **1** was tested in the triple-negative breast cancer (TNBC) cell line NFκB-MDA-MB-231 which is stably transfected with a NFκB-dependent luciferase reporter gene. The IC₅₀ value of **1** amounted to 15.5 μM in this assay. To exclude that inhibition of NFκB activation is caused by cytotoxicity, cell viability of TNBC cells was determined in parallel. Compound **1** was about 3 times more potent in the NFκB inhibition assay compared to its cytotoxicity (IC₅₀ 45.4 μM), thereby suggesting that the antitumor activity of compound **1** (Table 3) may be due to blockade of NFκB activation.

Moreover, all isolated compounds were subjected to an antibacterial screening. Compound **3** was the most active substance against drug-susceptible and drug-resistant strains of the Gram-positive bacteria *Staphylococcus aureus*, *Enterococcus faecalis* and *Enterococcus faecium*, with MIC values ranging from 3.1 to 6.3 μM (Table 4). Compound **1** likewise inhibited the growth of the latter bacteria with MICs ranging from 6.3 to 12.5 μM, whereas much weaker activity was observed for **2** compared to the two aforementioned analogues. Intriguingly, **1** and **3** were also found to be active against the Gram-negative bacterium *Acinetobacter baumannii*, with comparable MIC values of 3.1 μM, both tested in the presence of a sublethal concentration of colistin (0.1 μM). The activity of **1** against Gram-negative *A. baumannii* is not due to general toxicity of the compound as shown by comparison of the MIC of **1** with the IC₅₀ against MRC5 cells (Tables 3 and 4). Compounds with activity against *A. baumannii* are of substantial interest, as the increasing

emergence of multidrug-resistant strains has led to serious clinical challenges due to the limited number of effective antimicrobial drugs.^{31,32} Combination therapy of colistin with other antibacterial agents is currently considered as a promising alternative for the treatment of *A. baumannii* infections.^{33,34} All compounds were inactive against the Gram-positive bacterium *Mycobacterium tuberculosis* when tested up to 100 μM. On the basis of the antimicrobial activity of these alkaloids, the presence of a γ-lactam substructure as present in **1** and **3** seems to be preferable for the activity rather than a succinimide moiety as in **2**. As a lower potency towards Gram-positive bacteria was observed for **1** in comparison to **3**, it is suggested that the adenosine conjugate in **1** might attenuate its antimicrobial activity with regard to particular strains, while it had no effect on the tested Gram-negative bacterium.

Of note, biosynthetically related fungal alkaloids belonging to the decahydrofluorene-class, such as GKK1032s,^{35,36} pyrroci-dines,^{37–40} hirsutellones,^{41,42} trichobamide A,⁴³ and penicilpyrrodiether A,⁴⁴ were found in previous studies to exhibit antibacterial activity against Gram-positive bacteria including drug-resistant strains,^{36–38,44} and against *Mycobacterium tuberculosis*.^{41,42} These compounds furthermore exhibited antifungal activity,³⁷ were active as inhibitors of prolyl oligopeptidase,³⁹ and were shown to be cytotoxic against numerous cancer cell lines.^{35,40,43} The complex molecular architecture, consisting of a tricyclic polyketide fused to a 12 or 13-membered macroether ring which contains a γ-lactam or a succinimide moiety, combined with their intriguing bioactivities, have triggered tremendous efforts in synthetic and biosynthetic studies as well.^{45–47} However, decahydrofluorenes featuring a tetracyclic core as encountered in compound **1** are rarely reported. To date, only embellicines A and B, possessing cytostatic, cytotoxic and NFκB inhibitory activities, from a fungal endophyte *Embellisia eureka*,²³ antitubercular phomapyrrolidones A–C from an endophytic *Phoma* sp. NRRL 46751,¹⁶ and cytotoxic ascomylactams A–C from a mangrove associated fungus *Didymella* sp. CYSK-4,¹⁵ stand as examples. Thus, in light of the bioactivity results reported for didymellanosine (**1**) in this study and its new chemical feature bearing an adenosine unit attached to a pyrrolidinone, further studies on the pharmacological properties of this metabolite seem promising.

Experimental section

General procedures

HPLC analysis was carried out with a Dionex UltiMate 3000 system coupled with an UltiMate 3000 pump linked to a photodiode array detector (DAD 3000 RS). Detection wavelengths were set at 235, 254, 280, and 340 nm. The column was pre-filled with Eurospher 100-10 C₁₈, 125 × 4 mm (Knauer, Germany). The routine HPLC analysis was performed with the following gradient (MeOH : 0.1% HCOOH in H₂O): 0 min (10% MeOH); 5 min (10% MeOH); 35 min (100% MeOH); 45 min (100% MeOH). Semipreparative HPLC was conducted with a Merck Hitachi Chromaster HPLC system (UV detector 5410; pump 5110; column Eurospher 100-10 C₁₈, 300 × 8 mm, Knauer; flow rate at 5 mL min⁻¹). Silica gel 60 M (Macherey-Nagel)

Table 3 Cell viability assay (IC₅₀ in μM) of **1** towards L5178Y, Ramos, Jurkat J16 and MRC5 cells

	L5178Y ^a	Ramos ^b	Jurkat J16 ^b	MRC5 ^c
1	2.0	3.3 (6.4) ^d	4.4 (4.8) ^d	21.2

^a Kahalalide F (IC₅₀ 4.3 μM) as positive control. ^b Staurosporine (IC₅₀ 2.5 μM) as positive control. ^c Kahalalide F (IC₅₀ 10.3 μM) as positive control. ^d Selectivity index (SI): IC₅₀ value against MRC5 cells divided by IC₅₀ values against cancer cells.



Table 4 Antibacterial activity (MIC in μM) of compounds 1–3 and 6

	<i>M. tuberculosis</i> ^a		<i>S. aureus</i> ^b		<i>E. faecalis</i> ^b		<i>E. faecium</i> ^b		<i>A. baumannii</i> ^b
	H37Rv	ATCC 29213 ^c	ATCC 700699 ^d	ATCC 29212 ^c	ATCC 51299 ^e	ATCC 35667 ^c	ATCC 700221 ^f	BAA 1605 ^g	
1	>100	6.3	6.3	6.3	12.5	12.5	6.3	3.1	
2	>100	25	12.5	100	50	25	12.5	12.5	
3	>100	3.1	3.1	6.3	3.1	6.3	3.1	3.1	
6	>100	50	50	>100	>100	50	>100	>100	

^a Rifampicin as positive control. ^b Moxifloxacin as positive control. ^c Drug-susceptible strain. ^d Methicillin-resistant strain of *S. aureus* (MRSA). ^e Vancomycin-resistant strain of *E. faecalis*. ^f Vancomycin-resistant strain of *E. faecium*. ^g Tested in the presence of a sublethal concentration (0.1 μM) of colistin.

was used for vacuum liquid chromatography (VLC) and Sephadex LH-20 for column chromatography. TLC plates pre-coated with silica gel 60 F₂₅₄ (Macherey-Nagel) were used for routine analysis. One- and two-dimensional NMR spectra were recorded on Bruker AVANCE DMX 600 or 500 NMR spectrometers. ESIMS and HRESIMS data were acquired by a Finnigan LCQ Deca mass spectrometer and an UHR-QTOF maXis 4G (Bruker Daltonics) mass spectrometer, respectively. FT-IR spectra were recorded on a Bruker Tensor 37 IR spectrometer in a range of 4000–400 cm^{-1} with the resolution of 4 cm^{-1} as a KBr pellet. Optical rotations were measured on a Jasco P-2000 polarimeter.

Fungal isolation, identification and cultivation

The fungus, *Didymella* sp. IEA-3B.1, was isolated from healthy leaves of *Terminalia catappa* (Combretaceae), collected in April 2018, in Jimbaran in the south of Bali, Indonesia. The fungal culture was identified by a standard molecular biology protocol, through DNA amplification and sequencing of the ITS region as described before.⁴⁸ The sequence data have been submitted to the GenBank with accession No. MN227696.1. The voucher strain was deposited in the Institute of Pharmaceutical Biology and Biotechnology, Düsseldorf, Germany. The fungus was cultured on twenty 1 L Erlenmeyer flasks, each flask containing 100 g rice in 100 mL distilled water followed by autoclaving. Another set of fungal fermentation was carried out on five 1 L Erlenmeyer flasks by adding 3.5 g $(\text{NH}_4)_2\text{SO}_4$ to 100 g rice in 100 mL distilled water to each flask, followed by autoclaving. The fungal culture was maintained under static conditions at room temperature until the rice medium was completely covered by the fungus (30 days).

Extraction and isolation

The fungal culture grown on solid rice medium was extracted twice, each with 500 mL EtOAc added to each flask. The EtOAc extract was concentrated *in vacuo* and the obtained crude extract (32.9 g) was subjected to liquid–liquid partitioning between *n*-hexane and 90% aqueous MeOH. The 90% aqueous MeOH extract (5.0 g) was chromatographed on silica gel 60 (VLC) by a step gradient elution with *n*-hexane–EtOAc followed by CH_2Cl_2 –MeOH to afford 13 fractions (V1–V13). Based on HPLC chromatograms, fractions V3, V4, V5, V9, and V10 eluted with *n*-hexane–EtOAc (6 : 4), (4 : 6), (2 : 8), and CH_2Cl_2 –MeOH

(9 : 1), (7 : 3), respectively, were subjected to further separation. Fraction V3 (315.7 mg) was applied to a Sephadex LH-20 column and eluted with CH_2Cl_2 –MeOH (1 : 1) to obtain 4 subfractions. Purification of subfraction V3.2 (164.6 mg) was carried out with semipreparative HPLC employing MeOH–H₂O as mobile phase (from 85% to 100% MeOH) to afford 2 (45.6 mg). Meanwhile, compounds 4 (1.8 mg), 5 (5.8 mg) and 10 (2.1 mg) were obtained after purification of subfraction V3.3 (34.3 mg) by semipreparative HPLC with gradient elution of MeOH–H₂O (from 50% to 100% MeOH). Separation of fraction V4 (200.3 mg) on Sephadex LH-20 using CH_2Cl_2 –MeOH (1 : 1) as eluent, followed by purification using semipreparative HPLC eluted with MeOH–0.1% HCOOH in H₂O (from 85% to 100% MeOH), yielded 3 (3.4 mg). In a similar manner, fraction V5 (625.5 mg) was submitted to a Sephadex LH-20 column, to give 6 (263.0 mg) along with 5 subfractions. Subfraction V5.6 (37.8 mg) was purified by semipreparative HPLC, employing MeOH–0.1% HCOOH in H₂O (from 30% to 70% MeOH) as mobile phase, to yield 8 (11.6 mg) and 9 (2.2 mg). Furthermore, compound 7 (30.0 mg) was obtained by separation of fraction V9 (272.8 mg) on a Sephadex LH-20 column employing CH_2Cl_2 –MeOH (1 : 1) as eluent. Compound 1 (20.8 mg) was afforded through separation of fraction V10 (308.6 mg) over a Sephadex LH-20 column, eluted with CH_2Cl_2 –MeOH (1 : 1), followed by purification using semipreparative HPLC with MeOH–H₂O (from 85% to 100% MeOH). Following the same procedure, the fungal culture by supplementing rice medium with $(\text{NH}_4)_2\text{SO}_4$ was extracted with EtOAc, taken to dryness, and followed by liquid–liquid partition between *n*-hexane and 90% aqueous MeOH. The resulting MeOH fraction (340.2 mg) was rinsed with various solvents which yielded the pure compound 11 (3.0 mg).

Didymellanosine (1). White amorphous solid; $[\alpha]_{\text{D}}^{25}$ –28 (c 0.15, MeOH); UV (MeOH): λ_{max} 207 and 260 nm; IR ν_{max} (KBr) 3342, 2951, 2921, 2866, 1625, 1504, 1441, 1373, 1328, 1289, 1230, 1126, 1081, 1050, 950, 845, 648, 548 cm^{-1} ; 1D and 2D NMR data, see Table 1; HRESIMS m/z 795.4072 $[\text{M} + \text{H}]^+$ (calcd for $\text{C}_{44}\text{H}_{55}\text{N}_6\text{O}_8$, 795.4076).

Ascolactone C (4). White amorphous solid; $[\alpha]_{\text{D}}^{25}$ –98 (c 0.20, MeOH); UV (MeOH): λ_{max} 215, 228, and 264 nm; IR ν_{max} (KBr) 3438, 2970, 2932, 2876, 1713, 1619, 1458, 1343, 1312, 1270, 1150, 1113, 1061, 976, 837, 774, 720, 554 cm^{-1} ; 1D and 2D NMR data, see Table 2; HRESIMS m/z 279.1226 $[\text{M} + \text{H}]^+$ (calcd for $\text{C}_{15}\text{H}_{19}\text{O}_5$, 279.1227).



Ascochitamine (11). Yellowish brown amorphous solid; $[\alpha]_D^{25} -48$ (c 0.10, DMSO); UV (MeOH): λ_{\max} 264 and 357 nm; 1D and 2D NMR data, see Table S1 in the ESI;† HRESIMS m/z 276.1229 $[M + H]^+$ (calcd for $C_{15}H_{18}NO_4$, 276.1230).

Cytotoxicity assay

Cytotoxicity was tested against the murine lymphoma cell line L5178Y using the MTT method. Kahalalide F (IC_{50} 4.3 μ M) and culture media containing 0.1% DMSO were included as positive and negative controls, respectively.³⁰ Briefly, cells were seeded in 96-well plates (270 cells per well) and treated with tested compounds in the range of concentrations from 0.13 to 13 μ M in five points for 72 h. Next, 20 μ L of MTT (5 mg mL^{-1}) was added to each well and incubated for 3 h. After cell lysis, the absorbance of reduced MTT was measured by a Varioskan Flash (Thermo Scientific) at 595 nm.

Meanwhile, cytotoxicity of **1** against the human cell lines Ramos (Burkitt's lymphoma B cells), Jurkat J16 (adult lymphoblastic leukemia T cells) and non-malignant cells MRC5 (human fetal lung fibroblast cells) was determined by the resazurin reduction assay. In brief, cells were plated in 96-well plates (5×10^4 cells per well) and incubated with the indicated compound in concentrations ranging from 0.01 to 30 μ M for 72 h, respectively. Subsequently, resazurin was added to a final concentration of 40 μ M. After 3 h of incubation fluorescence of resorufin (excitation: 535 nm, emission: 590 nm) was measured *via* a microplate spectrophotometer. The reduction of resazurin to resorufin is proportional to aerobic respiration and therefore can be used as an indicator for cell viability.⁴⁹ Staurosporine (IC_{50} 2.5 μ M) was employed as a positive control for the cytotoxicity assay against Ramos and Jurkat J16 cells, while kahalalide F (IC_{50} 10.3 μ M) was used as a positive control for the assay against MRC5 cells. Culture medium containing 1% DMSO (concentration equal to the highest concentration of DMSO used in the dilutions of the tested compound) served as a negative control for the assay.

Cell culture for MDA-MB-231 cells and materials

Culture medium and supplements were purchased from Gibco (Fisher Scientific, Schwerte, Germany). Cell plates were purchased by Greiner bio-one (Frickenhausen, Germany). Cells were grown and incubated in a humidified 5% CO_2 atmosphere at constant 37 °C. The metastatic breast cancer cell line, MDA-MB-231, was obtained from the European Collection of Authenticated Cell Cultures (ECACC, Salisbury, UK). Subculture was done in RPMI 1640 medium (Cat# 21875-034) supplemented with 15% (v/v) fetal calf serum (FCS) and 1% (v/v) penicillin-streptomycin (pen-strep) (10 000 U mL^{-1}). The monoclonal NF κ B-MDA-MB-231 cell line contains a NF κ B response element to control the luciferase reporter gene. For the procedure of cell line generation see the publication of Sperlich *et al.* (2017).⁵⁰ Subculture was performed in high glucose DMEM (Cat# 41966-029) supplemented with 10% (v/v) FCS, 1% (v/v) pen-strep (10 000 U mL^{-1}) and 400 μ g mL^{-1} hygromycin B (Life Technologies, Darmstadt, Germany; Cat# 10687010) for selection. Starvation medium for the NF κ B inhibition assay was

composed of high glucose DMEM medium supplemented with 1% (v/v) FCS, 1% (v/v) pen-strep (10 000 U mL^{-1}). Cell detachment occurred by trypsinization in 0.25% trypsin-EDTA and cell counting was performed at 1 : 1 (v/v) dilution in erythrosin B (BioCat, Heidelberg, Germany; #L13002) using the LUNA II automated cell counter (BioCat). Compound **1** used for NF κ B inhibition and cell viability assay, was dissolved in DMSO to a final concentration of 10 mM and diluted in cell culture medium with final assay conditions of 1% DMSO.

Cell viability of MDA-MB-231 cells in presence of 1

Cytotoxicity of **1** against triple-negative breast cancer was determined using the cell line MDA-MB-231. Using the CyBio® Well vario pipetting robot (Analytik Jena, Jena, Germany; #OL3381-24-730), 18 μ L of the cell density of 2.8×10^5 cells per mL were seeded per well on a 384-well plate (Greiner; #781074) and incubated for 24 h. For treatment in quadruples, 2 μ L of RPMI + 1% DMSO (negative control) or the ten-fold concentrated substance was applied to reach a final volume of 20 μ L per well. The final concentration for compound ranged in two-fold serial dilution steps from 100 μ M to 0.78 μ M in eight points. As a positive control, doxorubicin (Sigma, CAS# 25316-40-9) was applied in a final concentration of 30 μ M. Compound stimulation endured for 2 h and final cell lysis and measurement was done as prescribed in the manufacturer's instruction of the CellTiter-Glo® Luminescent Cell Viability Assay (Promega, Mannheim, Germany; #G7570). In short, it was applied the equal volume of CellTiter-Glo® and luminescence was measured using the Spark® microplate reader (TECAN, Männedorf, Switzerland).

NF κ B inhibition in NF κ B-MDA-MB-231 cells in presence of 1

For testing compound **1** concerning NF κ B inhibitory activity, 4×10^4 NF κ B-MDA-MB-231 cells were seeded in total 100 μ L medium per well on a 96-well plate (Greiner; Cat# 655098). On the next day, medium was exchanged and cells pre-incubated for 20 min without (negative control) or with diluted substance in total 100 μ L starvation medium. The final concentration of the compounds ranged a two-fold serial dilution from 100 μ M downwards to 0.78 μ M in 8 points. To activate NF κ B signaling, untreated cells (positive control) or compound treated cells were subsequently stimulated for 2 h with 1 μ g mL^{-1} lipopolysaccharide (Sigma-Aldrich, Taufkirchen, Germany; #L2630). Last, cell lysis and measurement was done according to the manufacturer's instruction of the Nano-Glo Luciferase Assay System (Promega; #N1110). In short, it was applied the equal volume of 1 : 50 (v/v) diluted Nano-Glo reagent and luminescence was measured using the Spark® microplate reader (TECAN).

Antimicrobial activity

The tested bacteria included *Staphylococcus aureus* (ATCC 29213 and 700699), *Enterococcus faecium* (ATCC 35667 and 700221), *Enterococcus faecalis* (ATCC 29212 and 51299), *Acinetobacter baumannii* (ATCC BAA1605) and *Mycobacterium tuberculosis* (H37Rv). Except for *M. tuberculosis*, antimicrobial activity was



evaluated utilizing the microdilution method in accordance with the CLSI guidelines.⁵¹ Activity against *M. tuberculosis* was assessed employing the resazurin dye reduction method as described previously.⁵² Moxifloxacin was used as positive control for all tested Gram-positive and Gram-negative bacteria except for *Mycobacterium tuberculosis*, where rifampicin was used as a positive control. The tested compounds were pre-dissolved in DMSO and a final amount of 1% DMSO was included as a negative control.

Conflicts of interest

There are no conflicts to declare.

Acknowledgements

N. P. A. wishes to thank DAAD Program Biodiversity and Health for the doctoral scholarship. This work was supported by the Deutsche Forschungsgemeinschaft (DFG, German Research Foundation) – project number 270650915/GRK 2158 (to P. P., S. W. and R. K.). P. P. also wants to thank the Manchot Foundation for support. Furthermore, we wish to thank Mrs Birgit Tommes for technical assistance in FT-IR measurements.

Notes and references

- 1 A. H. Aly, A. Debbab, J. Kjer and P. Proksch, *Fungal Divers.*, 2010, **41**, 1–16.
- 2 G. Strobel, *J. Fungi*, 2018, **4**, 57.
- 3 H. Gao, G. Li and H. X. Lou, *Molecules*, 2018, **23**, 646.
- 4 J. G. Ondeyka, G. L. Helms, O. D. Hensens, M. A. Goetz, D. L. Zink, A. Tsiouras, W. L. Shoop, L. Slayton, A. W. Dombrowski, J. D. Polishook, D. A. Ostlind, N. N. Tsou, R. G. Ball and S. B. Singh, *J. Am. Chem. Soc.*, 1997, **119**, 8809–8816.
- 5 B. P. Bashyal, B. P. Wellensiek, R. Ramakrishnan, S. H. Faeth, N. Ahmad and A. A. L. Gunatilaka, *Bioorg. Med. Chem.*, 2014, **22**, 6112–6116.
- 6 A. Stierle, G. Strobel and D. Stierle, *Science*, 1993, **260**, 214–216.
- 7 S. C. Puri, A. Nazir, R. Chawla, R. Arora, S. Riyazul-Hasan, T. Amna, B. Ahmed, V. Verma, S. Singh, R. Sagar, A. Sharma, R. Kumar, R. K. Sharma and G. N. Qazi, *J. Biotechnol.*, 2006, **122**, 494–510.
- 8 S. Kusari, S. Zühlke and M. Spittler, *J. Nat. Prod.*, 2009, **72**, 2–7.
- 9 M. I. Chilvers, J. D. Rogers, F. M. Dugan, J. E. Stewart, W. Chen and T. L. Peever, *Mycol. Res.*, 2009, **113**, 391–400.
- 10 A. Cimmino, A. Andolfi, S. Fondevilla, M. A. Abouzeid, D. Rubiales and A. Evidente, *J. Agric. Food Chem.*, 2012, **60**, 5273–5278.
- 11 M. M. Aveskamp, J. de Gruyter, J. H. C. Woudenberg, G. J. M. Verkley and P. W. Crous, *Stud. Mycol.*, 2010, **65**, 1–60.
- 12 Q. Chen, J. R. Jiang, G. Z. Zhang, L. Cai and P. W. Crous, *Stud. Mycol.*, 2015, **82**, 137–217.
- 13 C. Li, Z. Hu, Q. Liu, X. Wu and S. Cao, *Tetrahedron Lett.*, 2018, **59**, 3381–3383.
- 14 Y. Chen, Z. Liu, H. Liu, Y. Pan, J. Li, L. Liu and Z. She, *Mar. Drugs*, 2018, **16**, 54.
- 15 Y. Chen, Z. Liu, Y. Huang, L. Liu, J. He, L. Wang, J. Yuan and Z. She, *J. Nat. Prod.*, 2019, **82**, 1752–1758.
- 16 E. M. K. Wijeratne, H. He, S. G. Franzblau, A. M. Hoffman and A. A. L. Gunatilaka, *J. Nat. Prod.*, 2013, **76**, 1860–1865.
- 17 M. Leyte-Lugo, M. González-Andrade, M. d. C. González, A. E. Glenn, C. M. Cerda-García-Rojas and R. Mata, *J. Nat. Prod.*, 2012, **75**, 1571–1577.
- 18 L. Colombo, C. Gennari, G. S. Ricca, C. Scolastico and F. Aragozzini, *J. Chem. Soc., Perkin Trans. 1*, 1980, 675–676.
- 19 S. F. Seibert, E. Eguereva, A. Krick, S. Kehraus, E. Voloshina, G. Raabe, J. Fleischhauer, E. Leistner, M. Wiese, H. Prinz, K. Alexandrov, P. Janning, H. Waldmann and G. M. König, *Org. Biomol. Chem.*, 2006, **4**, 2233–2240.
- 20 S.-X. Yang, J. Xiao, H. Laatsch, J. J. Holstein, B. Dittrich, Q. Zhang and J.-M. Gao, *Tetrahedron Lett.*, 2012, **53**, 6372–6375.
- 21 K. Kameda, H. Aoki, H. Tanaka and M. Namiki, *Agric. Biol. Chem.*, 1973, **37**, 2137–2146.
- 22 D. S. Zinad, K. A. Shaaban, M. A. Abdalla, M. T. Islam, A. Schöffler and H. Laatsch, *Nat. Prod. Commun.*, 2011, **6**, 45–48.
- 23 W. Ebrahim, A. H. Aly, V. Wray, A. Mándi, M.-H. Teiten, F. Gaascht, B. Orlikova, M. U. Kassack, W. Lin, M. Diederich, T. Kurtán, A. Debbab and P. Proksch, *J. Med. Chem.*, 2013, **56**, 2991–2999.
- 24 H. Rosemeyer, G. Toth and F. Seela, *Nucleosides Nucleotides*, 1989, **8**, 587–597.
- 25 P. Ciuffreda, S. Casati and A. Manocchi, *Magn. Reson. Chem.*, 2007, **45**, 781–784.
- 26 H. Mishima, M. Kurabayashhi, H. Oku and I. Iwai, *Annu. Rep. Sankyo Res. Lab.*, 1970, **22**, 67–79.
- 27 T. F. Lin, K. Yakushijin, G. H. Büchi and A. L. Demain, *J. Ind. Microbiol.*, 1992, **9**, 173–179.
- 28 X. Wang, J. G. S. Filho, A. R. Hoover, J. B. King, T. K. Ellis, D. R. Powell and R. H. Cichewicz, *J. Nat. Prod.*, 2010, **73**, 942–948.
- 29 K. Shi, D. Song, G. Chen, M. Pistolozzi, Z. Wu and L. Quan, *J. Biosci. Bioeng.*, 2015, **120**, 145–154.
- 30 N. P. Ariantari, G. Daletos, A. Mándi, T. Kurtán, W. E. G. Müller, W. Lin, E. Ancheeva and P. Proksch, *RSC Adv.*, 2019, **9**, 25119–25132.
- 31 J. Li, C. R. Rayner, R. L. Nation, R. J. Owen, D. Spelman, K. E. Tan and L. Liolios, *Antimicrob. Agents Chemother.*, 2006, **50**, 2946–2950.
- 32 L.-C. Kuo, C.-C. Lai, C.-H. Liao, C.-K. Hsu, Y.-L. Chang, C.-Y. Chang and P.-R. Hsueh, *Clin. Microbiol. Infect.*, 2007, **13**, 196–198.
- 33 S. Biswas, J.-M. Brunel, J.-C. Dubus, M. Reynaud-Gaubert and J.-M. Rolain, *Expert Rev. Anti-Infect. Ther.*, 2012, **10**, 917–934.
- 34 A. M. Peri, Y. Doi, B. A. Potoski, P. N. A. Harris, D. L. Paterson and E. Righi, *Diagn. Microbiol. Infect. Dis.*, 2019, **94**, 413–425.
- 35 F. Koizumi, Jpn. Kokat Tokyo Koho, Japanese Patent P2001-247574A, 2001.



- 36 X. Qi, X. Li, J. Zhao, N. He, Y. Li, T. Zhang, S. Wang, L. Yu and Y. Xie, *J. Antibiot.*, 2019, **72**, 237–240.
- 37 H. He, H. Y. Yang, R. Bigelis, E. H. Solum, M. Greenstein and G. T. Carter, *Tetrahedron Lett.*, 2002, **43**, 1633–1636.
- 38 T. M. Casella, V. Eparvier, H. Mandavid, A. Bendelac, G. Odonne, L. Dayan, C. Duplais, L. S. Espindola and D. Stien, *Phytochemistry*, 2013, **96**, 370–377.
- 39 Y. Shiono, A. Kosukegawa, T. Koseki, T. Murayama, E. Kwon, S. Uesugi and K.-i. Kimura, *Phytochem. Lett.*, 2012, **5**, 91–95.
- 40 S. Uesugi, N. Fujisawa, J. Yoshida, M. Watanabe, S. Dan, T. Yamori, Y. Shiono and K.-i. Kimura, *J. Antibiot.*, 2016, **69**, 133–140.
- 41 M. Isaka, N. Rugseree, P. Maithip, P. Kongsaree, S. Prabpai and Y. Thebtaranonth, *Tetrahedron*, 2005, **61**, 5577–5583.
- 42 M. Isaka, W. Prathumpai, P. Wongsang and M. Tanticharoen, *Org. Lett.*, 2006, **8**, 2815–2817.
- 43 S. Chen, H. Shen, P. Zhang, H. Cheng, X. Dai and L. Liu, *Chem. Commun.*, 2019, **55**, 1438–1441.
- 44 T. Song, M. Chen, Z.-W. Ge, W. Chai, X.-C. Li, Z. Zhang and X.-Y. Lian, *J. Org. Chem.*, 2018, **83**, 13395–13401.
- 45 H. Oikawa, *J. Org. Chem.*, 2003, **68**, 3552–3557.
- 46 H. Uchiro, R. Kato, Y. Arai, M. Hasegawa and Y. Kobayakawa, *Org. Lett.*, 2011, **13**, 6268–6271.
- 47 A. Ear, S. Amand, F. Blanchard, A. Blond, L. Dubost, D. Buisson and B. Nay, *Org. Biomol. Chem.*, 2015, **13**, 3662–3666.
- 48 J. Kjer, A. Debbab, A. H. Aly and P. Proksch, *Nat. Protoc.*, 2010, **5**, 479–490.
- 49 J. O'Brien, I. Wilson, T. Orton and F. Pognan, *Eur. J. Biochem.*, 2000, **267**, 5421–5426.
- 50 J. Sperlich, R. Kerr and N. Teusch, *Mar. Drugs*, 2017, **15**, 262.
- 51 CLSI, *Methods for Dilution Antimicrobial Susceptibility Tests for Bacteria That Grow Aerobically, Approved Standard Ninth ed. CLSI document M07-A9*, Clinical and Laboratory Standards Institute, Wayne, PA, 2012.
- 52 N. Rehberg, E. Omeje, S. S. Ebada, L. van Geelen, Z. Liu, P. Sureechachayan, M. U. Kassack, T. R. Ioerger, P. Proksch and R. Kalscheuer, *Antimicrob. Agents Chemother.*, 2019, **63**, e00136-19.



Publication 11

Manuscript “Induction of New Lactam Derivatives From the Endophytic Fungus *Aplosporella javeedii* Through an OSMAC Approach”:

Gao Y, Stuhldreier F, Schmitt L, Wesselborg S, Guo Z, Zou K, Mándi A, Kurtán T, Liu Z, Proksch P

Frontiers in Microbiology 11:600983 (2020). doi: 10.3389/fmicb.2020.600983



Induction of New Lactam Derivatives From the Endophytic Fungus *Aplosporella javeedii* Through an OSMAC Approach

Ying Gao¹, Fabian Stuhldreier², Laura Schmitt², Sebastian Wesselborg², Zhiyong Guo³, Kun Zou³, Attila Mándi⁴, Tibor Kurtán⁴, Zhen Liu^{1*} and Peter Proksch^{1,3*}

¹ Institute of Pharmaceutical Biology and Biotechnology, Heinrich Heine University Düsseldorf, Düsseldorf, Germany,

² Institute of Molecular Medicine I, Medical Faculty, Heinrich Heine University Düsseldorf, Düsseldorf, Germany, ³ Hubei Key Laboratory of Natural Products Research and Development, College of Biological and Pharmaceutical Sciences, China Three Gorges University, Yichang, China, ⁴ Department of Organic Chemistry, University of Debrecen, Debrecen, Hungary

OPEN ACCESS

Edited by:

Rosa Durán-Patrón,
University of Cádiz, Spain

Reviewed by:

Prasat Kittakoop,
Chulabhorn Graduate Institute,
Thailand
Javier Moraga,
University of Cádiz, Spain

*Correspondence:

Zhen Liu
zhenfeizi@sina.com
Peter Proksch
proksch@uni-duesseldorf.de

Specialty section:

This article was submitted to
Microbiotechnology,
a section of the journal
Frontiers in Microbiology

Received: 31 August 2020

Accepted: 16 October 2020

Published: 04 November 2020

Citation:

Gao Y, Stuhldreier F, Schmitt L,
Wesselborg S, Guo Z, Zou K,
Mándi A, Kurtán T, Liu Z and
Proksch P (2020) Induction of New
Lactam Derivatives From
the Endophytic Fungus *Aplosporella
javeedii* Through an OSMAC
Approach.
Front. Microbiol. 11:600983.
doi: 10.3389/fmicb.2020.600983

Fermentation of the endophytic fungus *Aplosporella javeedii* on solid rice medium in presence of either 3.5% NaNO₃ or 3.5% monosodium glutamate caused a significant change of the fungal metabolite pattern compared to fungal controls grown only on rice. Chemical investigation of the former fungal extracts yielded 11 new lactam derivatives, aplosporellins A–K (**2–12**), in addition to the known compound, pramanicin A (**1**). All of these compounds were not detected when the fungus was grown on rice medium without these activators thereby indicating the power of this OSMAC approach. The structures of the new compounds were elucidated by one- and two- dimensional NMR spectroscopy, DFT-NMR calculations and by mass spectrometry as well as by comparison with the literature whereas the absolute configuration of the lactam core was determined by TDDFT-ECD and OR calculations. Pramanicin A (**1**) showed strong cytotoxicity against human lymphoma (Ramos) and leukemia (Jurkat J16) cells with IC₅₀ values of 4.7 and 4.4 μM, respectively. Mechanistic studies indicated that **1** activates caspase-3 and induces apoptotic cell death.

Keywords: *Aplosporella javeedii*, lactam derivatives, OSMAC approach, DFT-NMR, TDDFT-ECD, OR calculations, apoptosis

INTRODUCTION

Endophytic fungi have been proven to be important sources for bioprospecting for new pharmaceutical lead compounds (Frank et al., 2015; Ancheeva et al., 2018; Bohler et al., 2018; Rehberg et al., 2018). However, conventional screening of endophytes that had been cultivated under standard laboratory conditions often fails to reveal the full biosynthetic potential of fungi and leads to re-isolation of already known metabolites. Strategies to activate silent biosynthetic gene clusters that are not expressed using conventional fermentation methods include co-cultivation of fungi with bacteria or the so called OSMAC (One Strain Many Compounds) approach (Daleto et al., 2017). The OSMAC approach makes use of altering cultivation parameters such as medium composition (carbon/nitrogen ratio, salinity, metal ions), physical parameters (temperature, pH, oxygen condition), or addition of enzyme inhibitors/inducers and biosynthetic precursors in order

to activate silent biosynthetic gene clusters and to expand the metabolite pattern produced by endophytes (Bode et al., 2002; Pan et al., 2019). Recent successful examples of OSMAC application from our own group include: addition of 2% tryptophan to rice medium which led to the accumulation of a new strongly cytotoxic bismacrolactone by the endophytic fungus *Trichocladium* sp. (Tran-Cong et al., 2019), addition of a mixture of salts (MgSO₄, NaNO₃, and NaCl) to solid Czapek medium which induced accumulation of nine new secondary metabolites by the endophytic fungus *Bulgaria inquinans* (Ariantari et al., 2019), and the accumulation of new brominated tyrosine-derived alkaloids by the soil fungus *Gymnascella dankaliensis* caused by addition of NaBr to solid rice medium (Wang et al., 2016).

As a part of our ongoing studies on fungal endophytes, we investigated the endophytic fungus *Aplosporella javeedii* derived from *Orychophragmus violaceus* (L.) O. E. Schul (Brassicaceae). *O. violaceus* is used in the Traditional Medicine of China for dissipating swelling and for treating unknown pyrogenic infections (Medicinal Plant Images Database, 2007). Recent studies have found that the plant also shows hepatoprotective effects (Huo et al., 2017). Previous chemical investigations of the fungus *A. javeedii* grown on solid rice medium resulted in the isolation of six new antifungal polyketides, five sesterterpenes including two new compounds, as well as a new macrolide, with some of the metabolites exhibiting cytotoxic and antimicrobial activities (Gao et al., 2020a,b). Due to the pronounced chemical diversity of natural products obtained from this fungus, we have now conducted an OSMAC study which involved the addition of different salts including 3.5% NaBr, 3.5% NaCl, 3.5% NaF, 3.5% KCl, 3.5% NH₄Cl, 3.5% (NH₄)₂SO₄, 3.5% C₅H₈NNaO₄·H₂O (monosodium glutamate), 3.5% NaNO₃, 3.5% Na₂HPO₄, 3.5% K₂HPO₄·3H₂O, 3.5% KH₂PO₄, 3.5% FeSO₄, 3.5% ZnSO₄, or 3.5% MgSO₄ to solid rice medium. The selection of most of these salts was based on previous studies which indicated their usefulness for activation of non-transcribed biosynthetic gene clusters (Hammerschmidt et al., 2015; Wang et al., 2016, 2018; Ariantari et al., 2019). The most striking effects with regard to an alteration of the fungal metabolite pattern, however, were detected following addition of either 3.5% NaNO₃ or of 3.5% monosodium glutamate to solid rice medium compared to fungal control cultures lacking either of these activators (**Figure 1**). Chemical investigation of fungal extracts obtained from fermentation of *A. javeedii* in presence of either 3.5% NaNO₃ or of 3.5% monosodium glutamate led to the isolation of 11 new lactam derivatives, aplosporellins A–K (2–12), in addition to the known compound, pramanicin A (1) (**Figure 2**), all of which were not detected when the fungus was grown on rice medium without these activators. Herein we report the structure elucidation of the new metabolites and the pro-apoptotic activity of pramanicin A (1).

MATERIALS AND METHODS

General Experimental Procedures

A Perkin-Elmer-241 MC polarimeter was used to measure optical rotations. ECD spectra were recorded on a J-810

spectropolarimeter. One- and two-dimensional NMR spectra were recorded on a Bruker ARX 600 spectrometer. Mass spectra (ESI) were recorded with a Finnigan LCQ Deca mass spectrometer. A UHR-QTOF maxis 4G mass spectrometer (Bruker Daltonics) was used to record HRESIMS data. A Dionex UltiMate-3400SD system with a LPG-3400SD pump and a photodiode array detector (DAD 3000RS) as well as a separation column (Eurosphere-10 C₁₈, 125 × 4 mm, Knauer) were used for HPLC analysis. Detection wave lengths were set at 235, 254, 280, and 340 nm. Semi-preparative HPLC analysis was performed with a Merck Hitachi Chromaster HPLC system (UV detector L7400; pump L7100; column Eurosphere-100 C₁₈, 300 × 8 mm, Knauer; flow rate at 5 mL/min). Silica gel 60 M (0.04–0.063 mm, Macherey-Nagel) or Sephadex LH-20 were used for column chromatography. TLC plates precoated with silica gel F₂₅₄ (Merck) were used to monitor isolation fractions. Distilled and spectral grade solvents were used for column chromatography and spectroscopic measurements, respectively.

Fungal Material and Fermentation

The fungus *A. javeedii* (ID code ZGB-B) was isolated from fresh, healthy stems of *Orychophragmus violaceus* (L.) O. E. Schul (Brassicaceae), collected in April 2018 in Beijing, China. Fungal identification was carried out according to a standard protocol as described previously (Kjer et al., 2010). The GenBank accession number is MN720704. The fungal strain is kept in the Institute of Pharmaceutical Biology and Biotechnology, Heinrich Heine University, Duesseldorf, Germany.

The fungus was cultivated in two 1 L Erlenmeyer flasks, of which each was filled with solid rice medium containing 100 g rice and 110 mL demineralized water. After autoclaving at 121°C for 20 min and cooling down to room temperature, the fungal strain that was preserved on the agar plates for a week was cut into pieces and added in each flask under sterile condition. The fermentation was maintained under static conditions at room temperature until the rice medium was completely overgrown by the fungus which lasted around 20 days (control cultivation). OSMAC cultivations were carried out following the same procedure by growing the fungus on solid rice medium containing 3.5% NaBr, 3.5% NaCl, 3.5% NaF, 3.5% KCl, 3.5% NH₄Cl, 3.5% (NH₄)₂SO₄, 3.5% C₅H₈NNaO₄·H₂O (monosodium glutamate), 3.5% NaNO₃, 3.5% Na₂HPO₄, 3.5% K₂HPO₄·3H₂O, 3.5% KH₂PO₄, 3.5% FeSO₄, 3.5% ZnSO₄, or 3.5% MgSO₄. Two flasks were used for each experiment and each flask contained 100 g rice, 110 mL demineralized water and 3.5 g salts. The usefulness of 3.5% salts in the OSMAC approach has been proved by previous experiments with other fungi (Hammerschmidt et al., 2015; Wang et al., 2016, 2018). Based on the chromatographic profiles obtained from the extractions of these fermentations, fungal cultivations with striking changes of metabolite patterns were selected for further investigation.

Extraction and Isolation

The fungal culture grown on solid rice medium with addition of 3.5% NaNO₃ or 3.5% monosodium glutamate was extracted with 800 mL EtOAc followed by evaporation to dryness to afford the crude extract. The obtained brown extracts from the 3.5%

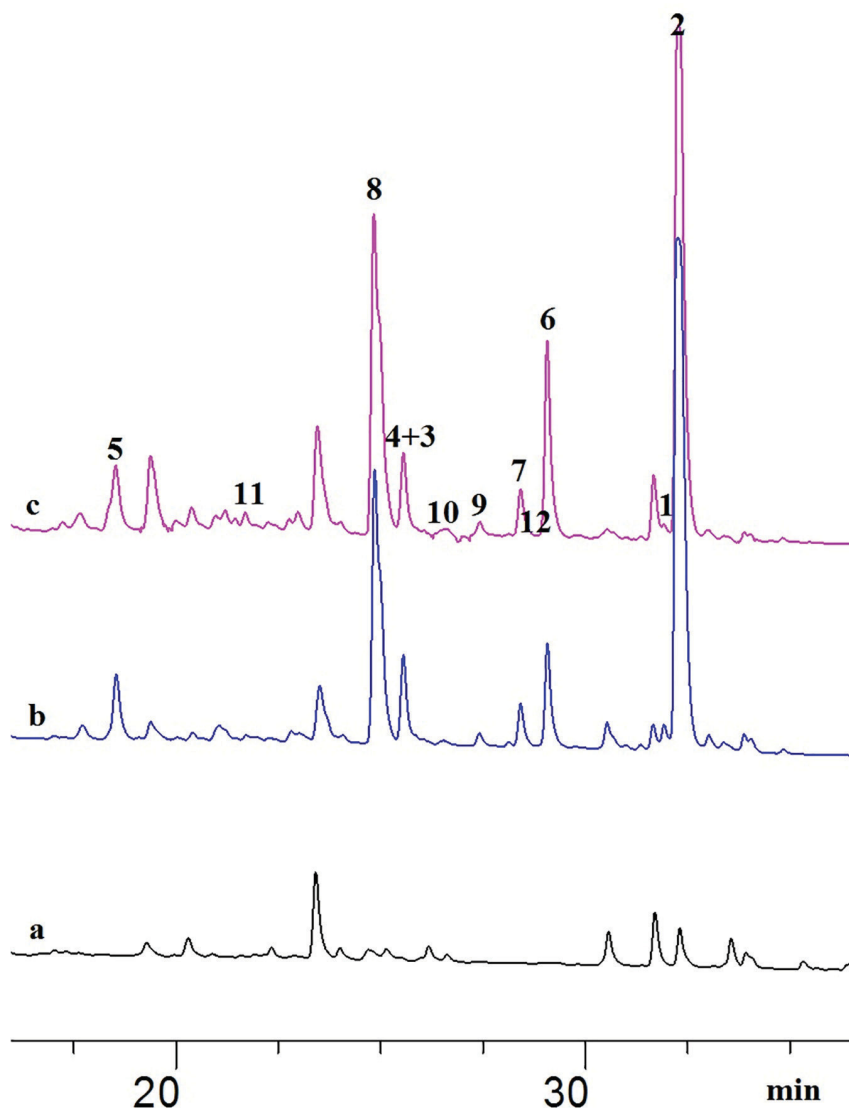


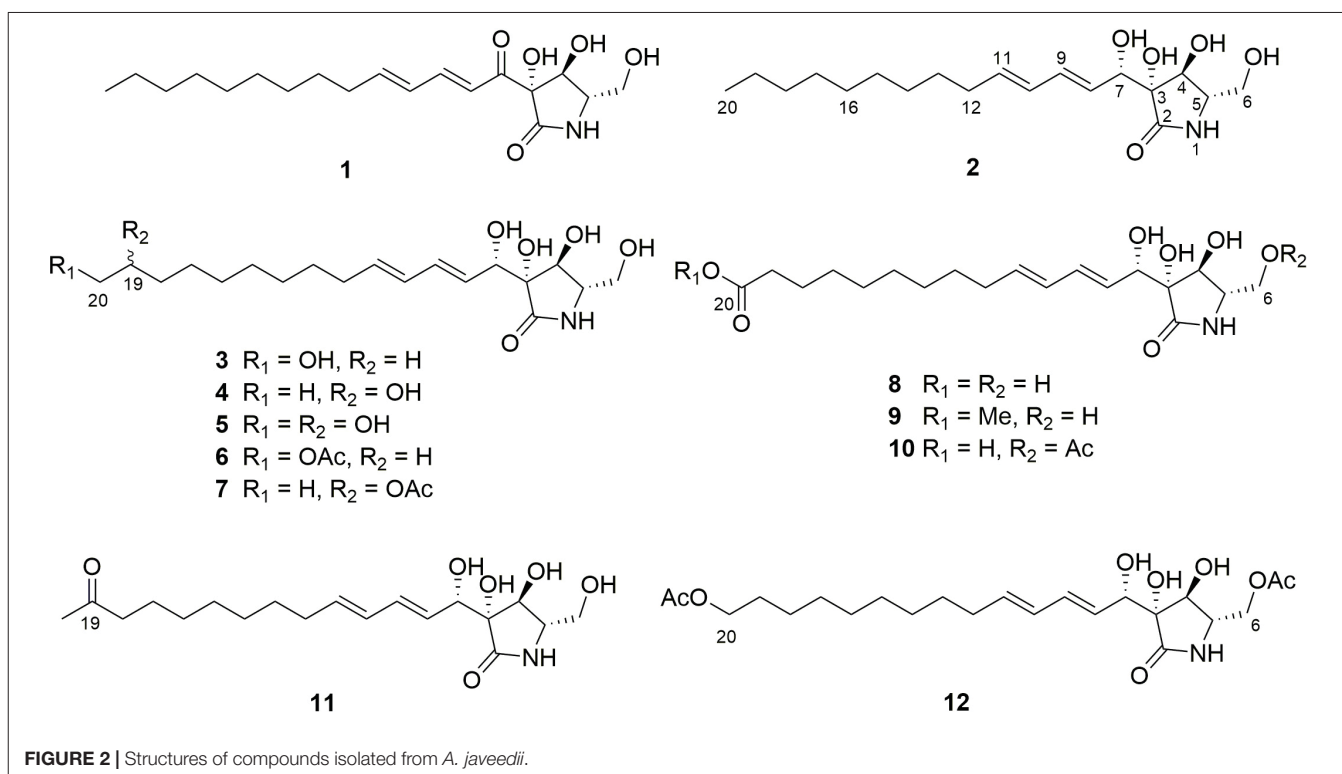
FIGURE 1 | HPLC chromatograms of the EtOAc extracts from OSMAC experiments detected at 235 nm: **(A)** *A. javeedii* control grown on solid rice medium; **(B)** *A. javeedii* cultured on solid rice medium with 3.5% NaNO_3 ; **(C)** *A. javeedii* cultured on solid rice medium with 3.5% monosodium glutamate.

NaNO_3 and 3.5% monosodium glutamate cultures were 2.3 and 2.8 g, respectively. The two crude extracts were subjected to a silica gel vacuum liquid chromatography (VLC) column, and eluted with 100% *n*-hexane, *n*-hexane-EtOAc (9:1), *n*-hexane-EtOAc (1:1), 100% EtOAc, CH_2Cl_2 -MeOH (1:1), and 100% MeOH, respectively, which resulted in 6 fractions (V1 to V6) for each extract.

From the 3.5% NaNO_3 culture extract, fraction V5 (0.55 g) was subjected to a Sephadex LH-20 column using 100% MeOH as eluent to give five subfractions (V5-S1 to V5-S5). Subfraction V5-S2 was then submitted to a RP-18 (40–63 μm) vacuum liquid chromatography column and eluted with 5–100% aqueous MeOH to yield 7 subfractions (V5-S2-RP1 to V5-S2-RP7). Subfraction V5-S2-RP4 was purified by semi-preparative HPLC using a mixture of MeCN and H_2O (10:90) containing 0.1%

HCOOH to give **4** (4.5 mg), **8** (8.2 mg), and **11** (4.3 mg). Subfraction V5-S2-RP5 was purified by semi-preparative HPLC using a gradient of MeCN and H_2O (15:85 to 50:50) containing 0.1% HCOOH to give **2** (23.5 mg), **3** (5.1 mg), **6** (6.0 mg), and **7** (5.9 mg).

From the 3.5% monosodium glutamate culture extract, fraction V4 (0.45 g) was subjected to a Sephadex LH-20 column using CH_2Cl_2 -MeOH (1:1) as eluent to obtain three subfractions (V4-S1 to V4-S3). Subfraction V4-S2 was then submitted to RP-18 (40–63 μm) vacuum liquid chromatography column and eluted with 10–100% aqueous MeOH to yield 10 subfractions (V4-S2-RP1 to V4-S2-RP10). Subfraction V4-S2-RP5 was purified by semi-preparative HPLC using MeOH-0.1% HCOOH in H_2O (50:50 to 72:28) to give **10** (2.3 mg). Subfraction V4-S2-RP7 was purified by semi-preparative HPLC



using MeOH-0.1% HCOOH in H₂O (65:35 to 86:14) to give **1** (25 mg) and **12** (1.4 mg). Fraction V5 (0.68 g) was subjected to a Sephadex LH-20 column using 100% MeOH as eluent to obtain eight subfractions (V5-S1 to V5-S8). Subfraction V5-S4 was submitted to a RP-18 (40–63 μm) vacuum liquid chromatography column and eluted with 10–100% aqueous MeOH to yield 10 subfractions (V5-S4-RP1 to V5-S4-RP10). Subfraction V5-S4-RP4 was purified by semi-preparative HPLC using MeOH-0.1% HCOOH in H₂O (50:50 to 70:30) to give **5** (2.5 mg). Subfraction V5-S4-RP6 was purified by semi-preparative HPLC using MeOH-0.1% HCOOH in H₂O (60:40) to give **9** (3.0 mg).

Pramanicin A (1): white solid; $[\alpha]^{20}_D$ -121 (c 0.1, MeOH).

Aplosporellin A (2): Colorless oil; $[\alpha]^{20}_D$ -21 (c 0.1, MeOH); UV (MeOH) λ_{max} 233 nm; ECD λ [nm] (ϕ): 239 (−1.54), 219 (1.06), 197 (−8.99); ¹H and ¹³C NMR data, see **Table 1**; HRESIMS [M + Na]⁺ *m/z* 378.2252 (calcd for C₁₉H₃₃NNaO₅ 378.2251) (**Supplementary Figures S1–S13**).

Aplosporellin B (3): Colorless oil; $[\alpha]^{20}_D$ -55 (c 0.1, MeOH); UV (MeOH) λ_{max} 233 nm; ECD λ [nm] (ϕ): 233 (−7.06), 199 (−8.83); ¹H and ¹³C NMR data, see **Table 1**; HRESIMS [M + Na]⁺ *m/z* 394.2197 (calcd for C₁₉H₃₃NNaO₆ 394.2200) (**Supplementary Figures S14–S21**).

Aplosporellin C (4): Colorless oil; $[\alpha]^{20}_D$ -26 (c 0.1, MeOH); UV (MeOH) λ_{max} 234 nm; ECD λ [nm] (ϕ): 233 (−0.98), 197 (−2.03); ¹H and ¹³C NMR data, see **Table 2**; HRESIMS [M + Na]⁺ *m/z* 394.2201 (calcd for C₁₉H₃₃NNaO₆ 394.2200) (**Supplementary Figures S22–S29**).

Aplosporellin D (5): Colorless oil; $[\alpha]^{20}_D$ -24 (c 0.1, MeOH); UV (MeOH) λ_{max} 234 nm; ¹H and ¹³C NMR data, see **Table 2**;

HRESIMS [M + Na]⁺ *m/z* 410.2145 (calcd for C₁₉H₃₃NNaO₇ 410.2149) (**Supplementary Figures S30–S37**).

Aplosporellin E (6): Colorless oil; $[\alpha]^{20}_D$ -33 (c 0.1, MeOH); UV (MeOH) λ_{max} 233 nm; ¹H and ¹³C NMR data, see **Table 2**; HRESIMS [M + Na]⁺ *m/z* 436.2307 (calcd for C₂₁H₃₅NNaO₇ 436.2306) (**Supplementary Figures S38–S45**).

Aplosporellin F (7): Colorless oil; $[\alpha]^{20}_D$ -36 (c 0.1, MeOH); UV (MeOH) λ_{max} 234 nm; ¹H and ¹³C NMR data, see **Table 3**; HRESIMS [M + Na]⁺ *m/z* 436.2304 (calcd for C₂₁H₃₅NNaO₇ 436.2306) (**Supplementary Figures S46–S53**).

Aplosporellin G (8): Colorless oil; $[\alpha]^{20}_D$ -57 (c 0.1, MeOH); UV (MeOH) λ_{max} 233 nm; ECD λ [nm] (ϕ): 234 (−2.59), 197 (−7.64); ¹H and ¹³C NMR data, see **Table 3**; HRESIMS [M + Na]⁺ *m/z* 408.1990 (calcd for C₁₉H₃₁NNaO₇ 408.1993) (**Supplementary Figures S54–S61**).

Aplosporellin H (9): Colorless oil; $[\alpha]^{20}_D$ -26 (c 0.1, MeOH); UV (MeOH) λ_{max} 232 nm; ¹H and ¹³C NMR data, see **Table 3**; HRESIMS [M + Na]⁺ *m/z* 422.2150 (calcd for C₂₀H₃₃NNaO₇ 422.2149) (**Supplementary Figures S62–S69**).

Aplosporellin I (10): Colorless oil; $[\alpha]^{20}_D$ -31 (c 0.1, MeOH); UV (MeOH) λ_{max} 233 nm; ¹H and ¹³C NMR data, see **Table 4**; HRESIMS [M + Na]⁺ *m/z* 450.2102 (calcd for C₂₁H₃₃NNaO₈ 450.2098) (**Supplementary Figures S70–S76**).

Aplosporellin J (11): Colorless oil; $[\alpha]^{20}_D$ -7 (c 0.1, MeOH); UV (MeOH) λ_{max} 234 nm; ¹H and ¹³C NMR data, see **Table 4**; HRESIMS [M + Na]⁺ *m/z* 392.2048 (calcd for C₁₉H₃₁NNaO₆ 392.2044) (**Supplementary Figures S77–S84**).

Aplosporellin K (12): Colorless oil; $[\alpha]^{20}_D$ -17 (c 0.1, MeOH); UV (MeOH) λ_{max} 232 nm; ¹H and ¹³C NMR data, see **Table 4**;

HRESIMS $[M + Na]^+$ m/z 478.2410 (calcd for $C_{23}H_{37}NNaO_8$ 478.2411) (**Supplementary Figures S85–S91**).

Cytotoxicity and Apoptosis Assays

Cytotoxicity against adult Burkitt's lymphoma B cells (Ramos, No. ACC-603) and lymphoblastic leukemia T cells (Jurkat J16, No. ACC-282) was tested as described previously (Harwoko et al., 2019). In the apoptosis assays, the protein kinase inhibitor staurosporine (STS, 2.5 μ M, #S5921, Sigma-Aldrich) was used as positive control, and standard growth medium supplemented with 0.1% DMSO was used as negative control. Determination of cell viability, western blot analysis and measurement of caspase-3 activity were performed as described previously (Manns et al., 2011; Liu et al., 2017). All experiments were carried out in triplicate.

Computational Methods

Mixed torsional/low-mode conformational searches were carried out by means of the MacroModel 10.8.011 software using the MMFF with an implicit solvent model for $CHCl_3$ applying a 21 kJ mol^{-1} energy window (MacroModel, 2015). Geometry reoptimizations of the resultant conformers [B3LYP/6-31 + G(d,p) level *in vacuo*, ω B97X/TZVP with PCM solvent model for MeCN and MeOH], DFT-NMR, TDDFT-ECD and SOR calculations were performed with Gaussian 09 (Frisch et al.,

2013). For NMR calculations the mPW1PW91/6-311 + G(2d,p) level while for the ECD and SOR calculations the B3LYP/TZVP, BH&HLYP/TZVP, CAM-B3LYP/TZVP and PBE0/TZVP levels were applied with the same or no solvent model as in the preceding DFT optimization level. ECD spectra were generated as the sum of Gaussians with 4200 and 3000 cm^{-1} half-height widths, using dipole-velocity-computed rotational strengths (Stephens and Harada, 2010). Computed NMR shift data were corrected with $I = -185.6277$ and $S = -1.0175$ (Pierens, 2014). Boltzmann distributions were estimated from the B3LYP and the ω B97X energies. The MOLEKEL program was used for visualization of the results (Varetto, 2009).

RESULTS

Chemical Identification of the Isolated Compounds

Compound **2** was obtained as a colorless oil, with UV absorption at λ_{max} 233 nm. Its molecular formula was established as $C_{19}H_{33}NO_5$ on the basis of HRESIMS data, accounting for four degrees of unsaturation. The NMR spectra of **2** (**Table 1**) were recorded in methanol- d_4 as well as in DMSO- d_6 . The latter solvent revealed the exchangeable protons of one NH proton

TABLE 1 | ^1H and ^{13}C NMR data of compounds **2** and **3**.

No.	2^a		2^b		3^b	
	δ_{C} , type	δ_{H} (J in Hz)	δ_{C} , type	δ_{H} (J in Hz)	δ_{C} , type	δ_{H} (J in Hz)
1	NH	7.69, br s				
2	174.4, C		177.3, C		177.4, C	
3	78.8, C		80.8, C		80.8, C	
4	76.1, CH	3.89, t (5.9)	77.9, CH	4.12, d (6.6)	78.0, CH	4.12, d (6.5)
5	59.5, CH	3.16, ddd (5.9, 5.5, 3.5)	61.2, CH	3.38, ddd (6.6, 5.8, 3.2)	61.2, CH	3.38, ddd (6.5, 5.8, 3.3)
6	61.6, CH ₂	3.54, ddd (11.1, 5.0, 3.5) 3.30, ddd (11.1, 5.5, 5.0)	62.9, CH ₂	3.76, dd (11.6, 3.2) 3.52, dd (11.6, 5.8)	62.9, CH ₂	3.76, dd (11.6, 3.3) 3.52, dd (11.6, 5.8)
7	73.0, CH	4.22, dd (6.5, 5.9)	74.5, CH	4.43, d (7.1)	74.6, CH	4.43, d (7.0)
8	130.8, CH	5.82, dd (15.4, 6.5)	129.6, CH	5.83, dd (15.4, 7.1)	129.6, CH	5.82, dd (15.4, 7.0)
9	131.0, CH	6.14, dd (15.4, 10.6)	134.6, CH	6.32, dd (15.4, 10.4)	134.6, CH	6.32, dd (15.4, 10.5)
10	130.2, CH	6.00, dd (15.1, 10.6)	131.2, CH	6.07, dd (15.0, 10.4)	131.2, CH	6.07, dd (15.0, 10.5)
11	133.6, CH	5.62, dt (15.1, 7.3)	136.3, CH	5.70, dt (15.0, 7.3)	136.3, CH	5.70, dt (15.0, 7.3)
12	32.0, CH ₂	2.04, q (7.3)	33.7, CH ₂	2.08, q (7.3)	33.6, CH ₂	2.08, q (7.3)
13	28.8, CH ₂	1.34, m	30.5, CH ₂	1.39, m	30.4, CH ₂	1.39, m
14	29.0, CH ₂	1.24, m	30.7, CH ₂	1.29, m	30.7, CH ₂	1.31, m
15	28.9, CH ₂	1.24, m	30.6, CH ₂	1.29, m	30.6, CH ₂	1.31, m
16	28.7, CH ₂	1.24, m	30.5, CH ₂	1.29, m	30.5, CH ₂	1.31, m
17	28.6, CH ₂	1.24, m	30.3, CH ₂	1.29, m	30.3, CH ₂	1.31, m
18	31.3, CH ₂	1.23, m	33.1, CH ₂	1.28, m	26.9, CH ₂	1.35, m
19	22.1, CH ₂	1.25, m	23.7, CH ₂	1.31, m	33.7, CH ₂	1.52, m
20	13.9, CH ₃	0.85, t (6.9)	14.4, CH ₃	0.90, t (7.0)	63.0, CH ₂	3.54, t (6.7)
3-OH		5.03, s				
4-OH		5.47, d (5.9)				
6-OH		4.74, t (5.0)				
7-OH		4.75, d (5.9)				

^aRecorded at 600 (^1H) and 150 MHz (^{13}C) in DMSO- d_6 . ^bRecorded at 600 (^1H) and 150 MHz (^{13}C) in CD_3OD .

TABLE 2 | ^1H and ^{13}C NMR data of compounds 4–6.

No.	4 ^a		5 ^a		6 ^a	
	δ_{C} , type	δ_{H} (J in Hz)	δ_{C} , type	δ_{H} (J in Hz)	δ_{C} , type	δ_{H} (J in Hz)
2	177.3, C		177.4, C		177.4, C	
3	80.8, C		80.8, C		80.8, C	
4	77.9, CH	4.12, d (6.5)	78.0, CH	4.12, d (6.5)	78.0, CH	4.12, d (6.5)
5	61.2, CH	3.38, ddd (6.5, 5.8, 3.2)	61.2, CH	3.38, ddd (6.5, 5.8, 3.3)	61.2, CH	3.38, ddd (6.5, 5.8, 3.2)
6	62.9, CH ₂	3.76, dd (11.5, 3.2) 3.52, dd (11.5, 5.8)	63.0, CH ₂	3.76, dd (11.6, 3.3) 3.52, dd (11.6, 5.8)	63.0, CH ₂	3.76, dd (11.5, 3.2) 3.52, dd (11.5, 5.8)
7	74.5, CH	4.43, d (7.1)	74.6, CH	4.43, d (7.1)	74.5, CH	4.43, d (7.0)
8	129.6, CH	5.82, dd (15.3, 7.1)	129.6, CH	5.82, dd (15.3, 7.1)	129.7, CH	5.82, dd (15.3, 7.0)
9	134.6, CH	6.32, dd (15.3, 10.5)	134.6, CH	6.32, dd (15.3, 10.5)	134.6, CH	6.32, dd (15.3, 10.5)
10	131.2, CH	6.07, dd (15.0, 10.5)	131.2, CH	6.07, dd (15.0, 10.5)	131.2, CH	6.07, dd (15.0, 10.5)
11	136.3, CH	5.70, dt (15.0, 7.3)	136.3, CH	5.70, dt (15.0, 7.3)	136.3, CH	5.70, dt (15.0, 7.3)
12	33.7, CH ₂	2.08, q (7.3)	33.7, CH ₂	2.09, q (7.3)	33.7, CH ₂	2.08, q (7.3)
13	30.4, CH ₂	1.39, m	30.4, CH ₂	1.40, m	30.3, CH ₂	1.39, m
14	30.7, CH ₂	1.31, m	30.8, CH ₂	1.33, m	30.6, CH ₂	1.31, m
15	30.6, CH ₂	1.31, m	30.5, CH ₂	1.33, m	30.5, CH ₂	1.31, m
16	30.2, CH ₂	1.31, m	30.2, CH ₂	1.33, m	30.4, CH ₂	1.31, m
17	26.9, CH ₂	1.40, m 1.33, m	26.7, CH ₂	1.48, m 1.34, m	30.2, CH ₂	1.31, m
18	40.2, CH ₂	1.44, m 1.40, m	34.4, CH ₂	1.49, m 1.36, m	27.0, CH ₂	1.35, m
19	68.6, CH	3.70, m	73.3, CH	3.56, m	29.7, CH ₂	1.62, m
20	23.5, CH ₃	1.14, d (6.2)	67.4, CH ₂	3.46, dd (11.2, 4.5) 3.41, dd (11.2, 6.5)	65.7, CH ₂	4.05, t (6.7)
20-OAc					20.8, CH ₃ 173.1, C	2.02, s

^aRecorded at 600 (^1H) and 150 MHz (^{13}C) in CD₃OD.**TABLE 3** | ^1H and ^{13}C NMR data of compounds 7–9.

No.	7 ^a		8 ^a		9 ^a	
	δ_{C} , type	δ_{H} (J in Hz)	δ_{C} , type	δ_{H} (J in Hz)	δ_{C} , type	δ_{H} (J in Hz)
2	177.3, C		177.3, C		177.3, C	
3	80.8, C		80.9, C		80.8, C	
4	77.9, CH	4.12, d (6.5)	77.9, CH	4.12, d (6.6)	78.0, CH	4.12, d (6.6)
5	61.2, CH	3.38, ddd (6.5, 5.8, 3.2)	61.1, CH	3.39, ddd (6.6, 5.8, 3.2)	61.2, CH	3.38, ddd (6.6, 5.8, 3.3)
6	62.9, CH ₂	3.76, dd (11.5, 3.2) 3.52, dd (11.5, 5.8)	62.9, CH ₂	3.76, dd (11.6, 3.2) 3.52, dd (11.6, 5.8)	63.0, CH ₂	3.76, dd (11.5, 3.3) 3.52, dd (11.5, 5.8)
7	74.5, CH	4.43, d (7.1)	74.5, CH	4.44, d (7.1)	74.6, CH	4.43, d (7.0)
8	129.6, CH	5.83, dd (15.3, 7.1)	129.5, CH	5.82, dd (15.3, 7.1)	129.7, CH	5.82, dd (15.4, 7.0)
9	134.6, CH	6.32, dd (15.3, 10.5)	134.6, CH	6.32, dd (15.3, 10.5)	134.6, CH	6.32, dd (15.4, 10.6)
10	131.2, CH	6.07, dd (15.1, 10.5)	131.2, CH	6.07, dd (15.0, 10.5)	131.2, CH	6.07, dd (15.0, 10.6)
11	136.3, CH	5.70, dt (15.1, 7.3)	136.3, CH	5.70, dt (15.0, 7.3)	136.3, CH	5.70, dt (15.0, 7.3)
12	33.6, CH ₂	2.08, q (7.3)	33.6, CH ₂	2.08, q (7.3)	33.7, CH ₂	2.08, q (7.3)
13	30.4, CH ₂	1.39, m	30.3, CH ₂	1.39, m	30.3, CH ₂	1.39, m
14	30.5, CH ₂	1.31, m	30.4, CH ₂	1.32, m	30.5, CH ₂	1.31, m
15	30.5, CH ₂	1.31, m	30.3, CH ₂	1.32, m	30.4, CH ₂	1.31, m
16	30.2, CH ₂	1.31, m	30.2, CH ₂	1.32, m	30.2, CH ₂	1.31, m
17	26.5, CH ₂	1.31, m	30.1, CH ₂	1.32, m	30.1, CH ₂	1.31, m
18	36.9, CH ₂	1.58, m 1.50, m	26.2, CH ₂	1.59, m	26.0, CH ₂	1.60, m
19	72.4, CH	4.86, m	35.2, CH ₂	2.27, t (7.4)	34.8, CH ₂	2.31, t (7.4)
20	20.2, CH ₃	1.20, d (6.2)	178.1, C		176.1, C	
19-OAc	21.2, CH ₃ 172.7, C	2.00, s				
20-OMe					52.0, CH ₃	3.65, s

^aRecorded at 600 (^1H) and 150 MHz (^{13}C) in CD₃OD.

at δ_H 7.69 (NH-1) as well as four OH protons at δ_H 5.47 (4-OH), 5.03 (3-OH), 4.75 (7-OH), and 4.74 (6-OH). The ^{13}C NMR spectrum of **2** displayed one carbonyl group at δ_C 174.4 (C-2), and four olefinic carbons at δ_C 133.6 (C-11), 131.0 (C-9), 130.8 (C-8), and 130.2 (C-10), accounting for three degrees of unsaturation. The presence of a γ -lactam ring was confirmed by the COSY correlations between 4-OH/H-4 (δ_H 3.89)/H-5 (δ_H 3.16)/H₂-6 (δ_H 3.54 and 3.30)/6-OH and the HMBC correlations from NH-1 to C-3, C-4, and C-5, from 3-OH to C-2, C-3 and C-4, from 4-OH to C-3, and from H-5 to C-2 (**Figure 3**). The COSY correlations between H-8 (δ_H 5.82)/H-9 (δ_H 6.14)/H-10 (δ_H 6.00)/H-11 (δ_H 5.62)/H₂-12 (δ_H 2.04)/H₂-13 (δ_H 1.34)/H₂-14 (δ_H 1.24), and between Me-20 (δ_H 0.85)/H₂-19 (δ_H 1.24) together with the HMBC correlations from Me-20 to C-19 (δ_C 22.1) and C-18 (δ_C 31.3) and the observation of characteristic aliphatic methylenes at 29.0, 28.9, 28.7, 28.6, and δ_H 1.24 (CH₂-14, 15, 16, and 17), established the presence of a trideca-1,3-diene subunit

in **2**. In addition, the COSY correlations between H-8/H-7 (δ_H 4.22)/7-OH along with the HMBC correlations from H-7 to C-2, C-3, and C-4, and from 3-OH to C-7 indicated the trideca-1,3-diene side chain to be connected to the γ -lactam moiety via the oxygenated carbon at C-7. Therefore, the planar structure of **2** was elucidated, which was similar to that of the co-isolated known compound, pramanicin A (**1**) (Schwartz et al., 1994; Harrison et al., 2000). The major difference between both compounds was the presence of an additional hydroxy group in **2** instead of the ketone group in **1** at position C-7. The trivial name aposporellin A is proposed for **2**.

The large values of $J_{8,9}$ (15.4 Hz) and $J_{10,11}$ (15.1 Hz) supported the *E* configuration for the double bonds at C-8/C-9 and C-10/C-11 in **2**. The relative configuration of the γ -lactam ring was deduced through the ROESY spectrum and by comparison with pramanicin A (**1**) (Harrison et al., 2000), virgaricins A and B (Ishii et al., 2012, 2015). The NOE

TABLE 4 | 1H and ^{13}C NMR data of compounds **10–12**.

No.	10 ^a		11 ^a		12 ^a	
	δ_C^b , type	δ_H (J in Hz)	δ_C , type	δ_H (J in Hz)	δ_C^b , type	δ_H (J in Hz)
2	177.3, C		177.3, C		177.4, C	
3	80.5, C		80.8, C		80.6, C	
4	78.1, CH	4.10, d (6.8)	77.9, CH	4.12, d (6.5)	78.1, CH	4.10, d (6.7)
5	58.2, CH	3.55, ddd (6.8, 6.2, 3.3)	61.2, CH	3.38, ddd (6.5, 5.8, 3.2)	58.3, CH	3.55, ddd (6.7, 6.2, 3.4)
6	65.0, CH ₂	4.30, dd (11.6, 3.3) 4.05, dd (11.6, 6.2)	63.0, CH ₂	3.76, dd (11.6, 3.2) 3.52, dd (11.6, 5.8)	65.0, CH ₂	4.30, dd (11.7, 3.4) 4.04, dd (11.7, 6.2)
7	74.5, CH	4.42, d (7.0)	74.5, CH	4.43, d (7.1)	74.6, CH	4.42, d (7.1)
8	129.4, CH	5.82, dd (15.3, 7.0)	129.7, CH	5.82, dd (15.3, 7.1)	129.4, CH	5.82, dd (15.4, 7.1)
9	134.5, CH	6.32, dd (15.3, 10.5)	134.6, CH	6.32, dd (15.3, 10.5)	134.5, CH	6.32, dd (15.4, 10.6)
10	131.2, CH	6.07, dd (15.1, 10.5)	131.2, CH	6.07, dd (15.0, 10.5)	131.2, CH	6.07, dd (15.0, 10.6)
11	136.3, CH	5.70, dt (15.1, 7.3)	136.3, CH	5.70, dt (15.0, 7.3)	136.3, CH	5.71, dt (15.0, 7.3)
12	33.6, CH ₂	2.08, q (7.3)	33.6, CH ₂	2.08, q (7.3)	33.6, CH ₂	2.08, q (7.3)
13	30.2, CH ₂	1.39, m	30.2, CH ₂	1.39, m	30.3, CH ₂	1.40, m
14	30.4, CH ₂	1.32, m	30.3, CH ₂	1.31, m	30.6, CH ₂	1.31, m
15	30.3, CH ₂	1.32, m	30.2, CH ₂	1.31, m	30.5, CH ₂	1.31, m
16	30.2, CH ₂	1.32, m	30.1, CH ₂	1.31, m	30.4, CH ₂	1.31, m
17	30.1, CH ₂	1.32, m	24.8, CH ₂	1.54, m	30.2, CH ₂	1.31, m
18	26.7, CH ₂	1.59, m	44.3, CH ₂	2.47, t (7.3)	27.0, CH ₂	1.35, m
19	36.6, CH ₂	2.22, t (7.4)	212.3, C		29.6, CH ₂	1.62, m
20	179.8, C		29.8, CH ₃	2.13, s	65.7, CH ₂	4.05, t (6.7)
6-OAc	20.5, CH ₃ 172.5, C	2.07, s			20.6, CH ₃ 172.4, C	2.07, s
20-OAc					20.8, CH ₃ 173.0, C	2.02, s

^aRecorded at 600 (1H) and 150 MHz (^{13}C) in CD₃OD. ^bData extracted from HSQC and HMBC spectra.

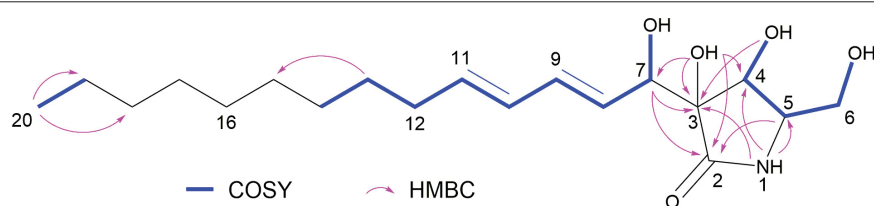


FIGURE 3 | COSY and key HMBC correlations of compound **2**.

correlations between 3-OH/H-4, H-4/H₂-6 indicated that 3-OH, H-4 and H₂-6 were located on the same side of the ring. In contrast, the NOE correlations between H-7/4-OH, 4-OH/H-5, indicated that 4-OH and H-5 were located on the opposite side compared to 3-OH, H-4 and H₂-6. On the basis of these findings, the relative stereochemistry of **2** in the γ -lactam moiety was assigned to be identical to that of pramanicin A (**1**).

Pramanicin A (**1**) was reported together with pramanicin from the fungus *Stagonospora* sp. (Schwartz et al., 1994), the latter contained an epoxide group at C-10/C-11 instead of a double bond. The absolute configuration of pramanicin A (**1**) was deduced by comparison to pramanicin through biogenetic considerations (Duspara et al., 1998; Harrison et al., 1998, 2000; Chen and Harrison, 2004) and by total synthesis (Cow et al., 1997; Barrett et al., 1999a,b; Tan et al., 2014, 2015, 2017), which confirmed that the compound has (3*S*,4*S*,5*S*) configuration. The large absolute value of the specific optical rotation (SOR) of **1** allowed testing the TDDFT-SOR method (Polavarapu, 2002; Mándi and Kurtán, 2019) and the ω B97X functional (Chai and Head-Gordon, 2008; Bremond et al., 2016), which was also applied for the TDDFT-ECD calculations of **2**. Merck Molecular Force Field (MMFF) conformational searches of **1** and the epimers of **2** resulted in a large number of conformers [c.a. 18 thousand by generating 100 thousand structures for (3*R*,4*S*,5*S*,7*S*)-**2**] and the searches were not complete, since many conformers were found only a few times (Mándi et al., 2015). Thus, model compounds were utilized for the calculations, in which the C-3 side-chain was truncated at the C-12 position (Figure 4).

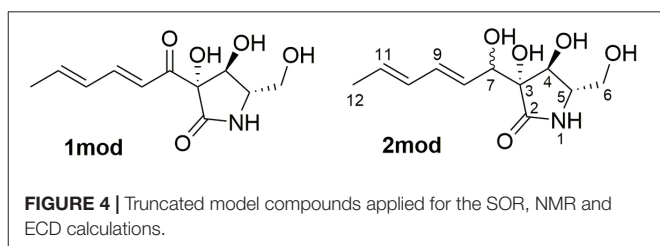
The MMFF conformational search of (3*S*,4*S*,5*S*)-**1mod** resulted in 79 conformers in a 21 kJ/mol energy window, which were re-optimized at the ω B97X/TZVP PCM/MeOH level yielding 16 low-energy conformers over 1% Boltzmann-distribution (Supplementary Figure S92). SOR values were computed at four levels (B3LYP/TZVP, BH&HLYP/TZVP, CAM-B3LYP/TZVP and PBE0/TZVP all with the PCM solvent model for MeOH) and nice agreements were found with the experimental SOR value (computed SOR values in the range from -91 to -115 compared to the -121 experimental value) (Supplementary Table S1).

The absolute configuration of the γ -lactam ring of compound **2** is assumed to be identical to that of **1** based on biogenetic considerations whereas that of the OH group in the side chain at C-7 could not be elucidated. In order to solve this problem, DFT-NMR calculations were performed on the epimeric model compounds (3*R*,4*S*,5*S*,7*R*)-**2mod** and (3*R*,4*S*,5*S*,7*S*)-**2mod** (Lodewyk et al., 2012; Kicsák et al., 2018; Mándi and

Kurtán, 2019). B3LYP/6-31 + G(d,p) re-optimization of the initial 169 and 205 conformers resulted in 8 and 15 low-energy conformers over 1% Boltzmann population, respectively (Supplementary Figures S93, S94). The ¹³C NMR chemical shift data of (3*R*,4*S*,5*S*,7*S*)-**2mod** computed at the mPW1PW91/6-311 + G(2d,p) level reproduced much better the experimental values than those of the other epimer (Supplementary Table S2). Mean absolute error (MAE) values were 1.70 vs. 2.17 favoring the (3*R*,4*S*,5*S*,7*S*) epimer. The signal of the terminal C-12 was neglected, since it has an abnormal shift in the computations due to the truncation. Computed and the experimental ¹³C NMR chemical shift data in the vicinity of the C-7 chirality center also clearly showed superior agreement for the (3*R*,4*S*,5*S*,7*S*) epimer. DP4 + statistical analysis was utilized for the comparison of the experimental and calculated ¹³C NMR data resulting in 97.31% confidence for the (3*R*,4*S*,5*S*,7*S*) epimer (Smith and Goodman, 2010; Grimblat et al., 2015; Li et al., 2020). Although the experimental SOR value of **2** is small, the SOR calculations performed the same way as for **1mod** were in agreement with the results of the NMR calculation suggesting also (3*R*,4*S*,5*S*,7*S*) absolute configuration. The (3*R*,4*S*,5*S*,7*R*) epimer of **2mod** gave computed SOR values ranging from +4 to +7 while the (3*R*,4*S*,5*S*,7*S*) one in the range from -18 to -23 reproducing better the -21 experimental value of **2** (Supplementary Tables S3, S4). For the TDDFT-ECD method, the same MMFF conformers of (3*R*,4*S*,5*S*,7*R*)-**2mod** and (3*R*,4*S*,5*S*,7*S*)-**2mod** were re-optimized at the ω B97X/TZVP PCM/MeCN level and ECD calculations were performed at various levels. Although both epimers gave rather diverse computed ECD spectra for the individual conformers and Boltzmann populations were small, the average ECD spectra of the (3*R*,4*S*,5*S*,7*S*) epimer were found to be similar to the experimental one (Figure 5) in line with the NMR and the SOR calculations. Consequently, the absolute configuration of **2** could be elucidated as (3*R*,4*S*,5*S*,7*S*).

The molecular formula of compound **3** was assigned as C₁₉H₃₃NO₆ based on its HRESIMS data, containing an additional oxygen atom when compared to **2**. The NMR data of **3** (Table 1) were similar to those of **2**, except for the presence of an oxygenated methylene group resonating at δ_C 63.0 and δ_H 3.54 (t) (CH₂-20) and the absence of the terminal methyl group in the side chain. The COSY correlation between H₂-20/H₂-19 (δ_H 1.52)/H₂-18 (δ_H 1.35) together with the HMBC correlations from H₂-20 to C-18 (δ_C 26.9) and C-19 (δ_C 33.7) indicated the attachment of a hydroxy group at C-20 in the side chain of **3**. Detailed analysis of its 2D NMR spectra revealed that the remaining substructure of **3** was identical to that of **2**. The absolute configuration of **3** was identical to that of **2** based on their similar ROESY correlations and ECD data.

Aplosporellin C (**4**) exhibited the same molecular formula as **3** as determined by HRESIMS data. The ¹H and ¹³C NMR data of **4** (Table 2) were likewise similar to those of **3**, yet showed the signal of a doublet methyl group at δ_C 23.5 and δ_H 1.14 (Me-20) in the side chain and the presence of an oxygenated methine at δ_C 68.6 and δ_H 3.70 (CH-19). The COSY correlations between Me-20/H-19, and between H-19/H₂-18 (δ_H 1.44 and 1.40) together with the HMBC correlations from Me-20 to C-19 and C-18 (δ_C 40.2) indicated the presence of a hydroxy group at C-19 in **4**



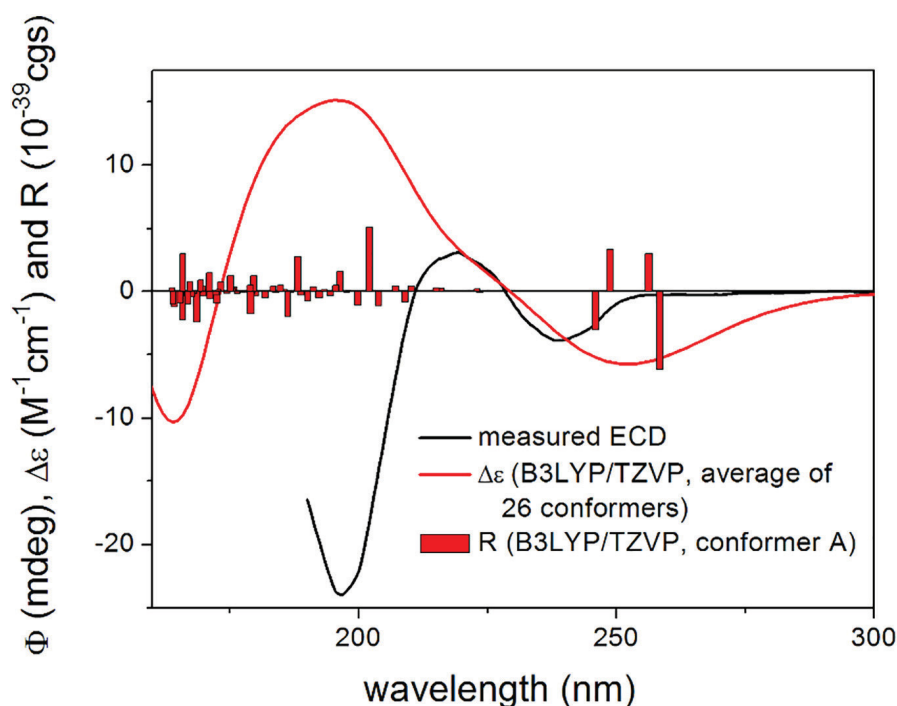


FIGURE 5 | Experimental ECD spectrum of **2** in MeCN compared with the Boltzmann-weighted B3LYP/TZVP PCM/MeCN ECD spectrum of (3R,4S,5S,7S)-**2mod**. Level of optimization: ω B97X/TZVP PCM/MeCN. Bars represent the rotatory strength values of the lowest-energy conformer. The experimental spectrum was scaled to the computed one.

instead of C-20 as in **3**. The remaining substructure of **4** was identical to that of **2** as confirmed by detailed interpretation of the 2D NMR spectra of **4**. Due to the limited amount, the absolute configuration at C-19 of **4** could not be determined by converting the compound to its Mosher ester.

Compound **5** had the molecular formula $C_{19}H_{33}NO_7$ as determined by HRESIMS data, containing one additional oxygen atom when compared to **3** and **4**. Detailed analysis of the 2D NMR of **5** (Table 2) revealed that it was similar to **3** except for the presence of one additional oxygenated methine at δ_C 73.3 and δ_H 3.56 (CH-19). The signal of the terminal oxygenated methylene at C-20 appeared as two dd peaks in the 1H NMR spectrum of **5** instead of a triplet peak of **3**. This suggested that the additional hydroxy group of **5** was located at C-19, which was further confirmed by the COSY correlations between H₂-20/H-19/H₂-18 together with the HMBC correlations from H₂-20 to C-19 and C-18. Thus, compound **5** was elucidated as 19,20-dihydroxy derivative of **2**.

Aplosporellin E (**6**) was found to have the molecular formula $C_{21}H_{35}NO_7$ on the basis of HRESIMS data, requiring five degrees of unsaturation. Comparison of the NMR data (Table 2) indicated compound **6** to be closely related to compound **3** except for the presence of an additional methyl group (δ_H 2.02 and δ_C 20.8) and an additional carbonyl carbon (δ_C 173.1). The HMBC correlations from protons of the additional methyl and H₂-20 (δ_H 4.05) to the additional carbonyl carbon indicated the attachment of an additional acetoxy group at C-20 in **6** when compared to **3**.

The molecular formula of compound **7** was the same as **6** as deduced from HRESIMS. The 1H and ^{13}C NMR data of **7** (Table 3) were very similar to those of **6**, except for the appearance of a terminal methyl group at δ_H 1.20 (Me-20) which was split into a doublet peak in the 1H NMR spectrum of **7**. Detailed analysis of the HSQC and HMBC spectra revealed an oxygenated methine at δ_C 72.4 and δ_H 4.86 (CH-19). The COSY correlations between Me-20/H-19/H₂-18 (δ_H 1.58 and 1.50) together with the HMBC correlations from H-19 and the methyl group at δ_H 2.00 (3H, s) to the carbonyl carbon at δ_C 172.7 indicated the presence of an acetoxy group at C-19. Thus, compound **7** was elucidated as 19-O-acetyl derivative of compound **4**.

Compound **8** exhibited the molecular formula $C_{19}H_{31}NO_7$ as determined by the HRESIMS data. Its 1H and ^{13}C NMR data (Table 3) were similar to those of **2** except for that signals of the terminal methyl group in the side chain was replaced with a carbonyl group at δ_C 178.1 (C-20). The HMBC correlations from H₂-18 (δ_H 1.59) and H₂-19 (δ_H 2.27, t) to C-20, together with the COSY correlations between H₂-18/H₂-19 indicated a terminal carboxylic acid group in the side chain. The remaining substructure of **8** was identical to that of **2** as confirmed by detailed analysis of the 2D NMR spectra of **8**.

The HRESIMS data of **9** gave the molecular formula $C_{20}H_{33}NO_7$. From the 2D NMR spectra of **9** (Table 3) it was evident that compound **9** was the 20-O-methyl derivative of **8** as indicated by the presence of an additional methoxy

group at δ_{H} 3.65 (3H, s) and δ_{C} 52.0, together with the HMBC correlations from the methoxy group and H₂-19 (δ_{H} 2.31, t) to the carbonyl carbon at δ_{C} 176.1 (C-20).

Aplosporellin I (**10**) exhibited the molecular formula C₂₁H₃₃NO₈ as determined by HRESIMS, requiring six degrees of unsaturation. The NMR data of **10** (Table 4) were similar to those of **8** except for the presence of a methyl group (δ_{H} 2.07 and δ_{C} 20.5) and a carbonyl carbon (δ_{C} 172.5) in addition to minor differences of the chemical shifts of the protons at the γ -lactam ring moiety. The COSY correlations between H-4 (δ_{H} 4.10)/H-5 (δ_{H} 3.55)/H₂-6 (δ_{H} 4.30 and 4.05) together with the HMBC correlations from H₂-6 and the additional methyl group at δ_{H} 2.07 to the carbonyl carbon at δ_{C} 172.5 indicated the attachment of an acetoxy group at C-6. Detailed analysis of the 2D NMR spectra and the ROESY spectra of compound **10** revealed that the remaining substructure and relative configuration were identical to compound **8**. Thus, compound **10** was identified as the 6-*O*-acetyl derivative of **8**.

The molecular formula of **11** was determined as C₁₉H₃₁NO₆ based on HRESIMS data, accounting for five degrees of unsaturation. The NMR data of **11** (Table 4) were similar to those of **2** but exhibited the signal of an additional carbonyl group at δ_{C} 212.3 (C-19). Moreover, the methyl group in the side chain was shifted to down field at δ_{C} 29.8, δ_{H} 2.13 (Me-20) and appeared as singlet in the ¹H NMR spectrum. The HMBC correlations from Me-20, H₂-18 (δ_{H} 2.47) and H₂-17 (δ_{H} 1.54) to C-19 indicated the presence of a ketone group in the side chain at C-19 in **11**. The remaining substructure of **11** was identical to that of **2** as confirmed by detailed analysis of the 2D NMR spectra.

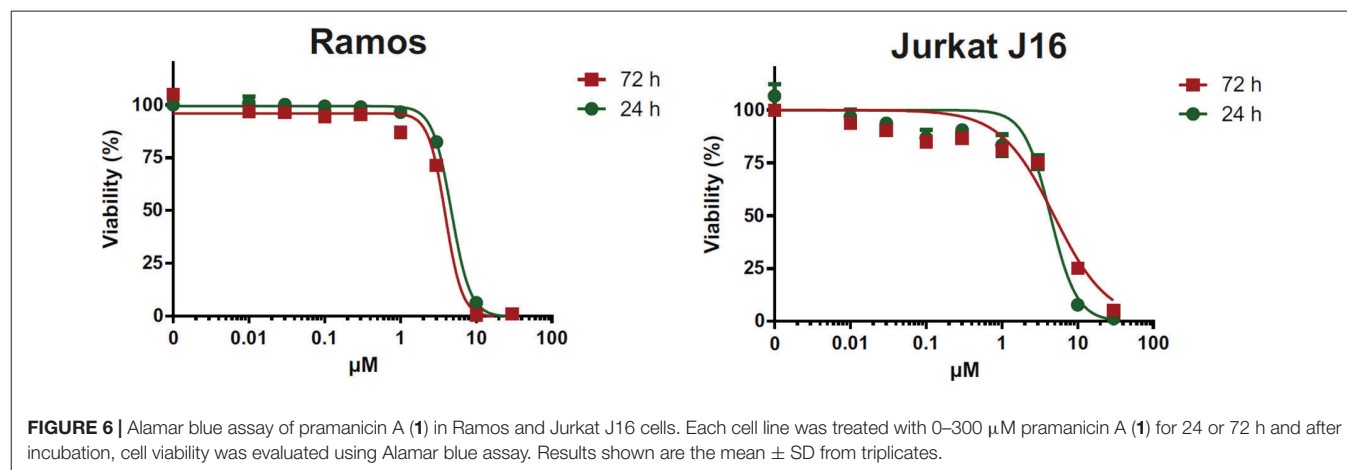
On the basis of the HRESIMS data, the molecular formula of **12** was established as C₂₃H₃₇NO₈ with six degrees of unsaturation. The NMR data of **12** (Table 4) were similar to those of **6**, except for the presence of an additional methyl group (δ_{H} 2.07 and δ_{C} 20.6) and a carbonyl carbon (δ_{C} 172.4). Moreover, the chemical shifts of the protons of the γ -lactam ring in **12** were more comparable to those of **10** rather than **6**. These findings suggested compound **12** was a 6-*O*-acetyl derivative of **6**, which was confirmed by the HMBC correlations from H₂-6 (δ_{H} 4.30

and δ_{C} 4.04) and the additional methyl group at δ_{H} 2.07 to the carbonyl carbon at δ_{C} 172.4.

Bioactivities of the Isolated Compounds

All isolated compounds were tested for their cytotoxicity against human lymphoma (Ramos) and leukemia (Jurkat J16) cell lines. Pramanicin A (**1**) exhibited IC₅₀ values of 4.7 and 4.4 μM after 24 h of incubation respectively, whereas after 72 h of incubation these values were 3.9 and 4.9 μM , respectively. Treatment with pramanicin A (**1**) significantly affected cell viability in a dose-dependent manner (Figure 6) whereas the remaining compounds showed no cytotoxicity in these two cell lines in the observed concentration ranging up to 30 μM . The ketone group at C-7 of pramanicin A (**1**) which is conjugated to the olefinic function at C-8/C-9 is obviously the key factor responsible for the cytotoxicity against human Ramos and Jurkat J16 cell lines. It was suggested that the α,β -unsaturated ketone functionality in pramanicin A (**1**) could be Michael acceptors that can react with a thiol group of cysteine amino acid of proteins or enzymes, and thus causing cytotoxic activity (Amslinger, 2010; Darsih et al., 2015).

In order to evaluate whether the pronounced cytotoxicity of pramanicin A (**1**) is attributable to the induction of apoptosis, we followed the activation of the effector caspases such as caspase-3 in response to pramanicin A (**1**) treatment. In the Western blot experiment, after 2–8 h treatment of Ramos and Jurkat J16 cell lines with 10 μM pramanicin A (**1**) respectively, an explicit cleavage of PARP1 (poly [ADP-ribose] polymerase 1) was observed (Figure 7). Cleavage of PARP1, which is a substrate of caspase-3, serves as a surrogate marker for activation of caspase-3 and therefore indicated that pramanicin A (**1**) is able to induce apoptosis. Moreover, we also measured caspase-3 activity by detecting the profluorogenic caspase-3 substrate Ac-DEVD-AMC. After treatment with 10 μM pramanicin A (**1**) in the two cell lines, cleavage of Ac-DEVD-AMC was observed within a few hours, which was more obvious in Ramos cells than in Jurkat J16 cells (Figure 8). These results further proved the activation of caspase-3 and thus induction of apoptosis in Ramos and Jurkat J16 cells by pramanicin A (**1**).



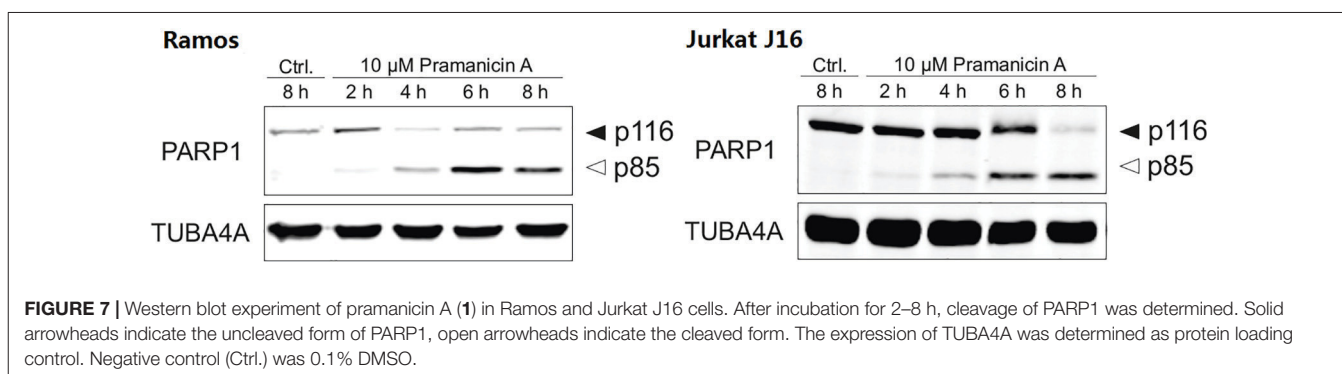


FIGURE 7 | Western blot experiment of pramanicin A (**1**) in Ramos and Jurkat J16 cells. After incubation for 2–8 h, cleavage of PARP1 was determined. Solid arrowheads indicate the uncleaved form of PARP1, open arrowheads indicate the cleaved form. The expression of TUBA4A was determined as protein loading control. Negative control (Ctrl.) was 0.1% DMSO.

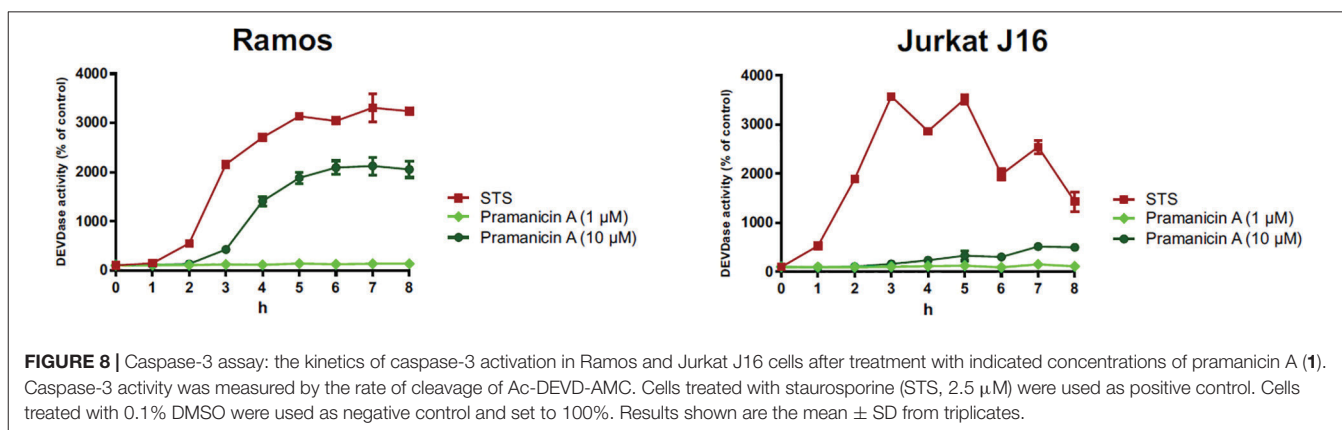


FIGURE 8 | Caspase-3 assay: the kinetics of caspase-3 activation in Ramos and Jurkat J16 cells after treatment with indicated concentrations of pramanicin A (**1**). Caspase-3 activity was measured by the rate of cleavage of Ac-DEVD-AMC. Cells treated with staurosporine (STS, 2.5 μ M) were used as positive control. Cells treated with 0.1% DMSO were used as negative control and set to 100%. Results shown are the mean \pm SD from triplicates.

DISCUSSION

In the previous biosynthetic study on pramanicin, which differs from pramanicin A (**1**) by the presence of an epoxide group at C-10/C-11 instead of the double bond, in the fungus *Stagonospora* sp., Duspara et al. (1998) and Harrison et al. (2000) conducted a feeding experiment using ^2H , ^{13}C , ^{15}N , and ^{18}O isotopically labeled precursors. It was concluded that pramanicin originates from one starter molecule acetate and six extender malonates to generate the aliphatic acyl tail, whereas L-serine interacts with one acetate to form the pyrrolidone ring. Acetylation of these two moieties provides 3-acetyltetramic acid, followed by a series of oxidation and reduction reactions to form pramanicin (Harrison et al., 2000). Proline or glutamate on the other hand were shown not be precursors of the pyrrolidone moiety (Harrison et al., 1998). In our study, the addition of 3.5% NaNO_3 or of 3.5% $\text{C}_5\text{H}_8\text{NNaO}_4 \cdot \text{H}_2\text{O}$ to solid rice medium was found to induce the accumulation of pramanicin-like compounds. Thus, a feeding study using labeled glutamate as a potential precursor of compounds **1**–**12** would be of interest as a follow up study of this investigation.

CONCLUSION

In summary, 11 new lactam derivatives, aposporellins A–K (**2**–**12**), together with the known analog, pramanicin A (**1**), were isolated from fermentation of *A. javeedii* on solid rice medium

with addition of either 3.5% NaNO_3 or 3.5% monosodium glutamate. All of these compounds were not detected when the fungus was grown on rice medium without these activators. To the best of our knowledge, this study was the first report to regulate secondary metabolites from *A. javeedii* applying an OSMAC approach. The results proved the power of the OSMAC approach on mining new secondary metabolites from endophytic fungi. DFT-NMR, TDDFT-ECD and OR calculations were carried out to determine the absolute configuration. Pramanicin A (**1**) exhibited strong cytotoxicity against human lymphoma (Ramos) and leukemia (Jurkat J16) cell lines with IC_{50} values of 4.7 and 4.4 μM , respectively. Furthermore, mechanistic studies indicated that pramanicin A (**1**) activates caspase-3 and induces apoptotic cell death.

DATA AVAILABILITY STATEMENT

The original contributions presented in the study are included in the article/**Supplementary Material**, further inquiries can be directed to the corresponding authors.

AUTHOR CONTRIBUTIONS

YG sentence contributed to extraction, isolation, and manuscript preparation. FS, LS, and SW carried out the cytotoxicity assay. ZG and KZ contributed to part of structure elucidation. AM and TK performed the DFT-NMR, TDDFT-ECD, and OR

calculations. ZL and PP supervised the research work and revised the manuscript. All the authors contributed to the article and approved the submitted version.

FUNDING

This study was supported by the Deutsche Forschungsgemeinschaft (DFG, German Research Foundation) – project number 270650915/GRK 2158 (to PP and SW). PP and YG also want to thank the Jürgen Manchot Foundation for support. The Hungarian authors were supported by the EU and co-financed by the European Regional Development Fund under the project

GINOP-2.3.2-15-2016-00008. TK thanks the National Research Development and Innovation Office (K120181) and AM thanks the János Bolyai Research Scholarship of the Hungarian Academy of Sciences. The Governmental Information-Technology Development Agency (KIFÜ) is acknowledged for CPU time.

SUPPLEMENTARY MATERIAL

The Supplementary Material for this article can be found online at: <https://www.frontiersin.org/articles/10.3389/fmicb.2020.600983/full#supplementary-material>

REFERENCES

- Amslinger, S. (2010). The tunable functionality of α,β -unsaturated carbonyl compounds enables their differential application in biological systems. *ChemMedChem*. 5, 351–356. doi: 10.1002/cmde.200900499
- Ancheeva, E., Daletos, G., and Proksch, P. (2018). Lead compounds from mangrove-associated microorganisms. *Mar. Drugs*. 16:319. doi: 10.3390/md16090319
- Ariantari, N. P., Daletos, G., Mándi, A., Kurtán, T., Müller, W. E. G., Lin, W. H., et al. (2019). Expanding the chemical diversity of an endophytic fungus *Bulgaria inquinans*, an ascomycete associated with mistletoe, through an OSMAC approach. *RSC Adv*. 9, 25119–25132. doi: 10.1039/c9ra03678d
- Barrett, A. G. M., Head, J., Smith, M. L., Stock, N. S., White, A. J. P., and Williams, D. J. (1999a). Fleming–tamao oxidation and masked hydroxyl functionality: total synthesis of (+)-pramanicin and structural elucidation of the antifungal natural product (–)-pramanicin. *J. Org. Chem*. 64, 6005–6018. doi: 10.1021/jo9905672
- Barrett, A. G. M., Head, J., Smith, M. L., and Stock, N. S. (1999b). Total synthesis of (+)-pramanicin and stereochemical elucidation of the natural product. *Chem. Commun*. 1999, 133–134. doi: 10.1039/a807988i
- Bode, H. B., Bethe, B., Hof, R., and Zeeck, A. (2002). Big effects from small changes: possible ways to explore nature's chemical diversity. *Chembiochem* 3, 619–627. doi: 10.1002/1439-7633(20020703)3:7<619::AID-CBIC619<3.0.CO;2-9
- Bohler, P., Stuhldreier, F., Anand, R., Kondadi, A. K., Schlutermann, D., Berleth, N., et al. (2018). The mycotoxin phomoxanthone A disturbs the form and function of the inner mitochondrial membrane. *Cell Death Dis*. 9:e286. doi: 10.1038/s41419-018-0312-8
- Bremont, E., Savarese, M., Su, N. Q., Perez-Jimenez, A. J., Xu, X., Sancho-Garcia, J. C., et al. (2016). Benchmarking density functionals on structural parameters of small-/medium-sized organic molecules. *J. Chem. Theory. Comput*. 12, 459–465. doi: 10.1021/acs.jctc.5b01144
- Chai, J. D., and Head-Gordon, M. (2008). Systematic optimization of long-range corrected hybrid density functionals. *J. Chem. Phys*. 128:084106. doi: 10.1063/1.2834918
- Chen, H., and Harrison, P. H. M. (2004). Investigation of the origin of C2 units in biosynthesis of streptolydigin. *Org. Lett*. 6, 4033–4036. doi: 10.1021/ol048317h
- Cow, C., Valentini, D., and Harrison, P. (1997). Synthesis of the fatty acid of pramanicin. *Can. J. Chem*. 75, 884–889. doi: 10.1139/v97-106
- Daletos, G., Ebrahim, W., Ancheeva, E., El-Neketi, M., Lin, W. H., and Proksch, P. (2017). "Microbial co-culture and OSMAC approach as strategies to induce cryptic fungal biogenetic gene clusters," in *Chemical Biology of Natural Products*, eds D. J. Newman, G. M. Cragg, and P. G. Grothaus (Boca Raton FL: CRC Press), 233–284. doi: 10.1201/9781315117089-9
- Darsih, C., Prachyawarakorn, V., Wiyakrutta, S., Mahidol, C., Ruchirawat, S., and Kittakoop, P. (2015). Cytotoxic metabolites from the endophytic fungus *Penicillium chermesinum*: discovery of a cysteine-targeted Michael acceptor as a pharmacophore for fragment-based drug discovery, bioconjugation and click reactions. *RSC Adv*. 5, 70595–70603. doi: 10.1039/C5RA13735G
- Duspara, P., Jenkins, S. I., Hughes, D. W., and Harrison, P. H. M. (1998).). The biosynthesis of pramanicin: intact incorporation of serine and absolute configuration of the antibiotic. *Chem. Commun*. 1998, 2643–2644. doi: 10.1039/a807401a
- Frank, M., Niemann, H., Bohler, P., Stork, B., Wesselborg, S., Lin, W., et al. (2015). Phomoxanthone A—from mangrove forests to anticancer therapy. *Curr. Med. Chem*. 22, 3523–3532. doi: 10.2174/0929867322666150716115300
- Frisch, M. J., Trucks, G. W., Schlegel, H. B., Scuseria, G. E., Robb, M. A., Cheeseman, J. R., et al. (2013). *Gaussian 09, Revision E.01*. Wallingford, CT: Gaussian, Inc.
- Gao, Y., Stuhldreier, F., Schmitt, L., Wesselborg, S., Wang, L., Müller, W. E. G., et al. (2020a). Sesterterpenes and macrolide derivatives from the endophytic fungus *Aplosporella javeedii*. *Fitoterapia* 146:104652. doi: 10.1016/j.fitote.2020.104652
- Gao, Y., Wang, L., Kalscheuer, R., Liu, Z., and Proksch, P. (2020b). Antifungal polyketide derivatives from the endophytic fungus *Aplosporella javeedii*. *Bioorg. Med. Chem*. 28:115456. doi: 10.1016/j.bmc.2020.115456
- Grimblat, N., Zanardi, M. M., and Sarotti, A. M. (2015). Beyond DP4: an improved probability for the stereochemical assignment of isomeric compounds using quantum chemical calculations of NMR shifts. *J. Org. Chem*. 80, 12526–12534. doi: 10.1021/acs.joc.5b02396
- Hammerschmidt, L., Aly, A. H., Abdel-Aziz, M., Müller, W. E. G., Lin, W. H., Daletos, G., et al. (2015). Cytotoxic acyl amides from the soil fungus *Gymnascella dankaliensis*. *Bioorg. Med. Chem*. 23, 712–719. doi: 10.1016/j.bmc.2014.12.068
- Harrison, P. H. M., Duspara, P. A., Jenkins, S. I., Kassam, S. A., Liscombe, D. K., and Hughes, D. W. (2000). The biosynthesis of pramanicin in *Stagonospora* sp. ATCC 74235: a modified acyltetramic acid. *J. Chem. Soc., Perkin Trans*. 2000, 4390–4402. doi: 10.1039/b006007k
- Harrison, P. H. M., Hughes, D. W., and William, R. R. (1998). The biosynthesis of pramanicin: origin of the carbon skeleton. *Chem. Commun*. 1998, 273–274. doi: 10.1039/a706799b
- Harwoko, H., Daletos, G., Stuhldreier, F., Lee, J., Wesselborg, S., Feldbrugge, M., et al. (2019). Dithiodiketopiperazine derivatives from endophytic fungi *Trichoderma harzianum* and *Epicoccum nigrum*. *Nat. Prod. Res*. 2019, 1–9. doi: 10.1080/14786419.2019.1627348
- Huo, X., Liu, C., Gao, L., Xu, X., Zhu, N., and Cao, L. (2017). Hepatoprotective effect of aqueous extract from the seeds of *Orychophragmus violaceus* against liver injury in mice and HepG2 cells. *Int. J. Mol. Sci*. 18:1197. doi: 10.3390/ijms18061197
- Ishii, T., Nonaka, K., Iwatsuki, M., Masuma, R., Ōmura, S., and Shiomi, K. (2012). Virgarcin produced by *Virgaria* sp. FKI-4860. *J. Antibiot*. 65, 139–141. doi: 10.1038/ja.2011.123
- Ishii, T., Nonaka, K., Sugawara, A., Iwatsuki, M., Masuma, R., Hirose, T., et al. (2015). Cinatrins D and E, and virgarcin B, three novel compounds produced by a fungus, *Virgaria boninensis* FKI-4958. *J. Antibiot*. 68, 633–637. doi: 10.1038/ja.2015.45
- Kicsák, M., Mándi, A., Varga, S., Herczeg, M., Batta, G., Bényei, A., et al. (2018). Tricyclanos: conformationally constrained nucleoside analogues with a new heterotricyclic obtained from a d-ribofuranose unit. *Org. Biomol. Chem*. 16, 393–401. doi: 10.1039/c7ob02296d
- Kjer, J., Debbab, A., Aly, A. H., and Proksch, P. (2010). Methods for isolation of marine-derived endophytic fungi and their bioactive secondary products. *Nat. Protoc*. 5, 479–490. doi: 10.1038/nprot.2009.233

- Li, W. S., Yan, R. J., Yu, Y., Shi, Z., Mándi, A., Shen, L., et al. (2020). Determination of the absolute configuration of super-carbon-chain compounds by a combined chemical, spectroscopic, and computational approach: gibbosols A and B. *Angew. Chem., Int. Ed. Engl.* 59, 13028–13036. doi: 10.1002/anie.202004358
- Liu, Y., Stuhldreier, F., Kurtán, T., Mándi, A., Arumugam, S., Lin, W. H., et al. (2017). Daldinone derivatives from the mangrove-derived endophytic fungus *Annulohyphoxylon* sp. *RSC Adv.* 7, 5381–5393. doi: 10.1039/c6ra27306h
- Lodewyk, M. W., Siebert, M. R., and Tantillo, D. J. (2012). Computational prediction of ¹H and ¹³C chemical shifts: a useful tool for natural product, mechanistic, and synthetic organic chemistry. *Chem. Rev.* 112, 1839–1862. doi: 10.1021/cr200106v
- MacroModel (2015). *SchrödingerLLC*. Available online at: <https://www.schrodinger.com/MacroModel> (accessed June 18, 2020).
- Mándi, A., and Kurtán, T. (2019). Applications of OR/ECD/VCD to the structure elucidation of natural products. *Nat. Prod. Rep.* 36, 889–918. doi: 10.1039/c9np00002j
- Mándi, A., Mudianta, I. W., Kurtán, T., and Garson, M. J. (2015). Absolute configuration and conformational study of psammaphysins A and B from the balinese marine sponge *Aplysina strongylata*. *J. Nat. Prod.* 78, 2051–2056. doi: 10.1021/acs.jnatprod.5b00369
- Manns, J., Daubrawa, M., Driessen, S., Paasch, F., Hoffmann, N., Löffler, A., et al. (2011). Triggering of a novel intrinsic apoptosis pathway by the kinase inhibitor staurosporine: activation of caspase-9 in the absence of Apaf-1. *FASEB J.* 25, 3250–3261. doi: 10.1096/fj.10-177527
- Medicinal Plant Images Database (2007). *School of Chinese Medicine*. Hong Kong: Baptist University.
- Pan, R., Bai, X., Chen, J., Zhang, H., and Wang, H. (2019). Exploring structural diversity of microbe secondary metabolites using OSMAC strategy: a literature review. *Front. Microbiol.* 10:294. doi: 10.3389/fmicb.2019.00294
- Pierens, G. K. (2014). ¹H and ¹³C NMR scaling factors for the calculation of chemical shifts in commonly used solvents using density functional theory. *J. Comput. Chem.* 35, 1388–1394. doi: 10.1002/jcc.23638
- Polavarapu, P. L. (2002). Optical rotation: recent advances in determining the absolute configuration. *Chirality* 14, 768–781. doi: 10.1002/chir.10145
- Rehberg, N., Akone, H. S., Ioerger, T. R., Erenkamp, G., Daletos, G., Gohlke, H., et al. (2018). Chlorflavonin targets acetoxyhydroxyacid synthase catalytic subunit IlvB1 for synergistic killing of *Mycobacterium tuberculosis*. *ACS Infect. Dis.* 4, 123–134. doi: 10.1021/acinfeddis.7b00055
- Schwartz, R. E., Helms, G. L., Bolessa, E. A., Wilson, K. E., Giacobbe, R. A., Tkacz, J. S., et al. (1994). Pramanicin, a novel antimicrobial agent from a fungal fermentation. *Tetrahedron* 50, 1675–1686. doi: 10.1016/s0040-4020(01)80843-7
- Smith, S. G., and Goodman, J. M. (2010). Assigning stereochemistry to single diastereoisomers by GIAO NMR calculation: the DP4 probability. *J. Am. Chem. Soc.* 132, 12946–12959. doi: 10.1021/ja105035r
- Stephens, P. J., and Harada, N. (2010). ECD cotton effect approximated by the Gaussian curve and other methods. *Chirality* 22, 229–233. doi: 10.1002/chir.20733
- Tan, S. W. B., Chai, C. L. L., and Moloney, M. G. (2014). Synthesis of 3-acetyltetramates by side chain manipulation and their antibacterial activity. *Org. Biomol. Chem.* 12, 1711–1716. doi: 10.1039/c4ob00095a
- Tan, S. W. B., Chai, C. L. L., and Moloney, M. G. (2017). Mimics of pramanicin derived from pyroglutamic acid and their antibacterial activity. *Org. Biomol. Chem.* 15, 1889–1912. doi: 10.1039/c6ob02828d
- Tan, S. W. B., Chai, C. L. L., Moloney, M. G., and Thompson, A. L. (2015). Synthesis of mimics of pramanicin from pyroglutamic acid and their antibacterial activity. *J. Org. Chem.* 80, 2661–2675. doi: 10.1021/jo502810b
- Tran-Cong, N. M., Mándi, A., Kurtán, T., Müller, W. E. G., Kalscheuer, R., Lin, W. H., et al. (2019). Induction of cryptic metabolites of the endophytic fungus *Trichocladium* sp. through OSMAC and co-cultivation. *RSC Adv.* 9, 27279–27288. doi: 10.1039/c9ra05469c
- Varetto, U. (2009). *MOLEKEL*, v. 5.4. Manno: Swiss National Supercomputing Centre.
- Wang, H., Dai, H., Heering, C., Janiak, C., Lin, W., Orfali, R. S., et al. (2016). Targeted solid phase fermentation of the soil dwelling fungus *Gymnascella dankaliensis* yields new brominated tyrosine-derived alkaloids. *RSC Adv.* 6, 81685–81693. doi: 10.1039/c6ra14554j
- Wang, H., Eze, P. M., Höfert, S. P., Janiak, C., Hartmann, R., Okoye, F. B. C., et al. (2018). Substituted l-tryptophan-l-phenyllactic acid conjugates produced by an endophytic fungus *Aspergillus aculeatus* using an OSMAC approach. *RSC Adv.* 8, 7863–7872. doi: 10.1039/c8ra00200b

Conflict of Interest: The authors declare that the research was conducted in the absence of any commercial or financial relationships that could be construed as a potential conflict of interest.

Copyright © 2020 Gao, Stuhldreier, Schmitt, Wesselborg, Guo, Zou, Mándi, Kurtán, Liu and Proksch. This is an open-access article distributed under the terms of the Creative Commons Attribution License (CC BY). The use, distribution or reproduction in other forums is permitted, provided the original author(s) and the copyright owner(s) are credited and that the original publication in this journal is cited, in accordance with accepted academic practice. No use, distribution or reproduction is permitted which does not comply with these terms.

Publication 12

Manuscript “High-throughput screening for natural compound-based autophagy modulators reveals novel chemotherapeutic mode of action for arzanol”:

Deitersen J, [Stuhldreier E](#), Ceccacci S, Schlütermann D, Berning L, Wu W, Sun Y, Berleth N, Mendiburo MJ, Seggewiß S, Monti MC, Proksch P, Stork B *Manuscript in preparation*

1 High-throughput screening for natural compound-based
2 autophagy modulators reveals novel chemotherapeutic mode of
3 action for arzanol

4

5 Jana Deitersen¹, Fabian Stuhldreier¹, Sara Ceccacci², David Schlütermann¹, Lena Berning¹, Wenxian
6 Wu¹, Yadong Sun¹, Philip Böhler¹, Niklas Berleth¹, Maria José Mendiburo¹, Sabine Seggewiß¹, Maria
7 Chiara Monti², Peter Proksch³, Björn Stork^{1,*}

8

9

10 ¹Institute of Molecular Medicine I, Medical Faculty, Heinrich Heine University, Universitätsstraße 1,
11 40225 Düsseldorf, Germany

12 ²Department of Pharmacy, University of Salerno, Via Giovanni Paolo II 132, 84084 Fisciano Salerno,
13 Italy

14 ³Institute of Pharmaceutical Biology and Biotechnology, Faculty of Mathematics and Natural Sciences,
15 Heinrich Heine University, Universitätsstraße 1, 40225 Düsseldorf, Germany

16

17

18 *Correspondence: bjoern.stork@hhu.de

19

20

21 RUNNING TITLE: Mode of action of arzanol

22 KEYWORDS: arzanol, autophagy, natural compounds, chemotherapy, mitochondria

23 **Abstract**

24 Autophagy is an intracellular recycling pathway with implications for intracellular homeostasis and cell
25 survival. Its pharmacological modulation can aid chemotherapy by sensitizing cancer cells towards
26 approved drugs and overcoming chemoresistance. Recent translational data on autophagy modulators
27 show promising results in reducing tumor growth and metastasis, but also reveal a need for more specific
28 compounds and novel lead structures. Here, we searched for such autophagy-modulating compounds
29 in a flow cytometry-based high-throughput screening of an in-house natural compound library. We
30 successfully identified novel inducers and inhibitors of the autophagic pathway. Among these, we
31 identified arzanol as autophagy-modulating drug that is able to sensitize RT-112 bladder cancer cells
32 towards cisplatin (CDDP). Its anticancer activity was further confirmed in monotherapy against both
33 CDDP-sensitive and -resistant bladder cancer cells. We classified arzanol as novel mitotoxin, inducing
34 the fragmentation of mitochondrial membranes, and we identified a series of new targets for arzanol that
35 involve proteins of the class of mitochondria-associated quinone-binding oxidoreductases. Using
36 fluorescence microscopy, we show that arzanol further causes the accumulation of ATG16L1-positive
37 structures, while it also induces the accumulation of lipidated LC3. Surprisingly, we observed a reduction
38 of the size of autophagosomes compared to the bafilomycin control and a pronounced accumulation of
39 p62/SQSTM1 in response to arzanol treatment in HeLa cells. We therefore speculate that arzanol acts
40 both as inducer of early autophagosome biogenesis and as inhibitor of later autophagy events.
41 Collectively, our results suggest arzanol as valuable tool for autophagy research and cancer therapy.

42 **Introduction**

43 As of today, the discovery of approved anticancer drugs falls behind the rapid increase in cancer-related
44 mortality. Cancer drug discovery therefore focusses on repurposing approved and identifying novel
45 bioactive compounds that can serve as lead compounds or clinical drug candidates. Most drugs
46 developed over the last decades are based on natural compounds^{1,2}. Their advantages lie in the
47 inexhaustible quantity of compounds available in nature, their often non-synthesizable complexity, and
48 a high degree of stereochemistry³. They often target evolutionarily conserved pathways that play central
49 roles in cell fate decisions leading to apoptosis, necrosis, senescence, or autophagy.

50 Autophagy is a lysosomal pathway with mainly cytoprotective purpose that plays a role in different
51 human pathologies such as neurodegeneration or cancer⁴⁻⁷. The main characteristic of macroautophagy
52 (henceforth referred to as autophagy) is the sequestration of aggregates, long-lived proteins, or
53 damaged organelles by an autophagosomal membrane and its subsequent fusion with the lysosome for
54 the degradation of bulk or selected cargo. Autophagy is a conserved pathway that is basally active in
55 most cell types, but can also be induced by stimuli like withdrawal of growth factors, nutrient deficiency,
56 hypoxia, aggregates or mitochondrial damage⁸⁻¹⁰. Dependent on the inducing stimulus, specific
57 autophagy receptors can target and help to eliminate sources of damage such as aggregates in
58 aggrephagy, parts of the ER in ERphagy, bacterial or viral components in xenophagy, isolated damaged
59 mitochondria in mitophagy and many more.

60 In canonical autophagy, 5'-AMP-activated protein kinase (AMPK)-dependent activation and
61 mechanistic/mammalian target of rapamycin (mTOR)-dependent inhibition regulate the autophagy-
62 initiating unc-51-like kinase 1 (ULK1) complex, which consists of ULK1, autophagy-related protein (ATG)
63 13, ATG101, and RB1-inducible coiled-coil protein 1 (RB1CC1/FIP200). Upon induction of autophagy,
64 the ULK1 complex activates the class III phosphatidylinositol 3-kinase (PIK3C3/VPS34) lipid kinase
65 complex that produces phosphatidylinositol 3-phosphate (PI3P) at subregions of the ER forming so
66 called omegasomes¹¹. ATG9A as well as the PI3P-binding proteins DCFP1 and WIPI1/2 are involved in
67 membrane elongation and recruit the ubiquitin-like ATG12—ATG5-ATG16L1 complex. In coordination
68 with ATG7 and ATG3, the ATG12—ATG5-ATG16L1 complex conjugates phosphatidylethanolamine to
69 LC3 (ref.¹²). Lipidated LC3 decorates autophagosomal membranes and serves as “anchor” for the
70 recruitment of autophagosomal cargo or downstream autophagy regulators. For instance, LC3 binds
71 p62 (also known as sequestosome 1, SQSTM1), which is an autophagic receptor for ubiquitinated
72 proteins and organelle surfaces¹³. After fusion of autophagosome and lysosome, lysosomal hydrolases

73 degrade not only autophagic cargo but also LC3 itself and LC3-bound receptors such as p62/SQSTM1.
74 Accordingly, a reduction in both LC3 and p62/SQSTM1 levels serves as a readout for autophagic flux.
75 As intracellular quality control, autophagy ensures cell survival and prevents the accumulation of
76 carcinogenic stimuli in healthy cells. Knockdown or deletion of ATG7 or of Beclin-1 (BECN1), a protein
77 member of the PIK3C3 complex, promotes tumor development^{14,15}. In line with this, biomarkers for poor
78 prognosis in leukemia are degraded by chaperone-mediated autophagy, suggesting a protective role of
79 autophagy against tumorigenesis¹⁶⁻¹⁹. In late-stage cancer, on the other hand, autophagy can be tumor-
80 promoting due to its catabolic function, supporting solid tumors in hypoxic regions and enabling the
81 tumor microenvironment to contribute nutrients and growth factors²⁰⁻²⁴. In these solid tumors, autophagy
82 has been found to contribute to cancer cell survival and poor outcome^{25,26}. Recent attempts in
83 translational cancer research therefore investigate the inhibition of autophagy in both monotherapy and
84 combinational treatment in order to sensitize cancer to chemotherapy²⁷⁻³⁰. In contrast, inducers of
85 autophagy are also discussed as potential chemotherapeutics, driving cancer cells into the so-called
86 autophagy-associated or autophagic cell death³¹⁻³⁵.

87 This work investigates an in-house library of natural compounds in order to find modulators of
88 autophagy, which can be applied as novel chemotherapeutics for monotherapy or combinational
89 therapy. We found that arzanol, a phloroglucinol derivative isolated from the plant *Helichrysum italicum*
90 (Asteraceae), impairs the viability of bladder cancer cells, and we investigated its molecular mode of
91 action. We identify arzanol as dual modulator of autophagy and expand the list of arzanol targets by
92 mitochondria-related oxidoreductases and autophagy-related proteins. Taken together, we propose
93 arzanol as new tool to study autophagic mechanisms and as a potential lead structure for combinational
94 chemotherapy with CDDP in urothelial bladder carcinoma cells.

95 **Results**

96 *High-throughput Screening Reveals Novel Modulators of Autophagy*

97 To identify novel modulators of autophagy among natural compounds, we screened an in-house library
98 of 300 natural compounds derived from marine sponges, endophytic fungi and higher plants, using a
99 flow cytometric high-throughput screening (Figure 1). The autophagic flux was measured in mouse
100 embryonic fibroblasts (MEFs) stably expressing mCitrine-tagged LC3 as a marker. As growth medium,
101 we used serum-supplied full medium including amino acids, while for starvation, we used serum-free
102 and amino acid-deficient starvation medium. During serum- and amino acid starvation, mCitrine-LC3
103 anchored to the inner autophagosomal membrane is quenched by the low lysosomal pH and degraded
104 by lysosomal hydrolases, causing a reduction of the mCitrine-LC3 signal (Figure 1A). Upon treatment
105 with the lysosomal inhibitor bafilomycin A₁ (baf A₁), both basal and starvation-induced autophagic flux
106 is inhibited and the mCitrine-LC3 signal increases (Figure 1A). These data confirm the sensitivity of this
107 assay to identify both inducers and inhibitors of autophagy.

108 For the classification of inducers and inhibitors, we set the threshold at 15% decrease or increase of the
109 mCitrine-LC3 signal upon treatment with the compounds. In addition, we set our threshold to compounds
110 with a fairly moderate and higher effect according to statistical analyses of high-throughput data ($|\text{SSMD}$
111 $\text{score}| \geq 1$) (Figure 1; Table 1 and 2; Supplementary Table 1)³⁶. In doing so, the screening of MEFs
112 treated with natural compounds in full medium revealed five potential inhibitors of basal autophagy
113 (Figure 1B) and eight potential novel inducers of autophagy (Figure 1B, Table 1).

114 The screening upon starvation conditions revealed in total 64 potential inhibitors of autophagic flux
115 (Figure 1C, Table 2). In addition to the aforementioned five inhibitors, and four dual modulators (i.e.,
116 activating in full medium, but inhibitory under starvation), 55 compounds were classified as potential
117 autophagy inhibitors. Of the 300 tested natural compounds, two thirds did not have a considerable effect
118 on autophagy in our screening (Figure 1D).

119

120 *Arzanol Interferes with Late-Stage Autophagy*

121 Among the novel modulators of autophagy, we identified the phloroglucinol α -pyrone arzanol (Figure
122 2A; marked as red dots in Figures 1B and 1C), which was isolated from the aerial parts of *Helichrysum*
123 *italicum*³⁷. Arzanol is known for its anti-inflammatory, anti-viral³⁸, anti-oxidative and cytotoxic effects³⁹,
124 however no effect on autophagy has been reported before. To identify the pathway affected by arzanol,

125 we performed immunoblotting analyses of key components of the canonical autophagy pathway along
126 the mTOR/ULK1-axis (Figures 2B-G).

127 During normal growth, AKT phosphorylates tuberous sclerosis complex 2 (TSC2) and thus destabilizes
128 and inactivates it⁴⁰. Upon nutrient deprivation, TSC2 is stabilized and suppresses mTOR signaling via
129 inactivation of Ras homolog enriched in brain (RHEB)⁴¹. Thus, nutrient starvation causes a reduction in
130 the mTOR-dependent phosphorylation of the target proteins ribosomal protein S6 kinase beta-1 (p70
131 S6K) at Ser371 (ref.⁴²) and ULK1 at Ser758 (ref.⁴³). Hypo-phosphorylation of ULK1 at Ser758 is
132 associated with the dissociation of mTOR from the ULK1 complex, allowing its activation and the
133 initiation of autophagosome formation⁴⁴. During the early biogenesis of autophagosomes, cytosolic LC3-
134 I gets lipidated to autophagosomal membrane-bound LC3-II, which is—along with the autophagy
135 receptor protein p62/SQSTM1—later degraded by lysosomal hydrolases⁴⁵.

136 Checking for these parameters, we observed that arzanol does not inhibit starvation-induced inactivation
137 of mTOR; however, it causes the accumulation of LC3-II and p62 during starvation-induced autophagy
138 (Figures 2B-F). For improved reproducibility, we also validated these effects using commercially
139 available arzanol. As determined by immunoblotting of HeLa cell lysates and similar to self-isolated
140 arzanol, commercially available arzanol had a minimum effective dose on LC3-II accumulation below 3
141 μM and a maximal effective dose of 5 μM (Figure 2H). The effect of arzanol on p62/SQSTM1
142 accumulation was more prominent upon amino acid starvation (Figure 2I). We further validated the
143 accumulation of LC3 in human HeLa cells expressing the GFP-LC3-RFP-LC3 ΔG reporter construct⁴⁶
144 by flow cytometry, measuring the autophagic degradation of GFP-LC3 indicated by a decrease in
145 fluorescence (Figure 2J). The effect of arzanol on autophagy is consistent within all our assays (i.e.,
146 murine vs. human cells, immunoblotting vs. flow cytometric assays, and self-isolated vs. commercial
147 arzanol), which is why we used commercially available arzanol in all further experiments. Of note, we
148 found that arzanol was ineffective in serum-supplied growth medium due to its serum-binding capacity
149 (Supplementary figure 1A), which also explains the absence of effects in our screening upon full medium
150 (Figure 1B). In serum-free and amino acid-rich medium, however, arzanol caused accumulation of LC3-
151 II, which resembles its effects in the amino acid-free starvation medium (Figure 2H). Furthermore, we
152 exclude the involvement of antioxidative or scavenging effects of arzanol during amino acid starvation
153 to be the reason for the observed effects, although antioxidative effects could be observed in serum-
154 free and amino acid-rich medium (Supplementary figure 1B).

155 *Arzanol Changes ATG16L1 Localization*

156 An increase in LC3 can be indicative of disrupted autophagic degradation or increased protein
157 expression, while an increase in LC3-II can additionally hint to its enhanced lipidation. To determine the
158 circumstances that led to the accumulation of the autophagic markers LC3 and p62/SQSTM1 upon
159 serum- and amino acid starvation (Figure 2), we detected both overexpressed GFP-LC3 (Figure 3A)
160 and endogenous LC3 (Figure 3B) using fluorescence microscopy and quantified both size and amount
161 of LC3-positive dots that commonly represent autophagosomes⁴⁷. A clear trend towards increasing
162 numbers of LC3 dots upon arzanol treatment was observed (Figures 3A and 3B). However, the size of
163 these LC3 dots appeared rather small, making them partly indistinguishable for the quantification
164 software. Nevertheless, we think one can appreciate the increase in number of both overexpressed and
165 endogenous LC3 dots and their significantly smaller size compared to bafilomycin A₁-treated cells
166 (Figures 3A and 3B, i. and ii.). Further, we examined the location, amount and size of ATG16L1 dots,
167 which is a core component of the LC3 lipidation machinery. Arzanol treatment caused a significant
168 increase in the number of ATG16L1-positive structures (Figure 3C, i.), while the size of the dots and the
169 total protein level of ATG16L1 remained unaltered (Figure 3C, ii and data not shown). These data are
170 in line with increased LC3-II in response to arzanol treatment we described above (Figures 2E, 2H, and
171 2J). Finally, we confirmed the autophagy-inhibiting properties of arzanol by analyzing autophagic flux
172 using the combination of arzanol with bafilomycin A₁ (Supplementary figure 1C).

173 Next, we aimed at investigating which other components of the autophagic machinery are involved in
174 the response to the treatment with arzanol during serum- and amino acid starvation. During
175 autophagosomal membrane expansion and cargo sequestration, ATG16L1 is recruited to PE-containing
176 phagophores by PI3P-binding WIPI2 (ref.^{48,49}). Recruitment of WIPI2 in turn depends on the interaction
177 between ATG13 and ATG101 that are both components of the ULK1 complex⁵⁰. We therefore performed
178 colocalization studies to determine mutual recruitment of ATG16L1 and WIPI2 or ATG13 upon arzanol
179 exposure in order to evaluate if the ATG16L1 dots that we observed are regular phagophores. We
180 observed colocalization of ATG16L1 dots with both WIPI2 and ATG13 (Figures 4A and 4B) by
181 immunofluorescence microscopy in response to arzanol treatment. Further, some of these ATG16L1
182 dots show a perinuclear localization, and are surrounded by a dense population of LC3 positive dots
183 (Figure 4C), which look similar in our previous observations (Figures 3A and 3B). Of note, we did not
184 observe an increased number of WIPI2 dots in response to arzanol (Supplementary figure 2).

185

186 *Arzanol as anti-Cancer Drug in Mono- and CDDP-Combination Therapy*

187 In addition to monotherapy, combinational therapies of approved drugs with autophagy modulators have
188 been proposed to overcome tumor survival⁵¹⁻⁵³. In order to test the cytotoxic effect of arzanol on cancer
189 cells, we performed MTT assays after 24 h of either arzanol monotherapy or combinational therapy with
190 cisplatin (CDDP) in RT-112 urothelial bladder carcinoma cells. We tested the cytotoxic effect of arzanol
191 both in serum-free growth medium containing amino acids (Figures 5A-C) and in serum- and amino
192 acid-deficient starvation medium (Figures 5D-F). The results of the cell viability assays reveal that
193 arzanol is a moderate chemotherapeutic alone during amino acid supply in both CDDP-resistant cells
194 (IC₅₀: 9.6 μM; Figure 5A), and in CDDP-sensitive RT-112 cells (IC₅₀: 6.6 μM; Figure 5B). For the amino
195 acid-supplied CDDP-sensitive RT-112 cells, arzanol sensitizes the cells towards CDDP treatment (IC₅₀
196 shift from 22.5 μM to 7.1 μM; Figure 5C). Similarly, arzanol is also a moderate chemotherapeutic alone
197 during amino acid starvation in both CDDP-resistant cells (IC₅₀: 22.6 μM; Figure 5D), and in CDDP-
198 sensitive RT-112 cells (IC₅₀: 13.2 μM; Figure 5E). Thereby, arzanol appears less toxic during amino
199 acid starvation in relation to the non-starved samples in both cell lines. For the amino acid-starved
200 CDDP-sensitive RT-112 cells, arzanol still sensitizes the bladder cancer cells towards CDDP-treatment
201 (IC₅₀ shift from 20.7 μM to 6.3 μM; Figure 5F). Upon both nutrient statuses, arzanol did not sensitize
202 the CDDP-resistant cell line (Supplementary figure 3A).

203 Surprisingly, when we compared these MTT assay data with similar samples from an Alamar blue assay
204 (Supplementary figure 3B), we noticed that especially for CDDP-resistant cells the treatment with low
205 amounts of arzanol resulted in an increased reduction of MTT, but a decreased reduction of resazurin
206 in the Alamar blue assay (Supplementary figure 3C). While both assays are colorimetric assays, the
207 MTT assay measures the metabolic activity of enzymes that are capable to reduce the tetrazolium dye
208 MTT 3-(4,5-dimethylthiazol-2-yl)-2,5-diphenyltetrazolium bromide to its insoluble formazan, whereas the
209 Alamar blue assay depends on enzymes that reduce resazurin to resofurin. Similarly to our results,
210 Hamid et al. observed the same phenomenon for the NAD(P)H quinone dehydrogenase 1 (NQO1)
211 inhibitor dicoumarol⁵⁴, which shares structural similarity with arzanol. In contrast to their observations
212 on dicoumarol, we still witnessed that the cells die at higher concentrations of arzanol. Nevertheless,
213 we suspect an effect of arzanol on the oxidoreductases involved in these cytotoxicity assays.

214

215 *Arzanol Targets Mitochondria*

216 In our search for upstream causes of ATG16L1 accumulation upon arzanol treatment during amino acid
217 deficiency, we next investigated mitochondrial integrity. Different mitotoxins stimulate mitophagy as
218 means of cell survival. They induce the fragmentation of damaged mitochondria as well as the
219 recruitment of mitophagy-associated proteins PTEN-induced putative kinase protein 1 (PINK) and the
220 E3 ubiquitin ligase Parkin⁵⁵⁻⁵⁷.

221 In microscopy assays, arzanol induced the fragmentation of the inner and outer mitochondrial
222 membrane determined with mito-DsRed localizing to the mitochondrial matrix and staining of
223 translocase of outer membrane 20 kDa subunit (TOM20) (Figure 6A, Supplementary figure 4A). In line
224 with this, arzanol caused the mitochondrial stress-induced cleavage of optic atrophy protein 1 (OPA1),
225 presumable ubiquitination of Parkin, and stabilization of PINK primarily during amino acid starvation
226 (Figure 6B). Interestingly, the fragmented mitochondria seem adjacent to but not colocalized with the
227 ATG16L1 dots observed upon arzanol treatment during serum- and amino acid starvation
228 (Supplementary figure 4B).

229 Consistent with mitochondrial damage, we identified a series of mitochondrial proteins as novel protein
230 targets for arzanol, using two approaches: we performed affinity purification with arzanol covalently
231 immobilized on beads and fished for binding-partners in HeLa and MEF cellular lysates and lysates from
232 isolated mitochondria. We also carried out Drug Affinity Responsive Target Stability (DARTS) assays in
233 mitochondrial lysates to evaluate the enhanced stability of arzanol binding targets against protease
234 degradation. This strategy is based on the evidence that under physiological conditions, a protein
235 fluctuates between multiple alternative conformations. But upon small molecule-binding, the equilibrium
236 shifts to favor the thermodynamically more stable bound-ligand state and this leads to a decrease of
237 protein susceptibility to enzymatic proteolysis⁵⁸. Both approaches were followed by mass spectrometry
238 or immunoblotting to identify and confirm the arzanol targets. Among the potential novel target proteins
239 of arzanol (Figure 7A, Supplementary table 2), we identified the autophagy-relevant proteins RAB1B
240 member RAS oncogene family (RAB1B), heat shock protein 90 alpha family class A member 1 and
241 class B member 1(HSP90AA1/B1), ribosomal protein S27a (RPS27A), and the mitochondria-related
242 proteins TNF receptor associated protein 1 (TRAP1) and superoxide dismutase 2 (SOD2). We further
243 found heterogeneous nuclear ribonucleoprotein H1 (HNRNPH1), acidic nuclear phosphoprotein 32
244 family member A (ANP32A), and annexin A2 (ANXA2) bound to arzanol-beads in affinity purification of
245 both cytosolic and mitochondrial HeLa lysates. DARTS assays further revealed carbamoyl-phosphate

246 synthase 1 (CPS1), glycyl-tRNA synthetase 1(GARS1), and heat shock protein family A (Hsp70)
247 member 9 (HSPA9) as arzanol binders. Of special interest to us, we identified mitochondrial respiratory
248 chain complex III proteins ubiquinol-cytochrome c reductase hinge protein (UQCRH) and cytochrome c
249 somatic (CYCS), and complex I-related NADH:ubiquinone oxidoreductase subunit S4 (NDUFS4) bound
250 to immobilized arzanol in affinity purification in mitochondrial lysates. We therefore tested arzanol in
251 mitochondrial activity assays for the respiratory chain complexes, and found that arzanol mostly inhibited
252 complexes II and III (Figure 7B). In line with these data, the succinate dehydrogenase complex iron
253 sulfur subunit B (SDHB, respiratory chain complex II) and the ubiquinol-cytochrome c reductase Rieske
254 iron-sulfur polypeptide 1 (UQCRFS1, respiratory chain complex III) were validated by immunoblotting
255 assays of DARTS samples (Figure 7C). Moreover, these immunoblotting assays also verified CPS1,
256 GARS and HSP9A as arzanol targets. With the structural similarity of arzanol and dicoumarol, and the
257 divergent effects of arzanol in MTT versus Alamar blue assays in mind, we also tested arzanol in a
258 NQO1 activity assay. Arzanol reduced the activity of NQO1 in concentrations of 10 μ M (Figure 7D).
259 Taken together, our results show that arzanol is a promising and versatile new anti-cancer drug and
260 modulator of autophagy. It sensitizes RT-112 bladder carcinoma cells towards CDDP, and reduces cell
261 viability of both normal and CDDP-resistant RT-112 in monotherapy. Arzanol is able to target different
262 quinone-dependent reductases such as NQO1 and oxidoreductases of the mitochondrial respiratory
263 chain that maintain mitochondrial integrity. Arzanol reduces mitochondrial respiration, targeting complex
264 II and III, and induces fission of the mitochondrial membranes independent from reactive oxygen
265 species. We observed the accumulation of ATG16L1 and lipidated LC3, but also smaller
266 autophagosomal structures and the accumulation of p62/SQSTM1 upon arzanol treatment during
267 starvation.

268 **Discussion**

269 The modulation of autophagy is used as anti-cancer treatment in more than eighty clinical trials treating
270 several different cancer types (<https://clinicaltrials.gov/>; accessed on December 14, 2020). We used the
271 top-down drug discovery approach to identify eight potential inducers and sixty-four potential inhibitors
272 of autophagy in our high-throughput autophagy screening. Among these compounds, we identified
273 arzanol as a novel modulator of autophagy. Due to its strong effect on LC3-II accumulation and
274 beneficial chemical characteristics like feasible compound isolation, commercial availability, and
275 chemical stability, we selected it for a more detailed characterization.

276 In our assays, arzanol was initially identified as inhibitor of starvation-induced autophagy by causing
277 accumulation of overexpressed mCitrine-LC3 in murine fibroblasts. Consistently, it also caused
278 accumulation of overexpressed GFP-LC3 and endogenous total LC3 as well as lipidated LC3 in human
279 cancer cells as determined by flow cytometry, fluorescence microscopy, and immunoblot analyses.
280 Lipidation of LC3 is facilitated by the activation of the ubiquitin-like LC3 processing cascade involving
281 ATG16L1, which is essential for LC3 lipidation⁵⁹. Dudley et al. showed that ATG16L1 homodimerizes in
282 order to bind to PI3P-covered pre-autophagosomal sites, and that modulating the PI3P-binding capacity
283 of ATG16L1 impairs lipidation of LC3 (ref.¹²). It is therefore likely that the accumulation of ATG16L1 dots
284 upon arzanol treatment under starvation conditions is the cause of the increase in LC3-II that we
285 observed in immunoblot analysis, which in turn contributes to the observed increase in total LC3
286 measured by flow cytometry. As platforms for autophagosome biogenesis, ATG16L1-positive dots are
287 also likely to account for the number of small LC3-positive dots detected by microscopy. However, also
288 the inhibition of the autophagic flux can account for these phenomena by preventing autophagosome
289 maturation and lysosomal LC3 degradation.

290 It was shown that accumulation of ATG16L1 increases during autophagy to ensure autophagosome
291 maturation and autophagic activity¹². During starvation-induced autophagy, ATG16L1 dots are known
292 to colocalize with proteins of the autophagic machinery such as ULK1, ATG14, and WIPI1 at the
293 phagophore⁶⁰. The colocalization of ATG16L1 with ATG13 and WIPI2, and the accumulation of LC3-
294 positive dots around the ATG16L1-positive structures therefore indicate that the ATG16L1-positive
295 structures, which accumulate upon arzanol treatment, are phagophores. In addition, Bansal et al.
296 observed that ATG16L1 is able to colocalize with LC3-binding mitophagy receptors such as ubiquitin-
297 binding optic neuropathy inducing protein (optineurin/OPTN)⁶¹⁻⁶⁴. Mitophagy is the selective autophagy
298 of damaged mitochondria and aims to deplete damaged organelles and their associated triggers such

299 as mitotoxins⁵⁵⁻⁵⁷. To induce mitophagy, PINK accumulates at the outer membrane of damaged
300 mitochondria where it recruits and activates the E3 ubiquitin ligase Parkin, which then ubiquitinates
301 mitochondrial surface proteins. This allows the recruitment of autophagic receptors such as LC3 and
302 OPTN, but also ULK1, FIP200, ATG9A, WIPI proteins and ATG16L1 to form a mature autophagosome
303 around the damaged organelle⁶⁵⁻⁶⁷. When we checked for mitochondrial damage induced by arzanol
304 during serum- and amino acid starvation, we observed the fragmentation of the inner and outer
305 mitochondrial membranes. We further found accumulation of PINK in immunoblot analysis, and
306 observed GFP-Parkin to run at a higher molecular mass, which we interpret as ubiquitinated Parkin.
307 Along with the markers for mitochondrial damage, we detected cleaved OPA1, a protein involved in
308 mitochondrial fusion⁶⁸⁻⁷¹. In line with these data, we found arzanol to reduce the activity of mitochondrial
309 respiratory complexes, mainly complexes II and III. Interestingly, among protein targets from affinity
310 purification, we also identified NDUFS4, a protein of respiratory complex I. As novel targets for arzanol,
311 we identified not only the respiratory complexes I, II and III, but also NQO1 and SOD2, which all function
312 as quinone-dependent reductases required for mitochondrial integrity⁷²⁻⁷⁶. Combined with structural data
313 of arzanol, we hypothesize that arzanol binds to the quinone-binding pockets of these proteins and
314 accounts for the observed mitochondrial damage. TRAP1, another potential target of arzanol, regulates
315 a metabolic switch between mitochondrial oxidative phosphorylation and glycolysis in cancer cells⁷⁷. It
316 is reported to maintain mitochondrial integrity downstream of respiratory complex I and PINK1⁷⁸. We
317 speculate that arzanol-induced mitochondrial damage provokes autophagosome formation and explains
318 ATG16L1 accumulation. Additionally, we identified autophagy-relevant proteins, such as RAB1B as
319 potential binding-partner of arzanol. RAB1B colocalizes with ATGs and is involved in autophagosome
320 biogenesis⁷⁹⁻⁸², and knockdown of RAB1B induced the accumulation of LC3-II⁸³. Inhibition of RAB1B
321 could support increased lipidation of LC3 upon arzanol treatment.

322 While we observed smaller autophagosomes upon arzanol treatment, it also caused accumulation of
323 p62. We interpret the pronounced accumulation of p62 upon arzanol treatment during starvation as an
324 indicator of an inhibited autophagic flux. This is further supported by our flux analysis using the
325 combination of arzanol and bafilomycin A₁. It remains unclear whether the dysregulation in LC3 lipidation
326 itself is ultimately sufficient to inhibit autophagy or if additional targets are involved. In support of the
327 latter, we found HSP90AA1 bound to arzanol in affinity purification. HSP90AA1 acts as chaperone for
328 many client proteins, some of which are involved in autophagy, e.g. AKT, Beclin-1, ULK1, or lysosome-
329 associated membrane protein 2 (LAMP2)⁸⁴. Dissociation of chaperones can destabilize their client

330 proteins, preventing them from fulfilling their tasks. HSP90AA1 inhibition by arzanol could result in
331 subsequent destabilization of LAMP2A, a protein that is essential for maintaining the integrity of
332 lysosomes and autolysosomes⁸⁵⁻⁸⁷. Non-functional lysosomes are prevented from fusing with
333 autophagosomes and cause the accumulation of different autophagic markers such as LC3 and p62
334 (ref.^{88,89}). Therefore, HSP90AA1 could be a target of arzanol accounting for a disturbed autophagosome
335 maturation and autolysosomal degradation of p62. Admittedly, we could not validate all identified targets
336 of arzanol, due to methodical blind spots of each assay, i.e. sterical problems in affinity purification, or
337 detectability issues of small proteins in DARTS. Accordingly, further validation experiments are required.
338 We tested the novel modulator of autophagy in monotherapy and combinational therapy with CDDP
339 against sensitive and CDDP-resistant bladder cancer cells. CDDP-based chemotherapy is the first-line
340 treatment in many cases of advanced or metastatic urothelial carcinoma according to The European
341 Association of Urology⁹⁰. However, innate and acquired chemoresistance remain a main reason for
342 cancer-related lethality in patients. Similar to other autophagy inhibitors that reduced tumor growth rate
343 and prolonged patient survival⁹¹⁻⁹⁵, we found that monotherapy with arzanol reduced the viability of both
344 CDDP-sensitive and -resistant bladder carcinoma cells while it sensitized the parental RT-112 cells to
345 CDDP treatment in combination therapy.

346 Conclusively, from our data we characterize arzanol as an inducer of mitochondrial damage and
347 autophagosome formation and as inhibitor of autophagy. Its different targets might account for the
348 multifaceted mode of action that leads to cytotoxic effects in bladder cancer cells. Taking into
349 consideration its pharmacological activities, we propose arzanol as a new lead structure for the
350 treatment of bladder cancer and suggest further investigations on its target- and cancer-specificity.

351 **Acknowledgements**

352 This study was supported by the Deutsche Forschungsgemeinschaft GRK 2158 (to P.P. and to B.S.),
353 STO 864/4-1 (to B.S.), STO 864/5-1 (to B.S.) and STO 864/6-1 (to B.S.), and the Düsseldorf School of
354 Oncology (to B.S.; funded by the Comprehensive Cancer Center Düsseldorf/Deutsche Krebshilfe and
355 the Medical Faculty of the Heinrich Heine University Düsseldorf). S. C. and M C. M. were supported by
356 POR CAMPANIA FESR 2014/2020 Asse 1 - Obiettivo specifico 1.2 – Azione 1 .2. Progetto: Campania
357 OncoTerapie CUP: B61G18000470007. We thank Andreas Reichert (Institute of Biochemistry and
358 Molecular Biology I, Medical Faculty, Heinrich Heine University Düsseldorf, Germany) for providing
359 *PRKN* cDNA and the OPA1 antibody. We thank Aviva M. Tolkovsky (Department of Clinical
360 Neurosciences, University of Cambridge, Cambridge, United Kingdom) for providing mito-DsRed-
361 expressing HeLa cells. We thank Margaretha Skowron (Department of Urology, Medical Faculty,
362 Heinrich Heine University, Düsseldorf, Germany) for providing RT-112 bladder carcinoma cells. We
363 thank Julia Werner (Institute of Pharmaceutical Biology and Biotechnology, Faculty of Mathematics and
364 Natural Sciences, Heinrich Heine University, Düsseldorf, Germany) for isolating arzanol used in Figures
365 1 and 2. We thank Tullia Lindsten (Memorial Sloan Kettering Cancer Center, New York City, USA) for
366 providing wild-type mouse embryonic fibroblasts. We thank Toshio Kitamura (Institute of Medical
367 Science, University of Tokyo, Japan) for providing Plat-E cells.

368

369 **Author contributions**

370 JD designed the experiments, performed flow cytometry analyses, microscopy and cell viability assays,
371 performed the NQO1 activity assay and immunoblot analyses, and prepared samples for AP-MS and
372 DARTS. JD analyzed and interpreted the data and wrote the manuscript. FS performed the Mito Check
373 experiments. SC and MCM performed DARTS and AP-MS. DS provided expertise on microscopy and
374 quantifications. LB performed cell viability assays. PB generated EGFP-Parkin- and mito-DsRed-
375 expressing HeLa cells. MJM, WW, YS, NB, and SS gave technical support. PP provided an in-house
376 natural compound library. PP and BS supervised the project. All authors discussed the results and
377 commented on the manuscript.

378

379 **Conflict of Interest**

380 The authors declare no conflict of interest.

381 **Materials and Methods**

382 *Reagents*

383 Natural compounds isolated from endophytic fungi, lichens, marine sponges or plants were provided by
384 Peter Proksch (Institute of Pharmaceutical Biology and Biotechnology of the Heinrich Heine University
385 (Düsseldorf, Germany). Bafilomycin A₁ (Sigma-Aldrich, #B1793) and arzanol (Sigma-Aldrich,
386 #SBR00002) were dissolved in dimethyl sulfoxide (DMSO; AppliChem GmbH, #A3672). We purchased
387 respiratory chain complex inhibitors antimycin A from Sigma (#A8674) and oligomycin A from Toronto
388 Research Chemicals (#O532970). For transfection of cells, we used FuGENE[®] 6 (Promega, #E2692)
389 and polybrene (hexadimethrine bromide; Sigma-Aldrich, #H9268-106). Immunoblots were performed
390 using Immobilon[™]-FL PVDF membrane (Merck-Millipore, #IPFL00010), milk powder (Carl Roth,
391 #T145.2), and Protease Inhibitor Cocktail powder (Sigma-Aldrich, #P2714-1BTL). Cells were cultivated
392 using full medium DMEM (Gibco[®] by Life Technologies, #41965-039), starvation medium EBSS (Gibco[®]
393 by Life Technologies, #24010-043), PBS (Gibco[®] by Life Technologies, #14190-094), fetal bovine serum
394 (GE Healthcare, #A15-101), 0.05% trypsin/EDTA solution (Gibco[®] by Life Technologies, #25300-062),
395 penicillin/streptomycin (10,000 U/ml, Biochrom GmbH, #A2213), puromycin (InvivoGen, ant-pr), or
396 blasticidin (InvivoGen, ant-bl).

397 For immunoblotting, antibodies against ACTB/ β -actin (Sigma-Aldrich, #A5316), LC3 (Cell Signaling
398 Technology, #2775), SQSTM1/p62 (PROGEN Biotechnik, GP62-C), ULK1 (clone D8H5, Cell Signaling
399 Technology, #8054), phospho ULK1 Ser758 (Cell Signaling Technology, #6888), phospho TSC2 Ser939
400 (Cell Signaling Technology, #3615), phospho p70S6K Ser371 (Cell Signaling Technology, #9208),
401 OPA1 (described previously⁹⁶; kindly provided by Andreas Reichert), PINK (Cell Signaling Technology,
402 #6946), Parkin (Abcam, #ab15954), SDHB (Thermo Fisher, #459230), UQCRRFS1 (Invitrogen, #MA5-
403 27471), CPS1 (Proteintech, #65011-1-Ig), GAPDH (Invitrogen, #437000), HSPA9/GRP 75 (clone D-9,
404 Santa Cruz Biotechnology, #sc-133137) and GARS1/GlyRS (clone D-10, Santa Cruz Biotechnology,
405 #sc-365311) were used. IRDye 800- or IRDye 680-conjugated secondary antibodies were purchased
406 from LI-COR Biosciences (#926-32210/11, #926-68070/71, #926-68024, #926-68077, #926-32214).
407 For immunofluorescence, antibodies against ATG16L (MBL #PM040), LC3B (MBL #PM036 and #M152-
408 3), WIPI2 (AbD Serotec/BIORAD, #MCA5780GA), ATG13 (MBL, #M183-3), TOM20 (Santa Cruz
409 Biotechnology, #17764) were used. Alexa Fluor[®] 488-conjugated and Alexa Fluor[®] 647-conjugated
410 antibodies were purchased from Jackson ImmunoResearch Laboratories.

411 NQO1 activity of HeLa cells was measured using the NQO1 Activity Assay Kit (Abcam, #184867)
412 according to the manufacturer. Respiratory chain complex activities were measured from isolated
413 mitochondria using the MitoCheck Complex Activity Assay Kits (Cayman Chemicals, #700930,
414 #700940, #700950, #700990, #701000). Both assays were measured using a microplate reader
415 (BioTek, Synergy Mx).

416

417 *Generation and culture of cell lines*

418 Wild-type mouse embryonic fibroblasts (MEFs) (kindly provided by Tullia Lindsten, Memorial Sloan
419 Kettering Cancer Center, New York City, USA) were retrovirally transfected with pMSCVblast/mCitrine-
420 LC3B. Generation of pMSCVblast/mCitrine-LC3B was described previously⁹⁷. For transfection, Plat-E
421 cells (kindly provided by Toshio Kitamura, Institute of Medical Science, University of Tokyo, Japan) were
422 transfected with 1.9 µg pMSCV-based retroviral vectors using FuGENE® 6 (Promega) transfection
423 reagent according to the manufacturer's manual. After 48 h, retroviral supernatant was collected and
424 used for the infection of MEFs in combination with 9 µg/mL polybrene (Sigma-Aldrich; H9268-106). The
425 cells were incubated for three days prior to selection with 35 µg/ml blasticidin.

426 Wild-type HeLa cells (kindly provided by Richard Youle, John Edward Porter Neuroscience Research
427 Center, Bethesda, USA) were retrovirally transfected with pMRX-IP/GFP-LC3-RFP-LC3ΔG (kindly
428 provided by Noboru Mizushima, Department of Biochemistry and Molecular Biology, University of Tokyo,
429 Tokyo, Japan; Addgene plasmid # 84572; <http://n2t.net/addgene:84572>; RRID:Addgene_84572).
430 Alternatively, mito-DsRed-expressing HeLa cells (kindly provided by Aviva M. Tolkovsky, Department of
431 Clinical Neurosciences, University of Cambridge, Cambridge, United Kingdom) were retrovirally
432 transfected with pMSCVpuro/EGFP-Parkin. This plasmid was generated by inserting EGFP cDNA and
433 human Parkin cDNA (kindly provided by Andreas Reichert, Institute of Biochemistry and Molecular
434 Biology I, Medical Faculty, Heinrich Heine University Düsseldorf, Germany) into pMSCVpuro. For
435 retroviral transfection of HeLa cells, Plat-E cells were transfected with 1.9 µg pMRX- or pMSCVpuro-
436 based retroviral vectors and 1.0 µg pVSV-G vector DNA using FuGENE® 6 (Promega) transfection
437 reagent according to the manufacturer's manual. After 48 h, retroviral supernatant was collected and
438 used for the infection of HeLa cells in combination with 9 µg/mL polybrene (Sigma-Aldrich; H9268-106).
439 The cells were incubated for three days prior to selection with 2.5 µg/ml puromycin. For Figure 2J, cells
440 were subcloned in order to isolate clones that properly express GFP-LC3-RFP-LC3ΔG, since
441 homologous recombination can occur between the two LC3 sequences during transfection⁴⁶.

442 All cell lines including urothelial bladder carcinoma cells RT-112 and their CDDP-resistant equivalent
443 cell line (previously described⁹⁸ and kindly provided by Margaretha Skowron, Department of Urology,
444 Medical Faculty, Heinrich Heine University, Düsseldorf, Germany) were cultured in high glucose (4.5
445 g/l) DMEM supplemented with 10% FCS at 37°C in a 5% CO₂ humidified atmosphere. For CDDP-
446 resistance, RT-112 cells were kept at 12 µg/ml CDDP. For amino acid starvation, cells were washed
447 once with PBS and incubated for the indicated times in EBSS.

448

449 *High-throughput autophagy screening*

450 Mouse embryonic fibroblasts stably expressing mCitrine-LC3 were incubated with 10 µM of each natural
451 compound solved in DMSO in serum-containing full medium or starvation medium for 6 h. During
452 screening, compound samples were blinded by labelling with a randomized code and unblinded post-
453 experiments. Cells were harvested by trypsination, washed using PBS and centrifugation at 300 g, and
454 measured via flow cytometry of 10,000 events in the FITC channel of an LSRFortessa (Becton
455 Dickinson, Heidelberg, Germany). Median fluorescence intensities were measured in biological
456 triplicates and normalized to the DMSO control.

457

458 *GFP-LC3-RFP-LC3ΔG assay*

459 HeLa cells stably expressing GFP-LC3-RFP-LC3ΔG were incubated with the indicated concentrations
460 of self-isolated or commercial arzanol solved in DMSO in starvation medium for 6 h. Cells were
461 harvested and analyzed using flow cytometry as described above.

462

463 *Immunoblotting*

464 Cleared cell lysates were prepared and subjected to immunoblotting as described before⁹⁷. Signal
465 intensities of protein bands were quantified using Image Studio lite 4.0 (LI-COR) and each band was
466 normalized to the average protein signal to correct for technical variance. The signals were then
467 normalized to the corresponding loading control (ACTB). Panels for at least three biological replicates
468 were prepared using GraphPad Prism 7.0.

469

470 *Fluorescence microscopy*

471 On the day before treatment, cells were grown on glass cover slips (Marienfeld). After treatment, cells
472 were fixed with 4% formaldehyde-PBS for 30 min on ice, and quenched with 50 mM NH₄Cl for 15 min.

473 For immunofluorescence labelling, cells were then permeabilized with 0.2% Triton X-100-PBS for 15
474 min, or 50 µg/ml digitonin (Roth, #4005) for 5 min according to the antibody manufacturers. Samples
475 were blocked with 3% BSA (Roth, #8076)-PBS for 30 min and incubated with primary antibodies for
476 1-2 h. After washing and 30 min of secondary antibody incubation, samples were again washed three
477 times with PBS. Cells were embedded in ProLong Glass Antifade Mountant (Thermo Fisher Scientific,
478 #P36980) including DAPI. Imaging was performed with a Zeiss Axio Observer 7 fluorescence
479 microscope (Zeiss, Köln, Germany) with a Plan Apochromat 40x/1.4 oil objective (Zeiss, Köln,
480 Germany). Quantification of images was performed with ImageJ. For that, signals and nuclei were
481 counted per image and a signal-to-nuclei ratio was calculated. Macros for the quantifications are
482 provided in supplementary Methods.

483

484 *Cell viability assays*

485 Cell viability was determined using the colorimetric Alamar Blue and MTT assays, which measure the
486 reduction of non-fluorescent dyes to the fluorescent metabolites resorufin and formazan, respectively.
487 For both assays, cells were cultivated in 96 well plates. The following day, the cells were treated with
488 cisplatin and/or arzanol for 24 h. For the MTT assay, MTT (Roth #4022) was added to the cells at 0.5
489 mg/ml concentration and incubated at 37°C for 1 h. Afterwards, the plates were centrifuged at 600 rcf
490 and 4°C for 5 minutes, and cells were lysed in DMSO for 20 min in the dark. Finally, the absorbance
491 was measured at 570 nm and 650 nm for reference, using a microplate reader (BioTek, Synergy Mx).
492 For the Alamar blue assay, 40 µM resazurin sodium salt (Cayman Chemicals, #14322) was added to
493 the cells and incubated at 37°C for 3 h. Afterwards, the absorbance was measured at 590 nm, using a
494 microplate reader (BioTek, Synergy Mx). The mean of the absorbance of untreated control samples was
495 set as 100%.

496

497 *Isolation of Mitochondria*

498 For isolation of mitochondria, wild-type HeLa cells were cultivated on 150 mm diameter tissue culture
499 treated dishes (Sarstedt) and $\sim 3.6 \times 10^8$ cells were harvested the next day via scraping. Cells were
500 pelleted at 500 g for 5 min and washed twice with PBS (Gibco). The pellet was resuspended in 10 ml
501 mitochondria isolation buffer (210 mM mannitol, 70 mM sucrose, 1 mM EDTA, 20 mM HEPES and
502 protease inhibitor cocktail [Sigma-Aldrich, #P2714]) for 5 min on ice before rupturing by seven strokes
503 through a 26 G canule. The cell lysate was then centrifuged at 1000 g and 4°C for 5 min and the

504 supernatant was collected. The remaining pellet of non-lysed cells was resuspended in 2 ml
505 mitochondria isolation buffer and ruptured again before centrifugation, and the two fractions were
506 pooled. The pooled lysate was centrifuged again at 1000 g and 4°C for 5 min and the pellet was
507 discarded. The remaining lysate was centrifuged at 8000 g and 4°C for 10 min. The supernatant
508 (cytosolic fraction) was collected and centrifuged again before transferring into a new tube and freezing
509 in liquid nitrogen. The pellet (mitochondrial fraction) was washed three times at 8000 g for 10 min in 250
510 µl mito isolation buffer. The pellet was finally centrifuged at 10,000 g and 4°C for 10 min. The supernatant
511 was discarded and the pellet containing isolated mitochondria was frozen in liquid nitrogen and stored
512 at -80°C.

513

514 *Preparation of cellular and mitochondrial HeLa lysates*

515 Cellular HeLa lysates were obtained by mechanical lysis in PBS pH 7.4 (137 mM NaCl, 2,7 mM KCl, 10
516 mM Na₂HPO₄, 2 mM KH₂PO₄) containing 0.1% IGEPAL CA-630 and a protease inhibitor cocktail (Sigma
517 Aldrich). Mitochondria were lysed in a buffer composed of 1,5 % digitonin, a protease inhibitor cocktail
518 (Sigma Aldrich), 150 mM NaCl, 10 mM Tris/HCl (pH 7.5) and 5 mM EDTA. After 15 min at 4°C, debris
519 were discarded by centrifugation at 20,000 × g (30 min at 4°C). Protein concentration of the obtained
520 supernatants was determined by Bradford spectrophotometric assay (BioRad Laboratories, Hercules,
521 CA) and adjusted to 3 mg/ml.

522

523 *Affinity purification from lysates and isolated mitochondria*

524 Arzanol bearing resin has been obtained as reported by Del Gaudio *et al*⁹⁹. The arzanol-containing and
525 the control resin were separately incubated with a solution containing 800 µg of proteins, for 1 h under
526 stirring at 4°C. After the incubation period, unspecifically adsorbed proteins were removed performing 3
527 washings with PBS, whereas bound proteins were eluted with 50 µl of 100 mM Tris (pH 6.8), 4% (v/v)
528 sodium dodecyl sulfate (SDS), 0.2% (v/v) Blue Bromophenol, 20% (v/v) glycerol and 2%
529 β-mercaptoethanol buffer. Each resin was then boiled at 95°C for 5 min and 15 µl of the obtained eluates
530 were subjected to 1D-SDS-PAGE (12% polyacrylamide). The resulting gel was then treated with 40%
531 MeOH, 10% CH₃COOH and 50% H₂O and stained by Coomassie Blue.

532

533 *Drug Affinity Responsive Target Stability*

534 300 µg proteins aliquots were either incubated with DMSO (vehicle control) or with arzanol (1 and 10
535 µM final concentrations) for 1 h at room temperature and under agitation. The obtained samples were
536 then treated with the unspecific protease subtilisin (Sigma-Aldrich, #P5380) (enzyme to proteins ratio of
537 1:500 w/w) and left shaking for 30 min at 25°C. Proteolysis was then quenched by adding PMSF
538 (phenylmethylsulfonyl fluoride, Sigma Aldrich, #P7626, 1 mM final concentration) to each sample.
539 Subsequently, all of the samples were prepared for 1D-SDS-PAGE and 20 µg were loaded on a 4-12%
540 Bis-Tris Criterion™ XT Precast Gel (BioRad Laboratories, #3450123), which was then stained with a
541 Coomassie solution. The experiment was carried out in duplicate.

542

543 *In situ gel digestion*

544 Protein bands were excised from the gels and submitted to an *in situ* tryptic digestion protocol¹⁰⁰. Briefly,
545 gel slices were reduced by 6.5 mM 1,4-dithiothreitol (DTT) and alkylated by 54 mM iodoacetamide. A
546 12 ng/µl trypsin/LysC solution (Promega, Madison, Wisconsin) was used to digest proteins. The enzyme
547 excess was then discarded and replaced with ammonium bicarbonate (AmBic, 40 µl, 50 mM, pH 8.5),
548 allowing protein digestion to carry on overnight at 37°C. Subsequently, supernatants were collected and
549 peptides were extracted from each gel slice using 100% CH₃CN. The obtained peptides mixtures were
550 dried *in vacuo* and dissolved in formic acid (FA, 10%) for LC-MS/MS analysis.

551

552 *Liquid chromatography and mass spectrometry analysis (LC-MS/MS)*

553 5 µl of each sample were injected into a nano-ACQUITY UPLC system (Waters, Milford, MA, USA),
554 equipped with a 1.7 µm BEH C18 column (Waters). Peptide elution was achieved with a linear gradient
555 of mobile phase B from 20% to 90% in 65 min (mobile phase A: 95% H₂O, 5% CH₃CN, 0.1% acetic acid;
556 mobile phase B: 95% CH₃CN, 5% H₂O, 0.1% acetic acid) at a flow rate of 280 nl/min. MS and MS/MS
557 data were acquired on an LTQ Orbitrap XL high-performance liquid chromatography MS system
558 (Thermo-Scientific, Waltham, MA, USA), interfaced with a nanoESI source. The ten most intense doubly
559 and triply charged peptide ions were fragmented. MS data were then processed by the MS Converter
560 General User Interface software (ProteoWizard; <http://proteowizard.sourceforge.net/project.html>) and

561 submitted to MASCOT Daemon (version 5.1, Matrix Science, London, UK) for protein identification,
562 employing the SwissProt database (release November 2019, 561344 entries) and the following settings:
563 two missed cleavages; carbamidomethyl (C) as fixed modification; oxidation (M) and phosphorylation
564 (ST) as variable modifications; peptide tolerance 30 ppm; MS/MS tolerance 0.8 Da.

565

566 *Statistics*

567 Sample sizes were chosen with reference to pragmatic considerations and the principle of saturation
568 due to previously published work in this field and preliminary experiments. For high-throughput analysis
569 of the flow cytometric mCitrine-LC3-based autophagy screening we used uniformly minimal variance
570 unbiased estimate (UMVUE) of strictly standardized mean difference (SSMD)³⁶. For the quantifications
571 of the immunoblots shown in Figure 2, statistical analysis was performed using a 2way ANOVA with
572 Dunnett's multiple comparison test comparing treated to untreated control samples. For comparing size
573 and number of dots in Figure 3, statistical analysis was performed using an ordinary 1way ANOVA with
574 Tukey's multiple comparison test comparing all treatments with each other. All IC₅₀ values in Figure 5
575 were calculated using GraphPad Prism 7.01 (function log[inhibitor] vs. response - variable slope [four
576 parameters]). For NQO1 activity data, statistical analysis was performed using a 1way ANOVA with
577 Dunnett's multiple comparison test comparing treated to untreated control samples. Representative data
578 or means of biological replicates are shown for every experiment with error bars that indicate standard
579 error. All statistical analyses were performed using Prism v7.01 (GraphPad Software, La Jolla, CA,
580 USA).

Table 1. List of potential autophagy inducers. Data show mean difference \pm SD (% of control) of mCitrine-LC3 decrease upon full medium monitored by flow cytometry. In total, 8 compounds causing equal to or greater than 15% LC3 degradation at a fairly moderate and higher effect ($|$ SSMD score $| \geq 1$) at 10 μ M after 6 h of treatment were classified as potential inducers of autophagy.

Compound	Mean difference of mCit-LC3 (%)	SD	SSMD
P05E07	-34.4	± 6.0	-3.25
P02E06	-28.8	± 1.3	-12.58
P04C02	-27.4	± 5.6	-2.75
P01F03	-22.0	± 11.2	-1.11
P05C06	-19.9	± 4.6	-2.43
P01G08	-18.1	± 8.1	-1.26
P03F08	-17.7	± 3.3	-3.04
P02B03	-17.3	± 6.0	-1.62

SD: standard deviation; SSMD: strictly standardized mean difference

Table 2. List of potential autophagy inhibitors. Data show mean difference \pm SD (% of control) of mCitricine-LC3 increase upon starvation medium monitored by flow cytometry. In total, 64 compounds causing equal to or greater than 15% LC3 protection at a fairly moderate and higher effect ($|\text{SSMD score}| \geq 1$) at 10 μ M after 6 h of treatment were classified as potential inhibitors of autophagy.

Compound	Mean difference of mCit-LC3 (%)	SD	SSMD
P05D05	+2590.4*	\pm 765.1	1.91
P05C04	+536.3	\pm 294.2	1.03
P02D03	+336.7	\pm 182.2	1.04
P05D10	+335.7	\pm 85.5	2.21
P04C10	+256.2	\pm 45.0	3.21
P01B11	+249.9	\pm 38.4	3.67
P03B08	+243.9	\pm 45.4	3.03
P01F02	+240.8	\pm 49.9	2.72
P03B06	+235.2	\pm 32.0	4.14
P05B05	+234.4*	\pm 44.8	2.95
P01E05	+224.6	\pm 19.1	6.65
P05E10	+221.8	\pm 21.1	5.92
P01C06	+220.6	\pm 37.8	3.29
P01F11	+209.4	\pm 55.6	2.13
P01G06	+174.5	\pm 21.1	4.67
P04E03	+174.3	\pm 30.7	3.21
P02D05	+170.9	\pm 67.0	1.44
P04E04	+166.1	\pm 48.5	1.93
Arzanol	+164.6	\pm 63.9	1.45
P01F08	+159.6	\pm 45.8	1.97
P05B09	+158.8	\pm 53.8	1.67
P01G09	+158.7	\pm 52.9	1.69
P04D02	+158.2	\pm 19.3	4.63
P05B06	+153.1	\pm 69.7	1.24
P05B02	+149.6	\pm 47.0	1.80
P05C03	+149.0	\pm 32.9	2.55
P03F09	+138.3	\pm 37.5	2.08
P02E04	+122.0	\pm 63.9	1.08
P02F04	+105.1	\pm 55.0	1.08
P04G07	+98.3	\pm 29.4	1.88
P02B07	+93.7	\pm 44.5	1.19
P04B04	+93.4	\pm 34.7	1.52
P04B07	+87.2	\pm 39.5	1.24
P04F06	+78.1	\pm 19.0	2.32
P05E07	+67.4	\pm 19.5	1.95
P04B02	+67.1	\pm 15.6	2.43
P04G08	+66.9	\pm 30.5	1.24
P02B02	+60.7	\pm 25.1	1.36
P05F02	+59.4	\pm 12.7	2.64
P03F08	+53.3	\pm 13.2	2.28
P05F03	+46.0	\pm 14.1	1.84
P01C05	+41.8	\pm 16.6	1.42
P04C02	+40.0	\pm 16.0	1.41
P02E08	+38.7	\pm 3.4	6.44
P05E06	+36.9	\pm 15.9	1.31
P04E10	+35.4	\pm 17.2	1.16

*could be caused by autofluorescence; SD: standard deviation; SSMD: strictly standardized mean difference

Continued table 2. List of potential autophagy inhibitors. Data show mean difference \pm SD (% of control) of mCitricine-LC3 increase upon starvation medium monitored by flow cytometry. In total, 64 compounds causing equal to or greater than 15% LC3 protection at a fairly moderate and higher effect ($|\text{SSMD score}| \geq 1$) at 10 μ M after 6 h of treatment were classified as potential inhibitors of autophagy.

Compound	Mean difference of mCit-LC3 (%)	SD	SSMD
P05C06	+34.8	\pm 5.1	3.85
P03E07	+33.6	\pm 17.6	1.08
P05D06	+33.2	\pm 12.4	1.51
P05G05	+33.2	\pm 2.4	7.93
P02D07	+32.1	\pm 17.3	1.05
P05E04	+31.3	\pm 6.8	2.59
P01G02	+29.8	\pm 14.2	1.18
P04C11	+27.6	\pm 5.6	2.76
P01C09	+25.1	\pm 6.8	2.10
P05F04	+23.8	\pm 7.2	1.86
P04B10	+23.1	\pm 8.3	1.57
P05D07	+22.9	\pm 5.5	2.36
P01E03	+22.0	\pm 9.0	1.39
P05E02	+21.1	\pm 4.0	3.01
P04E02	+18.2	\pm 9.2	1.12
P04D04	+17.2	\pm 8.0	1.21
P05B10	+17.2	\pm 7.5	1.30
P03E06	+15.9	\pm 3.5	2.56

SD: standard deviation; SSMD: strictly standardized mean difference

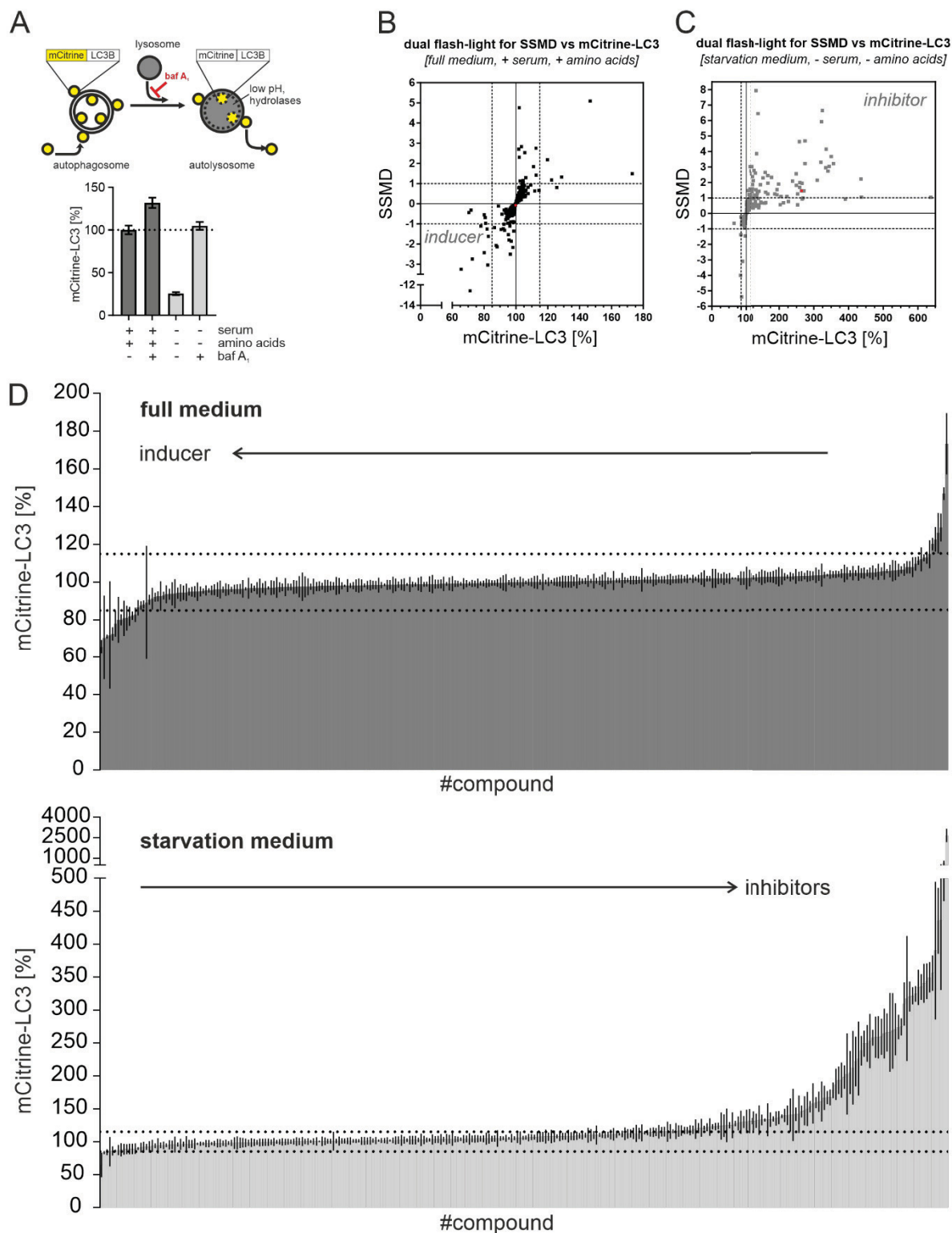


Figure 1: High-throughput screening for natural compound-based autophagy modulators.

(A) Detection of starvation-induced and bafilomycin A₁-inhibited autophagy in a flow cytometric screening. MEF cells stably expressing mCitrine-LC3 were cultured either in full medium plus serum or in starvation medium and were treated with either 10 nM bafilomycin A₁ or mock treatment (DMSO) for

6 h ($n \geq 19$). The mCitrine fluorescence is shown as a percentage relative to that of mock-treated cells. Data represent means \pm SEM. **(B, C)** High-throughput autophagy screening of 300 natural compounds. The diagram shows dual-flashlight plots for strictly standardized mean difference (SSMD) versus average percentage of mCitrine-LC3. Dotted lines define potential inducer and inhibitors of autophagy. Cells were treated with 10 μ M of each compound for 6 h ($n = 3$). Arzanol is highlighted in red. **(D)** The diagram shows individual levels of mCitrine-LC3 fluorescence from (B, C) for each of the 300 compounds in full or starvation medium. Dotted lines mark the $\pm 15\%$ difference in mCitrine-LC3 levels. Data represent means \pm SEM.

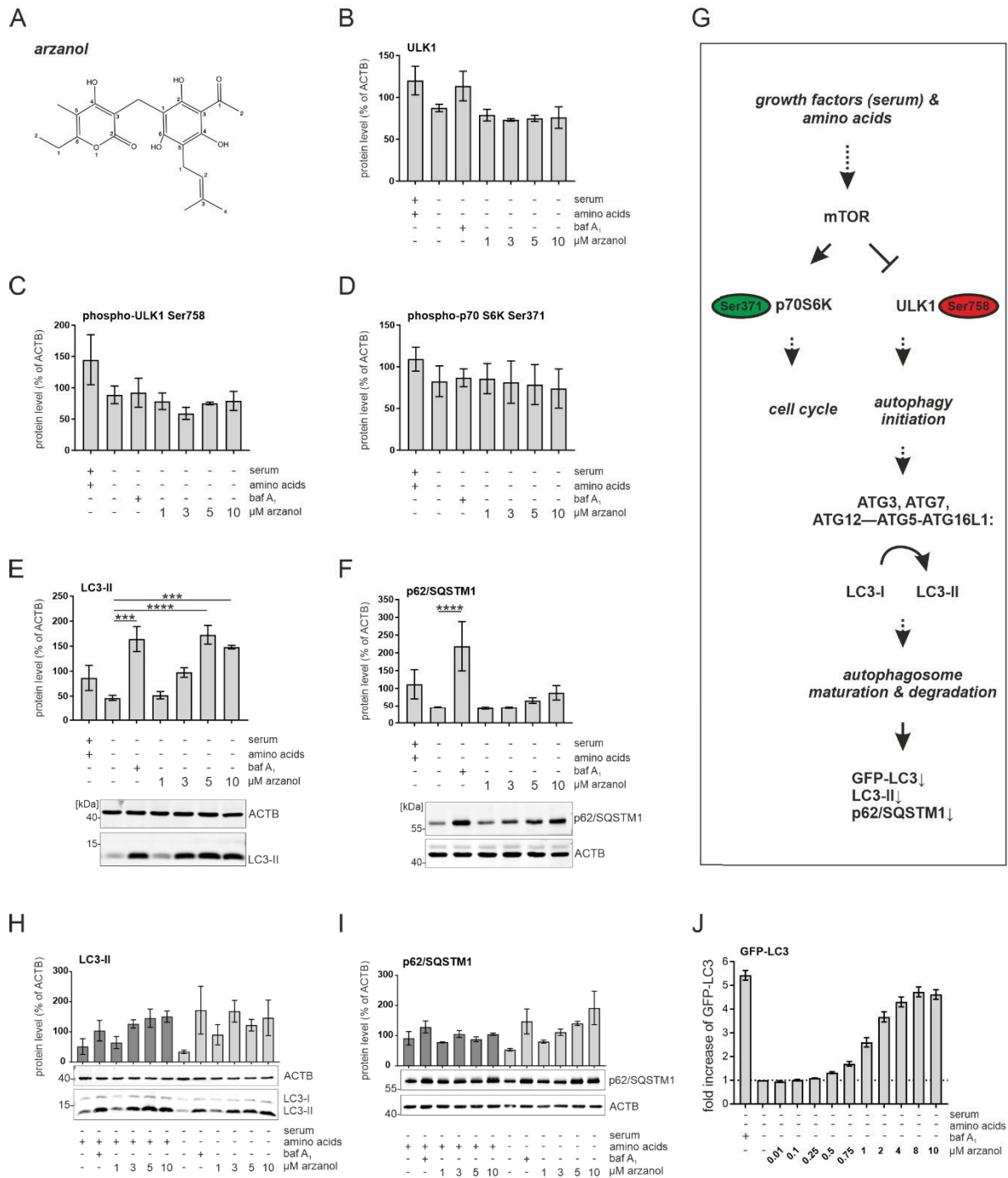


Figure 2: Arzanol drives LC3-II accumulation independent of the AKT/mTOR-pathway.

(A) Structure of arzanol. (B-F) Immunoblot analysis of mTOR/ULK1-pathway proteins during serum- and amino acid-starvation. Wild-type HeLa cells were starved in serum- and amino acid-free medium for 6 h while being incubated with baf A₁ or different concentrations of self-isolated arzanol. Data show quantified means of biological triplicates normalized to ACTB ± SEM. For (E) and (F), representative immunoblots are additionally shown. Statistical analysis was performed using 2way ANOVA with

Dunnett's multiple comparison test comparing treated to untreated samples, *** $p < 0.001$, **** $p < 0.0001$.

(G) Simplified pathway of key proteins of the mTOR/ULK1-axis in starvation-induced autophagy. **(H, I)** Immunoblot analysis of LC3-II and p62/SQSTM1 during serum-starvation. Wild-type HeLa cells were starved in serum-free (dark bars) or serum- and amino acid-free (light bars) medium for 6 h while being incubated with baf A₁ or different concentrations of commercially available arzanol. Data show quantified means of biological triplicates normalized to ACTB \pm SEM. **(J)** HeLa cells stably expressing GFP-LC3-RFP-LC3 Δ G were starved in serum- and amino acid-free medium for 6 h while incubated with different concentrations of commercially available arzanol. Data show fold increase of GFP-LC3 fluorescence relative to mock treated control as means \pm SEM of three biological replicates.

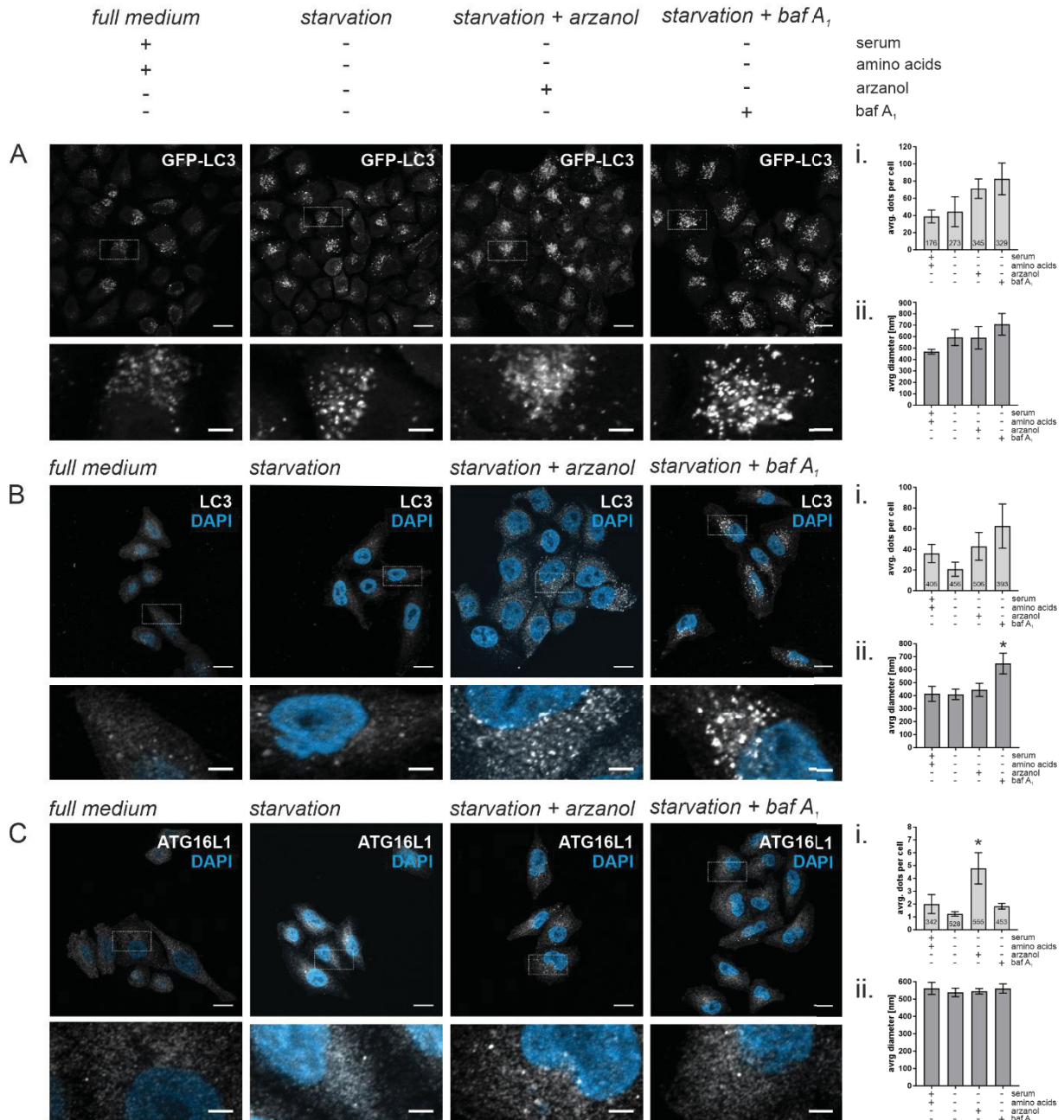


Figure 3: Arzanol interferes with autophagosome biogenesis.

Shown are representative microscopy images of HeLa cells stably expressing GFP-LC3-RFP-LC3ΔG (A), or wild-type HeLa cells immunofluorescently labelled for endogenous LC3 (B) or ATG16L1 (C). All cells were starved in serum- and amino acid-free medium for 2 h while incubated with 3 μM arzanol or 10 nM bafilomycin A₁. Scale bars in upper panels are 15.5 μm, scale bars in magnifications are 3.875 μm. (i.) Data show average number of dots per cell from biological triplicates for GFP-LC3, and n=6 for LC3 and ATG16L1 as mean ± SEM. Digits in bars show total number of cells quantified using ImageJ software. (ii.) Data show average diameter of dots in nm as mean ± SEM. Statistical analysis was performed using ordinary 1way ANOVA with Tukey's multiple comparison test, *p<0.1.

starvation + arzanol

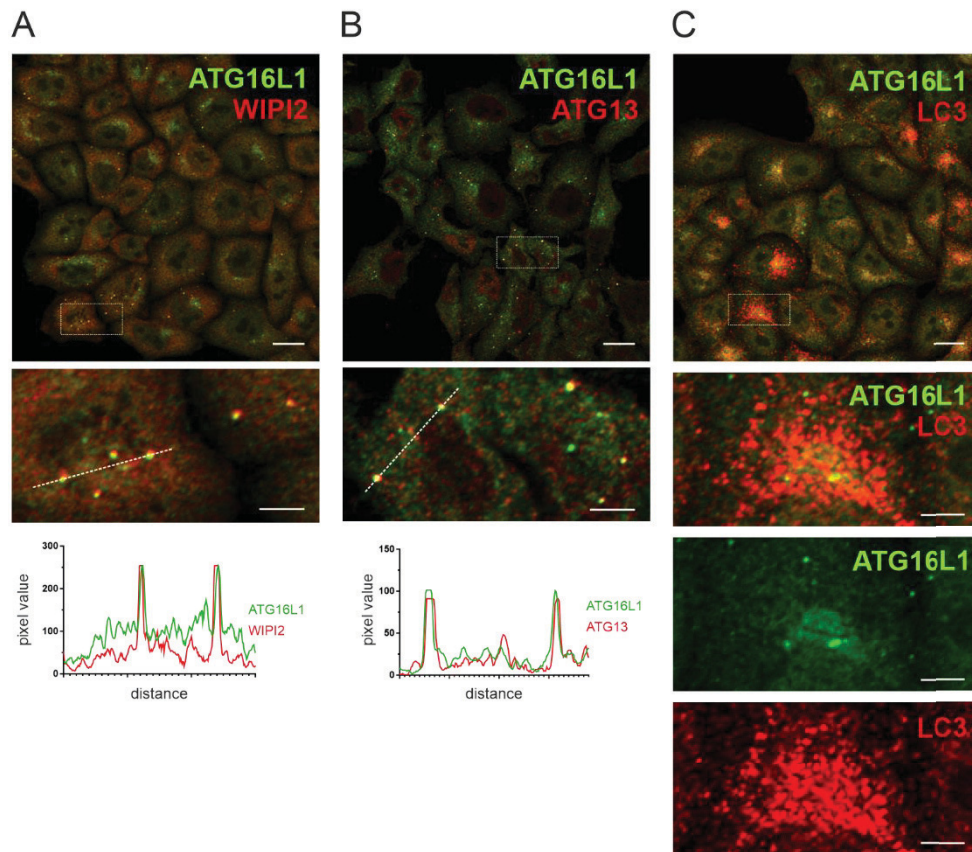
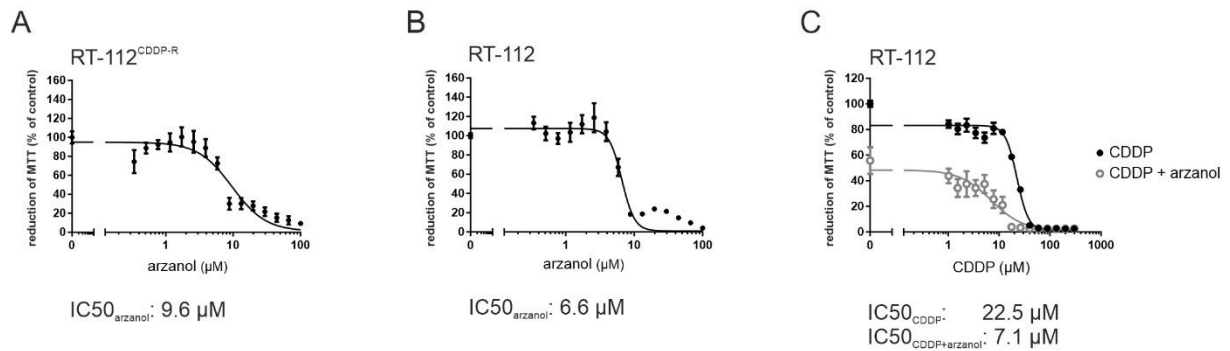


Figure 4: Arzanol-induced ATG16L1 accumulations at perinuclear regions colocalize with ATG13 and WIPI2.

Shown are representative microscopy images of wild-type HeLa cells immunofluorescently labelled for endogenous ATGs. Upon starvation, arzanol-induced ATG16L1 dots colocalize with WIPI2 (**A**) and ATG13 (**B**). These ATG16L1 dots accumulate at perinuclear regions that are also surrounded by LC3 dots (**C**). Cells were starved in serum- and amino acid-free medium for 2 h while incubated with 3 μM arzanol. Scale bars in panels are 15.5 μm, scale bars in magnifications are 3.875 μm. Diagrams show immunofluorescence intensities for the indicated proteins measured using ImageJ software for the cross sections marked as white dotted lines.

with amino acids



without amino acids

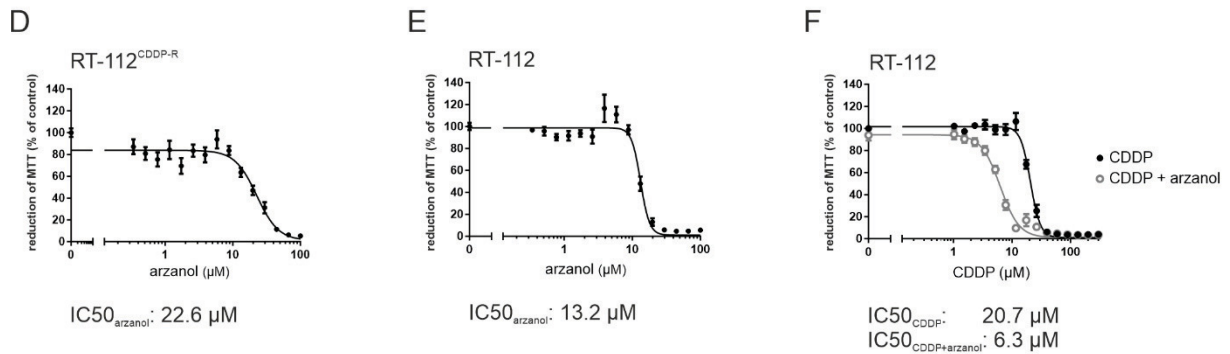


Figure 5: Arzanol is cytotoxic for bladder carcinoma cells in mono- and CDDP-combination therapy.

Arzanol reduces cell viability in bladder cancer cells as determined by the MTT assay. CDDP-resistant (CDDP-R) RT-112 bladder carcinoma cells (**A**) and CDDP-sensitive RT-112 bladder carcinoma cells (**B**) were incubated for 24 h with indicated concentrations of arzanol in serum-free, amino acid-supplied medium. (**C**) CDDP-sensitive RT-112 bladder carcinoma cells were incubated with indicated concentrations of CDDP in mono-therapy or in a combination with 5 μM arzanol in serum-free, amino acid-supplied medium. CDDP-resistant (CDDP-R) RT-112 bladder carcinoma cells (**D**) and CDDP-sensitive RT-112 bladder carcinoma cells (**E**) were incubated for 24 h with indicated concentrations of arzanol in serum- and amino acid-free medium. (**F**) CDDP-sensitive RT-112 bladder carcinoma cells were incubated with indicated concentrations of CDDP in mono-therapy or in a combination with 5 μM arzanol in serum- and amino acid-free medium.

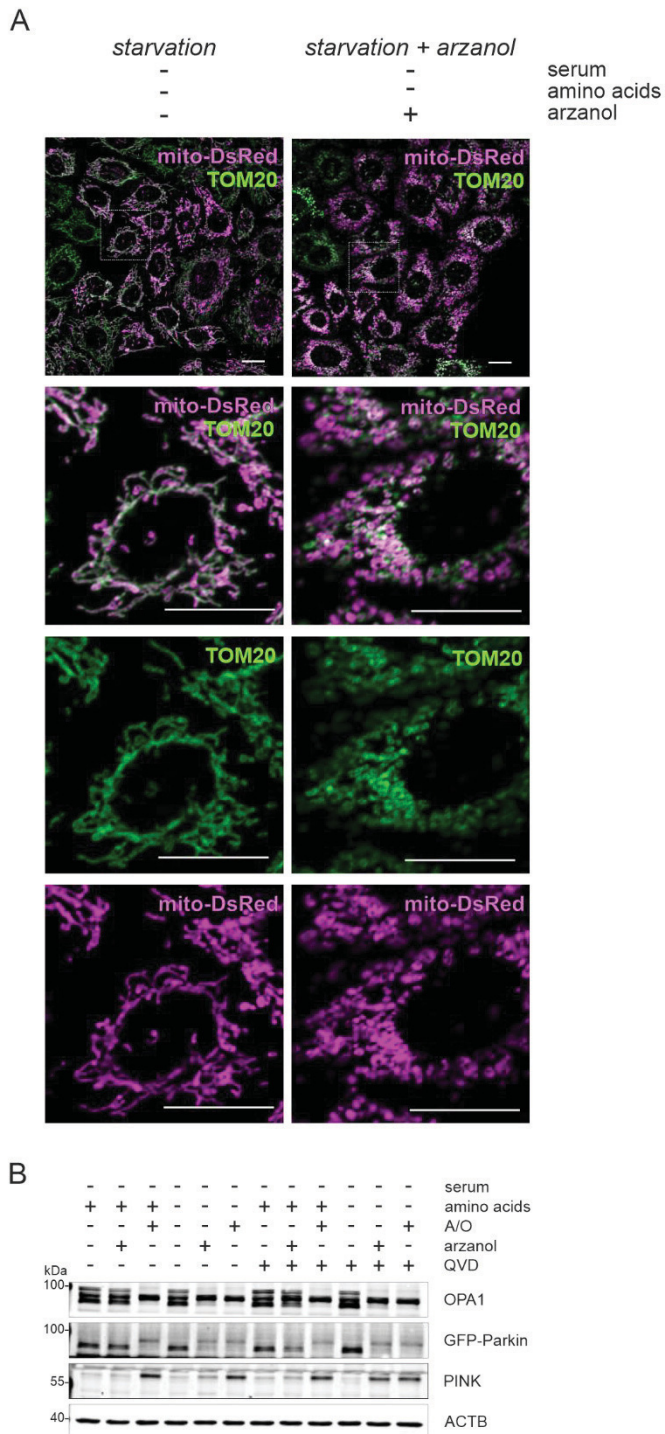


Figure 6: Arzanol causes damage-induced fragmentation of mitochondrial membranes during starvation.

(A) Shown are microscopy images of mito-DsRed-expressing HeLa cells immunofluorescently labelled for endogenous TOM20. During starvation, arzanol induces a fragmentation of both inner (mito-DsRed) and outer (TOM20) mitochondrial membranes. Cells were starved in serum- and amino acid-free medium for 2 h while incubated with 5 μ M arzanol. Scale bars in all panels are 20 μ m. (B) Immunoblot

for markers of mitochondrial damage (OPA1 fragmentation, Parkin ubiquitination, PINK accumulation) reveals that arzanol induced mitochondrial fragmentation independent of apoptosis induction. HeLa cells stably expressing mito-DsRed GFP-Parkin were incubated with serum-free full medium or starvation medium and treated with 5 μ M arzanol or a combination of 4 μ M antimycin and 10 μ M oligomycin (A/O) with/without 10 μ M QVD for 6 h. Shown blots are representative of three independent experiments.

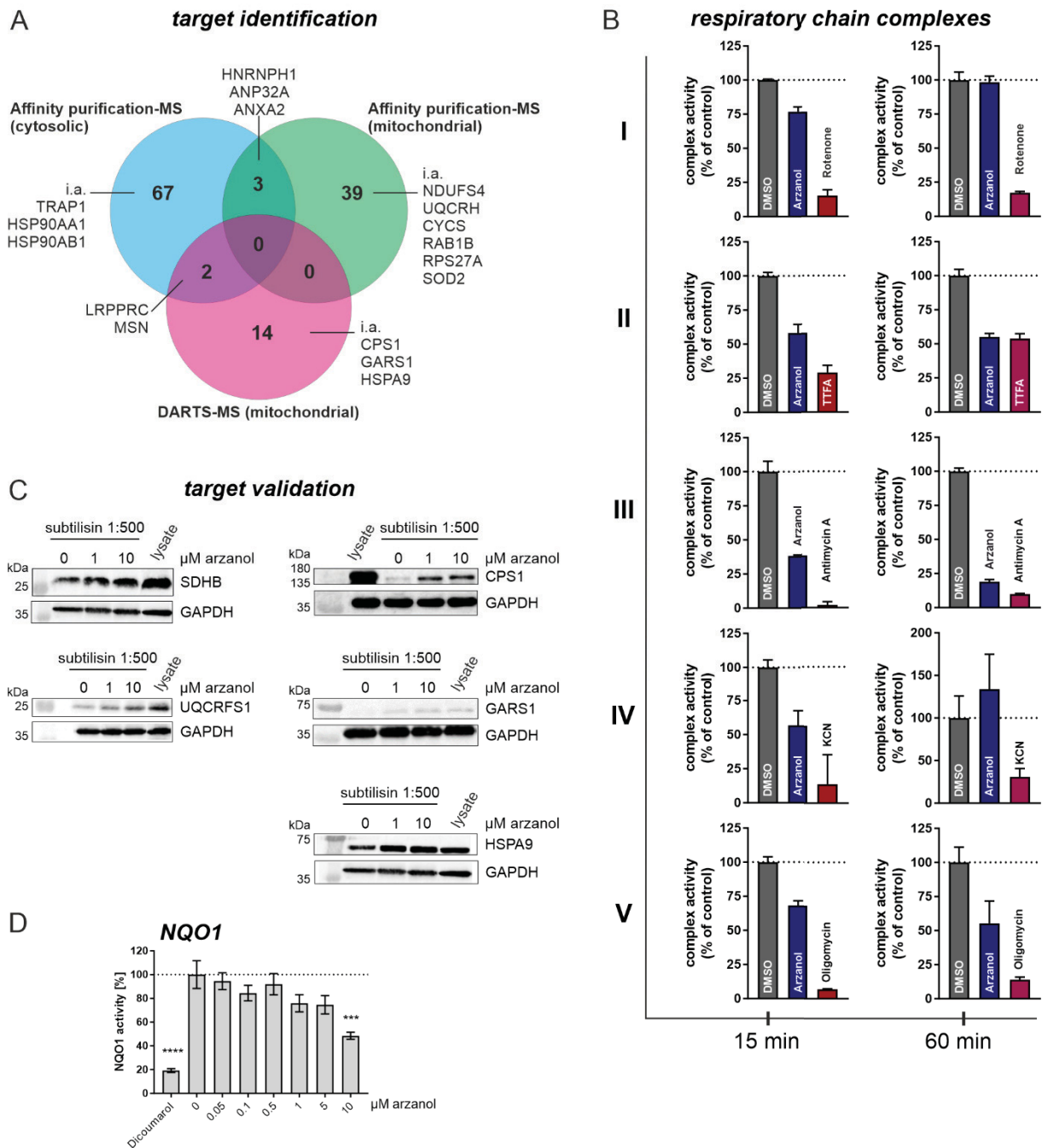


Figure 7: Target identification for arzanol reveals respiratory chain complexes II and III as targets for arzanol.

(A) Mass spectrometry (MS)-based target identification by affinity purification from HeLa cell whole lysates, and affinity purification and DARTS experiments from lysates of isolated mitochondria from HeLa cells reveal 125 novel potential targets of arzanol. (B) Arzanol inhibits mainly respiratory chain complexes II and III in a respiratory chain activity assay of isolated mitochondria after incubation for 15 min and 60 min. Complex activities were measured using the MitoCheck® kits in technical triplicates and normalized to the DMSO control. Bars show mean + SEM. (C) DARTS experiment validates selected

respiratory chain complex proteins of complexes II and III. The lysate from isolated mitochondria from HeLa cells was incubated with 1 or 10 μ M arzanol and then subjected to subtilisin-dependent proteolytic cleavage. Arzanol stabilized SDHB, UQCRC1, CPS1, GARS1 and HSP9A against subtilisin treatment. **(D)** Arzanol reduces the enzyme activity in an NQO1 activity assay similar to the positive control 20 μ M dicoumarol. Lysate from wild-type HeLa cells was subjected according to the manufacturer's manual. Bars show mean \pm SEM of biological quadruplets. Statistical analysis was performed using a 1way ANOVA with Dunnett's multiple comparison test comparing treated to untreated control samples; *** $p < 0.001$, **** $p < 0.0001$.

References

1. Choi H, Cho SY, Pak HJ, Kim Y, Choi JY, Lee YJ, *et al.* NPCARE: database of natural products and fractional extracts for cancer regulation. *Journal of cheminformatics* 2017, **9**: 2.
2. Newman DJ, Cragg GM. Natural Products as Sources of New Drugs from 1981 to 2014. *Journal of natural products* 2016, **79**(3): 629-661.
3. Baker DD, Chu M, Oza U, Rajgarhia V. The value of natural products to future pharmaceutical discovery. *Natural product reports* 2007, **24**(6): 1225-1244.
4. Frake RA, Ricketts T, Menzies FM, Rubinsztein DC. Autophagy and neurodegeneration. *The Journal of clinical investigation* 2015, **125**(1): 65-74.
5. Harris H, Rubinsztein DC. Control of autophagy as a therapy for neurodegenerative disease. *Nature reviews Neurology* 2011, **8**(2): 108-117.
6. Levine B, Kroemer G. Biological Functions of Autophagy Genes: A Disease Perspective. *Cell* 2019, **176**(1-2): 11-42.
7. Mizushima N, Levine B, Cuervo AM, Klionsky DJ. Autophagy fights disease through cellular self-digestion. *Nature* 2008, **451**(7182): 1069-1075.
8. Graef M, Nunnari J. Mitochondria regulate autophagy by conserved signalling pathways. *The EMBO journal* 2011, **30**(11): 2101-2114.
9. Li L, Chen Y, Gibson SB. Starvation-induced autophagy is regulated by mitochondrial reactive oxygen species leading to AMPK activation. *Cellular signalling* 2013, **25**(1): 50-65.
10. Papandreou I, Lim AL, Laderoute K, Denko NC. Hypoxia signals autophagy in tumor cells via AMPK activity, independent of HIF-1, BNIP3, and BNIP3L. *Cell death and differentiation* 2008, **15**(10): 1572-1581.
11. Axe EL, Walker SA, Manifava M, Chandra P, Roderick HL, Habermann A, *et al.* Autophagosome formation from membrane compartments enriched in phosphatidylinositol 3-phosphate and dynamically connected to the endoplasmic reticulum. *The Journal of cell biology* 2008, **182**(4): 685-701.
12. Dudley LJ, Cabodevilla AG, Makar AN, Sztacho M, Michelberger T, Marsh JA, *et al.* Intrinsic lipid binding activity of ATG16L1 supports efficient membrane anchoring and autophagy. *The EMBO journal* 2019, **38**(9).
13. Lee Y, Wehl CC. Regulation of SQSTM1/p62 via UBA domain ubiquitination and its role in disease. *Autophagy* 2017, **13**(9): 1615-1616.
14. Takamura A, Komatsu M, Hara T, Sakamoto A, Kishi C, Waguri S, *et al.* Autophagy-deficient mice develop multiple liver tumors. *Genes & development* 2011, **25**(8): 795-800.
15. Yue Z, Jin S, Yang C, Levine AJ, Heintz N. Beclin 1, an autophagy gene essential for early embryonic development, is a haploinsufficient tumor suppressor. *Proceedings of the National Academy of Sciences of the United States of America* 2003, **100**(25): 15077-15082.
16. Goussetis DJ, Gounaris E, Wu EJ, Vakana E, Sharma B, Bogyo M, *et al.* Autophagic degradation of the BCR-ABL oncoprotein and generation of antileukemic responses by arsenic trioxide. *Blood* 2012, **120**(17): 3555-3562.
17. Isakson P, BJORAS M, Boe SO, Simonsen A. Autophagy contributes to therapy-induced degradation of the PML/RARA oncoprotein. *Blood* 2010, **116**(13): 2324-2331.
18. Larrue C, Saland E, Boutzen H, Vergez F, David M, Joffre C, *et al.* Proteasome inhibitors induce FLT3-ITD degradation through autophagy in AML cells. *Blood* 2016, **127**(7): 882-892.
19. Li P, Ji M, Lu F, Zhang J, Li H, Cui T, *et al.* Degradation of AF1Q by chaperone-mediated autophagy. *Experimental cell research* 2014, **327**(1): 48-56.
20. Degenhardt K, Mathew R, Beaudoin B, Bray K, Anderson D, Chen G, *et al.* Autophagy promotes tumor cell survival and restricts necrosis, inflammation, and tumorigenesis. *Cancer cell* 2006, **10**(1): 51-64.
21. Martinez-Outschoorn UE, Balliet RM, Rivadeneira DB, Chiavarina B, Pavlides S, Wang C, *et al.* Oxidative stress in cancer associated fibroblasts drives tumor-stroma co-evolution: A new

- paradigm for understanding tumor metabolism, the field effect and genomic instability in cancer cells. *Cell cycle (Georgetown, Tex)* 2010, **9**(16): 3256-3276.
22. Mathew R, Karantza-Wadsworth V, White E. Assessing metabolic stress and autophagy status in epithelial tumors. *Methods in enzymology* 2009, **453**: 53-81.
 23. New J, Arnold L, Ananth M, Alvi S, Thornton M, Werner L, *et al.* Secretory Autophagy in Cancer-Associated Fibroblasts Promotes Head and Neck Cancer Progression and Offers a Novel Therapeutic Target. *Cancer research* 2017, **77**(23): 6679-6691.
 24. Rouschop KM, van den Beucken T, Dubois L, Niessen H, Bussink J, Savelkoul K, *et al.* The unfolded protein response protects human tumor cells during hypoxia through regulation of the autophagy genes MAP1LC3B and ATG5. *The Journal of clinical investigation* 2010, **120**(1): 127-141.
 25. Karantza-Wadsworth V, Patel S, Kravchuk O, Chen G, Mathew R, Jin S, *et al.* Autophagy mitigates metabolic stress and genome damage in mammary tumorigenesis. *Genes & development* 2007, **21**(13): 1621-1635.
 26. Lazova R, Camp RL, Klump V, Siddiqui SF, Amaravadi RK, Pawelek JM. Punctate LC3B expression is a common feature of solid tumors and associated with proliferation, metastasis, and poor outcome. *Clinical cancer research : an official journal of the American Association for Cancer Research* 2012, **18**(2): 370-379.
 27. Wiedmer T, Blank A, Pantasis S, Normand L, Bill R, Krebs P, *et al.* Autophagy Inhibition Improves Sunitinib Efficacy in Pancreatic Neuroendocrine Tumors via a Lysosome-dependent Mechanism. *Molecular cancer therapeutics* 2017, **16**(11): 2502-2515.
 28. Cook KL, Warri A, Soto-Pantoja DR, Clarke PA, Cruz MI, Zwart A, *et al.* Hydroxychloroquine inhibits autophagy to potentiate antiestrogen responsiveness in ER+ breast cancer. *Clinical cancer research : an official journal of the American Association for Cancer Research* 2014, **20**(12): 3222-3232.
 29. Degtyarev M, De Maziere A, Orr C, Lin J, Lee BB, Tien JY, *et al.* Akt inhibition promotes autophagy and sensitizes PTEN-null tumors to lysosomotropic agents. *The Journal of cell biology* 2008, **183**(1): 101-116.
 30. Ratikan JA, Sayre JW, Schae D. Chloroquine engages the immune system to eradicate irradiated breast tumors in mice. *International journal of radiation oncology, biology, physics* 2013, **87**(4): 761-768.
 31. Chen JL, David J, Cook-Spaeth D, Casey S, Cohen D, Selvendiran K, *et al.* Autophagy Induction Results in Enhanced Anoikis Resistance in Models of Peritoneal Disease. *Molecular cancer research : MCR* 2017, **15**(1): 26-34.
 32. Cui L, Song Z, Liang B, Jia L, Ma S, Liu X. Radiation induces autophagic cell death via the p53/DRAM signaling pathway in breast cancer cells. *Oncology reports* 2016, **35**(6): 3639-3647.
 33. Kim DE, Kim Y, Cho DH, Jeong SY, Kim SB, Suh N, *et al.* Raloxifene induces autophagy-dependent cell death in breast cancer cells via the activation of AMP-activated protein kinase. *Molecules and cells* 2015, **38**(2): 138-144.
 34. Peng PL, Kuo WH, Tseng HC, Chou FP. Synergistic tumor-killing effect of radiation and berberine combined treatment in lung cancer: the contribution of autophagic cell death. *International journal of radiation oncology, biology, physics* 2008, **70**(2): 529-542.
 35. Yu P, Zhang C, Gao CY, Ma T, Zhang H, Zhou MM, *et al.* Anti-proliferation of triple-negative breast cancer cells with physagulide P: ROS/JNK signaling pathway induces apoptosis and autophagic cell death. *Oncotarget* 2017, **8**(38): 64032-64049.
 36. Zhang XD. Illustration of SSMD, z score, SSMD*, z* score, and t statistic for hit selection in RNAi high-throughput screens. *Journal of biomolecular screening* 2011, **16**(7): 775-785.
 37. Werner J, Ebrahim W, Ozkaya FC, Mandi A, Kurtan T, El-Neketi M, *et al.* Pyrone derivatives from *Helichrysum italicum*. *Fitoterapia* 2019, **133**: 80-84.

38. Appendino G, Ottino M, Marquez N, Bianchi F, Giana A, Ballero M, *et al.* Arzanol, an anti-inflammatory and anti-HIV-1 phloroglucinol alpha-Pyrone from *Helichrysum italicum* ssp. *microphyllum*. *Journal of natural products* 2007, **70**(4): 608-612.
39. Rosa A, Atzeri A, Nieddu M, Appendino G. New insights into the antioxidant activity and cytotoxicity of arzanol and effect of methylation on its biological properties. *Chemistry and physics of lipids* 2017, **205**: 55-64.
40. Inoki K, Li Y, Zhu T, Wu J, Guan KL. TSC2 is phosphorylated and inhibited by Akt and suppresses mTOR signalling. *Nature cell biology* 2002, **4**(9): 648-657.
41. Inoki K, Li Y, Xu T, Guan KL. Rheb GTPase is a direct target of TSC2 GAP activity and regulates mTOR signaling. *Genes & development* 2003, **17**(15): 1829-1834.
42. Saitoh M, Pullen N, Brennan P, Cantrell D, Dennis PB, Thomas G. Regulation of an activated S6 kinase 1 variant reveals a novel mammalian target of rapamycin phosphorylation site. *The Journal of biological chemistry* 2002, **277**(22): 20104-20112.
43. Shang L, Chen S, Du F, Li S, Zhao L, Wang X. Nutrient starvation elicits an acute autophagic response mediated by Ulk1 dephosphorylation and its subsequent dissociation from AMPK. *Proceedings of the National Academy of Sciences of the United States of America* 2011, **108**(12): 4788-4793.
44. Alers S, Löffler AS, Wesselborg S, Stork B. Role of AMPK-mTOR-Ulk1/2 in the regulation of autophagy: cross talk, shortcuts, and feedbacks. *Molecular and cellular biology* 2012, **32**(1): 2-11.
45. Mizushima N, Yoshimori T. How to interpret LC3 immunoblotting. *Autophagy* 2007, **3**(6): 542-545.
46. Kaizuka T, Morishita H, Hama Y, Tsukamoto S, Matsui T, Toyota Y, *et al.* An Autophagic Flux Probe that Releases an Internal Control. *Molecular cell* 2016, **64**(4): 835-849.
47. Klionsky DJ, Abdelmohsen K, Abe A, Abedin MJ, Abeliovich H, Acevedo Arozena A, *et al.* Guidelines for the use and interpretation of assays for monitoring autophagy (3rd edition). *Autophagy* 2016, **12**(1): 1-222.
48. Dooley HC, Razi M, Polson HE, Girardin SE, Wilson MI, Tooze SA. WIPI2 links LC3 conjugation with PI3P, autophagosome formation, and pathogen clearance by recruiting Atg12-5-16L1. *Molecular cell* 2014, **55**(2): 238-252.
49. Polson HE, de Lartigue J, Rigden DJ, Reedijk M, Urbe S, Clague MJ, *et al.* Mammalian Atg18 (WIPI2) localizes to omegasome-anchored phagophores and positively regulates LC3 lipidation. *Autophagy* 2010, **6**(4): 506-522.
50. Wallot-Hieke N, Verma N, Schlütermann D, Berleth N, Deitersen J, Bohler P, *et al.* Systematic analysis of ATG13 domain requirements for autophagy induction. *Autophagy* 2018, **14**(5): 743-763.
51. Quan Y, Lei H, Wahafu W, Liu Y, Ping H, Zhang X. Inhibition of autophagy enhances the anticancer effect of enzalutamide on bladder cancer. *Biomedicine & pharmacotherapy = Biomedecine & pharmacotherapie* 2019, **120**: 109490.
52. Schlütermann D, Skowron MA, Berleth N, Böehler P, Deitersen J, Stuhldreier F, *et al.* Targeting urothelial carcinoma cells by combining cisplatin with a specific inhibitor of the autophagy-inducing class III PtdIns3K complex. *Urologic oncology* 2018, **36**(4): 160.e161-160.e113.
53. White E, DiPaola RS. The double-edged sword of autophagy modulation in cancer. *Clinical cancer research : an official journal of the American Association for Cancer Research* 2009, **15**(17): 5308-5316.
54. Hamid R, Rotshteyn Y, Rabadi L, Parikh R, Bullock P. Comparison of alamar blue and MTT assays for high through-put screening. *Toxicology in vitro : an international journal published in association with BIBRA* 2004, **18**(5): 703-710.
55. Vives-Bauza C, Zhou C, Huang Y, Cui M, de Vries RL, Kim J, *et al.* PINK1-dependent recruitment of Parkin to mitochondria in mitophagy. *Proceedings of the National Academy of Sciences of the United States of America* 2010, **107**(1): 378-383.

56. Tanaka A, Cleland MM, Xu S, Narendra DP, Suen DF, Karbowski M, *et al.* Proteasome and p97 mediate mitophagy and degradation of mitofusins induced by Parkin. *The Journal of cell biology* 2010, **191**(7): 1367-1380.
57. Twig G, Shirihai OS. The interplay between mitochondrial dynamics and mitophagy. *Antioxidants & redox signaling* 2011, **14**(10): 1939-1951.
58. Lomenick B, Olsen RW, Huang J. Identification of direct protein targets of small molecules. *ACS chemical biology* 2011, **6**(1): 34-46.
59. Fujita N, Itoh T, Omori H, Fukuda M, Noda T, Yoshimori T. The Atg16L complex specifies the site of LC3 lipidation for membrane biogenesis in autophagy. *Molecular biology of the cell* 2008, **19**(5): 2092-2100.
60. Itakura E, Mizushima N. Characterization of autophagosome formation site by a hierarchical analysis of mammalian Atg proteins. *Autophagy* 2010, **6**(6): 764-776.
61. Wong YC, Holzbaur EL. Temporal dynamics of PARK2/parkin and OPTN/optineurin recruitment during the mitophagy of damaged mitochondria. *Autophagy* 2015, **11**(2): 422-424.
62. Bansal M, Moharir SC, Sailasree SP, Sirohi K, Sudhakar C, Sarathi DP, *et al.* Optineurin promotes autophagosome formation by recruiting the autophagy-related Atg12-5-16L1 complex to phagophores containing the Wipi2 protein. *The Journal of biological chemistry* 2018, **293**(1): 132-147.
63. Moore AS, Holzbaur EL. Dynamic recruitment and activation of ALS-associated TBK1 with its target optineurin are required for efficient mitophagy. *Proceedings of the National Academy of Sciences of the United States of America* 2016, **113**(24): E3349-3358.
64. Wild P, Farhan H, McEwan DG, Wagner S, Rogov VV, Brady NR, *et al.* Phosphorylation of the autophagy receptor optineurin restricts Salmonella growth. *Science (New York, NY)* 2011, **333**(6039): 228-233.
65. Itakura E, Kishi-Itakura C, Koyama-Honda I, Mizushima N. Structures containing Atg9A and the ULK1 complex independently target depolarized mitochondria at initial stages of Parkin-mediated mitophagy. *Journal of cell science* 2012, **125**(Pt 6): 1488-1499.
66. Heo JM, Ordureau A, Paulo JA, Rinehart J, Harper JW. The PINK1-PARKIN Mitochondrial Ubiquitylation Pathway Drives a Program of OPTN/NDP52 Recruitment and TBK1 Activation to Promote Mitophagy. *Molecular cell* 2015, **60**(1): 7-20.
67. Lazarou M, Sliter DA, Kane LA, Sarraf SA, Wang C, Burman JL, *et al.* The ubiquitin kinase PINK1 recruits autophagy receptors to induce mitophagy. *Nature* 2015, **524**(7565): 309-314.
68. Duvezin-Caubet S, Jagasia R, Wagener J, Hofmann S, Trifunovic A, Hansson A, *et al.* Proteolytic processing of OPA1 links mitochondrial dysfunction to alterations in mitochondrial morphology. *The Journal of biological chemistry* 2006, **281**(49): 37972-37979.
69. Baricault L, Segui B, Guegant L, Olichon A, Valette A, Larminat F, *et al.* OPA1 cleavage depends on decreased mitochondrial ATP level and bivalent metals. *Experimental cell research* 2007, **313**(17): 3800-3808.
70. Guillery O, Malka F, Landes T, Guillou E, Blackstone C, Lombes A, *et al.* Metalloprotease-mediated OPA1 processing is modulated by the mitochondrial membrane potential. *Biology of the cell* 2008, **100**(5): 315-325.
71. Ishihara N, Fujita Y, Oka T, Mihara K. Regulation of mitochondrial morphology through proteolytic cleavage of OPA1. *The EMBO journal* 2006, **25**(13): 2966-2977.
72. Benit P, Lebon S, Rustin P. Respiratory-chain diseases related to complex III deficiency. *Biochimica et biophysica acta* 2009, **1793**(1): 181-185.
73. Byun HO, Kim HY, Lim JJ, Seo YH, Yoon G. Mitochondrial dysfunction by complex II inhibition delays overall cell cycle progression via reactive oxygen species production. *Journal of cellular biochemistry* 2008, **104**(5): 1747-1759.
74. Kwon J, Han E, Bui CB, Shin W, Lee J, Lee S, *et al.* Assurance of mitochondrial integrity and mammalian longevity by the p62-Keap1-Nrf2-Nqo1 cascade. *EMBO reports* 2012, **13**(2): 150-156.

75. Li Y, Huang TT, Carlson EJ, Melov S, Ursell PC, Olson JL, *et al.* Dilated cardiomyopathy and neonatal lethality in mutant mice lacking manganese superoxide dismutase. *Nature genetics* 1995, **11**(4): 376-381.
76. Voets AM, Huigsloot M, Lindsey PJ, Leenders AM, Koopman WJ, Willems PH, *et al.* Transcriptional changes in OXPHOS complex I deficiency are related to anti-oxidant pathways and could explain the disturbed calcium homeostasis. *Biochimica et biophysica acta* 2012, **1822**(7): 1161-1168.
77. Yoshida S, Tsutsumi S, Muhlebach G, Sourbier C, Lee MJ, Lee S, *et al.* Molecular chaperone TRAP1 regulates a metabolic switch between mitochondrial respiration and aerobic glycolysis. *Proceedings of the National Academy of Sciences of the United States of America* 2013, **110**(17): E1604-1612.
78. Zhang L, Karsten P, Hamm S, Pogson JH, Muller-Rischart AK, Exner N, *et al.* TRAP1 rescues PINK1 loss-of-function phenotypes. *Human molecular genetics* 2013, **22**(14): 2829-2841.
79. Mochizuki Y, Ohashi R, Kawamura T, Iwanari H, Kodama T, Naito M, *et al.* Phosphatidylinositol 3-phosphatase myotubularin-related protein 6 (MTMR6) is regulated by small GTPase Rab1B in the early secretory and autophagic pathways. *The Journal of biological chemistry* 2013, **288**(2): 1009-1021.
80. Ao X, Zou L, Wu Y. Regulation of autophagy by the Rab GTPase network. *Cell death and differentiation* 2014, **21**(3): 348-358.
81. Kakuta S, Yamaguchi J, Suzuki C, Sasaki M, Kazuno S, Uchiyama Y. Small GTPase Rab1B is associated with ATG9A vesicles and regulates autophagosome formation. *FASEB journal : official publication of the Federation of American Societies for Experimental Biology* 2017, **31**(9): 3757-3773.
82. Zoppino FC, Militello RD, Slavin I, Alvarez C, Colombo MI. Autophagosome formation depends on the small GTPase Rab1 and functional ER exit sites. *Traffic (Copenhagen, Denmark)* 2010, **11**(9): 1246-1261.
83. Winslow AR, Chen CW, Corrochano S, Acevedo-Arozena A, Gordon DE, Peden AA, *et al.* alpha-Synuclein impairs macroautophagy: implications for Parkinson's disease. *The Journal of cell biology* 2010, **190**(6): 1023-1037.
84. Wang B, Chen Z, Yu F, Chen Q, Tian Y, Ma S, *et al.* Hsp90 regulates autophagy and plays a role in cancer therapy. *Tumour biology : the journal of the International Society for Oncodevelopmental Biology and Medicine* 2016, **37**(1): 1-6.
85. Bandyopadhyay U, Kaushik S, Varticovski L, Cuervo AM. The chaperone-mediated autophagy receptor organizes in dynamic protein complexes at the lysosomal membrane. *Molecular and cellular biology* 2008, **28**(18): 5747-5763.
86. Eskelinen EL, Illert AL, Tanaka Y, Schwarzmann G, Blanz J, Von Figura K, *et al.* Role of LAMP-2 in lysosome biogenesis and autophagy. *Molecular biology of the cell* 2002, **13**(9): 3355-3368.
87. Huynh KK, Eskelinen EL, Scott CC, Malevanets A, Saftig P, Grinstein S. LAMP proteins are required for fusion of lysosomes with phagosomes. *The EMBO journal* 2007, **26**(2): 313-324.
88. Tanida I, Minematsu-Ikeguchi N, Ueno T, Kominami E. Lysosomal turnover, but not a cellular level, of endogenous LC3 is a marker for autophagy. *Autophagy* 2005, **1**(2): 84-91.
89. Zhang X, Garbett K, Veeraraghavalu K, Wilburn B, Gilmore R, Mirnics K, *et al.* A role for presenilins in autophagy revisited: normal acidification of lysosomes in cells lacking PSEN1 and PSEN2. *The Journal of neuroscience : the official journal of the Society for Neuroscience* 2012, **32**(25): 8633-8648.
90. Alfred Witjes J, Leuret T, Comperat EM, Cowan NC, De Santis M, Bruins HM, *et al.* Updated 2016 EAU Guidelines on Muscle-invasive and Metastatic Bladder Cancer. *European urology* 2017, **71**(3): 462-475.
91. Abdel Karim NF, Ahmad I, Gaber O, Eldessouki I, Olowokure OO, Farooq M, *et al.* Phase I trial of chloroquine (CQ)/hydroxychloroquine (HCQ) in combination with carboplatin-gemcitabine (CG) in patients with advanced solid tumors. *American Society of Clinical Oncology*; 2019.

92. Qin L, Xu T, Xia L, Wang X, Zhang X, Zhang X, *et al.* Chloroquine enhances the efficacy of cisplatin by suppressing autophagy in human adrenocortical carcinoma treatment. *Drug design, development and therapy* 2016, **10**: 1035-1045.
93. Yu L, Gu C, Zhong D, Shi L, Kong Y, Zhou Z, *et al.* Induction of autophagy counteracts the anticancer effect of cisplatin in human esophageal cancer cells with acquired drug resistance. *Cancer letters* 2014, **355**(1): 34-45.
94. Zhang HQ, Fang N, Liu XM, Xiong SP, Liao YQ, Jin WJ, *et al.* Antitumor activity of chloroquine in combination with Cisplatin in human gastric cancer xenografts. *Asian Pacific journal of cancer prevention : APJCP* 2015, **16**(9): 3907-3912.
95. Zhao XG, Sun RJ, Yang XY, Liu DY, Lei DP, Jin T, *et al.* Chloroquine-enhanced efficacy of cisplatin in the treatment of hypopharyngeal carcinoma in xenograft mice. *PloS one* 2015, **10**(4): e0126147.
96. Barrera M, Koob S, Dikov D, Vogel F, Reichert AS. OPA1 functionally interacts with MIC60 but is dispensable for crista junction formation. *FEBS Lett* 2016, **590**(19): 3309-3322.
97. Hieke N, Löffler AS, Kaizuka T, Berleth N, Bohler P, Driessen S, *et al.* Expression of a ULK1/2 binding-deficient ATG13 variant can partially restore autophagic activity in ATG13-deficient cells. *Autophagy* 2015, **11**(9): 1471-1483.
98. Skowron MA, Petzsch P, Hardt K, Wagner N, Beier M, Stepanow S, *et al.* Distinctive mutational spectrum and karyotype disruption in long-term cisplatin-treated urothelial carcinoma cell lines. *Sci Rep* 2019, **9**(1): 14476.
99. Del Gaudio F, Pollastro F, Mozzicafreddo M, Riccio R, Minassi A, Monti MC. Chemoproteomic fishing identifies arsanol as a positive modulator of brain glycogen phosphorylase. *Chemical communications (Cambridge, England)* 2018, **54**(91): 12863-12866.
100. Shevchenko A, Tomas H, Havlis J, Olsen JV, Mann M. In-gel digestion for mass spectrometric characterization of proteins and proteomes. *Nature protocols* 2006, **1**(6): 2856-2860.

Publication 13

Manuscript “Cancer-specific pro-apoptotic effects of the mycotoxin viriditoxin”:

Stuhldreier E, Lenz T, Jäger P, Schmitt L, Liu Y, Geyh S, Berleth N, Berning L, Deitersen J, Hinxlage I, Schlütermann D, Sun Y, Wu W, Haas R, Stühler K, Proksch P, Stork B, Wesselborg S

Manuscript in preparation

1 **Cancer-specific pro-apoptotic effects of the mycotoxin viriditoxin**

2 Fabian Stuhldreier¹, Thomas Lenz², Laura Schmitt¹, Paul Jäger³, Laura Schmitt¹, Yang Liu⁴, Stefanie
3 Geyh³, Niklas Berleth¹, Lena Berning¹, Jana Deitersen¹, Ilka Hinxlage¹, Maria Jose Mendiburo¹, David
4 Schlütermann¹, Yadong Sun¹, Wenxian Wu¹, Rainer Haas³, Kai Stühler², Peter Proksch⁴, Björn Stork¹,
5 Sebastian Wesselborg¹

6
7 ¹ Institute for Molecular Medicine I, Medical Faculty, Heinrich Heine University, Universitätsstraße 1,
8 40225 Düsseldorf, Germany

9 ² Proteomics Laboratory (BMFZ), Medical Faculty, Heinrich Heine University, Universitätsstraße 1,
10 40225 Düsseldorf, Germany

11 ³ Department of Hematology, Oncology and Clinical Immunology, University Hospital Düsseldorf,
12 Moorenstraße 1, 40225 Düsseldorf, Germany

13 ⁴ Institute of Pharmaceutical Biology and Biotechnology, Faculty of Mathematics and Natural Sciences,
14 Heinrich Heine University, Universitätsstraße 1, 40225 Düsseldorf, Germany

15

16

17 *Correspondence: sebastian.wesselborg@hhu.de

18

19

20 **RUNNING TITLE:** Cancer-specific pro-apoptotic effects of the mycotoxin viriditoxin

21 **KEYWORDS:** viriditoxin, apoptosis, natural products, mitochondria

22 **Abstract**

23 Despite the great efforts in cancer research in recent decades, cancer remains one of the dominant
24 causes of death, so that new drugs are urgently needed. Here we identified the mycotoxin viriditoxin
25 (VDT), derived from the endophytic fungus *Cladosporium cladosporioides* as a promising candidate for
26 a novel cancer therapeutic. VDT acted highly cytotoxic in leukemia and lymphoma cells, which was
27 evidenced by IC₅₀ values in the nanomolar range and by the cells being irreversibly primed to death by
28 even a short exposure to the natural product. We could show that VDT displays a strong apoptotic
29 potential with rapid onset, which is reflected by activation of caspase-3 within 2-4 h followed by cleavage
30 of PARP and apoptotic degradation of DNA. Most interestingly, the cytotoxicity of VDT in hematopoietic
31 stem and progenitor cells derived from healthy donors was found to be drastically reduced. Moreover,
32 the colony-forming capacity of these cells was affected only at very high concentrations of VDT, which
33 correspond to a multiple of the determined IC₅₀ values in leukemia and lymphoma cells. The specificity
34 of the substance thus verified suggests a therapeutic window that can be utilized in cancer treatment.
35 Surprisingly, we were able to show that the demonstrated effect of VDT on leukemia and lymphoma
36 cells was independent of tubulin inhibition as a mechanism previously described for VDT and was rather
37 related to a multifaceted intervention of mitochondrial functionality. The mitochondrial toxicity of VDT
38 was manifested by breakdown of the mitochondrial membrane potential ($\Delta\Psi_m$), impairment of cellular
39 respiration most likely by inhibition of complex I of the electron transport chain and processing of the
40 dynamin-like GTPase OPA1 with subsequent fragmentation of the mitochondria. In summary, our results
41 encourage the initiation of follow-up studies that could further specify the benefit of VDT in cancer
42 therapy.

43 Introduction

44 In a world in which life expectancy has been rising globally for centuries, the incidence of cancer, which
45 is usually strongly age-associated, has also increased sharply as a “quintessential product of modernity”
46 (Siddhartha Mukherjee).¹ Although the great financial and technical efforts in the field of cancer research
47 have prevented a similar increase in cancer-related mortality, cancer today is the second most frequent
48 cause of death.² Since cancer patients frequently suffer from limited treatment efficacy and serious side
49 effects³, there is a great need for new potent and low side-effect agents for anticancer therapy. The
50 majority of newly approved drugs are based directly on natural substances or derived structures, due to
51 their multifaceted positive properties for drug development.⁴ Natural products offer an enormous degree
52 of structural diversity including highly complex carbon scaffolds and often show more advantageous
53 pharmacodynamic and pharmacokinetic properties than synthesized substances due to their formation
54 and evolution in biological systems.⁵ Since the deregulation of apoptosis as a form of programmed cell
55 death is a hallmark of cancer,⁶ and bioactive natural products often intervene in cell fate-regulating
56 pathways, it is not surprising that for a large number of natural products an antitumorigenic effect by
57 inducing apoptosis has been described.⁷⁻⁹

58 In general, cells undergoing apoptotic cell death are characterized by specific morphological and
59 biochemical changes, including cell shrinkage, plasma membrane blebbing and nuclear fragmentation.
60 A distinction is made between different apoptosis pathways, the two main ones being intrinsic and
61 extrinsic apoptosis. While intrinsic apoptosis is triggered by cellular stress stimuli and originates in the
62 mitochondria, extrinsic apoptosis is initiated by extracellular signals through the activation of
63 transmembrane receptors called death receptors.^{10,11} Both pathways are characterized by activation of
64 *cysteine-aspartic proteases* (caspases), which are divided into initiator and effector caspases. Activation
65 of caspase-3 as the most prominent effector caspase by the initiator caspases leads to proteolytic
66 processing of several downstream substrates, finally leading to the apoptotic phenotype. For instance,
67 caspase-3 inactivates *poly [ADP-ribose] polymerase 1* (PARP1) by proteolytic cleavage and activates
68 *caspase-activated DNase* (CAD) by cleaving the corresponding inhibitor of caspase-activated DNase
69 (ICAD), resulting in degradation of chromosomal DNA.^{12,13}

70 Natural products primarily trigger the intrinsic pathway of apoptosis, presumably because formation of
71 secondary metabolites targeting mitochondria can efficiently protect organisms from microbial
72 infestation. Impairment of mitochondrial functionality is toxic to almost all eukaryotic cells, since
73 mitochondria are central to a variety of major cellular processes. Besides the initiation of intrinsic

74 apoptosis, their most important functionality is the production of ATP as the primary cellular energy
75 carrier. The four complexes of the electron transport chain (ETC) embedded in the inner mitochondrial
76 membrane generate a membrane potential ($\Delta\Psi_m$) by pumping protons from the mitochondrial matrix
77 into the mitochondrial intermembrane space under the consumption of oxygen. The resulting proton
78 gradient then serves as a drive for the ATP synthase and thus for the production of ATP via oxidative
79 phosphorylation (OXPHOS).^{14,15} Since OXPHOS is therefore fundamentally dependent on $\Delta\Psi_m$,
80 mitochondrial depolarization severely impairs energy metabolism, making it necessary to ensure the
81 timely removal of depolarized mitochondria. For the purpose of quality control and to ensure
82 homogeneous distribution of the generated ATP, the mitochondria form a highly dynamic network that
83 is permanently subject to balanced fusion and fission processes. Depolarized or otherwise damaged
84 mitochondria are first separated from the network by enhanced fission and then recycled by
85 mitophagy.¹⁶⁻¹⁸

86 Furthermore, mitochondria carry mitoribosomes, specialized ribosomes that are responsible for the
87 translation of 13 proteins, all of which are components of the OXPHOS complexes. Components of the
88 mitoribosomes are apparently also involved in the regulation of apoptotic cell death.¹⁹

89 The natural product viriditoxin (VDT), characterized by its 6,6'-binaphthopyranone structure, has been
90 isolated from different fungal species including *Paecilomyces variotii*, *Cladosporium cladosporioides* and
91 *Aspergillus fumigatus*, which can infect organisms as diverse as jellyfishes (*Nemopilema nomurai*) or
92 flowering plants (*Lawsonia alba*).²⁰⁻²² Care should be taken not to mix the mycotoxin with the
93 hemorrhagic poison of the prairie rattlesnake (*Crotalus viridis viridis*), also referred to as viriditoxin. VDT
94 exhibits broad-spectrum antibacterial activity against Gram-positive bacteria via inhibition of the
95 bacterial protein FtsZ, which is a close structural homologue of eukaryotic tubulin and is involved in
96 bacterial cell division.^{23,24} Moreover, Kundu et al. reported, that VDT induces apoptosis, mitotic
97 catastrophe, G₂/M phase cell cycle arrest and autophagic cell death in human prostate cancer cells.²⁰

98 The aim of this study was to identify natural compounds that potently induce apoptosis in cancer cells
99 and thus represent promising lead compounds for anticancer therapy. After characterizing the mycotoxin
100 viriditoxin as a strong, rapid and selective inducer of apoptosis in human leukemia and lymphoma cells,
101 we have further investigated the underlying biochemical processes in order to provide a basis for future
102 *in vivo* studies. We were able to classify VDT as a mitochondrial toxin, which causes collapse of the
103 mitochondrial membrane potential, inhibition of the ETC and mitochondrial fragmentation.

104 **Materials and Methods**

105 **Cell lines and cell culture**

106 HCT116 (#ACC-581), HeLa (#-57), HT-29 (#ACC-299), Jurkat (#ACC-282), MCF7(#ACC-115), RT-112
107 (#ACC-418) and SH-SY5Y (#ACC-209) cells were obtained from DSMZ, 143B cells from ATCC (#CRL-
108 8303). Ramos cells were kindly provided by Michael Engelke (Institute of Cellular and Molecular
109 Immunology, University Hospital Göttingen, Göttingen, Germany). HeLa cells stably expressing mito-
110 DsRed were kindly provided by Aviva M. Tolkovsky (Department of Clinical Neurosciences, University
111 of Cambridge, England, UK) and have been described previously.²⁵ Jurkat cells and Ramos cells were
112 cultivated in RPMI 1640 medium supplemented with 10% FCS, 100 U/ml penicillin, and 100 µg/ml
113 streptomycin at 37 °C and 5% CO₂ in a humidity-saturated atmosphere. HCT116, HT-29, MCF7, 143B
114 and RT-112 cells were cultivated under the same conditions but in high-glucose Dulbecco's Modified
115 Eagle's medium (DMEM) instead of RPMI 1640. Peripheral blood mononuclear cells (PBMC) were
116 obtained from the blood of healthy donors by apheresis and subsequent density gradient centrifugation.
117 Remaining erythrocytes were removed by a washing step in lysis buffer containing 0.83% ammonium
118 chloride. Hematopoietic stem and progenitor cells (HSPC) were then separated by magnetic cell
119 separation (MACS) using an antibody against the stem cell marker CD34.²⁶ The cells were subsequently
120 cultivated under the same conditions as described for Ramos and Jurkat cells, but with an additional
121 supplementation of cytokines (interleukin 3 [IL-3], interleukin 6 [IL-6], stem cell factor [SCF], Flt3-ligand,
122 10 ng/ml each, all purchased from PreproTech GmbH, Hamburg, Germany). The study of PBMCs and
123 HSPCs was approved by the local ethical review committee (study number: 5944R; registration ID:
124 2017044215), and all patients gave written informed consent.

125 **Extraction and isolation of VDT**

126 VDT was isolated as described before.²¹ Briefly, the fungus *Cladosporium cladosporioides* was isolated
127 from the sediment of a hypersaline lake in Egypt and cultivated on solid rice medium. After 35 d the
128 fungal culture was extracted with EtOAc. Subsequently, VDT was purified from the crude extract via
129 liquid-liquid partitioning, vacuum liquid chromatography, column chromatography and reversed-phase
130 HPLC. In order to exclude any unwanted metabolization or isomerization we prepared VDT in small,
131 lyophilized aliquots and dissolved it in DMSO immediately before usage.

132 **Reagents**

133 Antimycin A (#A8674), carbonyl cyanide m-chlorophenyl hydrazone (CCCP, #C2759), paclitaxel (TXL,
134 #T7402), potassium cyanide (# 60178), rotenone (#45656), sodium azide (NaN₃, #S200),
135 thenoyltrifluoroacetone (TTFA, #88300) and vinblastine (VBL, #V1377) were purchased from Sigma
136 (Munich, Germany), N-(2-Quinolyl)valyl-aspartyl-(2,6-difluorophenoxy)methyl ketone (QVD, #S7311)
137 from Sellekchem (Houston, TX, USA), oligomycin A (#O532970) from Toronto Research Chemicals
138 (Toronto, Canada) and staurosporine (STS, #9300) from LC Laboratories (Woburn, MA, USA). All other
139 substances for which a manufacturer is not explicitly named were obtained from Carl Roth.

140 **Replicates and statistical analysis**

141 Experiments were replicated at least three times, and representative data are shown. Error bars indicate
142 standard deviation. All statistical analysis was performed using Prism v7.01 (GraphPad Software, La
143 Jolla, CA, USA).

144 **Cytotoxicity measurements**

145 For the measurement of cytotoxicity in Ramos and Jurkat cells resazurin reduction assay (also known
146 as alamarBlue® assay) was performed as previously described.²⁷ In short, cells were seeded at a certain
147 density depending on the intended incubation time (0.5 x 10⁶ cells/ml for 8 or 24 h, 0.1 x 10⁶ cells/ml for
148 72 h), treated with ascending substance concentrations and after the specified incubation time, resazurin
149 (Sigma, #R7017) was added to a final concentration of 40 µM. After 90 min of incubation the fluorescence
150 of resorufin (excitation: 535 nm, emission: 590 nm) was measured with a microplate spectrophotometer.
151 Since the reduction of resazurin to resorufin is proportional to aerobic respiration it serves as a measure
152 of cell viability. For technical reasons, the MTT assay was used for the determination of cytotoxicity in
153 solid tumor cell lines and HSPC, after an initial comparative check showed that both assays represent
154 the cytotoxicity of VDT equivalently. The assay was performed as previously described.⁹ In principle,
155 the procedure is similar to that already described for the AlamarBlue assay. However, the cell densities
156 were adjusted (0.1 x 10⁶ cells/ml for solid cancer cell lines, 4 x 10⁵ cells/ml for HSPC) and the cells were
157 loaded with 1 mg/ml 3-(4,5-dimethylthiazol-2-yl)-2,5-diphenyltetrazolium bromide (MTT, Sigma, #M2128)
158 instead of resazurin for 60 min after treatment with the test substance. Subsequently, the formazan
159 crystals formed were solubilized with DMSO and absorbance was measured (test wavelength 570 nm,
160 reference wavelength 650 nm). For both assays, the viability of cells treated with DMSO (0.1% v/v) was

161 set to 100% and the dose-response curves were then fitted with Prism v7.01 (GraphPad Software, La
162 Jolla, CA, USA).

163 **Fluorometric caspase-3 activity assay**

164 The caspase-3 activity assay was performed as described in detail before.⁹ Briefly, Ramos or Jurkat
165 cells were seeded at a density of 1×10^6 cells/ml, treated with the test substances for the specified time
166 and then lysed on ice in lysis buffer containing leupeptin, aprotinin and pepstatin. A reaction buffer
167 containing the profluorescent caspase substrate Ac-DEVD-AMC (Biomol GmbH, Hamburg, Germany,
168 #ABD-13402) was subsequently added with a multistepper and the increase in DEVDase-dependent
169 fluorescence was measured by a Synergy Mx microplate reader at 37°C for at least 60 min (Ex 360 nm,
170 Em 450 nm). The slope of the linear range of fluorescence increase was regarded as correlated with
171 caspase-3 activity. To correct for differences in endogenous caspase activity between the independent
172 experiments, all values were normalized in a two-step process. In the first step, all values were divided
173 by the mean of all values measured at the respective time point. In the second step, this value was then
174 divided by the mean of the solvent controls of all independent experiments at the respective time point.

175 **Immunoblotting**

176 Ramos or Jurkat cells were treated as specified and then harvested by centrifugation (1000 g, 5 min)
177 and quick-frozen in liquid nitrogen. The cell pellets were thawed on ice, mixed with lysis buffer and lysed
178 by incubation for 30 min accompanied by occasional pulse-vortexing. Subsequently, the cell lysates
179 were purified from cell debris by centrifugation (20.000 g, 15 min) and the protein concentration in the
180 supernatant was determined by Bradford assay. The samples were then diluted down to a
181 homogeneous protein concentration with sample buffer and both SDS-PAGE and Western blot were
182 conducted in accordance with standard workflows. Finally, target protein specific primary antibodies
183 [anti-OPA1 (described earlier²⁸); anti-PARP1 (Enzo, #BML-SA250); Total OXPHOS Human WB
184 Antibody Cocktail (Abcam, #ab110411); anti-TUBA4A (Sigma, #T5168); or anti-VCL (Sigma, #V9131)]
185 and fluorescence-coupled secondary antibodies (LI-COR Biosciences) were used for the detection of
186 proteins on the membrane using the LI-COR Odyssey® imaging system.

187 **FACS-based analysis of apoptotic cell death**

188 After treatment with the indicated concentrations of VDT or the positive control staurosporine, nuclei of
189 Ramos or Jurkat cells were prepared by lysing cells in hypotonic lysis buffer [1% sodium citrate, 0.1%

190 Triton X-100, 50 µg/ mL propidium iodide (PI)] for at least 60 min. After the lysis step the PI fluorescence
191 was measured via flow cytometry. Since PI binds stoichiometrically to DNA, PI fluorescence mirrors the
192 DNA content of the nuclei.²⁹ Hypodiploid nuclei were considered as apoptotic.

193 **Colony formation assay in healthy hematopoietic stem and progenitor cells (HSPC)**

194 HSPC were gained from healthy donors as described above. The cells were then seeded in 12-well
195 plates with a density of 400 cells/ml and a final volume of 400 µl per well in semisolid ready-to-use
196 methylcellulose growth medium (MethoCult™ SF H4436; Stem Cell Technologies, Vancouver, BC,
197 Canada). After incubation for 14 days at 37 °C and 5% CO₂ under humidified conditions the resulting
198 colonies were counted and differentiated into different colony types via microscopy according to their
199 morphology (types: colony-forming unit-erythroid (CFU-E); burst-forming unit-erythroid (BFU-E); colony-
200 forming unit-granulocyte; colony-forming unit-granulocyte/macrophage; colony-forming unit-
201 macrophage (summed up as CFU-G/GM/M) and colony-forming unit-
202 granulocyte/erythrocyte/macrophage/megakaryocyte (CFU-GEMM)).

203 **Measurement of mitochondrial membrane potential**

204 To track changes in mitochondrial membrane potential, Ramos cells were loaded with the cell-
205 permeable and positively charged dye tetramethylrhodamine ethyl ester (TMRE), which accumulates in
206 active mitochondria characterized by a negative net charge, while depolarized mitochondria do not retain
207 the dye. For this purpose, Ramos cells were resuspended in fresh medium containing 10 mM HEPES
208 and supplemented with 100 nM TMRE (AAT Bioquest, Sunnyvale, CA, USA; #22220). After incubation
209 for 15 min at 37°C, the cells were washed twice with RPMI medium (+ HEPES) and incubated for another
210 15 minutes in order to allow the cells to recover and to ensure that the dye has accumulated in active
211 mitochondria. Subsequently, the fluorescence of TMRE was measured by flow cytometry (excitation
212 wavelength: 488 nm, emission wavelength: 575 ± 26 nm). First, the basic fluorescence level of active
213 mitochondria was recorded for at least one minute and then the test substance was added, the sample
214 tube was mixed, and the measurement continued for the specified time. The basic fluorescence level
215 before addition of the test substance was set to 100%. Treatment with the protonophore CCCP served
216 as a control for complete mitochondrial depolarization.

217 **Microscopy**

218 Imaging of HeLa cells stably expressing mito-DsRed was performed using an Axio Observer 7 inverted
219 microscope (Zeiss) equipped with a Plan-Apochromat 40x/1.4 Oil DIC (UV) VIS-IR M27 oil-immersion
220 objective and a Colibri7 LED light source and using optical sectioning via Zeiss apotome.2. The cells
221 were seeded on glass bottom 8-well chamber slides (Ibidi, Planegg, Germany) and maintained in full
222 growth medium supplemented with 10mM HEPES during imaging. Images were taken once every hour
223 and in the time between the recordings the cells were incubated at 37°C in an incubator.

224 **Measurement of cellular ROS level**

225 In order to quantify the cellular ROS level, Ramos cells were cultivated in RPMI medium lacking phenol
226 red for the duration of the experiment. First the cells were loaded with 20 µM 2',7'-
227 dichlorodihydrofluorescein diacetate (H₂DCF-DA, Sigma, #D6883) and incubated for 30 minutes in the
228 dark at 37°C. Subsequently, the cells were washed, seeded in 96-well plates and treated with the test
229 compounds for 6 h. ROS rapidly oxidize H₂DCF-DA to highly fluorescent 2',7'-
230 dichlorodichlorodihydrofluorescein (DCF).³⁰ Finally, the fluorescence of DCF, which therefore is directly
231 correlated to cellular ROS level, was measured by spectrophotometer (excitation wavelength: 485 nm,
232 emission wavelength: 530 nm). ROS level of cells treated with DMSO (0.1% v/v) was set to 100%.

233 **Fluorometric O₂ consumption assay**

234 Measurement of cellular oxygen consumption rate was performed using the MITO-ID® Extracellular O₂
235 Sensor Kit (High Sensitivity) (Enzo Life Sciences, Lörrach, Germany; #51045) according to
236 manufacturer's instructions. Fluorescence was analyzed using a Synergy Mx microplate reader (Ex
237 340–400 nm, Em 630–680 nm; time-resolved fluorescence, delay time 30 µs, integration time 100 µs).

238 **Measurement of cellular ATP levels**

239 Measurements of cellular ATP levels were performed using the *Mitochondrial ToxGlo™ Assay*
240 (Promega, Mannheim, Germany; #G8000) according to manufacturer's instructions. To increase the
241 sensitivity for the detection of mitochondrial toxins, the cells were cultivated during measurement in
242 medium containing either glucose or galactose as the only sugar. Since glycolytic processing of
243 galactose does not produce a net ATP gain, the cells are completely dependent on OXPHOS for ATP

244 production when cultivated in galactose medium and are therefore particularly sensitive to disturbances
245 of this.

246 **Activity measurements for electron transport chain complexes**

247 These measurements were performed using the *MitoCheck® Complex I-IV Activity Assay Kits* (Cayman
248 Chemical, Ann Arbor, MI, USA; #700930/700940/700950/700990) according to manufacturer's
249 instructions. For each complex, appropriate positive controls were used and the activity of DMSO-
250 treated (0.1% v/v) mitochondria was set to 100%.

251

252 **Results**

253 *VDT acts highly cytotoxic in leukemia and lymphoma cells with short latency and rapid kinetics*

254 With the aim of identifying potent structures with properties that qualify them as lead compounds in the
255 development of new drugs for the treatment of oncological diseases, we have investigated a large
256 number of natural products in a tiered approach. Under the premise of finding candidates for the
257 development of cancer drugs, cytotoxicity is a useful indicator to pre-sort the substances to be tested
258 according to bioactivity in the first step of a screening. Ramos (human Burkitt's lymphoma, B
259 lymphocytes) and Jurkat (human acute T cell leukemia, T lymphocytes) cells were used for screening
260 because their rapid growth and tolerance of high-density cultivation conditions make it convenient to
261 provide the required cell numbers for the investigations. In addition, their high sensitivity to noxious
262 substances ensures reasonable sensitivity in the detection of cytotoxic substances.
263 As it was found that one of the natural substances tested, the mycotoxin viriditoxin (VDT), is extremely
264 cytotoxic, especially in Ramos cells, and also showed favorable properties in the further stages of our
265 screening, we concentrated our further investigations on this compound.

266 The resulting IC₅₀ values after a 24-hour incubation period were in the lower nanomolar range for Ramos
267 cells and also below 1 µM for Jurkat cells, classifying VDT as a highly potent candidate (Figures 1B and
268 1C). In addition to a high potency, a rapid onset of action is desirable for clinical use in order to avoid
269 issues such as metabolic inactivation and elimination. For this reason, we have further tested the effect
270 of incubation time on the cytotoxicity of VDT. Since the IC₅₀ values shifted only slightly when the
271 incubation time was tripled and, in addition, significant cytotoxicity occurred in both tested cell lines after
272 a very short incubation time of only 8 h, a rapid onset of effect can be noted for VDT (Figures 1B and

273 1C). In the course of evaluating pharmacodynamic issues such as the speed of action and latency after
274 administration of the substance, it is also helpful to determine how quickly the substance can reach its
275 target. First indications can be obtained by measuring the cytotoxicity after a short pulse treatment with
276 the test substance, followed by washing out the substance and further incubation for 24 hours. Using
277 this test setup, we were able to show that even a 5-minute exposure to VDT is sufficient to cause a
278 severe cytotoxic effect (Figure 1D). Finally, we tested VDT in a panel of solid tumor cell lines to
279 determine whether its strong cytotoxic effect is limited to hemato-oncological diseases. The resulting
280 IC₅₀ values were all at least 10 times higher than in Ramos or Jurkat cells. For the majority of the solid
281 cell lines used, significant cytotoxicity was found only at high concentrations above 10 μM (Figure 1E).
282 The determined IC₅₀ values for all cell lines were summarized in Figure 1F.

283 *VDT is a potent inducer of apoptosis in leukemia and lymphoma cells*

284 Given the disrupted cell death machinery of cancer cells, their unlimited replicative potential as well as
285 their genomic instability that fires up rapid mutations, obviously the focus in the search for new drug
286 candidates must not be on growth inhibition as the desired endpoint, but on the direct killing of the cancer
287 cells. In the course of necrotic cell death, the plasma membrane ruptures, releasing intracellular
288 components that trigger inflammatory reactions in the adjacent tissue. For this reason, induction of
289 apoptotic cell death is the more suitable starting point for the development of novel cancer drugs. In
290 order to take this into account, we assessed if the substances have proapoptotic efficacy in the second
291 step of our screening approach. Since Kundu et al. have already shown that VDT can induce apoptosis
292 in human prostate cancer cells, our next step therefore was to determine whether the strong cytotoxicity
293 of VDT in Ramos and Jurkat cells is also due to the induction of apoptosis.
294 A characteristic hallmark for the occurrence of apoptotic cell death is the activation of effector caspases.
295 Consequently, we used a profluorescent caspase-3 substrate to monitor the activity of caspase-3 after
296 treatment with VDT. For this purpose, Ramos and Jurkat cells were treated with fixed concentrations of
297 1 or 10 μM VDT and the increasing caspase-3 activity was measured over a period of 8 h, allowing us
298 to determine how fast VDT is able to induce apoptosis. The measurement of the 8-hour kinetics revealed
299 a distinct activation of caspase-3 already after 3 h in Ramos cells and after 4 h in Jurkat cells (Figures
300 2A and 2B). Similar to the cytotoxicity measurements, the observation that in Jurkat cells only the
301 increased concentration of 10 μM caused this clear activation demonstrated again the higher sensitivity
302 of Ramos cells to VDT. Activated caspase-3 cleaves poly(ADP-ribose) polymerase-1 (PARP), a protein

303 mainly involved in the processing of DNA damage, proteolytically, which makes cleaved PARP indicative
304 of apoptotic processes. In both Ramos and Jurkat cells VDT induced a marked cleavage of PARP after
305 eight hours of treatment. This cleavage was prevented by co-treatment with the pan-caspase inhibitor
306 QVD (Figures 2C and 2D). To assess VDT's ability to induce apoptosis with a further endpoint, we
307 additionally determined the amount of hypodiploid nuclei, which are indicative for DNA fragmentation
308 caused by active caspases. VDT caused a pronounced and dose-dependent increase in hypodiploid
309 nuclei in both cell lines, with Ramos cells once again being more sensitive (Figures 2E and 2F).

310 *VDT shows a pronounced specificity against lymphoma cells and appears to offer a therapeutic window*

311 Suitable candidates for the development of new cancer drugs have to be able to kill cancer cells quickly
312 and effectively on the one hand, but on the other hand, they have to be able to spare healthy tissue, i.e.,
313 offer a high degree of selectivity. Since the cell lines we used as test systems are hemato-oncological
314 in nature, we used healthy hematopoietic stem and progenitor cells (HSPC) to test for selectivity. After
315 72 hours of treatment of HSPC, VDT showed a significantly reduced cytotoxicity compared to the effect
316 in Ramos cells (Figure 3A). In the next step, we tested whether HSPC are also less susceptible to the
317 pro-apoptotic effect of VDT by measuring the amount of hypodiploid nuclei. Again, significantly higher
318 concentrations of VDT were required in HSPC to produce the same effect as in Ramos cells, which
319 proves the specificity of the substance (Figure 3B). The most important task of hematopoietic stem cells
320 is obviously to provide a constant supply of fresh blood cells. To determine whether VDT interferes with
321 this process in healthy HSPC, we performed colony formation assays. Even HSPC treated with high
322 concentrations of VDT up to 3 μM did not show reduced proliferation or differentiation. In comparison,
323 the cancer drugs vinblastine and paclitaxel, which are used in the clinic for the treatment of leukemias
324 and lymphomas, completely inhibited proliferation and differentiation already at very low concentrations
325 (Figures 3C and 3D). In order not to limit our evaluation of possible hematotoxic effects to tests with
326 stem cells alone, we additionally tested the cytotoxicity of VDT in mononuclear cells of the peripheral
327 blood (PBMC). It was shown that VDT in PBMC is only slightly toxic with an IC_{50} value of over 30 μM
328 (Figure 3E)

329 *VDT impairs mitochondrial structure and function*

330 VDT is known to exhibit broad-spectrum antibacterial activity based on the inhibition of the bacterial
331 protein FtsZ, whose three-dimensional structure is closely related to that of eukaryotic tubulin.
332 Furthermore, Kundu et al. reported that VDT induces mitotic catastrophe and autophagic cell death in

333 prostate cancer cells by disrupting tubulin polymerization²⁰. Based on these observations, we wondered
334 whether the mechanism underlying the observed specificity of VDT is also related to targeting of tubulin.
335 However, since our measurements showed no influence of VDT on the polymerization rate of tubulin
336 and we did not observe either an accumulation of polymerized tubulin or a cell cycle arrest as it would
337 be expected for an antimetabolic toxin (supplemental Figure 1), we excluded tubulin as the primary target.
338 In the following, we first narrowed down the possible targets by phenotypic considerations. Since VDT
339 was capable of inducing apoptosis in caspase-8 deficient Jurkat cells, but not in caspase-9 deficient
340 Jurkat cells (data not shown), we focused on the intrinsic apoptosis pathway and thus the mitochondria.
341 First, we measured the effect of VDT on the mitochondrial membrane potential, as this is a key indicator
342 for mitochondrial functionality. While the mitochondrial membrane potential collapsed abruptly when
343 treated with the protonophore CCCP, here used as a positive control, it decreased gradually over a
344 longer period of more than 30 minutes after the addition of VDT (Figure 4A). The dynamin-like GTPase
345 OPA1 is a central regulator in the maintenance of mitochondrial homeostasis, serves as a sensor of
346 mitochondrial stress such as impaired mitochondrial membrane potential and interconnects
347 mitochondrial quality control and intrinsic apoptosis. The activity of OPA1 is regulated via proteolytic
348 processing through OMA1 and YME1L1 and balances fusion and fission of the mitochondrial network.
349 Stress-induced cleavage of OPA1 and the associated loss of the long isoforms shifts the balance
350 towards increased fission, leading to mitochondrial fragmentation and increased sensitivity to
351 proapoptotic stimuli. We could show that VDT causes a rapid cleavage of OPA1 within several minutes,
352 which cannot be prevented by inhibiting caspase signaling via co-treatment with QVD (Figure 4B). The
353 VDT-induced loss of long OPA1 isoforms was reversible allowing them to be detected again within 6
354 hours after washing out the substance (Figure 4B). Subsequently, we carried out microscopic
355 investigations on HeLa cells that stably express the fluorescent dye DsRed targeted to the mitochondrial
356 matrix to test whether VDT actually causes fragmentation of the mitochondrial network. We were thus
357 able to show that VDT causes a complete collapse of the network within a few hours (Figure 4C). Since
358 severe mitochondrial damage and oxidative stress are often mutually dependent, the next step was to
359 test if VDT treatment influences the cellular reactive oxygen species (ROS) level. Our measurements
360 using the fluorescent dye H₂-DCF-DA revealed, that VDT distinctly increase the ROS level compared to
361 the DMSO-treated control, indicating induction of oxidative stress (Figure 4D). To determine whether
362 the observed oxidative stress was causative for the measured cytotoxicity, we performed cytotoxicity
363 assays involving co-treatment with the antioxidant NAC. And indeed, co-treatment with NAC caused

364 reduced toxicity, suggesting that oxidative stress is at least partially responsible for VDT's cytotoxicity
365 (Figure 4E). Furthermore, we could show that co-treatment with NAC rescues the long OPA1 isoforms
366 (Figure 4F).

367 *VDT impairs mitochondrial respiration*

368 In order to further narrow down its underlying mode of action in the following, we then took a closer look
369 at possible VDT-induced disturbances of mitochondrial functional processes. Since a key task of
370 mitochondria is providing energy for the cell in the form of ATP, we have therefore investigated whether
371 VDT affects cellular ATP level. In order to be able to separate potential effects on glycolysis or oxidative
372 phosphorylation, we provided the cells with either glucose or galactose as the only available sugar in
373 the medium. The glycolytic degradation of galactose instead of glucose does not lead to net ATP gain,
374 forcing the cell to rely entirely on OXPHOS for energy production, making it particularly sensitive to
375 disrupters of the respiratory chain.³¹ Under galactose conditions, VDT caused a drastic and rapid drop
376 in cellular ATP levels, similar to a series of electron transport chain inhibitors used for control (Figure
377 5A). We were able to verify this result, which suggests inhibition of mitochondrial respiration, by
378 demonstrating that VDT causes a rapid and significant decrease in oxygen consumption rate (Figure
379 5B). To determine whether VDT may directly inhibit one of the five OXPHOS complexes, we measured
380 the activities of each complex under treatment with VDT and with the use of appropriate positive controls.
381 In addition, we carried out immunoblot analyses against specific subunits of the individual complexes,
382 which are degraded in case of incorrect assembly and can therefore provide information about functional
383 losses of these complexes. For both complexes I and IV a VDT-induced decrease in activity was
384 observed (Figure 5C). The reduced activity level of complex I is reflected by decreased levels of the
385 corresponding subunit (NDUFB8) in the immunoblots (Figure 5D). At low doses of VDT, this decrease
386 is accompanied by an increase in the expression of the subunit belonging to complex 2 (SDHB), before
387 it also decreases with rising concentrations (Figure 5D). Using thermal proteome profiling, we further
388 demonstrated that treatment with VDT decreases the thermal stability of a number of mitoribosomal
389 proteins, suggesting a pronounced binding affinity of VDT to them and making them potential targets
390 (supplemental Figure 2).

391 **Discussion**

392 The mycotoxin VDT is a toxic natural product that is so far primarily known for its antibiotic effects and
393 whose mechanisms of action in eukaryotic cells are not yet fully understood. In this study we
394 characterize VDT as a highly potent and rapid apoptosis inducer in human lymphoma and leukemia
395 cells. We show that this effect is based on the multifaceted intervention of VDT in mitochondrial
396 functionality, which leads to a disturbance of mitochondrial respiration, most likely by inhibition of
397 complex I of ETC, and to fragmentation of the mitochondrial network. Most interestingly, our studies
398 show that VDT's specific activity profile opens a therapeutic window for the treatment of hematological
399 neoplasia, making it a promising lead structure for the development of new anticancer drugs.
400 Finally, we introduce and discuss mitochondrial ribosomes as potential targets of VDT.

401 VDT shows a significantly higher cytotoxicity in leukemia and lymphoma cells than previously observed
402 for VDT in cancer cells²⁰, which is reflected in IC₅₀ values in the nanomolar range and a rapid onset of
403 action. However, in comparison with the prostate carcinoma cells used by Kundu et al., hemato-
404 oncological cell lines generally often show an increased sensitivity to cytotoxic noxae³², for example due
405 to the larger contact surface to the agent-containing medium. VDT is also found to be particularly toxic
406 in murine lymphoma cells.²¹

407 Due to their high number of functional groups, complex substances often exhibit many metabolic soft
408 spots, which can lead to rapid metabolic inactivation within a few minutes.³³ In particular natural
409 substances, including VDT, often carry methoxy groups and ester groups, which can potentially become
410 the target of rapid metabolic inactivation through O-demethylation respectively hydrolysis.^{34,35} The rapid
411 and irreversible onset of action of VDT is thus a valuable property from a pharmacokinetic perspective,
412 since it can save extensive substance optimization with the aim of achieving the desired metabolic
413 stability.³⁶

414 Compared to Ramos cells, the proapoptotic effect of VDT in Jurkat cells is less pronounced. This is
415 reflected by a higher threshold for caspase-3 activation and induction of hypodiploid nuclei as well as a
416 reduced caspase-dependent cleavage of PARP1. The lower sensitivity is in line with the lower
417 cytotoxicity in Jurkat cells. If the studies carried out by Kundu et al. in prostate cancer cells, which
418 showed a significantly lower cytotoxicity and apoptosis rate²⁰, are taken into account, it becomes clear
419 that both indices correlate for VDT.

420 VDT offers a distinct specificity towards the leukemia and lymphoma cells tested. This is shown by a up
421 to twentyfold lower sensitivity of HSPC to VDT-induced cytotoxicity and apoptosis and a high tolerance
422 to possible effects of VDT on their ability to form colonies. A comparison with the drugs paclitaxel and
423 vinblastine used in the therapy of leukemia and lymphoma³⁷⁻⁴¹ showed that these drugs drastically affect
424 the colony-forming potential even at much lower concentrations, which is indicative of hematotoxic side
425 effects. These results are consistent with the dose-limiting myelosuppressive side effects often
426 described for paclitaxel, vinblastine and other vinca alkaloids, most notably neutropenia.⁴²⁻⁴⁴ Malerba et
427 al. also found complete paclitaxel-induced inhibition of colony growth of HSPC in concentrations lower
428 than the lowest concentration used in our experiments.⁴⁵ In general, a drug is assumed to have a
429 favorable safety profile in case its therapeutic index surpasses the value of 10^{46} , which applies to VDT,
430 but not to Paclitaxel or Vinblastine, both classified as narrow therapeutic index (NTI) drugs.^{47,48} In
431 summary, it can be stated that VDT is apparently superior to these common cytostatic drugs with regard
432 to their hematotoxicity profile.

433 Maintaining the mitochondrial membrane potential ($\Delta\Psi_m$) is of fundamental importance for the cell, as it
434 drives essential processes such as ATP synthesis and mitochondrial protein import⁴⁹ and depolarization
435 below a certain threshold is accordingly associated with major implications for the viability of the cell.⁵⁰
436 The gradual collapse of $\Delta\Psi_m$, as caused by VDT, is therefore a symptom of severe mitochondrial
437 damage. Similar effects on $\Delta\Psi_m$ have been described for a variety of substances, on the one hand for
438 ionophores such as the electroneutral $\text{Ca}^{2+}/2\text{H}^+$ exchanger ionomycin⁵¹ or the protonophore CCCP⁵²
439 and on the other hand for inhibitors of ETC.^{53,54} However, while CCCP in high concentrations causes an
440 abrupt collapse of $\Delta\Psi_m$ by shuttling protons through the IMM⁵⁵, inhibitors of ETC complexes I - IV
441 mediate a slow decrease of $\Delta\Psi_m$ as observed for VDT. Off note, inhibition of complex V (ATP synthase),
442 can either lead to a decrease of $\Delta\Psi_m$ or to hyperpolarization, depending on the cell type.⁵⁶

443 Since $\Delta\Psi_m$ and cellular ATP levels are tightly interconnected parameters⁴⁹, inhibition of $\Delta\Psi_m$ by VDT is
444 accompanied by a rapid decrease in ATP levels within 2 h. Noteworthy, ETC inhibitors also cause a
445 comparably fast breakdown of the cellular ATP level of Ramos cells, while the literature describes a
446 significantly lower sensitivity towards ETC inhibitors for other cell lines, which is reflected in longer
447 latency periods until the breakdown and the need for higher concentrations.^{31,54} Apparently, Ramos cells
448 are highly dependent on OXPHOS, resulting in a pronounced sensitivity towards OXPHOS disruption.
449 Furthermore, it is of interest that VDT already causes a significant reduction of the ATP level under

450 glucose conditions. This could be due to an induction of an unidentified ATPase in rat liver mitochondria
451 described for VDT by Wong et al. as early as 1976.⁵⁷ However, it is also conceivable that this ATPase
452 activity is attributable to a reversely working ATP synthase. Depending on its direction of rotation, the
453 ATP synthase can either synthesize ATP using $\Delta\Psi_m$ or hydrolyze ATP to increase $\Delta\Psi_m$.⁵⁸ This latter,
454 reverse activity provides a protective mechanism for maintaining the $\Delta\Psi_m$ -driven import of proteins and
455 ions into the mitochondria, such as Fe^{2+} , which is crucial for the biogenesis of the ETC complexes.⁵⁹ On
456 the other hand, the VDT-induced decrease in ATP level is also critical for cell survival, since an ATP
457 undersupply can cause a highly cell-damaging acidosis, even when ATP-consuming enzymes are still
458 saturated.⁴⁹ Accordingly, Izyumov et al. report that even a transient three-hour drop in the ATP level to
459 one third induces apoptotic cell death in HeLa cells.⁶⁰

460 VDT rapidly causes a dramatic inhibition of mitochondrial respiration, suggesting that the demonstrated
461 decrease in $\Delta\Psi_m$ and ATP levels is due to an inhibition of OXPHOS. Indeed, we could show that VDT
462 reduces the activity of complex I of the respiratory chain and at the same time causes a compensatory
463 upregulation of complex II. Wong et al. observed that VDT is capable of chelating metallic cations.⁵⁷
464 Since complex I contains eight iron-sulfur (Fe-S) clusters⁶¹ and it is also known that iron chelating agents
465 can remove iron from protein-bound Fe-S clusters⁶², one can speculate whether VDT's ability to chelate
466 can explain the inhibitory effect on complex I. Interestingly, Chen et al. described a natural product that
467 inhibits activity of complex I by specifically targeting one of its iron-sulfur protein components and
468 thereby potentially induces cell death in leukemia and lymphoma cells.⁶³

469 As stated, VDT causes a breakdown of $\Delta\Psi_m$ and cellular ATP levels, both being sufficient conditions for
470 proteolytic processing of OPA1⁶⁴ by OMA1^{65,66}, leading to loss of L-OPA1. In addition, it should be noted
471 that $\Delta\Psi_m$ and OPA1 appear to be mutually interrelated. Thus, the loss of OPA1 in turn supports the
472 decrease of $\Delta\Psi_m$.⁶⁷ Consequently, after treatment with VDT, loss of L-OPA can be detected, which
473 correlates in time with impairment of $\Delta\Psi_m$ and ATP levels. To allow reversibility of the OMA1-mediated
474 stress response in case of recovery of $\Delta\Psi_m$ or ATP levels, activation of OMA1 is accompanied by an
475 autocatalytic turnover of the protease.⁶⁸ Hence, 4-6 h after removal of VDT, a recovery of long OPA1
476 forms can be observed, similar to the recovery after removal of CCCP. However, there have been
477 reported cases of irreversible L-OPA1 depletion, the mechanism of which is still unclear.⁹ The fast OPA1
478 processing by VDT in combination with the long recovery time required could also be an explanation
479 why even a short contact to VDT is highly cytotoxic. Loss of fusion-competent L-OPA1 shifts the balance

480 towards mitochondrial fission, resulting in mitochondrial fragmentation.^{67,69,70} The emerging fission
481 processes are canonically ascribed to the activity of DRP1^{50,71}, although DRP1-independent
482 mitochondrial fission has been shown recently.⁹ In addition, in isolated cases even an opposite effect
483 has been described for ETC inhibitors in the form of an increased mitochondrial fusion, which is
484 attributed to an inhibitory phosphorylation of Drp1 and is assumed to be a compensatory effect that
485 increases respiration.⁷² Since VDT-mediated mitochondrial fragmentation takes several hours, while
486 CCCP causes immediate and complete fragmentation, one could speculate that VDT does not actively
487 increase Drp1 activity as CCCP⁷¹, but merely triggers gradual fragmentation by inhibiting fusion.

488 The connections between mitochondrial fragmentation as a result of OMA1-dependent OPA1
489 processing and apoptotic cell death are extensively discussed in the literature. It has been clearly
490 demonstrated that the loss of L-OPA1 increases the sensitivity to proapoptotic stimuli, presumably
491 because the resulting aberrant cristae morphology favors the release of cytochrome C.⁷³⁻⁷⁶ Furthermore,
492 it is also known that in the course of intrinsic apoptosis a processing of OPA1 can be induced by Bax-
493 Bak oligomerization.⁷⁷ Since VDT cleaves OPA1 within minutes, while activation of caspase-3 as a
494 marker of apoptotic signaling can first be measured after hours, it can be assumed that the processing
495 of OPA1 is an upstream event of apoptotic signaling here. However, whether OPA1 processing alone
496 is sufficient to induce apoptosis is still a matter of research.

497 Adverse alterations in mitochondrial morphology and functionality are frequently associated with
498 increasing ROS levels, which is primarily described as a consequence of partial inhibition of the ETC⁷⁸⁻
499 ⁸⁰ or mitochondrial fragmentation.⁸¹ But at the same time, oxidative stress can also be the cause of
500 OMA1-dependent OPA1 cleavage^{68,82-84}, so that increased ROS levels and aberrant mitochondrial
501 fragmentation are mutually interdependent. We could show that VDT causes an increase in cellular ROS
502 levels and that co-treatment with the antioxidant NAC can rescue the levels of L-OPA1, resulting in a
503 decreased cytotoxicity. Therefore, it can be concluded that the axis of VDT-induced mitochondrial
504 damage, fragmentation and apoptotic cell death is at least partially ROS-dependent.

505 Thermal proteome profiling revealed several mitoribosomal proteins as top hits, suggesting
506 mitochondrial ribosomes as a target of VDT. Except for complex II, all ECT complexes contain mito-
507 encoded subunits, which makes mitochondrial translation essential for respiration.⁸⁵ Therefore, inhibition
508 of these is a possible mechanism to explain the VDT-induced inhibition of OXPHOS. However, since a
509 subsequent differential proteome analysis showed only a decrease of proliferation- and cell cycle-

510 associated proteins after treatment with VDT, but none of mito-encoded proteins (data not shown), an
511 inhibition of mitochondrial translation by VDT seems unlikely. But also independently of the process of
512 translation, mitoribosomes are associated with mitochondrial dynamics, morphology and intrinsic
513 apoptosis. For example, the loss of the mitoribosomal protein DAP3 leads to a collapse of $\Delta\Psi_m$, a
514 decrease in ATP-level, DRP1-dependent fragmentation of mitochondria and a sensitization to intrinsic
515 apoptosis.⁸⁶

516 The significantly increased sensitivity of lymphoma and leukemia cells to VDT compared to healthy
517 hematopoietic cells and cell lines derived from solid tumors raises the question why these cells are
518 particularly susceptible to VDT. Part of the explanation may be the induction of oxidative stress, as
519 cancer cells are known to have intrinsically elevated ROS levels and disturbed redox regulatory
520 mechanisms and are therefore particularly sensitive to the generation of ROS.⁸⁷ Silic-Benussi et al.
521 further proved that the use of ROS inducers is a suitable method to selectively kill T-ALL cells.⁸⁸
522 Analogous to VDT, they observed mitochondrial fragmentation and cleavage of OPA1, which could be
523 prevented by co-treatment with ROS scavengers.

524 Another explanation is the high dependence of blood cancer cells on OXPHOS. Typically, cancer cells
525 show an increased glycolysis rate even in the presence of abundant oxygen, which has been known for
526 almost 100 years as the so-called Warburg effect.⁸⁹ However, it is now known that not all cancer cells
527 share this characteristic, but that in some cases even the OXPHOS rate is upregulated to the detriment
528 of glycolysis, a kind of inverse Warburg effect.⁹⁰ For example, AML cells show an increased respiratory
529 activity, which makes them particularly sensitive to mitotoxic drugs.^{91,92} Burkitt's lymphoma cells like
530 Ramos are characterized by a *Myc proto-oncogene protein* (MYC)-dependent increase of mitochondrial
531 mass and respiratory activity. Škrtić et al. investigated the effect of the antibiotic tigecycline, which
532 inhibits complexes I/IV of the ETC and mitochondrial translation in Burkitt's lymphoma cells with and
533 without MYC repression. Only in Burkitt's lymphoma cells with functional MYC and thus increased
534 mitochondrial mass, the substance showed cytotoxic potency, proving the increased sensitivity of
535 Ramos cells towards ETC inhibition.⁹²

536 There are already several examples of successful exploitation of these discussed vulnerabilities of blood
537 cancer cells described. Arsenic trioxide for example, which induces apoptotic cell death by inhibition of
538 complex I and generation of ROS,⁹³ is FDA approved for the therapy of promyelocytic leukemia. The
539 vitamin E derivative (+) α -tocopheryl succinate (α -TOS), whose effects are similar to those of VDT in

540 many respects, also shows promising effects in leukemia and lymphoma cells.⁹⁴⁻⁹⁷ The substance
541 causes inhibition of complexes I/II,^{94,97} a breakdown of $\Delta\Psi_m$,⁹⁶ increases ROS levels⁹⁸ and, like VDT,
542 does not affect the ability of HSPC to differentiate.⁹⁵ However, treatment with arsenic trioxide is often
543 associated with the serious side effects of arsenic poisoning,⁹³ while α -TOS induces apoptosis only at
544 substantially higher concentrations than VDT and with a much longer latency period.⁹⁵

545 Whether the fate of a cell ends in apoptotic cell death is always determined by a complex interplay of
546 pro- and anti-apoptotic factors. VDT causes several adverse events that can directly trigger intrinsic
547 apoptosis (ROS) or reduce the threshold for triggering it (mitochondrial fragmentation, OXPHOS
548 inhibition). The complex, often mutually dependent effects orchestrated by VDT lead to its selective
549 induction of apoptotic cell death in lymphoma and leukemia cells. Future studies will have to show to
550 what extent mitochondrial ribosomes are involved in these processes.

551 In summary, we identified VDT as a mitochondrial toxin that rapidly induces apoptosis in leukemia and
552 lymphoma cells by causing inhibition of OXPHOS, breakdown of $\Delta\Psi_m$, oxidative stress and
553 fragmentation of the mitochondrial network. The beneficial combination of these effects leads to a
554 pronounced specificity that may open a therapeutic window for the treatment of leukemias and
555 lymphomas and encourages to further explore VDT's usefulness as a novel lead compound by
556 upcoming *in vivo* studies.

557

558 **Acknowledgment**

559 This work was supported by grants from Deutsche Forschungsgemeinschaft (RTG 2158 (to BS and SW)
560 and RTG 2578 (to BS and SW)) and the Düsseldorf School of Oncology (funded by the Comprehensive
561 Cancer Center Düsseldorf/Deutsche Krebshilfe and the Medical Faculty of the Heinrich Heine University
562 Düsseldorf (to BS and SW)).

563

564 **Conflict of Interest**

565 The authors declare no conflict of interest.

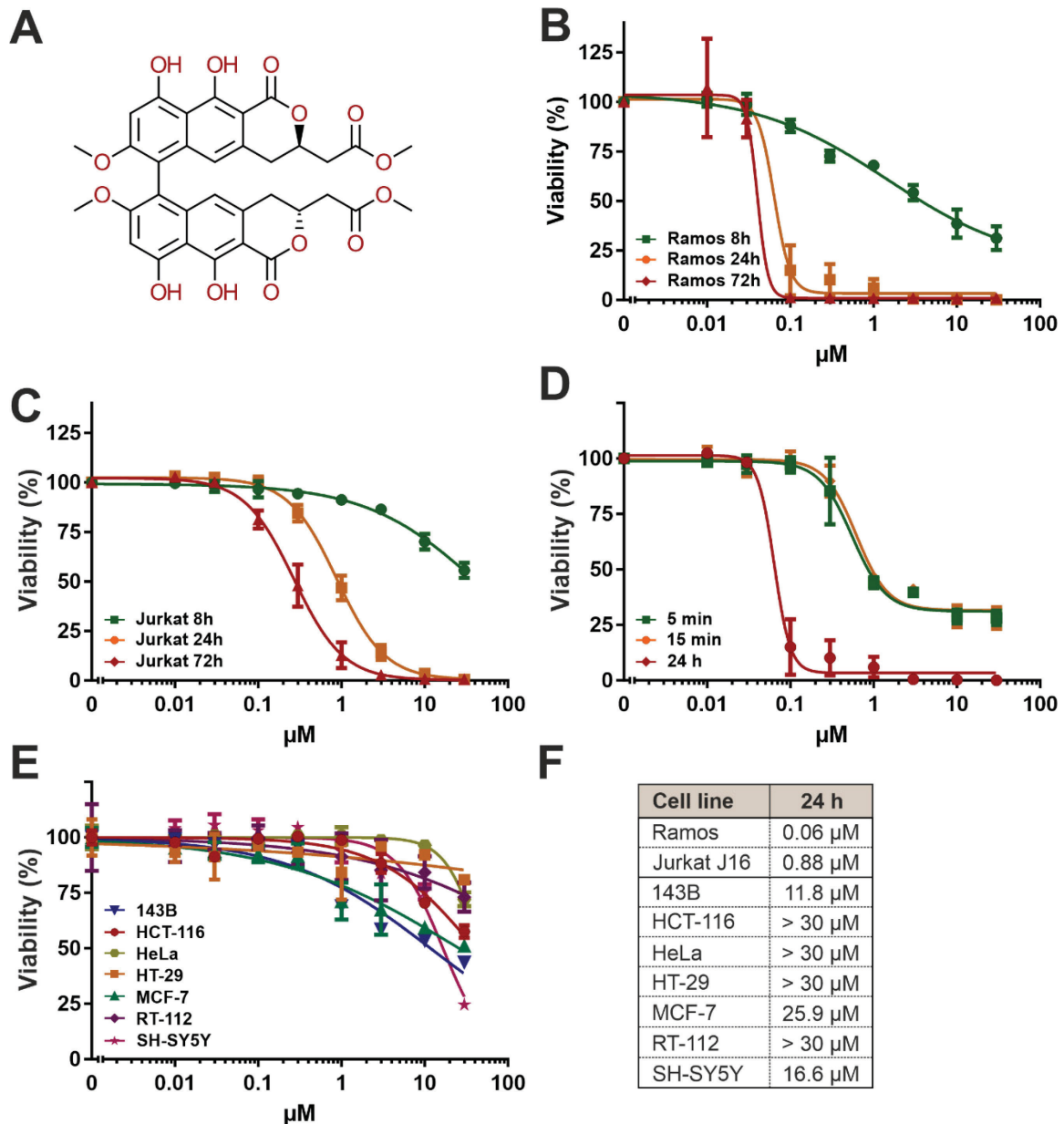


Fig. 1. VDT acts highly cytotoxic in leukemia and lymphoma cells with short latency and rapid kinetics.

(A) Structure of viriditoxin (VDT). Cytotoxicity in Ramos (B) or Jurkat (C) cells was determined after the indicated incubation periods using the MTT viability assay. (D) Ramos cells were treated with escalating VDT concentrations for 5 min, 15 min or 24 h. In the first two treatment series, VDT was washed out at the end of the incubation period and cells were further cultivated in growth medium until 24 h after the start of the experiment. Finally, cytotoxicity was determined by MTT assay. (E) Cytotoxicity of VDT after 24 h of incubation was determined in a panel of human solid tumor cell lines including 143B (osteosarcoma), HCT 116 (colorectal carcinoma), HeLa (cervix carcinoma), HT-29 (colorectal adenocarcinoma), MCF7 (breast adenocarcinoma), RT-112 (urinary bladder transitional cell carcinoma) and SH-SY5Y (neuroblastoma) cells was determined using the MTT assay. (F) Overview of the resulting IC_{50} values in the individual tested cell lines after incubation for 24 h.

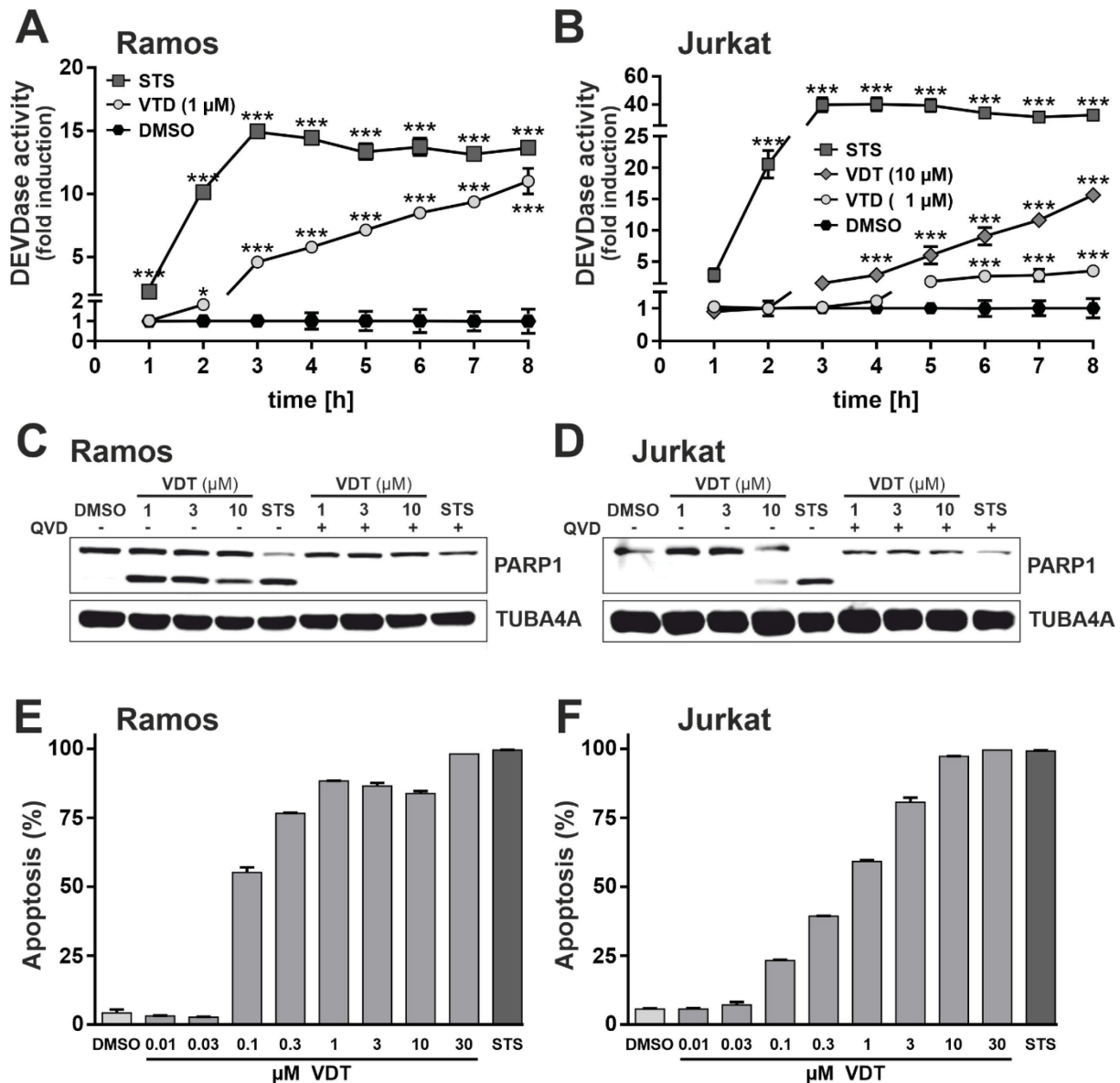


Fig. 2. VDT is a potent inducer of apoptosis in leukemia and lymphoma cells.

Ramos (A) or Jurkat (B) cells were treated with escalating concentrations of VDT or 2.5 μ M staurosporine (STS), serving as a positive control for induction of apoptosis, for 24 h. Subsequently, DEVDase activity as a surrogate marker for activation of procaspase-3 was determined via measurement of the fluorescence of the profluorescent caspase-3 substrate DEVD-AMc in a microspectrophotometer. The slope of the linear range of fluorescence increase served as a measure for DEVDase activity. The DMSO control values were set to 1 and the normalized relative fold induction was calculated as described in methods. Error bars = SD of three independent experiments performed in triplicates; p values were calculated by two-way ANOVA with the Holm-Sidak post-test; * = $p \leq 0.05$, *** = $p \leq 0.001$. Cleavage of the caspase-3 substrate *poly [ADP-ribose] polymerase 1* (PARP1) as an indicator for apoptotic cell death was measured in (C) Ramos and (D) Jurkat cells after 8 h of incubation via immunoblotting. Cells were treated with the indicated concentrations of VDT (in μ M) or 2.5 μ M STS either alone or in combination with the pan-caspase inhibitor QVD. Apoptosis-related DNA degradation was detected after 24 h of incubation via flow-cytometric measurement of propidium iodide stained hypodiploid nuclei in (E) Ramos or (F) Jurkat cells.

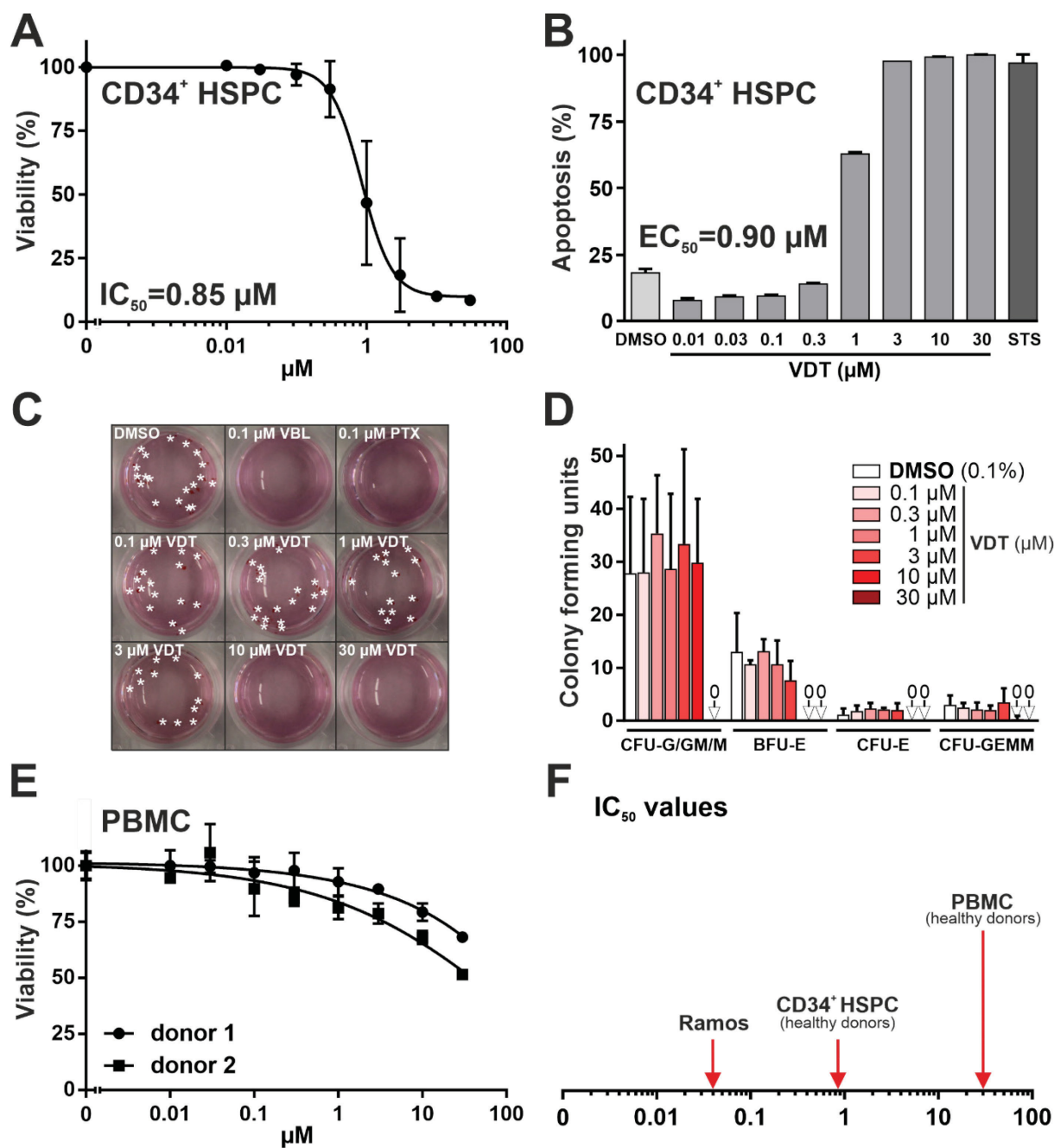


Fig. 3. VDT shows a pronounced specificity against lymphoma cells and appears to offer a therapeutic window.

(A) Cytotoxicity in hematopoietic stem and progenitor cells (HSPC) gained from healthy donors via apheresis and magnetic-activated cell sorting (MACS) against the stem cell marker CD34 was determined after 72 h of incubation with VDT using the MTT viability assay. (B) HSPC from healthy donors were treated for 24 h with either escalating concentrations of VDT or staurosporine (STS) as positive control for apoptosis induction. Subsequently, apoptotic events were identified via flowcytometric measurement of hypodiploid nuclei. (C) HSPC were plated at low cell density in semi-solid medium supplemented with appropriate cytokines and treated with 0.1% (v/v) DMSO, viriditoxin (VDT), paclitaxel (PTX) or vinblastine (VBL) for 14 d. Afterwards, the resulting colonies were classified and counted. Depicted are representative pictures. (D) Quantification of the colony formation assay (colony-forming unit-erythroid [CFU-E], burst-forming unit-erythroid [BFU-E], colony-forming unit-

granulocyte, colony-forming unit-granulocyte/macrophage, colony-forming unit-macrophage [summed up as CFU-G/GM/M], colony-forming unit-granulocyte/erythrocyte/macrophage/mega-karyocyte [CFU-GEMM]. (E) Cytotoxicity in PBMC (peripheral blood mononuclear cells) gained from healthy donors via apheresis and density gradient centrifugation was determined after 72 h of incubation with VDT using the MTT viability assay. (F) Overview of the determined IC_{50} values for 72 h of incubation with VDT in transformed (Ramos) and untransformed ($CD34^+$ HSPC, PBMC) cells.

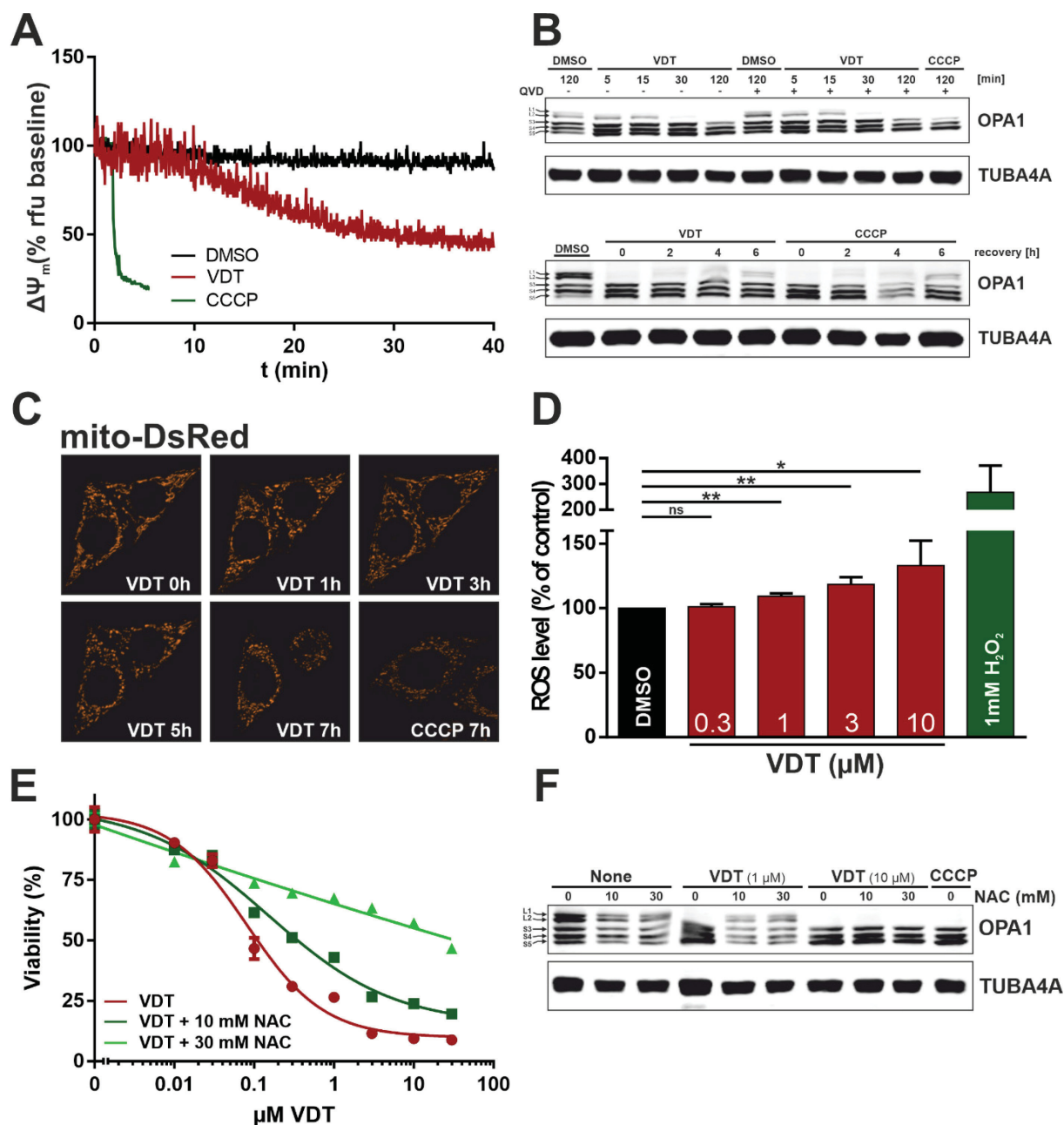


Fig. 4. VDT impairs mitochondrial structure and function.

(A) Monitoring of the mitochondrial membrane potential of Ramos cells over a period of at least 30 min after addition of 10 μ M VDT, 0.1 % (v/v) DMSO (negative control) or 10 μ M CCCP (mitochondrial uncoupler, positive control) by flow cytometric measurement of TMRE fluorescence. (B) Upper panel: The kinetics of VDT-induced OPA1 cleavage as determined via immunoblotting in Ramos cells. Co-treatment with the pancaspase-inhibitor QVD (10 μ M) was conducted in order to ensure independence from apoptotic signaling. Treatment with CCCP (10 μ M) served as a positive control. Lower panel: In order to study the recovery of long forms of OPA1 Ramos cells were treated for 30 min with either VDT (10 μ M) or CCCP (10 μ M), followed by substance removal and a recovery time of up to 6 h. (C) Changes in mitochondrial morphology after treatment with VDT (10 μ M) for up to 7 h were assessed by microscopy of HeLa cells stably expressing the fluorescent dye mito-DsRed, which stains the inner mitochondrial membrane. Shown are representative pictures. (D) VDT-induced effects on intracellular reactive oxygen species (ROS) activity as analyzed via DCF-Assay. Ramos cells were loaded with the

fluorogenic dye 2',7'-dichlorodihydrofluorescein diacetate (H₂DCF-DA, 20 μM) and then treated with the indicated concentrations of VDT for 6 h. Finally, the fluorescence of DCF was measured with a microplate reader (485/535 nm). Endogenous ROS level of cells treated with DMSO (0.1% v/v) was set to 100% and treatment with 100 mM H₂O₂ served as a positive control. Error bars = SD of three independent experiments performed in triplicates; p values were calculated by one sample t-test; * = p ≤ 0.05, ** = p ≤ 0.01. **(E)** Comparative measurement of the cytotoxicity of VDT with or without co-treatment with the ROS scavenger N-acetylcysteine (NAC) after an incubation period of 24 h via resazurin reduction assay. **(F)** Immunoblot of Ramos cells treated for 60 min with VDT (1 or 10 μM) with or without NAC pretreatment (10 or 30 mM). CCCP served as positive control for OPA1 cleavage.

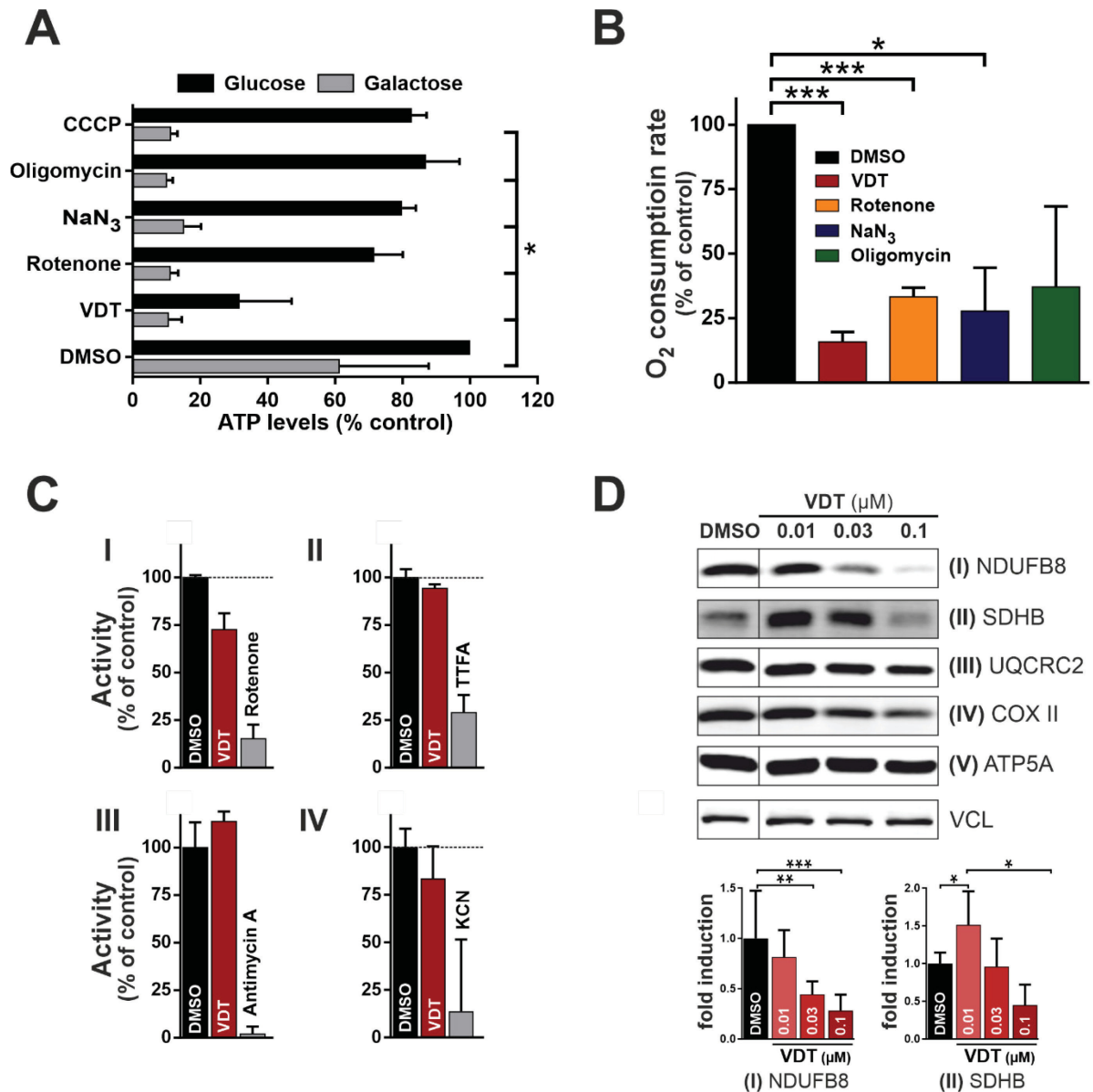


Fig. 5. VDT impairs mitochondrial respiration.

(A) Measurement of the effect of VDT and a selection of known mitochondrial toxins on the ATP levels of Ramos cells. Ramos cells were treated for 90 min with the indicated substances in full growth medium containing either glucose or galactose as the only available sugar. Subsequently, the ATP levels were measured using the luminescence-based Mitochondrial ToxGlo™ Assay (Promega). Galactose alone forces the cells to rely entirely on OXPHOS for ATP synthesis. The depicted values were normalized to cells treated with DMSO (0.1% v/v) in glucose containing growth medium (set to 100%). Error bars = SD of three independent experiments performed in triplicates; p values were calculated by two-way ANOVA with the Holm-Sidak post-test; * = $p \leq 0.05$. (B) Comparative measurement of the oxygen consumption rate of Ramos cells treated with VDT or a range of known complex-specific inhibitors of the respiratory chain (rotenone [complex I, 10 μ M], sodium azide [NaN₃, complex IV, 1 mM], oligomycin A [complex V, 10 μ M]) using the MITO-ID® Extracellular O₂ Sensor Kit (High Sensitivity) (Enzo). Oxygen consumption rate of cells treated with 0.1% DMSO (v/v) was set to 100%. Error bars = SD of three independent experiments performed in triplicates; p values were calculated by one sample t-test; * = p

≤ 0.05 , *** = $p \leq 0.001$. **(C)** The activities of the individual complexes of the respiratory chain were measured after treatment with VDT or a complex-specific positive control for 15 min using the corresponding MitoCheck® kits (Cayman Chemical). Depicted activities were normalized to cells treated with DMSO (0.1% v/v). **(D)** For each complex of the respiratory chain a subunit was selected which is unstable if the respective complex is incorrectly assembled. Ramos cells were treated with nanomolar concentrations of VDT for 24 h before a immunoblot was performed against these subunits. Vinculin served as loading control. The bar chart below shows the quantification of the signal for the subunits of complex I and II, based on at least three independent experiments. Error bars = SD of at least three independent experiments; p values were calculated by two-way ANOVA with the Holm-Sidak post-test; * = $p \leq 0.05$, ** = $p \leq 0.01$, *** = $p \leq 0.001$.

References

- 1 Mukherjee S. (2011) *The Emperor of All Maladies: A Biography of Cancer*. Fourth Estate Ltd: London, 2011.
- 2 Bray F, Ferlay J, Soerjomataram I, Siegel RL, Torre LA. (2018) Global Cancer Statistics 2018 : GLOBOCAN Estimates of Incidence and Mortality Worldwide for 36 Cancers in 185 Countries. *CA Cancer J Clin* **0**:01–31. doi:10.3322/caac.21492.
- 3 Pearce A, Haas M, Viney R, Pearson S-A, ... Ward R. (2017) Incidence and severity of self-reported chemotherapy side effects in routine care : A prospective cohort study. *PLoS One* **12**:e0184360. doi:https://doi.org/10.1371/journal.pone.0184360 Editor:
- 4 Newman DJ, Cragg GM. (2016) Natural Products as Sources of New Drugs from 1981 to 2014. *J Nat Prod* **79**:629–661. doi:10.1021/acs.jnatprod.5b01055.
- 5 Chin Y-W, Balunas MJ, Chai HB, Kinghorn AD. (2006) Drug Discovery From Natural Sources. *AAPS J* **8**:239–253. doi:10.1007/BF02854894.
- 6 Hanahan D, Weinberg RA. (2011) Hallmarks of cancer : The next generation. *Cell* **144**:646–674. doi:10.1016/j.cell.2011.02.013.
- 7 Safarzadeh E, Shotorbani SS, Baradaran B. (2014) Herbal Medicine as Inducers of Apoptosis in Cancer Treatment. *Adv Pharm Bull* **4**:421–427. doi:10.5681/apb.2014.062.
- 8 Taraphdar AK, Roy M, Bhattacharya RK. (2001) Natural products as inducers of apoptosis : Implication for cancer therapy and prevention. *Curr Sci* **80**:1387–1396.
- 9 Böhler P, Stuhldreier F, Anand R, Kondadi AK, ... Stork B. (2018) The mycotoxin phomoxanthone A disturbs the form and function of the inner mitochondrial membrane. *Cell Death Dis* **9**:286. doi:10.1038/s41419-018-0312-8.
- 10 Elmore S. (2007) Apoptosis: a review of programmed cell death. *Toxicol Pathol* **35**:495–516. doi:10.1080/01926230701320337.
- 11 Lopez J, Tait SWG. (2015) Mitochondrial apoptosis: killing cancer using the enemy within. *Br J Cancer* **112**:957–962. doi:10.1038/bjc.2015.85.
- 12 Li X, Darzynkiewicz Z. (2000) Cleavage of Poly (ADP-Ribose) Polymerase Measured in Situ in Individual Cells : Relationship to DNA Fragmentation and Cell Cycle Position during Apoptosis. *Exp Cell Res* **255**:125–132. doi:10.1006/excr.1999.4796.
- 13 Larsen BD, Sørensen CS. (2017) The caspase-activated DNase : apoptosis and beyond. *FEBS J* **284**:1160–1170. doi:10.1111/febs.13970.
- 14 Nunnari J, Friedman JR. (2014) Mitochondrial form and function. *Nature* **505**:335–343. doi:10.1038/nature12985.
- 15 Nunnari J, Suomalainen A. (2012) Mitochondria: In Sickness and in Health. *Cell* **148**:1145–1159. doi:10.1016/j.cell.2012.02.035.
- 16 McBride H, Soubannier V. (2010) Mitochondrial Function: OMA1 and OPA1, the Grandmasters of Mitochondrial Health. *Curr Biol* **20**:R274–R276. doi:10.1016/j.cub.2010.02.011.
- 17 Ni H-M, Williams JA, Ding W-X. (2015) Mitochondrial dynamics and mitochondrial quality control. *Redox Biol* **4**:6–13. doi:10.1016/j.redox.2014.11.006.
- 18 Ding W-X, Yin X-M. (2013) Mitophagy: mechanisms, pathophysiological roles, and analysis. *Biol Chem* **393**:547–564. doi:10.1515/hsz-2012-0119.
- 19 Kim HJ, Maiti P, Barrientos A. (2017) Mitochondrial ribosomes in cancer. *Semin Cancer Biol* **47**:67–81. doi:10.1016/j.semcan.2017.04.004.
- 20 Kundu S, Kim TH, Yoon JH, Shin H-S, ... Kim HS. (2014) Viriditoxin regulates apoptosis and autophagy via mitotic catastrophe and microtubule formation in human prostate cancer cells. *Int J Oncol* **45**:2331–2340. doi:10.3892/ijo.2014.2659.
- 21 Liu Y, Kurtán T, Wang CY, Lin WH, ... Proksch P. (2016) Cladosporinone , a new viriditoxin

- derivative from the hypersaline lake derived fungus *Cladosporium cladosporioides*. *J Antibiot (Tokyo)* **69**:702–706. doi:10.1038/ja.2016.11.
- 22 Abbas Z, Siddiqui BS, Shahzad S, Sattar S, ... Choudhary MI. (2020) Lawsozaheer, a new chromone produced by an endophytic fungus *Paecilomyces variotii* isolated from *Lawsonia Alba Lam.* inhibits the growth of *Staphylococcus aureus*. *Nat Prod Res* :1–6. doi:10.1080/14786419.2020.1729148.
 - 23 Wang J, Galgoci A, Kodali S, Herath KB, ... Singh S. (2003) Discovery of a small molecule that inhibits cell division by blocking FtsZ, a novel therapeutic target of antibiotics. *J Biol Chem* **278**:44424–44428. doi:10.1074/jbc.M307625200.
 - 24 Amos LA, Löwe J. (1998) Crystal structure of the bacterial cell-division protein FtsZ. **391**:203–206.
 - 25 Bampton ETW, Goemans CG, Niranjana D, Mizushima N, Tolkovsky AM. (2005) The dynamics of autophagy visualized in live cells: from autophagosome formation to fusion with endo/lysosomes. *Autophagy* **1**:23–36. doi:10.4161/auto.1.1.1495.
 - 26 Sidney LE, Branch MJ, Dunphy SE, Dua HS, Hopkinson A. (2014) Concise Review: Evidence for CD34 as a Common Marker for Diverse Progenitors. *Stem Cells* **32**:1380–1389. doi:10.1002/stem.1661.
 - 27 Drießen D, Stuhldreier F, Frank A, Stark H, ... Müller TJJ. (2019) Novel meriolin derivatives as rapid apoptosis inducers. *Bioorganic Med Chem* **27**:3463–3468. doi:10.1016/j.bmc.2019.06.029.
 - 28 Barrera M, Koob S, Dikov D, Vogel F, Reichert AS. (2016) OPA1 functionally interacts with MIC60 but is dispensable for cristae junction formation. *FEBS Lett* **590**:3309–3322. doi:10.1002/1873-3468.12384.
 - 29 Riccardi C, Nicoletti I. (2006) Analysis of apoptosis by propidium iodide staining and flow cytometry. *Nat Protoc* **1**:1458–1461. doi:10.1038/nprot.2006.238.
 - 30 Kalyanaraman B, Darley-Usmar V, Davies KJA, Dennerly PA, ... Ischiropoulos H. (2012) Measuring reactive oxygen and nitrogen species with fluorescent probes: challenges and limitations. *Free Radic Biol Med* **52**:1–6. doi:10.1016/j.freeradbiomed.2011.09.030.
 - 31 Marroquin LD, Hynes J, Dykens JA, Jamieson JD, Will Y. (2007) Circumventing the Crabtree Effect : Replacing Media Glucose with Galactose Increases Susceptibility of HepG2 Cells to Mitochondrial Toxicants. *Toxicol Sci* **97**:539–547. doi:10.1093/toxsci/kfm052.
 - 32 Barretina J, Caponigro G, Stransky N, Venkatesan K, ... Murray L. (2012) The Cancer Cell Line Encyclopedia enables predictive modeling of anticancer drug sensitivity. *Nature* **483**:603–607. doi:10.1038/nature11003.
 - 33 Li C, Lu Y, Narayanan R, Miller DD, Dalton JT. (2010) Drug Metabolism and Pharmacokinetics of 4-Substituted Methoxybenzoyl-aryl-thiazoles. *DRUG Metab Dispos* **38**:2032–2039. doi:10.1124/dmd.110.034348.
 - 34 Laizure S. C, Herring V, Hu Z, Witbrodt K, Parker RB. (2013) The role of human carboxylesterases in drug metabolism: have we overlooked their importance? *Pharmacotherapy* **33**:210–222. doi:10.1002/phar.1194.
 - 35 Zhang Z, Tang W. (2018) Drug metabolism in drug discovery and development. *Acta Pharm Sin B* **8**:721–732. doi:10.1016/j.apsb.2018.04.003.
 - 36 Trunzer M, Faller B, Zimmerlin A. (2009) Metabolic Soft Spot Identification and Compound Optimization in Early Discovery Phases Using MetaSite and LC-MS / MS Validation. *J Med Chem* **52**:329–335. doi:10.1021/jm8008663.
 - 37 Beinlich P, Riedel C, Escherich A, Sudhop T, Broich K. (2019) Projektstudie zur Evaluierung von Daten nach §§ 303a ff SGB V i.V.m. der DaTraV hinsichtlich ihrer Verwendbarkeit zur Gewinnung statistisch belastbarer Aussagen zur Quantität (...) des in Deutschland praktizierten Off-Label Use zu Lasten der GKV. 2019https://www.bundesgesundheitsministerium.de/fileadmin/Dateien/5_Publikationen/Minister

ium/Berichte/2019-05-23_Machbarkeitsstudie_zum_praktizierten_Off-Label-Use_zu_Lasten_der_GKV_Abschlussbericht_mit_Anlage.pdf.

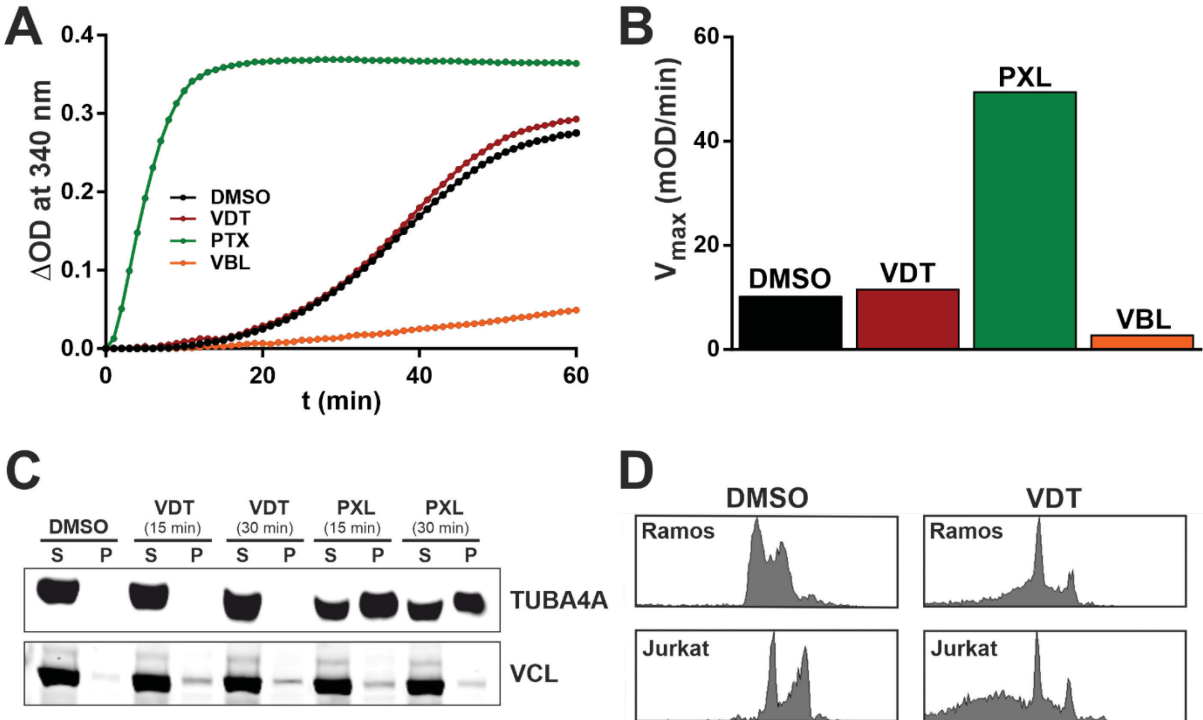
- 38 Pro B, Hagemeister FB, McLaughlin P, Romaguera J, ... Younes A. (2006) Phase 2 study of fludarabine and paclitaxel in patients with recurrent low-grade non-Hodgkin ' s lymphoma. *Leuk Lymphoma* **47**:1818–1821. doi:10.1080/10428190600684999.
- 39 Juliusson G. (2002) A dexamethasone, vinblastine, cyclophosphamide, etoposide, methotrexate and bleomycin (D-VICEMB) protocol as first-line treatment of patients aged 70 years or older affected by intermediate/high grade non-Hodgkin's lymphoma. *Haematologica* **87**:1227–1229.
- 40 Hay AE, Meyer RM. (2015) Balancing Risks and Benefits of Therapy for Patients with Favorable-Risk Limited-Stage Hodgkin Lymphoma: The Role of ABVD Chemotherapy Alone. *Hematol Oncol Clin North Am* **28**:1–17. doi:10.1016/j.hoc.2013.10.001.
- 41 Canellos GP, Petroni GR, Barcos M, Duggan DB, Peterson BA. (1995) Etoposide, Vinblastine, and Doxorubicin: An Active Regimen for the Treatment of Hodgkin's Disease in Relapse Following MOPP. *J Clin Oncol* **13**:2005–2011. doi:10.1200/JCO.1995.13.8.2005.
- 42 Horiguchi J, Rai Y, Tamura K, Taki T, ... Tajima T. (2009) Phase II Study of Weekly Paclitaxel for Advanced or Metastatic Breast Cancer in Japan. *Anticancer Res* **29**:625–630.
- 43 Cersosimo RJ, Bromer R, Licciardello JTW, Hong WK. (1983) Pharmacology , Clinical Efficacy and Adverse Effects of Vindesine Sulfate , A New Vinca Alkaloid. *Pharmacotherapy* **3**:259–274. doi:10.1002/j.1875-9114.1983.tb03269.x.
- 44 Moudi M, Go R, Yien CYS, Nazre M. (2013) Vinca alkaloids. *Int J Prev Med* **4**:1231–1235.
- 45 Malerba I, Casati S, Diodovich C, Parent-Massin D, Gribaldo L. (2004) Inhibition of CFU-E / BFU-E and CFU-GM colony growth by Cyclophosphamide , 5-Fluorouracil and Taxol : development of a high-throughput in vitro method. *Toxicol Vitro* **18**:293–300. doi:10.1016/j.tiv.2003.09.001.
- 46 Tamargo J, Le Heuzey J-Y, Mabo P. (2015) Narrow therapeutic index drugs : a clinical pharmacological consideration to flecainide. *Eur J Clin Pharmacol* **71**:549–567. doi:10.1007/s00228-015-1832-0.
- 47 Ratain MJ, Vogelzang NJ. (1986) Phase I and pharmacological study of vinblastine by prolonged continuous infusion. *Cancer Res* **46**:4827–4830.
- 48 Wishart DS, Feunang YD, Guo AC, Lo EJ, ... Wilson M. (2018) DrugBank 5.0 : a major update to the DrugBank database for 2018. *Nucleic Acids Res* **46**:1074–1082. doi:10.1093/nar/gkx1037.
- 49 Zorova LD, Popkov VA, Plotnikov EY, Silachev DN, ... Zorov DB. (2018) Mitochondrial membrane potential. *Anal Biochem* **552**:50–59. doi:10.1016/j.ab.2017.07.009.
- 50 Jones E, Gaytan N, Garcia I, Herrera A, ... Gilkerson R. (2017) A threshold of transmembrane potential is required for mitochondrial dynamic balance mediated by DRP1 and OMA1. *Cell Mol Life Sci* **74**:1347–1363. doi:10.1007/s00018-016-2421-9.
- 51 Nicholls DG. (2006) Simultaneous Monitoring of Ionophore- and Inhibitor-mediated Plasma and Mitochondrial Membrane Potential Changes in Cultured Neurons. *J Biol Chem* **281**:14864–14874. doi:10.1074/jbc.M510916200.
- 52 Kane MS, Paris A, Codron P, Cassereau J, ... Chevrollier A. (2018) Current mechanistic insights into the CCCP-induced cell survival response. *Biochem Pharmacol* **148**:100–110. doi:10.1016/j.bcp.2017.12.018.
- 53 Michelakis ED, Rebeyka I, Wu X, Nsair A, ... Archer SL. (2002) O₂ Sensing in the Human Ductus Arteriosus - Regulation of Voltage-Gated K⁺ Channels in Smooth Muscle Cells by a Mitochondrial Redox Sensor. *Circ Res* **91**:478–486. doi:10.1161/01.RES.0000035057.63303.D1.
- 54 Zuo Y, Hu J, Xu X, Gao X, ... Zhu S. (2019) Sodium azide induces mitochondria - mediated apoptosis in PC12 cells through Pgc - 1 α - associated signaling pathway. *Mol Med Rep*

- 19:2211–2219. doi:10.3892/mmr.2019.9853.
- 55 Benz R, McLaughlin S. (1983) The molecular mechanism of action of the proton ionophore FCCP (Carbonyl cyanide-p-trifluoromethoxyphenylhydrazone). *Biophys J* **41**:381–398. doi:10.1016/S0006-3495(83)84449-X.
- 56 Kalbacova M, Vrbacky M, Drahota Z, Melkova Z. (2003) Comparison of the Effect of Mitochondrial Inhibitors on Mitochondrial Membrane Potential in Two Different Cell Lines Using Flow Cytometry and Spectrofluorometry. *Cytom Part A* **54A**:110–116. doi:10.1002/cyto.a.10031.
- 57 Wong DT, Hamill RL. (1976) Viriditoxin induces swelling and ATPase by activation of calcium transport in liver mitochondria. *Biochem Biophys Res Commun* **71**:332–338. doi:https://doi.org/10.1016/0006-291X(76)90287-4.
- 58 Walker JE. (2013) The ATP synthase: the understood, the uncertain and the unknown. *Biochem Soc Trans* **41**:1–16. doi:10.1042/BST20110773.
- 59 Zorov DB, Isaev NK, Plotnikov EY, Zorova LD, ... Khrjapenkova TG. (2007) The Mitochondrion as Janus Bifrons. *Biochem* **72**:1371–1384. doi:DOI: 10.1134/S0006297907100094.
- 60 Izyumov DS, Avetisyan A V., Yu O, Sakharov D V., ... Skulachev VP. (2004) “Wages of Fear”: transient threefold decrease in intracellular ATP level imposes apoptosis. *Biochim Biophys Acta* **1658**:141–147. doi:10.1016/j.bbabi.2004.05.007.
- 61 Couch VA, Medvedev ES, Stuchebrukhov AA. (2009) Electrostatics of the FeS Clusters in Respiratory Complex I. *Biochim Biophys Acta* **1787**:1266–1271. doi:10.1016/j.bbabi.2009.05.001.
- 62 Wu S, Cowan JA. (2007) Iron-sulfur cluster stability . Kinetics and mechanism of ligand-promoted cluster degradation. *Chem Commun* :82–84. doi:10.1039/b610665j.
- 63 Hu Y, Huang P, Chen G, Chen Z. (2011) Inhibition of Mitochondrial Respiration and Rapid Depletion of Mitochondrial Glutathione by β -Phenethyl Isothiocyanate : Mechanisms for Anti-Leukemia Activity. *Antioxid Redox Signal* **15**:2911–2921. doi:10.1089/ars.2011.4170.
- 64 Baricault L, Ségui B, Guégand L, Olichon A, ... Lenaers G. (2007) OPA1 cleavage depends on decreased mitochondrial ATP level and bivalent metals. *Exp Cell Res* **313**:3800–3808. doi:10.1016/j.yexcr.2007.08.008.
- 65 Head B, Griparic L, Amiri M, Gandre-Babbe S, van der Blik AM. (2009) Inducible proteolytic inactivation of OPA1 mediated by the OMA1 protease in mammalian cells. *J Cell Biol* **187**:959–966. doi:10.1083/jcb.200906083.
- 66 Zhang K, Song Z. (2014) Membrane depolarization activates the mitochondrial protease OMA1 by stimulating self-cleavage. *EMBO Rep* **15**:576–585.
- 67 Olichon A, Baricault L, Gas N, Guillou E, ... Lenaers G. (2002) Loss of OPA1 Perturbates the Mitochondrial Inner Membrane Structure and Integrity, Leading to Cytochrome c Release and Apoptosis. *J Biol Chem* **278**:7743–7746. doi:10.1074/jbc.C200677200.
- 68 Baker MJ, Lampe PA, Stojanovski D, Korwitz A, ... Langer T. (2014) Stress-induced OMA1 activation and autocatalytic turnover regulate OPA1-dependent mitochondrial dynamics. *EMBO J* **33**:578–93. doi:10.1002/embj.201386474.
- 69 Lee H, Smith SB, Yoon Y. (2017) The short variant of the mitochondrial dynamin OPA1 maintains mitochondrial energetics and cristae structure. *J Biol Chem* **292**:7115–7130. doi:10.1074/jbc.M116.762567.
- 70 Duvezin-Caubet S, Jagasia R, Wagener J, Hofmann S, ... Reichert AS. (2006) Proteolytic processing of OPA1 links mitochondrial dysfunction to alterations in mitochondrial morphology. *J Biol Chem* **281**:37972–37979. doi:10.1074/jbc.M606059200.
- 71 van der Blik AM, Shen Q, Kawajiri S. (2013) Mechanisms of mitochondrial fission and fusion. *Cold Spring Harb Perspect Biol* **5**:a011072. doi:10.1101/cshperspect.a011072.
- 72 Trotta AP, Gelles JD, Serasinghe MN, Loi P, ... Chipuk JE. (2017) Disruption of mitochondrial

- electron transport chain function potentiates the pro- apoptotic effects of MAPK inhibition. *J Biol Chem* **292**:11727–11739. doi:10.1074/jbc.M117.786442.
- 73 Macvicar T, Langer T. (2016) OPA1 processing in cell death and disease – the long and short of it. *J Cell Sci* **129**:2297–2306. doi:10.1242/jcs.159186.
- 74 Frezza C, Cipolat S, Martins de Brito O, Micaroni M, ... Scorrano L. (2006) OPA1 controls apoptotic cristae remodeling independently from mitochondrial fusion. *Cell* **126**:177–189. doi:10.1016/j.cell.2006.06.025.
- 75 Griparic L, van der Wel NN, Orozco IJ, Peters PJ, van der Bliek AM. (2004) Loss of the Intermembrane Space Protein Mgm1/OPA1 Induces Swelling and Localized Constrictions along the Lengths of Mitochondria. *J Biol Chem* **279**:18792–18798. doi:10.1074/jbc.M400920200.
- 76 Xiao X, Hu Y, Quirós PM, Wei Q, ... Dong Z. (2014) OMA1 mediates OPA1 proteolysis and mitochondrial fragmentation in experimental models of ischemic kidney injury. *Am J Physiol Ren Physiol* **306**:1318–1326. doi:10.1152/ajprenal.00036.2014.
- 77 Jiang X, Jiang H, Shen Z, Wang X. (2014) Activation of mitochondrial protease OMA1 by Bax and Bak promotes cytochrome c release during apoptosis. *Proc Natl Acad Sci U S A* **111**:14782–14787. doi:10.1073/pnas.1417253111.
- 78 Fato R, Bergamini C, Bortolus M, Maniero AL, ... Lenaz G. (2010) Differential effects of mitochondrial Complex I inhibitors on production of reactive oxygen species. *Biochim Biophys Acta* **1787**:384–392. doi:10.1016/j.bbabi.2008.11.003.
- 79 Jacobson J, Duchon MR, Hothersall J, Clark JB, Heales SJR. (2005) Induction of mitochondrial oxidative stress in astrocytes by nitric oxide precedes disruption of energy metabolism. *J Neurochem* **95**:388–395. doi:10.1111/j.1471-4159.2005.03374.x.
- 80 Joseph LC, Barca E, Subramanyam P, Komrowski M, ... Morrow JP. (2016) Inhibition of NADPH Oxidase 2 (NOX2) Prevents Oxidative Stress and Mitochondrial Abnormalities Caused by Saturated Fat in Cardiomyocytes. *PLoS One* **11**:1–17. doi:10.1371/journal.pone.0145750.
- 81 Yu T, Robotham JL, Yoon Y. (2006) Increased production of reactive oxygen species in hyperglycemic conditions requires dynamic change of mitochondrial morphology. *Proc Natl Acad Sci U S A* **103**:2653–2658. doi:10.1073/pnas.0511154103.
- 82 Wu S, Zhou F, Zhang Z, Xing D. (2011) Mitochondrial oxidative stress causes mitochondrial fragmentation via differential modulation of mitochondrial fission-fusion proteins. *FEBS J* **278**:941–954. doi:10.1111/j.1742-4658.2011.08010.x.
- 83 Garcia I, Innis-Whitehouse W, Lopez A, Keniry M, Gilkerson R. (2018) Oxidative insults disrupt OPA1-mediated mitochondrial dynamics in cultured mammalian cells. *Redox Rep* **23**:160–167. doi:10.1080/13510002.2018.1492766.
- 84 Schapira AHV. (2012) Mitochondrial diseases. *Lancet* **379**:1825–1834. doi:10.1016/S0140-6736(11)61305-6.
- 85 Ott M, Herrmann JM. (2010) Co-translational membrane insertion of mitochondrially encoded proteins. *Biochim Biophys Acta* **1803**:767–775. doi:10.1016/j.bbamcr.2009.11.010.
- 86 Xiao L, Xian H, Lee KY, Xiao B, ... Liou Y-C. (2015) Death-associated protein 3 regulates mitochondrially encoded protein synthesis and mitochondrial dynamics. *J Biol Chem* **290**:24961–24974. doi:10.1074/jbc.M115.673343.
- 87 Trachootham D, Alexandre J, Huang P. (2009) Targeting cancer cells by ROS-mediated mechanisms: A radical therapeutic approach? *Nat Rev Drug Discov* **8**:579–591. doi:10.1038/nrd2803.
- 88 Silic-Benussi M, Scattolin G, Cavallari I, Minuzzo S, ... Ciminale V. (2018) Selective killing of human T-ALL cells: an integrated approach targeting redox homeostasis and the OMA1/OPA1 axis. *Cell Death Dis* **9**:822. doi:10.1038/s41419-018-0870-9.
- 89 Nakajima EC, Van Houten B. (2013) Metabolic symbiosis in cancer: Refocusing the Warburg lens. *Mol Carcinog* **52**:329–337. doi:10.1002/mc.21863.

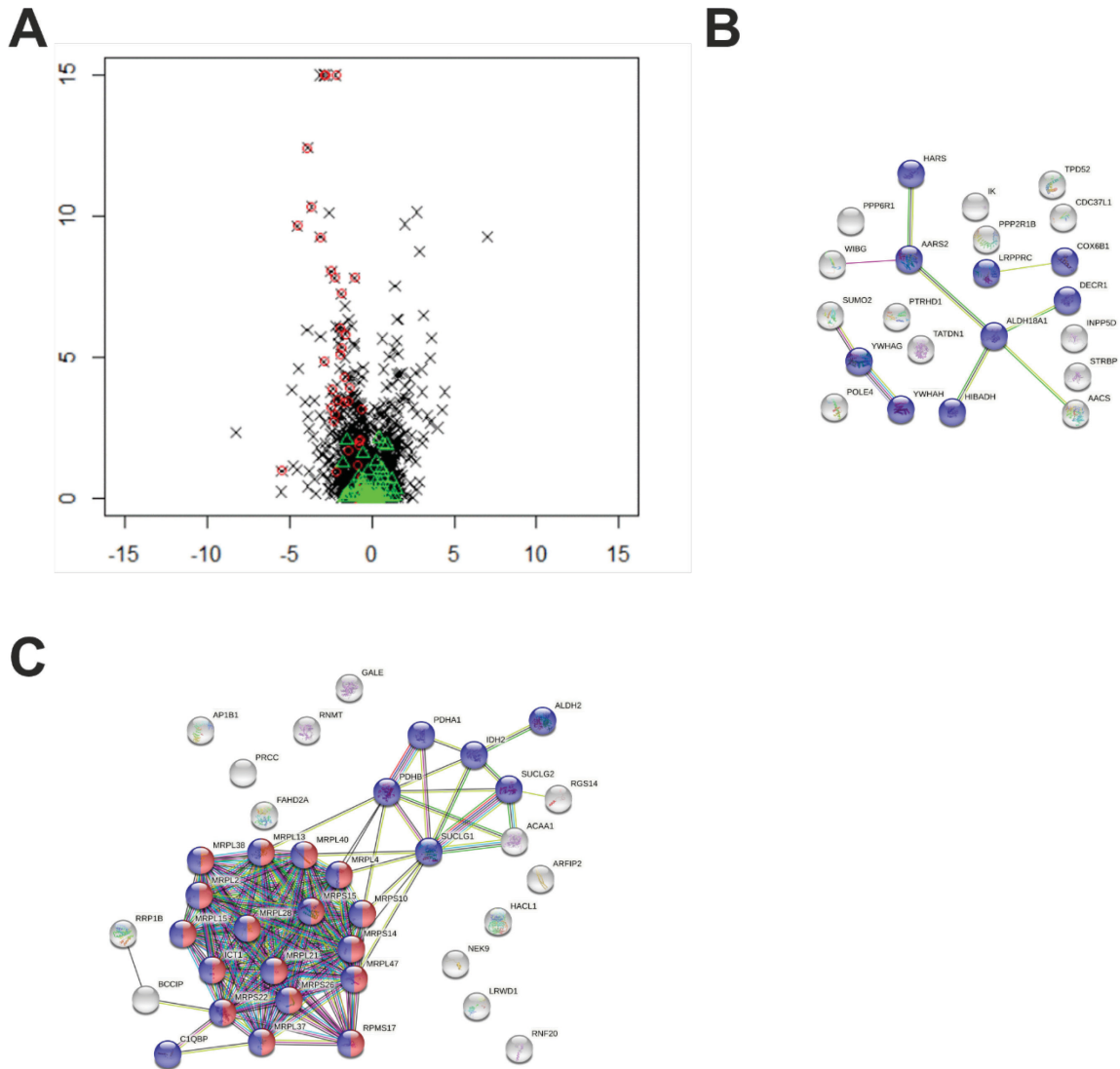
- 90 Demetrius LA, Simon DK. (2012) An inverse-Warburg effect and the origin of Alzheimer's disease. *Biogerontology* **13**:583–594. doi:10.1007/s10522-012-9403-6.
- 91 Panina SB, Baran N, Brasil da Costa FH, Konopleva M, Kirienko N V. (2019) A mechanism for increased sensitivity of acute myeloid leukemia to mitotoxic drugs. *Cell Death Dis* **10**:617. doi:10.1038/s41419-019-1851-3.
- 92 Škrtić M, Sriskanthadevan S, Jhas B, Gebbia M, ... Schimmer AD. (2012) Inhibition of mitochondrial translation as a therapeutic strategy for human acute myeloid leukemia. **20**:674–688. doi:10.1016/j.ccr.2011.10.015.
- 93 Hosseini M-J, Shaki F, Ghazi-Khansari M, Pourahmad J. (2013) Toxicity of Arsenic (III) on Isolated Liver Mitochondria: A New Mechanistic Approach. *Iran J Pharm Res* **12**:121–138. doi:10.22037/ijpr.2013.1279.
- 94 Dong LF, Low P, Dyason JC, Wang XF, ... Neuzil J. (2008) α -Tocopheryl succinate induces apoptosis by targeting ubiquinone-binding sites in mitochondrial respiratory complex II. *Oncogene* **27**:4324–4335. doi:10.1038/onc.2008.69.
- 95 Freitas RA, Silva dos Santos GA, Gimenes Teixeira HL, Scheucher PS, ... Rego EM. (2009) Apoptosis induction by (+) α -tocopheryl succinate in the absence or presence of all-trans retinoic acid and arsenic trioxide in NB4, NB4-R2 and primary APL cells. *Leuk Res* **33**:958–963. doi:10.1016/j.leukres.2008.09.035.
- 96 Yamamoto S, Tamai H, Ishisaka R, Kanno T, ... Utsumi K. (2000) Mechanism of α -tocopheryl succinate-induced apoptosis of promyelocytic leukemia cells. *Free Radic Res* **33**:407–418. doi:10.1080/10715760000300941.
- 97 Dos Santos GAS, Abreu E Lima RS, Pestana CR, Lima ASG, ... Rego EM. (2012) (+) α -Tocopheryl succinate inhibits the mitochondrial respiratory chain complex I and is as effective as arsenic trioxide or ATRA against acute promyelocytic leukemia in vivo. *Leukemia* **26**:451–460. doi:10.1038/leu.2011.216.
- 98 Neuzil J, Tomasetti M, Zhao Y, Dong L-F, ... Ralph SJ. (2007) Vitamin E Analogs, a Novel Group of 'Mitocans,' as Anticancer Agents: The Importance of Being Redox-Silent. *Mol Pharmacol* **71**:1185–1199. doi:10.1124/mol.106.030122.

Supplemental figures:



suppl. Fig. 1. The mode of action of VDT in leukemia and lymphoma cells is independent from tubulin polymerization.

(A) Measurement of the polymerization rate of porcine neuronal tubulin under treatment with either DMSO, vinblastine (VBL, as positive control for tubulin destabilization), paclitaxel (PXL, as positive control for tubulin stabilization) or VDT. Polymerization was started by incubation at 37°C and followed by absorption readings at 340 nm. Absorption at 340 nm is proportional to the concentration of microtubule polymer. (B) Maximum polymerization rates of tubulin calculated based on the data shown in panel A. (C) Soluble (S) and polymerized (P) tubulin from Ramos cells treated with VDT or PXL was separated by centrifugation and detected via immunoblotting. (D) Ramos or Jurkat cells were treated with VDT for 24 h. Subsequently, DNA was stained with propidium iodide and cell cycle distribution was determined via flowcytometry.



suppl. Fig. 2. VDT affects stability of mitoribosomal proteins.

(A) Thermal proteome profiling of Ramos cells treated with either 10 μ M VDT or 0.1% DMSO (v/v) was performed as described in methods. The VDT treated samples were compared to the vehicle controls using the NPARC algorithm resulting in adjusted p-values for each protein. The negative decadic logarithm of this adjusted NPARC p-value, $-\lg(\text{adj. } p, \text{NPARC})$, was plotted against the difference of the means of the melting points, ΔT_m , of the VDT treated samples and the vehicle controls for each protein. Mitoribosomal proteins (red circles) and membrane proteins (green triangles) were marked according to their annotation in the UniProt database. Proteins with $-\lg(\text{adj. } p, \text{NPARC}) > 4$ were regarded as significantly stabilized ($\Delta T_m > 0$: 24 proteins) or destabilized ($\Delta T_m < 0$: 42 proteins) caused by direct or indirect effects of VDT treatment. Shown are protein-protein association networks of the stabilized (B) or destabilized (C) hits using the online string data base. Blue markers indicate proteins of the mitochondrial matrix and red markers indicate proteins of the mitochondrial ribosome according to gene ontology (cellular component).

suppl. Table 1. List of proteins stabilized by VDT as identified by thermal proteome profiling which was performed as described in Methods. Proteins with $-\lg(\text{adj. } p, \text{ NPARC}) > 4$ and $\Delta T_m > 0$ were regarded as significantly stabilized.

Gene	Protein
TATDN1	Putative deoxyribonuclease TATDN1
LRPPRC	Leucine-rich PPR motif-containing protein, mitochondrial
INPP5D	Phosphatidylinositol 3,4,5-trisphosphate 5-phosphatase 1
AACS	Acetoacetyl-CoA synthetase
ALDH18A1	Delta-1-pyrroline-5-carboxylate synthase
STRBP	Spermatid perinuclear RNA-binding protein
PTRHD1	Putative peptidyl-tRNA hydrolase PTRHD1
GRSF1	G-rich sequence factor 1
HYOU1	Hypoxia up-regulated protein 1
YWHAH	14-3-3 protein eta
AARS2	Alanine—tRNA ligase, mitochondrial
IK	Protein Red
PPP6R1	Serine/threonine-protein phosphatase 6 regulatory subunit 1
HARS1	Histidine—tRNA ligase, cytoplasmic
POLE4	DNA polymerase epsilon subunit 4
HIBADH	3-hydroxyisobutyrate dehydrogenase, mitochondrial
YWHAG	14-3-3 protein gamma
CDC37L1	Hsp90 co-chaperone Cdc37-like 1
COX6B1	Cytochrome c oxidase subunit 6B1
DECR1	2,4-dienoyl-CoA reductase [(3E)-enoyl-CoA-producing], mitochondrial
PYM1	Partner of Y14 and mago
TPD52	Tumor protein D52
SUMO2	Small ubiquitin-related modifier 2
PPP2R1B	Serine/threonine-protein phosphatase 2A 65 kDa regulatory subunit A beta isoform

suppl. Table 2. List of proteins destabilized by VDT as identified by thermal proteome profiling which was performed as described in Methods. Proteins with $-\lg(\text{adj. } p, \text{ NPARC}) > 4$ and $\Delta T_m < 0$ were regarded as significantly stabilized.

Gene	Protein
MRPL4	39S ribosomal protein L4, mitochondrial
PDHB	Pyruvate dehydrogenase E1 component subunit beta, mitochondrial
MRPL28	39S ribosomal protein L28, mitochondrial
MRPL13	39S ribosomal protein L13, mitochondrial
MRPL21	39S ribosomal protein L21, mitochondrial
MRPL2	39S ribosomal protein L2, mitochondrial
MRPL58	Peptidyl-tRNA hydrolase ICT1, mitochondrial
MRPL37	39S ribosomal protein L37, mitochondrial
MRPS22	28S ribosomal protein S22, mitochondrial
MRPS26	28S ribosomal protein S26, mitochondrial
MRPS10	28S ribosomal protein S10, mitochondrial
MRPL15	39S ribosomal protein L15, mitochondrial
MRPL38	39S ribosomal protein L38, mitochondrial
RNF20	E3 ubiquitin-protein ligase BRE1A
SUCLG1	Succinate--CoA ligase [ADP/GDP-forming] subunit alpha, mitochondrial
PRCC	Proline-rich protein PRCC
IDH2	Isocitrate dehydrogenase [NADP], mitochondrial
MRPS18B	28S ribosomal protein S18b, mitochondrial
HADH	Hydroxyacyl-coenzyme A dehydrogenase, mitochondrial
HACL1	2-hydroxyacyl-CoA lyase 1
MRPL40	39S ribosomal protein L40, mitochondrial
PDHA1	Pyruvate dehydrogenase E1 component subunit alpha, somatic form, mitochondrial
FAHD2A	Fumarylacetoacetate hydrolase domain-containing protein 2A
OARD1	ADP-ribose glycohydrolase OARD1
ALDH2	Aldehyde dehydrogenase, mitochondrial
BCCIP	BRCA2 and CDKN1A-interacting protein
MRPL47	39S ribosomal protein L47, mitochondrial
MRPS14	28S ribosomal protein S14, mitochondrial
ARFIP2	Arfaptin-2
MRPS15	28S ribosomal protein S15, mitochondrial
AP1B1	AP-1 complex subunit beta-1
RGS14	Regulator of G-protein signaling 14
NEK9	Serine/threonine-protein kinase Nek9
SUCLG2	Succinate--CoA ligase [GDP-forming] subunit beta, mitochondrial
GALE	UDP-glucose 4-epimerase
ACAA1	3-ketoacyl-CoA thiolase, peroxisomal
AP2M1	AP-2 complex subunit mu
MRPS17	28S ribosomal protein S17, mitochondrial
C1QBP	Complement component 1 Q subcomponent-binding protein, mitochondrial
LRWD1	Leucine-rich repeat and WD repeat-containing protein 1
RRP1B	Ribosomal RNA processing protein 1 homolog B
RNMT	mRNA cap guanine-N7 methyltransferase

Supplemental methods:

Measurement of tubulin polymerization velocity

Measurements of tubulin polymerization velocity under treatment with VDT and suitable positive controls were performed using the *OD based Tubulin Polymerization Assay Kit* (Cytoskeleton, Inc., Denver, CO, USA; #BK006P) in porcine mitochondria according to manufacturer's instructions. The kit is based on the observation that polymerization of monomeric tubulin is accompanied by an increase in absorption at 340 nm, which can therefore be used as a measure of the underlying reaction. The velocity of polymerization has been calculated using the formulas provided by the manufacturer. Paclitaxel stabilizes tubulin and therefore increases the polymerization rate, while vinblastine destabilizes tubulin and consequently reduces the polymerization rate.

Detection of *in situ* tubulin polymerization via immunoblotting

In order to trace a possible shift in the ratio between soluble (cytosolic) and polymerized (cytoskeletal) tubulin, as it can be evoked by tubulin poisons, an immunoblot-based method was used, similar to that previously described by Hood et al.¹ Briefly, Ramos cells were treated with the test compounds, harvested by centrifugation (1000 g, 5 min) and subsequently lysed by exposure to an hypotonic lysis buffer [1 mM MgCl₂, 2 mM EGTA, 1% NP40, 2 mM phenylmethylsulfonyl fluoride, 1 µg/ml aprotinin, 2 µg/ml pepstatin, and 20 mM Tris-HCl (pH 6.8)] for 5 min at 37°C. Then the soluble tubulin was separated from the polymerized tubulin by centrifugation (10 min, 18.000 g). After dissolving the resulting pellet in 20 µl sample buffer (8 M urea, 4% 3-[(3-cholamidopropyl)dimethylammonio]-1- propanesulfonic acid, 3 M thiourea, and 40 mM DTT) and adding loading buffer to all samples, SDS-PAGE and immunoblot were performed as described above. Finally, the tubulin content in the two fractions was detected using the aforementioned antibody from Sigma.

Cell cycle analysis via flow cytometry

In order to determine whether VDT-treatment is related to changes in the distribution of cell cycle phases, nuclei of Ramos cells were stained with PI and PI fluorescence was subsequently measured via flow cytometry as described in the section "FACS-based analysis of apoptotic cell death". The classification into the cell cycle phases was then carried out based on the nuclei's PI intensity, which correlates with their DNA content.

Thermal proteome profiling (modified protocol according to Jafari et al., 2014; Reinhard et al., 2015; Franken et al., 2015; Huber et al., 2015)²⁻⁵

Compound treatment:

Ramos cells were expanded as described in "Cell lines and cell culture" to 2.4×10^8 cells (2x T175 cell culture flasks with 90 ml and 1.33×10^6 cells/ml each). VDT was prepared as 5 mM solution in DMSO immediately before usage. The cells were combined in one cell culture flask and gently mixed to generate a homogeneous cell suspension. The cell number and vitality were determined and after gentle mixing to generate a homogeneous cell suspension, the cells were divided into two individual cell culture flasks for compound treatment and vehicle control. 180 μ l 5 mM VDT in DMSO (compound treatment, 10 μ M final VDT concentration) or 180 μ l DMSO (vehicle control) were added and the cell suspensions were gently mixed immediately after addition. After incubation (0.5 h, 37°C, 5% CO₂, in cell culture CO₂ incubator), the cell suspensions were transferred into 50 ml Falcon tubes and the cell number and vitality were determined again. The cells were pelleted by centrifugation (800 rcf, 3 min, r.t.), the supernatants were discarded and the cell pellets were resuspended in 35 ml PBS, respectively, by aspiration and dispensing using 25 ml serological pipettes. The cells were pelleted again by centrifugation (800 rcf, 3 min, r.t.), the supernatants were discarded and the cells were transferred into two pre-weighed 2 ml Eppendorf tubes using 1 ml PBS (r.t.) for resuspending, combining all VDT treated cells in one tube and all vehicle control cells into the other tube. After centrifugation (800 rcf, 3 min, r.t.) and removing as much as possible of the supernatants, the cell wet weights were determined.

Temperature treatment:

The cell pellets were put on ice, resuspended in 2 ml, respectively, of ice-cold PBS supplemented with protease inhibitor cocktail (cOmplete ULTRA EDTA-free Protease Inhibitor Cocktail Tablets, Roche) (PBS+PI) and divided into 100 μ l each in PCR tube strips, so that the samples to be compared (2x with and 2x without VDT treatment) were placed together in one strip (10x strips of 4 PCR tubes: 2x with and 2x without VDT treatment). The suspensions were spun down as briefly as possible in a benchtop PCR tube centrifuge to release trapped air and to achieve an even liquid level without pelleting the cells. The 100 μ l cell suspensions were then temperature treated by a 7 min pre-incubation at r.t., a 3 min incubation at the following different temperatures in the PCR cycler (DNA Engine Tetrad 2, lid temperature 70°C), and a 3 min post-incubation at r.t. in a metal heating block for uniform heat dissipation.

PCR strip	1	2	3	4	5	6	7	8	9	10
Temperature	36.5°C	41.2°C	44.0°C	47.1°C	49.8°C	53.3°C	56.0°C	59.2°C	64.0°C	67.0°C

After the temperature treatment procedure, half of the samples (i.e., 1x with and 1x without VDT treatment for each different temperature) were supplemented with 4.2 µl 10% w/v Nonidet P-40 (NP-40, final 0.4% w/v) for solubilization of membrane proteins, or 4.2 µl water was added to the other half of the samples.³⁵ The samples were shock frozen in liquid nitrogen and stored at -80°C or were further processed directly.

Preparation of cell extracts containing the fraction of soluble, non-denatured proteins:

The cells were lysed by four freeze/thaw cycles consisting of thawing the samples (in a heat block set to 37°C and shaking at 1250 rpm) accompanied by mixing several times by inversion and shock freezing again in liquid nitrogen. Then, the PCR tube strips were cut (including the caps; any excess material cut off) into individual tubes and the closed tubes were transferred into 1.5 ml Eppendorf tubes and pressed down to the bottom (e.g., using a cut-off pipette tip). After centrifugation (20,000 rcf, 30 min, 4°C), the supernatants were transferred into new PCR tube strips (It is important, not to touch the pellet and to leave a bit of the supernatant over the pellet. The PCR tubes remain inside the 1.5 ml Eppendorf tubes and their caps can be removed best with the help of pointed tweezers.). The pellets were discarded and, after determining the protein content (Pierce 660 nm Protein-Assay, Thermo Scientific, BSA as standard), the cell extracts containing the fraction of soluble, non-denatured proteins were shock frozen in liquid nitrogen and stored at -80°C.

The whole above procedure was repeated to obtain two independent biological replicates, resulting in 80 samples in total: 2 (replicates) x 2 (+/- VDT) x 2 (+/- NP-40) x 10 (temperatures).

Normalization and SDS-PAGE:

For each of the eight sample sets (2 replicates, +/- VDT, +/- NP-40) comprising the ten temperature samples, the same volume was used for further analysis. This volume was determined using the three lowest temperature samples per sample set so that they contained an average of 30 µg protein (e.g., 15 µl for all temperature samples of a sample set whose three lowest temperature samples contain an average of 2.0 mg/ml protein). This volume was respectively transferred into 0.5 ml LoBind Eppendorf tubes and evaporated to dryness using vacuum centrifugation (SpeedVac concentrator). The dried proteins were reconstituted in respectively 10 µl of SDS sample buffer containing dithiothreitol (DTT)

(25 mM DTT, 7.5% glycerol, 3% SDS, 37.5 mM Tris/HCl pH 7.0, 0.005% bromophenol blue) and incubated for 30 min at 50°C with shaking (700 rpm). To each sample, 1.111 µl 1 M iodoacetamide (IAA) was added (final 100 mM IAA), mixed (yellow staining) and incubated for 30 min at r.t. in the dark. Sample quality was controlled by SDS-PAGE/silver staining using 0.926 µl of each sample (2.5 µg on average for the three lowest temperature samples; 26-well 4–12% Bis-Tris polyacrylamide gels, Novex NuPAGE, Thermo Scientific; 15 min at 50 V, 1.5 h at 200 V using the recommended MOPS running buffer). For later MS analysis, 4.63 µl per sample (12.5 µg on average for the three lowest temperature samples) were subjected to short SDS-PAGE (30 min at 50 V) using the same SDS-PAGE setup. The remaining halves of the samples (5.555 µl) were stored as backup samples at -80°C. The gels containing the MS samples were incubated for 1 h in fixing solution (40% ethanol, 2% acetic acid), stained for 3 min in CBB staining solution (25 ml 0.1% w/v Brilliant blue G, 0.29 M H₃PO₄, 16% saturated (NH₄)₂SO₄ mixed with 6.25 ml ethanol per gel), decolorized with decolorizing solution (25% ethanol, 5% acetic acid) until the gel background was almost colorless and washed with water until the water remained colorless. The short gel lanes were cut out of the gel on a clean glass plate with a scalpel and transferred, respectively, into 0.5 ml LoBind Eppendorf tubes, which were stored at -80°C.

In-Gel digestion:

In the following, it was ensured that the gel lanes were immersed in the added solutions after each addition. This was achieved, e.g., by means of short centrifugations in a table top centrifuge or by manually flicking against the tubes.

The gel lanes were decolorized and dehydrated by incubating each gel lane twice with 300 µl 40% (v/v) ethanol in 5 mM tetraethylammonium bicarbonate (TEAB) for 45 min at 55°C and, thereafter, twice with 300 µl ethanol (p.a., undenatured) for 5 min at r.t., discarding the supernatant after each incubation. The dehydrated gel lanes were then completely dried using vacuum centrifugation (SpeedVac concentrator) and stored at -80°C. 24 µl 1 µg/µl Trypsin/Lys-C-Mix (Mass Spec Grade, Promega, V5073, reconstituted in the supplied "Resuspension Buffer": 50 mM acetic acid, pH < 3) were mixed with 1176 µl 5 mM TEAB (from 1 M solution, Thermo scientific, 90114, diluted with HPLC-MS grade water) and 14 µl of the resulting 0.02 µg/µl Trypsin/Lys-C-Mix solution was added to each dry gel lane. After at least 15 min incubation at r.t. to completely absorb the solution, each gel lane was completely immersed by addition of 60 µl of 5 mM TEAB, followed by a 3.5 h incubation at 37°C within an incubator. The supernatants of the gel lanes were transferred respectively into new 0.5 ml LoBind Eppendorf tubes and stored at -80°C.

To the gel lanes, 21 μl 0.02 $\mu\text{g}/\mu\text{l}$ Trypsin/Lys-C-Mix (prepared analogously as described above) were added, respectively, followed by an overnight incubation at 37°C within an incubator.

Extraction of the peptides from the gel lanes after digestion:

The supernatants of the gel lanes after overnight digestion were combined with the first supernatants (after 3.5 h digestion) in the corresponding 0.5 ml LoBind Eppendorf tubes. 15 μl 5% formic acid (FA; in HPLC-MS grade water) were added to the gel lanes, respectively. Then, 60 μl 1% FA were added to the gel lanes, followed by an incubation for at least 30 min at r.t. The supernatants of the gel lanes were combined with the corresponding previous supernatants. Addition to the gel lanes, incubation and combining with the corresponding previous supernatants was repeated using again 60 μl 1% FA, then 60 μl 60% acetonitrile (ACN; Secu Solv for HPLC) in 1% FA, and finally 90 μl of ACN (incubation > 15 min instead of >30 min for the last step). The extracted gel lanes were discarded. 40%, respectively, of the collected supernatants containing the extracted peptides were transferred into new LoBind 0.5 ml Eppendorf tubes, shock frozen in liquid nitrogen, and evaporated to dryness using vacuum centrifugation (SpeedVac concentrator). The remaining 60% were stored at -80°C as backup.

TMT labeling:

The dried peptides were reconstituted each in 5 μl 180 mM TEAB in 10% (v/v) ACN (repeatedly vortexed and spun down) and allowed to equilibrate to r.t. The tandem mass tag (TMT) labeling reagents (Tandem Mass Tag 10-plex isobaric label reagent set, Thermo Scientific, #90110, 0.8 mg per tag; at r.t.) were reconstituted in 41 μl ACN (anhydrous HPLC-MS grade) each, and 2 μl each were added to the reconstituted peptides according to the following scheme and homogenized immediately by aspiration and dispensing:

TMT label:	131	130C	130N	129C	129N	128C	128N	127C	127N	126
Treatment temp. /°C:	36.5	41.2	44.0	47.1	49.8	53.3	56.0	59.2	64.0	67.0

After vortexing and spinning down, the samples were incubated for 1 h at r.t. and then quenched by addition of 0.8 μl 5% hydroxylamine each (homogenize immediately after addition) and incubation for more than 15 min at r.t. All samples of a sample set comprising the different TMT labels (e.g., replicate 1 with VDT treatment and NP-40 during cell lysis) were combined in the tube containing the sample with the highest temperature treatment (67°C, TMT label 126). The empty tubes of the respective sample set were rinsed successively from the lowest (36.5°C, TMT label 131) towards higher temperatures (TMT

labels 130C, 130N, 129C, etc.) using 5 μ l 180 mM TEAB in 10% (v/v) ACN, which was finally combined with the respective combined labeling solutions. The combined TMT labeled peptide samples of each sample set were shock frozen in liquid nitrogen, evaporated to dryness using vacuum centrifugation (SpeedVac concentrator), and stored at -80°C.

High pH reversed-phase peptide fractionation:

Offline peptide pre-fractionation was performed using a commercially available kit (Pierce High pH Reversed-Phase Peptide Fractionation Kit, #84868, Thermo scientific) according to the manufacturer's specifications for TMT-labeled peptides. For the 8 sample sets (2 replicates, +/- VDT, +/- NP-40), the elution solutions for Thermo Scientific TMT-labeled peptides were prepared as stated in table 1. The resulting eight fractions (300 μ l each) per sample set were stored at -80°C.

Table 1:

Fraction No.	ACN (%)	ACN (μ l)	0.1% Triethylamine (μ l)
Wash	5	150	2850
1	10	300	2700
2	12.5	375	2625
3	15	450	2550
4	17.5	525	2475
5	20	600	2400
6	22.5	675	2325
7	25	750	2250
8	50	1500	1500

Mass spectrometric (MS) measurement:

28.4 μ l per fraction were evaporated to dryness using vacuum centrifugation (SpeedVac concentrator), reconstituted each in 17 μ l 0.1% trifluoroacetic acid (TFA) and 15 μ l, respectively, of the resulting 64 samples were subjected to MS measurement employing the following setup and conditions.

Peptide separation was performed on a Rapid Separation Liquid Chromatography System (Ultimate 3000, Thermo Fisher). First, peptides were concentrated on a trap column (Acclaim PepMap100, 3 μ m C18 particle size, 100 Å pore size, 75 μ m inner diameter, 2 cm length, Thermo Fisher Scientific, Dreieich, Germany) using a flow rate of 6 μ L/min for 10 min with 0.1% TFA as mobile phase. Then, the peptides were separated on the analytical column (Acclaim PepMapRSLC, 2 μ m C18 particle size, 100 Å pore size, 75 μ m inner diameter, 25 cm length, Thermo Fisher Scientific, Dreieich, Germany) heated to 60°C using a flow rate of 300 nL/min and a 2 h gradient from 4 to 40% solvent B (solvent A: 0.1% (v/v) formic acid in water; solvent B: 0.1% (v/v) formic acid, 84% (v/v) ACN in water).

Peptides were eluted via a nano-source ESI interface equipped with distally coated SilicaTip emitters (New Objective, Woburn, MA, USA) into the online coupled Orbitrap Fusion Lumos Tribrid mass spectrometer (Thermo Fisher Scientific, Dreieich, Germany; Software: Xcalibur 4.3.73.11, SII 1.5, Orbitrap Fusion Lumos 3.3.2782.34) operated in positive mode with a spray voltage of 1400 V, a capillary temperature set to 275°C and advanced peak determination enabled. Precursor mass spectra were recorded in the orbitrap analyzer within a mass range of 375-1500 m/z and a resolution of 120000 (maximum injection time 50 ms, automatic gain control target value 400000, profile mode). For a maximum of three seconds, precursors with charge states +2 to +7 and a minimum intensity of 5000 were isolated with a 0.7 m/z isolation window and fragmented via collisional induced dissociation with a normalized collision energy of 35% and 10 ms activation time ($Q = 0.25$). Precursors chosen for fragmentation were excluded from further isolation for the next 60 s. MS2 spectra were recorded with scan rate 'turbo' (125000 Da/s) in the linear ion trap in centroid mode with a maximal injection time of 50 ms and a target value for the automatic gain control set to 10000. Precursors for MS3 spectra were selected in a mass range of 400-1200 m/z with a 2 m/z isolation window using isobaric tag exclusion filtering with TMT as the reagent tag type as well as synchronous precursor selection (SPS, maximum 10 notches). The precursors were fragmented via higher-energy collisional dissociation with a normalized collision energy of 65% and MS3 spectra were recorded in the orbitrap analyzer within a mass range of 100-500 m/z and a resolution of 50000 (maximum injection time 105 ms, automatic gain control target value 100000, centroid mode). The desired minimum points across the peak were set to six for all MS_n (n=1-3) levels.

Mass spectrometric data analysis, protein identification and quantification:

Mass spectrometric data was processed with MaxQuant version 1.6.6.0 (Max Planck Institute for Biochemistry, Planegg, Germany). If not stated otherwise, standard parameters were used for protein identification and quantification. Searches were carried out based on 74416 Homo sapiens protein entries downloaded from the UniProtKB on 19th June 2019 using tryptic cleavage specificity (behind K and R) and a maximum of three missed cleavage sites. Methionine oxidation and N-terminal acetylation as well as a carbamidomethylation at cysteine residues were considered as variable and fixed modifications, respectively. First, an initial search was carried out using a precursor mass tolerance of 20 ppm and after recalibration, a second search was performed with 4.5 ppm precursor mass tolerance. Tolerances for fragment spectra were 20 ppm. Peptides and proteins were identified with an FDR of

1%. The eight MS raw files corresponding to the eight high-pH fractions of each sample set were defined as fractions (Fraction 1-8) of the respective experiment in the table under the "Raw data" folder in the MaxQuant GUI, resulting in eight experiments (2 biological replicates, +/- Viriditoxin, +/- NP-40) with eight fractions, respectively. The settings "Label-free quantification" and "Match between runs" were explicitly disabled.

The following settings were explicitly enabled:

- Group-specific parameters -> Type -> Type -> Reporter ion MS3 with 10plex TMT and Reporter mass tolerance of 0.003 Da. Correction factors were not used for the single TMT labels, because their effect had been found neglectable in previous tests on published data sets (Pride ID: PXD013774).⁴

- Global parameters -> Protein quantification -> Discard unmodified counterpart peptides and Advanced ratio estimation

- Global parameters -> Tables -> Write ms3Scans table

Protein melting curve analysis:

In total, 4434 proteins (without reverse hits, contaminants and "by site" identifications) were identified in the 8 experiments and quantified by their TMT label intensities. These reporter intensities (10 TMT labels coding for 10 temperature treatment points) gathered in the proteinGroups.txt file by the MaxQuant software were normalized at each of the 10 temperature points (corresponding to the respective TMT label) in each of the 8 experiments towards a fitted intensity at this temperature point (fitting procedure described below) by multiplying the reporter intensity for each protein at the respective temperature point and experiment with the constant ratio (for the respective temperature point and experiment) of the fitted intensity at this temperature point and the median of all valid protein reporter intensity values at this temperature point within this experiment.

The above-described fitted intensity $f(T)$ at each temperature point T was obtained by a least square fit to the mean – over the 8 experiments – of the median reporter intensity values (derived from all valid protein reporter intensities per temperature point and experiment) at this temperature point using the logistic function

$$f(T) = f_{\min} + (f_{\max} - f_{\min}) / \{ 1 + \exp \{ b * [\log_{10}(T) - \log_{10}(T_m)] \} \},$$

with the fitting parameters f_{\min} as the lower limit, f_{\max} as the upper limit, b as a slope parameter, and T_m as a melting point parameter.

The normalized reporter intensities were then used as input for melting curve (TPP-TR) analysis using the TPP analysis package written in the "R" programming language⁶. The four VDT treated samples were compared to the four vehicle controls using the NPARC algorithm⁷ within the TPP software package resulting in adjusted p-values for each protein. The negative decadic logarithm of this adjusted NPARC p-value, $-\lg(\text{adj. } p, \text{NPARC})$, was plotted against the difference of the means of the melting points, ΔT_m , of the VDT treated samples and the vehicle controls for each protein. Proteins with an incomplete set of valid melting point values were omitted from the analysis resulting in a set of 2688 proteins comprising a complete set of valid melting point values. Four proteins (uniprot identifiers K7ES61, P11177, Q13084, Q9BYD1) with a zero value software output for their adjusted NPARC p-values were manually assigned with an arbitrary reasonable value of $-\lg(\text{adj. } p, \text{NPARC}) = 15$ (the lowest non-zero adjusted NPARC p-value was 3.9×10^{-13} , i.e., $-\lg(\text{adj. } p, \text{NPARC}) = 12.4$, in this analysis) after checking the correctness of data and melting curves. Mitochondrial proteins (red circles) and membrane proteins (green triangles) were marked according to their annotation in the UniProt database.

Proteins with $-\lg(\text{adj. } p, \text{NPARC}) > 4$ were regarded as significantly stabilized ($\Delta T_m > 0$: 24 proteins) or destabilized ($\Delta T_m < 0$: 42 proteins) caused by direct or indirect effects of VDT treatment and were further analyzed for protein-protein association networks using the online string data base.⁸

Of the 66 significantly affected proteins (stabilized or destabilized), 60 could be mapped to entries in the string data base, of which 33 were mitochondrial proteins, of which 27 were part of the mitochondrial matrix, of which 17 were part of the mitochondrial ribosome according to gene ontology (cellular component).

Of the 42 significantly destabilized proteins (caused by VDT treatment), 38 could be mapped to entries in the string data base, of which 24 were part of the mitochondrial matrix, of which 17 were part of the mitochondrial ribosome according to gene ontology (cellular component).

Of the 24 significantly stabilized proteins (caused by VDT treatment), 22 could be mapped to entries in the string data base, of which 9 were mitochondrial proteins according to gene ontology (cellular component).

Supplemental References

1. Hood, K. A. *et al.* Peloruside A, a Novel Antimitotic Agent with Paclitaxel-like Microtubule-stabilizing Activity. *Cancer Res.* **62**, 3356–3360 (2002).
2. Jafari, R. *et al.* The cellular thermal shift assay for evaluating drug target interactions in cells. *Nat. Protoc.* **9**, 2100–2122 (2014).
3. Reinhard, F. B. M. *et al.* Thermal proteome profiling monitors ligand interactions with cellular membrane proteins. *Nat. Methods* **12**, 1129–1131 (2015).
4. Franken, H. *et al.* Thermal proteome profiling for unbiased identification of direct and indirect drug targets using multiplexed quantitative mass spectrometry. **10**, 1567–1593 (2015).
5. Huber, K. V. M. *et al.* Proteome-wide drug and metabolite interaction mapping by thermal-stability profiling. *Nat. Methods* **12**, 1055–1057 (2015).
6. Childs, D. *et al.* TPP: Analyze thermal proteome profiling (TPP) experiments, R package version 3.18.0. (2020).
7. Childs, D. *et al.* Nonparametric analysis of thermal proteome profiles reveals novel drug-binding proteins. *Mol. Cell. Proteomics* **18**, 2506–2515 (2019).
8. Szklarczyk, D. *et al.* STRING v11: Protein-protein association networks with increased coverage, supporting functional discovery in genome-wide experimental datasets. *Nucleic Acids Res.* **47**, D607–D613 (2019).

Eidesstattliche Erklärung

Ich versichere an Eides Statt, dass die Dissertation von mir selbständig und ohne unzulässige fremde Hilfe unter Beachtung der „Grundsätze zur Sicherung guter wissenschaftlicher Praxis an der Heinrich-Heine-Universität Düsseldorf“ erstellt worden ist. Zudem versichere ich, dass ich die vorliegende Dissertation nur in diesem und keinem anderen Promotionsverfahren eingereicht habe und diesem kein früheres Promotionsverfahren vorausgegangen ist.

Ort, Datum

Fabian Stuhldreier